Topics in Applied Physics
Volume 109

Available online at
SpringerLink.com

Topics in Applied Physics

Topics in Applied Physics is a well-established series of review books, each of which presents a comprehensive survey of a selected topic within the broad area of applied physics. Edited and written by leading research scientists in the field concerned, each volume contains review contributions covering the various aspects of the topic. Together these provide an overview of the state of the art in the respective field, extending from an introduction to the subject right up to the frontiers of contemporary research.

Topics in Applied Physics is addressed to all scientists at universities and in industry who wish to obtain an overview and to keep abreast of advances in applied physics. The series also provides easy but comprehensive access to the fields for newcomers starting research.

Molecular Building Blocks for Nanotechnology

From Diamondoids to Nanoscale Materials and Applications

Edited by

G. Ali Mansoori
University of Illinois at Chicago

Thomas F. George
University of Missouri–St. Louis

Lahsen Assoufid
Argonne National Laboratory

Guoping Zhang
Indiana State University

Springer

G. Ali Mansoori
University of Illinois at Chicago
Chicago, IL 60607
USA
mansoori@uic.edu

Thomas F. George
University of Missouri–St. Louis
St. Louis, MO 63121
USA
tfgeorge@umsl.edu

Lahsen Assoufid
Argonne National Lab
Argonne, IL 60439
USA
assoufid@aps.anl.gov

Guoping Zhang
Indiana State University
Terre Haute, IN 47809
USA
gpzhang@indstate.edu

Preface

Molecular Building Blocks for Nanotechnology: From Diamondoids to Nanoscale Materials and Applications is a result of the research and educational activities of a group of outstanding scientists worldwide who have authored the chapters of this book dealing with the behavior of nanoscale building blocks. It contains a variety of subjects covering computational, dry and wet nanotechnology. The state-of-the-art subject matters are presented in this book which can provide the reader with the latest developments on the ongoing bottom-up nanoscience and nanotechnology research.

The editors would like to thank all the chapter authors whose scholarly contributions have made publication of this book possible. We would like to thank Springer for agreeing to publish this book as part of its *Topics in Applied Physics Series*. We also acknowledge the support of the U.S. Army Research Office under contract W911NF-04-1-0383.

<div align="right">

G. Ali Mansoori
Thomas F. George
Guoping Zhang
Lahsen Assoufid
2007

</div>

Contents

List of Contributors

Pulickel M. Ajayan
Rensselaer Nanotechnology Center
  and Department of Materials Science
  and Engineering
Rensselaer Polytechnic Institute
Troy, NY, USA.

R. L. Axelbaum
Department of Mechanical
  Engineering
Center for Materials Innovation
Washington University in St. Louis
St. Louis, MO, USA.

P. Biswas
Environmental Engineering Science
  Program
Department of Chemical Engineering
Center for Materials Innovation
Washington University in St. Louis
St. Louis, MO, USA.

V. D. Blank
Technological Institute for Superhard
  and Novel Carbon Materials
Troitsk, Moscow Region, Russia.

S. G. Buga
Technological Institute for Superhard
  and Novel Carbon Materials
Troitsk, Moscow Region, Russia.

Soo Jin Chua
Department of Electrical and Computer
  Engineering
National University of Singapore
Singapore.

S. I. Chukhaeva
Russian Federal Nuclear Center
Zababakhin All-Russian Research
  Institute of Technical Physics
Snezhinsk, Chelyabinsk Region,
  Russia.

Aron W. Cummings
Department of Electrical Engineering
Arizona State University
Tempe, AZ, USA.

P. Ya. Detkov
Russian Federal Nuclear Center –
  Zababakhin
All-Russian Research Institute of
  Technical Physics
Snezhinsk, Chelyabinsk Region,
  Russia.

G. A. Dubitsky
Technological Institute for Superhard
  and Novel Carbon Materials
Troitsk, Moscow Region, Russia.

P. Fraundorf
Department of Physics & Astronomy
Center for Molecular Electronics
University of Missouri-St. Louis
St. Louis, MO, USA.

V. K. Ganesh
Faculty of Dentistry
National University of Singapore
Singapore.

Hota Garudadhwaj
Department of Mechanical Engineering
National University of Singapore
Singapore.

Thomas F. George
Office of the Chancellor and Center
  for Molecular Electronics
Departments of Chemistry &
  Biochemistry and Physics &
  Astronomy
University of Missouri-St. Louis
St. Louis, MO, USA.

K. V. Gogolinsky
Technological Institute for Superhard
  and Novel Carbon Materials
Troitsk, Moscow Region, Russia.

Renuga Gopal
Nanoscience and Nanotechnology
  Initiative
National University of Singapore
Singapore.

Satinderpal Kaur
Nanoscience and Nanotechnology
  Initiative
National University of Singapore
Singapore.

V. G. Kulichikhin
Topchiev Institute of Petrochemical
  Synthesis

Russian Academy of Sciences
Moscow, Russia.

Neeta L. Lala
Nanoscience and Nanotechnology
  Initiative
National University of Singapore
Singapore.

Kian Ping Loh
Department of Chemistry, National
  University of Singapore
Singapore.

G. Ali Mansoori
Departments of Bio & Chemical
  Engineering
University of Illinois at Chicago
Chicago, IL, USA.

R. Murugan
National University of Singapore
Singapore.

Mohamed. A. Osman
School of Electrical Engineering and
  Computer Science
Washington State University
Pullman, WA, USA.

Fabio Pichierri
COE Laboratory
Tohoku University
Sendai, Japan.

V. A. Popov
Moscow Institute of Steel and Alloys
Moscow, Russia.

V. M. Prokhorov
Technological Institute for Superhard
  and Novel Carbon Materials
Troitsk, Moscow, Russia.

Seeram Ramakrishna
Department of Mechanical Engineering
Nanoscience and Nanotechnology
    Initiative
National University of Singapore
Singapore.

Ramakrishnan Ramaseshan
Nanoscience and Nanotechnology
    Initiative
National University of Singapore
Singapore.

Hamid Ramezani
Departments of Pharmacy
Mashhad University of Medical
    Sciences
Mashhad, Khorasan, Iran.

N. R. Serebryanaya
Technological Institute for
    Superhard and Novel Carbon
    Materials
Troitsk, Moscow, Russia.

Z. X. Shen
Division of Physics and Applied
    Physics
School of Physical and Mathematical
    Sciences
Nanyang Technological University
Singapore.

Deepak Srivastava
NASA Ames Center for
    Nanotechnology and UARC/UCSC
Moffett Field, CA, USA.

K. L. Teo
Information Storage Materials
    Laboratory
Department of Electrical and Computer
    Engineering

National University of Singapore
Singapore.

C. J. Unrau
Department of Mechanical Engineering
    and Center for Materials
    Innovation
Washington University in St. Louis
St. Louis, MO, USA.

Robert Vajtai
Rensselaer Nanotechnology Center
Rensselaer Polytechnic Institute
Troy, NY, USA.

G. R. Vakili-Nezhaad
Department of Chemical Engineering
University of Kashan
Kashan, Iran.

Feng Wang
Division of Bioengineering
Faculty of Engineering
National University of Singapore
Singapore.

Xue-Sen Wang
Department of Physics
National University of Singapore
Singapore.

Binqing Wei
Department of Electrical and Computer
    Engineering
Center for Applied Information
    Technology and Learning
Louisiana State University
Baton Rouge, LA, USA.

G. P. Zhang
Department of Physics
Indiana State University
Terre Haute, IN, USA.

Yong Zhang
Division of Bioengineering
Faculty of Engineering and
  Nanoscience and Nanotechnology
  Initiative
National University of Singapore
Singapore.

Ma Zuwei
Nanoscience and Nanotechnology
  Initiative
National University of Singapore
Singapore.

Introduction

Two different methods are envisioned to build nanostructured systems, components and materials: One method is the "top-down" approach, and the other is the "bottom-up" approach [1,2]. In the top-down approach, the idea is to miniaturize macroscopic structures, components and systems towards a nanoscale size. In the bottom-up approach, the atoms and molecules constituting the building blocks are the starting point to build the desired nanostructure.

In the top-down approach, a macrosized material is reduced in size to reach nanoscale dimensions. Photolithography used in the semiconductor industry is one example of the top-down approach. In the bottom-up strategy, we need to start with molecular building blocks (MBBs) and assemble them to build a nanostructured material. The emphasis of this book is on the bottom-up approach.

The most fundamentally-important aspect of the bottom-up approach is that the nanoscale building blocks, because of their sizes of a few nanometers, impart to the nanostructures created from them new and possibly preferred properties and characteristics heretofore unavailable in conventional materials and devices. For example, metals and ceramics produced by consolidating nanoparticles with controlled nanostructures are shown to possess properties substantially different from materials with coarse microstructures. Such differences in properties include greater hardness, higher yield strength and ductility in ceramic materials. The band gap of nanometer-scale semiconductor structures increases as the size of the microstructure decreases, raising expectations for many possible optical and photonic applications. Considering that nanoparticles have much higher specific surface areas, in their assembled forms there are large areas of interfaces. One needs to know in detail not only the structures of these interfaces, but also their local chemistries and the effects of segregation and interaction among MBBs, and also between MBBs and their surroundings. Nanostructure sizes, size distributions, compositions and assemblies are key aspects of nanoscience and nanotechnology, and it is important to understand these aspects as well as possible.

Nanotechnology MBBs are distinguished for their unique properties. They include, for example, graphite, fullerene, carbon nanotubes, diamondoids, nanowires, nanocrystals and amino acids. All these MBBs, and more, are candidates for various applications in nanotechnology. These building blocks have

quite unique properties not found in small molecules. Some of these MBBs are electrical conductors, some are semiconductors, some are photonic, and the characteristic dimension of each is a few nanometers. For example, carbon nanotubes are about five times lighter and five times stronger than steel. Many nanocrystals are photonic, and they guide light through air since their spacing of the crystal pattern is much smaller than the wavelength of light being controlled. Nanowires can be made of metals, semiconductors, or even different types of semiconductors within a single wire. They are upwards of ten nanometers and can be made into a conductor or semiconductor. Amino acids and DNA, the basis for life, can also be used to build nanomachines. Adamantane (a diamondoid) is a tetrahedrally-symmetric stiff hydrocarbon that provides an excellent building block for positional (or robotic) assembly as well as for self-assembly. In fact, over 20,000 variants of adamantane have been identified and synthesized, and even more are possible [2], providing a rich and well-studied set of MBBs.

The applications of MBBs would enable the practitioner of nanotechnology to design and build systems on a nanometer scale. The controlled synthesis of MBBs and their subsequent assembly (self-assembly, self-replication or positional-assembly) into nanostructures is a fundamental theme of nanotechnology. These promising nanotechnology concepts with far-reaching implications (from mechanical to chemical processes; from electronic components to ultra-sensitive sensors; from medical applications to energy systems; and from pharmaceuticals to agricultural and food chains) will impact every aspect of our future. This book consists of sixteen chapters written by authorities from all around the world on MBBs and their applications in bottom-up nanotechnology.

In Chapter 1, the thermodynamic properties of diamondoids are reported by by G. R. Vakili-Nezhaad. In this chapter, the author focuses on two main subjects. First, thermodynamic properties of pure diamondoids (adamantane and diamantane), and second, solubilities of diamondoids and phase behavior of the binary systems consisting of diamondoids and other hydrocarbons are presented in detail.

In Chapter 2, the development of composite materials based on improved nanodiamonds is reported by P. Ya. Detkov, V. A. Popov, V. G. Kulichikhin and S. I. Chukhaeva. The authors describe methods for improving the quality of diamond nanopowders obtained by detonation synthesis, as well as some commercial applications of nanodiamonds. The authors prove that the synthetic detonation diamond is a promising material that can be used in many fields. Of special interest are its applications in compos ite materials both with a metal and polymer matrix. Commercial production of ultradisperse diamonds (or nanodiamonds) has been developed, and it is synthesized on a scale sufficient for particular industries.

In Chapter 3, the use of diamondoids as MBBs is reported by H. Ramezani and G. A. Mansoori. In this chapter, the authors present at first a general discussion about molecular building blocks for nanotechnology. Then, the remaining major part of the chapter is devoted to diamondoid molecules and their role as MBBs. The authors conclude that diamondoids are one of the best candidates for molecular building blocks in molecular nanotechnology to design nanostructures with predetermined physicochemical properties.

In Chapter 4, surface modification and applications of functionalized polymer nanofibers are reported by R. Gopal, M. Zuwei, S. Kaur and S. Ramakrishna. Electrospun polymer nanofibers are receiving extensive research interest for applications in such diverse fields as separation technology and biotechnology. The authors review the current trend to develop sub-micron scale fibers and nanofibes to tap a number of favorable properties, such as an increase in surface area to volume ratio, decrease in pore size, drop in structural defects and superior mechanical characteristics. They argue that the potential target areas of application for these nanofibrous structures are as affinity membranes, scaffolds for tissue engineering, sensors and protective clothing, to name a few.

In Chapter 5, zinc oxide nanorod array properties and hydrothermal synthesis are presented by K. P. Loh and S. J. Chua. The authors report their synthesis results of hexagonally-packed zinc oxide nanorod bundles on hydrotalcite (HTlc) sheets by reacting zinc acetate with aluminum-coated silicon in alkali hydrothermal conditions. They indicate that HTlc sheets are a unique product of the alkali hydrothermal environments, and cannot be readily produced by dry chemical vapor deposition methods. They conclude that controlling the thickness of the Al film is key to obtaining a range of secondary structures, ranging from self-assembled ZnO nanorod bundles on HTlc sheets, which precipitate randomly on the silicon substrate, to well-aligned ZnO nanorods growing on silicon substrates.

In Chapter 6, nanoparticles, nanorods and other nanostructures assembled on inert substrates are reported by X.-S. Wang. The author demonstrates that the geometric and surface properties of nanostructures can deviate significantly from those of bulk crystals and are sensitively size-dependent. Consequently, these properties affect the interactions of nanostructures with the substrates and with each other, as well as the texture of films derived from these nanoparticles. A few examples of selective nanostructural self-assembly are shown, and it is demonstrated that: (i) the selectivity can be expanded based on the experiments over broader ranges of growth conditions (e.g., flux, substrate temperature, type of surfactant); (ii) the details of nanoparticle migration, rotation and coarsening can be captured at a reduced substrate temperature; and (iii) self-assembly and morphology of nearly free-standing compound nanostructures can be explored on inert substrates. Such explorations are beneficial to the integration of nanostructure-based electronic, optoelectronic and spintronic devices with Si-based integrated circuits.

In Chapter 7, the thermal properties of carbon nanotubes are discussed by M. Osman, A. Srivastava and D. Srivastava. The authors first present the physical structure of nanotubes and their electrical properties. Then, theoretical analytical approaches to thermal conductivity and specific heat calculations are introduced. This is followed by a review of the recent experimental measurement of thermal conductivity of single-wall nanotubes (SWNTs) and multiwall nanotubes. They also present a molecular dynamical simulation approach and its application to the investigation of thermal conductivity of SWNTs, Y-junction nanotubes and heat pulse propagation in SWNTs.

In Chapter 8, chemical vapor deposition of organized architectures of carbon nanotubes for applications is discussed by R. Vajtai, B. Wei, T. F. George and

P. M. Ajayan. In the first part of this chapter, the authors summarize the short history and achievements of the last several years regarding carbon nanotube growth. They also demonstrate their state-of-the-art methods of tailored nanotube growth and their efforts to prepare nanotube structures capable of fulfilling the high expectations for these new and highly-advanced materials. They then address applications of carbon nanotubes. Devices based on electron-field emission, low-voltage gas breakdown, filtering on the micro, nano and even molecular scale, and equipment based on the enhanced properties of different composite materials consisting of nanotubes are explored.

In Chapter 9, the online size characterization of nanofibers and nanotubes is discussed by C. J. Unrau, R. L. Axelbaum, P. Biswas and P. Fraundorf. First, a review of this subject is introduced and a method for online size characterization of carbon nanotubes developed by the authors is presented. This method employs a differential mobility analyzer, which classifies particles by their electrical mobility. It is concluded that: (i) the presented method of online size characterization allows for faster optimization of gas-phase carbon nanotube production; (ii) it could be valuable for online air quality measurements related to nanofibers and nanotubes; and (iii) by identifying functional relationships between length and width, microscopy can make it possible for the online techniques described here to infer the size distribution of both.

In Chapter 10, theoretical investigations in retinal and cubane are presented by G. Zhang and T. F. George. The authors use the first-principles method to investigate the reaction path of isomerization of retinal segments and explain why the isomerization is so efficient in rhodopsin. They find that the dipole transition moment has an important effect on the reaction path. They compute the potential energy surface for cubane as a function of C-C and C-H bond lengths and find that those realistic ab initio potentials can not always be fitted to a general potential.

In Chapter 11, the polyhedral heteroborane clusters for nanotechnology applications is presented by F. Pichierri. Polyhedral heterocarborane clusters are promising materials for nanotechnology. This is evident from the interesting applications discussed in this chapter, which include molecular nanoparticles, nanomedicines, molecular-scale machines and devices. The author provides an overview of the potential applications of polyhedral heteroborane clusters to nanotechnology. These include the synthesis of molecular nanoparticles with controlled dimensions, nanomedicines for use in boron-neutron capture therapy, molecular-scale machines and devices, and nanostructured materials. Finally, a general strategy for the computational design of functional molecular materials that makes use of both structural and synthetic chemistry information is discussed.

In Chapter 12, properties of germanium nanostructures are reported by K. L. Teo and Z. X. Shen. The authors report on high-pressure Raman studies on germanium nanostructures using diamond anvil cells. They demonstrate that it is possible to obtain strain information on quantum dots and nanocrystals. They also show that their electronic and vibrational properties are indeed different from bulk samples. The results reported in this chapter should help provide a general understanding of the elastic properties of different multi-component nanosystems.

In Chapter 13, nanoengineered biomimetic bone-building blocks are discussed by R. Murugan and S. Ramakrishna. The authors suggest that bone is a paradigm for a dynamic tissue since it has a unique capability of self-regenerating or self-remodeling throughout the life span without leaving a scar. However, many circumstances call for a bone grafting owing to bone defects arising either from traumatic or non-traumatic destructions. The authors suggest that: (i) a combination of osteoconductive matrix with osteogenic cells and osteoinductive growth factors creates an ideal bone graft; (ii) the biomimetic approach is a good choice and, perhaps, one of the promising methods for making such bone grafts with enhanced functions, mimicking a real bone that may even alleviate the demerits of the currently available bone grafting procedures, including donor site morbidity of autogenic bone and possible disease transformation of allogenic bone; and (iii) biomimetic design of bone grafts is, however, still at the laboratory research level, and the development of such grafts for all length scales is in fact a critical task for biomaterialists. The authors conclude that with the advances of nanotechnology and tissue engineering, there is a bright chance in the near future to formulate biomimetic nanocomposite bone grafts in place of autogenic bone grafts.

In Chapter 14, the use of nanoparticles as building blocks for bio-applications is presented by Y. Zhang and F. Wang. In this chapter, the authors review the current and envisioned uses of nanoparticles as building blocks for for bio-applications. They argue that: (i) the sizes of the nanoparticles are close to those of biomolecules, which allows an integration of nanotechnology and biotechnology, leading to major advances in multiplexed bioassays, clinical therapies, ultra-sensitive biodetection and bioimaging; (ii) nanoparticles can be used as building blocks for the fabrication of micro/nanoscale structures with highly-ordered architectures; (iii) increasing interest has been attracted to build close-packed solids of nanoparticles, control their microstructure, and engineer their properties on a nanometer scale. The authors also review the strategies available for the ordering of nanoparticles into structured assemblies, and construction of large and complex systems including shape-directed assembly and programmed assembly of nanoparticles comprising surface-attached molecules, ligands and recognition sites, the formation of complex hybrid nanostructures by *in situ* transformation of unstable nanoparticle-based precursors, and template-directed assembly using nanoparticle building blocks. The authors conclude that these materials can bring new and unique capabilities to a variety of biomedical applications ranging from diagnostics to therapies.

In Chapter 15, the applications of polymer nanofibers for biosensors is presented by S. Ramakrishna, N. L. Lala, H. Garudadhway, R. Ramaseshan and V. K. Ganesh. This chapter gives a brief description of biosensors and their existing limitations. Much emphasis is focused on the replacement of the sensing interface with polymer nanofibers, and improvements in the sensor's performance have been highlighted. The various applications where nanofiber-based biosensors could possibly fit are also described. It is concluded that polymer nanofibers have great potential for sensor applications, and further research is needed in this area.

In Chapter 16, the high-pressure synthesis of carbon nanostructured superhard materials is presented by V. D. Blank, S. G. Buga, G. A. Dubitsky, K. V. Gogolinsky,

V. M. Prokhorov, N. R. Serebryanaya and V. A. Popov. The authors of this chapter believe that a high-pressure/high-temperature/large deformation treatment is an effective tool for the development of unique new structures of solids (named 3D-polymerized fullerites), unknown earlier in nature and possessing novel physical and chemical properties. A distinctive feature of these new structures is the extremely-high values of hardness and the bulk module of elasticity—close to corresponding values for diamond and exceeding them. At the same time, the value of the shear modulus and Joung's modulus are lower that the values for diamond. The authors believe that 3D-polymerized fullerites represent a new class of superhard materials which can find wide areas of applications as various functional materials and also as components of various composite, construction and tool materials.

References

[1] R. W. Siegel, E. Hu, and M.C. Roco, Editors, *Nanostructure Scence and Technology— A Worldwide Study. Prepared under the guidance of the IWGN, NSTC* (WTEC, Loyola College, Maryland, 1999).
[2] G. A. Mansoori, *Principles of Nanotechnology: Molecular Based Study of Condensed Matter in Small Systems* (World Scientific, New York, 2005).

1
Thermodynamic Properties
of Diamondoids

G. R. Vakili-Nezhaad

1.1. Introduction

Diamondoid hydrocarbons are ringed compounds that have a diamondlike structure consisting of a number of six-member carbon rings fused together [1,2]. They have high melting points and low strain energy, which highlights their relative stability [1,3]. The first diamondoid isolated from petroleum, adamantane, was later synthesized and this molecule and its derivatives show a number of unusual chemical and physical properties [1,3]. Adamantane derivatives have shown promise in pharmaceutical applications [1,4], and have been used as templates for crystallization of zeolite catalysts [1,5], and the synthesis of high-temperature polymers [6], so interest in this molecule and higher diamondoids has both pure and applied roots. Recently, interest in higher diamondoids has been renewed by molecular simulation studies suggesting possible applications in nanotechnology [1,7–9], and use as seed crystals in CVD diamond production [10]. Besides the attractions of diamondoids due to their applications to nanotechnology, these organic nanostructures cause severe problems in oil and gas production. Therefore for reducing the problems due to the precipitation of diamondoids in the petroleum production process of knowledge of the phase behavior of these components with hydrocarbons is important.

Considering the above, in this chapter we focus on the following main subjects. First, thermodynamic properties of pure diamondoids (adamantane and diamantane) are considered. Second, solubilities of diamondoids and phase behavior of the binary systems are given in detail.

1.2. Pure Component Thermodynamic Properties

In this section thermodynamic properties of light diamondoids such as adamantane and diamantane are presented.

Based on the temperature-dependence of the heat capacity of adamantane in the condensed state between 5 and 600 K taken from the results of measurements [11,12] presented this dependency as shown in Figure 1.1. The smoothed values of
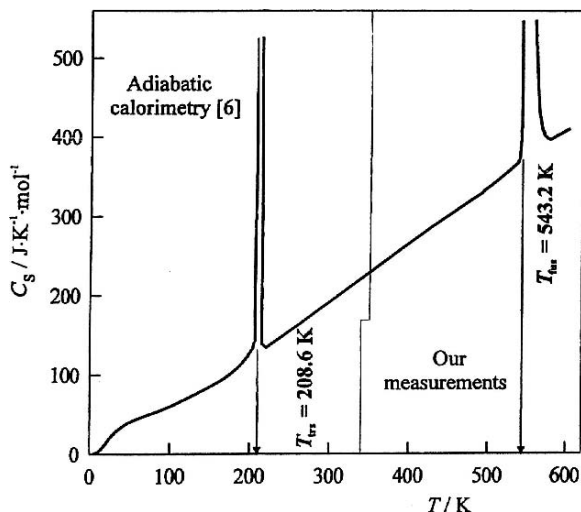
7

FIGURE 1.1. The temperature dependence of the heat capacity in the condensed state for adamantane.

the molar heat capacity and the standard thermodynamic functions of adamantane in the interval from 340 to 600 are listed in Table 1.1. Thermodynamic quantities associated with the phase transitions of the compound are given in Table 1.2. The enthalpy of sublimation of adamantane was determined in a series of calorimetric experiments which can be seen in Table 1.3 [12]. Also the experimental saturated vapor pressures over crystal adamantane are given in Table 1.4 [12].

TABLE 1.1 Molar thermodynamic functions for adamantane.

	T (K)	$C_{s,m}/R$	$\Delta S_m/R$	$\Delta H_m/RT$	Φ_m/R
Crystal I					
	340	26.26	26.64	13.66	12.98
	360	28.41	28.21	14.42	13.78
	380	30.27	29.79	15.21	14.58
	400	31.98	31.39	16.01	15.38
	420	33.61	32.99	16.81	16.18
	440	35.24	34.59	17.61	16.98
	460	36.91	36.19	18.41	17.78
	480	38.65	37.80	19.22	18.59
	500	40.46	39.42	20.03	19.39
	520	42.32	41.04	20.85	20.19
	540	44.18	42.67	21.68	20.99
	543.2	44.48	42.93	21.81	21.12
Liquid					
	543.2	44.48	46.02	24.81	21.21
	560	45.99	47.40	25.42	21.98
	580	47.65	49.04	26.16	22.88
	600	49.05	50.68	26.90	23.78

TABLE 1.2 Temperatures, the molar enthalpies, and entropies of phase transitions of adamantane.

Transition	T_{trans}(K)	ΔH_m(Jmol^{-1})	ΔS_m(JK^{-1}mol^{-1})	Reference
CrII→CrI	208.60	3376	16.19	Kabo et al., 1998
CrI→I	543.20	13958 ± 279	25.7 ± 0.5	Kabo et al., 2000

The entropy of crystal adamantane from the low-temperature measurements based on the work of Chang and Westrum (1960) is ΔS_m (cr I; 303.54 K) = (199.27 ± 0.40) JK^{-1} mol^{-1}. Thermodynamic parameters of sublimation Δ_{crI} H$_m$(303.54 K) = (58.52 ± 0.15) kJ mol^{-1} and Δ_{crI}S$_m$(303.54 K) = (192.79 ± 0.49) JK^{-1}mol^{-1} were calculated on the basis of results given in Table 1.3 and the mean value Δ_{crI}C$_p$ = −44.35 JK^{-1} mol^{-1}. The experimental standard entropy of adamantane in the gas state S$_m$(g; 303.54 K) = (324.62 ± 0.76) JK^{-1} mol^{-1} was obtained using the value of P$_{sat}$ = (30.4 ± 1.5) Pa (Table 1.4).

The entropy of gaseous adamantane at T = 303.54 K, S$_m$(g) = (324.83 ± 1.62) JK^{-1}mol^{-1} determined from the above-mentioned data is in very good agreement with the experimental value [12]. Thermodynamic functions of adamantane in the ideal gas state between 100 and 1000 K are given in Table 1.5 [12].

TABLE 1.3 The results of calorimetric of the enthalpy of sublimation for adamantane.[a]

No.	m (g)	T (K)	$\int \Delta V d\tau$ (mVs)	Type of Cell	ΔH (J)	ΔH_m (kJ mol^{-1})
1	0.05016	306.14	4790.37	A	20.50	58.40
2	0.06792	305.86	6498.38	A	29.17	58.51
3	0.07126	306.52	6854.55	A	30.77	58.82
4	0.07615	309.06	7211.37	A	32.37	57.91
5	0.09246	309.14	8852.84	A	39.74	58.55
6	0.07291	309.47	6953.20	A	31.21	58.32
7	0.06815	308.11	6494.41	A	29.15	58.28
8	0.11800	308.40	11278.84	A	50.63	58.45
9	0.06363	309.04	5702.89	B	26.95	57.70
10	0.08484	309.09	7659.34	B	36.19	58.12
11	0.07283	309.37	6611.68	B	31.24	58.45
12	0.10855	308.51	9819.18	B	46.40	58.24
13	0.04533	306.08	4104.92	B	18.52	58.29
14	0.07410	305.81	6703.16	B	30.25	58.24
15	0.05741	306.50	5226.57	B	23.58	58.61

[a] The calorimetrically measured enthalpy change ΔH and molar enthalpies ΔH$_m$ were calculated from expressions: $\Delta H = K^{-1} \int_{\tau=0}^{\tau} \Delta V d\tau$; $\Delta H_m = \Delta H$ (M/m), where m is the mass of a specimen; M is the molar mass; K is the calorimetric constant (K$_A$ = 228.78 mVsK^{-1} and K$_B$ = 211.62 mVsK^{-1}); ΔV is the thermocouple potential difference corresponding to the temperature difference between the cell and the calorimetric thermostat at time τ; τ is the experiment duration; T is the temperature of the calorimeter. The value of m is corrected for the mass of saturated vapor in the free volume of the ampoule immediately before the experiment.

TABLE 1.4 Saturated vapor pressures P_{sat} over crystal adamantane.

$T(K)$	$\tau(s)$	Δm (mg)	P_{sat}(Pa)
303.58	5454	19.57	30.37
303.52	3054	10.87	30.14
303.46	3054	11.06	30.65
303.53	3054	10.90	30.21
303.56	3054	10.72	29.71
303.59	3054	11.24	31.15

Δm is the sample mass decrease; τ is the duration of effusion.

At this point we present the phase diagrams of adamantane and diamantane according to the work of Reiser et al. [13].

The results of the phase boundary experiments are summarized in Figure 1.2 for adamantane. The equation representing adamantane has been presented by the least squares linear regression method. The result of this regression can be expressed in the following form.

$$\ln P(kPa) = -4670/T + 14.75 \qquad T > 543 \text{ K}. \tag{1.1}$$

with the correlation coefficient of 0.997. Also the equation representing the solid–vapor pressure curve that has been obtained by the least squares method can be written as

$$\ln P(kPa) = -6570/T + 18.18 \qquad 483 < T < 543 \text{ K}. \tag{1.2}$$

The correlation coefficient of this curve is 0.995. The dashed lines in Figure 1.2 also provide Boyd's vapor pressure correlations.

$$\ln P(kPa) = -6324.7/T + 17.827 \qquad 366 < T < 443. \tag{1.3}$$
$$\ln P(kPa) = -9335.6/T - 15.349 \log T + 65.206 \qquad 313 < T < 443. \tag{1.4}$$

TABLE 1.5 Standard molar thermodynamic functions for adamantane in the ideal gas state.

| T (K)	C_p/R	$\Delta S/R$	$\Delta H/R$	Φ/R	$\Delta_f H$	$\Delta_f G$
100	5.144	28.26	4.225	24.04	-98.57	-40.54
200	10.38	33.29	5.887	27.40	-117.1	24.76
298.15	17.73	38.75	8.530	30.22	-134.6	98.16
300	17.88	38.86	8.587	30.27	-134.9	99.61
303.54	18.17	39.07	8.697	30.37	-135.4	102.5
400	26.01	45.12	11.93	33.19	-150.1	180.2
500	33.23	51.73	15.49	36.23	-162.1	264.2
600	39.24	58.33	18.97	39.37	-171.1	350.3
700	44.19	64.77	22.23	42.54	-177.5	437.8
800	48.31	70.94	25.24	45.71	-181.9	526.5
900	51.76	76.84	28.00	48.84	-184.4	614.6
1000	54.68	82.45	30.52	51.92	-185.3	703.5
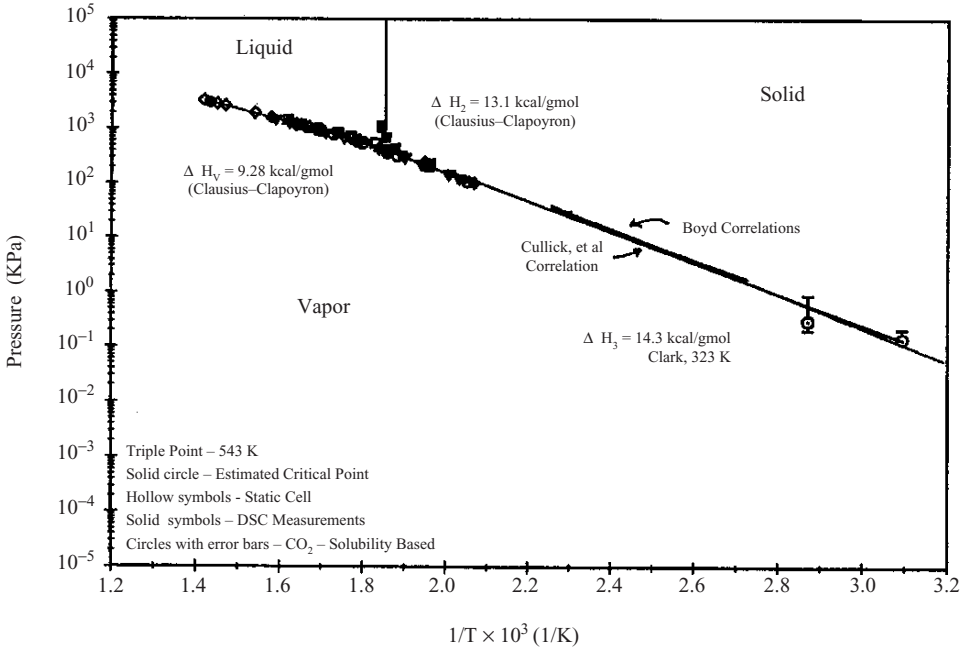
FIGURE 1.2. Phase diagram of adamantane.

The results of Cullick, Magouirik, and Ng [14] are also presented as the solid line in Figure 1.2.

$$\ln P(kPa) = -7300/T - 4.376 \log T + 31.583 \qquad 323 < T < 499. \qquad (1.5)$$

The phase diagram for diamantane, Figure 1.3, has been generated in a similar manner to that of the adamantane diagram. The fundamental distinction between these systems is that three solid phases of diamantane, S_1, S_2, and S_3 were observed. The equation representing the liquid–vapor curve is

$$\ln P(kPa) = -5680/T + 14.858 \qquad 516 < T < 716. \qquad (1.6)$$

The correlation coefficient of this curve is 0.989. The equation for the S_3 vapor pressure curve of diamantane has been obtained using the least squares linear regression method which can be read as

$$\ln P(kPa) = -7330/T + 18.00 \qquad 498 < T < 516\,K. \qquad (1.7)$$

This equation had a correlation coefficient of 0.986. The solid curves in Figure 1.3 are based on the correlations of Cullick et al. [14] and they can be written in the following forms.

$$\ln P(kPa) = 18.333 - 7632.5/T \qquad 353 < T < 493\,K. \qquad (1.8)$$

$$\ln P(kPa) = 190.735 - 18981.3/T - 55.4418 \log T \quad 332 < T < 423\,K. \quad (1.9)$$
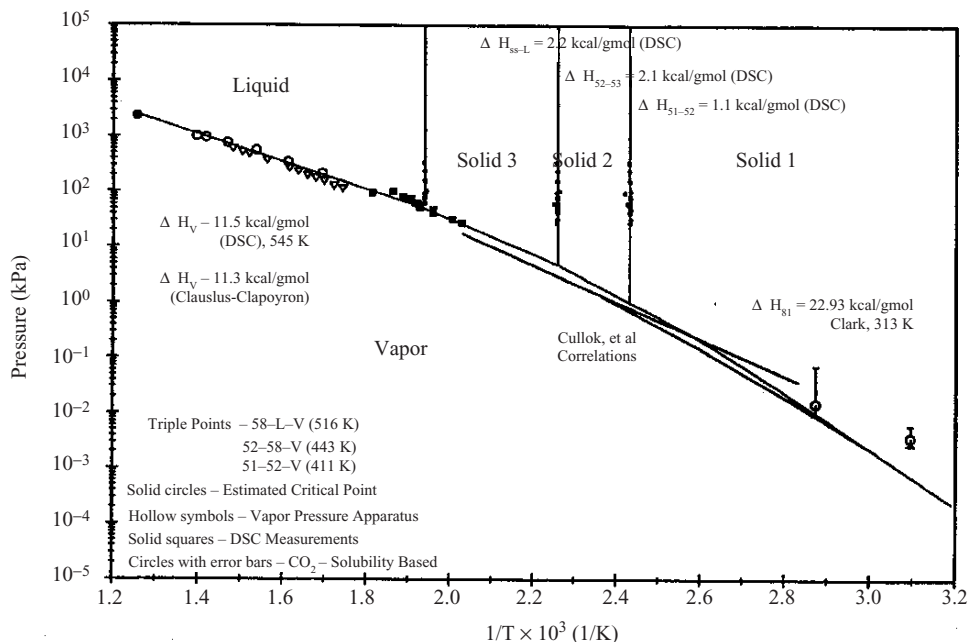
FIGURE 1.3. Phase diagram of diamantane.

1.3. Solubilities of Diamondoids and Phase Behavior of the Binary Systems

In this section the experimental data and modeling of the solubilities of diamondoids in supercritical solvents such as carbon dioxide, methane, and ethane are presented first, followed by the solubilities of these components in liquid organic solvents. In the last part of this section high-pressure phase behavior of the binary systems of diamondoids containing butane and isobutene is explained.

1.3.1. Solubilities of Diamondoids in Supercritical Solvents

As mentioned before, adamantane and diamantane are the first two members in the diamondoid series, and the most prevalent diamondoid compounds in natural gas. Their measured solubilities in methane, ethane, and carbon dioxide, which are three major components of natural gas, have been reported here [15]. The experimental solubilities of adamantane ($C_{10}H_{16}$) in ethane, carbon dioxide, and methane at 333 K are presented in Table 1.6, whereas solubility data for diamantane ($C_{14}H_{20}$) in ethane and carbon dioxide at 333 K and in methane at 353 K are presented in Table 1.7. The solubility of diamantane in methane is also reported in Table 1.7. Solubility data are reported in terms of the solute mole fraction y_2 in the supercritical phase. The solubility data for adamantane in carbon dioxide produced

TABLE 1.6 Experimental solubility of adamantane in CO_2, CH_4, and C_2H_6 at 333 K.

CO₂		CH₄		C₂H₆	
P/MPa	y_2*10^4	P/MPa	y_2*10^5	P/MPa	y_2*10^3
7.70	4.13 ± 0.35	5.62	8.27 ± 1.23	6.07	3.75 ± 0.23
10.17	8.85 ± 0.38	7.64	7.18 ± 2.66	8.10	8.73 ± 0.06
12.59	23.3 ± 0.78	10.14	6.17 ± 1.28	11.04	18.8 ± 0.70
16.65	43.9 ± 1.39	12.58	15.5 ± 1.54	12.72	26.5 ± 0.35
20.06	64.0 ± 1.02	15.27	25.9 ± 0.88	15.93	34.3 ± 0.31
16.57	36.8 ± 3.18	20.06	38.4 ± 0.26	20.08	42.3 ± 5.72

by Smith and Teja [15] as well as the previously published data of Swaid et al. [16] are plotted in Figure 1.4. The solubility data for the six systems measured by Smith and Teja [15] are plotted in Figure 1.5 versus the reduced density of the solvent. As can be seen in Figure 1.5 the trends are linear which shows that the diamondoid solubilities increase with density at 333 K (or 353 K) in the range of pressures studied. The statistics of the linear regressions are given in Table 1.8. The solubility of the heavier compound diamantane is less than that of adamantane in the same solvent, as expected. The measured solubilities are much greater than predicted, assuming ideal gas behavior [15]. The extent to which solubility is enhanced is shown by an examination of the enhancement factors E of solutes, where

$$E = \frac{y_2 P}{P_2^{Sat}} \tag{1.10}$$

and y_2 is the experimental solubility of the solute, P is the total system pressure, and P_2^{sat} is the saturation (or, for solid solutes, sublimation) pressure of the pure solute. Sublimation pressures for adamantane and diamantane were taken from Cullick et al. [14]. Enhancement factors versus solvent-reduced density are plotted in Figure 1.6 for the systems in which carbon dioxide or ethane was the solvent, and linear fits of the data are shown for each solute. Solubility enhancement increases as the solvating power of the solvent increases.

The calculated enhancement factors by Smith and Teja [15] were found to be greater for the higher molecular weight diamantane, because the sublimation

TABLE 1.7 Experimental solubility of diamantane in CO_2 and C_2H_6 at 333 K and at CH_4 at 353 K.

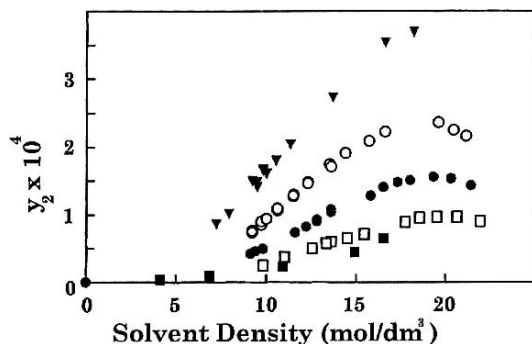| CO₂		CH₄		C₂H₆	
P/MPa	y_2*10^5	P/MPa	y_2*10^5	P/MPa	y_2*10^4
8.13	2.95 ± 1.00	17.37	7.08 ± 1.89	7.65	5.25 ± 0.40
10.14	5.69 ± 0.89	18.06	7.26 ± 1.52	10.10	13.8 ± 0.34
12.62	17.5 ± 1.12	19.77	8.43 ± 3.00	13.13	27.3 ± 0.76
15.12	36.9 ± 1.90	20.09	10.9 ± 3.98	16.58	63.4 ± 1.18
17.55	64.0 ± 1.02	20.06	52.4 ± 0.99	20.10	70.8 ± 3.52

FIGURE 1.4. Comparison of solubilities of adamantane in CO_2: (■), Smith and Teja (333 K); Swaid et al. (□) (343 K), (●) (362.5 K), (○) (382 K), (▼) (402 K).

pressure of this substance is lower. Diamantane enhancement in both solvents exhibited the same general trend, as shown by the trend line on the graph through both sets of diamantane measurements. Adamantane enhancement in both carbon dioxide and ethane also exhibited a linear trend. The slopes of the trend lines for each solute in methane were different from the slopes of the trend lines for each solute in carbon dioxide and ethane, because of the difference in reduced temperature between methane and the other solvents.

Solubilities for the six systems were correlated by Smith and Teja [15] using the equation of state of Patel and Teja [17]. The critical temperatures and pressures of the solutes, which are required by the Patel–Teja equation of state, have not been measured because the substances decompose below their critical points. Instead, these values have been estimated by averaging the results of two group contribution methods [18–20]. In both methods, critical temperature is a function of normal
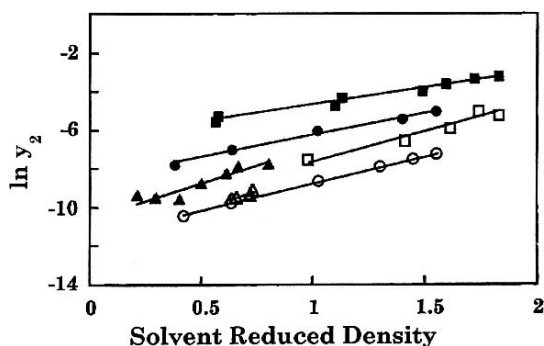

FIGURE 1.5. Diamondoid solubilities versus solvent reduced density: (■) adamantane + ethane (333 K); (●) adamantane + carbon dioxide (333 K); (□) diamantane + ethane (333 K); (▲) adamantane + methane (333 K); (△) diamantane + methane (353 K); (○) diamantane + carbon dioxide (333 K).

TABLE 1.8 Correlation of the solubility of diamondoids in supercritical solvents.

System	Slope	Intercept	R^2
Adamantane + CO_2	2.269	−8.558	0.991
Adamantane + CH_4	3.510	−10.49	0.873
Adamantane + C_2H_6	2.019	−6.891	0.981
Diamantane + CO_2	2.791	−11.58	0.999
Diamantane + CH_4	3.817	−12.01	0.784
Diamantane + C_2H_6	3.017	−10.56	0.953

boiling point. Normal boiling points for each diamondoid were obtained from Wingert [2].

The mixture constants for the Patel and Teja equation of state were calculated using several mixing rules. Results of the calculations using classical one- and two-parameter van der Waals mixing rules are summarized in Table 1.9. The one-parameter mixing rule (denoted by vdW1 in Table 1.9) contains one adjustable parameter k_{ij} in the cross term a_{ij} as follows,

$$a_{ij} = \sqrt{a_i a_j}(1 - k_{ij}), \tag{1.11}$$

whereas the two-parameter rule (denoted by vdW2 in Table 1.9) introduces a second adjustable l_{ij} in the calculation of b_{ij} as follows,

$$b_{ij} = \frac{1}{2}(b_i + b_j)(1 - l_{ij}). \tag{1.12}$$

The objective function (OF) used to obtain the adjustable parameters from experimental data for each mixing rule is

$$OF = \sum_i \frac{(y_{i,calc} - y_{i,exp})^2}{\sigma_{\Delta y_i}^2}, \tag{1.13}$$

where σ is the experimental uncertainty of each data point. Each mixing rule was evaluated by examining the percent average absolute deviation (%AAD) between
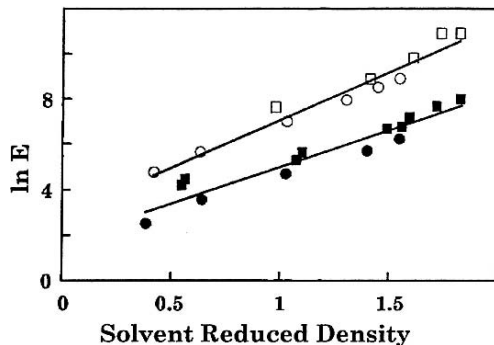

FIGURE 1.6. Solute enhancement factor versus solvent-reduced density: (■) adamantane + ethane; (●) adamantane + carbon dioxide; (□) diamantane + ethane; (○) diamantane + carbon dioxide.

TABLE 1.9 Correlation of the solubility of diamondoids in
supercritical solvents using the Patel–Teja equation of state.

	vdW1		vdW2		
System	k_{ij}	%AAD	k_{ij}	l_{ij}	%AAD
$C_2H_6 + C_{10}H_{16}$	0.02530	17.49	0.05747	0.06367	16.45
$CO_2 + C_{10}H_{16}$	0.15033	23.47	0.27090	0.29386	3.40
$CH_4 + C_{10}H_{16}$	0.22695	55.34	1.1913	2.9717	26.84
$C_2H_6 + C_{16}H_{20}$	0.00556	20.08	0.04955	0.10956	19.81
$CO_2 + C_{16}H_{20}$	0.13082	18.43	0.21992	0.24430	11.90
$CH_4 + C_{16}H_{20}$	0.04867	6.83	0.15309	0.28642	6.93

experimental and correlated solubilities, as follows,

$$\%AAD = \frac{100}{N} \sum_i \frac{|y_{i,calc} - y_{i,\exp}|}{y_{i,\exp}}, \tag{1.14}$$

where N is the total number of data points per system. The results for each
mixing rule, including the optimized parameters and %AAD for each system,
are given in Table 1.9. One binary interaction parameter had been sufficient
to correlate the solubilities in five of the systems studied. However, the CH_4-
adamantane system could not be correlated satisfactorily even with two adjustable
parameters [15].

1.3.2. Solubilities of Adamantane in Near and Supercritical Fluids by Using a New Equation of State

For the optimization and scale-up of a technical high-pressure process, as many
properties as possible, in particular phase behavior and solubilities, should be
known as widely as possible. Although the relevance of the pT-range for applica-
tions is normally limited, process design will strongly benefit from knowledge of
the phase equilibrium behavior over a wider pT-range than finally applied in the
process. The validity of a model over a wide pT-range also contributes to the safety
in process development. There are several approaches to correlate the solubility of
low volatile substances in supercritical solvents. Popular simple models such as
the Chrastil model give a linear dependence of the solubility on the solvent density
in the double logarithm plot [21,24,25].

Besides these models, which are valid over a limited pressure range, cubic
equations of state have also been employed for modeling the solvent properties
[21,26]. In a 1989 review article by Brennecke and Eckert [21,27] the need to
achieve a sufficiently detailed understanding of the actual molecular circumstances
in supercritical fluid (SCF) mixtures is demanded. With the extension of the cubic
equations of state to dilute solutions by a fugacity approach one can model the
solubility in supercritical solvents.

Further improvement has been accomplished by the use of a more realistic equation with respect to the molecular interaction such as the Carnahan–Starling–van der Waals type of equation of state for the description of the solvent [28]. However, the cubic equations as well as the Carnahan–Starling kind of equations are not accurate in the critical region [27]. The computational method preserved here is based on a Carnahan–Starling–van der Waals kind of equation but expected by a perturbation term that corrects the pVT-behavior in the critical region. This approach is expected to be a promising tool for the correlation of solubility behavior even up to pressures above 100 MPa.

The basis for a good correlation of solubility data in supercritical solvents is an equation of state that is able to model the pVT-data of the pure solvent in the critical region accurately. Most equations of state including empirical equations, such as the cubic equations of state as well as molecular-based equations of state, are not able to describe the pVT-behavior in the critical region correctly [27]. Special models have been developed that are able to describe accurately the behavior of fluids at the critical point [21,29,30]. These models account for the singular behavior of the thermodynamic properties at the critical point. Because most of these models are anchored at the critical point, they become less accurate away from the critical region. Early approaches of linking the equations for critical behavior with equations of state for the liquid and gas phase region mathematically by switch functions yielded inconsistencies in derived thermodynamic properties [21,31–33].

Another approach is the physically based crossover from nonanalytic near-critical behavior to the classical behavior proposed by Sengers and co-workers [34–36]. This particular model yields accurate descriptions of the thermodynamic properties in the critical region as well as in the liquid and in the gas phase region. The combination of this approach with classical equations of state is possible and requires numerical iterations and several substance-dependent parameters.

In order to combine a good description of the pVT behavior in the critical region and a mathematical function that does not require a numerical iteration, a semi-empirical approach for an equation of state has recently been developed [21,37]. This approach is based on a classical equation of state consisting of the Carnahan–Starling repulsion term [38] and a van der Waals-like attraction term [39]. Such an equation usually shows deviations from experimental data in the critical region. The correlation of the deviations is accomplished by a perturbation term that describes the deviation of a local density from the average density.

Mathematically, this perturbation procedure is a convolution of the classical equation of state with a density distribution function. Because the integration within the convolution cannot be accomplished analytically, it is performed with a Taylor expansion of the reference equation of state. The integration of the expansion terms can be achieved analytically for the Gauss density distribution function. The convolution generates additional terms in the power series that depend on a parameter σ describing the width of the density distribution. The terms of the

power series can be separated into terms that are independent of and those that depend on the σ-dependent terms representing the perturbation term, whereas the reference can be reassembled from the σ-independent terms.

$$p = \langle p_{ref}(\rho, T) \rangle_\rho = p_{ref}(\rho, T) + p_{pert}(\rho, T, \sigma). \tag{1.15}$$

The perturbation term is a general expression depending on the new parameter σ. In the limit of vanishing σ-value the perturbation term vanishes.

$$\lim_{\sigma \to 0} p_{pert}(\rho, T, \sigma) = 0. \tag{1.16}$$

The dependence of σ on the density has been introduced as a semi-empirical function [37]. The parameters of this function have been obtained by fitting to experimental and theoretically obtained data of the critical isotherm of argon. Argon has been chosen as the reference fluid because of its simple molecular interaction. With scaling parameters this function obtained for argon can be applied to other substances.

The resulting expression for the perturbation as Kraska et al. [21] have been proposed can be read as

$$p_{pert,rep} = \frac{RT}{V_m} \left(\frac{Ay + By^2 + Cy^3}{(3 - 4y)(1 - c_1 y)} \right), \tag{1.17}$$

where

$$A = 4.757 \times 10^{-5}\sigma_n + 12.22\sigma_n^2 - 0.5568\sigma_n^3. \tag{1.18}$$

$$B = -0.001692\sigma_n + 47.57\sigma_n^2 - 1.886\sigma_n^3. \tag{1.19}$$

$$C = \frac{-0.0204\sigma_n + 189.3\sigma_n^2 + 434.2\sigma_n^3 - 1711\sigma_n^4}{1 + 2.35\sigma_n}. \tag{1.20}$$

$$c_1 = 1.424 - 0.1\sigma_n + 8.114\sigma_n^2 - 4.916\sigma_n^3 \ . \tag{1.21}$$

$$y \equiv \frac{b}{V_m}. \tag{1.22}$$

$$\sigma_n \equiv \frac{\sigma V_m}{b_0}. \tag{1.23}$$

Here, y is the packing fraction defined with the parameter b which is four times the co-volume, and $b_0 = 1 \ \text{dm}^3\text{mol}^{-1}$ is the volume unit. The complete perturbation term corresponding to Eq. (24) in reference [21,37] is then:

$$p_{pert} = p_{pert,rep} - 8RbT^*\Psi(T)\sigma^2. \tag{1.24}$$

The remaining unknown functions such as the density and temperature dependence of σ or the temperature dependence of the attraction term $\Psi(T)$ are listed below. The coefficients C_i can be looked up in reference [21,37].

$$\sigma = \sigma_c y \left(\frac{1}{y_c} - \frac{B_\xi}{y_c^2}\Delta y + \sum_{i=2}^{n_{coeff}} C_i \Delta y^i \right) \exp\left(-\left(\frac{\Delta T}{B_T} \right)^2 \right). \tag{1.25}$$

$$\Delta y = \frac{y - y_c}{B_\xi} \quad \Delta T = \frac{T - T_c}{T_c}. \tag{1.26}$$

TABLE 1.10 Parameter of the equation of state for the solvent $CClF_3$.

Substance	$T^*(K)$	$B(cm^3\,mol^{-1})$	σ_c	B_ξ	f_T	B_T
$CClF_3$	422.64145	23.348332	0.00186167	1.0067467	0.344025	300.0

The reference equation of state is listed below:

$$p_{ref} = \frac{RT}{V_m}\left(1 + \frac{4y - 2y^2}{(1-y)^3}\right) - \frac{8RbT^*}{V_m^2 \Psi(T)}. \tag{1.27}$$

$$\Psi(T) = 1 + f_T^* \frac{T_c - T}{T_c}. \tag{1.28}$$

Here, f_T^* is equal to f_T if $T \leq T_c$ and it is equal $0.25\,f_T$ for $T > T_c$. Kraska et al. [21] have applied this equation of state for the modeling of the pVT behavior of pure $CClF_3$ which is used as a supercritical solvent. The parameters are listed in Table 1.10 and those for CO_2 are given in [21,37]. This equation of state has been employed by Kraska et al. [21] for the calculation of the solubility of several low-volatile substances in supercritical fluids with the fugacity approach.

$$x_2 = \frac{p_2^{sat}}{p\varphi_2(x_2)} \exp\left(\frac{V_{m,2}(p - p_2^{sat})}{RT}\right), \tag{1.29}$$

where $V_{m,2}$ is the molar volume of the pure solute, p^{sat} the saturation pressure of the pure solute, and φ_2 the fugacity of the solute. This approach is based on the solvent equation of state and accounts for the solute by its vapor pressure, its interaction parameters, and its molar volume. For the solute the following parameters have been obtained from adjustment to the solubility data: the attraction parameter of the pure solute T_{22}^* and its volume parameter b_{22}, and, in some cases, the corresponding cross-parameters k_{12} and l_{12}. The quadratic one-fluid mixing rules have been used for the calculation of the mixture parameters T^* and b.

$$b = x_1^2 b_{11} + 2x_1 x_2 b_{12} + x_2^2 b_{22}. \tag{1.30}$$

$$T^* = \frac{x_1^2 b_{11} T_{11}^* + 2x_1 x_2 b_{12} T_{12}^* + x_2^2 b_{22} T_{22}^*}{b}. \tag{1.31}$$

$$b_{12} = l_{12}\frac{b_{11} + b_{22}}{2}. \tag{1.32}$$

$$T_{12}^* = k_{12}\sqrt{T_{11}^* T_{22}^*}. \tag{1.33}$$

Because saturation pressure data for many solutes are not available in the literature, Kraska et al. [21] chose an indirect way of estimating the saturation pressures. The relevant function is

$$p_{sat} = p_0 \exp\left(-\frac{A_{sat}}{T} + B_{sat}\right), \tag{1.34}$$

where $p_0 = 1$ MPa is the unit pressure. The parameters A_{sat} and B_{sat} have been treated as adjustable parameters similar to the equation of state parameters. All

these parameters have been optimized by least square minimization of the difference of experimental data and model. In order to obtain A_{sat} and B_{sat}, which determine the temperature dependence of the saturation pressure, it is necessary to use several solubility isotherms at once for fitting.

The isothermal compressibility κ_T of the solute has been taken from the literature where available.

$$V_{m,2} = \left[1 - \kappa_T\left(p - p_2^{sat}\right)\right] V_{m,2}^{p=p_2^{sat}} \tag{1.35}$$

In general, this equation of state can be extended to multicomponent mixtures. For mixtures of two dissolved low-volatile compounds one can extend the fugacity approach. For the description of systems of one solute in a solvent mixture the mixing rules for all parameters have to be evaluated [21].

It has been shown that this equation of state is able to give a good correlation in the overall pressure range, whereas the Redlich–Kwong equation of state, as reported earlier [21,40,41], cannot represent solubility maxima.

1.3.3. Solubilities of Diamondoids in Liquid Organic Solvents

The solubilities of adamantane and diamantane have been determined in various liquid organic solvents at ambient temperature. Data were obtained by adding approximately 0.05 grams of diamondoids to a vial. A Mettler AM100 scale, with a precision of ± 0.0001 gram has been used in all measurements of Reiser et al. [13]. The solubilities of adamantane and diamantane in liquid solvent are listed in Table 1.11.

1.3.4. High-Pressure Phase Behavior of the Binary Systems

In this section (solid + liquid) and (vapor + liquid) equilibria for the binary systems (butane + adamantane), (butane + diamantane), and (isobutene + diamantane) were reported. Solid liquid and vapor liquid equilibria for these systems have been reported and the three phase curves were introduced.

1.3.4.1. Solid Liquid Equlibria and Vapor Liquid Equilibria for the Systems Butane + Adamantane and Butane + Diamantane

Poot et al. [22] have determined experimentally the high-pressure phase behavior of the binary systems (butane + adamantane) and (butane + diamantane). The phase behavior of these binary systems is shown schematically in Figure 1.7. Because the phase diagrams of pure adamantane and diamantane show a solid–solid $(s_1 + s_2)$ transition line the curve representing the (solid diamondoids + liquid + vapor) equilibrium will split into two branches. One branch corresponds to the $(s_1 + l + v)$ equilibrium and the other branch corresponds to the $(s_2 + l + v)$ equilibrium. Both branches intersect at the $(s_1 + s_2)$ equilibrium line of the pure diamondoids. The

TABLE 1.11 Solubilities of diamondoids in liquid
solvents at 25°C.

Solvent	Adamantane Wt%	Diamantane Wt%
Pentane	11.6	4.0
Hexane	10.8	3.9
Cyclohexane	11.1	6.3
Heptane	10.4	3.7
Octane	10.0	3.9
Decane	8.9	3.5
Undecane	7.9	3.2
Tridecane	7.3	2.7
Tetradecane	7.5	2.3
Pentadecane	7.1	2.2
Carbon Tetra	7	5
m-Xylene	9.8	4.5
p-Xylene	9.6	4.5
o-Xylene	9.6	4.1
Toluene	9.9	4.5
THF	12	4
Benzene	10.9	4.3
Diesel fuel	7.5	2.7
1,3-Dimethyl adamantane	6	2
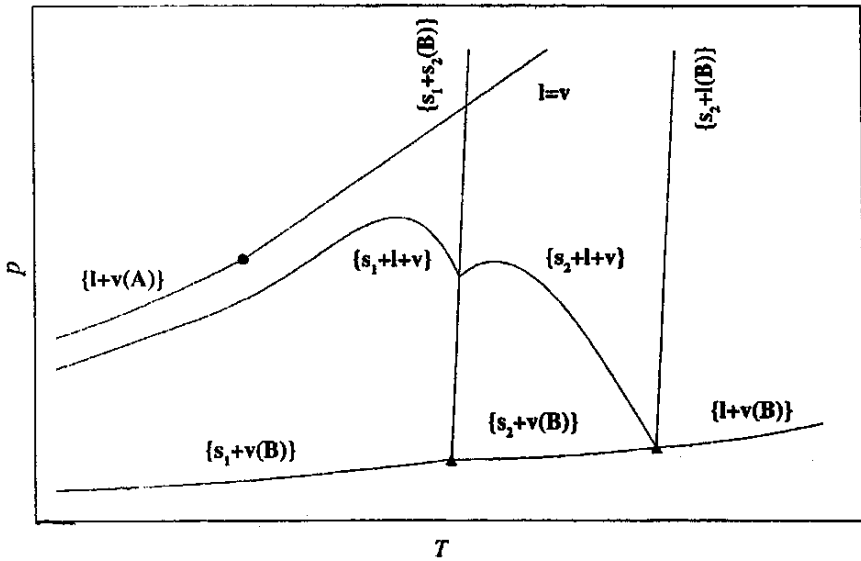
FIGURE 1.7. (P,T) Projection of {butane (A) and diamantane (B)}, with a discontinuity in the slope of the $(s + 1 + v)$ equilibrium line at the intersection with the $(s + s)$ transition line of diamantane.
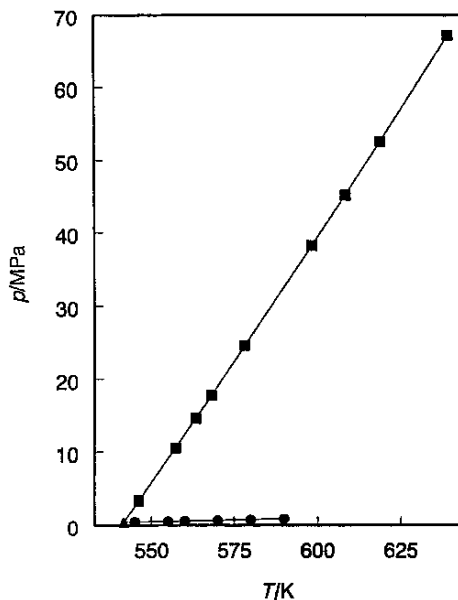
FIGURE 1.8. Phase diagram of adamantane. ■, Poot et al. (2003), $(s + 1)$ transition; •, $(1 + v)$ Ref. (1 in Poot et al. 2003); ▲, triple point.

$(s + 1 + v)$ line starts at low temperature in the quadruple point (solid butane + solid diamondoids + liquid + vapor). The line ends at higher temperature in the triple point of the pure diamondoids. The $(s_1 + s_2)$ equilibrium line of diamantane can be constructed using the atmospheric data of Reiser et al. [13] and data for other binary diamantane systems [22,23]. The $(s_1 + s_2)$ equilibrium line of adamantane is found at temperatures that are lower than the temperature range investigated, so for (butane + adamantane) only the $(s_2 + 1 + v)$ branch of the $(s + 1 + v)$ equilibrium curve can be found.

The phase diagrams of pure adamantane and pure diamantane are presented in Figures 1.8 and 1.9, respectively. These phase diagrams have been constructed by Poot et al. [22].

From the intersection of the vapor pressure curve and the melting curves (listed in Table 1.12) which were determined by Poot et al. [22], the coordinates of the triple point $(s + 1 + v)$ can be obtained. The triple-point temperature for adamantane is 541.7 K and the triple-point pressure about 0.45 MPa. This means that adamantane does not melt at atmospheric pressure, but sublimates. The triple-point temperature for diamantane is 517.65 K and the triple-point pressure about 0.05 MPa. The triple-point temperature for both compounds is very high compared with the triple-point temperature of n-alkanes with the same carbon number. It is also striking that the triple-point temperature of adamantane is higher than the triple-point
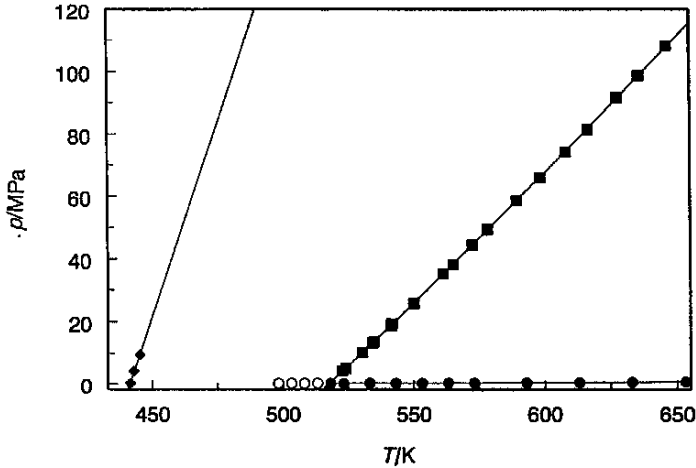
FIGURE 1.9. Phase diagram of diamantane. ■, Poot et al. (2003), $(s_2 + l)$; •, $(l + v)$ Ref. (1 in Poot et al); ▲, triple point; ○, $(s_2 + v)$ Ref. (1 in Poot et al. 2003); ♦, $(s_2 + s_1)$ at temperature T and pressure p.

temperature. Another striking feature of these phase diagrams is that the slope of the melting curve is five times smaller than the slope of the melting curves of alkanes.

The experimentally determined $(l + v)$ equilibrium points for (butane + adamantane) are given in Table 1.13 and for (butane + diamantane) in Table 1.14. Also critical points were obtained at diamondoids mole fractions 0.0495, 0.1008, and 0.1478 for (butane + adamantane) and 0.0223, 0.0493, and 0.1011 for (butane + diamantane). At higher mole fractions dew points and critical points could not be measured due to the temperature limitations of the equipment.

TABLE 1.12 The melting curves of adamantane and diamantane at temperature T and pressure p.

Adamantane				Diamantane	
T/K	p/MPa	T/K	P/MPa	T/K	p/MPa
546.18	3.4	522.7	4.1	598.44	66.0
557.26	10.5	530.34	10.2	608.12	74.2
563.36	14.6	534.86	13.6	616.58	81.5
568.09	17.8	541.27	18.7	627.52	91.5
578.13	24.6	549.99	25.8	627.85	91.8
598.33	38.3	561.23	35.2	635.89	98.6
608.26	45.2	572.62	44.4	646.36	108.1
618.72	52.6	578.43	49.3	655.04	115.2
639.08	67.2	589.61	58.5		

TABLE 1.13 Vapor + liquid equilibria for $\{(1-x) \text{ butane } +x \text{ adamantane}\}$: phase boundaries at T and p and constant adamantane mole fraction x.

		T/K	p/MPa	T/K	p/MPa	T/K	p/Mpa
$X = 0$	$1 = v$	333.60	0.655	373.64	1.550	397.70	2.405
		343.62	0.827	377.79	1.675	407.64	2.845
		353.63	1.032	383.61	1.871	413.70	3.145
		363.65	1.272	387.65	2.010	417.66	3.355
		367.67	1.380	393.69	2.241		
	$1 = v$	425.03	3.785				
$x = 0.0495$ 1 to (1 + v)		285.10	0.169	353.13	0.978	412.96	2.857
		293.25	0.217	363.06	1.196	423.12	3.320
		303.17	0.289	373.03	1.450	433.13	3.813
		313.24	0.380	382.98	1.740	443.15	4.294
		323.44	0.499	392.95	2.070	448.16	4.468
		333.33	0.632	402.95	2.442	448.27	4.472
		343.25	0.791				
	$1 = v$	448.38	4.474				
	v to (1 + v)	448.49	4.477	449.19	4.497	453.17	4.599
		448.68	4.483				
$x = 0.1008$ 1 to (1 + v)		327.51	0.525	393.42	1.954	453.54	4.481
		333.51	0.605	403.43	2.295	463.14	4.874
		343.47	0.756	413.45	2.674	465.15	4.942
		353.44	0.933	423.46	3.089	467.13	5.003
		363.38	1.138	433.51	3.538	469.12	5.059
		373.53	1.380	443.52	4.009	470.14	5.087
		383.45	1.649				
	$1 = v$	470.21	5.089				
	v to (1 + v)	470.38	5.094				
$x = 0.1478$ 1 to (1 + v)		353.28	0.894	413.07	2.515	463.22	4.668
		363.19	1.088	423.11	2.897	473.23	5.096
		373.11	1.310	433.27	3.318	483.46	5.443
		383.26	1.568	443.25	3.756	488.37	5.570
		393.15	1.850	453.23	4.211	489.72	5.602
		403.14	2.167				
	$1 = v$	489.83	5.605				
	v to (1 + v)	489.95	5.608	490.85	5.629	493.40	5.686
$x = 0.2003$ 1 to (1 + v)		375.67	1.288	412.79	2.342	452.73	3.905
		383.09	1.466	422.75	2.693	462.72	4.343
		393.00	1.730	432.71	3.073	472.72	4.784
		402.92	2.022	442.72	3.479	482.71	5.208
$x = 0.2504$ 1 to (1 + v)		392.54	1.633	422.67	2.537	452.58	3.656
		402.92	1.917	432.61	2.886	462.59	4.069
		412.74	2.212	442.58	3.261	472.57	4.494
$x = 0.3016$ 1 to (1 + v)		408.51	1.923	433.58	2.701	463.38	3.799
		413.51	2.067	443.58	3.053	473.46	4.198
		423.63	2.376	453.59	3.423		
$x = 0.3503$ 1 to (1 + v)		419.03	2.123	448.05	3.035	478.02	4.123
		428.03	2.388	458.06	3.385	488.02	4.504
		438.05	2.702	468.04	3.748		
$x = 0.3996$ 1 to (1 + v)		431.20	2.288	453.27	2.959	473.18	3.632
		433.34	2.346	463.22	3.286	483.10	3.982
		443.30	2.643				
$x = 0.4518$ 1 to (1 + v)		441.46	2.388	450.93	2.657	470.84	3.265
		444.96	2.486	460.89	2.955	480.82	3.585

TABLE 1.13 (*Continued*)

	T/K	p/MPa	T/K	p/MPa	T/K	p/Mpa
x = 0.5003 1 to (1 + v)	451.36	2.444	470.97	2.988	480.91	3.281
	460.94	2.704				
x = 0.55203 1 to (1 + v)	461.69	2.477	470.92	2.713	480.89	2.977
	465.97	2.585	475.90	2.844	485.88	3.113
x = 0.6023 1 to (1 + v)	471.25	2.432	477.03	2.568	483.00	2.712
	474.05	2.497	480.03	2.640	486.02	2.786

TABLE 1.14 (Vapor + liquid) equilibria for $\{(1 - x)\,\text{butane} + x\,\text{diamantane}\}$: phase boundaries at constant diamantane mole fraction x.

	T/K	p/MPa	T/K	p/MPa	T/K	p/MPa
X = 0.0223 1 to (l + v)	342.68	0.795	382.54	1.780	423.10	3.480
	353.01	0.995	392.73	2.135	432.79	3.990
	363.03	1.225	402.90	2.535	437.80	4.235
	372.14	1.465	413.06	2.975		
1 = v	441.27	4.375				
v to (1 + v)	442.78	4.435	452.80	4.770	462.77	4.980
	473.76	5.030				
x = 0.0493 1 to (1 + v)	357.84	1.070	398.20	2.250	437.95	4.070
	367.93	1.305	408.39	2.660	447.92	4.590
	378.02	1.585	417.86	3.075	457.91	5.055
	388.13	1.900	427.93	3.560		
1 = v	461.24	5.195				
v to (1 + v)	462.93	5.270	482.96	6.045	502.83	6.225
	472.91	5.680	492.88	6.235		
x = 0.1011 1 to (1 + v)	377.52	1.510	417.93	2.955	457.81	4.895
	387.78	1.810	427.91	3.375	467.71	5.410
	397.86	2.145	437.88	3.855	477.70	5.905
	407.95	2.515	447.85	4.365	478.64	6.355
1 + v	491.41	6.515				
v to (1 + v)	500.65	6.890				
x = 0.1508 1 to (1 + v)	387.91	1.730	432.88	3.430	482.83	5.985
	392.84	1.885	442.82	3.905	492.77	6.480
	402.89	2.215	452.83	4.405	502.77	6.940
	412.86	2.585	462.84	4.925		
	422.89	2.990	472.82	5.465		
x = 0.3495 1 to (1 + v)	412.85	2.135	442.84	3.185	472.88	4.425
	422.85	2.460	452.86	3.580	482.75	4.860
	432.82	2.815	462.81	3.990	492.77	5.305
x = 0.5481 1 to (1 + v)	432.79	2.145	462.92	2.970	492.72	3.860
	442.94	2.400	472.91	3.260	502.78	4.175
	452.93	2.675	482.84	3.555		
x = 0.6489 1 to (1 + v)	447.73	1.960	477.62	2.615	502.61	3.200
	457.68	2.170	483.02	2.740		
	468.06	2.400	492.64	2.970		
x = 0.7589 1 to (1 + v)	463.76	1.650	479.78	1.895	499.78	2.215
	469.76	1.740	489.78	2.055	507.77	2.345
x = 0.8697 1 to (1 + v)	487.69	1.100	502.83	1.230	522.87	1.415
	492.87	1.145	512.80	1.325		

TABLE 1.15 Vapor–liquid equilibria in the system $[(1 − x)$ isobutane $+ x$ diamantane]: phase boundries at constant diamantane mole fraction x.

	T/K	p/MPa	T/K	p/MPa	T/K	p/MPa
$x = 0.000 L \rightarrow V$	328.58	0.79	358.57	1.50	393.63	2.86
	338.56	0.99	363.57	1.66	403.66	3.39
	343.51	1.10	368.52	1.82	407.70	3.62
	348.56	1.23	373.52	1.99	407.74	3.63
	353.50	1.35	383.60	2.40		
$x = 0.05 L \rightarrow L + V$	365.20	1.617	403.16	3.069	441.09	4.99
	368.18	1.700	413.13	3.558	442.13	5.03
	373.20	1.863	423.14	4.078	442.98	5.07
	383.19	2.221	433.13	4.60		
	393.18	2.623	439.12	4.89		
$L = V$	443.13	5.08				
$V \rightarrow L + V$	443.23	5.09	453.15	5.55	493.11	6.86
	443.61	5.10	463.10	5.98	503.09	6.94
	444.09	5.13	473.13	6.37		
	445.17	5.18	483.13	6.67		
$x = 0.198 L \rightarrow L + V$	401.67	2.682	434.00	4.184	483.92	6.92
	402.64	2.722	443.99	4.670	493.89	7.41
	403.92	2.772	453.87	5.25	503.90	7.86
	413.96	3.208	463.87	5.83		
	424.00	3.678	473.92	6.38		
$x = 0.400 L \rightarrow L + V$	421.26	2.932	453.27	4.225	493.24	5.98
	423.30	3.006	463.28	4.658	503.20	6.41
	433.35	3.396	473.26	5.10		
	443.29	3.804	483.25	5.55		
$x = 0.600 L \rightarrow L + V$	438.22	2.572	463.19	3.260	493.29	4.124
	443.34	2.713	473.20	3.546	503.30	4.421
	453.44	2.994	483.23	3.841		
$x = 0.840 L \rightarrow L + V$	482.15	1.613	493.16	1.737		
	483.17	1.623	503.26	1.852		

In addition to the above systems, Miltenburg et al. [23] determined the high-pressure phase behavior of the binary system isobutene + diamantane according to a synthetic method in the temperature range (320–530) K and the pressure range (0.3–10) Mpa which are presented in Table 1.15 for their experimentally determined LV equilibrium points.

References

[1]   Dahl, J.E., Liu, S.G., and R.M.K. Carlson, Scienceexpress/www.sciencexpress.org/28November2002/page1–3/101126/science.1078239

[2]   Wingert, W.S., *Fuel*, 1992, 71, 37–43.

[3]   Fort, R.C., *Adamantane The Chemistry of Diamond Molecules*, Dekker, New York, 1976.

[4]   Marchand, A.P., *Aldrichim. Acta*, 28, 95, 1995.

[5]   Zones, S.I., Nakagawa, Y., Lee, G.S., Chen, C.Y., and Yuen, L.T., *Micropor. Mesopor. Mater.*, 21, 199, 1998.

[6]   Meador, M.A., *Annu. Rev. Mater. Sci.*, 28, 599, 1998.

[7]   Brenner, B.W., Shenderova, O.A., Areshkin, D.A., Schall, J.D., and Frankland, S.J.V., *CMES*, 3, 643, 2002.

[8]   Cagin, T., Che, J., Gardos, M.N., Fijani, A., and Goddard, III, W.A., *Nanotechnology*, 10, 278, 1999.

[9]   Drexler, K.E., *Nanosystems: Molecular Machinery, Manufacturing and Computation*, Wiley, New York, 1992.

[10]   Lifshitz, Y., *Science*, 297, 1531, 2002.

[11]   Chang, S.S. and Westrum, E.F., *J. Phys. Chem.*, 94, 1960, 1547.

[12]   Kabo, G.J., Blokhin, A.V., Charapennikan, M.B., Kabo, A.G., and Sevruk, V.M., *Thermochim. Acta*, 345, 2000, 125–133.

[13]   Reiser, J., McGregor, E., Jones, J., Enick, R., and Holder, G., *Fluid Phase Equilibria*, 117, 1996, 160–167.

[14]   Cullick, Magourik, and Ng, Paper presented at the 73rd Annual Convention of the GPA, New Orleans, 1994.

[15]   Smith, V.S. and Teja, A.S. *J. Chem. Eng. Data*, 1996, 41, 923–925.

[16]   Swaid, I., Nickel, D., and Schneider, G.M., *Fluid Phase Equilibria*, 1985, 21, 95–112.

[17]   Patel, N. and Teja, A.S., *Chem. Eng. Sci.*, 1982, 37, 463–473.

[18]   Ambrose, D., NPL Report Chemistry 92, National Physical Laboratory: Teddington, UK, 1978.

[19]   Ambrose, D., NPL Report Chemistry 98, National Physical Laboratory: Teddington, U.K, 1979.

[20]   Reid, R.C., Prausnitz, J.M., and Poling, B.E., *The Properties of Gases and Liquids*, McGraw-Hill: New York, 1987.

[21]   Kraska, T., Leonhard, K.O., Tuma, D., and Schneider G.M., *J. Supercrit. Fluids*, 23, 2002, 209–224.

[22]   Poot, W., Kruger, K.M., and de Loos, T.W., *J. Chem. Thermodynamics*, 35, 2003, 591–604.

[23]   Van Miltenburg, A., Poot, W., and de Loos, T.W., *J. Chem. Eng. Data*, 45, 2000, 977–979.

[24]   Chrastil, J., *J. Phys. Chem.*, 86, 1982, 3016.

[25]   Mendez-Santiago, J. and Teja, A.S., *Fluid Phase Equilibria*, 158–160, 1999, 501.

[26]   Coutsikos, P., Magoulas, K., and Tassios, D., *J. Chem. Eng. Data*, 42, 1997, 463.

[27]   Brennecke, J.F. and Eckert, C.A., *AIChE J.*, 35, 1989, 1409.

[28]   Trabelsi, F., Abaroudi, K., and Recasens, F., *J. Supercrit. Fluids*, 14, 1999, 151.

[29]   Widom, B., *J. Chem. Phys.*, 43, 1965, 3898.

[30]   Schofield, P., *Phys. Rev. Lett.*, 22, 1969, 606.

[31]   Chapela, G.A., and Rowlinson, J.S., *J. Chem. Soc., Faraday Trans.*, I 70, 1974, 584.

[32]   Wooley, H.W., *Int. J. Thermophys.*, 4, 1983, 51.

[33]   Fox, J.R., *Fluid Phase Equilibria*, 14, 1983, 45.

[34]   Chen, Z.Y., Albright, P.C., and Sengers, J.V., *Phys. Rev. A*, 41, 1990, 3161.

[35]   Van Pelt, A., and Sengers, J.V., *J. Supercrit. Fluids*, 8, 1995, 81.

[36]   Krostowicka Wyczalkowska, A., Anisimov, M.A., and Sengers, J.V., *Fluid Phase Equilibria*, 158–160, 1999, 523.

[37]   Leonhard, K., and Kraska, T., *J. Supercrit. Fluids*, 16, 1999, 1.

[38]   Carnahan, N.F. and Starling, K.E., *J. Chem. Phys.*, 51, 1969, 635.

[39]   Yelash, L.V. and Kraska, T., *Fluid Phase Equilibria*, 162, 1999, 115.

[40]   Deiters, U.K. and Swaid, I., *Ber. Bunsenges. Phys. Chem.*, 88, 1984, 791.

[41]   Deiters, U.K., *Fluid Phase Equilibria*, 20, 1985, 275.

2
Development of Composite Materials Based on Improved Nanodiamonds

P. Y. DETKOV, V. A. POPOV, V. G. KULICHIKHIN, AND S. I. CHUKHAEVA

2.1. Introduction

This chapter describes the methods of improving the quality of diamond nanopowders obtained by detonation synthesis, and some commercial applications of nanodiamonds that have been developed.

Due to its unique physicochemical characteristics, diamond is widely used in industry. Interest in fabrication of artificial diamond crystals, specifically, those obtained by detonation transformation of explosives, was already evinced in the 1940s. Attention was paid to the fact that thermodynamic conditions for the existence of carbon as diamond crystals are realized in the zone of the detonation complex. Nanodiamond powder synthesis and the properties of synthesized materials were studied in numerous works performed at various research centers [1–11]. In subsequent decades, many attempts were undertaken to develop detonation diamond technology. One of these technologies was developed and patented by the Russian Federal Nuclear Center–Zababakhin All-Russian Research Institute of Technical Physics (RFNC–VNIITF).

2.2. Description of the Existing and Improved Techniques of Diamond Nanopowder Synthesis

The theoretical bases of the mechanism of diamond crystal formation and graphitization (transition of carbon of the diamond phase to other nondiamond forms) in the expansion of the explosion products are given in the published papers [4,5], which present the carbon phase diagrams and consider the fundamental principles of the existence of carbon in a phase.

To date, considerable theoretical and experimental material has been accumulated, which enables formulation of not only the principles of the existence of carbon in a phase, but also of the physical characteristics of the conditions for the formation of diamond-phase crystals and their graphitization. The major ones are as follows.

- The rate of graphite–diamond transformation goes up as pressure (P) and temperature (T) are increased.
- The characteristic time of the formation of diamond phase from graphite is $\sim 10^{-6}$–10^{-7} s (under certain conditions the diamond nucleation time can be $\sim 10^{-10}$ s)[6].
- Presumably, the diamond phase is formed from elemental carbon (this point of view coincides with the opinion of other authors).
- Crystals with defects are mainly graphitized.
- The threshold temperature of graphitization is $\sim 2500°C$ (defect-free crystalline structure) and $\sim 1500°C$ (crystal with defects).
- The ratio of graphitization rate and characteristic time of explosion products' expansion determines the stability of the diamond phase.
- According to [6,7], N and O can occur in crystalline-lattice nodes by the substitution mechanism; and H and other elements, by the mechanism of diffuse impurities, by forming defects in diamond crystals.
- The works [6,7] also maintain that the rate of incorporation of diffuse impurities into the crystal in the shock wave is significant.

Fabrication of diamonds using explosives is a dynamic synthesis method. It began to be used in the past 15–20 years. The sources of carbon for the diamond phase are (i) nonexplosive carbon materials or (ii) carbon-containing explosives.

In the former case, explosives are used for dynamic compression of ampules with carbon-containing material to yield diamonds.

In the latter case, transition of the carbon of an explosive into the diamond phase occurs as a result of explosive transformation of the explosive, that is, in the detonation wave. The method was called detonation synthesis. Diamonds are also formed in the degradation of some inert (nonexplosive) organic substances in the detonation wave, if they are used as additives to potent explosives. An attractive feature of detonation synthesis of diamonds is that it uses charges from explosives obtained in the disposal of weapons. Thus, the detonation synthesis of diamonds can help utilize explosives obtained in weapons dismantlement.

The detonation method is relatively simple: an explosive charge is exploded in a sealed armored chamber; after the explosion the condensed products of explosive conversion, diamonds included, remain in the chamber from where they are recovered and cleared of impurities. The impurities are metal particles of the armored chamber and of construction elements required to install and explode the charge (suspensions, wires, detonators, etc.), and also nondiamond forms of carbon. The condensed nondiamond carbon is formed both during the detonation together with the diamond phase and in the subsequent expansion of the detonation products, when the diamond phase is subject to partial graphitization.

To reduce graphitization and enhance the yield of diamonds, before the explosion the volume of the armored chamber is filled with an inert gas (nitrogen, carbon dioxide, gaseous products of the previous explosions).

Inert gas in this case plays the role of coolant for expanding detonation products. Liquids and solids inert with respect to the detonation products can also be used

as coolants. The choice of coolant is determined by not only the condition of preventing the graphitization, but also by the possibility of clearing the diamond phase of impurities in the presence of the coolant.

The explosives most frequently used at present in the synthesis of detonation diamonds are mixtures of trinitrotoluene and hexogen. Trinitrotoluene is an explosive with a high negative oxygen balance. Explosive decomposition of trinitrotoluene releases a large amount of free carbon. Therefore, trinitrotoluene is the major source of carbon for the diamond phase in trinitrotoluene–hexogen mixtures. Hexogen (trimethylenetrinitramine) is a more potent explosive than trinitrotoluene and is used to maintain the detonation parameters of the mixture at a required level.

Diamond particles formed in the detonation synthesis are 2–6 nm in size. Particles of detonation diamond have a cubic lattice with lattice parameter $\alpha = 0.3575$ nm (in natural diamond, $\alpha = 0.3566$ nm). Due to the small size of particles, the detonation diamonds are called ultradisperse diamonds (UDD) or nanodiamonds.

Besides the diamond phase, the condensed products of explosion recovered from the armored chamber after the explosion of a charge contain the nondiamond modifications of carbon and metal impurities. Depending on the method of synthesis, the diamond phase in the condensed carbon products of explosion is 30 to 75% of the weight of these products. Optimization of the detonation synthesis by the ratio of trinitrotoluene and hexogen in the mixture, by the ratio of the weight of exploded charge and the volume of the chamber and also the use of special coolants enables a stable 75% yield of the diamond phase in the condensed products of explosion.

Metal impurities are removed from nanodiamond powders by dissolving them in mixtures of strong inorganic acids.

To date, four types of diamond nanopowders are produced depending on how they are separated from the mixture: standard, ozone, pure type 1, and pure type 2.

The essence of the purification method used in the production of diamond nanopowders is to dissolve impurities of metals and their compounds and oxidize nondiamond forms of carbon by chromic anhydride in the presence of sulfuric acid. The use of such a strong oxidant in the presence of a strong acid makes it possible to combine in one stage the purification of diamonds both from nondiamond carbon forms and from metal impurities. The suspension of the nanodiamond-containing mixture is filtered through a set of sieves to remove mechanical impurities, the metal part is removed by magnetic treatment, and the solid phase is concentrated by nutsch filters. Dissolution of impurities of metals and their compounds and oxidation of nondiamond forms of carbon is carried out in a reactor (further on, this operation is called "oxidation"). One run of oxidation to purify 3.3–3.7-kg solid phase of the mixture requires 24–27-kg sulfuric acid and 6.9–7.5-kg chromic anhydride. In the oxidation, when a solution of chromic anhydride is added, the temperature in the reactor reaches 125–130°C; the mixture is kept in the reactor with sulfuric acid and chromic anhydride for 3–4 h. Following the oxidation, the reaction mixture is washed with water to remove chromium and sulfuric-acid salts. The yield is a nanodiamond suspension that contains 2.3–2.5-kg solid phase.

The nanodiamond powder is separated from the suspension by centrifugation and drying at 150°C.

Nanodiamonds purified according to this method contain no less than 97% ultradisperse diamond in the carbon component (1.4–1.7% incombustible impurities; density, 3.1–3.2 g/cm^3).

Thus, purification of ultradisperse diamond in the production process yields powders or suspensions of the above quality of the solid phase. They are called type or standard powders/suspensions. Pure powders/suspensions are those with lower impurity content.

Nanodiamonds synthesized in the standard process contain nondiamond forms of carbon, metal, and silicon compounds as major impurities. Metal impurities include compounds from the diamond-containing mixture that were not dissolved during oxidation or were formed during purification (mainly chromium hydroxide and major chromium sulfates). Production of pure powders requires additional expenditures, and the effect of this or that impurity on particular consumer properties of ultradisperse diamond remains an open issue. Nanodiamond powders were obtained in a more pure form with respect to:

- Incombustible impurities and nondiamond carbon
- Any one of these parameters

The purity with respect to nondiamond carbon can be improved by:

- Changing the oxidation modes in the chosen purification technique by increasing the concentration of reagents, temperature, and time of the process
- Using another oxidant with a higher redox potential as compared with chromium anhydride (e.g., potassium permanganate) during the purification in a liquid medium, or a strong oxidant during the gas-phase purification (e.g., ozone)

In liquid-phase purification, the purity with respect to metal impurities initially present in the mixture is improved simultaneously with that with respect to nondiamond carbon. The content of impurities of chromium compounds introduced with the purification decreases in the alkaline treatment based on a better solubility of the amphoteric chromium compounds in a weak alkaline solution rather than in an acid, and also by the treatment with ion-exchange resins (in particular, cation-exchange resins).

A technique increasing the concentration of the reagents and, therefore, the rate of the process, can be further purification of standard purified diamond powders and suspensions. Usually, this is of importance for liquid-phase oxidation, in which there are no byproducts from the reaction mixture (except the gaseous products).

Based on these considerations, pure diamond powders were produced by the following techniques.

- From the mixture by treatment with sulfuric acid and chromium anhydride with an increased proportion of the reagents, temperature, and time of the process
- From nanodiamonds (powders and suspensions) purified by the standard process by retreatment with sulfuric acid and chromium anhydride at various ratios

TABLE 2.1 Characteristics of nanodiamond powders obtained by various purification techniques.

| Quality Index | Samples of Ultradisperse Diamond Powders | | | |
	Standard	Ozone	Pure Type 1	Pure Type 2
Volatile impurities and moisture, %	3.0	2.0	2.0	2.0
Incombustible residue, %	1.4–1.7 (No more than 2.0 according to [8])	1.0	0.2	0.45
Oxidized carbon, %	2.0	0.5	0.5	2.0
Density, g/cm^3	3.1–3.15 (No less than 3.0 according to [8])	3.3–3.4	3.2–3.3	3.1
pH of the 10% nanodiamond suspension in distilled water	5.6–6.2	1.6–2.0	3.5–4.5	5.6–6.2

- By purification of the diamond-containing mixture with potassium permanganate in the presence of sulfuric acid
- By ozone oxidation of nondiamond forms of carbon in the mixture purified from metal compounds
- By alkaline treatment of nanodiamond powders and suspensions purified in the standard process
- By cationite treatment of nanodiamond powders and suspensions purified in the standard process

After the purification by these methods, incombustible impurities and oxidized forms of carbon in the synthesized powders were assayed. For some samples, the pycnometric density was determined. The efficiency of the methods used to produce pure powders of ultradisperse diamonds was assessed based on these solid-phase parameters (Table 2.1).

2.2.1. Properties of Nanodiamonds Demonstrating Their Diamondlike Structure

The characteristics of nanodiamonds demonstrating their diamondlike (crystalline and molecular) structure include:

- Crystalline diamond structure parameters: cubic syngony with $a = 3.55$ Å.
- Optical spectra of Raman scattering (RS) have the following values.
  - Region of RS spectrum absorption, 1321–1328 cm^{-1} (diamond phase).
  - Ratio of diamond and oxidized carbon was determined as 97–98/3–2%.

2.2.2. Dispersity

Calculated from the shape of the lines, the distribution of ultradisperse diamond particles by size on the X-ray patterns of UDD samples gives the values 10–100 Å with the average size of 31 Å. Small-angle X-ray scattering determines the fractal character of nanoparticles with the size of 18 Å.

2.2.3. Density

Determined experimentally by the pychometric method, the density of the four types of UDD varies from 3.1 g/cm^3 (type 2 pure nanodiamond) up to 3.3–3.4 g/cm^3 (ozone purified).

2.2.4. Chemical Composition

The basis of the UDD samples was determined to be carbon, no less than 85 wt%. Major impurity elements were oxygen, nitrogen, hydrogen; microimpurities—mainly elemental metals (Ca, Cr, Cu, Zn, Ti, Fe, Na, K, Ba, Al, Mg, B, Mn, Si, S, Cl)—were in total from 0.2% (type 2 pure UDD) up to 2% (standard UDD). The concentration of each impurity element and especially microimpurities varied depending on the particular features of synthesis and the purification technique. Thus, additional purification of UDD with cation-exchange resins included the separation of the aqueous suspension of the nanopowder into two fractions: upper, nonprecipitating; and lower, residue. In the upper fraction the content of incombustible residue was 20–50% smaller than in the lower fraction.

The nanodiamond powder has a complex multilevel structure. Primary nanodiamond particles ($d \sim 4$ nm) are combined into strong cluster aggregates 40 to 400 nm in size. In turn, primary aggregates are combined into secondary aggregates and agglomerates of 0.4–4 μm in size (Figure 2.1). Residual non-diamond forms of carbon, not removed in oxidation, are distributed mainly on the surface of crystallites inside the aggregates. The surface of the diamond particles was found to have significant amounts of various oxygen-containing hydroxyl, carboxyl, and so on groups, and also, to a lesser extent, methyl and nitrile groupings. On the whole, the experimental facts taken together suggest that UDD belong to fractal systems, and the most important stages of the UDD structure-forming mechanism is fractal formation according to the cluster–particle and cluster–cluster type with multilevel macrostructures formed.

A commercial technology of ultradisperse detonation diamond powder (technical specifications TU 2-037-677-94) has been developed and its production has been organized at the Russian Federal Nuclear Center–Zababakhin All-Russian Research Institute of Technical Physics (RFNC–VNIITF), Snezhinsk, Chelyabinsk Region. The major physicochemical parameters of this product are given in Table 2.2.

Besides, the RFNC–VNIITF produces 1- to 2-kg test batches of diamond powders of increased purity (incombustible residue, 0.2%).
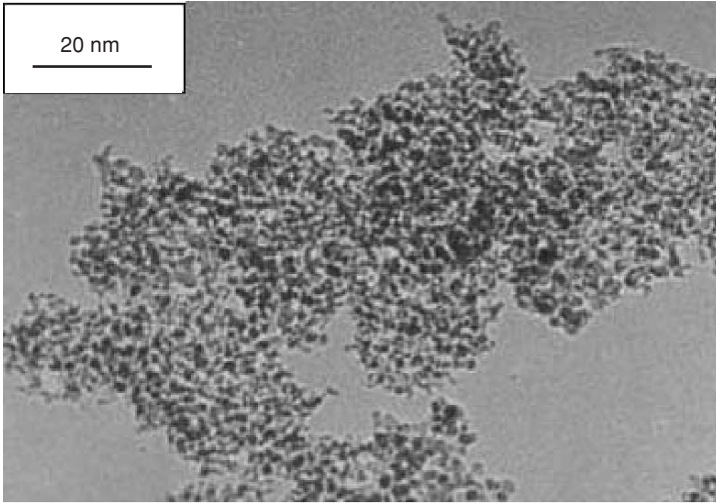
FIGURE 2.1. Agglomerated nanodiamond particles.

2.3. Fields of Application of Nanodiamond Powders

The most developed application of UDD is their use for strengthening composite electrochemical chromium-based coatings. Ultradisperse diamond is introduced into the standard chromium-plating electrolyte usually as suspension. The

TABLE 2.2 The major physicochemical parameters of ultradisperse detonation diamond powder produced at the Russian Federal Nuclear Center–Zababakhin All-Russian Research Institute of Technical Physics, Snezhinsk, Chelyabinsk Region.

S. No.	Parameter	Value
1	Appearance	Light-gray powder
2	Mass fraction of diamond in the base substance, determined by X-ray diffraction analysis, %, no less than	98.0–99.0
3	Mass fraction of incombustible residue, %, no less than	1.0–1.5
4	Mass fraction of moisture and volatiles, %, no less than	2.0–3.0
5	Density (pycnometric), g/cm^3, no less than	3.10–3.20
6	Mass fraction of oxidized forms of carbon, %	1.0–2.0
7	Bulk density, g/cm^3	0.25–0.35
8	Specific surface, m^2/g	350
9	Average size of primary particles, determined by X-ray diffraction method, nm (Å)	3(30)
10	Average size of aggregated particles, determined by traditional dispersion analysis methods, μm	1.3
11	Heat resistance, determined by derivatographic method	In an air atmosphere, the powder is oxidized at 450°C
12	Heat resistance in vacuum	800°C
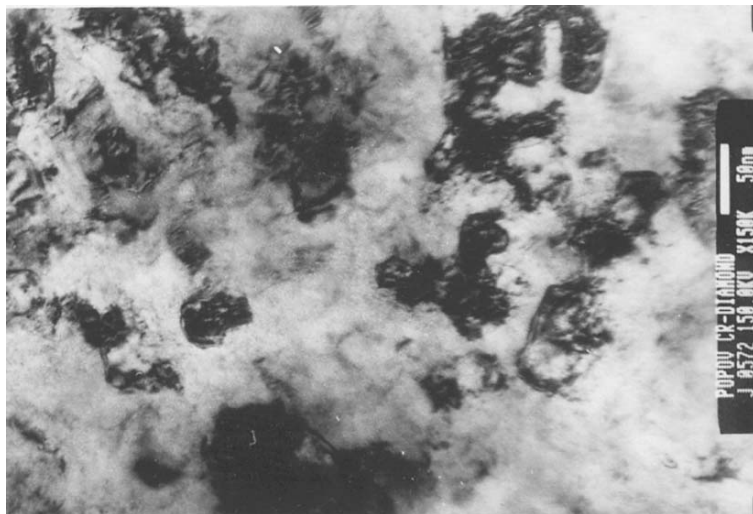
FIGURE 2.2. Structure of the chromium-nanodiamond coating (planar section).

concentration of UDD in the electrolyte is maintained at 15–30 g/l. Chemical pre-activation of UDD and their UV dispersion are used to increase the sedimentation stability of diamond particles in the electrolyte. The content of the diamond phase in the chromium–diamond coating is 0.1–1%.

The chromium coating thus obtained was studied using a JEM 2000 EX transmission electron microscope at an accelerating voltage of 150 kV. Diamond nanoparticles in this process were shown to be, first of all, a strong structure former. The structure of the coating was more even and monocrystalline (see Figure 2.2) and its hardness was higher. The studies of macro- and microdiffraction patterns supported the fine-crystalline structure of diamond particles and chromium in the coating. Any discontinuities, ruptures, cracks, or other defects were absent.

Chromium–diamond coatings applied on the friction surfaces of workpieces and mechanisms increase their wear resistance many times (Table 2.3). The greatest effect was achieved in coatings of multiedged nonresharpened tools (screw taps, reamers, multiflute drills, milling cutters, etc.). Plated press tools for ferrous and nonferrous metals, powders, plastics, and also for valves of highly loaded pipelines had a much greater wear resistance. It also appears promising to use ultradisperse diamond in electrochemical coatings with other metal matrices (nickel, copper, silver, cobalt, etc.).

Nanodiamond powder technology began to be rapidly developed in the mid-1980s. UDD is close to this class of materials by its characteristics. A large body of information on the positive effect of nanofillers on the mechanical properties of various composite materials, polymer composites included, appeared in the patent and technical literature. Still, in spite of UDD evidently being technically

TABLE 2.3 Results of tests of chromium–diamond-coated tools.

Type of Tool	Sample for Comparison	Test Conditions	Wear Resistance Increase Coefficient
Saws	Series-produced	Cutting of: Rods 2″ × 4″ steel 1010	8.5
		Plates 1.4″ × 4″ stainless steel 316L	9.2
End mills *d* 1/4″ 6061 and 3/4″ steel 1018	Standard	Aluminum	8–15
Facing tools	Standard		5
Roughing mills			2
Finishing mills			2
Screw taps with nanodiamonds	Standard	Tapping nuts (steel 4140)	1.9
Screw taps	Standard	Tapping nuts M20–M27 (steels 10, 35, 20G2R)	1.3–2
Flat files (GOST 1465-80)	Standard	Workpieces from steel 12Kh18N9 and titanium alloy VT 14	2–3
Special screw taps M1 to M6	Standard	Titanium alloy VT 14	1.2
Drill bits M5 (fast-cutting steel R6)		Moulding material AG-4	2.3
Screw taps M4		Moulding material AG-4	2.0
Screw taps M20 × 0.75 (GOST 3266-81)	Standard	Steel 12Kh18N10T	1.5
Dental drills	Standard	Sheet glass, 3.2 mm	2.8
Aluminum friction discs	Non-coated	Sea water	28
Friction pairs of various configurations	Non-coated	(*T* up to 600°C)	1.5–5
Sealing surfaces of saddle and wedge of pipeline gate-valve ZKS 160 *d* 150	Non-coated	air	40

attractive, work on its applications as a disperse filler of polymer composites has been sporadic.

Polymers containing a nanodiamond powder filler find wide use. Nanodiamond powder fillers are added into polymers to enhance their strength and increase their elasticity modulus. These effects depend on the nature of the polymer and filler, their interaction, and on how discrete the filler particles are. The effect of strength increase is the most pronounced at the addition of highly disperse fillers to elastomers. In the case of amorphous plastics, the effect of the elasticity modulus increase predominates.

Of significant interest is the use of nanodiamond powders for strengthening polymer materials. Nanopowders of oxides obtained from clay are used for these purposes at present. In commercial production of nanopowders by detonation the cost of nanodiamond powders and nanooxides obtained from clay becomes commensurate. That is, there are almost no obstacles of economic character for broad introduction of diamond nanopowders.
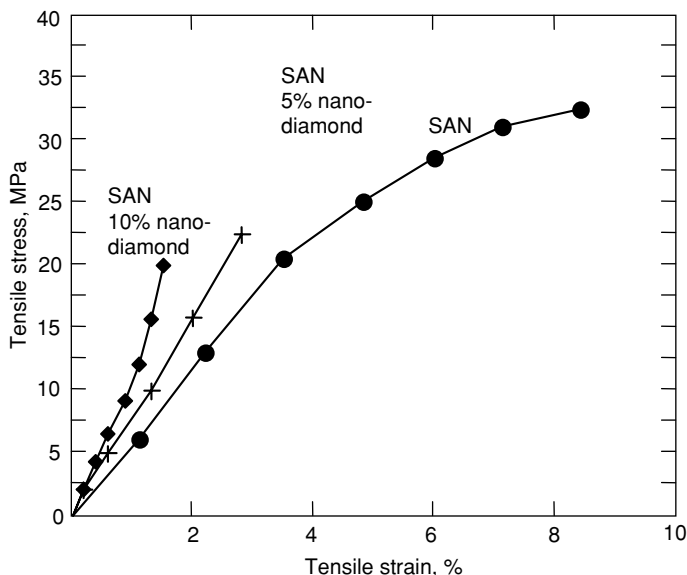
FIGURE 2.3. Deformation curves for styrene acrylonitrile copolymer (SAN) and its mixtures with nanodiamonds.

This work studied the mechanical characteristics of amorphous plastic styrene acrylonitrile copolymer (SAN). Nanodiamond powder particles (2.5, 5, and 10%) were added to copolymer granules and mixed in a microextruder-type mixer (auger diameter, 9 mm; 2 rpm, 200°C, mixing time 5 min). Samples of the mixture as extrudates were tested at room temperature on an Instron testing machine.

Figure 2.3 shows deformation curves plotted in tensile strain versus tensile stress coordinates. The endpoints on the curves conform to the time of sample rupture with respective stress and strain. The elasticity modulus of the samples was calculated by the tangent of the angle of slope of the initial segments of the deformation curves. The deformation curves of filled SAN are characteristic of plastics with brittle failure. Nonfilled SAN exhibits considerable deformations. As seen in Figure 2.3 and Table 2.4, addition of up to 10% diamond carbon to SAN

TABLE 2.4 Effect of nanodiamond powders on the mechanical properties of polymer materials.

Sample	Elasticity Modulus, MPa	Modulus of Rupture, MPa	Elongation at Rupture, %
SAN	550	42 max 50 min 38	10
SAN + 5% C	800	23 max 31 min 19	5
SAN + 10% C	1100	20 max 33 min 14	3
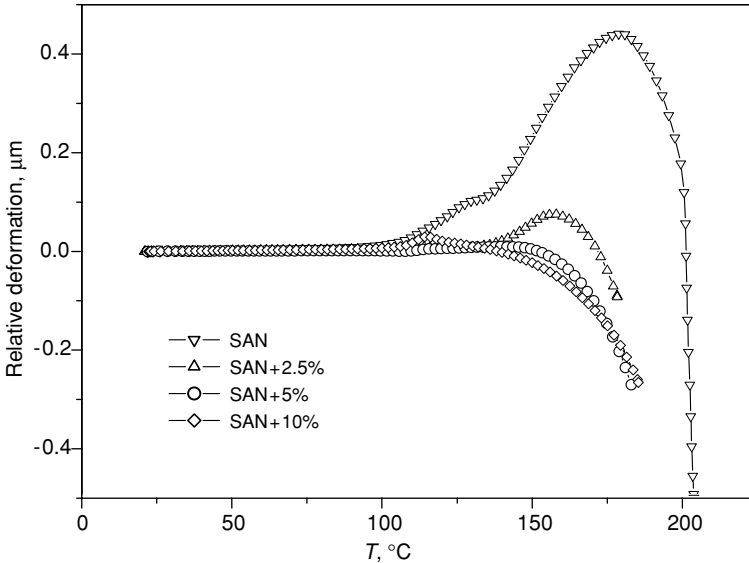
FIGURE 2.4. Thermomechanical curves of SAN composites filled with diamond nanoparticles.

leads to a significant decrease of the tensile strain from 10 to 3% and a decrease of strength from 42 to 20 MPa. At the same time, the initial elasticity modulus (E) of the material markedly increases proportionally to the concentration of the filler. Herewith, modulus E increases almost proportionally to the content of the filler from 550 MPa for pure SAN up to 1100 MPa for a composite with a 10% filler. The increase of modulus E is due to the presence of rigid diamond-powder particles in the composite.

The thermomechanical studies on a DTMD instrument, that is, studies of the relative deformation (δ) of the sample at the application of a small load ($\sim$1.5 g/cm³), showed that $\delta \approx 0$ in the temperature range conforming to the solid state. At the vitrification temperature $T_v \approx 110°C$ for initial SAN, the deformation increases up to the fluidity temperature $T_f \approx 170°C$, after which the deformation decreases due to the transition to a fluid state. Addition of up to 10% nanodiamond powder particles to SAN decreases the deformability of the material, but has almost no effect on its T_v and T_f (Figure 2.4).

Dynamic small-amplitude deformation tests using a torsion pendulum at a frequency of 25–27 Hz within the temperature range of 25–160°C showed that at room temperature the dynamic modulus of elasticity (G') weakly rose as the content of diamond powder in the composite was increased up to 10%. However, at a concentration of 2.5%, G' rapidly increased $\sim$1.8-fold (Figure 2.5).

The temperature-dependence of G' and the tangent of the angle of mechanical losses tan δ (Figure 2.6) demonstrates a sharp decrease of G' and the passage of tan δ through a maximum at the vitrification temperature studied. Herewith,
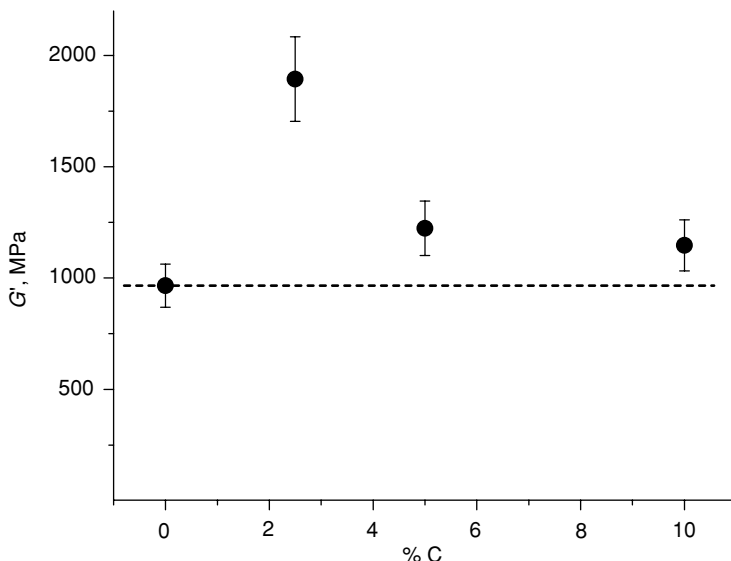
FIGURE 2.5. Concentration dependence of the elasticity modulus of SAN composites with nanodiamonds.

within the range of 140–150°C (i.e., above the T_v of the composites), an additional relaxation region is revealed at the introduction of a nanodiamond powder filler.

These results show that small additions of diamond nanopowders to thermoplastics can be useful for solving the essential problem of increasing the elasticity modulus of polymers.

In addition, the following interesting results were obtained under laboratory conditions.

1. Upon addition of 3% UDD to polytetrafluoroethylene its wear resistance increased almost 30-fold at an insignificant increase of the friction coefficient.
2. Upon addition of UDD to hard rubbers their processability was improved (they were better milled) and the major physicochemical parameters were noticeably increased (rupture strength, tear resistance, resistance to multiple tension, abrasion resistance).

Thus, UDD can be used in polymer composites as active filler and potent structure former increasing their strength, wear resistance, and heat resistance. This is due to record values of specific surface and, therefore, surface energy; the presence of surface functional groups; and high heat conduction. Also, owing to the sphericity of its particles UDD plays the role of dry lubricant decreasing the friction coefficient.

The use of nanodiamond particles not only at the stage of fabrication of items, but also at the stage of polymer synthesis could lead to unexpected positive effects. Of practical importance, first of all, can be the following directions.
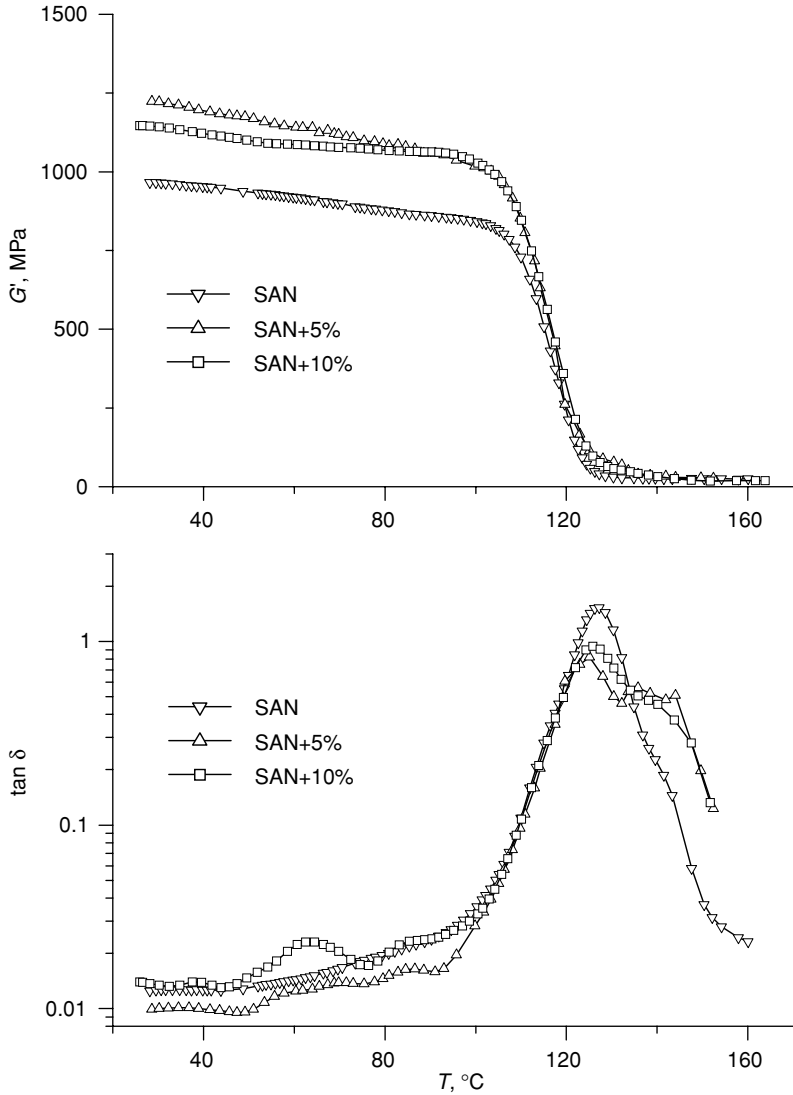
FIGURE 2.6. Temperature-dependences of G' and $\tan\delta$ of SAN composites with diamond nanoparticles.

1. Development of construction polymer composites with improved tribomechanical characteristics (wear, friction)
2. Modification of consumer properties of polymers (heat conduction, resistance to aggressive media, etc.)
3. Development of technologies of applying protective polymer coatings with embedded diamond nanoparticles

Ultrasmall size of primary particles, specificity of structure formation processes, extremely high dispersity and specific surface, coordination unsaturation of surface atoms of carbon, and the presence of functional groupings on them, all these significantly distinguish detonation diamonds from natural diamonds and static-synthesis diamonds. As the detonation method of UDD synthesis developed, it became clear that ultradisperse diamonds could have not only traditional but also absolutely new applications.

Thus, for carbon diamond-containing products obtained by detonation synthesis and purified from only metal particles, such a field was oils and technological lubricants [11]. Well back in the 1980s, it was found that addition of only 0.1–0.3% of this product to oils improved their antifriction and antiwear properties. Studies of the properties of dispersions of ultradisperse diamond/graphite (UDDG) material in lubricating oils, carried out at that time, made it possible to develop a technology of UDDG concentrates in I-40A, I-50A, M-$6_3/10_g$ oils. These concentrates are used as additives to industrial and motor oils to improve their tribotechnical characteristics. Thus, for steel–iron and steel–bronze coupled pairs the friction coefficient decreased 2–3-fold and the wear of contact surfaces was 1.5–5 times lower. The temperature in the contact zone was found to decrease. The use of these antifriction additives to motor oils leads to faster green run of engines, increased service life, and fuel economy.

Many technological lubricants and solid lubricating coatings traditionally use graphite and molybdenum disulfide as additives. Addition of small-size solid particles into lubricants improves lubricity. The size of solid particles should not exceed 1–2 microns. UDD and diamond-containing carbon products of detonation synthesis conform to this requirement. The efficiency of using UDDG additives in this direction was confirmed during their introduction into process lubricants for cold die forging and drawing of high-alloy steels and alloys. This was also confirmed at their introduction into process lubricants for hot pressing of aluminum and titanium alloys in order to prevent the adhesion of deformed metal to the tool and scoring.

The tests show that addition of UDD and UDD-based materials to oils and lubricants is multifunctional. The major difficulty impeding the research in this direction is due to the insufficient sedimentation stability of UDD oil suspensions. If and when this problem is solved, a promising application of UDD suspension is its use in motor oil as an additive to fuels for two-stroke gasoline engines. In this case, the additives can improve the lubricating characteristics of fuel and, at the same time, increase its calorific value. RFNC–VNIITF carries out research on the separation of ultradisperse diamond powder into nanometer-range fractions, capable of yielding stable suspensions in various liquids.

Ultradisperse detonation diamonds can also be considered as promising sorbents. Positive properties characterizing UDD in this respect are its high strength (hardness), availability of micropores, considerably developed mesoporous and macroporous structures, and chemical and thermal stability. These properties suggest a successful use of UDD as catalyst or sorbent carrier, working under very severe conditions (high temperatures and pressure, aggressive media, etc.). UDD

can also be used as adsorbent for extracting precious metals—Au, Pd, Rh, Os etc.—from industrial wastes.

2.4. Conclusion

Thus, synthetic detonation diamond is a promising material that can be used in many fields. Of special interest are its applications in composite materials both with metal and polymer matrix. Commercial production of UDD has been developed, and it is synthesized on a scale sufficient for particular industries.

References

[1] Sakovich, G.V. (2003). In *Proc. Int. Symposium "Detonation Nanodiamonds: Technology, Properties and Applications,"* July 7–9, St. Petersburg, Russia.

[2] Vozniakovskii, A.P. (2003). In *Proc. Int. Symposium "Detonation Nanodiamonds: Technology, Properties and Applications,"* July 7–9, St. Petersburg, Russia.

[3] Chuhaeva, S.I. (2003). In *Proc. Int. Symposiuim "Detonation Nanodiamonds: Technology, Properties and Applications,"* July 7–9, St. Petersburg, Russia.

[4] Gubin, S.A., Odintsov, V.V., and Pepekin, V.V. (1984). *Khim. Fizika*, **5**:1 (in Russian).

[5] Gubin, S.A., Odintsov, V.V., and Pepekin, V.V. (1984). *Khim. Fizika*, **3**:5 (in Russian).

[6] Savvakin, G.I., Serdyuk, V.A., and Trefilov, V.N. (1983). *Dokl. Akad. Nauk SSSR*, **270**:2 (in Russian).

[7] Savvakin, G.I., Trefilov, V.N., and Fenochka, B.V. (1985). *Dokl. Akad. Nauk SSSR*, **282**:5 (in Russian).

[8] Lyamkin, A.I., Petrov, E.A., and Ershov, A.P. et al. (1988). *Dokl. Akad. Nauk SSSR*, **302**:3 (in Russian).

[9] Savvakin, G.I. and Trefilov, V.N. (1991). *Dokl. Akad. Nauk SSSR*, **321**:1 (in Russian).

[10] Petrov, E.A., Sakovich, G.V., and Brylyakov, P.M. (1990). *Dokl. Akad. Nauk SSSR*, **313**:4 (in Russian).

[11] Chepovetsky, I.Kh. and Budnik, S.N. (1993). *Sverkhtverd. Materialy*, **3**:48 (in Russian).

3
Diamondoids as Molecular Building Blocks for Nanotechnology

HAMID RAMEZANI AND G. ALI MANSOORI

3.1. Introduction

Two different methods are envisioned for nanotechnology to build nanostructured systems, components, and materials: One method is named the "top-down" approach and the other method is named the "bottom-up" approach [1,2]. In the top-down approach the idea is to miniaturize the macroscopic structures, components, and systems towards a nanoscale of the same. In the bottom-up approach the atoms and molecules constituting the building blocks are the starting point to build the desired nanostructure [3].

Various illustrations are available in the literature depicting the comparison of top-down and bottom-up approaches [2]. In the top-down method a macro-sized material is reduced in size to reach the nanoscale dimensions. The photolithography used in the semiconductor industry is one example of the top-down approach. In the bottom-up strategy, we need to start with MBBs and assemble them to build a nanostructured material.

3.2. Molecular Building Blocks (MBBs) in Nanotechnology

The most fundamentally important aspect of the bottom-up approach is that the nanoscale building blocks, because of their sizes of a few nms, impart to the nanostructures created from them new and possibly preferred properties and characteristics heretofore unavailable in conventional materials and devices. The band gap of nanometer-scale semiconductor structures increases as the size of the microstructure decreases, raising expectations for many possible optical and photonic applications. Considering that nanoparticles have much higher specific surface areas, thus in their assembled forms there are large areas of interfaces. One needs to know in detail not only the structures of these interfaces, but also their local chemistries and the effects of segregation and interaction among molecular building blocks (MBBs) and also between MBBs and their surroundings. Knowledge on means to control nanostructure sizes, size distributions, compositions, and assemblies are important aspects of nanoscience and nanotechnology.

The building blocks of all materials in any phase are atoms and molecules. All objects are comprised of atoms and molecules, and their arrangement and how they interact with one another define the properties of an object. Nanotechnology is the engineered manipulation of atoms and molecules in a user-defined and repeatable manner to build objects with certain desired properties. To achieve this goal a number of molecules are identified as the appropriate building blocks of nanotechnology. These nanosize building blocks are intermediate-size systems lying between atoms and small molecules and microscopic and macroscopic systems. These building blocks contain a limited and countable number of atoms. They can be synthesized and designed atom by atom. They constitute the means of our entry into new realms of nanoscience and nanotechnology.

The controlled and directed organization of molecular building blocks and their subsequent assembly into nanostructures is one fundamental theme of bottom-up nanotechnology. Such an organization can be in the form of association, aggregation, arrangement, or synthesis of MBBs through van der Waals forces, hydrogen bonding, attractive intermolecular polar interactions, electrostatic interactions, hydrophobic effects, and so on. The ultimate goal of assemblies of nanoscale molecular building blocks is to create nanostructures with improved properties and functionality heretofore unavailable with conventional materials and devices. Fabrication of nanostructures demands appropriate methods and molecular building blocks.

The applications of MBBs would enable the practitioner of nanotechnology to design and build systems on a nanometer scale. These promising nanotechnology concepts have far-reaching implications (from mechanical to chemical processes, from electronic components to ultrasensitive sensors, from medical applications to energy systems, and from pharmaceutical to agricultural and food chain) and will have an impact on every aspect of our future.

Through the controlled and directed assembly of nanoscale molecular building blocks one should be able to alter and engineer materials with desired properties. For example, ceramics and metals produced through controlled consolidation of their MBBs have been shown to possess properties substantially improved and different from materials with coarse microstructures. Such different and improved properties include greater hardness and higher yield strength in the case of metals and better ductility in the case of ceramic materials [4,5].

It should be pointed out that MBBs with three linking groups, such as graphite, could only produce planar or tubular structures. MBBs with four linking groups can form three-dimensional diamond lattices. MBBs with five linking groups can create three-dimensional solids and hexagonal planes. The ultimate present possibility is MBBs with six linking groups. Adamantane (see Figure 3.1) and buckyball (C_{60}), are of the latter category which can construct cubic structures [5,6]. Such MBBs can have many applications in nanotechnology and they are of major interest in designing shape-targeted nanostructures, nanodevices, molecular machines [4–7], nanorobots, and synthesis of supramolecules with manipulated architectures. A far-reaching example of the possibility of using diamondoids is in the conceptual and exploratory design of an artificial red blood cell, called
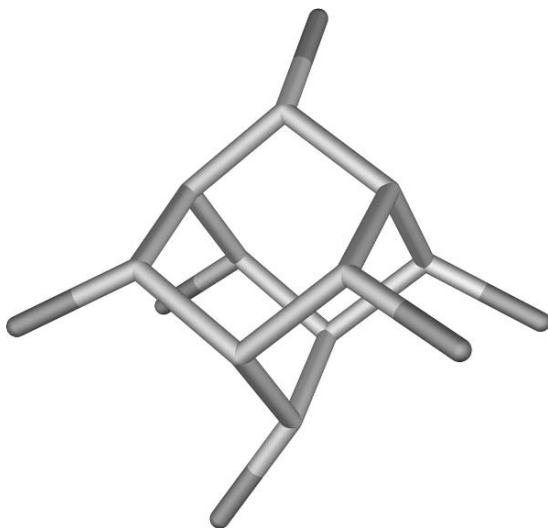
FIGURE 3.1. Six linking groups of adamantane.

Respirocyte, which would have the ability to transfer respiratory gases and glucose [8–10].

In general nanotechnology, molecular building blocks are distinguished for their unique properties. They include, for example, graphite, fullerene molecules made of a number of carbon atoms (C_{60}, C_{70}, C_{76}, etc.), carbon nanotubes, nanowires, nanocrystals, amino acids, and diamondoids [11]. All these molecular building blocks are candidates for various applications in nanotechnology.

The diamondoid family of compounds is one of the best candidates for molecular building blocks to construct organic nanostructures compared to other MBBs known so far [4–7]. Diamondoids offer the possibility of producing a variety of nanostructural shapes. They have quite high strength, toughness, and stiffness compared to other known MBBs. These are tetrahedrally symmetric stiff hydrocarbons that provide an excellent building block for positional (or robotic) assembly as well as for self-assembly. In fact, over 20,000 variants of diamondoids have been identified and synthesized and even more are possible [4–6], providing a rich and well-studied set of MBBs. Diamondoids have recently been named as the building blocks for nanotechnology [12].

3.2.1. Diamondoid Molecules

Diamondoid molecules are cagelike saturated hydrocarbons. These molecules are ringed compounds, that have a diamondlike structure consisting of a number of six-member carbon rings fused together. They are called "diamondoid" because they can be assumed as repeating units of the diamond. The most famous member of this group, adamantane, is a tricyclic saturated hydrocarbon (tricyclo [3.3.1.1]decane).
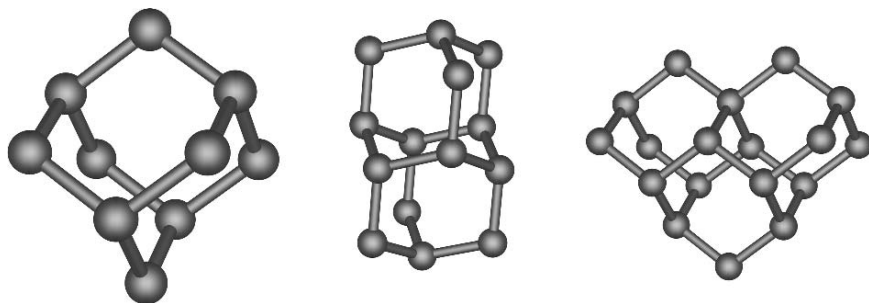
FIGURE 3.2. Molecular structures of adamantane, diamantane, and trimantane, the smaller diamondoids, with chemical formulas $C_{10}H_{16}$, $C_{14}H_{20}$, and $C_{18}H_{24}$, respectively.

The simplest of these polycyclic diamondoids is adamantane, followed by its homologues diamantane, tria-, tetra-, penta- and hexamantane. In Figure 3.2, adamantane ($C_{10}H_{16}$), diamantane ($C_{14}H_{20}$), and triamantane ($C_{18}H_{24}$), the smaller diamondoid molecules, with the general chemical formula $C_{4n+6}H_{4n+12}$ are reported. These are lower adamantologues, as each has only one isomer. Depending on the spatial arrangement of the adamantane units, higher polymantanes ($n \geq 4$) can have numerous isomers and nonisomeric equivalents. There are three possible tetramantanes, all of which are isomeric, respectively, iso-, anti-, and skew-tetramantane as depicted in Figure 3.3 Anti- and skew-tetramantanes each possess two quaternary carbon atoms, whereas iso-tetramantane has three. There are seven possible pentamantanes, six being isomeric ($C_{26}H_{32}$) obeying the molecular formula of the homologous series and one nonisomeric ($C_{25}H_{30}$). For hexamantane, there are 24 possible structures: among them, 17 are regular cata-condensed isomers with the chemical formula ($C_{30}H_{36}$), six are irregular cata-condensed isomers with the chemical formula ($C_{29}H_{34}$), and one is peri-condensed with the chemical formula ($C_{26}H_{30}$).
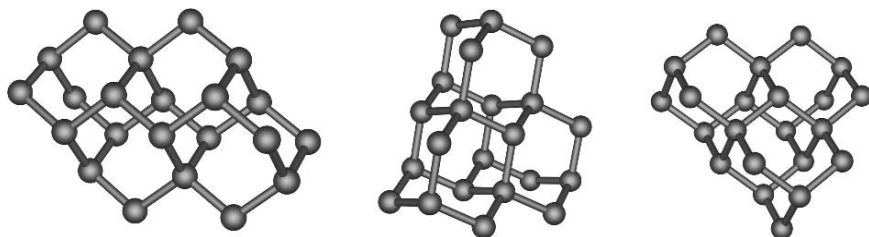
FIGURE 3.3. There are three possible tetramantanes all of which are isomeric, respectively, from left to right as anti-, iso-, and skew-tetramantane. Anti- and skew-tetramantanes each possess two quaternary carbon atoms, whereas iso-tetramantane has three quaternary carbon atoms. The number of diamondoid isomers increases appreciably after tetramantane.

When in solid state, diamondoids melt at much higher temperatures than other hydrocarbon molecules with the same number of carbon atoms in their structure. Inasmuch as they also possess low strain energy they are more stable and stiff, and resemble diamond in a broad sense. They contain dense, three-dimensional networks of covalent bonds, formed chiefly from first and second row atoms with a valence of three or more. Many of the diamondoids possess structures rich in tetrahedrally coordinated carbon. They are materials with a superior strength-to-weight ratio, as much as 100 to 250 times as strong as titanium, but much lighter in weight. In addition to applications in nanotechnology they are being considered to build stronger, but lighter, rocket and other space components and a variety of other earthbound articles for which the combination of weight and strength is a consideration [13,14].

It has been found that adamantane crystallizes in a face-centered cubic lattice, which is extremely unusual for an organic compound. The molecule therefore should be completely free from both angle and torsional strain, making it an excellent candidate for various nanotechnology applications. At the beginning of growth, crystals of adamantane show only cubic and octahedral faces. The effects of this unusual structure upon physical properties are striking (interested readers are referred to [15] for a further detailed description of thermodynamic and crystalline properties of adamantane). Adamantane is one of the highest melting hydrocarbons known (m.p. ∼266–268°C), yet it sublimes easily, even at atmospheric pressure and room temperature. Because of this, it can have interesting applications in nanotechnology such as possibilities for application in molding and cavity formation.

Diamondoids can be divided into two major clusters based upon their size: lower diamondoids (1–2 nm in diameter) and higher diamondoids (>2 nm in diameter).

Adamantane and other light diamondoids are constituents of petroleum and they deposit in natural gas and petroleum crude oil pipelines causing fouling [13,16,17]. Adamantane was originally discovered and isolated from Czechoslovakian petroleum in 1933. The isolated substance was named adamantane, from the Greek for diamond. This name was chosen because it has the same structure as the diamond lattice, highly symmetrical and strain free. Actually their carbon atom structure can be superimposed upon a diamond lattice. It is generally accompanied by small amounts of alkylated adamantane: 2-methyl-; 1-ethyl-; and probably 1-methyl-; 1,3-dimethyl; and others.

The unique structure of adamantane is reflected in its highly unusual physical and chemical properties, which can have many applications in nanotechnology, as do the diamond nanosized crystals, with a number of differences. The carbon skeleton of adamantane comprises a cage structure, which may be used for encapsulation of other compounds, such as drugs for drug delivery. Because of this, adamantane and other diamondoids are commonly known as cage hydrocarbons. In a broader sense they may be described as saturated, polycyclic, cagelike hydrocarbons.

Diamantane, triamantane, and their alkyl-substituted compounds, just as adamantane, are also present in certain petroleum crude oils. Their concentrations in crude oils are generally lower than that of adamantane and its alkyl-substituted

compounds. In rare cases, tetra-, penta-, and hexamantanes are also found in petroleum crude oils. Their diamondlike rigidity and strength make them ideal for molecular building blocks. Research along this line could have a significant impact on practical applications of diamondoids in nanotechnology. Vasquez et al. [13,16] succeeded in identifying diamondoids in petroleum crude oils, measuring their concentrations and separating them from petroleum. Recently, Dahl et al. have identified higher diamondoids, from $n = 4$–11, and their isomers in certain petroleum fluids [12].

Diamondoids show unique properties due to their exceptional atomic arrangements. These compounds are chemically and thermally stable and strain free. These characteristics make them have a high melting point in comparison with other hydrocarbons. For instance, the m.p. of adamantane is estimated to be in the range of 266–268°C and of diamantane in the range of 241–243°C. Such high melting points of diamondoids have caused fouling in oil wells, transport pipelines, and processing equipment during production, transportation, and processing of diamondoid-containing petroleum crude oil and natural gas [13,16].

One may exploit the large differences in melting points of diamondoids and other petroleum fractions for isolation of diamondoids from petroleum [14]. Many of the diamondoids can be brought to macroscopic crystalline forms with some special properties. For example, in its crystalline lattice, pyramidal [1(2,3)4]pentamantane has a large void in comparison with similar crystals. Although it has a diamondlike macroscopic structure, it possesses weak noncovalent intermolecular van der Waals attractive forces involved in forming a crystalline lattice [12,18].

The crystalline structure of 1,3,5,7-tetracarboxy adamantane is formed via carboxyl hydrogen bonds of each molecule with four tetrahedral nearest neighbors. The similar structure in 1,3,5,7-tetraiodoadamantane crystal would be formed by I...I interactions. In 1,3,5,7-tetrahydroxyadamantane, the hydrogen bonds of hydroxyl groups produce a crystalline structure similar to inorganic compounds, such as a CsCl, lattice [19] (see Figure 3.4).

Presence of chirality is another important feature in many derivatives of diamondoids. Such chirality among the unsubstituted diamondoids occurs first of all in tetramantane [12].

The vast number of structural isomers and stereoisomers is another property of diamondoids. For instance, octamantane possesses hundreds of isomers in five molecular weight classes. The octamantane class with formula $C_{34}H_{38}$ and molecular weight 446 has 18 chiral and achiral isomeric structures. Furthermore, there is unique and great geometric diversity with these isomers. For example, rod-shaped diamondoids (the shortest one of which is 1.0 nm), disc-shaped diamondoids, and screw-shaped ones (with different helical pitches and diameters) have been recognized [12].

Diamondoids possess great capability for derivatization. This matter is of importance in reaching suitable molecular geometries needed for molecular building blocks of nanotechnology. These molecules are substantially hydrophobic and their solubility in organic solvents is a function of that (adamantane solubility
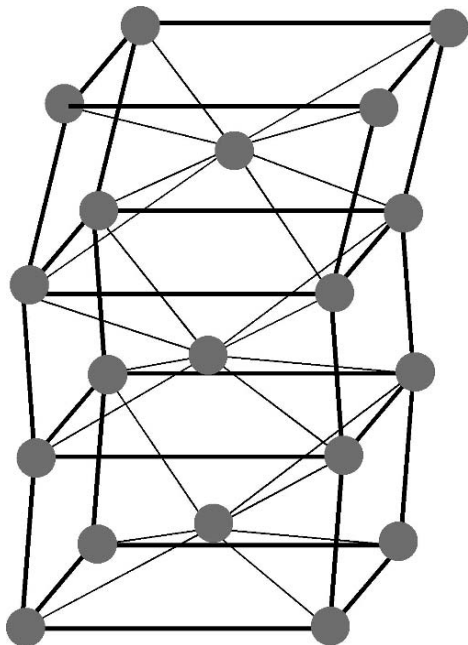
FIGURE 3.4. The quasi-cubic units of a crystalline network for 1,3,5,7-tetrahydroxyadamantane. Molecules have been shown as gray spheres and hydrogen bonds as solid linking lines [19].

in THF is higher than in other organic solvents [20]). Using derivatization, it is possible to alter their solubility. Functionalization by different groups can produce appropriate reactants for desired reactions.

The strain-free structures of diamondoids give them high molecular rigidity, which is quite important for a MBB. High density, low surface energy, and oxidation stability are some other preferred diamondoid properties as MBBs.

3.2.2. Synthesis of Diamondoids

Besides the natural gas and petroleum crude oils as the natural source for diamondoids one may produce lower diamondoids through Lewis acid-catalyzed rearrangement of hydrocarbons. Producing heavy diamondoids via synthetic method is not convenient because of their unique structural properties and especially their thermal stability. However, outstanding successes have been achieved in synthesis of adamantane and other lower-molecular-weight diamondoids. Adamantane was synthesized in 1941 for the first time, although the yield was very low [21,22]. Some new methods have been developed since that time and the yield has been increased to 60% [23]. Attempts to synthesize lower diamondoids (adamantane, diamantane, triamantane) have been successful through Lewis acid-catalyzed rearrangement but it is no longer a method of choice for synthesis of higher polymantanes [22]. However, synthesis of higher diamondoids is a challenging and complex process. As evidence, after numerous efforts the anti-isomer of tetramantane was

synthesized with only 10% yield [22]. The usage of zeolites as the catalyst in the synthesis of adamantane has been investigated and different types of zeolites have been tested for achieving better catalyst activity and selectivity in adamantane formation reactions [21]. Recently, Shibuya et al. have represented two convenient methods for synthesis of enantiomeric (optical antipode) adamantane derivatives [24].

3.3. General Applications of Diamondoids

Each successively higher diamondoid family shows increasing structural complexity and varieties of molecular geometries. Sui generis properties of diamondoids have provoked an extensive range of inquiries in different fields of science and technology. For example, they have been used as templates for crystallization of zeolite catalysts [25], the synthesis of high-temperature polymers [26], and in pharmacology.

In pharmacology, two adamantane derivatives, Amantadine (1-adamantaneamine hydrochloride) and Rimantadine (α-methyl-1-adamantane methylamine hydrochloride) have been well known because of their antiviral activity (Figure 3.5). The main indication of these drugs is prophylaxis and treatment of influenza A viral infections. They are also used in the treatment of Parkinsonism and inhibition of hepatitis C virus (HCV) [27]. Memantine (1-amino-3,5-dimethyladamantane) has been reported effective in slowing the progression of Alzheimer's disease [27].

Extensive investigations have been performed related to synthesis of new adamantane derivatives with better therapeutic actions and less adverse effects. For example, it has been proved that adamantylaminopyrimidines and -pyridines are strong stimulants of tumor necrosis factor-α (TNF-α) [28], and 1,6-diaminodiamantane possesses an antitumor and antibacterial activity [29]. Many derivatives of aminoadamantanes have antiviral activity and 3-(2-adamantyl) pyrolidines with two pharmacophoric amine groups have antiviral activity against influenza A virus [30].
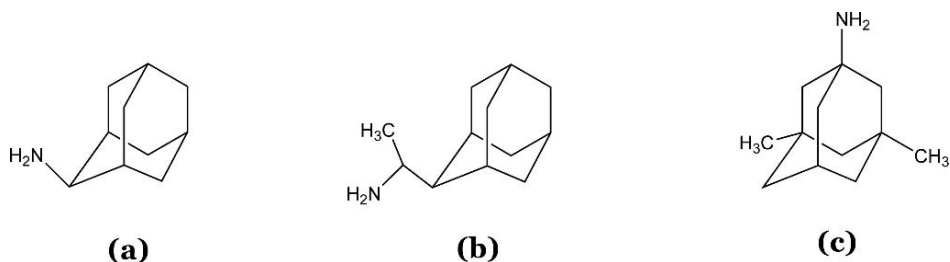
FIGURE 3.5. (a) Amantadine. (b) Rimantadine. (c) Memantine.

Some derivatives of adamantane with antagonist or agonist effects have also been synthesized. For instance, monocationic and dicationic adamantane derivatives block the α-amino-3-hydroxy-5-methylisoxazole-4-propionic acid (AMPA) and N-methyl-D-aspartate (NMDA) receptors [31–33] and also 5-hydroxytryptamine (5-HT3) receptors [34]. The monocationic and dicationic adamantane derivatives have been employed to investigate the topography of the channel binding sites of AMPA and NMDA receptors [32]. A dicationic adamantane derivative has been exploited as a selective and specific marker of the native AMPA receptor assembly to determine the distribution of AMPA receptors subtypes among populations of rat brain cells [31,33]. Other instances include antagonism of 5-HT3 and agonism of 5-HT4 receptors by aza(nor)adamantanes [35], P2X7 receptor antagonism by adamantane amides [36], antagonism of voltage-gated calcium channels and probably activation of γ-aminobutyric acid (GABA) receptors by an adamantane amine derivative that results in its anti-convulsive and antinociceptive actions [37], and inhibition of glucosylceramidase enzyme and glycolipid biosynthesis by a deoxynojirimycin-bearing adamantane derivative leading to strong anti-inflammatory and immunosuppressive activities [38].

Attaching some short peptidic sequences to adamantane makes it possible to design novel antagonists. The bradykinin antagonist is an example [39]. The adamantane-based peptidic bradykinin analogue was utilized in the structure–activity relationship (SAR) studies on the bradykinin receptors and showed a potent activity in inhibition of bradykinin-induced cytokine release and stimulation of histamine release [39]. In an attempt to design the β-turn peptide mimics, the aspartic acid and lysine were attached to each amine group of 1,3-diaminoadamantane in the form of an amide bond [40]. The said compound displayed some degrees of fibrinogen-GPIIB/IIIA antagonism [40].

3.3.1. Application of Diamondoids as MBBs

The importance of applications of diamondoids in nanotechnology is their potential role as MBBs. Diamondoids have noticeable electronic properties. In fact, they are H-terminated diamond and the only semiconductors that show a negative electron affinity [12].

Diamondoids may be used in self-assembly, positional assembly, nanofabrication, and many other important methods in nanotechnology. Although adamantane has been the subject of many research projects in the field of pharmacophore-based drug design, its application to nanoscale drug delivery and targeting systems is a matter of considerable importance. Furthermore, polymantanes have the potential to be utilized in the rational design of multifunctional drug systems and drug carriers. In host–guest chemistry there is plenty of room for working with diamondoids. The other potential application of diamondoids is in designing molecular capsules and nanocages for drug delivery.

Diamondoids, especially adamantane, its derivatives, and diamantane, can be used for improvement of thermal stability and other physicochemical properties of

FIGURE 3.6. (Left) 1,3-dichloro-5-(1-admantyl) benzene monomer and (Right) adamantyl-substituted poly(m-phenylene) which is shown to have a high degree of polymerization and stability decomposing at high temperatures of around 350°C [41].
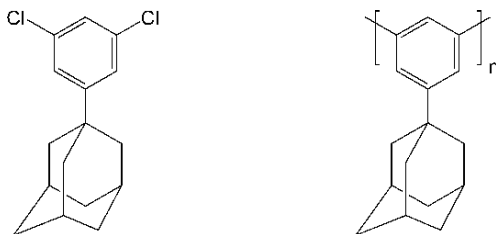
polymers and preparation of thermosetting resins that are stable at high temperatures. For example, diethynyl diamantane has been utilized for such an application [29]. As another example, adamantyl-substituted poly(m-phenylene) is synthesized starting with 1,3-dichloro- (1- adamantyl) benzene monomers (Figure 3.6) and it is shown to have a high degree of polymerization and stability, decomposing at a high temperature of around 350°C [41].

Diamantane-based polymers are synthesized because of their stiffness, chemical and thermal stability, high glass transition temperature, improved solubility in organic solvents, and retention of physical properties at high temperatures. Such improved properties result from the introduction of diamantane derivatives to their structures [42]. Polyamides are high-temperature polymers with a broad range of applications in different scientific and industrial fields. However, there are some problems with their processing because of poor solubility and lack of enough thermal stability retention [43]. Incorporation of 1,6- or 4,9-diamantylene groups into the polyamides would result in improved thermal stability and satisfactory retention of the storage modulus at temperatures above 350°C [42]. These characteristics, as well as improved viscosity and solubility in organic solvents, are specific to polyamides derived from 4,9-bis(4-aminophenyl)diamantane and also 4,9-bis[4-(4-aminophenoxy)phenyl]diamantane (Figure 3.7) [42,43].

Star polymers are another class of polymers based on diamondoids with interesting rheological and physical properties [44]. For example, the tetra-functionalized adamantane cores have been employed as initiators in the atom transfer radical polymerization (ATRP) method applied to styrene. Various acrylate monomers and starlike polymers have been prepared from rigid and stable adamantane cores with a wide range of molecular weights [44].

In another study, introducing adamantyl group to the poly (etherimide) structure caused polymer glass transition temperature, Tg, and solubility enhancement in some solvents such as chloroform and other aprotic solvents [45].

Introducing bulky side chains that contain adamantyl group to the poly(p-phenylenevinylene; PPV), a semiconducting conjugated polymer, elicits diminution of interchain interactions and thus, aggregation quenching would be reduced and polymer photoluminescence properties would be improved [46,47].

Substitution of the bulky adamantyl group on the C(10) position of the biliverdin pigment structure, would lead to the distortion of helical conformation and hence, the pigment color would shift from blue to red [48].

(a)

(b)

Ar =
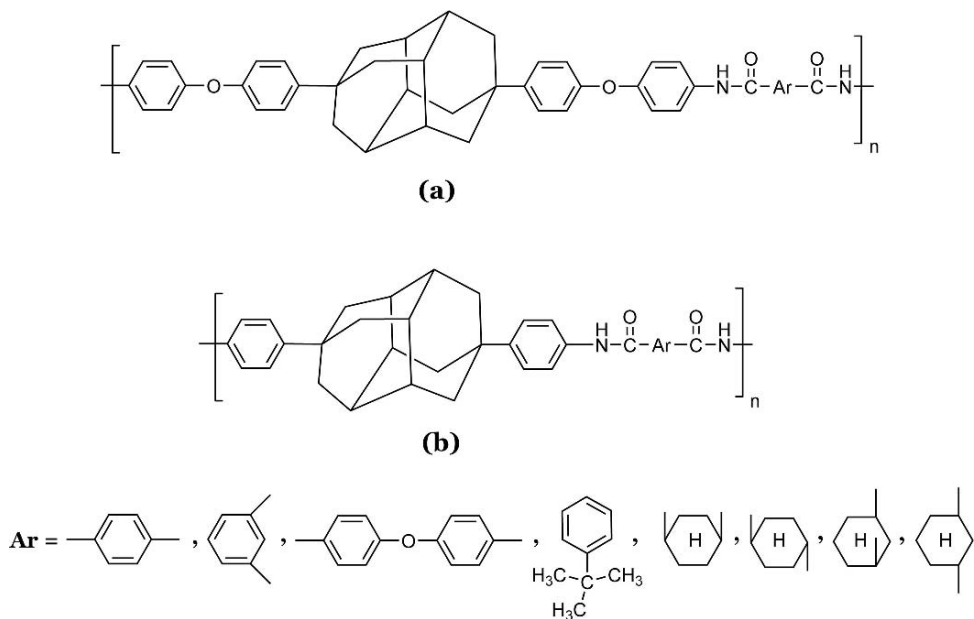
FIGURE 3.7. Diamantane-based polyamides; (a) derived from 4,9-bis[4-(4-aminophenoxy) phenyl]diamantane and (b) derived from 4,9-bis(4-aminophenyl)diamantane [42,43].

Adamantane can be used in molecular studies and preparation of fluorescent molecular probes [49]. Because of its incomparable geometric structure, the adamantane core can impede interactions of fluorophore groups and self-quenching would diminish due to steric hindrance. Hence, mutual quenching would be diminished and it becomes possible to introduce several fluorescent groups to the same molecular probe in order to amplify the signals. Figure 3.8 shows the general scheme of an adamantane molecule with three fluorophore groups (F) and a targeting group for attachment of biomolecules. Such a molecular probe can be very useful in DNA probing and especially in fluorescent in situ hybridization (FISH) diagnostics [50].
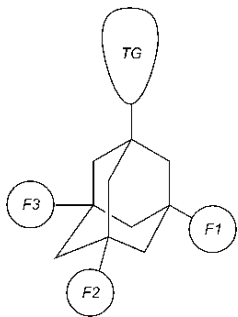
FIGURE 3.8. Schematic drawing showing adamantane as a molecular probe with three fluorophore groups (F) and a targeting part (TG) for specific molecular recognition [50].

   Due to their demanding synthesis, diamondoids are helpful models to study structure–activity relationships in carbocations and radicals, to develop empirical computational methods for hydrocarbons, and to investigate orientational disorders in molecular crystals as well [15,22].

3.3.2. Diamondoids for Drug Delivery and Drug Targeting

Adamantane derivatives can be employed as carriers for drug delivery and targeting systems. Due to their high lipophilicity, attachment of such groups to drugs with low hydrophobicity would lead to an increment of drug solubility in lipidic membranes and thus their uptake will increase. Furthermore, favorable geometric properties of adamantane and other diamondoids make it possible to introduce to them several functional groups, consisting of drug, targeting part, linker, and the like, without undesirable interactions between such groups. In fact, adamantane derivatives can act as a central core for such drug systems. Short peptidic sequences bound to adamantane will provide binding sites for connection of macromolecular drugs (such as proteins, nucleic acids, lipids, polysaccharides, etc.) as well as small molecules. Hence, short amino acid sequences can have linker roles, which are capable of drug release in the target site.

   There are some successful instances of adamantyl moiety application for brain delivery of drugs [51]. For this purpose, 1-adamantyl moiety was attached to several AZT (Azidothymidine) drugs via an ester spacer and these prodrugs could pass the blood–brain barrier (BBB) easily. The drug concentration after using such a lipophilized prodrug was measured in the brain tissue and showed an increase of 7–18 folds in comparison with the same AZT drug without the adamantane vector. The ester bond would be cleaved after passing BBB by brain tissue esterases. However, the ester link should be resistant to the plasma esterases. Inasmuch as the site of action for Memantine is the central nervous system (CNS) and it has CNS affinity and further, Amantadine and Rimantadine can penetrate to the CNS and cause some adverse effects, it has been proposed that adamantane might have an intimate CNS tropism [51]. Furthermore, because half-life of the two latter drugs in the bloodstream is long (12–18 hours for Amantadine and 24–36 hours for Rimantadine in young adults), utilization of adamantane derivative carriers can probably prolong drug presence time in blood circulation. However, related data for each system should be obtained. Ultimately, it is of importance to note that adamantane has appeared as a successful brain-directing drug carrier.

   Another example of adamantane utilization for brain delivery of poorly absorbed drugs is the conjugation of a Leu-enkephalin analogue, [D-Ala2] Leu-enkephalin, with a 1-adamantane moiety [52]. The antinociceptive effect of Leu-enkephalin disappears when it is administered peripherally because it would be decomposed by proteolytic enzymes and cannot penetrate into the CNS. It is feasible to conjugate the [D-Ala2] Leu-enkephalin with a 1-adamantane vector via an ester, amide, or a carbamate linkage in order to enhance the drug lipophilicity and thus facilitate its delivery across the blood–brain barrier [52]. The adamantane-conjugated [D-Ala2]

R
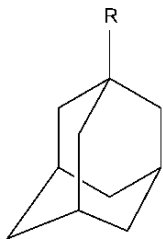
FIGURE 3.9. The adamantane-conjugated [D-Ala2] Leu-enkephalin prodrugs [52].

(I) R = NH₂-Tyr-(D-Ala)-Gly-Phe-Leu-CO-O-
(II) R = NH₂-Tyr-(D-Ala)-Gly-Phe-Leu-CO-NH

Leu-enkephalin prodrugs (Figure 3.9) are highly lipophilic and show a significant antinociceptive effect because of their ability to cross the BBB [52]. These results suggest that the adamantane moiety is a promising brain-directing drug vector providing a high lipophilicity, low toxicity, and high BBB permeability for sensitive and poorly absorbed drugs [52,53].

Adamantane has been also used for lipidic nucleic acid synthesis as a hydrophobic group [54]. Two major problems in gene delivery are nucleic acids low uptake by cells and instability in the blood medium. Probably, an increase in lipophilicity using hydrophobic groups would lead to improvement of uptake and an increase in intracellular concentration of nucleic acids [54]. In this case, an amide linker is used to attach the adamantane derivatives to a nucleic acid sequence [54]. Such a nucleic acid derivatization has no significant effect on hybridization with RNA as the target. Lipidic nucleic acids possessing adamantane derivative groups may be also exploited for gene delivery.

Recently, synthesis of a polyamine adamantane derivative has been reported which has a special affinity for binding to DNA major grooves [55]. Such DNA selectivity of this ligand is one of its outstanding features. It should be pointed out that most of the polyamines have an affinity for binding to RNA and thus making RNA stabilized. This positive-nitrogen-bearing ligand has more of a tendency to establish hydrophobic interaction with deeper DNA grooves due to its size and steric properties. Such an exclusive behavior occurs because this ligand fits better into the DNA major grooves. This bulky ligand size works the same as the zinc-finger protein, which also binds to DNA major grooves.

Higher affinity of adamantane-bearing ligands to DNA, instead of RNA, probably arises from the presence of adamantane and leads to DNA stabilization. Adamantane is actually the reason for lipophilicity increase as well as DNA stabilization of such ligands. This property may be exploited for using such ligands as stabilizing carriers in gene delivery. Furthermore, the ligand/groove size-based targeting may also be possible with less specificity by changing the bulk and conformation of the ligand.

Polymers conjugated with 1-adamantyl moieties as lipophilic pendent groups can be utilized to design nanoparticulate drug delivery systems. Polymer #1 (Figure 3.10), which is synthesized by homopolymerization of ethyladamantyl malolactonate, can be employed as a highly hydrophobic block to construct
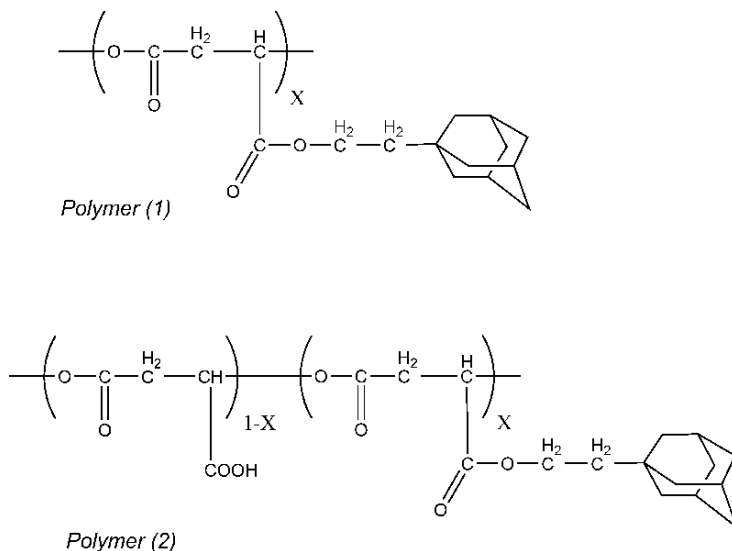
Polymer (1)

Polymer (2)

FIGURE 3.10. Polymer (1): poly (ethyladamantyl β-malate) and polymer (2): poly(β-malic acid-co-ethyladamantyl β-malate) [56].

polymeric drug carriers [56]. In contrast, polymer #2 (Figure 3.10), which is synthesized by copolymerization of polymer #1 with benzyl malolactonate, is water soluble. Its lateral carboxylic acid functions can be used to bind biologically active molecules in order to achieve targeting as well. These polymers may be also used to produce pH-dependant hydrogels and intelligent polymeric systems [56].

3.4. DNA-Directed Assembly and DNA–Adamantane–Amino acid Nanostructures

Due to the ability of adamantane for attachment to DNA, construction of well-defined constitutions consisting of DNA fragments as linkers between adamantane (and its derivatives) cores is possible. This kind of attachment can be a powerful tool to design nanostructured self-assemblies. The unique feature of DNA-directed assembly, namely site-selective immobilization, makes it possible to arrange completely defined structures. On the other hand, due to the possibility of introduction of a vast number of attachments (such as peptidic sequences, nucleoproteins, and hydrophobic hydrocarbon chains) to the adamantane core makes such a process capable of designing steric conformation via setting hydrophobic/hydrophilic (and other) interactions. In addition, due to the rigidity of diamondoid structure, strength and stiffness can be provided to the resulting structures.

Bifunctional adamantyl, as a hydrophobic central core, can be used to construct peptidic scaffolding [57] as shown in Figure 3.11. This indicates why adamantane is taken into account as one of the best MBBs. This may be considered an effective and practical strategy to substitute different amino acids or DNA segments on the
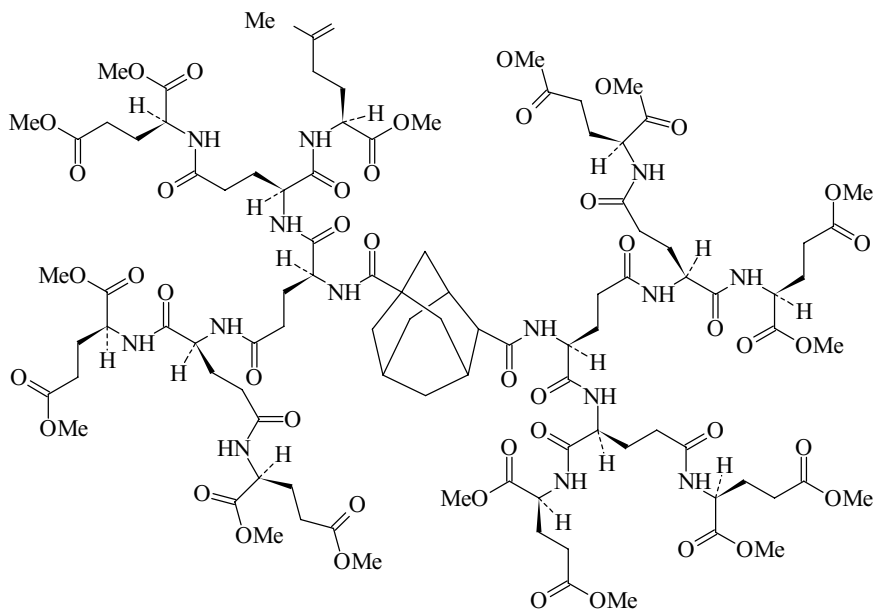
FIGURE 3.11. Adamantane nucleus with amino acid substituents creates a peptidic matrix. The reported structure in this figure is Glu4-Glu2-Glu-[ADM]-Glu-Glu2-Glu4 [57].

adamantane core (Figure 3.12). In other words, one may exploit nucleic acid (DNA) sequences as linkers and DNA hybridization as a tool to attach these modules (or adamantane cores) together. Thus, the DNA-adamantane-amino acid nanostructure may be produced.

The knowledge about protein folding and conformation in biological systems can be used to mimic the design of a desired nanostructure conformation from a particular MBB and to predict the ultimate conformation of the nanostructure.

a : Aaa = Asp ; b : Aaa = Glu
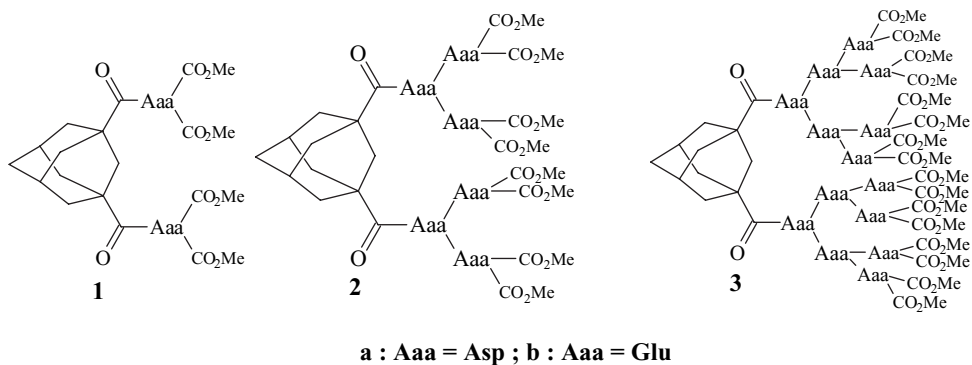
FIGURE 3.12. Amino acid substituted adamantane cores can be employed as diverse nanomodules [57].

Such biomimetic nanoassembly is generally performed step by step. This will allow observation of the effect of each new MBB on the nanostructure. As a result, it is possible to control accurate formation of the desired nanostructure. Biomimetic-controlled and directed assembly can be utilized to investigate molecular interactions, molecular modeling, and the study of relationships between the composition of MBBs and the final conformation of the nanostructures. Immobilization of molecules on a surface could facilitate such studies [58].

Nucleic acid attachments to an adamantane core (adamantyl) can be achieved in several ways. At least two nucleic acid sequences, as linkage groups, are necessary for each adamantyl to form a nanostructured self-assembly. Various geometrical structures may be formed by changing the position of the two nucleic acid sequences with respect to each other on two of the six linking positions available on an adamantane core or addition of more nucleic acid sequences (linkers) to the core on the other possible linkage positions. A number of alterations can be exerted on the nucleic acid sequences utilizing the new techniques developed in solid-phase genetic engineering for immobilized DNA alteration [59]. For instance, ligated DNA (two enzymatically joined linear DNA fragments through covalent bonds) may be employed to join the adamantyl nanomodules similar to what has been done on immobilized DNA in the case of gene assembly [59] provided some essential requirements could be met for the retention of enzyme activities. It may be possible to modify the amino acid parts, adamantane cores, and DNA sequences of the resulting nanostructure. For example, using some unnatural (synthetic) amino acids [60] with appropriate folding characteristics, the ability of conformation fine-tuning could be improved. Hence, assembling and composing adamantyls as central cores, DNA sequences as linkers, and amino acid substituents (on the adamantane) as conformation controllers may lead to design of DNA–adamantane–amino acid nanostructures with desired and predictable properties.

On the whole, the hypothesis of formation of DNA + adamantane + amino acid nanoarchitectures is currently immature and amenable to many technical modifications. Advancement in this subject requires a challenging combination of state-of-the-art approaches of organic chemistry, biochemistry, proteomics, and surface science.

A dendrimer-based approach for the design of globular protein mimics using glutamic (Glu) and aspartic (Asp) acids as building blocks has been developed [57]. The preassembled Glu/Asp dendrones were attached to a 1,3-bifunctional adamantyl based upon a convergent dendrimer synthesis strategy (Figure 3.12). Three successive generations of dendrimers composed of an adamantane central core and two, six, and fourteen chiral centers (all L-type amino acids) and thus four, eight, and sixteen peripheral carbomethoxy groups, respectively, were synthesized. The adamantane core was selected to render the dendrimer structures spherical with the capability of different ligand incorporation to their peripheral reactive arms. The Glu dendritic scaffoldings 2b and 3b (Figure 3.12) showed a noticeable feature from the solubility standpoint. The resulting dendrimers dissolved slowly in warm water to form a clear solution in spite of the fact that Glu dendrones, on their own, are quite insoluble in water. This solubility enhancement probably

results from the double-layer structures of dendritic scaffoldings 2b and 3b in which a hydrophilic outer shell encircles the hydrophobic adamantane core. In other words, this property can be attributed to the role of the adamantane core due to its ability to bring about a wide range of changes in physicochemical properties from a completely hydrophobic molecule to a hydrophilic one.

3.5. Diamondoids for Host–Guest Chemistry

The main aim in host–guest chemistry is to construct molecular receptors by a self-assembly process so that such receptors could, to some extent, gain molecular recognition capability. Such molecular recognition capability is for the goal of either mimicking or blocking a biological effect caused by molecular interactions [61].

Calixarenes, which are macrocyclic compounds, are one of the best building blocks to design molecular hosts in supramolecular chemistry [146]. Synthesis of Calix[4]arenes that had been adamantylated has been reported [61]. In these calix[4]arenes, adamantane or its ester/carboxylic acid derivatives were introduced as substituents (Figure 3.13). The purpose of this synthesis was to learn how to employ the flexible chemistry of adamantane in order to construct different kinds of molecular hosts. The X-ray structure analysis of p-(1-adamantyl) thiacalix[4]arene demonstrated that it contained four $CHCl_3$ molecules, one of them was located inside the host molecule cavity, as shown in Figure 3.14, and the host molecule assumed the conelike conformational shape (Figure 3.14).

Some other types of macrocycle compounds have been synthesized using adamantane and its derivatives. Recently, a new class of cyclobisamides has been synthesized using adamantane derivatives that shows the general profiles of amino acid (serine or cystine)-ether composites. They were shown to be efficient ion transporters (especially for Na^+ ions) in the model membranes [62]. Another interesting family of compounds to which adamantane derivatives have been introduced in order to obtain cyclic frameworks are "crown ethers" [63]. The outstanding feature of these adamantane-bearing crown ethers (which are also called "Diamond Crowns") is that α-amino acids can be incorporated to the adamantano-crown backbone [63]. This family of compounds provides valuable models for studying selective host–guest chemistry, ion transportations, and ion-complexation [63].

Adamantane has been also used as a cagelike alicyclic (both aliphatic and cyclic) bridge to construct a new class of tyrosine-based cyclodepsipeptides (tyrosinophanes) [64]. Macrocyclic peptides composed of an even number of D and L amino acids can self-assemble to form a tube through which ions and molecules can be transported across the lipid bilayers. Although they rarely exist in nature, they are synthesized to be employed in the host–guest studies (Figure 3.13a) and to act as ion transporters in the model membranes (Figure 3.15b,c) [64]. The adamantane-bridged, leucine-containing macrocycle 3.15-b shows a modest ability to transport Na^+/K^+ ions across the model membranes [64]. The adamantane-constrained macrocycle 3.15-c is also suitable for attachment of different functional
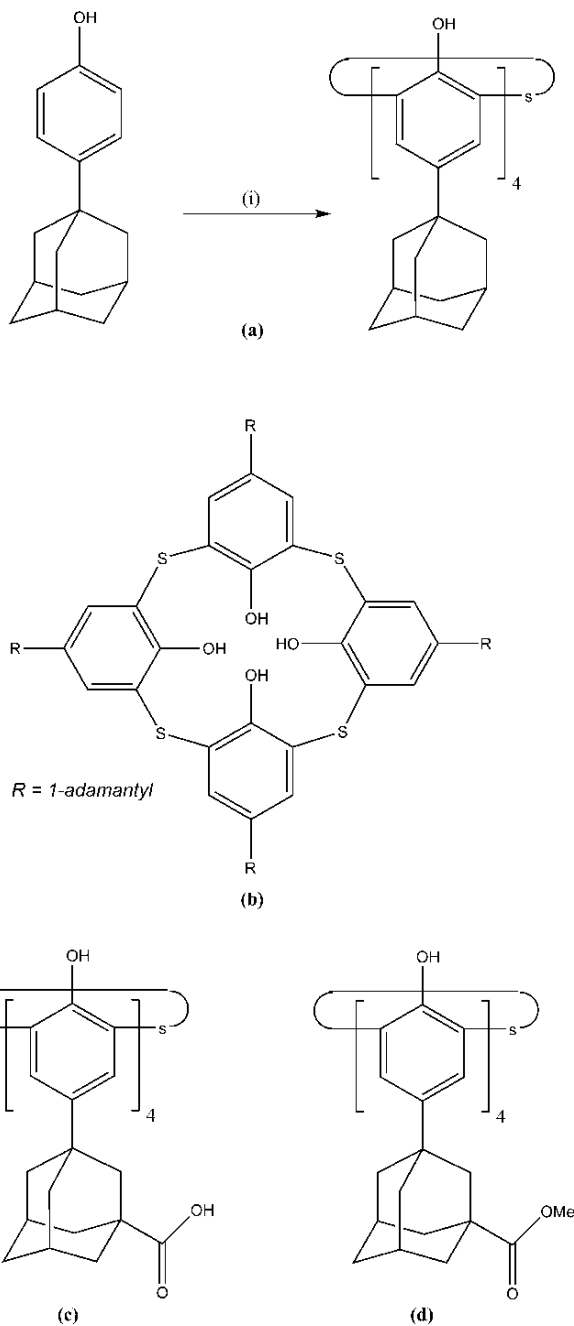
FIGURE 3.13. (a) Synthesis route of the molecule (b): (i) S8, NaOH, tetraethylenegly-col dimethyl ether, heat, (28%). (b) Adamantane Upper rim derivative based on the thia-calix[4]arene platform. (c),(d) The carboxylic acid and ester derivative of adamantane can be also used as substituents [61].
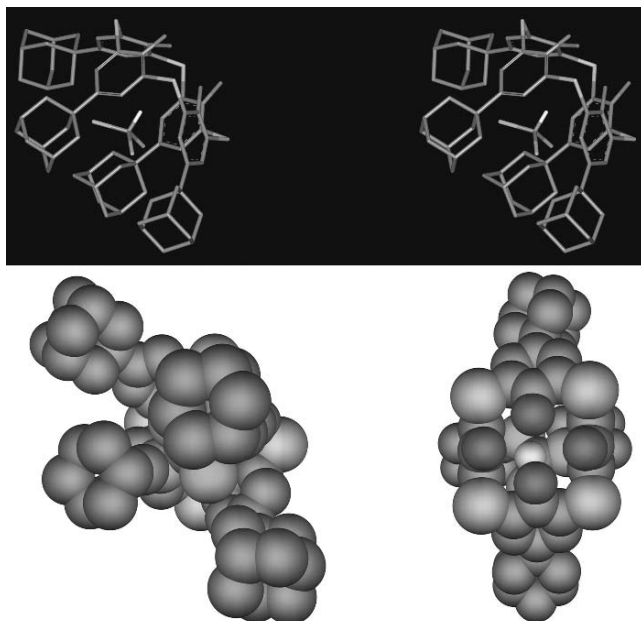
FIGURE 3.14. Lateral stereo views of adamantane-derivative thiacalix[4]arene (top) presented in Figure 3.13. A CHCl$_3$ molecule has been entrapped inside the inclusion compound. The bottom view (left bottom) and top view (right bottom) are also shown. H atoms have been removed from the inclusion compound for more clarity.

groups to design artificial proteins [64]. The adamantane-containing cyclic peptides are efficient metal ion transporters and utilization of adamantane in such compounds improves their lipophilicity and thus membrane permeability [65]. A new class of norbornene-constrained cyclic peptides has been synthesized using adamantane as a second bridging ligand (Figure 3.16). The macrocycle 16-a is a specific ion transporter for monovalent cations and the cyclic peptide 16-b is able to transport both mono- and divalent cations across the model membranes [65].

Peptidic macrocycles are especially useful models to discover the protein folding mechanisms and design novel peptide-made nanotubes as well as other biologically important molecules. These large cyclic peptides tend to fold in such a way that they can adopt a secondary structure such as β-turns, β-sheets, and helical motifs. A new series of double-helical cyclic peptides have been synthesized; among them are the adamantane-constrained cystine-based cyclic trimers {cyclo (Adm-Cyst)$_3$}. They have attracted a great deal of attention due to their figure-eightlike helical topologies and special way of hydrogen binding and symmetries [66,67] (Figure 3.17). The cyclo (Adm-Cyst)$_3$ molecule was able to transport K$^+$ ions through the model membranes and it was a valuable model to study the mechanism of secondary structure formation in proteins [68].
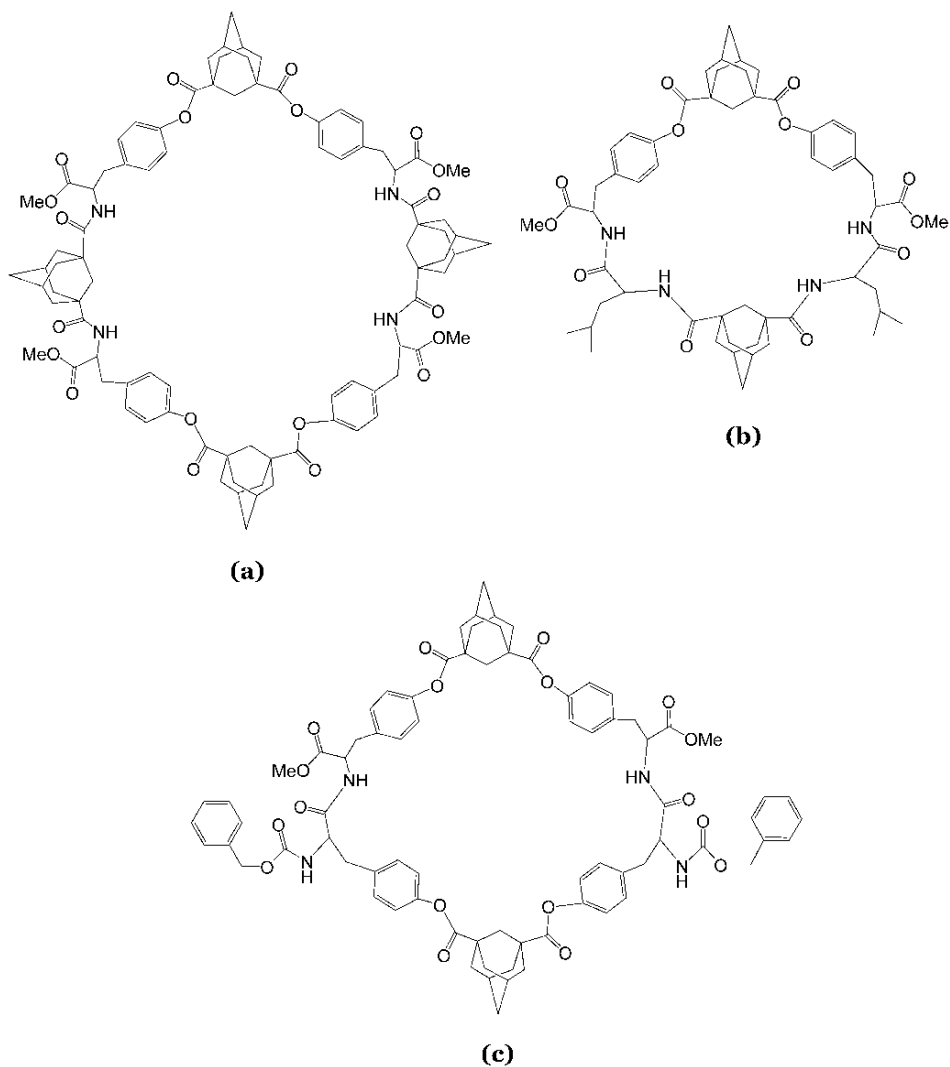
FIGURE 3.15. Adamantane-bridged tyrosine-based cyclodepsipeptides are suitable models for host–guest studies and they are also able to act as ion transporters [64].

Cyclodextrins (CDs) are inclusion compounds formed by enzymatic decomposition of starch to the cyclic oligosaccharides containing six to eight glucose units. Depending on the number of glucose units, there are three types of natural CDs, namely, α, β, and γ consisting of six, seven, and eight glucoses, respectively. The interior lining of the parent CD cavities is somehow hydrophobic. Adamantane is one of the best guests entrapped within the CDs' cavities [69]. Its noticeable association constant with CDs ($\sim 10^4$ to 10^5 M^{-1}) denotes a high affinity to interact

(a)   **(b)**

R = Val-Val-OMe
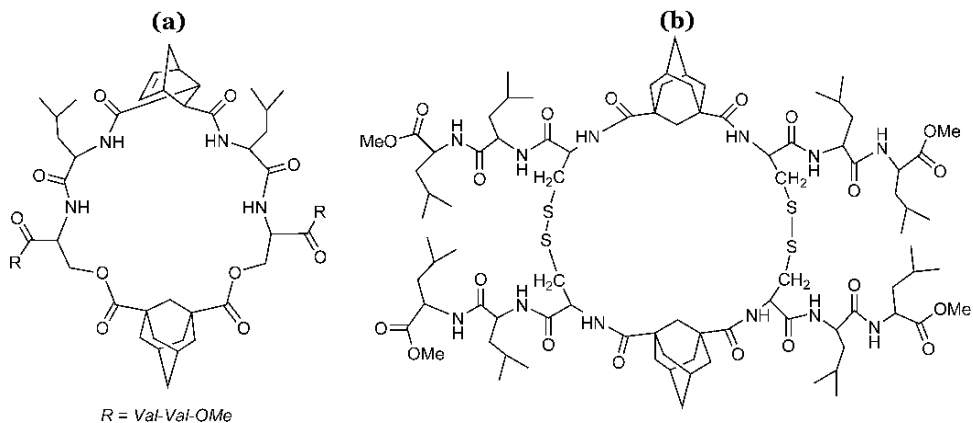
FIGURE 3.16. Adamantane-containing norbornene-constrained cyclic peptides possess the ability to transport ions across the model membranes in both specific and nonspecific ways [65].

with the hydrophobic pocket of CDs which is a valuable linking system to join different molecules together. Interestingly, this system is noteworthy to adsorb and immobilize molecules on a solid support and has been exploited to immobilize an adamantane-bearing polymer onto the surface of a β-CD-incorporated silica
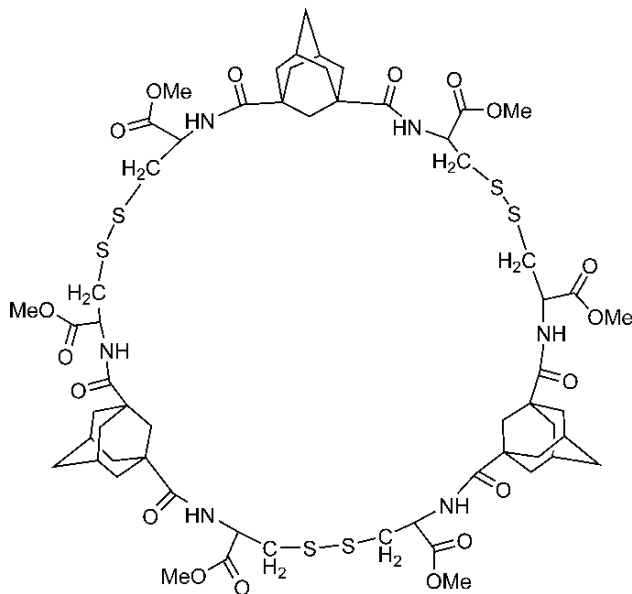
FIGURE 3.17. The cyclo (Adm-Cyst)3 adopts a figure-eightlike helical structure. The chiral amino acid, cystine, configuration determines the helix disposition (right-handed or left-handed helix). Adamantane plays an important role as a ring size-controlling agent [66].

FIGURE 3.18. Poly-adamantane molecular rods [71].

n= 1, 2, 3
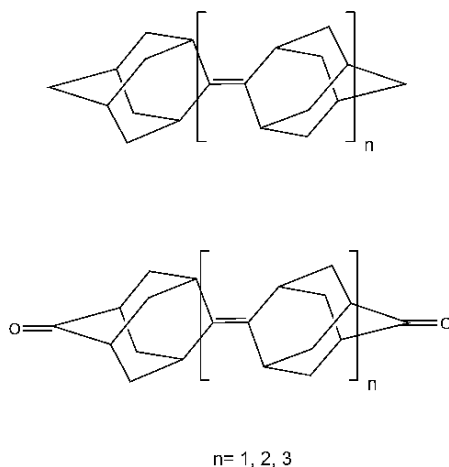
support [70]. In this case adamantane acts as a linker to attach a dextran-adamantane-COOH polymer to a solid support through a physical entrapment mechanism and thus contributes to the formation of a stationary phase for chromatographic purposes [70]. The aforementioned stationary phase could be readily prepared under mild conditions and is stable in aqueous media. It revealed some cation-exchange properties suggesting its application to the chromatography of proteins [70].

Covalent attachment of adamantane molecules is a key strategy to string them together and construct molecular rods. The McMurry coupling reaction was employed to obtain poly-adamantane molecular rods (Figure 3.18) [71]. As another example, synthesis of tetrameric 1,3-adamantane and its butyl derivative has been reported [72] (see Figure 3.19).

3.6. Discussion and Conclusions

Diamondoids are organic compounds with unique structures and properties. This family of compounds with over 20,000 variants is one of the best candidates for molecular building blocks (MBBs) to construct nanostructures compared to other MBBs known so far.
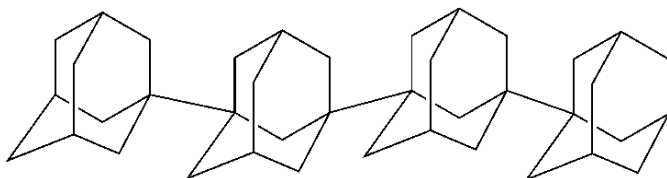
FIGURE 3.19. The tetrameric 1,3-adamantane [72].

Some of their derivatives have been used as antiviral drugs for many years. Due to their flexible chemistry, they can be exploited to design drug delivery systems and also in molecular nanotechnology. In such systems, they can act as a central lipophilic core and different parts such as targeting segments, linkers, spacers, or therapeutic agents can be attached to their central core. Their central core can be functionalized by peptidic sequences, nucleic acid sequences, and various other biomolecules.

Some adamantane derivatives possess a special affinity to bind to DNA, making it stabilized. This is an essential feature for a gene vector. Some polymers have been synthesized using adamantane derivatives, application of which is under investigation for drug delivery.

Adamantane can be used to construct peptidic scaffolding and in synthesis of artificial proteins. Adamantane has also been introduced into different types of synthetic peptidic macrocycles, which are useful nanotools for many applications including in peptide- and stereochemistry. Introduction of amino-acid-functionalized adamantane to the DNA nanostructures may lead to construction of DNA–adamantane–amino acid nanostructures with desirable stiffness and integrity. Diamondoids can be employed to construct molecular rods, nanocages, nanocapsules, and also for utilization in different methods of self-assembly. In fact, by development of self-assembly approaches and utilization of diamondoids in these processes, it should be possible to construct novel nanostructures especially to design effective and specific in vivo carriers for drugs.

The phase transition boundaries (phase envelope) of adamantane need to be investigated and constructed. Predictable and diverse geometries are important features for molecular self-assembly and pharmacophore-based drug design. Incorporation of higher diamondoids into solid-state systems and polymers will provide high-temperature stability, a property already found for polymers synthesized from lower diamondoids.

A concept named "molecular manufacturing" which was originally proposed by Drexler [7] has attracted the attention of a group of investigators [9,10]. Molecular manufacturing is defined as "the production of complex structures via nonbiological mechanosynthesis (and subsequent assembly operations)" [7]. Chemical synthesis as controlled by mechanical systems operating on atomic scale and performing direct positional selection of reaction sites by atomic-precision manipulation systems is known as mechanosynthesis.

Diamondoids, due to their strong and stiff structures containing dense, three-dimensional networks of covalent bonds, are one of the favorite sets of molecules considered for molecular manufacturing. Diamondoid materials, if they could be synthesized as proposed, will be quite strong but light. For example, diamondoids are considered to build stronger, but lighter, rocket and other space components and a variety of other earthbound articles for which the combination of weight and strength is a consideration [8–10].

Molecular manufacturing based on diamondoids is proposed to design an artificial red blood cell called Respirocyte, nanomotors, nanogears, molecular machines,

and nanorobots, just to name a few [4,8–10]. The other potential application of molecular manufacturing of diamondoids could be in designing molecular capsules and cages for various applications including drug delivery.

For the concept of molecular manufacturing to become successful a systematic study of the fundamental theory of molecular processes involved and possible technological and product capabilities is needed.

Finally here is a partial list of known applications of diamondoids in nanotechnology and the related fields:

- Antiviral drug
- Cages for drug delivery
- Designing molecular capsules
- Drug targeting
- Gene delivery
- Designing artificial red blood cells
- Host–guest chemistry
- Nanorobots
- Molecular machines
- Molecular probe
- Nanodevices
- Nanofabrication
- Nanomodule
- Organic molecular building blocks in formation of nanostructures
- Peptide chemistry
- Pharmacophore-based drug design
- Positional assembly
- Preparation of fluorescent molecular probes
- Rational design of multifunctional drug systems and drug carriers
- Self-assembly: DNA directed self-assembly
- Shape-targeted nanostructures
- Synthesis of supramolecules with manipulated architecture
- Semiconductors that show a negative electron affinity.

References

[1]   Mansoori, G.A.: Advances in atomic & molecular nanotechnology. In *Nanotechnology: The Emerging Cutting-Edge Technology*; *Sep–Oct 2002*. United Nations Tech Monitor; 2002: 53–59.

[2]   Siegel, R.W., Hu, E., Roco, M.C.: *Nanostructure Sci. and Technology—A Worldwide Study. Prepared under the guidance of the IWGN, NSTC*. WTEC, Loyola College in Maryland; 1999.

[3]   La Van, D.A., McGuire, T., Langer, R.: Small-scale systems for in vivo drug delivery. *Nature Biotechnol* 2003, **21:**1184–1191.

[4]   Merkle, R.C.: Biotechnology as a route to nanotechnology. *Trends Biotechnol* 1999, **17:**271–274.

[5]   Merkle, R.C.: *Nanotechnology* 2000, **11:**89.

[6]   Molecular building blocks and development strategies for molecular nanotechnology [http://www.zyvex.com/nanotech/mbb/mbb.html]

[7]   Drexler, K.E.: Building molecular machine systems. *Trends Biotechnol* 1999, **17:** 5–7.

[8]   Bogunia-Kubik, K. and Sugisaka, M.: From molecular biology to nanotechnology and nanomedicine. *Biosystems* 2002, **65:**123–138.

[9]   Freitas, R.A.: Respirocytes: High performance artificial nanotechnology red blood cell. *Nanotechnol* 1996, **2:**8–13.

[10]   Freitas, R.A., Jr.: Exploratory design in medical nanotechnology: a mechanical artificial red cell. *Artifficial Cells, Blood Substitutes Biotechnol* 1998, **26:**411–430.

[11]   Mansoori, G.A.: *Principles of Nanotechnology: Molecular-Based Study of Condensed Matter in Small Systems.* World Scientific, Singapore; 2005.

[12]   Dahl, J.E., Liu, S.G., and Carlson, R.M.: Isolation and structure of higher diamondoids, nanometer-sized diamond molecules. *Science* 2003, **299:**96–99.

[13]   Vazquez Gurrola, D., Excobedo, J., and Mansoori, G.A.: Characterization of crude oils from southern Mexican oilfields. In *Proceedings of the EXITEP 98, International Petroleum Technology Exhibition, Placio de Los Deportes*; *15th–18th November 1998; Mexico City, Mexico, D.F.*; 1998.

[14]   Rollmann, L.D., Green, L.A., Bradway, R.A., and Timken, H.K.C.: Adamantanes from petroleum with zeolites. *Catalysis Today* 1996, **31:**163–169.

[15]   Kabo, G.J., Blokhin, A.V., Charapennikau, M.B., Kabo, A.G., and Sevruk, V.M.: Thermodynamic properties of adamantane and the energy states of molecules in plastic crystals for some cage hydrocarbons. *Thermochim Acta* 2000, **345:**125–133.

[16]   Vazquez, D. and Mansoori, G.A.: Identification and measurement of petroleum precipitates. *J Petroleum Sci Eng* 2000, **26:**49–55.

[17]   Mansoori, G.A.: Modeling of asphaltene and other heavy organic depositions. *J Petroleum Sci Eng* 1997, **17:**101–111.

[18]   Mansoori, G.A., Assoufid, L., George, T.F., and Zhang, G.: Measurement, simulation and prediction of intermolecular interactions and structural characterization of organic nanostructures. In *Proceedings of the Conference on Nanodevices and Systems, Nanotech 2003*; *February 23–27; San Francisco*. 2003

[19]   Desiraju, G.R.: The supramolecular concept as a bridge between organic, inorganic and organometallic crystal chemistry. *J Mol Structure* 1996, **374:**191–198.

[20]   Reiser, J., McGregor, E., Jones, J., Enick, R., and Holder, G.: Adamantane and diamantane; phase diagrams, solubilities, and rates of dissolution. *Fluid Phase Equilibria* 1996, **117:**160–167.

[21]   Navratilova, M. and Sporka, K.: Synthesis of adamantane on commercially available zeolitic catalysts. *Appl Catalysis A: Gen* 2000, **203:**127–132.

[22]   Mckervey, M.A.: Synthetic approaches to large diamondoid hydrocarbons. *Tetrahedron* 1980, **36:**971–992.

[23]   Hopf, H.: *Classics in Hydrocarbon Chemistry: Syntheses, Concepts, Perspectives.* Weinheim: Wiley-VCH, 2000.

[24]   Shibuya, M., Taniguchi, T., Takahashi, M., and Ogasawara, K.: Chiral modification of adamantane. *Tetrahedron Lett* 2002, **43:**4145–4147.

[25]   Zones, S.I., Nakagawa, Y., Lee, G.S., Chen, C.Y., and Yuen, L.T.: Searching for new high silica zeolites through a synergy of organic templates and novel inorganic conditions. *Micropor Mesopor Mater* 1998, **21:**199–211.

[26] Meador, M.A.: *Annu Rev Mater Sci* 1998, **28:**599.

[27] Hardman, J.G. and Limbird, L.E.: *Goodman & Gilman's The pharmacological basis of Therapeutics.* 10th edition. New York: McGraw-Hill, 2001.

[28] Kazimierczuk, Z., Gorska, A., Switaj, T., and Lasek, W.: Adamantylaminopyrimidines and -pyridines are potent inducers of tumor necrosis factor-α *J. Bioorganic Medicinal Chem Lett* 2001, **11:**1197–1200.

[29] Yaw-Terng, C. and Jane-Jen, W.: Synthesis of 1,6-Diaminodiamantane. *Tetrahedron Lett* 1995, **36:**5805–5806.

[30] Stamatiou, G., Kolocouris, A., Kolocouris, N., Fytas, G., Foscolos, G.B., Neyts, J., and De Clercq, E.: Novel 3-(2-Adamantyl)pyrrolidines with potent activity against influenza A virus—identification of aminoadamantane derivatives bearing two pharmacophoric amine groups. *Bioorganic Medicinal Chem Lett* 2001, **11:**2137–2142.

[31] Samoilova, M.V., Buldakova, S.L., Vorobjev, V.S., Sharonova, I.N., and Magazanik, L.G.: The open channel blocking drug, IEM-1460, reveals functionally distinct α-amino-3-hydroxy-5-methyl-4-isoxazolepropionate receptors in rat brain neurons. *Neuroscience* 1999, **94:**261–268.

[32] Bolshakov, K.V., Tikhonov, D.B., Gmiro, V.E., and Magazanik, L.G.: Different arrangement of hydrophobic and nucleophilic components of channel binding sites in N-methyl-d-aspartate and AMPA receptors of rat brain is revealed by channel blockade. *Neurosci Lett* 2000, **291:**101–104.

[33] Buldakova, S.L., Vorobjev, V.S., Sharonova, I.N., Samoilova, M.V., and Magazanik, L.G.: **C**haracterization of AMPA receptor populations in rat brain cells by the use of subunit-specific open channel blocking drug, IEM-1460. *Brain Res* 1999, **846:**52–58.

[34] Rammes, G., Rupprecht, R., Ferrari, U., Zieglgänsberger, W., Parsons, C.G.: The N-methyl-d-aspartate receptor channel blockers memantine, MRZ 2/579 and other amino-alkyl-cyclohexanes antagonise 5-HT3 receptor currents in cultured HEK-293 and N1E-115 cell systems in a non-competitive manner. *Neuroscience Lett* 2001, **306:**81–84.

[35] Flynn, D.L., Becker, D.P., Spangler, D.P., Nosal, R., Gullikson, G.W., Moummi, C., and Yang, D.-C.: New aza(nor)adamantanes are agonists at the newly identified serotonin 5-HT4 receptor and antagonists at the 5-HT3 receptor. *Bioorganic Medicinal Chem Lett* 1992, **2:**1613–1618.

[36] Baxter, A., Bent, J., Bowers, K., Braddock, M., Brough, S., Fagura, M., Lawson, M., McInally, T., Mortimore, M., and Robertson, M.: Hit-to-Lead studies: The discovery of potent adamantane amide P2X7 receptor antagonists. *Bioorganic Medicinal Chem Lett* 2003, **13:**4047–4050.

[37] Zoidis, G., Papanastasiou, I., Dotsikas, I., Sandoval, A., Dos Santos, R.G., Papadopoulou-Daifoti, Z., Vamvakides, A., Kolocouris, N., and Felix, R.: The novel GABA adamantane derivative (AdGABA): design, synthesis, and activity relationship with gabapentin. *Bioorganic Medicinal Chem* 2005, **13:**2791–2798.

[38] Shen, C., Bullens, D., Kasran, A., Maerten, P., Boon, L., Aerts, J.M.F.G., van Assche, G., Geboes, K., Rutgeerts, P., and Ceuppens, J.L.: Inhibition of glycolipid biosynthesis by N-(5-adamantane-1-yl-methoxy-pentyl)-deoxynojirimycin protects against the inflammatory response in hapten-induced colitis. *Int Immunopharmacol* 2004, **4:**939–951.

[39] Reissmann, S., Pineda, F., Vietinghoff, G., Werner, H., Gera, L., Stewart, J.M., and Paegelow, I.: Structure activity relationships for bradykinin antagonists on the inhibition of cytokine release and the release of histamine. *Peptides* 2000, **21:**527–533.

[40] Hoekstra, W.J., Press, J.B., Bonner, M.P., Andrade-Gordon, P., Keane, P.M., Durkin, K.A., Liotta, D.C., and Mayo, K.H.: Adamantane and Nipecotic Acid Derivatives as Novel [beta]-Turn Mimics. *Bioorganic Medicinal Chem Lett* 1994, **4:**1361–1364.

[41] Mathias, L.J. and Tullos, G.L.: Synthesis of adamantyl and benzoxazole substituted poly(m-phenylene)s via the nickel catalysed coupling of aryl chlorides. *Polymer* 1996, **37:**3771–3774.

[42] Chern, Y.-T. and Wang, W.-L.: Synthesis and characterization of tough polyamides derived from 4,9-bis[4-(4-aminophenoxy)phenyl]diamantane. *Polymer* 1998, **39:** 5501–5506.

[43] Chern, Y.-T.: Synthesis of polyamides derived from 4,9-bis(4-aminophenyl) diamantane. *Polymer* 1998, **39:**4123–4127.

[44] Huang, C.-F., Lee, H.-F., Kuo, S.-W., Xu, H., and Chang, F.-C.: Star polymers via atom transfer radical polymerization from adamantane-based cores. *Polymer* 2004, **45:**2261–2269.

[45] Eastmond, G.C., Gibas, M., and Paprotny, J.: Pendant adamantyl poly(ether imide)s: synthesis and a preliminary study of properties. *Euro Polym J* 1999, **35:**2097–2106.

[46] Lee, Y.K., Jeong, H.Y., Kim, K.M., Kim, J.C., Choi, H.Y., Kwon, Y.D., Choo, D.J., Jang, Y.R., Yoo, K.H., Jang, J., and Talaie, A.: Synthesis of new PPV based polymer and its application to display. *Curr Appl Phys* 2002, **2:**241–244.

[47] Jeong, H.Y., Lee, Y.K., Talaie, A., Kim, K.M., Kwon, Y.D., Jang, Y.R., Yoo, K.H., Choo, D.J., and Jang, J.: Synthesis and characterization of the first adamantane-based poly(p-phenylenevinylene) derivative: an intelligent plastic for smart electronic displays. *Thin Solid Films* 2002, **417:**171–174.

[48] Kar, A.K. and Lightner, D,A,.: Circular dichroism of distorted helices. C(10)-Adamantyl and C(10)-tert-butyl biliverdins. *Tetrahedron: Asymmetry* 1998, **9:**3863–3880.

[49] Seidl, P.R. and Leal, K.Z.: Steric contributions to carbon-13 chemical shifts of 1- and 2-methyl adamantanes by DFT/GIAO. *J Mol Structure: THEOCHEM* 2001, **539:**159–162.

[50] Martin, V.V., Alferiev, I.S., Weis, A.L.: Amplified fluorescent molecular probes based on 1,3,5,7-tetrasubstituted adamantane. *Tetrahedron Lett* 1999, **40:**223–226.

[51] Tsuzuki, N., Hama, T., Kawada, M., Hasui, A., Konishi, R., Shiwa, S., Ochi, Y., Futaki, S., and Kitagawa, K.: **A**damantane as a brain-directed drug carrier for poorly absorbed drug. 2. AZT derivatives conjugated with the 1-adamantane moiety. *J Pharmaceut Sci* 1994, **83:**481–484.

[52] Tsuzuki, N., Hama, T., Hibi, T., Konishi, R., Futaki, S., and Kitagawa, K.: Adamantane as a brain-directed drug carrier for poorly absorbed drug: Antinociceptive effects of [D-Ala2]Leu-enkephalin derivatives conjugated with the 1-adamantane moiety. *Biochem Pharmacol* 1991, **41:**R5–8.

[53] Kitagawa, K., Mizobuchi, N., Hama, T., Hibi, T., Konishi, R., and Futaki, S.: Synthesis and antinociceptive activity of [D-Ala2]Leu-enkephalin derivatives conjugated with the adamantane moiety. *Chem Pharmaceut Bull (Tokyo)* 1997, **45:**1782–1787.

[54] Manoharan, M., Tivel, K.L., and Cook, P.D.: Lipidic nucleic acids. *Tetrahedron Lett* 1995, **36:**3651–3654.

[55] Lomadze, N. and Schneider, H.-J.: Reversal of polyamine selectivity for DNA and RNA by steric hindrance. *Tetrahedron Lett* 2002, **43:**4403–4405.

[56] Moine, L., Cammas, S., Amiel, C., Guerin, P., and Sebille, B.: Polymers of malic acid conjugated with the 1-adamantyl moiety as lipophilic pendant group. *Polymer* 1997, **38:**3121–3127.

[57] Ranganathan, D. and Kurur, S.: Synthesis of totally chiral, multiple armed, poly glu and poly asp scaffoldings on bifunctional adamantane core. *Tetrahedron Lett* 1997, **38:**1265–1268.

[58] Busch, K. and Tampé, R.: Single molecule research on surfaces: from analytics to construction and back. *Rev Mol Biotechnol* 2001, **82:**3–24.

[59] Kim, J.H., Hong, J.-A., Yoon, M., Yoon, M.Y., Jeong, H.-S., and Hwang, H.J.: Solid-phase genetic engineering with DNA immobilized on a gold surface. *J Biotechnol* 2002, **96:**213–221.

[60] Nanotechnology in medicine [http://www.foresight.org/Updates/Update16/Update 16.1.html#anchor576239]

[61] Shokova, E., Tafeenko, V., and Kovalev, V.: First synthesis of adamantylated thiacalix[4]arenes. *Tetrahedron Lett* 2002, **43:**5153–5156.

[62] Ranganathan, D., Samant, M.P., Nagaraj, R., and Bikshapathy, E.: Design, synthesis and membrane ion transport properties of cystine- and serine-based cyclo-4-oxa-heptane-1,7-bisamides. *Tetrahedron Lett* 2002, **43:**5145–5147.

[63] Ranganathan, D., Haridas, V., and Karle, I.L.: Diamond crowns: Design, synthesis and x-ray crystallographic studies of a novel family of adamantane-containing crown ethers. *Tetrahedron* 1999, **55:**6643–6656.

[64] Ranganathan, D., Thomas, A., Haridas, V., Kurur, S., Madhusudanan, K.P., Roy, R., Kunwar, A.C., Sarma, A.V., Vairamani, M., and Sarma, K.D.: Design, synthesis, and characterization of tyrosinophanes, a novel family of aromatic-bridged tyrosine-based cyclodepsipeptides. *J Organic Chem* 1999, **64:**3620–3629.

[65] Ranganathan, D., Haridas,V., Kurur, S., Nagaraj, R., Bikshapathy, E., Kunwar, A.C., Sarma, A.V., and Vairamani, M.: Norbornene-constrained cyclic peptides with hairpin architecture: design, synthesis, conformation, and membrane ion transport. *J Organic Chem* 2000, **65:**365–374.

[66] Ranganathan, D., Haridas, V., Nagaraj, R., and Karle, I.L.: Double-helical cyclic peptides: design, synthesis, and crystal structure of figure-eight mirror-image conformers of adamantane-constrained cystine-containing cyclic peptide cyclo (Adm-Cyst)(3). *J Organic Chem* 2000, **65:**4415–4422.

[67] Karle, I.L.: Hydrogen bonds in molecular assemblies of natural, synthetic and 'designer' peptides. *J Mol Structure* 1999, **474:**103–112.

[68] Karle, I. and Ranganathan, D.: Construction of polar and hydrophobic pores and channels by assembly of peptide molecules. *J Mol Structure* 2003, **647:**85–96.

[69] Jaime, C., Redondo, J., Sanchez-Ferrando, F., and Virgili, A.: [beta]-cyclodextrin inclusion complex with adamantane Intermolecular 1H{1H} NOE determinations and molecular mechanics calculations. *J Mol Structure* 1991, **248:**317–329.

[70] Karakasyan, C., Millot, M.-C., and Vidal-Madjar, C.: Immobilization of a (dextran-adamantane-COOH) polymer onto [beta]-cyclodextrin-modified silica. *J Chromatography B* 2004, **808:**63–67.

[71] Ayres, F.D., Khan, S.I., and Chapman, O.L.: Synthesis and x-ray crystal structures of poly-adamantane molecular rods. *Tetrahedron Lett* 1994, **35:**8561–8564.

[72] Ishizone, T., Tajima, H., Matsuoka, S., and Nakahama, S.: Synthesis of tetramers of 1,3-adamantane derivatives. *Tetrahedron Lett* 2001, **42:**8645–8647.

4
Surface Modification and Application of Functionalized Polymer Nanofibers

Renuga Gopal, Ma Zuwei, Satinderpal Kaur, and Seeram Ramakrishna

4.1. Attractiveness of Nanofibers

Past research in the field of polymeric micron fibers highlighted very unique and remarkable fiber properties such as ultraviolet resistance, electrical conductivity, and biodegradability, as compared to the material's bulk properties. With the immense promise of better properties and anticipated performance, and the ability to produce finer fibrous structures using a relatively straightforward method of electrospinning, the current trend is to develop submicron scale fibers, nanofibers, to tap a number of favorable properties such as increase in surface area-to-volume ratio, decrease in pore size, a drop in structural defects, and superior mechanical characteristics. The potential target areas of application for these nanofibrous structures are as affinity membranes, scaffolds for tissue engineering, sensors, and protective clothing, to name a few.

4.1.1. Affinity Membranes

Affinity membranes permit the purification of molecules based on physical/chemical properties or biological functions instead of molecular weight/size. Rather than operate purely on the sieving mechanism, affinity membrane separates based on the selectivity of the membrane to "capture" molecules, by immobilizing specific ligands onto the membrane surface. Affinity membrane reflects technological advances in both fixed-bed liquid chromatography and membrane filtration, combining both the outstanding selectivity of chromatography resins and the reduced pressure drops associated with filtration membranes [1].

The idea of using polymer nanofiber as affinity membrane is based on the fact that the polymer nanofibers deposited on the collector during electrospinning assemble into a membranelike nonwoven fiber mesh. This electrospun nonwoven mesh possesses properties such as high porosity, micron-scaled pore size, and high interconnectivity of the interstitial space. Above all, the nanoscaled fiber diameter gives rise to an increased surface area as compared with the conventional nonwoven filter media composed of currently available textile fibers with typical diameters of several microns. A large surface area-to-volume ratio is one of the most important

requirements for an ideal affinity membrane. In the same sense, they are also being considered for drug delivery applications [2,3].

4.1.2. Tissue Engineering Scaffolds

Polymeric nanofiber matrix has similar structure to nanoscaled nonwoven fibrous ECM proteins, and thus is a wonderful candidate for ECM-mimic materials [4]. In recent years, the ease of polymer nanofiber fabrication using electrospinning began to stimulate more and more researchers to explore the application of nanofiber matrix as a tissue engineering scaffold [5–8]. A successful tissue engineering scaffold should have cell-compatible surfaces to allow cell attachment and proliferation. Based on the understanding of the "biorecognition" mechanism [9] of the interaction between cells and biomaterial surfaces, most research work to improve biocompatibilities of polymeric tissue engineering scaffold center on immobilization of biomolecules that can be specifically recognized by cells on the biomaterial surfaces. These biomolecules include adhesive proteins such as collagen, fibronectin, RGD peptides, and growth factors such as bFGF, EGF, insulin, and the like. The biomolecules can either be covalently attached, statically adsorbed, or self-assembled on the biomaterial surfaces. Such kinds of surface modification can preserve the good mechanical strength of nanofibers while giving the nanofibers improved cell adhesion propeties.

4.1.3. Sensors

Due to its unique properties such as high surface area and acoustic/viscoelastic properties electrospun nanofiber is also receiving great research interest in sensor application [10–16]. High surface area is one of the most desired parameters for the sensitivity of conductimetric sensor film. The operating principle of these devices is associated primarily with the adsorption of the gas molecules on the surface of semiconducting oxides inducing electric charge transport between the two materials that changes the resistance of the oxide. The structure configuration of the metal oxide materials is one of the key parameters controlling the gas-sensing process. Now there is an increasing trend in chemical sensing to utilize nanostructured materials as gas sensing elements because the high surface areas and the unique structure features are expected to promote the sensitivity of the metal oxide to the gaseous component.

4.1.4. Protective Clothing

The current material system for protective clothes usually adopts a multilayer composite structure. An activated carbon-based chemical vapor filtration medium, a nonwoven or woven fabric, and a cover top layer are often incorporated. There is an opportunity to improve the performance of this system through the incorporation of one or several layers of nonwoven polymeric nanofiber mats. The polymeric

nanofibers can provide enhanced protection against aerosols without adding weight or thickness, while maintaining adequate permeability for wearer comfort.

An optimal protective cloth should be able to prevent infiltration of aerosols (e.g., chemical/biochemical agent microdroplets, bacteria, virus, radioactive dust, etc.) and at the same time must be highly permeable to the air and water vapor to improve wearer comfort. Nonwoven polymeric nanofibers are a natural fit for this application due to their enormous surface area and microscale pore size. By physical absorption and exclusion, the nanofiber mat can provide an impermeable barrier to toxic chemical agents, that is lightweight with remarkable breathing properties [17,18].

To meet these potential applications, a rich variety of electrospun polymeric fibers with diameters ranging from several tens to several hundreds nanometers are now being fabricated and studied for suitability. Unfortunately, most as-spun polymer nanofibers are chemically inert and do not have any specific functions. From the above descriptions, one can see that to realize these applications, there is a need to modify the polymer nanofibers to incorporate new functionalities on the surface. This in return enhances its property or produces unique surface properties required by the various applications. For example, for the nanofibers to be used as drug delivery carriers, drug molecules must be hybridized with the polymer nanofiber; for the nanofibers to be used as an affinity membrane for antibody purification, protein A or G should be covalently bonded on the nanofiber surface; for the nanofiber mesh to be used as protective cloth, capture agents need to be introduced on the nanofiber surface to capture and decompose molecules of toxic gas.

In this chapter, techniques of surface modification suitable for polymer nanofibers are introduced and followed by the significance of these techniques to develop the above-mentioned applications.

4.2. Polymer Surface Modification

Polymers have a vast number of advantages and attractiveness as a material system. However, despite these plus factors, polymers have limitations. In general, special surface properties with regard to chemical composition, hydrophilicity, roughness, crystallinity, conductivity, lubricity, and cross-linking density are required for successful application of polymers in such wide fields as adhesion, membrane filtration, coatings, friction and wear, composites, microelectronic devices, thin-film technology and biomaterials, and so on. Unfortunately, polymers very often do not possess the surface properties needed for these applications. In fact, polymers that are mechanically strong, chemically stable, and easy to process usually will have inert surfaces both chemically and biologically. Vice versa, those polymers having active surfaces usually do not possess excellent mechanical properties which are critical for their successful application.

Due to this dilemma, surface modification of the polymers without changing the bulk properties has been a classical research topic for many years, and is still receiving extensive studies as new applications of polymeric materials emerge,

especially in the fields of biotechnology, bioengineering, and most recently in nanotechnology.

The main purpose of surface modification is to alter surfaces by either chemically or physically altering the atoms/molecules in the existing surface (treatment, etching, chemical modification), changing the surface topography or coating over the existing surface with a material having a new composition (solvent coating or thin film deposition by chemical vapor deposition, radiation grafting, chemical grafting, or RF-plasmas) [19,20]. There are a few factors to consider when modifying a surface [21–24]:

1. Thickness of the surface is crucial. Thin surface modifications are desirable, otherwise mechanical and functional properties of the material will be altered. This is more so when dealing with nanofibers as there is less bulk material present.
2. Sufficient atomic or molecular mobility must exist for surface changes to occur in reasonable periods of time. The driving force for the surface changes is the minimization of the interfacial energy.
3. Stability of the altered surface is essential, achieved by preventing any reversible reaction. This can be done by cross-linking and/or incorporating bulky groups to prevent surface structures from moving.
4. In some cases a transparent scaffold is desired, especially in optical sensors or ophthalmology; after surface treatment they should remain transparent. Any cloudiness introduced is of real concern.
5. Uniformity, reproducibility, stability, process control, speed, and reasonable cost should be considered in the overall process of surface modification. The ability to achieve uniform surface treatment of complex shapes and geometries can be essential for sensor and biomedical applications.
6. Precise control over functional groups. This is a challenging yet difficult scope. Many functional groups might bond to the surface such as hydroxyl, ether, carbonyl, carboxyl, and carbonate groups, instead of one desired functional group.

Common surface modification techniques used on polymer substrates include treatments by blending, coating, surface segregation, layer by layer electrostatic interaction, radiation of electromagnetic waves, electron beam, ion beam [25,26] or atom beams [27], corona or plasma treatment [28–30], chemical vapor deposition (CVD), gas oxidation, metallization, chemical modifications using wet-treatment and surface grafting polymerization [31,32], and so on. In recent years, many advances have been made in developing surface treatments to alter the chemical and physical properties of polymer surfaces and progress in recent years has been summarized by many reviews [19,33,34].

To date, no specific method of surface modification has been developed for nanofibers. In principle, all the current techniques mentioned above may be considered for the surface modification of polymer nanofibers. Nevertheless, they have to be carried out under moderate conditions for nanofibers. Of the above-mentioned

techniques, only blending, grafting, radiation, and plasma treatment have been utilized to date on nanofibers with success.

4.3. Blending and Coating

Blending and coating are by far the simplest and easiest methods employed to functionalize a polymer. Both these techniques are physical approaches, whereby there is no chemical bonding or attachment involved between the polymer material and the functionalized species. It is a simple mixing of two or more materials (blending) or using another material of desired properties to "cover" the surface of the polymer (coating). Thus to some extent, they are prone to detachment and can be less reproducible and controlled. Nevertheless they have been proven to be effective methods for polymer nanofiber modifications. Until better chemical methods are formulated or current techniques better controlled, many emerging applications will use this approach as a starting block.

4.3.1. Application

The simplest method to introduce ligands is by blending ligand molecules into the polymer solution and then electrospinning the polymer solution. For example, an attempt [35] was made to incorporate chemically modified β-CD onto the surface of the nanofiber to target potential applications in organic waste treatment for water purification. Phenylcarbomylated or azido phenylcarbomylated β-CD was successfully blended with polymethyl methacrylate (PMMA) and electrospun into nanofibrous membrane, respectively. The presence of the β-CD derivatives on the surface of the nanofibers was confirmed by attenuated total reflectance fourier transform infrared spectrometry (ATR-FTIR) and X-ray photoelectron spectroscopy (XPS). To determine the functionalized membranes' ability to capture small organic molecules, a solution containing phenolphthalein (PHP), a small organic molecule, was used. Results obtained showed that the functionalized nanofibrous membranes were able to capture the PHP molecules effectively. Thus the functionalized nanofibrous membranes may have the potential to capture similar small organic waste molecules present in wastewater [35].

In another work, collagen was directly blended into the poly(L-lactic acid)-co-poly(ε-caprolactone) PLLA-co-PCL (70:30) nanofibers [36]. The blended nanofibers with different weight ratios of the polymer to collagen were fabricated by electrospinning a mixture of collagen and the copolymer solution. Morphology of the blended nanofibers was investigated by scanning electron microscope (SEM) and transmission electron microscope (TEM). ATR-FTIR spectra and X-ray photoelectron spectroscopy (XPS) verified existence of collagen molecules on the surface of nanofibers. Five characteristic endothelial cell (EC) markers including four cell adhesion molecules (CAMs) and one EC-preferential gene (von Willebrand factor, vWF) were studied by RT-PCR and the results showed that the collagen-blended polymer nanofibers preserved the EC's normal phenotype and showed

enhanced cell viability, spreading, and attachment, indicating a potential application as a vascular graft in tissue engineering.

The blending (or mixing) technique for the bulk modification of the polymer nanofibers has also been used for drug delivery applications. Drugs, growth factors, and genes can be directly mixed into the polymer solution and electrospun to prepare drug carriers with controlled release properties. Verreck et al. [3] prepared PU nanofibers containing the model drug itraconazole and ketanserin, using dimethylformide (DMF) and dimethylacetamide (DMAc) as solvent, respectively. The release of the drug showed a linear relation with time. In another instance, Luu et al. [4] mixed plasmid with PLA-PEG and PLGA solution in DMF and electrospun the mixture into nanofibers. Release of plasmid DNA from the scaffolds was sustained over a 20-day study period, with maximum release occurring at 2 h.

Coatings are also predominantly used to enhance the performance of nanofibrous scaffolds. Collagen, fibronectin, and laminin have been coated on electrospun silk fibroin nanofiber surface to promote cell adhesion [37]. Collagen-coated P(LLA-CL 70:30) nanofiber mesh (NFM) with diameter of 470 nm and porosity of 64–67% was fabricated using electrospinning followed by plasma treatment and collagen coating. The spatial distribution of the collagen in the NFM was visualized by labeling the collagen with fluorescent dye and it was found that the collagen can be uniformly coated around the polymer nanofiber. Endothelial cells were seeded onto the collagen-coated P(LLA-CL) nanofiber and the results showed that the collagen-modified material had higher cell attachment, spreading, and viability than the unmodified nanofiber [38].

To use nanofibers as a conductimetric sensor, it should be functionalized with metal oxide semiconductors. Gouma et al. produced MoO_3-containing PEO nanofibers by electrospinning a mixture of MoO_3 sol-gel and PEO solution [16]. A gas sensing test of the electrospun nanofiber mat was carried out using ammonia and nitroxide as the model gas. Electrical resistance of the sensing film as a function of the gas concentration was measured and the results showed that the nanoscaled metal oxide fiber offered high sensitivity and fast response to the harmful chemical gases. Drew et al. [13] coated SnO2 and TiO2 on polyacrylonitrile (PAN) nanofibers using a "liquid-phase deposition" technique. The coatings were thin enough to maintain the nanofibrous morphology, thereby retaining the large surface area of the electrospun membrane. Such metal oxide-coated nanofibrous membranes are expected to provide unusual and highly reactive surfaces for improved sensing, catalysis, and photoelectric conversion applications.

Likewise polymeric nanofibers can also be used as a carrier for active chemistry that may allow for improvements in chemical protective properties. The nanofibers can provide a huge surface area to be functionalized with chemical groups that are reactive with toxic gases and chemicals. Graham et al. [39] mixed polyoxometallate, a catalyst for the oxidative degradation of sulfur mustard (a chemical weapon agent) with the PU (Estane ∘ R 58238) solution and electrospun the mixture into nanofibers. The capability of the catalyst in the electrospun nanofiber was found to be even higher than the catalyst alone [39].

4.4. Chemical Methods

Chemical modification involves the introduction of one or more chemical species to a given surface so as to produce a surface that has enhanced chemical and physical properties. Chemical modification can be classified into four categories, namely physical modification, chemical reaction modification, physicochemical modification, and electrochemical modification [40].

Wet-chemical oxidation treatments are commonly employed to introduce oxygen-containing functional groups (such as carbonyl, hydroxyl, and carboxylic groups) at the surface of the polymer. This can be conducted using gaseous reagents or with solutions of vigorous oxidants. Oxygen-containing functional groups increase the polarity and the ability to hydrogen bond. This in turn results in the enhancement of wettability and adhesion. Overexposure to the treatment conditions tends to damage the polymer surface by producing microscopic pits [41].

Chemical reactions can also be carried out at sites that are vulnerable to electrophilic or nucleophilic attack. Structures such as benzene rings, hydroxyl groups, double bonds, halogen, and the like qualify for such attacks [41].

4.4.1. Applications

A study has been presented of the potentialities of an electrostatically spun poly(ether-urethane-urea) as an affinity separation membrane, via chemical modification [42]. A variety of chemical methods has been used for functionalizing and activating the membrane surfaces. Assessments of the capacities of the activated membranes for covalent coupling of protein A and human immunoglobulin G have given very encouraging data, 4 mg/g for protein A and 4 mg/g for bounded IgG, respectively.

A similar approach was adopted for cellulose, a common and important material for membrane preparation. To study the feasibility of applying electrospun cellulose nanofiber mesh as an affinity membrane, cellulose acetate (CA) solution (0.16 g/ml) in a mixture solvent of acetone/DMF/ trifluoroethylene (3:1:1) was electrospun into nonwoven fiber mesh with the fiber diameter ranging from 200 nm to 1 μm. The CA nanofiber mesh was heat treated under 208°C for 1 h to improve structural integrity and mechanical strength, and then treated in 0.1 M NaOH solution in H_2O/ethanol (4:1) for 24 h to obtain regenerated cellulose (RC) nanofiber mesh, which was used as a novel filtration membrane [43]. The RC nanofiber membrane was further surface functionalized with Cibacron Blue F3GA (CB), a general affinity dye ligand for separation of many biomolecules. The CB-derived RC nanofiber membrane has a CB content of 130 μmol/g, and capture capacity of 13 mg/g for bovine serum albumin (BSA) and 4 mg/g for bilirubin. The material's chemical and physical properties were studied by SEM, DSC, and ATR-FTIR. The novel RC membrane had a lower pressure drop (more energy efficient) and higher fluse compared to a commercial microfiltration membrane.

In another work [14], a fluorescent probe, hydrolyzed poly[2-(3-thienyl) ethanol butoxy carbonyl-methyl urethane] (H-PURET) was immobilized on the cellulose acetate electrospun nanofibrous membranes using a "layer by layer" electrostatic self-assembly method. Also by the quenching mechanism, the nanofiber can be used as an optical sensor to detect trace amounts of methyl viologen (MV2+) and cytochrome c (cyt c) in aqueous solutions. The high sensitivity is attributed to the high surface area-to-volume ratio of the electrospun membranes and efficient interaction between the fluorescent conjugated polymer and the analytes.

4.5. Graft Polymerization

Among the chemical modification techniques developed to date, surface grafting has emerged as a simple, useful, and versatile approach to improve surface properties of polymers for a wide variety of applications.

Grafting has several advantages: (1) the ability to modify the polymer surface to have very distinct properties through the choice of different monomers, (2) the ease and controllable introduction of graft chains with a high density and exact localization of graft chains to the surface with the bulk properties unchanged, and (3) covalent attachments of graft chains onto a polymer surface assuring long-term chemical stability of introduced chains, in contrast to physically coated polymer chains [31,44].

Many different synthetic routes can be employed to introduce graft chains onto the surface of polymeric substrates depending on a system of interest. Surface modification can be achieved by two methods [45]: graft coupling and graft polymerization. The former is applied when reactive groups are present on the polymer surface that can undergo a condensation reaction with a second polymer chain to be grafted onto its surface. The latter does not require any reactive functional groups on the surface; instead the surface of the polymer must be initiated in order for graft polymerization to occur.

Graft co-polymerization is one of the promising methods of modification for various polymers and polymer materials. Initiation of the surface can be achieved via direct chemical modification, ozone, gamma rays, electron beams, glow discharge, corona discharge, or UV irradiation [45]. The general scheme of how the surface of polymer can be grafted is reflected in Figure 4.1. There are two main approaches to graft co-polymerization of particular interest to nanofibers: radiation-induced graft co-polymerization and plasma-induced graft co-polymerization.

4.5.1. Radiation-Induced Graft Co-Polymerization

Radiation can generally be classified into two categories, high energy radiation (also known as ionization radiation) and low energy radiation. Each can be further subclassified. There are two types of low energy, visible light and UV radiation with particle energy of up to about 50 eV, commonly used for nanofiber irradiation. UV radiation interacts with the substance in the primary stages by the mechanism

Mutual-Irradiation grafting

Non-ionization radiation: UV light + P

Ionization radiation: electrons or gamma-rays

Monomer

Pre irradiation grafting

Irradiation by UV, electrons, or gamma-rays

Air

Chemical grafting

O_3

Air or oxygen

Plasma or corona

Plasma or corona discharge

Monomer | Heat
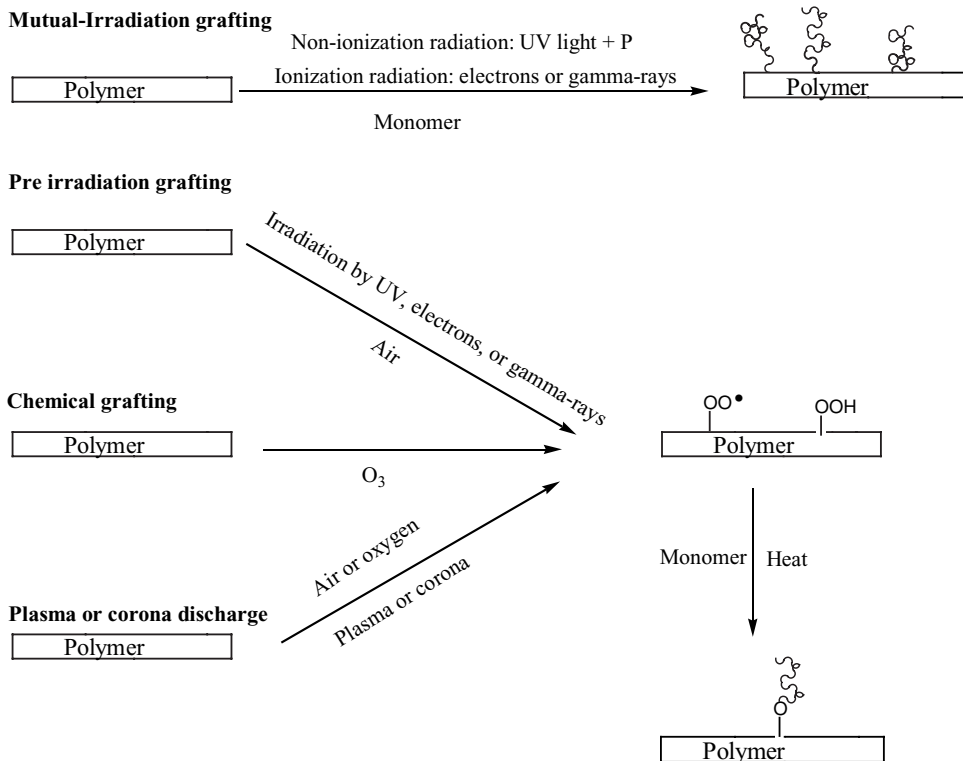
FIGURE 4.1. Various graft polymerization methods.

of excitation of its atoms and molecules, whereas high-energy radiation mainly induces an ionization mechanism, leading to the formation of ions with different signs.

Exposure of polymers to ultraviolet and higher-energy (ionizing) radiation can lead to extensive physical and chemical modification of polymeric materials. These changes in properties may have both detrimental and beneficial consequences in determining the end uses of polymer [46]. It is beneficial in the sense that it can cause cross-linking and grafting on the surface of the polymers but on the other hand it may cause chain scission (breaking of bond) as well, thus damaging the polymer. This is especially so for nanofibers. Strong reaction conditions such as plasma, UV, or gamma (γ) radiation, may destroy the polymer nanofibers easily, especially when the polymer nanofiber is biodegradable. Biodegradable polymers such as PLA and PGA nanofibers may have a much faster degradation rate compared with the macro- or microscale materials due to the high surface area. Our recent work found even PET showed considerable degradation when it is prepared into nanofibers. Therefore, the reaction condition for the surface modification of polymer nanofibers must be optimized to preserve the nanofibrous morphology. If

TABLE 4.1 Using empirical formula to predict the behavior of polymer upon irradiation [48].

Predominant behavior of polymer upon irradiation	Empirical formula of polymer
Cross-linking	∼CH2-CHR∼ (as long as there is a H atom on each C)
Degradation/Chain scission	∼CH2-CRR'∼
	∼CX2-CX2∼

the reaction is controlled, it can be used in nanofibers successfully as an initiator for graft polymerization: radiation-induced graft co-polymerization.

Radiation-induced graft co-polymerization is the irradiation of the polymer surfaces with a high energy source and eventually grafting a monomer (or monomers) on the surface. As mentioned above, radiation can promote both cross-linking as well as chain scission. A moderate number of cross-links can often improve the physical properties of polymers whereas scission processes usually produce deleterious effects, resulting in materials that are soft and weak. In many cases, cross-linking and scission occur simultaneously. However, depending on the molecular structure, one or the other prevails or predominates [47]. An empirical rule is used to predict the behavior of carbon chain polymers exposed to irradiation. This is reflected in Table 4.1. Given in Table 4.2 is a list of polymers that undergo

TABLE 4.2 List of polymers that undergoes predominantly cross linking or chain-scission [48].

Polymers predominantly undergoing cross-linking upon irradiation	Polymers predominantly undergoing chain scission upon irradiation
Polyethylene	Polytetrafluoroethylene
Polypropylene	Polytriflurochloroethylene
Polystyrene	Polyisobutylene
Poly(vinyl chloride)	Poly-α-methyl styrene
Poly(vinylidene fluoride)	Poly(vinylidene chloride)
Poly(vinyl acetate)	Polymethacrylic acid
Poly(vinylalkyl ethers)	Polymethacrylates
Polyacrylic acid	Polymethacrylamide
Polyacrylonitrile	Polymethacrylonitrile
Poly(vinyl pyrrolidone)	Butyl rubber
Polyamides	Polysulphide rubbers
Polyurethanes	Poly(ethylene terephthalate)
Poly(ethylene oxide)	Cellulose and its derivatives
Polyalkysiloxanes	
Polyesters	
Natural rubber	
Synthetic carbon-chain rubbers (except butyl rubber)	

Polymers that can cross-link and degrade depending on appropriate conditions:
Poly(vinyl chloride)
Polypropylene
Poly(ethylene terephthalate)

predominantly cross-linking or chain scission as well as polymers that can undergo either cross-linking or chain scission depending on appropriate conditions. Paths have been proposed allowing cross-linking of typically degrading polymers and vice versa [48].

4.5.1.1. Mechanism

Absorption of high-energy radiation by polymers induces excitation and ionization and these excited and ionized species are the initial chemical reactants for graft polymerization as shown in the following table. The ejected electron must lose energy until it reaches thermal stability. The resulting species can further react to give free radicals, which can cause monomers to polymerize (6) and polymers to crosslink and degrade (7 and 8) and, in mixtures, monomers to graft to polymers (9). As can be seen, the radiation chemistry of polymers is a chemistry of neutral, cation, and anion radical, cations and anions, and excited species. The chemical nature and morphology of the material determine which of these reactions are predominant [49,50].

$$P \dashrightarrow P^+ + e^- \quad (1)$$

$$P \dashrightarrow P^* \quad (2)$$

$$e^- \longrightarrow e_{th}^- \quad (3)$$

$$P^{\cdot +} + e_{th}^- \longrightarrow P \quad (4)$$

$$P^* \longrightarrow R^{\cdot}{}_1 + R^{\cdot}{}_2 \quad (5)$$

$$R + nM \longrightarrow RM_n \quad (6)$$

$$P_n \xrightarrow{R^{\cdot}} X \quad (7)$$

$$P_n \xrightarrow{R^{\cdot}} P_{n-m} + P_m \quad (8)$$

$$P_n + mA \xrightarrow{R^{\cdot}} P_n A_m \quad (9)$$

where,
P = polymer substrate
e^- = electron
A, M = monomers
X = crosslinked polymer
$R^{\bullet}$ = radical
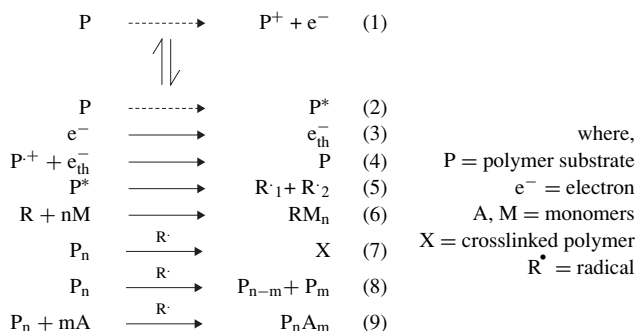
The primary reactive species involved in the radiation chemistry of macromolecules is the free radical. Free radicals are species having an unpaired electron, which results from cleavage of a chemical bond [46]. The electronic excitation or removal of valence electrons (ionization) can result in the formation of free radicals that may readily cross-link the polymer chains thereby increasing the molecular weight, hardness, and wear resistance [25]. The displacement of target atoms by energetic collisions can cause permanent damage in the polymer through chain scission by displacing atoms from polymer chains. This results in a deduction of average molecular weight. In other words, the reactions of the free radicals include: (1) abstractions (of H atoms, with preference for tertiary H, and of halogen atoms); (2) addition to double bonds, which are very efficient scavengers for radicals; (3) decomposition to give both small molecule products, such as carbon dioxide; and (4) chain scission and cross-linking of molecules.

Aromatic groups such as polyimides and polyetherimides are more resistant to irradiation compared to polymers that have groups such as C–Cl, for example, in PVC. Side chains such as methyl group in PP result in the production of CH4 on irradiation. The C–O–C linkage in polyoxymethylene is rather easily broken on

irradiation. It would be expected that polymers having a low heat of polymerization would be more susceptible to degradation by chain scission than polymers with high heat of polymerization. Polymers that predominantly cross-link eventually form highly interconnected, insoluble networks (giving a solvent-swelled gel on treatment with a compatible liquid solvent). Despite the excellent resistance of PTFE and other fluorinated polymers to chemical attack and elevated temperature, these materials are unfortunately among the least radiation resistant of polymers.

Oxidizing and nonoxidizing conditions play a very important part in surface modification. When oxygen is present it reacts very rapidly with radicals produced by irradiation. As a result, the free-radical reaction pathways and the molecular reaction products are dominated by oxidation chemistry and these differences are reflected in the physical property changes.

Based on the relative stabilities of different radicals, it is possible to understand which sites in a macromolecule should be preferentially oxidized, because radical migration can be expected to result in conversion to the most stable species. For example, if tertiary carbon atoms are present, radicals should prefer these sites to secondary carbon atoms, due to stability arguments. The time-dependent conversion of radicals to the most stable molecular sites can be observed by ESR spectroscopy. The relative radiation stabilities of different polymers have already been given [47]. It is a rough guide to show at what levels of dose the polymers can tolerate.

4.5.1.2. Application

In practice, the radiation-chemical method of initiation is often an easier method for preparing graft co-polymers. It is more universal because it can be used to generate any active centers and to prepare desired combinations of polymers and polymer materials for any substrates. Graft co-polymerization may proceed by both the free radical and the ionic mechanisms under the conditions generally chosen for grafting, but most often the free-radical mechanism is used [48]. Figure 4.2 illustrates the radiation-induced grafting on a polymer surface that was later used
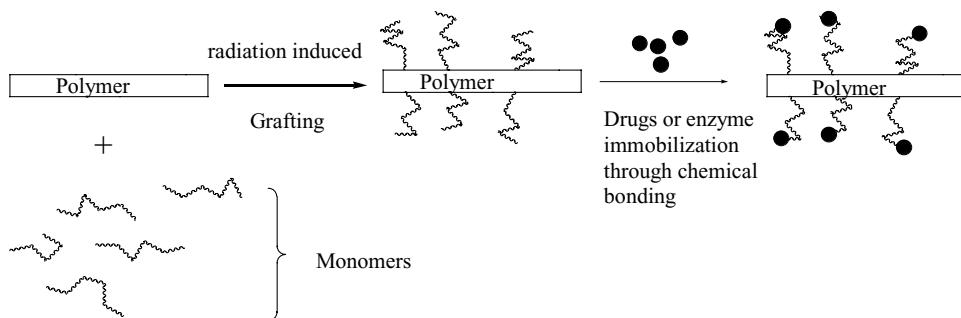
FIGURE 4.2. Illustrating the radiation-induced grafting on polymer surface and potential application.

to immobilize drugs or enzymes for further application [51]. The hydrophobic polymer is made hydrophilic via radiation-induced grafting. This hydrophilic surface has functional sites capable of binding chemically to enzymes or bioactive compounds [44].

Chua et al. used radiation-induced graft co-polymerization to develop a biofunctional poly(ε-caprolactone-co-ethyl ethylene phosphate; PCLEEP) nanofiber construct for hepatocyte culture [52]. This was achieved by conjugating hepatocyte-specific galactose ligands (AGH) onto the nanofiber surface. Poly(acrylic acid) was grafted onto the nanofiber scaffold via UV-induced polymerization using acrylic acid (AAc) monomers. The COOH sites on the grafted scaffold were then used as immobilization sites to conjugate AHG, using standard EDC chemistry. Studies have shown that AHG-congujated surfaces improve hepatocyte attachment and retain most of the cellular functions [53,54]. The functionalized AHG-P(AAc)-grafted nanofiber scaffolds exhibited much higher hepatocyte attachment as compared to unmodified scaffold [52]. Such nanofiber scaffolds would be advantageous in the design of a bioartificial liver-assist device, where the hepatocytes could attach to a scaffold with high surface area immobilized with a cell-specific ligand, maintain their differentiated functions, and remain stable against the perfusion and shear forces in the bioreactor [52].

4.5.2. Plasma-Induced Graft Co-Polymerization

Plasma is the fourth state of material and is composed of electrons, ions, free radicals, atoms, and molecules. There are two subdivisions for plasma: thermal equilibrium and nonthermal equilibrium plasma. For current use on polymers, the subdivision of nonthermal equilibrium is frequently used, which constitutes different plasma species having different temperatures. More precisely, the electrons usually have much higher temperature than the heavier particles (ions, atoms, molecules). In a plasma, important parameters include average electron temperature, ranging from 1 to 10 eV, electron density, varying from 109 to 1012 cm^{-3}, and degree of ionization, lying between 10^{-6} to 0.3 [27]. It is notable that, in plasma, compared to the high temperature of the electron, heavy particles have temperature around ambient condition (300 K or 0.025 eV) [28]. This heavy particle temperature is obviously suitable for treating many temperature-sensitive polymers, which will otherwise undergo degradation if exposed to a hot gas. Although the hot electrons, which are light and easily accelerated by the applied electromagnetic fields, can provide gas molecule energy through inelastic collision with them, to produce a chemically rich environment. Due to the advantages of plasma surface modifications, this technique is widely used in the polymer field. Many papers regarding this technique and its application are available [28,44,55]. The advantages of plasma surface include the following [27].

1. Modification can be limited to the surface layer, leaving the properties of the bulk material unaltered. Typically, the modification depth is several hundred angstroms.

FIGURE 4.3. Schematic of surface activation.

$$C\text{-}C\text{-}C\text{-}C\text{-}C \xrightarrow{\text{Ar}^*} C\text{-}C^{\cdot}\text{-}C\text{-}C\text{-}C$$

Substrate   Activated substrate
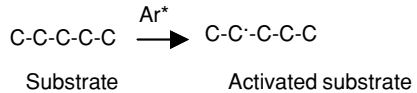
2. Nearly all polymer surfaces can be modified by plasma, no matter how the surface is composed.
3. It is possible to choose the type of chemical modification for the polymer through the choice of gas used in gas plasma.
4. Gas plasma treatment can avoid the problems encountered in wet chemical techniques such as residual solvent on the surface.
5. Plasma surface treatment is fairly uniform over the whole surface.

4.5.2.1. Mechanism

In plasma, as mentioned, many species exist:electrons, ions, and photons. The reaction of these species with the polymer can result in free radicals in the polymer main chain. The generation of free radicals can happen in two ways: the bombardment of the ions and photons can provide energy higher than the covalent C–C or C–H bonding energy and can break the C–C, or C–H bond to form C free radicals on the midpoint of the polymer main chain [56]; or through elastic or inelastic collision of the electron in the plasma with the polymer, the H can be abstracted, resulting in C free radicals.

When these activated polymers are exposed to monomers with unsaturated bonds, the radicals on the polymer play the role of initiator as in conventional polymerization and starts polymerization . This is called plasma-induced graft co-polymerization. One typical example is shown as follows.

1. Radicals are formed when the polymer are exposed to an inert gas (such as Argon) plasma (Figure 4.3).
2. Then the activated surface is exposed to the monomer (such as acrylic acid) with an unsaturated bond in the form of gas or liquid; a polymer layer is grafted on the polymer surface (Figure 4.4).

Another approach for this would be to expose the plasma-treated surface in air to form peroxides. This peroxide, after exposure to ultraviolet, decomposes and
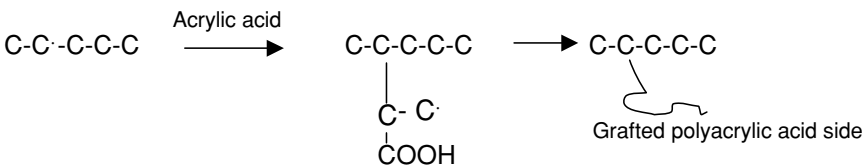
FIGURE 4.4. Grafting onto activated surface.

can later act as initiator to start a polymerization when the surface is exposed to monomers with unsaturated bond [32].

4.5.2.2. Applications

Via plasma surface modification, the surface properties, such as printability, wettability, hardness, and biocompatibility can be improved to a certain degree, thus this technique is widely used in fields such as print, plastic, and especially, these days, bioengineering. In this field, it can be used to make the surface more compatible, sterilizing the surfaces, to produce certain surface morphology to regulate cell functions, or to create a barrier to reduce undesirable diffusion of small molecules into or out of the substrate. Table 4.3 lists briefly some materials that have been plasma-surface modified in the bioengineering field.

In one instance, nonwoven mesh composed of polysulphone (PSU) ultrafine fibers (diameter, 1~2 μm) were fabricated via the electrospinning technique and

TABLE 4.3 Plasma surface modified materials employed in bioengineering field

Modified material	Modification method	Modification effect	Application field	Reference
PTFE and PET	Use argon plasma to activate surface , then graft collagen IV and laminin	Reduced fibrinogen adsorption and platelet adhesion	Vascular graft	57
PU	Si^+ and N^+ ion implantation	Improved wettability, anticoagulability and anticalcific behavior	Medical field	33,58
PLLA	Ammonia plasma	Improved growth in human vascular endothelial cell and rabbit microvascular endothelial cell	Cell transplantation and in vivo regeneration of vascular tissue	59
PMMA	Plasma activation followed by PEG grafting	Reduced cell adhesion and decreased incidents of retroprosthetic membrane formation after keratoprosthesis surgery	Artificial intraocular lens	60
SR	Argon plasma glow discharge followed by grafting PHEMA	Improved cell attachment and growth	Artificial cornea	61
SR	Ion implantation	Reduced biofouling and building up of thrombosis	Catheter	31,62
Titanium	Ion(nitrogen, calcium) implantation	Improved wear resistance, improved new bone regeneration	Orthopedic and dental	32,45,63
Cobalt-chromium	Ion implantation	Improved wear resistance	Artificial hip and joint	24

then surface modified using plasma-induced grafting towards development of a novel affinity membrane [64]. After heat treatment of the nanofiber mesh, carboxyl groups were introduced onto the PSU fiber surfaces through grafting co-polymerization of methacrylic acid (MAA) initiated by Ce(IV) after an air plasma treatment of the PSU fiber mesh. Toluidine Blue O (TBO), a dye which can form a stable complex with carboxyl groups, was used as a model target molecule to be captured by the PMAA-grafted PSU fiber mesh. Furthermore, the carboxyl groups on the PMAA-grafted PSU fiber mesh can be used as coupling sites for immobilization of other protein ligands. Bovine serum albumin (BSA) was chosen as a model protein ligand to be immobilized into the PSU fiber mesh with an encouraging capacity of 17 µg/mg, which implies other protein ligands can also be attached using the same method.

In addition to physical blending, to covalently graft ECM protein such as collagen and gelatin on nanofiber surfaces is the ultimate goal in development of biomimetic tissue engineering scaffolds. One of the most popular methods to covalently attach protein molecules on a polymer surface is grafting poly(methacrylic acid) on the biomaterial surface to introduce carboxyl groups at first, followed by the grafting of the protein molecules using water-soluble carbodiimide as the coupling reagent [65,66]. Nonwoven PET nanofiber meshes were prepared by electrospinning technology and were surface grafted with gelatin. The PET NF was first treated in formaldehyde to yield hydroxyl groups on the surface, followed by the grafting polymerization of methacrylic acid (MAA) initiated by Ce (IV). Finally the PMAA-grafted PET nanofiber was grafted with gelatin using water-soluble carbodiimide as coupling agent. For gelatin grafting on PCL nanofiber surfaces, the PCL nanofiber was first treated with air plasma to introduce -COOH groups on the surface followed by covalent grafting of gelatin molecules with the water-soluble carbodiimide as the coupling agent. Both the gelatin-modified PET and PCL nanofibers showed improved endothelial cell compatibility to those of the unmodified nanofibers [8]. Moreover, the gelatin-modified aligned PCL nanofiber also showed strong abilities to affect endothelial cell orientation.

4.6. Advantages and Disadvantageous

Each of the methods mentioned above has advantages and limitations. Some are better than others when viewed at a certain perspective. The following paragraphs give a brief description of the advantages and disadvantages of the methods as well as a comparison between the methods if applicable.

All the methods mentioned above allow surface modification (generally of several hundred Å) without affecting the bulk properties when appropriate conditions are selected. However, caution must be taken to ensure not too much of the nanofiber surface is eroded away.

Plasma treatment is probably one of the most versatile surface treatment techniques. Regardless of the structure and chemical reactivity of polymers, excited species generated in gas plasma allow the surface modification of any type of polymer. So if one is not aware of which method is the best for modifying a particular

polymer, this method would be a good choice with which to start. On top of this, by selecting an appropriate gas (argon, oxygen, nitrogen, fluorine, carbon dioxide, and water), it is possible to choose a desired type of chemical modification to produce unique surface properties required by various applications. Cross-linking can be induced via inert gas plasma. This method offers uniformity over the whole surface after modification. When compared to wet-chemical techniques, the use of gas plasma can avoid problems such as residual solvent on the surface as well as swelling of the substrate.

Plasma treatment seems to offer several advantages to a user, however, it can deter one from using it as well. The main drawback is that plasma treatments must be conducted in a vacuum system and hence the cost of operation is expensive. The process parameters are highly system-dependent; optimal parameters developed for one system cannot be adopted for another system. The scale-up of an experimental setup to a large production reactor is not a simple process. Last but not least, the plasma process is extremely complex. Achieving a good understanding of the interactions between the plasma and the surface is rather difficult [67].

Grafting as a technique is simple, useful, and versatile. The key advantage of this technique is that the surface of the same polymer can be modified to have very distinctive properties through the choice of different monomers. Grafting can occur both at the surface as well as in the bulk. The depth of grafting is controlled by the interaction between the substrate polymer and the solvent. If penetration of the solvent is limited to a very small depth, surface grafting predominates. On the other hand, if the solution can diffuse uniformly into the polymer substrate, homogeneous grafting prevails. This method cannot totally eliminate homopolymerization initiated by free radicals formed during irradiation of the monomer. However, a two-step method can be employed to minimize the formation of the homopolymer. The polymer is preirradiated in air to produce peroxide groups on the surface. Grafting is subsequently initiated thermally in contact with a monomer. Methods such as corona discharge, ozone treatment, and plasma treatment can also be used to generate peroxide groups on polymer surfaces [44]. Surface grafting has several interesting medical applications.

Chemical treatment usually employs harsh treatment, thus in most cases it can lead to undesirable surface changes such as severe surface roughening, excessive surface damage, and surface contamination, and also may not be environmentally green [68]. Also problems of yield and chemoselectivity might arise.

Radiation technology does not produce any harmful waste compared to chemical treatment. Also it requires less water consumption. It can generate radicals and promote grafting.

4.7. Summary

Electrospun polymer nanofiber is receiving an extensive research interest for applications in such diverse fields as separation technology and biotechnology. However, most of the polymer nanofibers do not possess any specific functional groups

and they must be specifically functionalized for successful applications. It can be seen that conventional polymer surface modification techniques can be applied to nanofibers. However, caution must be taken when applying these techniques. Nanofibers by virtue of their size require less harsh reaction conditions and controlled reactions to prevent the morphology from being destroyed. Nevertheless surface modification is a necessary tool to realize the potential of nanofibers as an affinity filtration membrane, tissue engineering scaffold, drug delivery carrier, biosensor/chemosensor, protective air filtration cloth, and other uses.

The successful modifications via blending, coating, and graft co-polymerization prove that nanofiber surfaces can be manipulated to design these for specific applications, endorsed by the successful preliminary results described within this chapter. Thus it gives us great hope that it is only a matter of time when immense research will begin to focus on surface modification of nanofibers, in particular to explore the possibility of employing other established techniques for nanofibers.

References

[1]   Klein, E. (2000). *J Membrane Sci* **179**, 1.
[2]   Luu, Y.K., Kim, K., Hsiao, B.S., et al. (2003). *J Controlled Release* **89**, 341.
[3]   Verreck, G., Chun, I., Rosenblatt, J., et al. (2003). *J Controlled Release* **92**, 349.
[4]   Ma, Z.W., Kotaki, M., Inai, R., et al. (2005). *Tissue Eng* **11**, 101.
[5]   Shin, M., Ishii, O., Sued, T., et al. (2004). *Biomaterials* **25**, 3717.
[6]   Xu, C.Y., Inai, R., Kotaki, M., et al. (2004). *Biomaterials* **25**, 877.
[7]   Yoshimoto, H., Shin, Y.M., Terai, H., et al. (2003). *Biomaterials* **24**, 2077.
[8]   Ma, Z.W., Kotaki, M., Yong, T., et al. (2005). *Biomaterials* **26**, 2527.
[9]   Elbert, D.L. and Hubbell, J.A. (1996). *Ann Rev Mater Sci* **26**, 365.
[10]   Kwoun, S.J., Lec, R.M., Han, B., et al. (2001). *The IEEE 27th Annual Northeast Bioengineering Conference*, March 31.
[11]   Wang, X., Drew, C., Lee, S.H., et al. (2002). *Nano Lett* **11**, 1273.
[12]   Lee, S.H., Ku, B.C., Wang, X., et al. (2002). *Mat Res Soc Symp Prog* 708, BB10.45.1.
[13]   Drew, C., Liu, X., Ziegler, D., et al. (2003). *Nano Lett* **3**, 143.
[14]   Wang, X., Kim, Y.G., Drew, C., et al. (2004). *Nano Lett* **4**, 331.
[15]   Ding, B., Kim, J.H., Miyazaki, Y., et al. (2004). *Sens Actuators B-Chem* **101**(3), 373.
[16]   Gouma, P.I. (2003). *Rev Adv Mater Sci* **5**, 147.
[17]   Timothy, H., Grafe, K., and Graham, M. (2003). *Fifth International Conference*, Stuttgart, Germany, March.
[18]   Gibson, P., Gibson, H.S., Rivin, D., (1995). *Colloids Surfaces A* **187**, 469.
[19]   Ratner, B.D. (2001). *Biosens Bioelectro* **10**, 797.
[20]   Fowkes, F.M. (1989). Acid-base interactions. In: *Encylcopedia of Polymer Science and Engineering Supplement* (John Wiley & Sons, New York) pp. 1–11.
[21]   Wu, S. (1982). *Polymer Interface and Adhesion* (Marcel Dekker, New York).
[22]   Griesser, H.J. and Chatelier, R.C. (1990). *J Appl Polym Sci Appl Polym Symp* **46**, 361.
[23]   Huang, J. and Hemminger, J.C. (1993). *J Am Chem Soc* **115**, 3342.
[24]   Gupta, B., Plummer, C., Bisson, I., et al. (2002). *Biomaterials* **23**(3), 863.
[25]   Dong, H. and Bell, T. (1999). *Surface Coatings Technol* **111**(1), 29.
[26]   Brown, I.G. (1993). *J Vacuum Sci Technol* A **11**, 1480.

[27] Chan, C.M., Ko, T.M., and Hiraoka, H. (1996). *Surface Sci Rep* **24**(1–2), 3.

[28] Liston, E.M., Martinu, L., and Wertheimer, M.R. (1993). *J Adhesion Sci Technol* **7**, 1091.

[29] Grace, J.M. and Gerenser, L.J. (2003). *J Dispersion Sci Technol* **24**(3–4), 305.

[30] Chu, P.K., Chen, J.Y., Wang, L.P., et al. (2002). *Mater Sci Eng R-Rep*orts **36**(5–6), 143.

[31] Uyama, Y., Kato, K., and Ikada, Y. (1998). *Adv Polym Sci* **137**, 1.

[32] Kato, K., Uchida, E., Kang, E.T., et al. (2003). *Prog Polym Sci* **28**(2), 209.

[33] Ikada, Y. (1994). *Biomaterials* **15**, 725.

[34] Desai, S.M. and Singh, R.P. (2004). *Adv Polym Sci* **169**, 231.

[35] Kaur, S., Gopal, R., Kotaki, M., et al. (2006). *Int J Nanosci* **5**(1), 1.

[36] He, W., Yong, T., Teo, W.E., et al. (2005). *Tissue Eng* **11**, 1575.

[37] Mina, B.M. Leea, G. Kimb. S.H. et al. (2004). *Biomaterials* **25**, 1289.

[38] He, W., Ma, Z.W., Yong T., et al. (2005). *Biomaterials* **26**(36), 7606.

[39] Graham, K., Gibson, H.S., and Gogins, M. (2003). *Technical Association of the Pulp & Paper Industry,* September 15–18.

[40] Mottola, H.A. (1992). Chemical immobilization in chemistry. In: *Chemically Modified Surfaces*, ed. H.A. Mottola, J.R. Steinmetz (Elsevier, New York) pp. 1–14.

[41] Penn, L.S. and Wang, H. (1994).: *Polym Adv Technol* **5**, 809.

[42] Bamford, C.H. and Al-Lamee, K.G. (1992). *J Chromatogr* **606**, 19.

[43] Ma, Z.W., Kotaki M., and Ramakrishna, S. (2005). *J Memb Sci* **265**, 115.

[44] Chan, C.M. (1993). *Polymer Surface Modification and Characterization* (Munich, New York).

[45] Ikada, Y. (1992). *Radiat Phys Chem* **39**(6), 509.

[46] Ghiggino, P.K. (1989). Chapter 3. In: *The Effects of Radiation on High-Technology Polymers*, ed. E. Reichmanis, and J.H. O'Donnell (American Chemical Society, Washington).

[47] Clough, R.L., Gillen, K.T., and Dole, M. (1991). Chapter 3. In: *Irradiation Effects on Polymers*, ed. D.W. Clegg, A.A. Collyer (Elsevier Applied Science, New York).

[48] Ivanov, V.S. (1992). Chapter 3. In: *New Concepts in Polymer Science: Radiation chemistry of Polymers*, ed. C.R.H.I. de Jonge (Utrecht, The Netherlands).

[49] O'Donnell, J.H. (1989). Chapter 1. In: *The Effects of Radiation on High-Technology Polymers*, ed. E. Reichmanis, J.H. O'Donnell, (American Chemical Society, Washington).

[50] Sangster, D. F. (1989). Chapter 2. In: *The Effects of Radiation on High-Technology Polymers*, ed. E. Reichmanis, J.H. O'Donnell, (American Chemical Society, Washington).

[51] Ivanov, V.S. (1992). Chapter 5. In: *New Concepts in Polymer Science: Radiation Chemistry of Polymers*, ed. C.R.H.I. de Jonge, (Utrecht, The Netherlands).

[52] Chua, K.N., Lim, W.S., Zhang, P.,et al. (2005). *Biomaterials* **26**, 2537.

[53] Yin, C., Ying, L., Zhang, P.C., et al. (2003). *J Biomed Mater Res* **67A**(4),1093.

[54] Ying, L., Yin, C., Zhuo, R.X., et al. (2003). *Biomacromolecules* **4**(1), 157.

[55] Mittal, K.L. (2000). *Polymer Surface Modification: Relevance to Adhesion, Vol. 2*, (Utrecht, Netherlands VSP).

[56] Wertheimer, M.R., Fozza, A.C., and Holländer, A. (1999). *Nuclear Instrument Meth Phys Res B* **151**, 65.

[57] van Wachem, P.B., Beugeling, T., Feijen, J. et al. (1985). *Biomaterials* **6**, 403.

[58] Lee, J.H., Jung, H.W., Kang, I-.K., et al. (1994). *Biomaterials* **15**, 705.

[59]   Hoffman, A.S., Achmer, C., Harris, C., et al. (1972). *Trans Am Soc Artif Intern Organs* **18**, 10.
[60]   Ma, Z., Gao, C., Yuan, J. et al. (2002). *J Appl Polym Sci* **5**, 2163.
[61]   Chu, C.F.L., Lu, A., Liszkowski, M., et al. (1999). *Biochim Biophys Acta*, **1472**, 479.
[62]   Ratner, B.D. (1996). Surface modification of polymers for biomedical applications: Chemical, biological, and surface analytical challenges. In: *Surface Modification of Polymeric Biomaterials*, ed. B.D. Ratner, D.G. Castner (Plenum, New York) pp.1–9.
[63]   Zhu, Y., Gao, C., and Shen, J. (2002). *Biomaterials* **23**, 4889.
[64]   Ma, Z.W., Kotaki, M., and Ramakrishna, S. (2006). *J Memb Sci* **272**, 179.
[65]   Steffensa, G.C.M., Nothdurfta, L., Busea, G., et al. (2002). *Biomaterials* **23**, 3523.
[66]   Ma, Z.W., Gao, C.Y., Ji, J., et al. (2002). *Europ Polym J* **38**, 2279.
[67]   Ford, W.T. (1992). Surface vs. internal reactivity of solid polymers. In: *Chemically Modified Surfaces*, ed. H.A. Mottola, and J.R. Steinmetz (Elsevier Science B.V.).
[68]   Mirzadeh, H., Katbab, A.A., Khorasani, M.T., et al. (1994). *Clinical Mater* **16**, 177.

5
Zinc Oxide Nanorod Arrays: Properties and Hydrothermal Synthesis

Kian Ping Loh and Soo Jin Chua

5.1. Introduction

5.1.1. Properties of ZnO Nanorods

With the emergence of nanoscience as a major research initiative in almost every research university today, there have been intense research efforts in the fabrication of one-dimensional semiconductor nanostructures [1]. These one-dimensional semiconductor nanostructures are considered to be the critical components in a wide range of potential nanoscale device applications due to the availability of a broad selection of composition and size in these materials [2]. Among them, ZnO possesses structural, electrical, and optical properties that make it useful for a diverse range of technological applications, such as ultraviolet/blue emission devices [3], piezoelectric devices [4], acoustic–optical devices, field emission [5,6], and chemical sensors [7]. ZnO (ΔEg $\geq$ 3.0 eV) is thought to be the most suitable material for UV laser devices among others such as ZnS, GaN, and ZnSe because of its large exciton binding energy of 60 meV, compared to 25 meV and 22 meV for GaN and ZnSe, respectively. For wide band-gap semiconductor materials, a high carrier concentration is usually required in order to reach an optical gain that is high enough for lasing action in an electron-hole plasma (EHP) process. Excitonic recombination in semiconductors is a more efficient radiative process and it can facilitate low threshold lasing. In order to achieve efficient excitonic laser action at room temperature, one critical factor is that the binding energy of the exciton must be much greater than the thermal energy at room temperature (26 meV). Therefore the large exciton binding energy of ZnO leads to very efficient near band-gap recombination at room temperature.

Room-temperature UV lasing from directionally grown ZnO nanorods was first reported by P.D. Yang's group at the University of Berkeley, with a threshold power density below $100 \, \text{kW cm}^{-2}$ [8]. The ZnO nanorods, which were grown on a-plane sapphire substrates via the vapor–liquid–solid (VLS) mechanism, were optically pumped by the fourth harmonic of Nd: yttrium–aluminum–garnet laser (266 nm) at room temperature. In the absence of any fabricated mirrors, it was observed that the evolution of the emission spectra with pump power from the ZnO nanorod was

typical of lasing action. When the excitation intensity exceeded the threshold, the integrated emission intensity increased rapidly with pump power. The narrow line width and the rapid increase of emission intensity indicate that stimulated emission takes place in these nanowires. These single-crystalline, well-faceted nanowires can be considered as natural resonance cavities. One end of the ZnO nanowire is the epitaxial interface between the sapphire and ZnO; the other end is the abrupt (0001) interface of the ZnO nanocrystals with air. The difference in refractive indices across the interfaces at the two ends of the nanorods allow the facets to serve as good laser cavity mirrors (refractive indices for sapphire, ZnO, and air are 1.8, 2.45, and 1, respectively). The ability of as-grown ZnO nanowire array to act as a natural resonant cavity or waveguide suggests that architectured arrays of these can be used as miniature laser components.

A p–n junction has been made from n-ZnO nanorod arrays grown epitaxially on p-GaN wafer by a Korean group [9]. The p–n junction shows high current density and strong luminescence even at a reverse bias of 3 volts, indicating that an electrically active nanojunction can be formed between the ZnO nanorod and GaN. It has also been demonstrated that an array of ZnO nanorods can exhibit enhanced photoconductivity [10]. For example, highly sensitive nanowire switches can be fabricated by tuning the photoconducting properties of individual ZnO nanowires. It has been found that the conductivity of ZnO nanowires is extremely sensitive to ultraviolet light exposure. The light-induced conductivity enables the wires to be reversibly switched between on and off states.

In addition to the high sensitivity, the nanowire photoconductors also exhibit excellent wavelength selectivity in terms of their photoconductivity. The light-induced photoconductivity has been proposed to be due to the combined effect of light and adsorbed oxygen on the ZnO. In the dark, oxygen molecules adsorbed on the nanowire surface as negatively charged ions formed by capturing free electrons from the n-type ZnO create a depletion layer with low conductivity near the nanowire surface. Upon exposure to UV-light, photo-generated holes migrate to the surface and discharge the adsorbed oxygen ions through surface electron hole recombination. At the same time, the photogenerated electrons significantly increase the conductivity of the nanowire. It follows therefore that the ZnO nanorod array can also be utilized as ultrasensitive gas sensors or photocatalyts due to its high surface area and photocatalytic properties.

The large surface area of nonpolar ZnO faces gives rise to an interesting size-property effect not related to the quantum confinement effect. Chen and co-workers [11] studied the cathodoluminescence (CL) from single-crystal ZnO nanorods with different diameters ranging from 50 to 180 nm. The CL spectra of individual nanorods show that the emission maxima move towards higher energy positions with decreasing nanorod diameter even though their sizes have not reached the quantum confinement effect regime. The anomalous energy shift has been explained by Chen to result from the enhanced surface resonance effect due to the higher surface-to-bulk ratio of the ZnO nanorod with a smaller diameter. Charge transfer from Zn to O in the nonpolar ($10\bar{1}0$) face results in an enhancement of

surface density of states beneath the bulk valence band maximum, resulting in an enlargement of the surface band-gap.

5.2. Synthesis Methods for ZnO Nanorod Arrays

5.2.1. *Chemical Vapor Deposition Methods*

In order to realize device applications in optoelectronics, the practical configuration will necessitate the growth of ZnO nanorod on a substrate, with an electrically active nanojunction. There are two main methods reported for the synthesis of aligned ZnO nanorods on substrates: either by chemical vapor deposition methods or hydrothermal synthesis. In both fabrication methods, the anisotropic growth of the ZnO crystal is due to a faster rate of growth in the c-axis, resulting in the morphology of a rod shape with the [0001] direction normal to the substrate. If the nucleation density on the substrate is high, as promoted by precoating the surface with a catalyst or a buffer layer of ZnO, the very dense vertical growth is a result of the crowding effect. Hence most of the vertically aligned growth reported in literature is not due to true epitaxial growth with respect to the substrate, but arises from the overcrowding effect.

It is now well established that vapor phase methods can produce high-quality aligned ZnO nanorod arrays, but gas phase reactions generally require prohibitively high growth temperatures of between 800–900°C. Yang and co-workers at the University of Berkeley demonstrated the fabrication of ZnO nanowire arrays on a-plane sapphire in a furnace [12]. The starting materials and the substrates were heated to 900°C in an argon flow and the Zn vapor was generated by carbothermal reduction of ZnO, and transported to the substrates where ZnO nanowires grew. A thin layer of Au catalyst was predeposited on the sapphire. The growth mechanism follows the well-known VLS mechanism. Selective growth can be readily achieved by patterning the Au thin film before growth. Wang and Summers [13] demonstrated large-scale hexagonal-patterned growth of aligned ZnO nanorods by using a catalyst template produced by a self-assembled monolayer of submicron polystyrene spheres.

Aligned growth of ZnO nanorods without catalyst has also been achieved using low-temperature chemical vapor deposition and metal organic chemical vapor deposition (MOCVD). Although no metal catalyst was coated on the sapphire, a very thin layer of ZnO buffer layer was grown at a low temperature prior to the ZnO nanorod growth. G. C. Yi et al. utilized diethylzinc (DEZn) and oxygen as reactants and ZnO nanorods can be grown on sapphire at 400–500°C [14].

5.2.2. *Solution Phase Methods Based on Hydrothermal Synthesis*

Wet-chemistry methods to grow ZnO nanowires are appealing because of the low growth temperatures and good potential for scale-up. The hydrothermal technique

Stainless
Steel cap

Stainless Steel
plate

Teflon Cap

Teflon
Liner

Stainless Steel
autoclave

Stainless Steel
plate
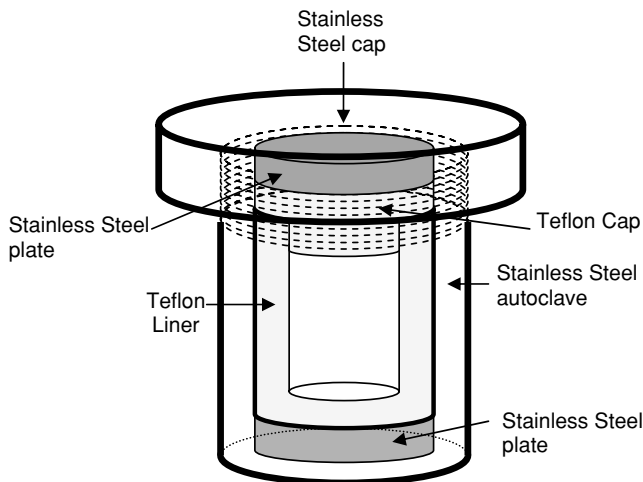
FIGURE 5.1. Schematic diagram of the mini-stainless steel autoclave and the Teflon liner.

has enjoyed a revived interest in the last five years due to the ease and flexibility in preparing a wide range of nanomaterials at low temperatures. The term "hydrothermal" is purely of geological origin. It was first coined by the British geologist, Sir Roderick Murchison, to describe the action of water under elevated temperature and pressure in bringing changes in the earth crust, leading to the formation of various rocks and minerals. Byrappa and Yoshimura proposed to define hydrothermal reaction as: "any heterogeneous chemical reaction in the presence of a solvent (whether aqueous or nonaqueous) above room temperature and at pressure greater than one atmosphere in a closed system" [15]. In a typical reaction, a precursor and a reagent capable of regulating the crystal growth are added into water in a certain ratio. This mixture is placed in an autoclave to allow the reaction to proceed at elevated temperature and pressures.

Figure 5.1 shows an example of the homemade autoclave employed in our experiment. The lid of the Teflon cup is specially machined to ensure that tension will be applied to seal the cup when the metal cap is tightened. The separate Teflon liner fits snugly into the autoclave without leaving any gap. The system is not provided with in situ pressure or temperature monitoring systems. Temperature gradients are appreciably lower in the liners than in the autoclaves without liners. This difference becomes more prominent when Teflon liners are used.

The reaction time ranges from a few hours to a few days. The major advantage of this approach is that most of the inorganic material can be made soluble in water at elevated temperatures and pressures. Figure 5.2 illustrates the different stages in the hydrothermal process, consisting of dissolution, supersaturation, and subsequent crystallization. Standard hydrothermal experiments are conducted under isothermal and isobar conditions without agitation. At the beginning of the experiment, the hydrothermal fluid consists only of water with solid precursor materials
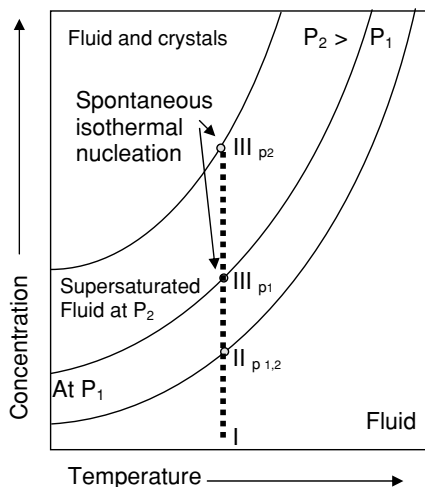
FIGURE 5.2. Isothermal-isobar hydrothermal processing: At (I) only water and precursor materials are present. Between (I) and (III): time-dependent precursor material dissolution. Nucleation occurs spontaneously if point (III) is achieved. A subsequent crystal growth process may only take place in the field of saturated solution.

(point I); it then gets more and more concentrated with time. Near the solubility limit of the product phase (point II, supersaturation), the precursor can still be dissolved. At a certain level of supersaturation (point III), spontaneous crystallization will finally occur, leading to a decrease of the concentration in the hydrothermal fluid [16].

Most of the nanomaterials synthesized using hydrothermal methods are dispersed in solution. The product, which is in powder form, is collected following sequential washing and centrifugation. Reports on the assembly of nanomaterials on substrate using the wet-chemistry method are relatively few. In this work, the focus is on the heterogeneous growth of one-dimensional nanorods on a substrate. When a substrate is introduced into an autoclave, instead of the homogeneous nucleation, there is additional heterogeneous nucleation that increases the complexity of the reaction.

The chemistry aspects of ZnO growth in a hydrothermal alkali environment has been reviewed previously by Demianets et al. [17], as well as Vayssieres [18,19]. Vayssieres proposed that controlling the interfacial tension is the key to controlling the shape and orientation of crystallites growing on a substrate from aqueous precursors. In an aqueous system, crystal nucleation will be induced when the solution is supersaturated. Initial nucleation can occur either in solution (homogeneous), or on the surfaces of solid phases (heterogeneous), depending on the net interfacial energy of the system. If the interaction between the growing nucleus and a substrate surface represents a lower net interfacial energy, heterogeneous nucleation is favored over homogeneous nucleation. It is well known that crystal–substrate adhesion energies (due to interfacial bond formation minus interfacial strain) can be dominant contributors to the net free energy for heterogeneous nucleation [20]. Thus far, almost all the templated hydrothermal synthesis methods rely on precoating the substrate with a ZnO buffer layer prior to the actual

hydrothermal synthesis to promote high density nucleation and oriented growth [21–27]. Because the ZnO buffer layer is prepared using chemical bath deposition, selected area synthesis via this approach is difficult. Moreover, regardless of whether vapor phase or wet-chemical synthetic methods are used for the growth of ZnO, the growth is mostly demonstrated on flat, two-dimensional substrates. The large area synthesis of ZnO nanorods via the solution methods has been achieved by Yang and co-workers [23] using a two-step procedure. The ZnO nanocrystals were first spin-cast several times on the Si wafer followed by the hydrothermal growth of ZnO nanorods.

5.2.3. Self-Assembly of Aligned ZnO Nanorods on Any Substrates via a Mineral Interface

As an alternative to using ZnO as a buffer layer to promote growth in hydrothermal synthesis, we research a method that can promote ZnO nanorod growth on any substrate, regardless of its crystal type and shape (flat or curved). One way to reduce the interfacial energy between the nucleus and substrate is through surface modification. Taking a cue from biomineralization, where organisms control surface nucleation and growth on substrate materials that are relatively inert, we have identified a mineral interface that will aid the nucleation of ZnO on any surface.

One complex mineral, which can only be achieved in a wet-chemistry environment, is the hydrotalcitelike (HTlc) zinc aluminum carbonate hydroxide hydrate (abbreviate as HTlc hereafter). HTlc belongs to anionic clays of general formula $[M(II)_{1-x}-M(III)_x(OH)_2].mH_2O)$, a family of layered solids with positively charged layers ($M(II) = Zn^{2+}$ or $Mg^{2+,}M(III) = Al^{3+}$) and interlayered charge balancing anions [27–29]. The compound has been extensively studied as catalysts, anionic exchanges, and sorbents [30,31]. The divalent (Zn^{2+}) and trivalent (Al^{3+}) metal are localized in the same layer, and occupy the octahedral holes in the close-packed configuration of the OH^- ions. The counteranions consist of carbonate ions and water that can freely migrate within the interlayer. Most of the synthetic HTlc are prepared by co-precipitation of the chosen M(II) and M(III) hydroxides with diluted NaOH or Na_2CO_3 solutions [27–30]. The calculated lattice mismatch between ZnO and HTlc–$Zn_{1-x}Al_xCO_3$ on the a-axis is about 5.78% if $x = 0.29$ (hexagonal ZnO, lattice constant $a = 3.2498$ Å, $Zn_{1-x}Al_xCO_3$ (hexagonal or rhombohedral), lattice constant $a = 3.052$ Å$\sim$3.079 Å, depending on the ratio between Al and Zn) [32]. The small lattice mismatch favors the nucleation of ZnO with its basal plane oriented parallel to the basal plane of HTlc. The preferential growth in the c-axis will result in a rise of well-aligned ZnO nanorods. In the actual experiments, controlling the concentration of Zn^{2+} and the thickness of the aluminum film is critical to allow the correct sequences of reactions to proceed.

The synthesis of HTlc and ZnO was performed in a mini-autoclave (refer to Figure 5.1) using NH_4OH and zinc acetate, and aluminum-coated silicon substrate. Aluminum-coated silicon was prepared by the electron beam evaporation

of aluminum on the silicon wafer. In a typical procedure, 6.83×10^{-4} mole (0.15 g) of zinc acetate ($ZnAc_2$) was dissolved in vigorously stirred deionized water (42 ml) to form clear solutions. Ammonia (28% NH_4OH) solution was added to the solution containing $ZnAc_2$ and this solution was transferred into a 50-ml Teflon-lined autoclave. Al-coated Si substrate was then suspended in the autoclave by a tantalum wire with the Al film facing downward. The autoclave was then put into the laboratory oven and the temperature was set at $100°C$ for three hours. Controlling the concentration of NH_4OH controls the amount of $Zn(OH)_4^{2-}$ in the solution. In aqueous solution at pH > 9, the concentration of Zn(II) hydroxyl complexes such as $Zn(OH)_4^{2-}$ increases. The chemical potential of OH^- in a system increases with increasing pH, and the forward equilibrium is to transform the hydroxyl complexes into solid Zn–O by dehydration.

$$OH^- + OH^- <—> O_2^- + H_2O \qquad (1)$$
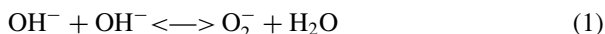
The crystal structure of ZnO was gradually constructed by dehydration between OH^- on the surface of the growing crystals and the OH^- ligands of the hydroxyl complexes. By controlling the ratio of the concentration of NH_4OH to the $ZnAc_2$ in the secondary growth experiment, the diameter of ZnO nanorods growing on the HTlc–$ZnAlCO_3$ can be controlled from 20 nm to 100 nm and the length from nm to sub-μm range.

By controlling the thickness of the Al film on silicon and the concentration of Zn^{2+} used in the hydrothermal synthesis, either thick multilayered HTlc sheets that roll up into a bundle (Figure 5.3a), or thin isolated hexagonal HTlc plates (Figure 5.3b), can be grown. Apparently the HTlc acts as an excellent lattice-matched template for the assembly and growth of c-plane oriented ZnO nanorods. Figures 5.3b–d display the SEM images whereby we interrupt the hydrothermal synthesis at intervals to study the sequences in the assembly process, starting from the synthesis of the thin HTlc template initially, as shown in Figure 5.3b, to the oriented assembly of ZnO nanorods on the edges of the HTlc hexagonal template in Figure 5.3c, and finally to the complete oriented coverage of the HTlc template by ZnO nanorods in Figure 5.3d. The preferential nucleation on the edges of the HTlc template at first gives rise to beltlike ZnO nanorod arrays in Figure 5.3c; this might be related to the higher surface free energy on the faceted edges.

Figure 5.4a shows the images of ZnO nanorods that have self-assembled on the hexagonal HTlc template; the hexagonal shape of the template can be clearly observed by the way all the ZnO nanorods packed to form two-dimensional hexagonal arrays. Both the top and bottom faces of the HTlc provide sites for the nucleation of the ZnO. The changes in the crystal phases have been monitored by grazing angle XRD, as shown in Figure 5.4b. Initially, the diffraction peaks are due to the rhombohedral phase of HTlc alone; after longer growth time, diffraction peaks due to hexagonal ZnO appear.

From the SEM images, it is clear that the ZnO nanorods are oriented with their growth axis perpendicular to the hexagonal template, and packed intimately. The ZnO nanorods are about 80 nm in diameter and have catalyst-free, pyramidal-shaped tips. High-resolution TEM images and the diffraction pattern of
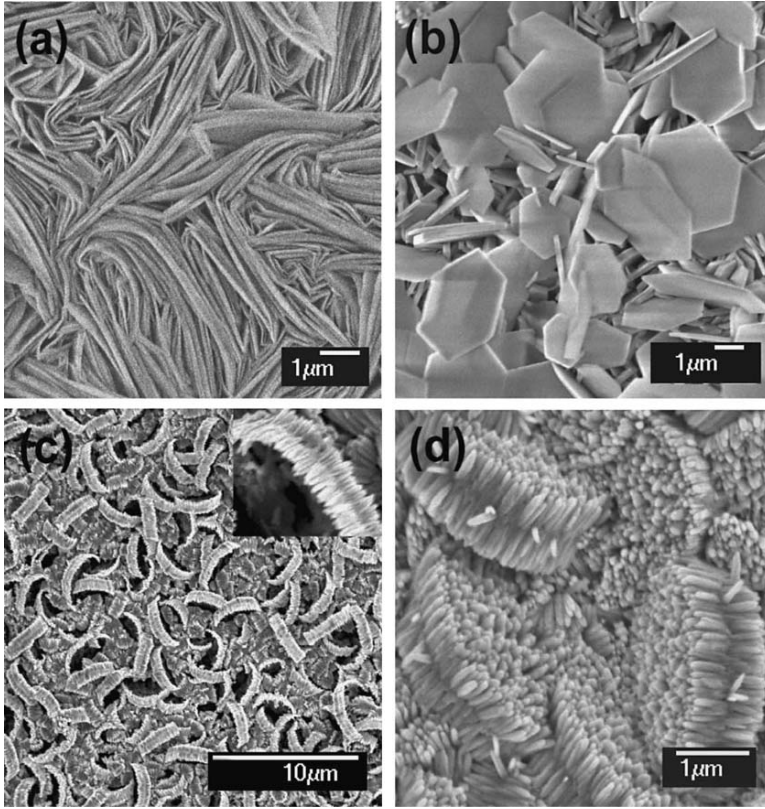
FIGURE 5.3. (a) Thick multilayered HTlc sheets obtained when Al thickness on silicon is ~1 μm, in 0.31 M of Zn(Ac)$_2$, pH 10, 100°C; (b) Isolated hexagonal HTlc plates obtained when Al thickness is ~1 μm, in 0.016 M of Zn(Ac)$_2$; (c) and (d) Various stages in the assembly of ZnO nanorods on HTlc-template when Al thickness on silicon is ~100 nm, in 0.016 M of Zn(Ac)$_2$.

the ZnO nanorod growing on the HTlc are shown in Figures 5.5a and b, respectively. The interplanar separation of 0.52 nm as indicated suggests that the growth axis is c-axis oriented, thus the (002) plane of the ZnO is oriented parallel to the (002) face of the rhombohedral HTlc template. The very tight packing density of the ZnO nanorods suggests a very efficient nucleation process on the HTlc template. One individual discrete unit of the ZnO array on an HTlc platform in Figure 5.4a may act as a free-standing, micron-size lasing array with hundreds of oriented ZnO nanorods, or as a photonic waveguide unit.

The process described in the preceding section is a kind of template-assisted assembly of ZnO nanorods. The question is: can we remove the ZnO nanorods from the HTlc template? The results show that delamination of the ZnO nanorods on both sides of thin HTlc–ZnAlCO$_3$ can be brought about by thermally annealing the entire
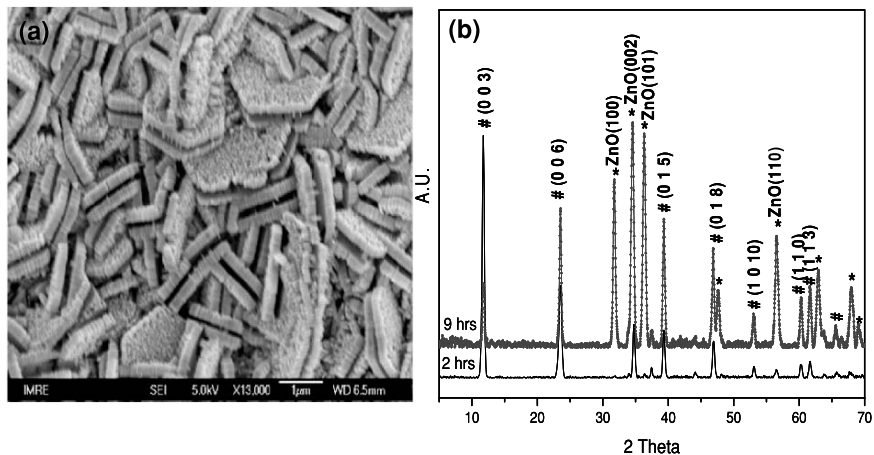
FIGURE 5.4. (a) SEM image showing the self-assembled hexagonal array of ZnO nanorods; (b) XRD pattern of ZnO nanorods grown on HTlc-template, where the peaks can be assigned to HTlc–$ZnAlCO_3$ (#-labeled peaks) and ZnO (*-labeled peaks). The presence of multiple diffraction peaks is due to the presence of differently oriented ZnO/HTlc platforms, but within one ZnO/HTlc unit, the ZnO nanorods adopt only c-axis orientation on the HTlc.

structure. Figure 5.6 illustrates the schematic showing how a twin ZnO nanoarray block can be separated following thermal annealing. Separation is possible only if the HTlc–$ZnAlCO_3$ template is thin, otherwise the HTlc–$ZnAlCO_3$ will be transformed into a mineral called garcite (i.e., $ZnAl_2O_4$), and the ZnO remains attached. Figures 5.6a and b show ZnO nanorod arrays on both sides of the thin HTlc–$ZnAlCO_3$ becoming nicely separated following annealing in air (10 torr) at 500°C for two hours. The delamination arises from the decarbonation of the HTlc sheets; the interlayer anions will be released as CO_2 and H_2O.

If the silicon sample is coated with Al film of 5-nm thickness, the thinness of the Al layers allows the assembly of vertically aligned ZnO to proceed rapidly on the silicon substrate, possibly through an ultrathin HTlc-mediated interface that is oriented flat on the substrate face, and thus is not visible to SEM visualization. Oriented assembly of ZnO nanorods on the entire silicon sample face could be achieved via this approach, as shown in Figure 5.5c. Grazing angle XRD analysis of the ZnO-coated silicon sample shows only one strong (002) peak in Figure 5.5d, which is clear evidence of oriented assembly of the single crystalline ZnO nanorods with their (002) plane parallel to the silicon face. The control experiment which is carried out without the aluminum precoat achieves only sparsely distributed ZnO crystals that show random orientation with respect to the plane of the silicon.

Although we have demonstrated that Al-coated silicon is effective for the fabrication of oriented ZnO nanorods, one question is whether the presence of Al introduces deep trap centers in the energy gap of ZnO. Figure 5.5e shows the room-temperature photoluminescence spectrum of the ZnO nanorods assembly,
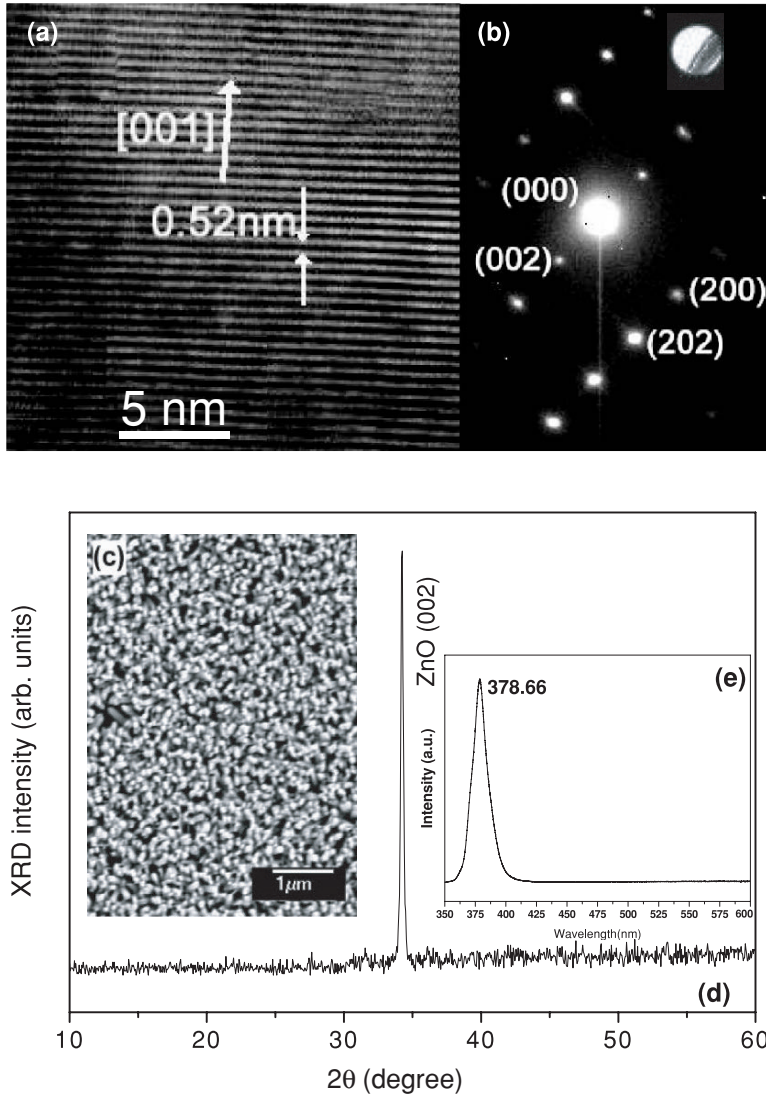
FIGURE 5.5. (a) and (b) HRTEM image and electron diffraction pattern of a ZnO nanorod, respectively; (c) Plan view SEM image of aligned ZnO nanorods synthesized on silicon coated with 5-nm Al film; (d) XRD 2θ scan showing only the (002) peak, indicating *c*-axis orientation; (e) Room-temperature PL spectrum of aligned ZnO nanorods.

exhibiting only one single strong luminescence peak centered at 382 nm which is associated with the exciton recombination. The absence of defect-related or impurity-related trap centers indicates that the optical properties of ZnO nanorods fabricated this way are of excellent optical quality.
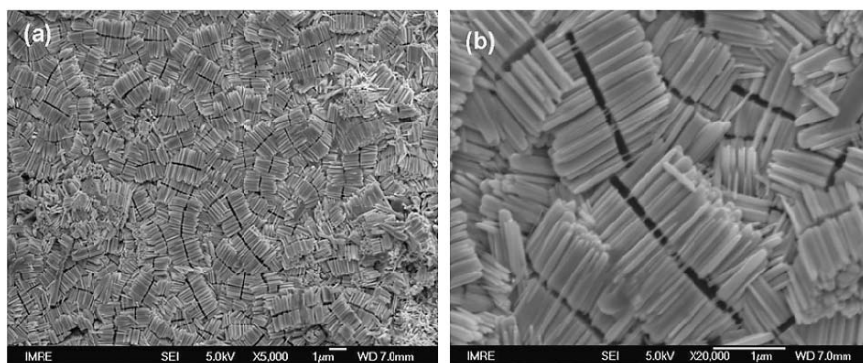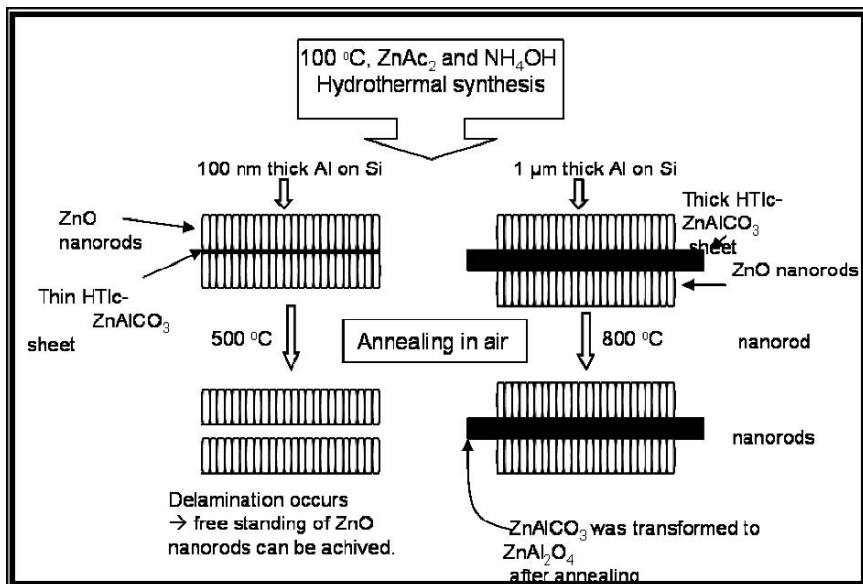
FIGURE 5.6. (Top) Schematic showing how the HTlc–$ZnAlCO_3$–ZnO assembly can separate into free-standing ZnO bundles after thermal annealing. (Bottom) (a) and (b) SEM images of ZnO bundles after annealing in air at $500°C$ for 2 h; the HTlc–$ZnAlCO_3$ template has vanished.

5.2.4. Field Emission

Field emission measurement was carried out on the ZnO nanorods array grown on silicon, as shown in Figure 5.7(a). The experiments were performed in a vacuum chamber with a base pressure of 1×10^{-7} Torr. The distance between an indium tin oxide anode and the sample is 150 μm. The measured emission area is 0.20 cm^2. The emission current-voltage characteristics are analyzed using the
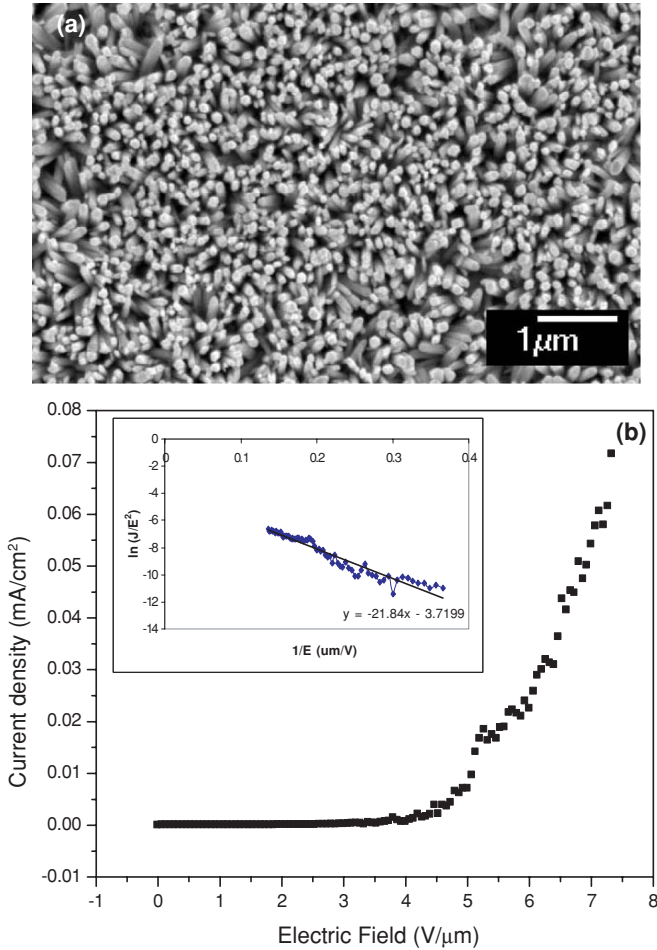
FIGURE 5.7. (a) SEM image of the ZnO nanorods grown on Si substrate with a very thin layer of Al precoat; (b) FE current density as a function of the applied electric field. Inset: FN-plot of FE density and electric field.

Fowler–Nordheim (FN) equation for field emission:

$$J = A\,(\beta^2 E^2/\phi)\exp(-B\phi^{3/2}/\beta E),$$

where J is the current density, $A = 1.56 \times 10^{-10}$ (amperes V^{-2} eV), $B = 6.83 \times 10^3$ (V $eV^{-3/2}\mu m^{-1}$), β is the field enhancement factor, ϕ is the work function, and E is the applied field which is equal to V/d (applied voltage over the distance between the anode and the cathode).

The ZnO nanorods used for field emission studies have diameters of approximately 100∼150 nm and lengths of 500 nm. Figure 5.7b illustrates the emission
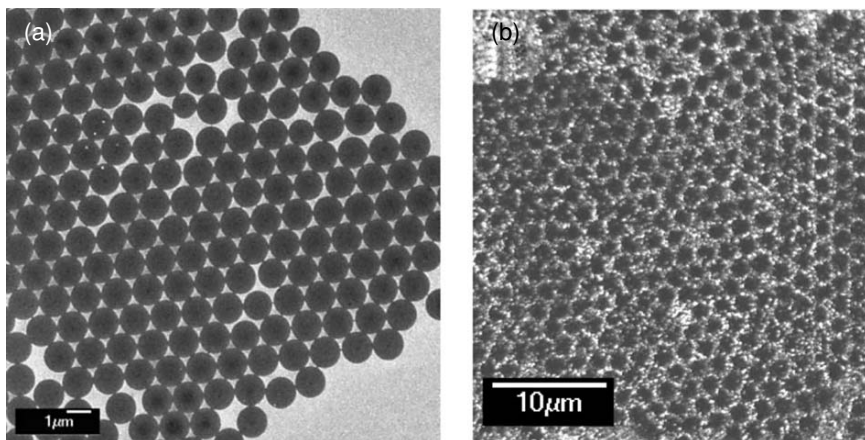
FIGURE 5.8. Selective growth of ZnO nanorods on patterned Al dots: (a) Patterned Al dots formed by the microsphere lithography methods, the triangularly shaped white regions between the black circles are areas coated with Al; (b) Selective nucleation of ZnO on the Al-coated regions.

current density from the ZnO nanorod arrays. The turn-on voltage was about 2.73 V/μm at a current density of 0.1 μA/cm^2. The current density increases to 70 μA/cm^2 at 7.5 V/μm. The FE properties of the ZnO nanorods prepared via hydrothermal method are superior to the one reported by Lee et al. [5], which has a higher turn-on voltage at 6.0 V/μm with a lower current density at 0.1 μA/cm^2. The plot of $\ln(J/E^2)$ versus $1/E$ (μm/V) exhibits typical Fowler–Nordheim behavior. The field enhancement factor β, a parameter related to the geometry and conductivity of the tip, is calculated to be 3800 from the gradient of the plot, using the reported work function of 5.3 eV from ZnO [5] 5.3 eV. The β value calculated here is comparable to CNT and it is sufficient for field emission application.

5.2.5. Selected Area Assembly

The heterogeneous growth suggests that the selective assembly of the ZnO nanorods should be possible by first lithographically patterning a thin film of Al on the substrate during hydrothermal synthesis. To demonstrate selective area growth on the Al-seeded areas, we apply the conventional microsphere lithography method to catalytically pattern the silicon surface with an hexagonal array of aluminum dots. Figures 5.8a and b demonstrate the patterned substrate before and after hydrothermal synthesis. Figure 5.8b shows that the nucleation of ZnO is specific to the region coated with Al. This is very clear evidence that the hydrothermal conditions utilized in this work are operating in regimes where interfacial energy controls the nucleation.

In another experiment, we coated Si pillars with a very thin layer of Al film (∼5 nm) via electron beam deposition. The Si pillars were prepared using the
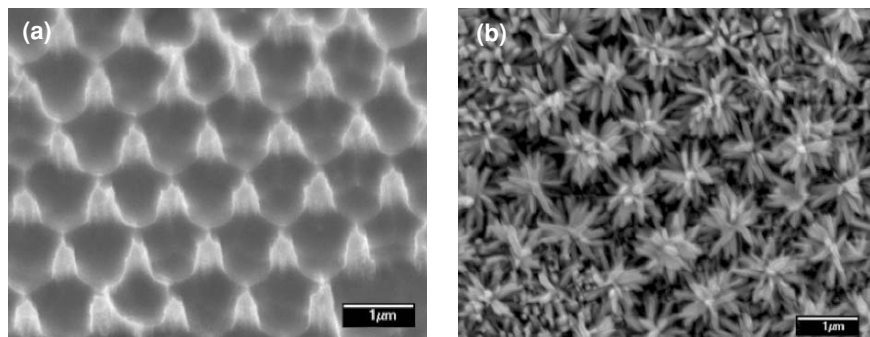
FIGURE 5.9. SEM images of (a) Si pillars prepared by microsphere lithography; (b) ZnO nanorods grown on Si pillars.

microsphere lithography method followed by plasma etching to create the desired pattern. A very thin layer of HTlc was formed on the Al-coated region and this facilitated the nucleation of ZnO on these surfaces, followed by the growth of ZnO nanorods, as shown in Figure 5.9.

5.2.6. Oriented Assembly of ZnO on Curved Surfaces

The challenge is to grow uniformly coated ZnO nanorods on curved surfaces. This is where hydrothermal synthesis affords unique advantages compared to vapor phase techniques due to the isotropic supply of reactants to the growing face in the solution phase. To evaluate this, carbon nanotube (CNT) arrays grown on silicon by chemical vapor deposition technique are used as the substrate. The CNT arrays are precoated with ~5-nm-thick Al film, and then subjected to hydrothermal synthesis using similar growth conditions. Remarkably, both radial as well as tangential coating of the CNT with ZnO nanorods could be achieved as shown in Figure 5.10a–c. The CNT two-dimensional array becomes a scaffold supporting
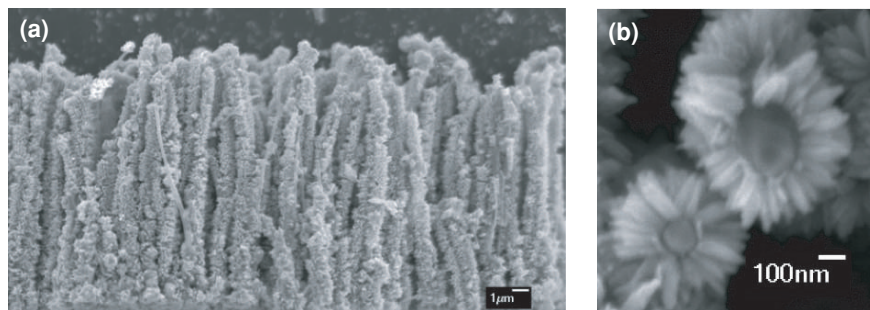
FIGURE 5.10. (a), (b) SEM image of ZnO nanorods grown on CNT.
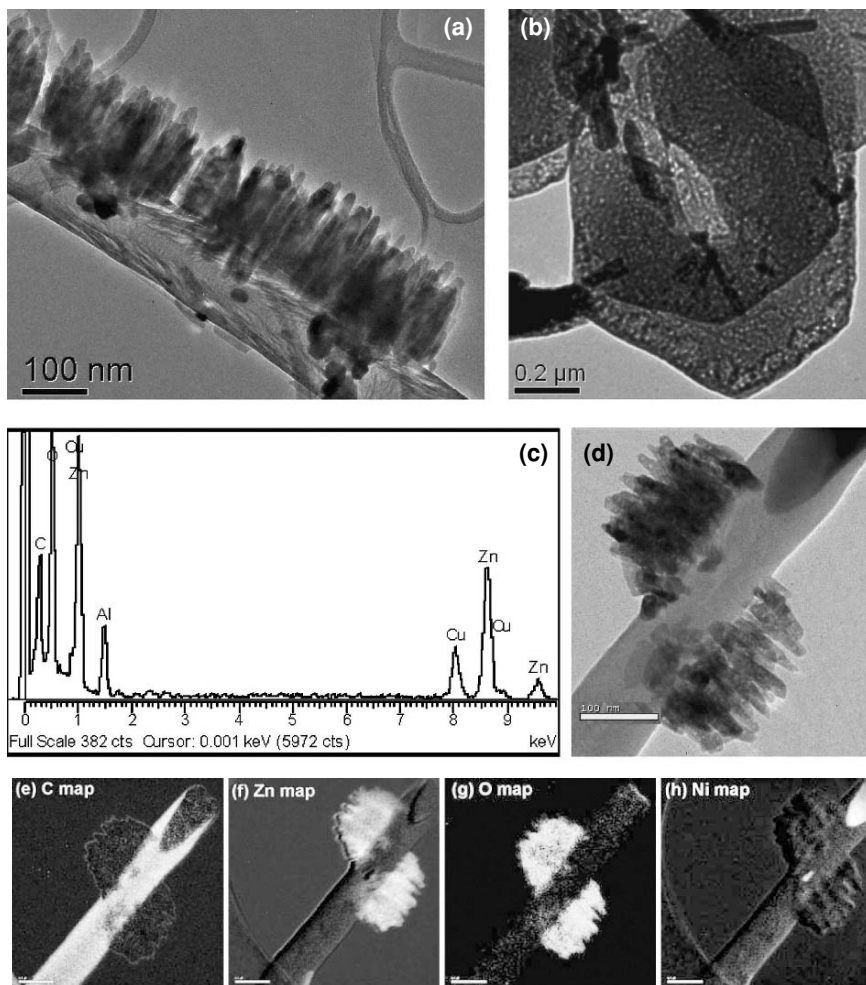
FIGURE 5.11. (a) TEM image of ZnO–CNT system; (b) TEM image of hexagonal HTlc–ZnAlCO$_3$sheet obtained when Al film is 100-nm thick; (c) EDX spectrum taken from the hexagonal HTlc–ZnAlCO$_3$ sheet shown in (b); (d) TEM image of ZnO–CNT before annealing. (e)–(h): EELS elemental mapping of ZnO–CNT shown in (d).

the high density of ZnO nanorods along the radial and tangential axes of individual nanotubes. The dimension of one single nanorod is about 30∼50 nm, which is smaller than that obtained on the flat surface (∼100 nm) shown earlier. This suggests that a curved surface will promote the growth of thinner ZnO rods due to the smaller contact area. The TEM images of the ZnO–CNT assembly are shown in Figures 5.11a and b. From Figure 5.11a, small hexagonal HTlc- sheets can be seen to adhere to the CNT; we believe that these HTlc sheets are responsible for

the nucleation of ZnO on CNT. Energy-dispersive X-ray (EDX) spectra recorded from a larger hexagonal sheet confirms the present of Al and Zn in these. Elemental mapping of Zn, C, O, and Ni using electron energy loss spectroscopy (EELS) is shown in Figures 5.11d, e, f, and g, respectively. The presence of the element is evidenced by areas of bright contrast. The results, as anticipated, indicate that the nanorods consist of Zn and O. The element Ni is observed at the CNT tip because it is used as a catalyst for CNT growth.

ZnO can have oxidative photocatalytical properties when it is excited with radiation with wavelength shorter than the energy of the band gap. During the photoexcitation process, holes and electrons will be generated and the holes can react with water and be converted into hydroxyl radicals which are strongly oxidizing species. These hydroxyl radicals can react with aromatic compounds through a diffusion-controlled process [33]. Our preliminary investigations show that supporting the ZnO nanorod on a 3-D scaffold enhances the effective surface area for photocatalysis compared to a ZnO nanorod grown on a 2-D substrate.

In one experiment, both types of samples that had base silicon areas of 25 mm^2 were placed into beakers containing 5 ml aqueous solution containing 30 ppm of phenol; these were then exposed to UV irradiation from a 125-W Hg lamp. After five hours, no measurable change was detected from the sample containing ZnO nanorod grown on the flat silicon substrate, whereas a 10% reduction in phenol concentration could be detected from the sample containing the ZnO-coated CNT array, suggesting that the higher density of 3-D supported ZnO nanorods is responsible for the improved photocatalytic effect. Similar experiments have been carried out on Al-coated polystyrene microbeads that have been spin-coated on silicon using microsphere lithography. We find that uniform coating of the ZnO nanorods around the microbeads can be obtained as well, as shown in Figures 5.12a and b. This indicates that hydrothermal synthesis can achieve high-density coating of ZnO on any type of surfaces precoated with an aluminum film.
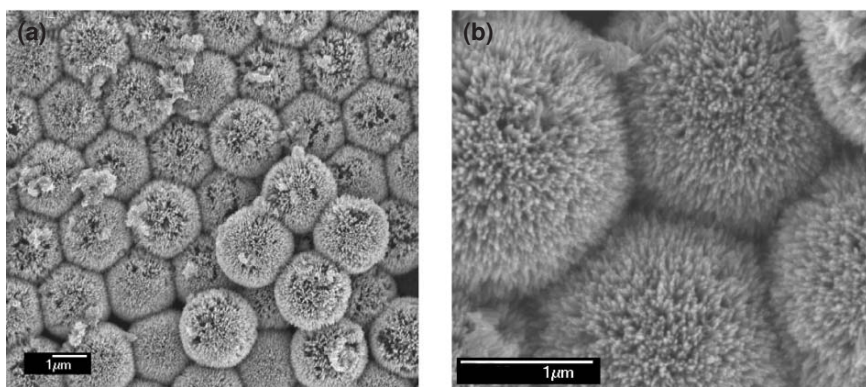
FIGURE 5.12. (a), (b) Assembly of ZnO nanorods on Al-coated polystyrene spheres.

5.2.6.1. Epitaxial Growth of ZnO on GaN Surfaces

The previous section describes a strategy to grow aligned ZnO nanorods on any surface by precoating the surface with an aluminum coat. Although this method may be useful for catalytic applications due to the ease of generating a high density of ZnO nanorods, the applications in optoelectronic devices are limited. The absence of a well-defined epitaxial interface means that a nanojunction between the ZnO and the substrate cannot be formed. In this section we describe the hydrothermal synthesis of ZnO on GaN where the growth of well-aligned ZnO nanorods occurs epitaxially. This process is highly relevant to the fabrication of n-ZnO/p-GaN type devices. In this section, the ZnO nanorods were epitaxially grown by using the aqueous solution described in the earlier section. This growth method showed some advantages compared with others, such as the use of simple equipment, low temperature deposition (100°C), low cost, and not requiring the use of hazardous metalorganics or metal catalysts. The GaN substrate was used as a template for the ZnO nanorod growth because these materials have the same wurtzite crystal structure, similar in band-gap energy (~3.7eV), and small lattice constant mismatch (1.9%).

Growing ZnO nanorods on GaN offers a new method to fabricate the GaN nanotube because the ZnO is easily decomposed in the hydrogen ambient at 600°C [34]. In addition, n-ZnO nanorod on p-GaN has a potential application in heterojunction-based devices [44] due to the increase in carrier injection efficiency in the nanojunction [45,46]. To the best of our knowledge, this is the first report on growth of ZnO nanorods on GaN using a wet-chemistry method.

Well-aligned ZnO nanorod arrays were grown directly on the GaN substrate. The experimental procedure is described as follows. $Zn(CH_3COO)_2 \cdot 2H_2O$ (0.016 M) was first dissolved in deionized water at room temperature. NH_4OH (0.095 M) was next added to the solution to create the alkaline environment (pH 10). The resulting suspension was transferred into a Teflon-lined stainless steel autoclave. A GaN substrate, after cleaning with deionized water, was dipped into the solution and suspended in the autoclave by a tantalum wire. Finally, the autoclave was sealed and put into the oven. The hydrothermal treatments were carried out from 60–150°C. After the growth, the autoclave was allowed to cool down naturally. The samples were taken out, washed in the deionized water several times, and dried in air.

The surface morphology and the crystalline quality were characterized using a scanning electron microscope (SEM) and X-ray diffraction (XRD), respectively. The photoluminescence measurement was carried out on the synthesized ZnO nanorods.

5.3. Characterization of ZnO Nanorods

5.3.1. Morphology of ZnO Nanorods

Figure 5.13 shows the SEM image of the ZnO nanorods, grown on the (0001) GaN substrate for five hours at a temperature of 100°C. The solution has a pH of approximately 9 to 10, containing 0.25 g zinc acetate at a concentration 0.016 M.

FIGURE 5.13. SEM image of ZnO nanorods with tilt angle.
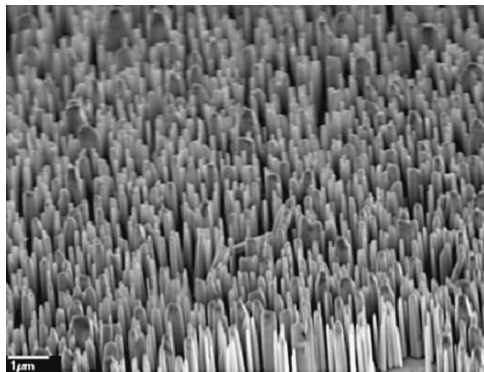
Nanorods uniformly covered the entire surface and each has a hexagonal cross-section with a sharp tip at the top. From the cross-section image, the rods are seen to grow vertically from the GaN substrate surface, with uniform thickness and length distributions. The diameter and length of the nanorods are 80–120 nm and approximately 1 μm, respectively. The hexagonal shape of the nanorods reveals that the rods grew epitaxially on the GaN film. The diameter, length, and density of the ZnO nanorods can be changed by varying the growth time and reactant concentration. The nanorods with diameter 60 nm and length up to 2 μm can be achieved by increasing the reactant concentration to 0.021 M and increasing the growth time to seven hours.

5.3.2. Crystalline Property of ZnO Nanorods

The crystal structure of the nanorods was characterized by XRD. During the measurement, the 2θ was scanned and the ω value was kept constant in order to avoid the GaN peak arising from the substrate. From the XRD spectrum shown in Figure 5.14, the strong peak at $2\theta = 34.42°$ is due to ZnO (0002) crystal plane, from which value a lattice constant of 5.206 Å was estimated. In addition, a small peak corresponding to the ZnO (0004) crystal plane was also observed. The strong (0002) diffraction peak is consistent with the SEM images, which show well-oriented arrays of ZnO nanorods with a preferential growth along the c-axis. All the observed diffraction peaks can be indexed to the hexagonal phase of ZnO.

5.3.3. Optical Properties of ZnO Nanorods

As a potential material for photonic applications, it is important to evaluate the optical properties of ZnO. Photoluminescence measurement was performed on the ZnO nanorod/GaN substrate because it is an effective method to investigate the presence of defects. Figure 5.15 shows the PL spectrum at room temperature of the ZnO nanorods grown on GaN substrate (full line) and of the GaN substrate
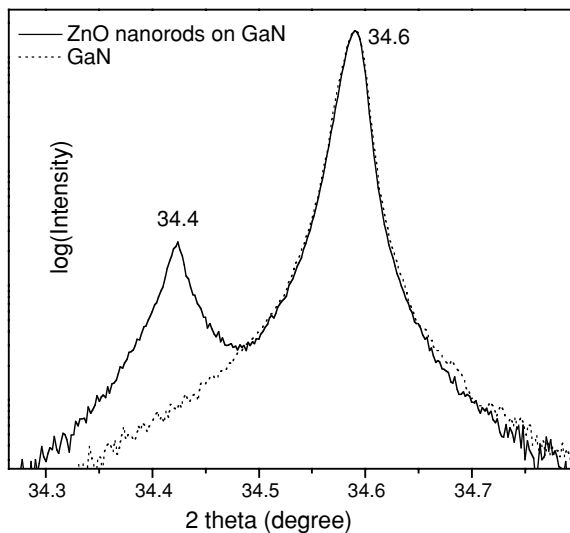
FIGURE 5.14. XRD spectrum of ZnO.
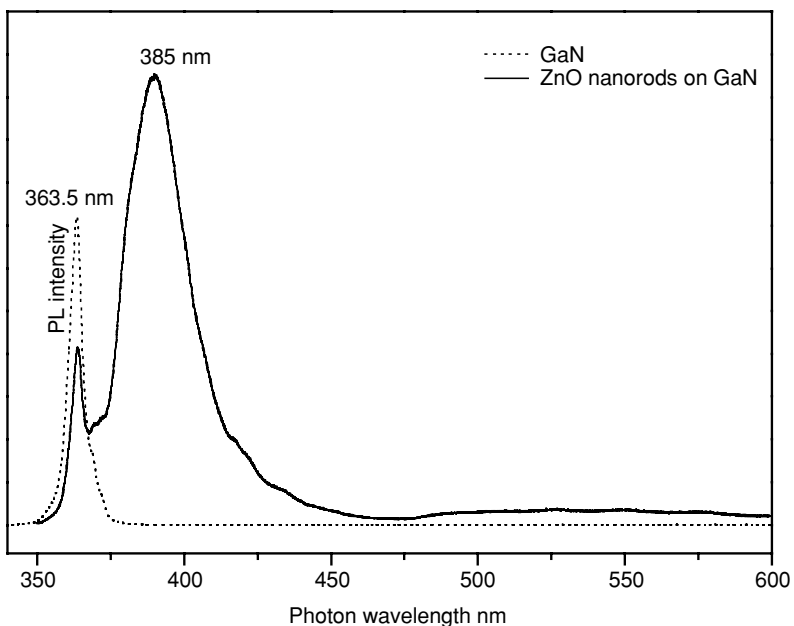
FIGURE 5.15. The photoluminescence spectra of ZnO nanorods (full line) and GaN substrate (dotted line) at room temperature.

(dotted line). The PL spectrum of the GaN substrate was confirmed by removing the ZnO nanorods from a small area of the GaN substrate. The nanorods exhibit a PL peak in the vicinity of the band edge at 385 nm (3.23 eV). This peak is attributed to the exciton-related recombination [38]. In addition, the small peak at 363.5 nm was also observed. This peak comes from the GaN substrate due to the fact that the ZnO nanorods did not cover the entire GaN surface. Besides, the defect peak, centered at 520 nm (2.38 eV) was also observed. This peak is attributed to singly ionized oxygen vacancies in ZnO and the emission results from the radiative recombination of a photo-generated hole with an electron occupying the oxygen vacancy [39–40]. To our knowledge, the ZnO nanorods we have grown have the highest intensity ratio of the band edge emission to the deep level emission among those obtained by solution methods [41–42].

5.3.4. Growth Mechanism of ZnO Nanorods

The growth mechanism of ZnO nanorods in aqueous solution is discussed next. The principle of aqueous solution techniques is based on heterogeneous nucleation and subsequent crystal growth on a specific surface. The heterogeneous nucleation is induced in a supersaturated solution at a relatively low degree of supersaturation. The condition of the aqueous solution can be controlled by adjusting the reactant concentration, growth temperature, and the pH. The crystal phase of the deposits was mainly determined by the pH of the aqueous solutions. If the pH is in the range 6 to 9, the Zn(OH) is predominantly formed. The wurtzite ZnO crystal is formed at pH 9–13 [43]. During the progress of the formation of ZnO, the complex ion $Zn(NH_3)_4^{2+}$ or $Zn(OH)_4^{2-}$ was formed first. The equations expressing the thermal equilibrium of the ZnO–H_2O system are given below:

$$Zn^{2+} + H_2O \leftrightarrow ZnO + 2H^+$$
$$ZnOH^+ \leftrightarrow ZnO + H^+$$
$$Zn(OH)_2 \leftrightarrow ZnO + H_2O$$
$$Zn(OH)_3^- + H^+ \leftrightarrow ZnO + 2H_2O$$
$$Zn(OH)_4^{2-} + 2H^+ \leftrightarrow ZnO + 3H_2O$$
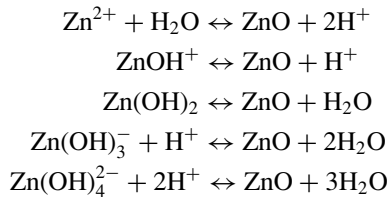
With an increase in temperature, these complexes will be dehydrated. The ZnO crystal forms a heterogeneous nucleus at the interface between substrate and solution. After that, the crystals begin to grow into the nanorods.

From Figure 5.16, it is seen that the ZnO nanorods grown on the GaN substrate have hexagonal cross-sections with well-formed faceted prismatic morphology at the tips. The possible mechanism suggested is that the formation of hexagonal-shaped ZnO rodlike crystal is attributed to the difference in the growth rates of the various crystal facets, resulting in the observed crystallite shape [44]. The relative growth rates of these crystal faces, which can be adjusted by the growth conditions, will determine the aspect ratio of the ZnO nanorods. Figure 5.17 shows the schematic sketch of an ideal ZnO rod. Growth in the $\langle 00 \cdot 1 \rangle$ direction has the fastest growth rate. Growth in the $\langle 10 \cdot 1 \rangle$ direction has intermediate growth
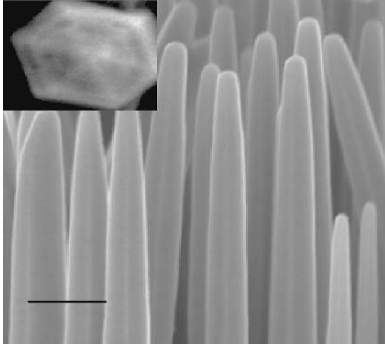
FIGURE 5.16. SEM image of ZnO nanorods with tilt angle at high resolution. The inset shows the shape of the nanorod's tip. Scale bar is 100 nm.

rate, and in the ⟨10 · 0⟩, the growth rate is smallest. Hence, the relationship of the growth rate of ZnO crystal face is R⟨00 · 1⟩ R⟨10 · 1⟩ R⟨10 · 0⟩. These relationships will result in the formation of 1-D ZnO nanorods with hexagonal cross-section.

5.3.5. Effect of ZnO Nanorod Morphology on Growth Temperature: From Nanoneedles to Nanorods

In the case of ZnO growth using an aqueous solution, the 1-D growth can be enhanced by controlling certain growth parameters such as pH, reactant concentration, and growth temperature. The dependence of ZnO nanorod morphology on the
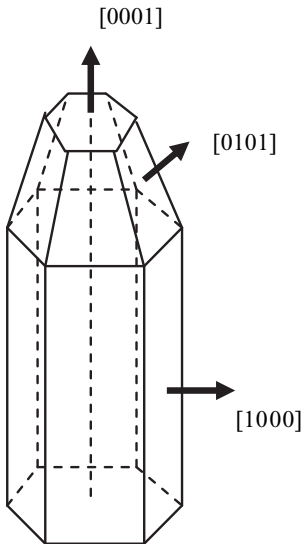
FIGURE 5.17. A schematic sketch of an ideal hexagonal rod.
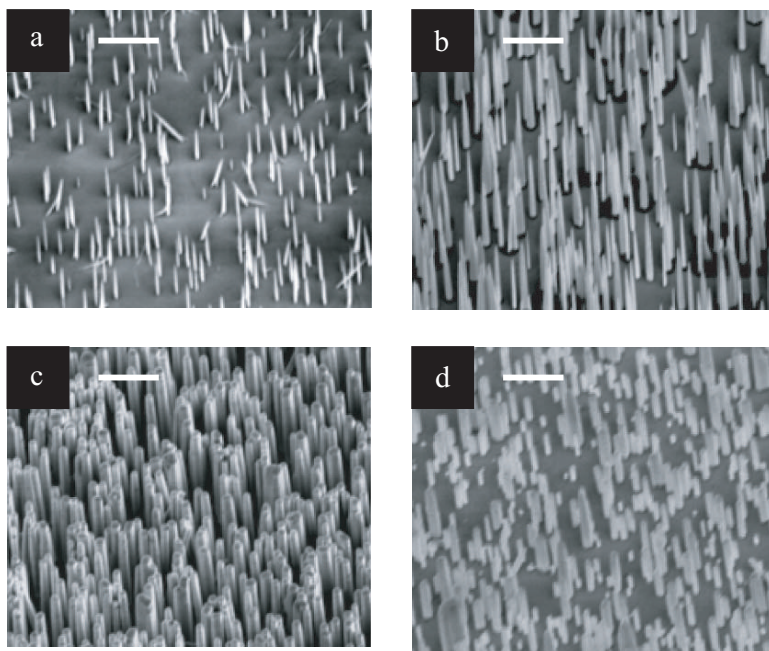
FIGURE 5.18. ZnO nanorods grown on GaN at different growth temperatures: (a) 60°C, nanorod density 3×10^4 cm^{-2}; (b) 80°C, nanorod density 7×10^4 cm^{-2}; (c) 100°C, nanorod density 2×10^5 cm^{-2}; (d) 150°C, nanorod density 1.2×10^5 cm^{-2}. Scale bars are 1 μm.

growth parameters has been investigated. The growth temperature, reactant concentration (zinc acetate concentration), and pH were changed so that the optimum value of growth parameters could be obtained. However, only the temperature-dependence of morphology is presented here to illustrate some interesting results.

The growth temperature was changed from 60°C to 150°C and other parameters (reaction concentration: Zn (CH$_3$COO)$_2$ .2H$_2$O, 0.25 g, 0.016 M; pH 9, NH$_4$OH 0.85 ml; growth time 5 h) were kept constant. The ZnO nanorods formed at different growth temperatures are shown in Figure 5.18. From Figure 5.18, the morphology of the ZnO nanorods changed from a sharp tip with high aspect ratio to a flat tip with smaller aspect ratio when the temperature was varied from 60°C to 150°C. In addition, the density of the nanorods was also affected. The temperature at 100°C seems to be the optimum value in order to obtain high density of nanorods $(2 \times 10^5$ cm$^{-2})$. The possible reason for these observed morphologies is the dependence of the relative growth rate of the crystal faces on growth temperature.

Figure 5.19 shows the cross-section image of the ZnO nanorods grown at temperatures of 100°C and 80°C. The average diameter and length of the nanorods are 90 nm and 1.5 μm, respectively. The diameter of the nanorods grown at 80°C is a little smaller, around 70–80 nm. These two types of morphology are found to be useful in laser and field emission application.
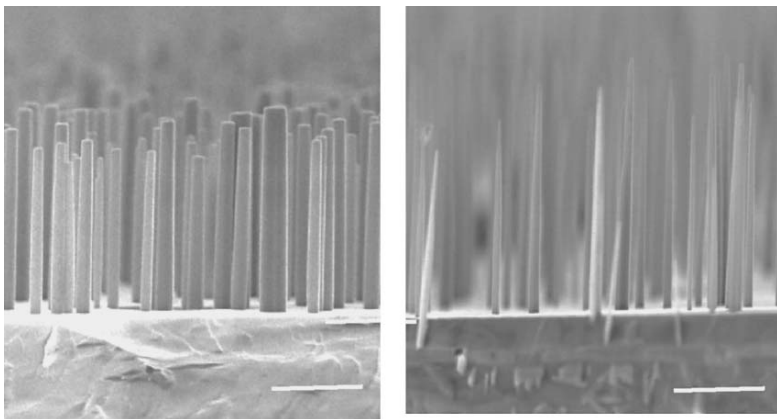
FIGURE 5.19. Cross-section SEM images of ZnO nanorods with different morphology: (a) ZnO nanorods with flat tip, growth temperature 100°C; (b) ZnO nanorods with sharp tip, growth temperature 80°C. Scale bars are 1 μm.

From Figure 5.19a, it is seen that all the nanorods have flat tips that can serve as miniature Fabry–Perot optical cavity facets. With a facet reflectivity of 42% formed by the difference in refractive indices between air ($n_r = 1$) and ZnO ($n_r = 2.45$), UV lasing emission can be generated.

The morphology of the ZnO nanorod (with sharp tip) shown in Figure 5.19b is useful for field emission application. In addition to the sharp tip and high aspect ratio, ZnO is well known as having negative electron affinity, and high mechanical strength and chemical stability. With these properties, ZnO has a potential for use in field emission display.

5.4. Conclusion

Hexagonally packed zinc oxide nanorod bundles have been synthesized on hydrotalcite (HTlc) sheets by reacting zinc acetate with aluminum-coated silicon in alkali hydrothermal conditions. The HTlc sheets are a unique product of the alkali hydrothermal environments, and cannot be readily produced by dry chemical vapor deposition methods. Controlling the thickness of the Al film is key to obtaining a range of secondary structures, ranging from self-assembled ZnO nanorod bundles on HTlc sheets which precipitate randomly on the silicon substrate, to well-aligned ZnO nanorods growing on silicon substrates.

A mild catalyst–free aqueous route has been successfully established to synthesize vertically aligned ZnO nanorod arrays on GaN. From the SEM and XRD measurements, the ZnO nanorods are seen to be vertically well aligned on the c-axis orientation, and have uniform hexagonal structure with diameter of 80–100 nm and length of about 1 μm. The photoluminescence spectrum also exhibits

strong exciton-related emission with a weak defect peak, which shows that the nanorods have good optical properties with low atomic defect. In addition, the growth mechanism of the ZnO nanorods has also been discussed.

The change of ZnO nanorod morphology from nanoneedle to nanorod was also observed when the growth temperature was changed from 60°C to 150°C. Control of growth temperatures offers a flexible method to obtain ZnO nanostructures with different shapes (needle or rod) suitable for different applications such as field emission and laser application .

With further improvement, the vertically aligned ZnO nanorods epitaxially grown on the GaN substrate seems to be a promising method for fabricating *p–n* heterojunction nanorod devices. Further work is needed to explore the lasing emission and field emission properties of the ZnO nanorods.

References

[1] Wang, Z.L., Ed. (2003). *Nanowires and Nanobelts*, Vol 1: *Metal and Semiconductor Nanowires*, and Vol II: *Nanowire and Nanobelt of Functional Oxide*; Norwell, MA: Kluwer Academic.

[2] Law, M., Goldberger, J., and Yang, P. (2004). Semiconductor nanowires and nanotubes, *Annu Rev Mater Sci* **34**: 83.

[3] Service, R.F., (1997). *Science* **276**: 895.

[4] Kong, X.Y. and Wang, Z.L. (2003), *Nano Lett* **3**: 1625.

[5] Liu, C., Zapien, J.A., Yao, Y., Meng, X., Lee, C.S., Fan, S., Lifschitz, Y., and Lee, S.T. (2003). *Adv Mater* **15**: 838.

[6] Bai, X.D., Wang, E.G., Gao, X.P., and Wang, Z.L. (2003). *Nano Lett* **3**: 1147.

[7] Arnold, M.S., Avouris, Ph., Pan, Z.W., and Wang, Z.L. (2003). *J Phys Chem B* **107**: 659.

[8] Hung, M.H., Mao, S., Feick, H., Yan, H., Wu, Y., Kind, H., Weber, E. Russo R., and Yang P. (2001). *Science* **292**: 1897.

[9] Park, W.I. and Yi, G.-C. (2004). *Adv Mater* **16**: 87.

[10] Kind, H., Yan, H., Messer, B., Law, M., and Yang, P. (2002). *Adv Mater* **14**(2): 158.

[11] Chen, C. L. Surface resonance.

[12] Huang, M.H., Mao, S. Feick, H., Yan, H.Q., Wu, Y., Kind, H., Weber, E., Russo, R., and Yang, P. (2001). *Science*, **292**:1897.

[13] Wang, X., Summers, C.J., and Wang, Z.L. (2004**).** *Nano Lett* **4**(3):423.

[14] Park, W.I., Yi, G.C., Kim, M., and Penycook, S.L. (2002). *Adv Mater* **14**:1841.

[15] Byrappa, K., and Yoshimura, M. (2001). *Handbook of Hydrothermal Technology*; New Jersey: Noyes, p. 76.

[16] Schaf, O., Ghobarkar, H., and Knauth, P. (2001) In *Nanostructured Materials-Selected Synthesis Method, Properties and Application*, Knauth, P., Schoonman, J., Eds., Boston: Kluwer Academic, p. 24.

[17] Demianets, L.N., Kostomarov, D.V., Kuz'mina, I.P., and Pushko, S.V. (2002). *Crystallogr Rep* **47** (suppl.1): S86.
[18] Vayssieres, L. (2003). *Adv Mater* **15**(5): 464–466.
[19] Vayssieres, L., Keis, K., Lindquist. S., and Hagfeldt. A. (2001). *J Phys Chem B* **105**: 3350
[20] Vayssieres, L., Keis, K., Lindquist. S., andHagfeldt. A. (2001). *Chem Mater* **13**(12): 4395.
[21] Bunker, B.C., Rieke, P.C., Tarasevich, B.J., Cambell, A.A., Fryxell, G.E., Graff, G.L., Song, L., Virden, J.W., and McVay, G.L. (1994) *Science*, **264**: 48.
[22] Tian, Z.R., Voigt, J.A., Liu, J., Mckenzie, B., and Mcdermott, M.J. (2002), *J Am Chem Soc* **124**: 12954.
[23] Greene, L.E., Law, M., Goldberger, J., Kim, F., Johnson, J.C., Zhang, Y., Saykally, R.J., and Yang, P. (2003). *Angew Chem Int Ed* **42**: 3031.
[24] Boyle, D.S., Govender, K., and O'Brien, P. (2002) *Chem Commun* **1**: 80.
[25] Choy, J.H., Jang, E.S., Won, J.H., Chung, J.H., Jang, D.J., and Kim, Y.W. (2003). *Adv Mater* **15**(22): 1911.
[26] Yamabi, S. and Imai, H. (2002). *J Mater Chem* **12**: 3773.
[27] Allmann, R. (1970). *Chimia*, **24**, 99.
[28] Thevenot, F., Szymanski, R., and Chaumette, P. (1989). *Clays Clay Minerals*, **37**(5): 396.
[29] Costantino, U., Marmottini, F., Nocchetti, M., and Vivani, R. (1998). *Eur J Inorg Chem* 1439.
[30] Tichit, D. and Coq, B. (2003). *CATTECH* **7**(6): 206.
[31] Cavani, F., Trifiro, F., and Vaccari, A.(1991). *Catalysis Today*, **11**: 173.
[32] *Powder Diffraction Database* JCPDS No. 481021–481024.
[33] Sehili, T., Boule, P., and Lemaire, J. (1989). *J Photochem Photobiol A: Chem*, **50**: 103.
[34] Hu, J.T., Odom, T.W., and Lieber, C.M. (1999). *Acc Chem Res*, **32**: 435.
[35] Wu, Y. and Yang, P. (2000). *Chem Mater* **12**: 605.
[36] Yazawa, M., Koguchi, M., Mutto, A., Ozawa, M., and Hiruma, K. (1992). *Appl Phys Lett* **61**: 2051.
[37] Chen, C.C. and Yen, C.C. (2000). *Adv Mat* **12**: 738.
[38] Heo, Y.W., Kaufman, M., Pruessner K., and Norton, D.P. (2003). *Solid State Electron* **47**: 2269.
[39] Park, W., Yi, I., and Kim, J.W. (2003). *Appl Phys Lett* **82**: 4358.
[40] Sharma, A.K., Narayan, J., Muth, J.F., Teng , C.W., Jin, C., and Kvit, A. (1999). *Appl Phys Lett* **75**: 3327.
[41] Minemoto, T. Negami, T., Nishiwaki, S., Takakura, H., and Hamakawa, Y. (2000). *Thin Solid Films* **372**: 173.
[42] Chik, H., Liang, J., Cloutier, S.G., Kouklin, N., and Xu, J.M. *Appl Phys Lett* (2003). **84**: 3376.
[43] Goldberger, J., He, R., Zhang, Y., Lee, S., and Yan, H. (2003). *Nature* **422**: 599.
[44] Smit, G.D.J., Rogge, S., and Klapwijk, T.M. (2002). *Appl Phys Lett* **81**: 3852.
[45] Park, W.I., Yi, G.-C., Kim, J.-W., and Park, S.-M. *Appl Phys Lett* (2003) **82**: 4358.
[46] Park, W.I. and Yi, G.C. (2004) *Adv Mater* **1**: 87.
[47] Kong, Y.C., Yu, D.P., Zhang , B., and Fang, W. (2001). *Appl Phys Lett* 78: 407.
[48] Vanheusden, K., Warren, W.L., Seager, C.H., Tallant, D.R., Voigt, J.A., and Gnade, B.E. (1996). *J Appl Phys* **79**:7983.

[49]   Zeuner, A., Alves, H., Hofmann, D.M., Mayer, B.K., and Heuken, M. (2002). *Appl Phys Lett* **80**: 2078.

[50]   Hsu, H.C., Tseng, Y.K., and Cheng, H.S. (2004). *J Crystal Growth* **261**: 520.

[51]   Zhang, J., Sun, L.D., and Liao, C. (2002). *Chem Commun* **262**.

[52]   Yamabi, S. and Imai, H. (2002) *J Mater Chem* **12**: 3773.

[53]   Laudies, R.A. and Ballman, A.A. (1960). *J Phys Chem* **64**, 688.

6
Nanoparticles, Nanorods, and Other Nanostructures Assembled on Inert Substrates

Xue-Sen Wang

6.1. Introduction

The geometric and surface properties of supported nanostructures (nanoparticles, nanorods, and other nanoscale objects) are closely related to many of their important applications. On relatively inert substrates, such as graphite, oxides, and nitrides, many nanostructures can be fabricated in a nearly free-standing state by simple physical vapor deposition, and be characterized using electron microscopy, scanning probe microscopy, and various spectroscopic methods. Their intrinsic properties, including the interaction among them, can be measured. In addition, the nanostructures on an inert support provide us with an arena to examine their interactions with other nanoobjects, such as biomolecules, without the influence of a solution.

The nucleation and growth on an inert substrate is generally portrayed as in a three-dimensional (3-D) islanding mode based on (macroscopic) surface/interface energy consideration. However, the morphology of self-assembled nanostructures can vary dramatically from one material to another, and even for the same material under different growth conditions. Such variations reflect the characteristics of the interactions among the deposited atoms/molecules, the nucleated structures, and the substrate in different systems. Many of these can be classified as kinetics that can be adjusted by controlling the growth conditions. This provides us with the possibility to fabricate the nanostructured materials that satisfy particular application requirements. To achieve this goal, it is essential to understand the basic thermodynamic and kinetic properties of deposited and nucleated species that determine the size, shape, and surface atomic structures of the self-assembled nanostructures.

6.2. Geometry and Surface Structures of Supported Nanostructures

The strong interest in nanostructural research originates from the novel properties of nanoparticles that can be quite different from the bulk, and the sensitive

dependence of these properties on particle size, shape, and surface atomic configuration [1–5]. The size- and shape-dependent properties are closely related to important applications of nanoparticles, including quantum dots (QDs) in electronics and optoelectronics [6,7], catalysts [8–11], and single-domain magnets [12,13]. Although some extrinsic factors such as a surface passivation layer may have a strong influence on nanoparticles' properties [14], most of their novel properties originate from their atomic configuration and geometry. Free-standing nanoparticles have been investigated extensively in past decades in order to extract their intrinsic properties [1,3,4,15–19]. But various experimental difficulties have limited the variety of completely free-standing nanoparticles that can be studied.

Taking advantage of the Volmer–Weber growth mode, nanoparticles in the form of cluster and crystallite can nucleate and grow on inert substrates such as graphite, oxide, and ceramic surfaces. To display the intrinsic properties of nanostructures, their interaction with the substrate should be significantly weaker than that in an epitaxial system. Nevertheless, the interaction is strong enough to maintain mechanical bonding required for analyses. In particular, graphite, oxide, and nitride thin films formed on conductive substrates provide us with the "inert" templates for growing nanostructures that can be characterized subsequently using popular analytical tools including photoelectron spectroscopy and scanning tunneling microscopy (STM) [9,10,20]. Such supported nanoparticles are relatively close to the state of their applications in catalysis and sensors [21]. They also make it relatively easy to extract geometric, electronic, chemical, and magnetic properties of a particular nanostructure and establish correlations among these properties [22,23].

In many applications, the surface atomic structure, shape, and crystal orientation with respect to the substrate are important to particular functions of nanoparticles. For example, the catalytic and sensor performances are closely related to the surface structures of nanoparticles. For single-domain nanomagnets in the patterned medium used for ultrahigh-density information storage, it is desirable to let all magnetic crystallites take an identical orientation and a unique shape so that full advantage may be taken of the shape and magnetocrystalline anisotropy to enhance the stability against superparamagnetism [12,13,24]. In addition, the nucleation and growth of nanoparticles are the initial stages of film growth on an inert substrate. The properties of nanoparticles, including interparticle mass transport kinetics, have intimate effects on the texture of films obtained at a later stage of growth [25–31].

Depending on the strength of the interaction with the supporting surface, the properties of nanoparticles grown on inert substrates vary between those formed in epitaxy and those of free-standing clusters without any support. The epitaxial film or island growth [32,33] on one extreme and free cluster formation [1–4] on the other have been quite well understood now. In epitaxy, the lattice parameters and orientation of islands nucleated initially are fixed largely by the requirement of registry with the substrate due to a strong interaction across the interface. For particles formed on an ideal inert substrate, their crystalline orientation could be completely random as a free-standing nanoparticle, and the shape and atomic configuration of clusters or crystallites are determined solely by minimizing the particle energy,

which includes contributions from electronic and atomic configurations. For the intermediate systems we deal with here, all the factors important in the extreme cases must be considered. Additionally, growth kinetics [26,31–34], surfactant [35–37], buffer layer [38], and surface termination [39,40] can be used to adjust the geometric and other properties of nanoparticles as well as the texture of thin film derived from these nanoparticles.

The equilibrium shape and surface atomic configuration of nanoparticles often show sensitive size dependence. Small metal clusters (consisting of $\leq 10^3$ atoms) are normally spherical (with a diameter within ~ 3 nm) to minimize quantum confinement energy of electrons [3,4,41]. In the intermediate size ($\sim 10^3$–10^4 atoms) range, both quantum confinement and atomic configuration energies are important so that the particles are usually in near-spherical crystalline or quasicrystalline polyhedral forms (e.g., cuboctahedron, icosahedron, and decahedron) [1,34]. At even larger particle size, the interior atomic configuration should take a crystal form the same as the bulk. But the particle shape may differ remarkably from the macroscopic equilibrium crystal shape (ECS) [32]. Quantum confinement may remain an important factor. Furthermore, the surface energy anisotropy of a nanocrystallite can deviate significantly from that of a macroscopic crystal due to reduced surface area to accommodate surface reconstruction. Additionally, the contribution to surface energy from atoms located at edge and corner sites, which scales as $\sim R^{-1}$ is no longer negligible for nanoparticles. All these factors favor an isotropic ECS. On the other hand, the interface binding with the substrate generally reduces the profile of supported nanoparticles and favors a relative anisotropic ECS [8,42].

To reveal the interplay of various factors, we performed a systematic study, mainly using in situ ultrahigh vacuum (UHV) STM, combining with Aüger electron spectroscopy (AES) and low-energy electron diffraction (LEED), on the nucleation and growth, shape, and surface atomic structures of nanostructures on highly oriented pyrolytic graphite (HOPG) [43,44] and silicon nitride (SiN$_x$) thin films obtained by thermal nitridation of Si [45–47]. Much previous research work has been carried out with (mostly ex situ) scanning electron microscopy (SEM), cross-sectional transmission electron microscopy (TEM), and X-ray scattering [3–5,8,29,34,48]. Although each of these techniques offers certain strength, UHV STM is unique in providing atomic-resolution surface structural and other geometric information of nanostructures under a well-controlled environment. Of course, STM normally can only image the top surface of an object, so investigations using STM and other techniques should be complementary to each other.

HOPG has been used as a prototypical inert substrate in many nanostructural nucleation and growth studies [8,26,49–54]. It has been found that the bonding of many metal and semiconductor atoms (e.g., Au, Ag , Sb, and Si) with HOPG is extremely weak (the sticking coefficient of Si on HOPG is much less than unity [49]), so a variety of nearly free-standing nanostructures has been observed to form on HOPG. HOPG is also used as an ideal template for studying the kinetics and thermodynamics governing the migration and coalescence of nanoparticles. Here, we present mainly our investigations of Al, Sb, and Ge nanostructures formed on HOPG.

For comparison, we also show some results of Ge and Si nucleation and growth on SiN_x films. SiN_x has been used widely as a high-quality dielectric material in microelectronics [55], and as coating and buffer layers with excellent thermal, mechanical, and chemical stabilities [56]. Crystalline and amorphous SiN_x thin films (thickness 1–3 nm) can be formed on Si(111) and Si(001) substrates, respectively, allowing us to examine processes relevant to different applications [45–47]. Semiconductor and magnetic nanoparticle growth on SiN_x has been investigated by a few groups including ours [22,37,57–60]. In general, studies of formation of semiconductor QDs and magnetic nanoparticles on Si-based substrates are important for integration of optoelectronic and magnetic functions on Si-based integrated circuits [5,61]. Si and Ge low-dimensional structures are especially attractive because their luminescence efficiency could be much higher than that of the bulk [2,6,7,62,63]. Clusters made of up to a few tens of Si or Ge atoms (size ∼1 nm) have been investigated extensively [15,16], and studies of free-standing particles of size beyond a few nm have been rather rare [17–19] because of experimental and calculation difficulties. For supported nanoparticles (besides the well-known epitaxial pyramidal and dome Ge (or SiGe) QDs on Si(001) [64,65]), experimental works of deposition on Si(111) [66], SiO_x [67,68], CaF_2 [69], HOPG [49], and Ag(111) [70] have been reported. It has been found that the electronic properties of Si nanoparticles on graphite depend sensitively on their size [71,72]. However, the evolution of shape and surface structures with the particle size, the effects of surfactants on nanoparticle growth, and the texture of continuous films obtained subsequently were not examined extensively. These issues are addressed in our study.

In the following, after a brief description of procedure and precautions in experiments and data analyses, results of nucleation, coarsening, morphology and surface atomic structures of Al, Sb and Ge nanostructures on HOPG are presented first, followed with the evolution from clusters via crystallites to continuous films of Si and Ge on SiN_x. The effects of an Sb atomic layer on the nucleation and shape evolution of nanoparticles on SiN_x will be briefly illustrated. Based on the comparison of nanostructures formed in different cases, a few general observations regarding the correlation between the nanostructural geometry and the thermodynamic and kinetic driving forces will be made. Particularly, we will explore the surface properties of nano-particles, their interaction with each other and with the substrates, and the consequences on the texture of more sophisticated nanostructures and continuous films they form later.

6.3. Experimental Procedure and Considerations

Our experiments were mostly carried out in UHV (base pressure $\sim 1 \times 10^{-10}$ mbar) chambers equipped with STM and LEED/AES apparatus. Samples can be annealed up to 1500 K by radiative and electron-bombardment heating with a W-filament on the back. Deposition fluxes were generated from well-degassed thermal evaporators loaded with high-purity source materials. Ge and Sb were deposited from Ta-boat evaporators, and Al was from a wetted W-coil and Si from
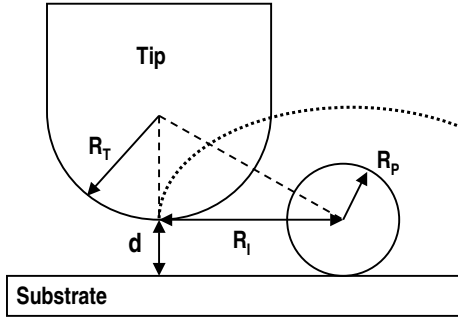
FIGURE 6.1. Schematic diagram for estimating the apparent shape and size of a spherical particle in STM image. The dotted line represents the tip trajectory.

an electron-bombardment source. A thermocouple was used to monitor the Sb source temperature which was normally in 340–380°C range, so the flux mostly consists of Sb_4 [73,74]. The flux was calibrated by measuring AES peak ratio and the island volume of a deposited material on a substrate in STM images (assuming a sticking probability near 1, which cannot be applied for some systems such as Ge on HOPG). The flux values carry an absolute error of about 30%, but the relative error should be within 15%. The deposition rate was typically on the order of 1 monolayer per minute (ML/min). The sources and substrates were kept as clean as possible in a UHV chamber to reduce impurity effects on cluster nucleation and surface morphology.

STM images were taken at RT using electrochemically etched and electron-beam treated W tips. The STM image scales were calibrated with well-known surface structures such as Si(111)–7 × 7, Si(001)–1 × 2 and atomic steps on these surfaces. In addition to conventional drift and the hysteresis effect of the piezoelectric scanner, a precise determination of distances on crystallite facets is handicapped by tilting of the facets. The finite tip size and multiple-tip effects often make the 3-D islands appear bigger than their real size, and generate artifacts in STM images [42,69]. Great care was taken in our experiments to avoid these effects. But they could not be eliminated completely, especially in imaging samples with relative large corrugation, so they must be taken into consideration in data analyses. On inert substrates, nanoparticles often grow initially in a near spheric or oblate shape [69]. A simple sketch shown in Figure 6.1 gives us an estimate on how the apparent size and shape of a spherical particle are related to the real size and STM tip geometry. Assuming a hemispheric shape of radius R_T for the STM tip front and a tip-sample tunneling gap d, for a spheric particle of radius R_P, the scanning trajectory of the tip gives an accurate measure of the particle's height. But the apparent lateral radius R_I of the particle in STM image is:

$$R_I \approx 2\sqrt{(R_T + d)R_P} \tag{1}$$

Typically, $d \leq 1$ nm. This equation is valid for $R_T \geq R_P$. If $R_T \leq R_P$, R_I is approximately $R_T + R_P$, because the tip cannot go underneath the spheric particle. For a nanoparticle of $R_P = 5$ nm imaged with a tip of $R_T = 10$ nm, we would get $R_I \approx 15$ nm, a quite large overestimate. The tip shape can be rather irregular, which leads to different values of R_T for nanoparticles in a different size range. In

addition, the supported nanostructures, especially small clusters on weak-binding sites, can be moved or even picked up by a STM tip. These possibilities have to be considered in selecting STM imaging parameters and interpreting images. Besides in situ characterizations, some samples were examined ex situ with SEM and high-resolution TEM.

Fresh HOPG substrates were obtained by cleaving in air and then quickly transferred into a UHV chamber through a load-lock. Before being used for nanostructural growth, they were degassed at 200–500°C for 10 hours. HOPG is made of graphite atomic sheets stacked in an identical polar (the [0001] direction) orientation, but the stacked sheets are not necessarily azimuthally aligned with each other. The lateral size of an individual sheet is also limited. Therefore, a cleaved HOPG sample surface commonly shows flat terraces of 100–500 nm in width separated by steps (see Figure 6.2a) [43,44]. The step heights vary from 3.4 Å (monatomic) to a
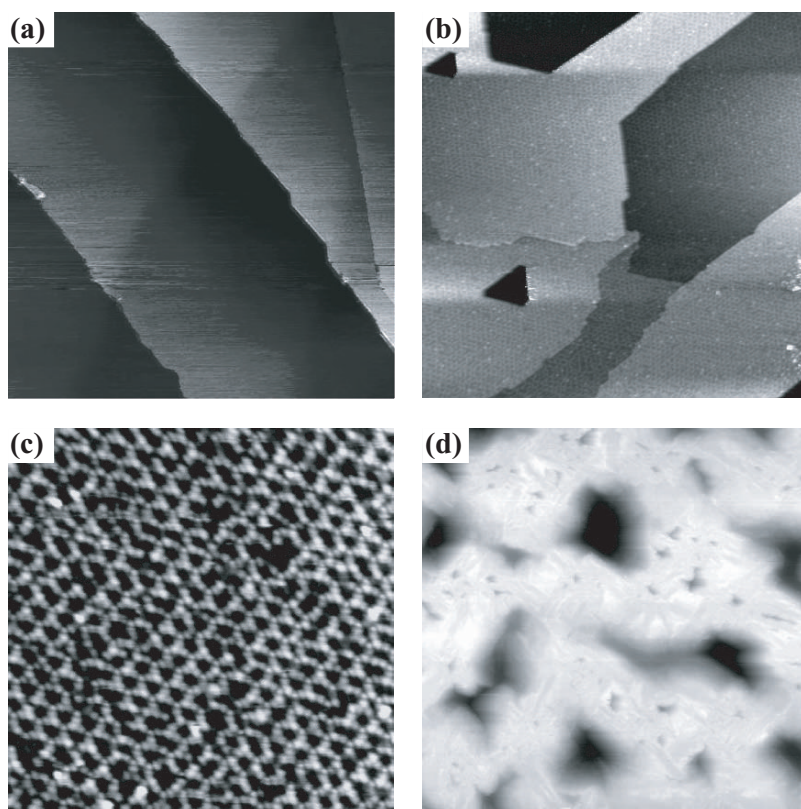
FIGURE 6.2. Grey-scale STM images of substrates used in our supported-nanostructure study: (a) a HOPG surface, (b) crystalline SiN_x film on Si(111), (c) a zoom-in scan showing the 30.7-Å superstructure on SiN_x/Si(111), and (d) amorphous SiN_x film on Si(001) with pinholes of depth ≤ 7 nm. Image area: (a) $(0.5 \mu m)^2$; (b) $(220 nm)^2$; (c) $(50 nm)^2$; (d) $(380 nm)^2$.

few nm. These steps have a much stronger power to trap atoms and nanoparticles [49,54,75] than terrace sites and even point defects on terrace. As we show later, there are subsurface step edges of graphite sheets covered by a thin (a few ML) surface sheet. These subsurface steps are normally invisible in STM images of bare HOPG, but play a noticeable role in nucleation and growth of nanostructures.

SiN$_x$ films were formed on clean Si(111) and Si(001) surfaces after NH$_3$ or NO exposure for 1–20 min at a temperature of 875–975°C [45,46,57,58]. AES measurement indicated saturation of SiN$_x$ growth after a 20-min exposure. On Si(111), the nitridation resulted in a crystalline SiN$_x$ film as shown in Figure 6.2b, with a 30.7-Å periodic superstructure (see Figure 6.2c), flat terraces, and atomic steps on the surface. The long-range order on the surface, however, was much inferior to that on a typical Si(111)–7 × 7. This gave rise to a high nucleation density in the initial stage of overlayer growth. TEM images confirmed that the thickness of SiN$_x$ films was in the 1–3 nm range. On Si(001), the SiN$_x$ film shown in Figure 6.2d is amorphous, with some voids penetrating down to the pure Si region.

6.4. Nanostructures Assembled on Graphite

For the three elements (Sb, Al, and Ge) deposited on HOPG at room temperature (RT $\sim$ 30°C here), due to weak interface bonding, 3-D island (Volmer–Weber) growth was observed. Nevertheless, the nucleation and growth of each element show its distinctive behavior.

6.4.1. Antimony on Graphite

Among various materials deposited on HOPG or amorphous carbon, particularly rich phenomena have been reported for Sb clusters (Sb$_n$) in a size range of $n = 4$ to 2300 [26,76–79]. Depending on the size n of Sb$_n$, the Sb islands formed on graphite vary from compact spheres for $n = 4$ to ramified fractals for $n \geq 90$. The fractal branch width decreases as n increases. These phenomena are explained in terms of the interplay of Sb$_n$ arriving rate at an existing island, and the time it takes for clusters in contact to coalesce. In all these studies, however, the possibility and consequences of Sb$_n$ decomposition were largely ignored.

In many processes, Sb$_n$ (particularly for Sb$_4$ generated from a thermal evaporator) decomposition and/or conversion from the physisorption to chemisorption state do occur [80]. This has strong effects on compound and alloy growth involving Sb [73,74,81]. The diffusion, nucleation, and growth kinetics of chemisorbed Sb species on HOPG are expected to differ remarkably from those of physisorbed Sb$_4$. It would be interesting to examine whether different structures form on HOPG if Sb$_4$ decomposition is significantly activated (or similarly if the deposition flux consists of a significant percentage of Sb$_2$ and Sb$_1$). In addition, due to experimental difficulties, the atomic structure of Sb(111) was revealed with STM only very recently [82], and the atomic structures of other surfaces of Sb crystal are largely
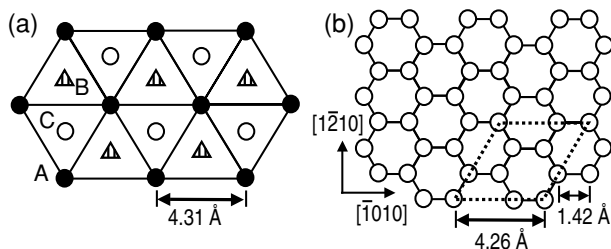
FIGURE 6.3. (a) α-Sb lattice viewed in [111] direction (the long diagonal of rhombohedral cell). A, B, and C mark sites in three layers separated by 3.76 Å. (b) Atomic configuration of graphite basal plane, a $(\sqrt{3} \times \sqrt{3})$ R30° cell is outlined with dotted lines.

unknown. The crystalline Sb structures formed on HOPG allow us to image other surfaces when they appear.

We observed that spherical 3-D islands, extended 2-D islands, and 1-D crystalline nanorods are formed on HOPG. The atomic-scale STM images of the surfaces on these different-dimensional Sb structures have been obtained. Furthermore, with a low Sb_4 flux and the substrate at RT, spherical islands nucleate and grow exclusively at the initial stage. In contrast, with a high Sb_4 flux and substrate at ~100°C, formation of a spherical island is completely suppressed, resulting in only the 2-D and 1-D structures. These results are explained in terms of a relatively large difference in the activation energies of Sb_4 diffusion and dissociation (or chemisorption) on HOPG, which leads to different rate changes in response to temperature increase. It is well known that the properties of different types of nanomaterials (i.e., nanoparticles, nanowires, and thin films) differ remarkably from their bulk counterparts and from each other due to their dimensionality [2,5–7,83]. Therefore, the ability to selectively grow certain dimensional nanostructural materials is highly desirable in nanoscience and nanotechnology [84,85].

The most stable α-Sb bulk crystals take a rhombohedral lattice structure [86], which can be derived by a slight distortion of a cubic lattice [87]. The distorted face-center cubic representation of α-Sb is illustrated in Figure 6.3a, with the ABC stacking at a 3.76-Å layer spacing. Each site represents a base of two Sb atoms, with the other atom 5.26 Å beneath the one shown in the figure. In this chapter, we use the rhombohedral index notation for the observed Sb structures [88], so Sb(0001) in Reference [82] is denoted Sb(111) here. For comparison, the atomic configuration of a graphite basal plane is sketched in Figure 6.3b.

6.4.1.1. Three Types of Sb Nanostructures

Figure 6.4a displays a STM image taken on a HOPG sample with 12 Å Sb deposited at a rate of 4 Å/min at RT. Three types of Sb structures are observed, labeled as 1-D, 2-D, and 3-D in the figure. The three large 3-D spherical-top islands have heights in the 50–56 nm range, and apparent lateral diameters 140–150 nm. STM
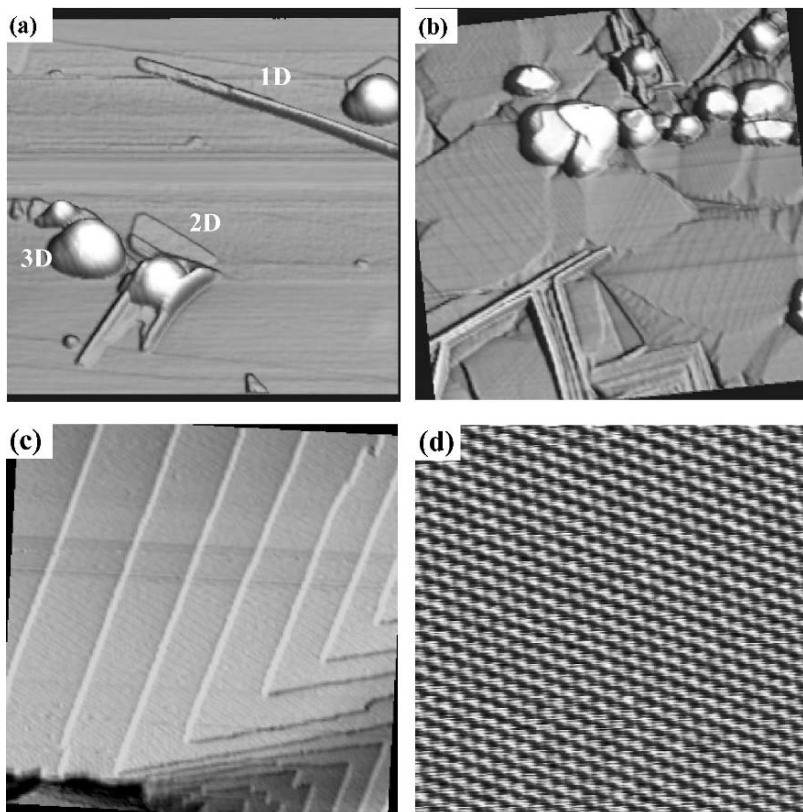
FIGURE 6.4. Three-dimensional view STM images of Sb structures on HOPG. (a) After 1.2-nm Sb deposited at RT and a flux of 4-Å/min; (b) after 10-nm Sb deposited at RT and a 4-Å/min flux. (c) and (d) are zoom-in images taken on a 2-D island. Image area: (a),(b) $(1 \ \mu m)^2$; (c) $(300 \ nm)^2$; (d) $(10 \ nm)^2$. Imaging conditions: $V_s = 0.45$ V, $I_t = 0.4$ nA.

tip cannot scan underneath the nanoparticles, so we cannot know their exact shape. Based on the inertness of the substrate, the observed 3-D particles are most likely spheres or oblate spheres at this stage.

In addition to these tall 3-D islands, lower and extended structures are observed. The 2-D islands (three of them: two unlabeled ones are in the upper part of Figure 6.4a) have heights in the 3.1–3.5 nm range, and with atomically flat terraces and straight step edges. These 2-D islands are not small graphite pieces, because they grow as more Sb is deposited later. The long linear (1-D) feature in the upper part of Figure 6.4a has a height 20 nm and a measured width ~35 nm. In addition to this relatively long Sb nanorod, there are two short rods on the side of a 3-D nanoparticle in the lower half of the image. The heights of these wires are about 13 nm. It should be mentioned that these Sb rods are not necessarily formed along the steps of HOPG.
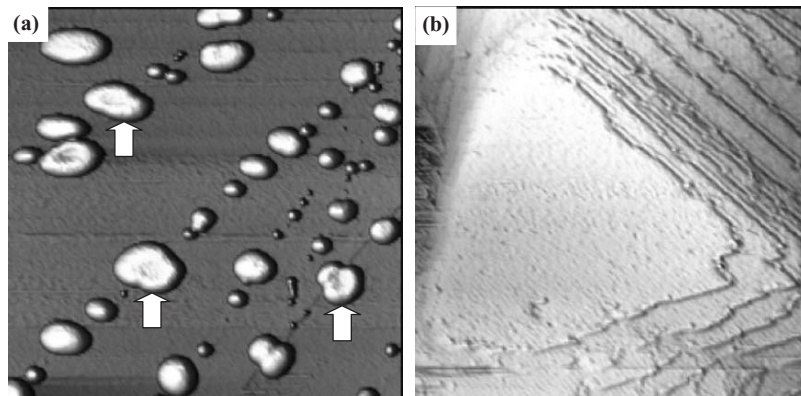
FIGURE 6.5. STM images of 3-D Sb islands on HOPG. (a) After 1.8-nm Sb deposited at RT and a flux of 1.8 Å/min; (b) a facet on top of a 3-D island. Image area: (a) $(2.5 \text{ } \mu\text{m})^2$; (b) $(60 \text{ nm})^2$.

As more Sb is deposited in the same condition, all three types of Sb structures grow in size, but at different rates. More characteristics of these structures can be revealed as they grow. Figure 6.4b displays an image taken on a sample after 10 nm Sb was deposited. Most of the surface is covered with multilayer 2-D film domains. In the zoom-in scan in Figure 6.4c, flat terraces separated with atomic steps are observed. The measured average height of the atomic steps on the 2-D islands is 3.96 ± 0.20 Å. Further zoom-in scans on a flat terrace reveal a hexagonal ordered structure as shown in Figure 6.4d, with a period 4.17 ± 0.12 Å. The steps are all along the $\langle 110 \rangle$ direction. Comparing with the lattice parameters of Sb (111) in α-phase [86], our measured average step height is 5% larger than the bulk layer spacing (3.76 Å), whereas the lateral period is shorter than the expected value (4.31 Å) by 3%.

The surface of 3-D islands is smoothly curved without any facet initially. In fact, some 3-D islands of heights ~55 nm and lateral size ~200 nm still have a smoothly curved surface. This type of islands can be observed in the image of Figure 6.5a taken on a HOPG sample with 1.8 nm Sb deposited at a rate of 1.8 Å/min at RT. In this condition, only 3-D spherical islands are formed at this early stage. Most 3-D islands are located along the steps on HOPG. Some islands (marked with an arrow in Figure 6.5a) have a concave top area, indicating coalescence of smaller islands to form these larger ones.

On the other hand, faceting has been observed on the surface of some relatively large 3-D islands, as illustrated in Figure 6.4b. In this image, several 3-D islands have heights in the 40–58 nm range when measured from surrounding 2-D film. Although some of these 3-D islands remain in spherical shape with a lateral dimension ~150 nm, most 3-D islands have grown to lateral size >300 nm and have developed a flat top facet with straight edges, indicating a crystalline structure inside. The top facets mostly form irregular hexagons or triangles, surrounded

with a smooth curved surface. One triangular top facet is shown in Figure 6.5b. Zooming-in STM scans on such top facets reveal a hexagonal periodic atomic structure similar to that in Figure 6.4d. But the period on the 3-D top facets is 4.27 ± 0.10 Å, basically the value on Sb(111) of bulk crystal. The faceted Sb crystallites observed here are similar to those observed by Kaiser et al. [79] using SEM. In their SEM image, the top hexagons of Sb islands are also surrounded with a smooth curved surface, indicating that the surrounding feature in our STM images is not totally due to tip-shape artifact.

The surface periodicity data indicate that the lattice parameters of the 3-D Sb islands on HOPG are basically the same as the bulk α-phase, with the (111) face parallel to the graphite basal plane. The lattice parameters of the 2-D films show a slight deviation from that of bulk Sb, in particular a contraction of 3% in lateral spacing. It can be seen in Figure 6.3b that the period of the $(\sqrt{3} \times \sqrt{3})$R30° superstructure on graphite (0001) (a cell outlined with dotted lines in Figure 6.3b) is 4.26 Å, which is quite close to the period in the (111) plane of bulk Sb. One would expect that a (111)-oriented Sb film of a few atomic layers matches with the graphite lattice underneath. But our results suggest that this is not necessarily the case. We found that the azimuthal orientation of the 2-D islands on one HOPG terrace can be different from each other, indicating that these islands do not all have a fixed azimuthal alignment with graphite substrate.

Our STM images, as those displayed in Figure 6.6, indicate that the 1-D Sb nanorods formed on HOPG are also crystalline. It is often observed that Sb nanorods grow out in two perpendicular directions, as illustrated in Figure 6.6a. Zoom-in images on Sb nanorods reveal the top surface structures mostly as rectangular periodic or rows along the rod axis. Rows displayed in Figure 6.6b, with a period of 3.70 ± 0.15 Å along the rows and 4.5 ± 0.2 Å between the rows are typically observed on tall nanorods with heights ≥ 20 nm, such as those shown in Figure 6.4a and those marked "T" in Figure 6.6a. Figure 6.6c shows an atomic-resolution image taken near the right-angle elbow of those relative lower Sb nanorods (marked "L", with height ≤ 15 nm). The surface lattice parameters vary from one area to another beyond experimental uncertainty. In the right-angle intersection area, we often found a nearly square order with a period of 4.18 ± 0.15 Å. In contrast, a rectangular order of period $(3.93 \pm 0.15$ Å$) \times (4.40 \pm 0.15$ Å$)$ is observed away from the intersection, as shown in Figure 6.6d, with the shorter side along the axis of nanorods. A rectangular cell is outlined in Figure 6.6d, with a bright spot observable inside. The average step height on the nanorod top surface is 2.83 ± 0.20 Å. As discussed in detail below, these observations suggest that these nanorods start in a simple cubic (SC) phase which forms for compressed Sb [86,89,90]. These Sb nanorods have (110) top facet, and their axes are along [1$\bar{1}$0] direction.

The lattice structure of 1-D Sb nanorods deviates significantly from α-Sb bulk. For the (110) surface of bulk α-Sb, the unit cell size is 4.31 Å $\times$ 4.51 Å. The lattice constants measured on top of Sb nanorods indicate a compressed state. It has been observed for Group V elements such as As, Sb, and Bi that a rhombohedral to SC phase transition occurs under pressure [86,87,89–91]. For Sb, the SC phase exists in a narrow pressure range around 7.0 GPa, in which the atomic volume is about
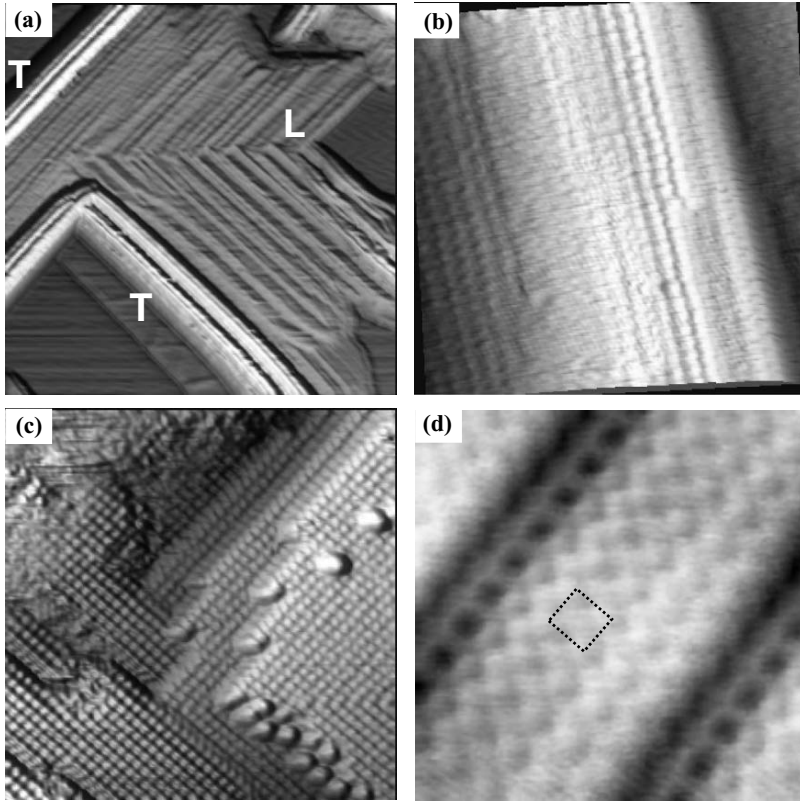
FIGURE 6.6. STM images of Sb nanorods. (a) Tall (T) and low (L) nanorods growing in perpendicular directions; (b) an image on a tall nanorod showing row structure; (c) an image taken at a right-angle intersection of a low nanorod; and (d) on a low nanorod but away from the intersection. Image area: (a) $(300 \text{ nm})^2$; (b) $(10 \text{ nm})^2$; (c) $(15 \text{ nm})^2$; (d) $(4 \text{ nm})^2$. Imaging conditions: (b) $V_s = 0.4$ V, $I_t = 0.3$ nA; (c), (d) $V_s = 0.63$ V, $I_t = 0.6$ nA.

85% of the normal state value and the atomic spacing is 2.966 ± 0.010 Å [89]. The 4.18 ± 0.15 Å square unit cells and 2.83 ± 0.20 Å step height observed on the top surface at the right-angle intersections of Sb nanorods fit closely to the SC lattice, with a $\sqrt{2} \times \sqrt{2}$ reconstructed $(001)_{SC}$ surface. The nanorods grow out from the SC along the equivalent $[110]_{SC}$ and $[1\bar{1}0]_{SC}$ directions. Away from the intersection, the nanorod lattice changes away from SC. The surface unit cell becomes rectangular, with atomic spacing expanded in the direction perpendicular to the rod axis while contracted along the axis. The transition seems continuous, with the atomic volume remaining 85% of the normal state.

Nanostructures can be in a stressed state even without an external force. For example, colloidal CdSe QDs have been observed in compressive or tensile stress state depending on how the QDs' surface is passivated [14]. The CdSe QDs are in

compressive stress if the passivation layer acts as an electron donor. It is quite likely that some electrons transfer from the graphite substrate to Sb nanorods to induce the compressive stress. Similar charge transfer to the 3-D and 2-D Sb islands can also occur. Its effect on 3-D crystalline islands seems negligible due to a large volume of 3-D crystallites and a weak interaction across the interface. The 2-D films, however, are expected to have a strong interaction with the substrate, but the lattice parameter changes are fairly small. Therefore, in addition to charge transfer, the surface atomic configurations on the top and side facets (the latter cannot be imaged with STM) as well as the growth kinetics must also be considered to explain the formation and lattice structure of the Sb nanorods.

6.4.1.2. Selective Growth of Different Dimensional Sb Nanostructures

We have illustrated that Sb can grow in three different types of nanostructures on HOPG, namely 3-D clusters or crystallites, 2-D films, and 1-D nanorods. Inasmuch as different-dimensional nanostructures can have quite different properties, it is valuable to understand the mechanism behind different structural formations, and to search for conditions to selectively grow nanostructures of one type and suppress others. To this end, we investigated nanostructural formation on HOPG under different Sb flux and/or substrate temperature. The STM image shown in Figure 6.5a is taken on a HOPG sample with 1.8 nm Sb deposited at a rate of 1.8 Å/min and at RT. In this condition, only 3-D spherical islands are formed at the early stage. Most 3-D islands are nucleated along the steps on HOPG. With further Sb deposition in this condition, 2-D and 1-D islands start forming.

The STM image shown in Figure 6.7 is taken on a sample with 5.4 nm Sb deposited at a rate of 18 Å/min and with sample at about 100°C. Here, only
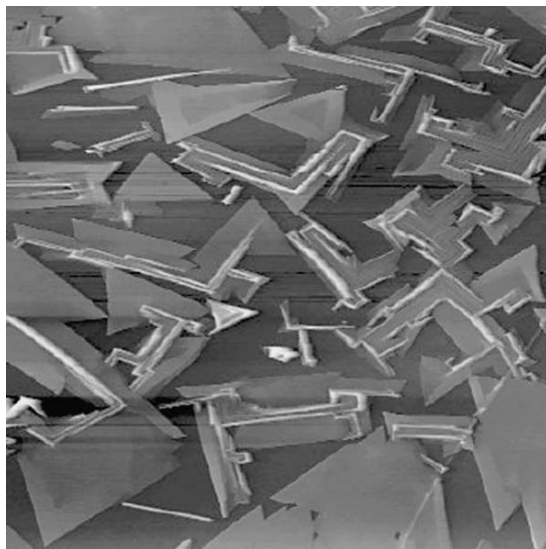
FIGURE 6.7. A(4-μm)^2 STM image of 5.4-nm Sb deposited on HOPG at 100°C and a flux of 18 Å/min.

2-D and 1-D Sb structures are observed. We found that substrate temperature is more important than the flux in determining what types of Sb structures grow initially. At RT, even with a flux of 6 Å/min, 3-D island nucleation and growth are dominant, whereas 3-D islands are totally suppressed with this flux but at 100°C. Raising substrate temperature further, we found that the growth cannot happen when $T \geq 135$°C. In addition, we observed that sublimation becomes significant at $T \geq 220$°C from the Sb structures grown on HOPG. After a 10-min annealing at 260°C, the nanorods almost all disappear, whereas many 2-D and 3-D islands remain. All Sb desorbs from HOPG after 10 min annealing at 375°C.

Previous studies of Sb growth on graphite have mostly addressed the nucleation and growth of compact and ramified 3-D structures [76–78,92]. Kaiser et al. [79] observed formation of other types of structures, and they obtained dominantly branched 3-D islands at a high flux (~60 Å/min), whereas a few different types of structures formed at ~3 Å/min. Supercooling of deposited Sb_4 was considered a possible driving force for viscous fingering and dendrite crystallization. With a relative low Sb_4 flux used in our experiments, however, this effect should be rather weak.

We now explain the observed phenomena in terms of a different adsorption state and diffusion rates of Sb species on HOPG. In the gas phase, Sb_4 is more stable than Sb_2 and Sb_1. The energy cost to dissociate an Sb_4 into two Sb_2 is 2.4 eV (i.e., 1.2 eV per Sb_2), and it is 8.4 eV for dissociating into four Sb_1 (i.e., 2.1 eV per atom) [93,94]. The most stable configuration of free-standing Sb_4 is a tetrahedron [95]. All these can change when Sb_4 is adsorbed on a substrate. For example, when deposited on Si(001) near RT, an Sb_4 ball (or tetrahedron) cluster first settles in a planar dumbbell precursor chemisorption state, then dissociates into two dimers [80]. The energy barrier is ~0.7 eV for ball-to-planar transition, and is ~0.8 eV for dissociation of a planar Sb_4 into two Sb_2. The binding energy of Sb on Si(001) is about 0.5 eV per atom with reference to Sb_4 in the gas phase, and a saturation coverage near 0.5 monolayer is maintained up to $T \approx 800$°C [93,94], much higher than the temperature at which such a coverage can be maintained on HOPG.

The binding of Sb with HOPG is expected to be significantly weaker than that with Si. Our results show that the initial sticking probability of Sb_4 on HOPG is near 1 at RT, but it starts dropping noticeably at ~100°C. When an Sb_4 lands on HOPG, it is most likely in a physisorption state. Similar to the case on Si(001), a physisorbed Sb_4 can transfer to a chemisorption state or even dissociate into two Sb_2. But these transformations require overcoming certain energy barriers, which are expected to be at least as high as those on Si(001) (i.e., ≥ 0.7 eV). The diffusion barrier E_d of physisorbed Sb_4 on HOPG seems quite low (significantly less than 0.3 eV based on a comparison with nucleation and growth on some metal surfaces [96]; here we assume $E_d \approx 0.1$ eV), so that at RT they can already quickly find defect sites such as steps. Three-dimensional island nucleation occurs as several Sb_4 clusters meet at a defect site. As more Sb_4 clusters arrive, the existing 3-D islands grow, and more 3-D islands nucleate until the island density reaches a certain saturation value.

On the other hand, when a physisorbed Sb_4 transforms to a chemisorbed Sb_4 or dissociates into dimers, the diffusion barriers of these Sb species on HOPG are expected to increase significantly from that of physisorbed Sb_4. We believe that the crystalline 2-D and 1-D structures are nucleated from these chemisorbed Sb species, and these nucleation events occur when the chemisorbed Sb clusters meet on a graphite terrace, not necessarily at defects. This offers a channel competing with 3-D island growth. Which channel is dominant depends on the kinetic parameters of these processes and deposition conditions.

At a relative low T (e.g., 30°C) and a low Sb_4 flux, the conversion to chemisorption or dissociation is strongly suppressed due to the Boltzmann factor exp[-$E_c/(kT)$], where E_c is the barrier of chemisorption or dissociation, and k is the Boltzmann constant. Because the diffusion barrier of physisorbed Sb_4 on HOPG is quite low, migration of Sb_4 clusters to step edges and other defects is highly activated. Consequently, 3-D island nucleation and growth are dominant, resulting in a sample shown in Figure 6.5.

Increasing substrate temperature enhances the rates of both Sb_4 diffusion and conversion to chemisorption (or dissociation). The ratio of these two rates changes with T approximately as $R_{\text{chemisorb}}/R_{\text{diffusion}} \propto \exp[-(E_c - E_d)/kT]$. Because $E_c > E_d$, the increment of the chemisorption rate with T is faster than that of Sb_4 diffusion, so that this ratio increases with T. Assuming $E_c - E_d = 0.8$ eV, this ratio at 100°C is about 300 times higher than that at RT. Correspondingly, the concentration of chemisorbed Sb species increases with T, which enhances the probability of nucleation and growth of 2-D and 1-D structures. Increasing the deposition flux further enhances this probability, because it lets chemisorbed Sb clusters more likely meet with each other.

In addition, Figures 6.4a and b show that, with a moderate flux and at RT, although all three types of Sb structures grow initially, most Sb_4 clusters deposited later go to 2-D and 1-D islands. This indicates that once 2-D and 1-D islands have nucleated, they can effectively attract Sb deposited later so that the supply of Sb_4 for 3-D island growth drops. At high T and high flux, this effect completely suppresses 3-D island growth, yielding only 2-D and 1-D islands on the sample as shown in Figure 6.7. At this stage, we are still searching for conditions to selectively grow either 1-D or 2-D Sb structures but not both.

6.4.2. Aluminum on Graphite

The growth and structure of aluminum on graphite have been studied by several groups [97–101]. Three-dimensional island growth of Al was observed using LEED, AES, and STM [97,98]. However, 2-D clusters of sputter-deposited Al up to 1 nm were imaged using STM in air [99]. XPS studies of Al sputter deposition on graphite indicated Al cluster formation with Al–C bonds and the carbidelike component Al_xC ($x \approx 1.4$) at the interface in early stage, followed by pure Al overlayer growth [100]. It is not clear if these controversies arise from different sample preparation methods or from ex situ characterization processes, especially considering the chemical sensitivity of Al atoms and clusters. An in situ UHV
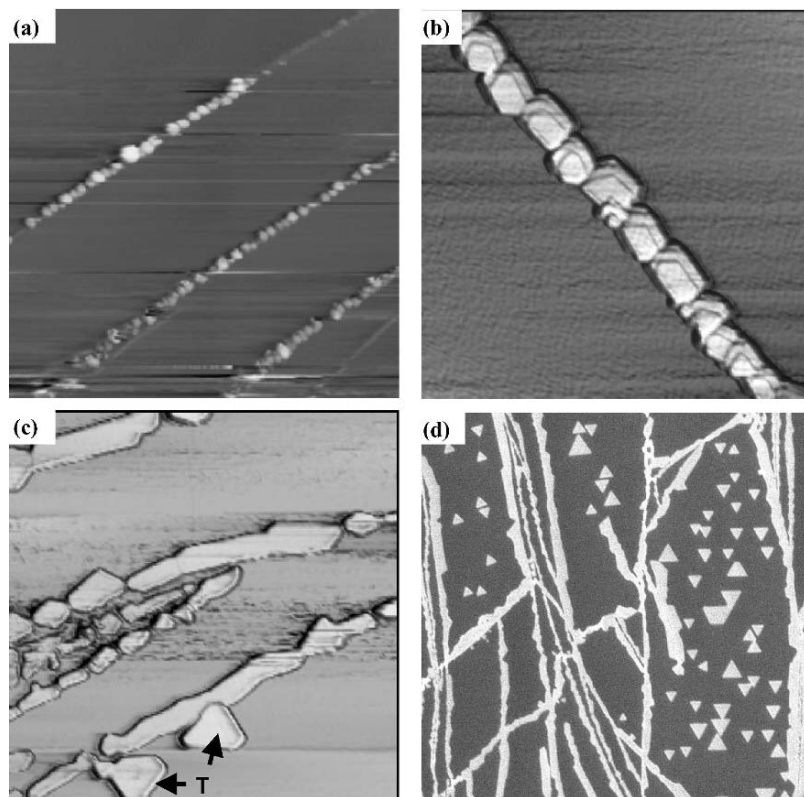
FIGURE 6.8. (a) Spherical Al clusters and cluster chains at step edges after 1.5 Å Al deposited on HOPG at RT; (b) flat-top faceted Al islands after deposition of 8 Å at RT; (c) triangular islands (T) on terrace and elongated ones at step edges after 6-nm Al deposited at RT; and (d) a SEM image of the sample in (c). Scan area: (a) $(0.5 \ \mu m)^2$; (b) $(250 \ nm)^2$; (c) $(2 \ \mu m)^2$; (d) $(15 \ \mu m)^2$.

STM investigation will be very helpful to clarify the growth and structure of Al on graphite.

We found that Al initially nucleate mostly at step edges of HOPG as 3-D spherical clusters at RT. With further deposition, the growth and coarsening of these clusters lead to interesting features. Figure 6.8a displays a STM image after 1.5 Å Al deposited at RT. Al cluster chains are observed along the steps at this stage, similar to the Ag and Au growth on HOPG [54,75,102]. The spherical 3-D clusters have height in the 4–8 nm range. Although none can be seen on terraces, Al clusters may also have nucleated on some isolated defect sites, but the binding between such small Al clusters and these defects is too weak to withstand STM scanning. This can explain the fluctuating scan lines in Figure 6.8a, and is consistent with previous in situ XPS and ab initio molecular dynamics studies [101,103].

After a total deposition of 8 Å, faceted Al islands with flat top and straight edges can be seen in the 3-D view STM image of Figure 6.8b, indicating crystallite formation. The double-edge of islands in this image is due to the multiple-tip effect. The island height is in the 3.0–5.5 nm range, and the lateral size in the 15–30 nm range. These islands are still only found at the step edges when a sample bias (V_S) of 0.5 V is used in the STM scan. However, after 6-nm Al deposition, isolated islands are observed on the terrace area along with those at step edges, as shown in Figure 6.8c. The SEM image in Figure 6.8d illustrates the distribution of Al islands over an even larger area. The islands on terraces, mostly in a (truncated) triangular shape, have an average height of ∼28 nm, nearly twice that of those along steps. During STM imaging with $V_S = 0.6$ V, isolated islands on the terrace of quite large lateral size (∼200 nm) can be dragged along by the tip. When these islands are dragged to be in contact with those at step edges, they will settle there. Similar behavior was observed for Au on HOPG [54,104,105]. When a large sample bias ($V_S > 3$ V) is used, even much smaller isolated islands on terraces (∼10 nm high and 90 nm lateral) can be stably imaged.

Zooming in on top of large Al islands in Figure 6.8c, we observe craters typically 4–8 nm in depth as those shown in Figure 6.9a. The craters on an elongated island are usually aligned as a chain roughly following the HOPG step edge. A large island on a terrace may have several craters on top. Further zooming in on a crater reveals atomic steps and terraces (see Figure 6.9b). The concentric rounded hexagonal step loops of the craters and the triangular shape of islands on the terrace indicate that the top facet is Al(111). The measured average height of atomic steps is 2.52 ± 0.20 Å, larger than the bulk value (2.34 Å).

Most of the isolated triangular islands shown in Figure 6.8d take two azimuthal orientations with a 60° rotation from each other. According to Maurice and Marcus [99], a preferential fitting of Al atomic rows with the $(\sqrt{3} \times \sqrt{3})$R30° superstructure on graphite (0001) leads to the alignment of Al crystallites with the substrate as Al(111)||HOPG(0001) and Al⟨110⟩||HOPG⟨10$\bar{1}$0⟩. Most of our observed islands agree with this alignment as the triangle island edges are along Al⟨110⟩, with the apexes of triangles pointing in two opposite directions. Deviations from the exact azimuthal alignment by several degrees are observed occasionally. A single atomic sheet of graphite is mirror symmetric with respect to ⟨10$\bar{1}$0⟩, Graphite (0001) is mirror symmetric with respect to ⟨10$\bar{1}$0⟩, so the opposite oriented Al triangular islands have equivalent interface bonding with graphite. The relative high mobility of Al islands manifested during STM imaging and the island coalescence discussed next indicates. a weak interaction between the Al islands and graphite, so the Al islands are indeed near the free-standing state.

The formation of 3-D islands with craters on top is a very unique growth behavior. Based on thermodynamic arguments, the typical Volmer–Weber growth with atomic deposition results in islands with a flat or protruding top surface. In most kinetic theories of island nucleation, growth, and coalescence based on atomic deposition, diffusion, attachment, and detachment processes, the curvature on the island top is normally flat or convex. The smaller Al islands, such as those in Figures 6.8a and b, are in such "normal" geometry. The craters on the large Al
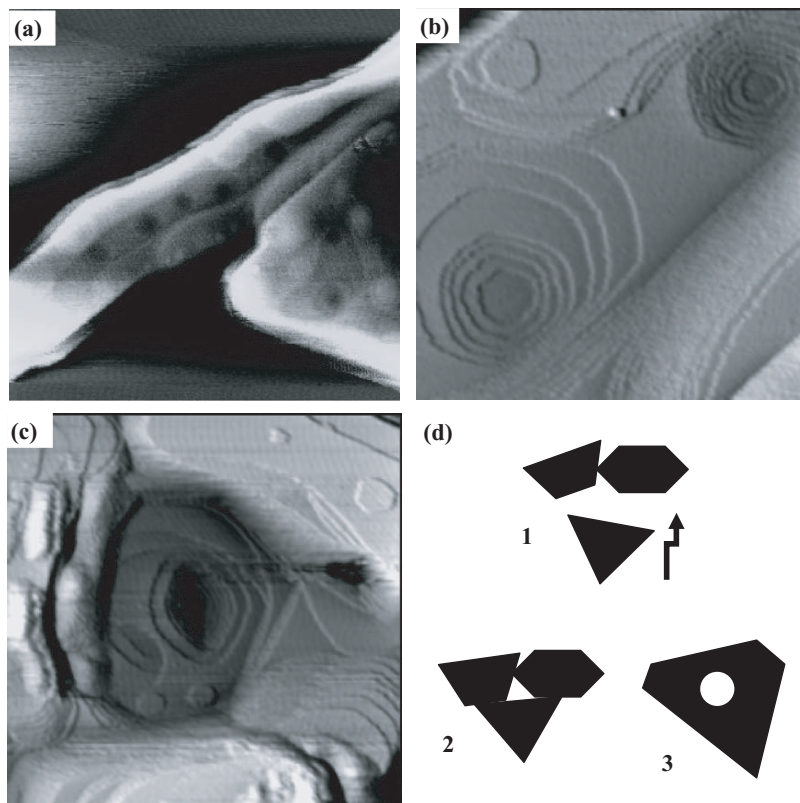
FIGURE 6.9. (a), (b): Craters formed on Al islands shown in Figure 6.8(c); (c): coarsening of three Al crystallites; and (d): schematics of island coarsening leading to crater formation. Image area: (a) $(500 \text{ nm})^2$; (b) $(110 \text{ nm})^2$; (c) $(200 \text{ nm})^2$.

islands disappear after a 25-min annealing at 350°C, indicating that they are not thermodynamically stable. Therefore, the formation of craters on large Al islands reflects a different kinetic situation in the coarsening of smaller islands.

In Figure 6.9c, we show an island group (not at step edge) in an early merging stage, in which the crater in the center and the boundaries between smaller islands near the perimeter can be easily identified. Based on this, a simple model is proposed for crater formation. Al atoms diffuse quickly on a HOPG surface due to a low diffusion energy barrier ($\sim$0.02 eV) [103], and the nucleation of small clusters occurs when Al atoms meet at the initial stage. These Al atoms and small clusters arrive and stay at defect sites with a relatively strong binding force. With further deposition of Al, small spherical clusters grow up to faceted crystallites. The relatively small faceted islands still can migrate on the defect-free area, although with their mobility decreasing gradually due to a higher diffusion barrier and/or lower attempt frequency.

When several islands meet, they merge from an island group to one large coherent island. In this process, Al atoms are required to fill in the bare HOPG surface area surrounded in the middle of the island group. Previous investigations have shown that coalescence happens at RT for Al islands, and kink and corner breaking induce a transition towards equilibrium-shaped islands [106,107]. However, even though the Ehrlich–Schwoebel barrier [108,109] for an Al atom to jump down a step is small (0.06–0.08 eV), the interlayer mass transport is hindered at RT due to a high energy barrier ($\sim$0.8 eV) for atom evaporation from the steps. Therefore, Al atom transport to the middle of the island group is much slower than the merging diffusion along the perimeter. Thus craters with a rounded hexagonal shape finally form in the central area at RT. The scenario of crater formation in three stages is sketched schematically in Figure 6.9d. To form a crater at the center, the minimum number of islands in a group is three. A similar process is applicable to the formation of crater chains on the elongated islands along HOPG steps.

In our model, the remarkable translational and rotational mobilities of Al crystallites are essential. In fact, the inertness of graphite usually leads to a very low diffusion barrier not just for adatoms, but also for clusters of some metals, even those consisting of several thousand atoms. For instance, it has been demonstrated that Sb and Au clusters migrate on HOPG surfaces at a surprisingly high diffusion rate of $\sim$$10^{-8}$ cm^2/s at RT [110,111], quite comparable to that of single atoms in similar conditions. Ag clusters with a diameter of $\sim$14 nm were also found to be mobile on graphite surfaces [112]. The behavior of Al clusters on HOPG surfaces seems similar to that of Au and Ag.

Most of the small islands are already crystalline when they form a group. In order to merge into a big coherent island, these small islands should have the same lattice orientation. As shown earlier, most crystalline islands take two azimuthal orientations, with some deviating a few degrees. Thus, for an island group coarsening into a single island with craters in the middle, it is necessary for some Al islands to adjust their orientation. We observed island rotation during the STM scan, especially for those in contact with each other. It is also possible that the grain boundary moves across a crystallite when coarsening with another of different orientation [29,30].

6.4.3. Germanium on Graphite

Ge cluster nucleation also occurs mostly at HOPG step edges. Initially, the clusters form a single-row chain along a step, the same as that of Al in Figure 6.8a. Later, clusters on both sides of the step as shown in Figure 6.10a are observed. With 0.9 nm Ge deposited, the height of Ge cluster is ≤9 nm. The cluster surface is curved with no observable atomic order. After 2.1 nm Ge are deposited, the cluster chains branch off the step edges and grow into the terrace region, as shown in Figure 6.10b. Most of the chains are nearly parallel to each other. The chain growth on the terrace is similar to that of a Si dimer row on Si(001) [113], suggesting the chain end as a most favorable site for cluster nucleation and trapping. Some chains change direction and even make a U-turn in the growth process. These chains
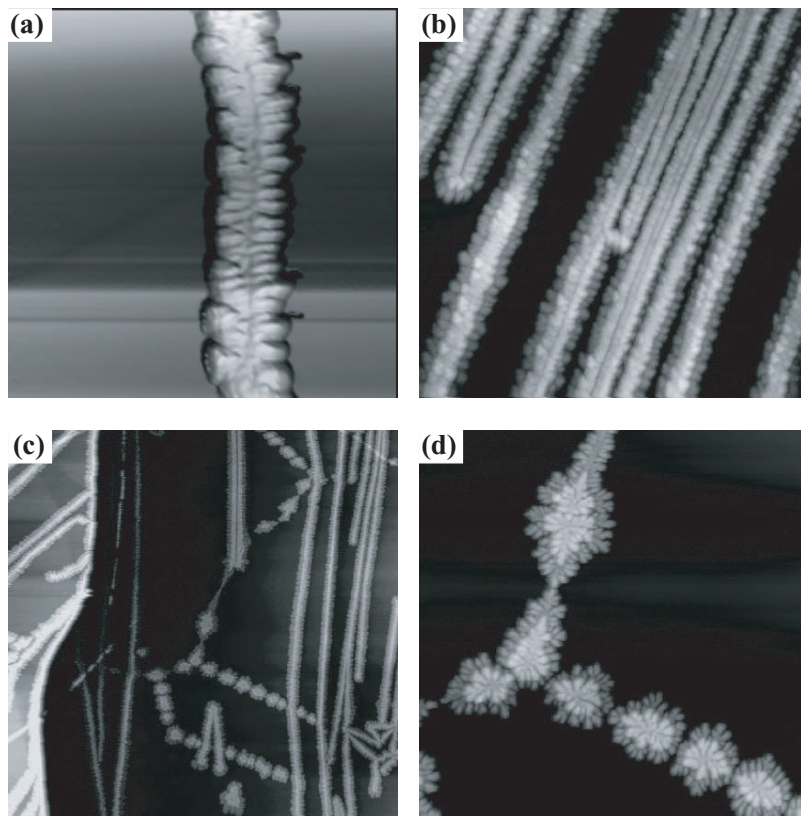
FIGURE 6.10. STM images of Ge deposition on HOPG at RT. (a) Clusters nucleated on both sides of a step after 0.9-nm Ge deposition; (b) double-layer cluster chains formed after 2.1-nm Ge deposition; (c) fractal islands grow along undersurface steps on wide terrace; and (d) a zoom-in scan on the double-layer fractals in (c). Image area: (a) $(0.3 \ \mu m)^2$; (b) $(0.6 \ \mu m)^2$; (c) $(2.5 \ \mu m)^2$; (d) $(0.8 \ \mu m)^2$.

mostly consist of two layers of Ge clusters now. The height of the lower layer is ≤ 9.5 nm, about the same as the single-layer chain in Figure 6.10a, and the height of the upper layer is ~ 15 nm as measured from the graphite surface. In the middle area of wide terraces such as the one shown in Figure 6.10c, the Ge clusters form fractal islands due to diffusion limited aggregation [114].

Figure 6.10d is a zoom-in STM scan on the ramified islands, which also show a double-layer structure. These connected ramified islands originate from clusters nucleated at sites of undersurface steps. The heights of the two layers are about the same as those of the chains. The second-to-first layer mass ratio is quite high. These double-layer structures form due to several factors: (1) Ge atoms deposited later are more likely to form new clusters rather than being integrated into existing ones, indicating a self-limiting cluster growth similar to Co on SiN_x [59]; (2) the
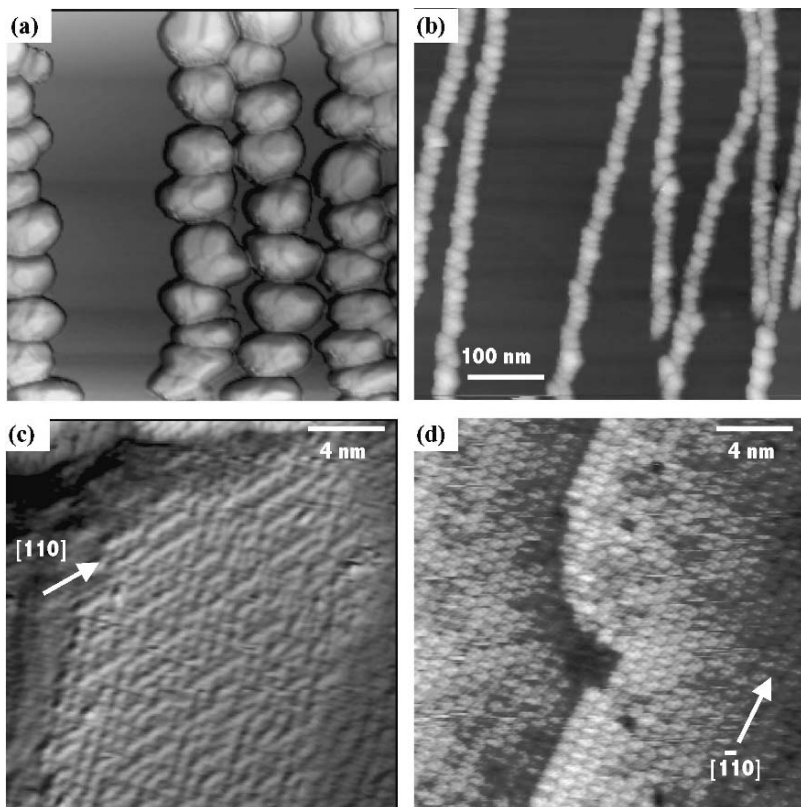
FIGURE 6.11. STM images of Ge crystallites with facets formed on HOPG. (a) With 4-nm Ge deposited at RT and annealed at 310°C; (b) 0.7 nm of Ge deposited at 175°C; (c) a facet imaged at $V_s = -1.8$ V; and (d) a facet imaged at $V_s = -0.6$ V after 22-nm Ge deposition. Image area: (a) $(0.6 \ \mu m)^2$, (b) $(0.5 \ \mu m)^2$, (c), (d) $(20 \ nm)^2$.

top of first-layer chains and fractals provides more stable sites for nucleation and/or binding of new clusters than a graphite surface adjacent to the first-layer Ge clusters; (3) Ge atoms or small clusters are mobile on HOPG and on the first-layer clusters to reach the top even at room temperature; and (4) the re-evaporation probability of Ge atoms on the HOPG terrace is quite high, so that only those landed on or very near a defect or existing Ge clusters can stay by quickly finding a binding site. The structures shown in Figure 6.10 are stable with respect to annealing at $T \leq 225°C$ for 10 min. Faceted crystallites of height $\sim$50 nm form from coarsening of clusters when annealed at a higher T, as shown in Figure 6.11a.

When Ge is deposited on HOPG held at $T \geq 175°C$, nanocrystallites are nucleated as chains along the steps first, and later the chains also branch off from the steps onto the terraces. Crystal facets develop on the particle surface at a certain stage of growth. Figure 6.11b displays an image of a sample after 0.7 nm Ge

deposited at 175°C. The cluster heights are in 10–13 nm range and their lateral size is ∼25 nm (without considering broadening due to tip shape). These clusters are easily moved by STM tip, indicating weaker adhesion to the substrate than the cluster islands formed at RT. This suggests that the nanoparticles are more compact now, so the area of contact with graphite is reduced. At this stage, no facet is observed on the island surface.

With 5 nm Ge deposited, the typical height of nanocrystallites becomes ∼45 nm and the apparent lateral size ∼90 nm when measured perpendicular to the chain, whereas along the chain the lateral spacing is about 50 nm (close to the height). Because the particles should be in contact with one another, the lateral spacing along the chain should be close to the real lateral size of the particles. Using Eq. (2.1) and assuming a nearly isotropic particle shape, the estimated radius of curvature of the STM tip is approximately 40 nm.

Crystal facets have developed on Ge crystallites of diameter ≥40 nm, similar to those in Figure 6.11a. These facets are oriented randomly with respect to the substrate and uncorrelated between different crystallites. Figure 6.11c displays a STM image of atomic-scale structure on a facet. The period along the arrow is 10.3 Å, whereas perpendicular to the arrow the period is 5.2 Å. The observed surface feature suggests that it is most probably a Ge{113} facet with the arrow pointing in the [110] direction [115–117]. Ge(113)–3 × 1 reconstruction has a period of 12 Å along [1$\bar{1}$0] and 6.6 Å along [33$\bar{2}$]. The shorter periods here can be explained with a tilting of the facet from the scanning plane by 30° in [1$\bar{1}$0] and 38° in [33$\bar{2}$].

The indices of some facets are difficult to identify. Figure 6.11d displays a facet with a period along the rows in the arrow direction 7.7 Å and a row spacing 8.1 Å. Ge(331)–2 × 1 superstructure fits these measured values relatively well, with the arrow pointing in the [1$\bar{1}$0] direction. This reconstruction should have a period of 8 Å along [1$\bar{1}$0] and a row spacing of 8.7 Å. Again, our measured values can be explained with a tilting of the facet from the imaging plane by 15° in [1$\bar{1}$0] and 21° in [11$\bar{6}$]. However, such a 2 × 1 superstructure has not been observed on macroscopic Ge(331) or Si(331) [118,119]. This discrepancy could originate from the environment on nanocrystal surfaces that could be rather different than the bulk surfaces. Effects of impurities cannot be completely excluded. It is important to notice that low-index facets, such as {100} and {111}, which have the lowest surface energies for a bulk crystal [120], have not been observed very often on the Ge nanocrystals grown on HOPG.

6.5. Silicon and Germanium on Silicon Nitride

On the crystalline SiN$_x$ film grown on Si(111) shown in Figure 6.2b, Si and Ge atoms also nucleate into 3-D islands. However, the nucleation takes place almost uniformly all over the surface, and the nucleation density does not change sensitively with substrate temperature. This is mainly due to the existence of many surface defects that act as nucleation sites. Figure 6.12a is an image of Si clusters
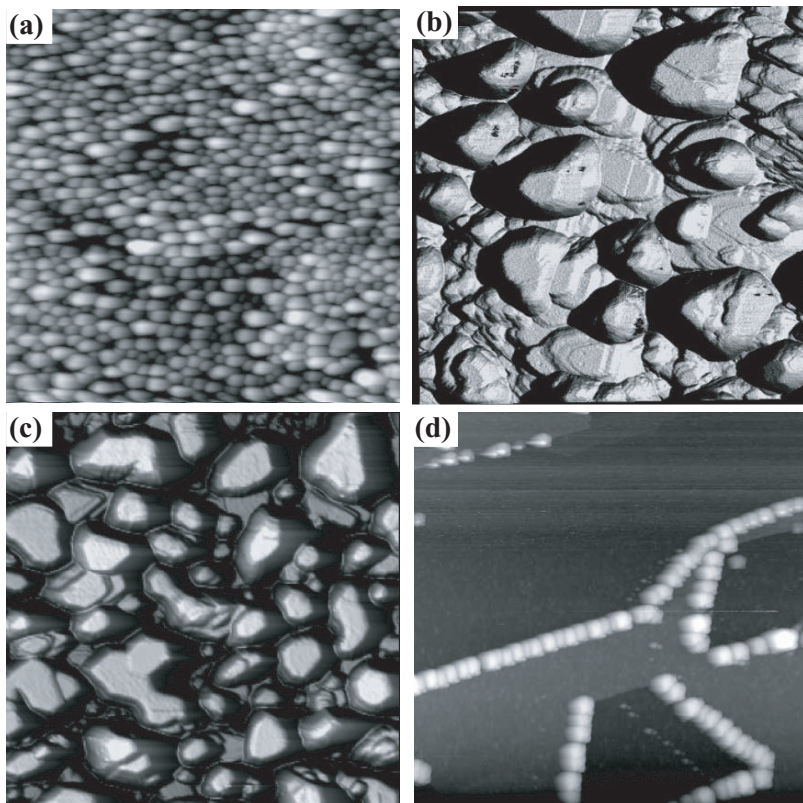
FIGURE 6.12. STM images of Si and Ge grown on crystalline SiN_x/Si(111). (a) 5-nm Si deposited at 750°C; (b) 50-nm Ge deposited at 550°C, the top facets on large islands are mostly (111); (c) 80-nm Si deposited at 800°C, the top facets of crystallites are mostly (111) aligned with Si substrate; and (d) Ge crystallites nucleated on Sb-covered SiN_x/Si(111). Scan area: (a), (b) $(0.22 \mu m)^2$; (c), (d) $(0.55 \mu m)^2$.

nucleated on SiN_x/Si(111) at 750°C. Si 3-D islands formed initially are spherical, without any facet and atomic feature resolvable with STM. Ge deposited at 550°C also forms spherical islands with high nucleation density. The islands are quite stable against tip disturbance during STM imaging. This indicates a stronger bonding of the nanoparticles on SiN_x than on HOPG. The Ge nanocrystals probably partially wet the substrate as a truncated sphere, instead of near the complete nonwetting state on HOPG.

As more Si or Ge is deposited, the average crystallite size increases. But the crystallites remain (truncated) spherical until their size reaches a threshold value. Here, facets become observable when the crystallites grow to a diameter of 40 ± 5 nm. This size threshold of faceting is comparable to that of Ge on HOPG. In Figure 6.12b, after 50-nm Ge deposited, relatively large islands show facets on

top, whereas the smaller ones remain round. The corrugation of this image is 15 nm, and many features between the islands are obviously the artifacts due to tip shape. Small-area scans indicate that most of the top facets are (111) faces (with the c(2 × 8) superstructure observed [121]) aligned with Si substrate. The nanocrystal surface adjacent to the (111) facets is still curved smoothly.

With more Si or Ge deposited, the islands grow further. As shown in Figure 6.12c, the top facets of the most protruded islands are almost exclusively the aligned (111). Other facets now appear around the (111). Non-(111) oriented islands can be found in STM and cross-section TEM images, but they grow much more slowly than the (111)-topped ones so they are shadowed or even buried by the latter.

We examined the effects of an Sb atomic layer as a surfactant on the nucleation, growth, and shape of Ge nanoparticles on SiN_x films [37]. Sb is deposited on SiN_x at RT, followed with an annealing at $\sim355°C$ to keep 1 ML Sb adsorbed. The nucleation density of Ge nanoparticles on such Sb-covered SiN_x surfaces is reduced dramatically. Figure 6.12d shows that Ge nanoparticles grown on Sb-SiN_x/Si(111) at 465°C mostly stay at step edges. The high nucleation density of Si and Ge is related to the high density of defects or unsaturated bonds on SiN_x surface, which is probably due to missing nitrogen atoms in the nitride film. Considering both N and Sb are Group V elements, Sb seems to passivate these defects quite effectively.

Si and Ge deposited on amorphous SiN_x films on Si(001) (see Figure 6.2d) initially also form round-shaped nanocrystals of high nucleation density. Facets start to appear as the crystallites become sufficiently large. However, there is no dominant orientation in which the nanocrystals would take; that is, the crystallite orientation remains completely random, as shown in Figure 6.13a. Furthermore, although low-index facets such as {111} and {100} exist, most of facets are high-index ones. In Figures 6.12b to d, small-scale images of Si and Ge crystallites are displayed, and the {111} and {100} facets are marked. The indices of high-index facets can be determined in some cases (e.g., {113}), especially when their area is large. But it is difficult to identify some of the small-area facets inasmuch as their surface configuration could be rather different from the large-area ones [122,123]. The facet on top of a Si crystallite displayed in Figure 6.13d has a rectangular supercell of size 7.5 Å × 5.3 Å. It can match with Si(110)–2 × 1, which should have a period of 7.68 Å along the [1$\bar{1}$0] and 5.43 Å along [001]. However, the 2 × 1 reconstruction is not observed on macroscopic Si(110). "n × 2" (with the 2 × along [001]) and 2 × 16 superstructures have been reported on Si(110) [124,125], and 2 × 16 and c(10 × 8) on Ge(110) [126].

6.6. From Clusters and Nanocrystallites to Continuous Film

As more material is deposited, more surface area is covered by clusters and crystallites, leading to a continuous film. The texture of such a film depends on the growth kinetics and the interaction between the nanoparticles. If the randomly oriented nanocrystals formed in an early stage grow at about the same rate, and the crystallites nucleated later remain in random orientation, a polycrystalline film
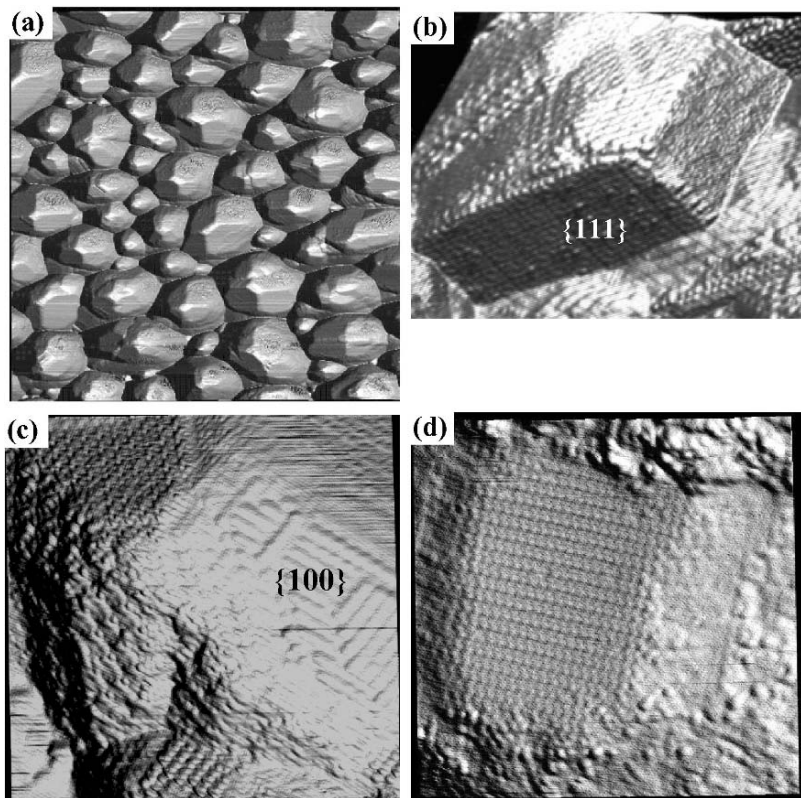
FIGURE 6.13. STM images of Si and Ge nano-crystallites on amorphous SiN_x/Si(001). (a) After 35-nm Ge deposited at 465°C; (b) {111} facet among others on Si crystallite, (c) {100} on Ge crystallite, and (d) a facet with rectangular atomic order on Si. Image area: (a) $(0.33 \ \mu m)^2$; (b) (40 nm × 32 nm); (c), (d) $(22 \ nm)^2$.

is expected. Ge growth on HOPG seems to proceed in this form. Figure 6.14a is taken on a sample with 30-nm Ge deposited at 190°C. The nanocrystals are in contact with each other in the chains, but the orientation of neighboring crystallites is basically not correlated. The random-oriented Ge crystallites do not coalesce with each other effectively. The Ge clusters formed at RT on HOPG show similar behavior. In contrast, coalescence among Al clusters and crystallites can proceed effectively to form large islands and continuous films along HOPG steps, as shown in Figure 6.14b. The coalescence rate between nanoparticles depends not only on the diffusivity of surface atoms, but also on the orientation order and mobility (translational and rotational) of the nanoparticles [26,127].

The Si or Ge films formed on SiN_x/Si(111) and on SiN_x/Si(001) have texture quite different from each other. In Figure 6.12, we have shown that most grown-up crystallites are aligned with the Si(111) substrate. However, cross-sectional TEM
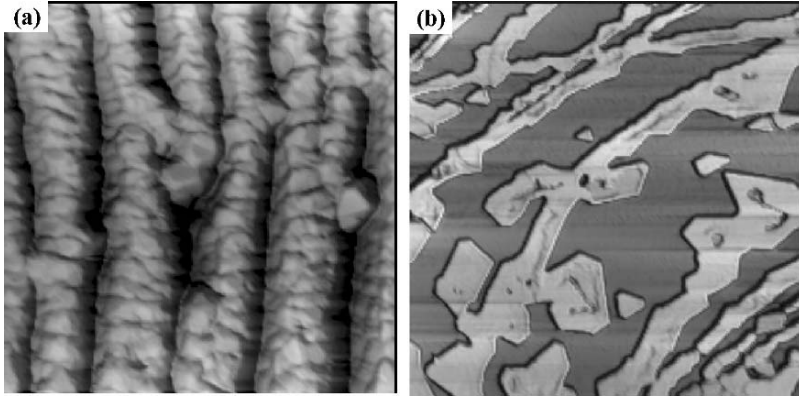
FIGURE 6.14. STM images of near-continuous films on HOPG. (a) After 30-nm Ge deposited at 190°C; and (b) 10-nm Al deposited at RT. Image area: (a) $(1.5\,\mu m)^2$; (b) $(3.5\,\mu m)^2$.

images reveal that, at the interface with SiN_x, many Si or Ge crystallites take other orientation in addition to the aligned ones. The average crystallite size is rather small compared with that observed away from the interface, indicating not much coarsening between the small crystallites at the interface. The STM and TEM images suggest that, in later stages of growth, the oriented crystallites grow faster and occupy more surface area. Most of the misoriented crystallites are screened later so they stop growing and get buried, but are not consumed or transformed to the aligned. The dominance of aligned crystallites leads to a (111)-oriented columnar film which gives rise to a fairly sharp single-phase LEED pattern. Figure 6.15a displays a STM image of a Ge overlayer with an average thickness ~300 nm deposited at 600°C. Now, the surface is fully covered with large aligned grains of dimension >200 nm. These grains come from the coalescence of smaller aligned crystallites. Although the top surfaces are rather flat (height variation <3 nm across the top), small-scale STM scans (see Figure 6.15b) reveal domain boundaries. An oriented film resulting from relative random nucleation was also observed in the growth of GaN or AlN on α-Al_2O_3(0001) [28].

Figure 6.15c shows a polycrystalline Si film on SiN_x/Si(001) obtained with ~450 nm of Si deposited at 770°C. The typical grain sizes are below 50 nm in these films. No particular orientation of crystallites becomes dominant. The orientation of new crystallites nucleated between the existing ones remains random. It is also well known that the difference in growth rate on different facets has a strong influence on the shape of a crystal [32–34,128]. A facet will disappear if atom incorporation on it is faster than on other facets if its surface area decreases in growth [29]. We have observed that the (001) top facets shrink rapidly as nanocrystals grow. Such facets disappear in film growth. This explains that, although quite a few (001)-oriented islands may grow epitaxially from the voids of the amorphous SiN_x film, they do not dominate in later growth stages.
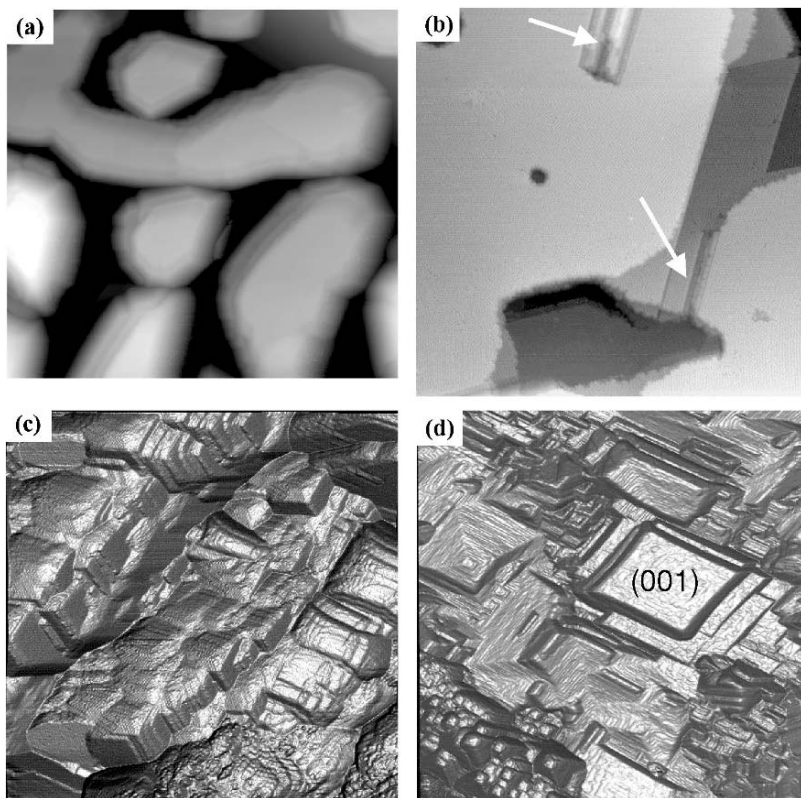
FIGURE 6.15. STM images of continuous films on SiN_x. (a) After 300-nm Ge deposited on SiN_x/Si(111) at 600°C; (b) zoom-in on a flat top area in (a), arrows point at domain boundaries; (c) 450-nm Si deposited at 770°C on SiN_x/Si(001); and (d) Sb-covered 230-nm Ge deposited on SiN_x/Si(001). Image area: (a) (1 μm × 0.9 μm); (b) (110 nm)^2; (c) (0.22 μm)^2; (d) (0.33 μm)^2.

When an Sb surfactant layer covers the Si or Ge nanocrystals on SiN_x/Si(001) (maintained with an Sb flux) during growth, their shape is significantly changed from the bare state. It is well known that an Sb surfactant layer on Ge lowers the surface energy of {001} relative to other orientations [35]. In addition, because SiN_x area is passivated by Sb, the nucleation and growth of Ge crystallites take place more likely at the voids exposing the Si substrate shown in Figure 6.2d. These crystallites are expected to be epitaxial to align with the Si(001) substrate [129]. These factors enhance the growth of (001)-oriented grains. The smoothness and orientation order of the overlayer films are significantly improved, as illustrated by the image in Figure 6.15d. For Si and Ge overlayers grown on SiN_x/Si(111), Sb surfactant does not improve the film smoothness. In fact, the modification of surface atomic structure by Sb adsorption favors {113} growth against {111}, so the overlayer surface is even rougher [37,130].

6.7. Conclusions and Future Outlook

Our results and remarks are summarized as the following.

1. Three-dimensional islands nucleate and grow for all the elements deposited on all inert substrates studied in our experiments. Comparatively speaking, graphite is nearly a perfect inert substrate to Al and Ge nanoparticles, and SiN_x surfaces show noticeable stronger binding with the nanoparticles, partly because of a high density of surface defects (or unsaturated bonds in the case of amorphous SiN_x).

2. In addition to 3-D islands, 2-D films and 1-D nanorods are also formed when Sb is deposited on HOPG. The formation of 2-D and 1-D structures is closely related to the chemisorption and dissociation of deposited Sb_4. By choosing proper deposition flux and substrate temperature, we can selectively grow either 3-D islands or 2-D and 1-D structures. Although the 3-D crystallites are close to α-phase Sb bulk, the 1-D and 2-D structures show noticeable deviation in lattice type or parameters from the bulk, possibly induced by a charge transfer from graphite to Sb.

3. The shape of 3-D nanoparticles is nearly spherical when they are small. The spherical shape can be maintained for Sb and Ge crystallites up to quite large size (consisting of $\geq 10^6$ atoms). Such faceting threshold sizes, beyond which crystalline facets appear on nanocrystal surface, are significantly bigger than those of many metallic crystallites [8,34,36,131], including Al in our study. The electronic energy factor, which favors spherical shape, should be insignificant in this size range. We believe that the key factor here is the surface energy of a nanoparticle that, due to limited size, can take very different values than that of macroscopic surfaces.

4. For Sb and Al on HOPG, and for Si and Ge on crystalline SiN_x/Si(111), most grown-up crystallites have definite polar (also azimuthal for some) orientation alignment with the substrate. In contrast, for Ge on graphite, and Si and Ge on amorphous SiN_x/Si(001), the orientation of the nanocrystals seems completely random, and high-index facets are observed quite often. Surface reconstructions not formed on bulk crystals are observed on some facets. These observations reflect the unique capacity of nanoscale facets to accommodate certain surface superstructures that are not observable on a macroscopic scale.

5. The growth competition and coarsening kinetics of nanoparticles vary dramatically among different elements and/or substrates, leading to different film texture in the later growth stage. The coarsening among aligned grains can occur easily, as in the cases of Al and Sb on HOPG, whereas that between crystallites with different orientations is difficult, as in the case of Ge and Si on SiN_x/Si(001) and on HOPG. The aligned Si and Ge crystallites on SiN_x/Si(111) prevail in growth competition with others, resulting in an oriented columnar film. In contrast, the (001)-oriented crystallites shrink in the growth competition, so the crystallite orientation remains random in further Si or Ge deposition on amorphous SiN_x (and on HOPG). This results in polycrystalline overlayer films later.

6. An Sb atomic layer effectively passivates the defects on SiN_x so nanoparticle nucleation only takes place along steps. Sb adsorption also modifies the shape of

nanocrystals due to a change in surface energy anisotropy. By favoring (001) facets against others, it improves the smoothness and orientation order of Si and Ge films on $SiN_x/Si(001)$. This effect could be further enhanced so that a (001)-oriented Si or Ge overlayer can grow on $SiN_x/Si(001)$ in epitaxial lateral overgrowth [132,133].

All these results indicate that the geometric and surface properties of nanostructures can deviate significantly from that of bulk crystals and are sensitively size-dependent. Consequently, these properties affect the interactions of nanostructures with the substrates and with each other, as well as the texture of films derived from these nanoparticles. We also showed a few examples of selective nanostructural self-assembly. The selectivity can be expanded based on the experiments over broader ranges of growth conditions (e.g., flux, substrate temperature, type of surfactant). The details of nanoparticle migration, rotation, and coarsening can be captured at a reduced substrate temperature. In addition, self-assembly and morphology of nearly free-standing compound nanostructures can be explored on inert substrates. Such exploration is beneficial to the integration of nanostructural electronic, optoelectronic, and spintronic devices on Si-based integrated circuits.

References

[1] Marks, L.D. (1994). Experimental studies of small particle structures, *Rep. Prog. Phys.* **57**, 603-649.

[2] Alivisatos, A.P. (1996). Semiconductor clusters, nanocrystals, and quantum dots, *Science* **271**, 933–937.

[3] Sugano, S. and Koizumi, H. (1998). *Microcluster Physics,* 2nd edition, Berlin: Springer.

[4] Meiwes-Broer, K.-H. (ed.) (2000). *Metal Clusters at Surfaces: Structure, Quantum Properties, Physical Chemistry*, New York: Springer.

[5] Moriarty, P. (2001). Nanostructured materials, *Rep. Prog. Phys.* **64**, 297–381.

[6] Yoffe, A.D. (2002). Low-dimensional systems: Quantum size effects and electronic properties of semiconductor microcrystallites (zero-dimensional systems) and some quasi-two-dimensional systems, *Adv. Phys.* **51**, 799–890.

[7] Yoffe, A.D. (2001). Semiconductor quantum dots and related systems: Electronic, optical, luminescence and related properties of low dimensional systems, *Adv. Phys.* **50**, 1–208.

[8] Henry, C.R. (1998). Surface studies of supported model catalysts, *Surf. Sci. Rep.* **31**, 231–325.

[9] Chusuei, C.C., Lai, X., Luo, K., and Goodman, D.W. (2001). Modeling heterogeneous catalysts: metal clusters on planar oxide supports, *Topics Catal.* **14**, 71–83.

[10] Freund, H.-J. (2002). Clusters and islands on oxides: From catalysis via electronics and magnetism to optics, *Surf. Sci.* **500**, 271–299.

[11] Cho, A. (2003). Connecting the dots to custom catalysts, *Science* **299**, 1684–1685.

[12] Chou, S.Y. (1997). Patterned magnetic nanostructures and quantized magnetic disks, *Proc. IEEE* **85**, 652–671.

[13] Ross, C.A. (2001). Patterned magnetic recording media, *Annu. Rev. Mater. Res.* **31**, 203–235.

[14] Meulenberg, R.W., Jennings, T., and Strouse, G.F. (2004). Compressive and tensile stress in colloidal CdSe semiconductor quantum dots, *Phys. Rev. B* **70**, 235311.

[15] Jarrold, M.F. and Constant, V.A. (1991). Silicon cluster ions: Evidence for a structural transition, *Phys. Rev. Lett.* **67**, 2994–2997.

[16] Ho, K.-M., Shvartsburg, A.A., Pan, B., Lu, Z.-Y., Wang, C.-Z., Wacker, J.G., Fye, J.L., and Jerrold M.F. (1998). Structures of medium-sized silicon clusters, *Nature* **392**, 582–585.

[17] Bachels, T. and Schäfer, R. (2000). Binding energies of neutral silicon clusters, *Chem. Phys. Lett.* **324**, 365–372.

[18] Pizzagalli, L., Galli, G., Klepeis, J.E., and Gygi, F. (2001). Structure and stability of germanium nanoparticles, *Phys. Rev. B* **63**, 165324.

[19] Weissker, H.-Ch., Furthmüller, J., and Bechstedt, F. (2003). Structural relaxation in Si and Ge nanocrystallites: Influence on the electronic and optical properties, *Phys. Rev. B* **67**, 245304.

[20] Ventrice, C.A., Jr. and Geisler, H. (1999). The growth and structure of epitaxial metal-oxide/metal interfaces, in: *Thin Films: Heteroepitaxial Systems*, ed. W.K. Liu, M.B. Santos, Singapore: World Scientific, pp. 167–210.

[21] Göpel, W. and Reinhardt, G. (1996). Metal oxide sensors: new devices through tailoring interfaces on atomic scale, *Sensors Update* **1**, 47–120.

[22] Baron, T., Martin, F., Mur, P., Wyon, C., Dupuy, M., Busseret, C., Souifi, A., and Guillot, G. (2000). Low pressure chemical vapor deposition growth of silicon quantum dots on insulator for nanoelectronics devices, *Appl. Surf. Sci.* **164**, 29–34.

[23] Millo, O., Steiner, D., Katz, D., Aharoni, A., Kan, S., Mokari, T., and Banin U. (2005). Transition from zero-dimensional to one-dimensional behavior in InAs and CdSe nanorods, *Physica E* **26**, 1–8.

[24] O'Handley, R.C. (1999). *Modern Magnetic Materials: Principles and Applications*. New York: Wiley.

[25] Yu, X., Duxbury, P.M., Jeffers, G., and Dubson, M.A. (1991). Coalescence and percolation in thin metal films, *Phys. Rev. B* **44**, 13163–13166.

[26] Jensen, P. (1999). Growth of nanostructures by cluster deposition: Experiments and simple models, *Rev. Mod. Phys.* **71**, 1695–1735.

[27] Jung, Y.-C., Miura, H., Ohtani, K., and Ishida M. (1999). High-quality silicon/insulator heteroepitaxial structures formed by molecular beam epitaxy using Al_2O_3 and Si, *J. Cryst. Growth* **196**, 88–96.

[28] Heffelfinger, J.R., Medlin, D.L., and McCarty, K.F. (1999). On the initial stages of AlN thin-film growth onto (0001) oriented Al_2O_3 substrates by molecular beam epitaxy, *J. Appl. Phys.* **85**, 466–472.

[29] Thompson, C.V. (2000). Structure evolution during processing of polycrystalline films, *Annu. Rev. Mater. Sci.* **30**, 159–190.

[30] Rost, M.J., Quist, D.A., and Frenken, J.W.M. (2003). Grains, growth, and grooving, *Phys. Rev. Lett.* **91**, 026101.

[31] Givargizov, E.I. (1991). *Oriented Crystallization on Amorphous Substrates*. New York: Plenum.

[32] Pimpinelli, A. and Villain, J. (1998). *Physics of Crystal Growth*. Cambridge: Cambridge University Press.

[33] Zhang, Z. and Lagally, M.G. (Eds.) (1998). *Morphological Organization in Epitaxial Growth and Removal*. Singapore: World Scientific.

[34] Wang, Z.L. (2000). Transmission electron microscopy of shape-controlled nanocrystals and their assemblies, *J. Phys. Chem. B* **104**, 1153–1175.

[35] Eaglesham, D.J., Unterwald, F.C., and Jacobson D.C. (1993). Growth morphology and the equilibrium shape: the role of "surfactants" in Ge/Si island formation, *Phys. Rev. Lett.* **70**, 966–969.

[36] Hansen, P.L., Wagner, J.B., Helveg, S., Rostrup-Nielsen, J.R., Clausen, B.S., and Topsøe, H. (2002). Atom-resolved imaging of dynamic shape changes in supported copper nanocrystals, *Science* **295**, 2053–2055.

[37] Hu, Y., Wang, X.-S., Cue, N., and Wang X. (2002). Ge islanding growth on nitridized Si and the effect of Sb surfactant, *J. Phys.: Condens. Matter* **14**, 8939–8946.

[38] Lee, H.N., Hesse, D., Zakharov, N., and Gösele, U. (2002). Ferroelectric $Bi_{3.25}La_{0.75}Ti_3O_{12}$ films of uniform a-axis orientation on silicon substrates, *Science* **296**, 2006–2009.

[39] Koch, R. and Poppa, H. (1987). The influence of the mica surface composition on the growth morphology of discontinuous epitaxial palladium vapor deposits, *J. Vac. Sci. Technol. A* **5**, 1845–1848.

[40] Polli, A.D., Wagner, T., Gemming, T., and Rühle M. (2000). Growth of platinum on TiO_2- and SrO-terminated $SrTiO_3$(100), *Surf. Sci.* **448**, 279–289.

[41] Lerme, J., Pellarin, M., Baguenard, B., Bordas, C., Cottancin, E., Vialle, J.L., and Broyer, M. (1996). Electronic shells and supershells in gallium and aluminum clusters, in: T.P. Martin (ed.) *Large Clusters of Atoms and molecules*. Dordrecht: Kluwer, pp. 71–88.

[42] Bäumer, M., and Freund, H.-J. (1999). Metal deposits on well-ordered oxide films, *Prog. Surf. Sci.* **61**, 127–198.

[43] Gan, Y., Chu, W., and Qiao, L. (2003). STM investigation on interaction between superstructure and grain boundary in graphite, *Surf. Sci.* **539**, 120–128.

[44] Sun, H.-L., Shen, Q.-T., Jia, J.-F., Zhang, Q.-Z., and Xue, Q.-K. (2003). Scanning tunneling microscopy study of superlattice domain boundaries on graphite surface, *Surf. Sci.* **542**, 94–100.

[45] Wang, X.-S., Zhai, G., Yang, J., and Cue, N. (1999). Crystalline Si_3N_4 thin films on Si(111) and the 4×4 reconstruction on Si_3N_4(0001), *Phys. Rev. B* **60**, R2146–R2149.

[46] Wang, X.-S., Zhai, G., Yang, J., Wang, L., Hu, Y., Li, Z., Tang, J.C., Wang, X., Fung, K.K., and Cue N. (2001). Nitridation of Si(111), *Surf. Sci.* **494**, 83–94.

[47] Ahn, H., Wu, C.-L., Gwo, S., Wei, C.M., and Chou, Y.C. (2001). Structure determination of the Si_3N_4/Si(111)–(8×8) surface: a combined study of Kikuchi electron holography, scanning tunneling microscopy, and *ab initio* calculations, *Phys. Rev. Lett.* **86**, 2818–2821.

[48] Renaud, G. (1998). Oxide surfaces and metal/oxide interfaces studied by grazing incidence X-ray scattering, *Surf. Sci. Rep.* **32**, 1–90.

[49] Scheier, P., Marsen, B., Lonfat, M., Schneider, W.-D., and Sattler, K. (2000). Growth of silicon nanostructures on graphite, *Surf. Sci.* **458**, 113–122.

[50] Ganz, E., Sattler, K., and Clarke, J. (1988). Scanning tunneling microscopy of the local atomic structure of two-dimensional gold and silver islands on graphite, *Phys. Rev. Lett.* **60**, 1856–1859.

[51] Nishitani, R., Kasuya, A., Kubota, S., and Nishina, Y. (1991). Dendritic aggregation of gold particles on graphite surface, *J. Vac. Sci. Technol. B* **9**, 806–809.

[52] Binns, C., Baker, S.H., Demangeat, C., and Parlebas, J.C. (1999). Growth, electronic, magnetic and spectroscopic properties of transition metals on graphite, *Surf. Sci. Rep.* **34**, 105–170.

[53] Marsen, B. and Sattler, K. (1999). Fullerene-structured nanowires of silicon, *Phys. Rev. B* **60**, 11593–11600.

[54] McBride, J.D., Van Tassell, B., Jachmann, R.C., and Beebe, T.P., Jr. (2001). Molecule corrals as templates for the formation of metal and silicon nanostructures, *J. Phys. Chem. B* **105**, 3972–3980.

[55] Ma, T.P. (1998). Making silicon nitride film a viable gate dielectric, *IEEE Trans. Electron Devices* **45**, 680–690.

[56] Narula, C.K. (1995). *Ceramic Precursor Technology and its Applications.* New York: Marcel Dekker.

[57] Wang, X.-S., Li, Z., Wang, L., Hu, Y., Zhai, G., Yang, J., Wang, Y., Fung, K.-K., Tang, T.C., Wang, X., and Cue, N. (2001). Characterization of silicon nitride thin films on Si and overlayer growth of Si and Ge, *Jpn. J. Appl. Phys.* **40**, 4292–4298.

[58] Wang, L., Hu, Y., Li, Z., Tang, J.-C., and Wang, X.-S. (2002). Shape, orientation and surface structure of Si and Ge nano-particles grown on SiN, *Nanotechnology* **13**, 714–719.

[59] Gwo, S., Chou, C.-P., Wu, C.-L., Ye, Y.-J., Tsai, S.-J., Lin, W.-C., and Lin, M.-T. (2003). Self-limiting size distribution of supported cobalt nanoclusters at room temperature, *Phys. Rev. Lett.* **90**, 185506.

[60] Liu X., Jia J.-F., Wang, J.-Z., and Xue Q.-K. (2003). Growth of Co nanoclusters on Si_3N_4 surface formed on Si(111), *Chin. Phys. Lett.* **20**, 1871–1874.

[61] Murray, C.B., Kagan, C.R., and Bawendi, M.G. (2000). Synthesis and characterization of monodisperse nanocrystals and close-packed nanocrystal assemblies, *Annu. Rev. Mater. Sci.* **30**, 545–610.

[62] Kovalev, D., Heckler, H., Ben-Chorin, M., Polisski, G., Schwartzkopff, M., and Koch, F. (1998). Breakdown of the k-conservation rule in Si nanocrystals, *Phys. Rev. Lett.* **81**, 2803–2806.

[63] Koshida, N. and Matsumoto, N.: (2003). Fabrication and quantum properties of nanostructured silicon, *Mater. Sci. Eng. R* **40**, 169–205.

[64] Mo, Y.-W., Savage, D.E., Swartzentruber, B.S., and Lagally, M.G. (1990). Kinetic pathway in Stranski-Krastanov growth of Ge on Si(001), *Phys. Rev. Lett.* **65**, 1020–1023.

[65] Brunner, K. (2002). Si/Ge nanostructures, *Rep. Prog. Phys.* **65**, 27–72.

[66] McComb, D.W., Collings, B.A., Wolkow, R.A., Moffatt, D.J., MacPherson, C.D., Rayner, D.M., Hackett, P.A., and Hulse, J.E. (1996). An atom-resolved view of silicon nanoclusters, *Chem. Phys. Lett.* **251**, 8–12.

[67] Dinh, L.N., Chase, L.L., Balooch, M., Siekhaus, W.J., and Wooten F. (1996). Optical properties of passivated Si nanocrystals and SiO_x nanostructures, *Phys. Rev. B* **54**, 5029–5037.

[68] Wu, Y., Takeguchi, M., and Furuya, K. (1999). High resolution transmission electron microscopy study on the structure of Ge nanoparticles by using an ultrahigh

vacuum-molecular beam epitaxy-transmission electron microscope system, *Jpn. J. Appl. Phys.* **38**, 7241–7246.

[69]   Andersson, M., Iline, A., Stietz, F., and Träger F. (2000). Silicon nanoclusters formed through self-assembly on CaF$_2$ substrates: morphology and optical properties, *Appl. Phys. A* **70**, 625–632.

[70]   Messerli, S., Schintke, S., Morgenstern, K., Sanchez, A., Heiz, U., Schneider, and W.-D. (2000). Imaging size-selected silicon clusters with a low-temperature scanning tunneling microscope, *Surf. Sci.* **465**, 331–338.

[71]   van Buuren, T., Dinh, L.N., Chase, L.L., Siekhaus, W.J., and Terminello, L.J. (1998). Changes in the electronic properties of Si nanocrystals as a function of particle size, *Phys. Rev. Lett.* **80**, 3803–3806.

[72]   Marsen, B., Lonfat, M., Scheier, P., and Sattler K. (2000). Energy gap of silicon clusters studied by scanning tunneling spectroscopy, *Phys. Rev. B* **62**, 6892–6895.

[73]   Rouillard, Y., Lambert, B., Toudic, Y., Baudet, M., and Gauneau, M. (1995). On the use of dimeric antimony in molecular beam epitaxy, *J. Cryst. Growth* **156**, 30–38.

[74]   Brewer, P.D., Chow, D.H., and Miles R.H. (1996). Atomic antimony for molecular beam epitaxy of high quality III-V semiconductor alloys, *J. Vac. Sci. Technol. B* **14**, 2335–2338.

[75]   Francis, G.M., Kuipers, L., Cleaver, J.R.A., and Palmer, R.E. (1996). Diffusion controlled growth of metallic nanoclusters at selected surface sites, *J. Appl. Phys.* **79**, 2942–2947.

[76]   Perez, A., Melinon, P., Dupuis, V., Jensen, P., Prevel, B., Tuaillon, J., Bardotti, L., Martet, C., Treilleux, M., Broyer, M., Pellarin, M., Vaille, J.L., Palpant, B., and Lerme, J. (1997). Cluster assembled materials: A novel class of nanostructured solids with original structures and properties, *J. Phys. D: Appl. Phys.* **30**, 709–721.

[77]   Yoon, B., Akulin, V.M., Cahuzac, P., Carlier, F., de Frutos, M., Masson, A., Mory, C., Colliex, C., and Bréchignac, C. (1999). Morphology control of the supported islands grown from soft-landed clusters, *Surf. Sci.* **443**, 76–88.

[78]   Heyde, M., Cappella, B., Sturm, H., Ritter, C., and Rademann, K. (2001). Dislocation of antimony clusters on graphite by means of dynamic plowing nanolithography, *Surf. Sci.* **476**, 54–62.

[79]   Kaiser, B., Stegemann, B., Kaukel, H., and Rademann, K. (2002). Instabilities and pattern formation during the self-organized growth of nanoparticles on graphite, *Surf. Sci.* **496**, L18–L22.

[80]   Mo, Y.W. (1993). Direct determination of the reaction path of Sb$_4$ on Si(001) with scanning tunneling microscopy, *Phys. Rev. B* **48**, 17233–17238.

[81]   Stegemann, B., Bernhardt, T.M., Kaiser, B., and Rademann, K. (2002). STM investigation of surface alloy formation and thin film growth by Sb$_4$ deposition on Au(111), *Surf. Sci.* **511**, 153–162.

[82]   Stegemann, B., Ritter, C., Kaiser, B., and Rademann, K. (2004).Characterization of the (0001) cleavage surface of antimony single crystals using scanning probe microscopy: Atomic structure, vacancies, cleavage steps, and twinned interlayers, *Phys. Rev. B* **69**, 155432.

[83]   Johnson, E.A. (2001). Electrons in quantum semiconductor structures: An introduction, in: *Low-dimensional Semiconductor Structures: Fundamentals and Device Applications*, ed. K. Barnham, D. Vvedensky Cambridge, UK: Cambridge University Press, pp. 56–78.

[84]   Peng, X., Manna, L., Yang, W., Wickham, J., Scher, E., Kadavanich, A., and Alivisatos A.P. (2000). Shape control of CdSe nanocrystals, *Nature* **404**, 59–61.

[85] Kan, S., Aharoni, A., Mokari, T., and Banin, U. (2004). Shape control of III-V semiconductor nanocrystals: Synthesis and properties of InAs quantum rods, *Faraday Discuss.* **125**, 23–38.

[86] Donohue, J. (1974). *The Structures of the Elements*. New York: Wiley.

[87] Beister, H.J., Strössner, K., and Syassen, K. (1990). Rhombohedral to simple-cubic phase transition in arsenic under pressure, *Phys. Rev. B* **41**, 5535–5543.

[88] Isshiki, T., Nishio, K., Saijo, H., and Shiojiri, M. (1994). Growth and crystallographic, surface and defect structures of antimony particles deposited in a high-resolution transmission electron microscope, *Thin Solid Films* **237**, 155–159.

[89] Aoki, K., Fujiwara, S., and Kusakabe, M. (1983). New phase transition into the b.c.c. structure in antimony at high pressure, *Solid State Commun.* **45**, 161–163.

[90] Iwasaki, H. and Kikegawa T. (1997). Structural systematics of the high-pressure phases of phosphorus, arsenic, antimony and bismuth, *Acta Cryst. B* **53**, 353–357.

[91] Kolobyanina, T.N., Kabalkina, S.S., Vereshchagin, L.F., and Fedina: L.V. (1969). Investigation of the crystal structure of antimony at high pressures, *Sov. Phys. JETP* **28**, 88–90.

[92] Bréchignac, C., Cahuzac, Ph., Carlier, F., Colliex, C., de Frutos, M., Kébaïli, N., Le Roux, J., Masson, A., and Yoon, B. (2001). Control of island morphology by dynamic coalescence of soft-landed clusters, *Eur. Phys. J. D* **16**, 265–269.

[93] Barnett, S.A., Winters, H.F., and Greene, J.E. (1986). The interaction of Sb₄ molecular beams with Si(100) surfaces: Modulated-beam mass spectrometry and thermally stimulated desorption studies, *Surf. Sci.* **165**, 303–326.

[94] Slijkerman, W.F.J., Zagwijn, P.M., van der Veen, J.F., Gravesteijn, D.J., and van de Walle G.F.A. (1992). The interaction of Sb overlayers with Si(001), *Surf. Sci.* **262**, 25–32.

[95] Kumar, V. (1993). Electronic and atomic structures of Sb₄ and Sb₈ clusters, *Phys. Rev. B* **48**, 8470–8473.

[96] Brune, H. (1998). Microscopic view of epitaxial metal growth: Nucleation and aggregation, *Surf. Sci. Rep.* **31**, 121–229.

[97] Fan, W.C., Strozier, J., and Ignatiev, A. (1988). Island formation of aluminum on the graphite (0001) surface: LEED and AES study, *Surf. Sci.* **195**, 226–236.

[98] Ganz, E., Sattler, K., and Clarke, J. (1989). Scanning tunneling microscopy of Cu, Ag, Au and Al adatoms, small clusters, and islands on graphite, *Surf. Sci.* **219**, 33–67.

[99] Maurice, V. and Marcus P. (1992). STM study of sputter-deposited Al clusters in chemical interaction with graphite (0001) surfaces, *Surf. Sci.* **275**, 65–74.

[100] Hinnen, C., Imbert, D., Siffre, J.M., and Marcus, P. (1994). An in situ XPS study of sputter-deposited aluminum thin films on graphite, *Appl. Surf. Sci.* **78**, 219–231.

[101] Ma, Q. and Rosenberg, R.A. (1997). Interaction of Al clusters with the (0001) surface of highly oriented pyrolytic graphite, *Surf. Sci.* **391**, L1224–L1229.

[102] Stabel, A., Eichhorst-Gerner, K., Rabe, J.P., and González-Elipe A.R. (1998). Surface defects and homogeneous distribution of silver particles on HOPG, *Langmuir* **14**, 7324–7326.

[103] Moullet, I. (1995). Ab-initio molecular dynamics study of the interaction of aluminum clusters on a graphite surface, *Surf. Sci.* **331**, 697–702.

[104] Zhu, Y.-J., Schnieders, A., Alexander, J.D., and Beebe T.P., Jr. (2002). Pit-templated synthesis and oxygen adsorption properties of gold nanostructures on highly oriented pyrolytic graphite, *Langmiur* **18**, 5728–5733.

[105]   Hövel, H., Becker, Th., Bettac, A., Reihl, B., Tschudy, M., and Williams, E.J. (1997). Crystalline structure and orientation of gold clusters grown in preformed nanometer-sized pits, *Appl. Surf. Sci.* **115**, 124–127.

[106]   Stumpf, R. and Scheffler, M. (1996). *Ab initio* calculations of energies and self-diffusion on flat and stepped surfaces of Al and their implications on crystal growth, *Phys. Rev. B* **53**, 4958–4973.

[107]   Bogicevic, A., Strömquist J., and Lundqvist B.I. (1998). Low-symmetry diffusion barriers in homoepitaxial growth of Al(111), *Phys. Rev. Lett.* **81**, 637–640.

[108]   Ehrlich, G. and Hudda, F.G. (1966). Atomic view of surface self-diffusion: tungsten on tungsten, *J. Chem. Phys.* **44**, 1039–1049.

[109]   Schwoebel, R.L. (1969). Step motion on crystal surfaces. II, *J. Appl. Phys.* **40**, 614–618.

[110]   Bardotti, L., Jensen, P., Hoareau, A., Treilleux, M., and Cabaud B. (1995). Experimental observation of fast diffusion of large antimony clusters on graphite surfaces, *Phys. Rev. Lett.* **74**, 4694–4697.

[111]   Lewis, L.J., Jensen, P., Combe, N., and Barrat J.-L. (2000). Diffusion of gold nanoclusters on graphite, *Phys. Rev. B* **61**, 16084–16090.

[112]   Goldby, I.M., Kuipers, L., von Issendorff, B., and Palmer, R.E. (1996). Diffusion and aggregation of size-selected silver clusters on a graphite surface, *Appl. Phys. Lett.* **69**, 2819–2821.

[113]   Zhang, Z., Lu, Y.-T., and Metiu, H. (1991). Pathways for dimer string growth during Si deposition on Si(100)–2×1, *Surf. Sci.* **255**, L543–L549.

[114]   Witten, T.A., Jr. and Sander, L.M. (1981). Diffusion-limited aggregation, a kinetic critical phenomenon, *Phys. Rev. Lett.* **47**, 1400–1403.

[115]   Gai, Z., Ji, H., Ga,o B., Zhao, R.G., and Yang, W.S. (1996). Surface structure of the (3 × 1) and (3 × 2) reconstructions of Ge(113), *Phys. Rev. B* **54**, 8593–8599.

[116]   Knall, J., Pethica, J.B., Todd, J.D., and Wilson, J.H. (1991). Structure of Si(113) determined by scanning tunneling microscopy, *Phys. Rev. Lett.* **66**, 1733–1736.

[117]   Hibino H. and Ogino T. (1997). Phase transitions on Si(113): A high-temperature scanning- tunneling-microscopy study, *Phys. Rev. B* **56**, 4092–4097.

[118]   Gai, Z., Zhao, R.G., and Yang, W.S. (1998). Atomic structure of the Ge(313) surface, *Phys. Rev. B* **58**, R4223–R4226.

[119]   Tanaka, H., Yokoyama, T., and Sumita, I. (1994). Giant adatom-like structures observed with scanning tunneling microscopy: Super adatoms on Si(331), *Appl. Surf. Sci.* **76**, 340–346.

[120]   Stekolnikov, A.A., Furthmüller J., and Bechstedt, F. (2002). Absolute surface energies of group-IV semiconductors: Dependence on orientation and reconstruction, *Phys. Rev. B* **65**, 115318.

[121]   Becker, R.S., Golovchenko, J.A., and Swartzentruber, B.S. (1985).Tunneling images of germanium surface reconstructions and phase boundaries, *Phys. Rev. Lett.* **54**, 2678–2680.

[122]   Baski, A.A., Erwin, S.C., and Whitman, L.J. (1995). A stable high-index surface of silicon: Si(5 5 12), *Science* **269**, 1556–1560.

[123]   Gai, Z., Yang, W.S., Zhao, R.G., and Sakurai, T. (1999). Macroscopic and nanoscale faceting of germanium surfaces, *Phys. Rev. B* **59**, 15230–15239.

[124]   Neddermeyer, H. and Tosch, St. (1988). Atomic nature of reconstructed Si(110), *Phys. Rev. B* **38**, 5784–5787.

[125]   An, T., Yoshimura, M., Ono, I., and Ueda, K. (2000). Elemental structure in Si(110)– "16 × 2" revealed by scanning tunneling microscopy, *Phys. Rev. B* **61**, 3006–3011.

[126] Ichikawa, T. (2004). Atomic geometry of the Ge(110)c(8×10) structure, *Surf. Sci.* **560**, 205–212.

[127] Zhu, H. and Averback, R.S. (1996). Sintering processes of two nanoparticles: A study by molecular dynamics simulations, *Philos. Mag. Lett.* **73**, 27–33.

[128] Wang, Z., Li, Y., and Adams, J.B. (2000). Kinetic lattice Monte Carlo simulation of facet growth rate, *Surf. Sci.* **450**, 51–63.

[129] Shibata, M., Nitta, Y., Fujita, K., and Ichikawa, M. (2000). Facets formation of pyramidal Si nanocrystals selectively grown on Si(001) windows in ultrathin SiO_2 films, *J. Crystal Growth* **220**, 449–456.

[130] Dabrowski, J., Müssig, H.-J., Wolff, G., and Hinrich, S. (1998). Surface reconstruction suggests a nucleation mechanism in bulk: Sb/Si(113) and {113} planar defects, *Surf. Sci.* **411**, 54–60.

[131] Hansen, K.H., Worren, T., Stempel, S., Lægsgaard, E., Bäumer, M., Freund, H.-J., Besenbacher, F., and Stensgaard, I. (1999). Palladium nanocrystals on Al_2O_3: structure and adhesion energy, *Phys. Rev. Lett.* **83**, 4120–4123.

[132] Tseng, H.-C., Chang,. C.Y., Pan, F.M., Chen, J.R., and Chen, L.J. (1997). Effects of isolation materials on facet formation for silicon selective epitaxial growth, *Appl. Phys. Lett.* **71**, 2328–2330.

[133] Langdo, T.A., Leitz, C.W., Currie, M.T., Fitzgerald, E.A., Lochtefeld, A., and Antoniadis D.A. (2000). High quality Ge on Si by epitaxial necking, *Appl. Phys. Lett.* **76**, 3700–3702.

7
Thermal Properties of Carbon Nanotubes

Mohamed. A. Osman, Aron W. Cummings, and Deepak Srivastava

7.1. Introduction

The experimental observation of carbon nanotubes by Sumio Iijima in 1991 [1], sparked a significant effort in theoretical and experimental investigation of carbon nanotubes and related structures. The studies of thermal properties, although very important from fundamental and applications points of view, have received less attention in comparison with other aspects such as the electrical and mechanical properties [2–18]. This might be due to the fact that one associates the nanoscale aspect of nanotubes with quantization of transport properties which applies to electrons at room temperature. On the other hand, thermal transport involves many phonon modes and these can form a continuum at room temperature and phonon quantization manifests itself in nanotubes at very low temperatures (less than 8 K) [5]. Carbon nanotubes can be viewed as rolled-up graphene sheets and therefore one can infer their thermal properties by comparing them with graphite. Graphite has a large in-plane thermal conductivity, second only to type II diamond, and significantly lower out-of-plane thermal conductivity [19,20]. Therefore, in carbon nanotubes or nanotube ropes, one can expect very high thermal conductivity along the tube axis compared to the radial component due to the large separation between the different layers in multiwall nanotubes [22,13].

The ability to grow single-wall nanotube (SWNT) and multiwall nanotubes (MWNT) with different diameters and chiralities opens the possibility of developing materials with tailored thermal properties for different applications including thermal management, switches, and sensors. Carbon nanotubes can be added to other materials to enhance the magnitude and directionality of their thermal properties. This has motivated several groups to investigate the thermal properties of carbon nanotubes using experimental and theoretical approaches. The physical structure of nanotubes and their electrical properties are briefly discussed in Section 7.2. In Section 7.3, the theoretical analytical approaches to thermal conductivity and specific heat calculations are introduced. This is followed by a review of the recent experimental measurement of thermal conductivity of single- and multiwall nanotubes. Sections 7.4 and 7.5 focus on the molecular dynamics (MD) simulation

FIGURE 7.1. The unrolled hexagonal lattice of a nanotube.

approach and its application to investigation of thermal conductivity of SWNT, Y-junction nanotubes, and heat pulse propagation in SWNT.

7.2. Background

7.2.1. Physical Structure

A single-wall carbon nanotube can be viewed as a single sheet of graphite rolled up into a cylinder. Figure 7.1 shows a representation of the 2-D hexagonal plane that makes up a graphitic sheet, where the carbon atoms lie at the corners of each hexagon. In this figure, one can see that if point O is connected to point A, and point B is connected to point B', then the sheet will be rolled into a cylindrical structure. However, this is just one of many possible cylindrical orientations that can be constructed. For example, points A and B' could lay directly to the right of points O and B, respectively, which would result in a different orientation of the hexagonal rings on the face of the cylinder [22] The chiral vector $\vec{C}_H$ uniquely determines the physical structure of a carbon nanotube, and is perpendicular to the tube axis $\vec{z}$. $\vec{C}_H$ can be written in terms of the unit vectors of the hexagonal lattice,

FIGURE 7.2. Carbon nanotube classification [22].

$\vec{a}_1$ and $\vec{a}_2$, such that $\vec{C}_H = n\vec{a}_1 + m\vec{a}_2$. Thus, the integer pair (n, m) is used to completely describe the geometry of a carbon nanotube. Because of the rotational symmetry of the 2-D hexagonal lattice, it is only necessary to consider n and m such that $0 \leq |m| \leq n$. In the case where $m = n$, the angle θ will be $30°$. In this case, as one moves along the chiral vector, the carbon bonds form an armchair-shaped pattern. Thus, a carbon nanotube of the form (n, n) is known as an armchair nanotube. In the case where $m = 0$, $\theta = 0°$ and the bonds along the chiral vector form a zigzag pattern. So, carbon nanotubes of the form $(n,0)$ are known as zigzag nanotubes. In all other cases, $0° < \theta < 30°$, and the tubes are known as chiral nanotubes. Figure 7.2 shows an example of each of the three different types of carbon nanotubes [22]. Note the zigzag and armchair patterns at the end rings of the zigzag and armchair carbon nanotubes. In Figure 7.2, all three nanotubes are single-wall carbon nanotubes. Multiwall carbon nanotubes consist of two or more concentric single-wall carbon nanotubes. Bundles of aligned single-wall nanotubes also form during growth with intertube separation of 1.7 nm [22].

An additional interesting structure is the Y-junction carbon nanotube which was first observed experimentally [22,23] and later produced in a controllable fashion using templates [24,25]. The Y-junction structure consists of a single "trunk" nanotube splitting into two "branch" nanotubes. Figure 7.3 shows some examples of Y-junction configurations. The structure of the trunk and branches of the Y-junction nanotube is the same as that for a straight single-wall carbon nanotube. The difference in structure lies at the junction, where the continuity of the hexagonal lattice cannot be conserved. To realize the Y-junction, nonhexagonal polygons with 4, 5, 7, or 8 edges must be introduced into the lattice. The number of extra edges introduced into the lattice is known as the bond surplus. Thus, an octagon

FIGURE 7.3. Examples of Y-junction nanotube configurations [29].
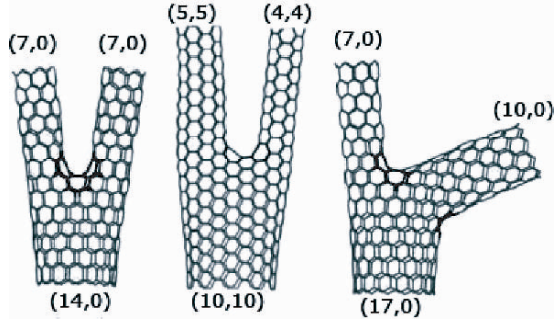
contributes a bond surplus of $+2$, and a pentagon contributes a bond surplus of -1. A rule for the bond surplus of carbon nanotube junctions based on application of Euler's rule for polygons on the surface of a closed polyhedron was proposed in [26]. The rule states that a junction consisting of N tubes would have a bond surplus of $12(N-2)$. Thus, a Y-junction should have a bond surplus of 12. However, this surplus can be shared between the two junctions, resulting in a need for six extra polygonal edges [26]. In Figure 7.3, the two Y-junctions on the left contain six heptagons, whereas the one on the right contains four heptagons and an octagon [27].

7.2.2. Electrical Properties

The electronic structure of carbon nanotubes can be determined starting from that of two-dimensional (2-D) graphite. When a plane of graphite (graphene sheet) is rolled up into a carbon nanotube, periodic boundary conditions are imposed in the circumferential direction described by the chiral vector $\vec{C}_H$, and the wave vector associated with this direction becomes quantized. Thus, the set of one-dimensional (1-D) energy dispersion relations of a carbon nanotube is made up of slices of the 2-D energy band structure of graphite [28]. In the energy dispersion relations for 2-D graphite, a finite band-gap is present along all points in the hexagonal Brillouin zone, except in the corners of the hexagon (K points). At these K points, the band-gap drops to zero, resulting in a degenerate energy state. If one of the N wave vectors of a carbon nanotube passes through a K point, then the 1-D energy bands will have a zero energy gap [22]. A finite density of states results from the crossing of two 1-D energy bands, which means the carbon nanotube will be metallic in nature. If the wave vectors of a carbon nanotube do not cross through one of the K points, then the 1-D energy bands will not overlap and the nanotube will be a semiconductor. The condition for an (n, m) carbon nanotube to be metallic is that $2n + m$ be a multiple of three [29]. An equivalent condition is that $n - m$ be a multiple of three [22]. Thus, a carbon nanotube can be
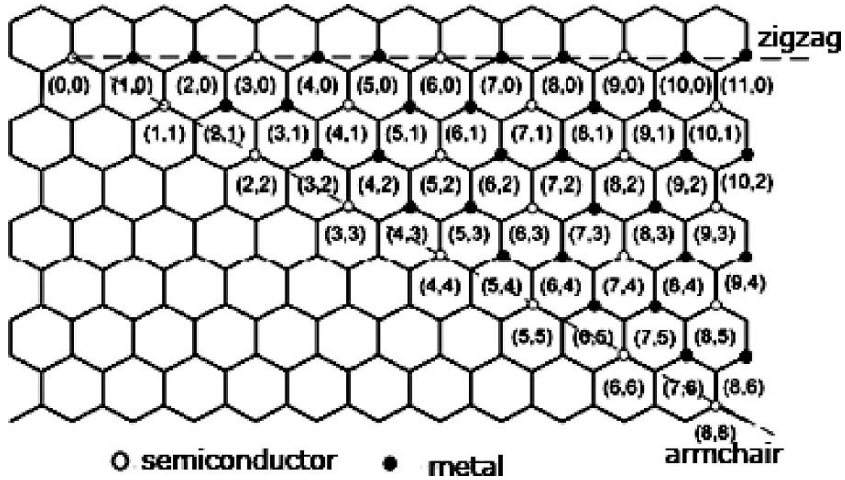
FIGURE 7.4. Geometries of nanotubes and their resulting electrical properties.

either metallic or semiconducting, depending on its diameter and its chiral angle. Figure 7.4 illustrates this condition.

Another important result is the dependence of the band-gap of semiconducting carbon nanotubes on the tube diameter. The band-gap of a semiconducting nanotube is inversely proportional to its diameter [22]. Because carbon nanotubes of different geometries exhibit different electrical characteristics, the connection of a metallic nanotube with a semiconducting nanotube will result in a Schottky barrier device, and the connection of two different semiconducting tubes will result in a heterojunction structure [30]. These structures have been shown to exhibit asymmetric electrical properties, both in carbon nanotubes and in traditional CMOS circuits [31]. The usefulness of these structures in present-day circuits underscores how useful carbon nanotubes may be in the development of next-generation electrical devices [32,33].

Given that a Y-junction carbon nanotube consists of a connection of two or more straight nanotubes of different geometries, it seems reasonable to assume that this structure will exhibit electrical rectification. Calculations of the quantum conductivity of a wide class of Y-junction structures using Green's function formalism [27], confirmed this assumption theoretically. Additionally, they found that the rectification and switching characteristics of these structures depends strongly on their symmetry, and less strongly on the chirality of each branch. Specifically, symmetric Y-junctions with a zigzag trunk always showed perfect rectification, where as symmetric Y-junctions without a zigzag trunk exhibited imperfect rectification, an asymmetric I–V characteristic with small leakage currents in cutoff mode. Furthermore, asymmetric Y-junction structures showed much weaker rectification behavior. Experimental data have also shown the presence of electrical

rectification in individual and parallel arrays of Y-junction carbon nanotubes [34].

7.3. Thermal Conductivity

7.3.1. Theory

Carbon nanotubes can either be classified as metals or semiconductors depending on the chirality. Furthermore, as the nanotube diameter increases in semiconducting nanotubes, the energy gap decreases, approaching metallic behavior at very large diameters approximating graphite structure. Therefore both electrons and phonons contribute to heat flow in carbon nanotubes. Also, quantization of the transport properties of electrons and phonon modes due to size effect depends on temperature. Consequently, the relative contribution of electrons and phonons to the thermal conductivity will not be the same as bulk metals and crystals. However, the thermal conductivity behavior in bulk provides a starting point in understanding thermal transport in nanotubes. In metals electrons are the major heat carriers, whereas phonons carry heat in nonmetallic crystals.

A qualitative temperature-dependence of the thermal conductivity κ in metals and crystals is shown in Figure 7.5. The thermal conductivity is defined by the following simple relationship,

$$\kappa = \frac{1}{3}Cv\lambda, \tag{1}$$

where C is the lattice (electron) heat capacity, v is the average phonon (electron) velocity, and λ is the mean free path of the phonons (electrons) in a nonmetallic crystal (metal) [35]. In metals, electrons form a highly degenerate system and the velocity v is effectively independent of temperature whereas C is proportional to
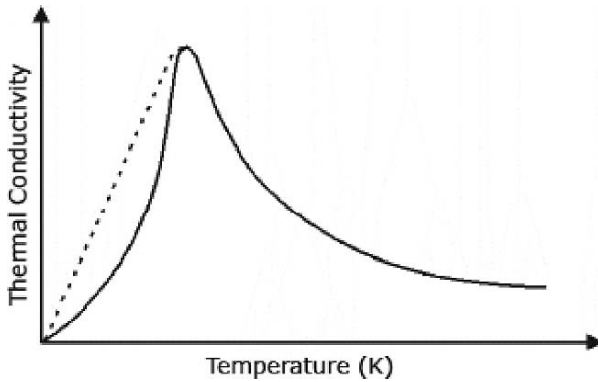
FIGURE 7.5. Qualitative temperature-dependence of thermal conductivity in metals (dashed line) and nonmetals (solid line).

the temperature T. The mean free path λ for electrons in metals exhibits a $1/T$ dependence at high T due to scattering by phonons leading to a faster than $1/T$ drop in κ at high T. At low temperatures, the scattering events are less frequent and λ is mainly determined by material imperfections such as defects and impurities. For nonmetallic crystals, velocity v is approximately equal to the sound velocity in the crystal whereas λ is limited by direct phonon–phonon Umklapp interactions, at normal and high temperatures exhibiting a $1/T$ dependence at very high T [35]. As T is decreased, phonon–phonon interactions become less frequent and λ increases at a rate determined by the material characteristics and imperfections. At low temperatures, λ is limited by the boundaries of the crystal and can be comparable to sample dimensions. Therefore, the shape of the curve in Figure 7.5 will be determined by the details of the heat capacity C.

The equilibrium distribution of phonons of energy $\hbar\omega$ at temperature T is given by

$$N^o = \frac{1}{\exp(\hbar\omega/k_B T) - 1},\tag{2}$$

where k_B is the Boltzmann constant. The presence of a temperature gradient in a material with finite conductivity disturbs the phonon distribution and the difference in contributions of $+q$ and $-q$ phonon modes gives rise to a heat current flux $J = \sum n(q)\hbar\omega v_G(q)$, where q is the phonon wavevector, v_G is the phonon group velocity, and $n(q)$ is the deviation from equilibrium phonon distribution due to the temperature gradient. In the relaxation time approximation, $n(q) = -\tau(q)(v_G(q) \cdot \nabla T)(\nabla N^o)$, where τ is the phonon relaxation time. In the Fourier approximation, the heat flux $\vec{J} = -\kappa \cdot \nabla T$, where κ is the thermal conductivity. Assuming a temperature gradient along the z-axis leads to the following relation for the thermal conductivity κ

$$\kappa = \frac{J}{(\partial T/\partial z)} = \frac{1}{3} \int_0^{\omega_{max}} \tau(q) v_G^2 \hbar\omega g(\omega) \frac{\partial N^o}{\partial T} d\omega,\tag{3}$$

where τ is the relaxation time, $g(\omega)$ is the phonon density of states, v_z is the z-component of the group velocity with $v_Z^2 = v_G^2/3$. The frequency maximum is usually expressed in terms of the Debye temperature $\theta = \hbar\omega_{max}/k_B$ which is chosen such that only $3N$ phonon modes exist [35]. The details of $g(\omega)$ depend on the dimensionality of the system and the phonon frequency dispersion. As the contribution from phonon modes in the frequency range ω to $\omega + \omega$ to heat capacity C_{ph} is $(d/dT)\{N^o(\omega)\hbar\omega g(\omega)\}$, the above integral can be simplified to provide an equation relating the thermal conductivity to heat capacity as

$$\kappa = \frac{1}{3} v \int \lambda(x) C_{ph}(x) dx,\tag{4}$$

where $\lambda(x) = v\tau(x)$ is the mean free path length. The above equation demonstrates that accurate evaluation of κ requires knowledge about both C_{ph}, which depends on the phonon density of states and λ, which is determined by phonon–phonon scattering over the phonon spectrum. Even though λ dependence on phonon–phonon, boundary, and defect scattering is quite involved, one can still gain better insight into κ by decoupling C_{ph} from λ and understanding how each one behaves as a function of temperature, phonon mode, and dimensionality. The heat capacity C_{ph} provides information about the details of the phonon spectrum and is defined by

$$C_{ph} = k_B \int_0^{\omega_{max}} dx \frac{g(x)x^2 e^x}{(e^x - 1)^2}. \tag{5}$$

The phonon density of states $g(\omega)$ is determined by the phonon dispersion $\omega(q)$ of different modes and the dimensionality of the system. To examine the C_{ph} of carbon nanotubes, a Debye model that assumes a simple linear dispersion of the form $\omega(q) = vq$ for each phonon spectrum branch and that $v_G \approx v_s$ for all branches where v_s. is the speed of sound was used in [2]. For an isotropic m-dimensional system, $g(x)$ reduces to

$$g(x) = \frac{m\pi^{m/2} \Omega \gamma k_B^m T^m x^{m-1}}{(2\pi)^m \left(\frac{m}{2}\right)! \hbar^m v_s^m}, \tag{6}$$

where γ is the number of acoustic phonon mode polarizations and Ω is the m-dimensional system volume. Therefore, for a single-wall nanotube of radius R at temperature $T \ll \frac{\hbar v}{k_B R}$, the phonon contribution to the heat capacity is

$$C_{ph} = \frac{3Lk_B^2 T}{\pi \hbar v_s} \int_0^\infty dx \frac{x^2 e^x}{(e^x - 1)^2} = 3.292 \frac{3Lk_B^2 T}{\pi \hbar v_s}, \tag{7}$$

where L is the tube length [2]. Equation (7) shows that for small R and T, the heat capacity exhibits linear T dependence. The same model also predicts a temperature-dependence of C_{ph} for a multiwall nanotube (MWNT) that depends strongly on the radius R and number of layers N and exhibits 1-D to 3-D behavior. The measured specific heat for MWNT in [3] showed a linear dependence over a wide temperature range (10–300 K) which was attributed to the weak interwall coupling in MWNT compared to graphite.

In carbon nanotubes and graphite, the total heat capacity $C = C_{ph} + C_{el}$ and the low temperature behavior of C in a nanotube depends strongly on the relative magnitudes of these contributions. The electron concentration in semiconducting nanotubes is proportional to $\exp[-E_g/2k_B T]$, where the energy gap $E_g = 2.5\pi/\sqrt{3(m^2 + n^2 + mn)}$ eV for (m, n) semiconducting nanotubes.

Consequently, C_{el} is negligibly small as long as $k_B T \ll E_g$, which is satisfied for most SWNTs such as (7,0) and (10,0) nanotubes even at room temperature. On the other hand, there is a degenerate electron concentration in metallic nanotubes over the whole temperature range, which contributes to heat capacity. It was also shown in [2] that in a metallic nanotube with one partially filled band, provided $T \ll \hbar v_F / k_B R$,

$$C_{el} = \frac{4\pi L k_B^2 T}{3\hbar v_F},$$
(8)

where v_F is the Fermi velocity, $v_F \approx 10^8 \ cm/s$. From equations (3) and (5) one can show that

$$\frac{C_{el}}{C_{ph}} \approx \frac{v_s}{v_F} \approx 10^{-2}.$$
(9)

Consequently, the phonon contribution dominates in metallic nanotubes even at very low temperatures ($T \approx 0 \ K$). This is consistent with the observations in graphite which are considered to be semi-metallic with low density of electrons near the Fermi level.

The measured low-temperature specific heat of MWNT and nanotube ropes in [4] showed a graphitelike behavior for MWNT that deviated from that of nanotube ropes below 20 K. In order to understand the strong temperature dependence, they modeled the nanotube rope by an hexagonal array of nanotubes taking into account the longitudinal, doubly degenerate transverse, and twisted-mode acoustic phonon branches. Additional terms were also included to account for intertube interactions. However, predictions of the simple model underestimated the measured data and they concluded that the steep temperature dependence was due to impurities. The low temperature for specific heat measurement of SWNT bundles was extended to 2 K in [5] and 0.1 K in [6]. The measured data in [5] followed the theoretical prediction for SWNT above 4 K and were significantly different from that of graphite and graphene up to 100 K. The results from these measurements after corrections that account for nuclear hypercontributions arising from residual catalyst particles was fitted to $0.043T^{0.62} + 0.035T^3$. The second term reflects 3-D- like behavior, whereas the first term cannot be accounted for by either electronic or defect contributions. To account for the $T^{0.62}$ dependence observed in [6], a quadratic dependence of the transverse acoustic phonon frequency on wave vector q was proposed in [7]. This model leads to $T^{0.5}$ behavior of the C at very low temperatures that crosses over to linear dependence on T as the diameter of the nanotube increases leading to stronger contributions from LA (longitudinal acoustic) and TW (twisted) acoustic phonon modes. The low-temperature C calculations using a continuum model for nanotubes in [8], overestimate C up to 100 K when compared to the measured data in [5].

To account for the ballistic nature of phonon transport in nanotubes and the quantized thermal conductance in CNT at low temperatures, an approach analogous

to the Landauer theory of electronic transport was proposed in [9]. The SWNT is assumed to be sandwiched between a hot and a cold heat bath which gives rise to a thermal current density that is described by the Landauer energy flux

$$J_{ph} = \sum_m \int_0^\infty \frac{dq}{2\pi} \hbar\omega_m(q) v_m(q) \left[N(\omega_m, T_{hot}) - N(\omega_m, T_{cold}) \right] \zeta_m(q), \qquad (10)$$

where m is the phonon mode, q is the phonon wave vector, $\hbar\omega_m(q)$ is the phonon energy, $v_m(q) = d\omega_m(q)/dq$ is the group velocity, $N(\omega_m, T_b)$ is the Bose–Einstein phonon distribution of the phonon heat bath at temperature T_b, and $\zeta_m(q)$ is the transmission coefficient between the heat baths and the system. To arrive at an analytical solution in [9], they assumed (1) an adiabatic contact between the heat baths and the system, $\zeta_m(q) \approx 1$, (2) linear response condition, $\Delta T = T_{hot} - T_{cold} \ll T \equiv (T_{hot} + T_{cold})/2$, and (3) the frequencies of the mth phonon dispersion are limited to a range between $\omega_m^{\min}$ and $\omega_m^{\max}$. These assumptions lead to thermal conductance κ_{ph} given by

$$\begin{aligned} K_{ph} &= \frac{J_{ph}}{\Delta T} = \frac{k_B^2 T}{2\pi\hbar} \sum_m \int_{x_m^{\min}}^{x_m^{\max}} dx \frac{x^2 e^x}{(e^x - 1)^2} \\ &= \frac{2k_B^2 T}{h} \sum_m \left[\varphi(2, e^{-x_m^\alpha}) + x_m^\alpha \varphi(1, e^{-x_m^\alpha}) + \frac{(x_m^\alpha)^2}{2} N(x_m^\alpha) \right], \qquad (11) \end{aligned}$$

where $x_m^\alpha = \hbar\omega_m^\alpha / k_B T$, and α denotes min or max, $\varphi(y, s) = \sum_{n=1}^\infty (s^n/n^y)$ is the Appel function which for a gapless (acoustic) mode $\omega_m^{\min} = 0$ ($s = 1$), yields the Rieman zeta function. This mode contributes a universal quantum of $\kappa_0 = \pi^2 k_B^2 T/3h$ to the thermal conductance. There are four acoustic modes that are responsible for the quantization of thermal conductance in nanotubes at temperatures below the excitation of the lowest two optical modes with energy gap $\hbar\omega_{op}$ which is equal to 2.1 meV in (10,10) nanotubes. A similar approach was used to calculate the thermal conductance of electrons. This model predicts values for ratio K_{el}/K_{ph} of the thermal conductance by electrons to that of by phonons that ranges from 1 close to 0 K to 0.1 at 350 K as can be seen in Figure 7.6. However, the calculated ratios were an order of magnitude higher than the measured ratio in [10].

7.3.2. Measurements

The thermal conductivity measurements in [10] used a comparative method on SWNT from 8 K to 350 K on as-grown and sintered SWNT mat samples. The measured values at room temperature ranged from to 2.3 W/m-K to 35 W/m-K for sintered and as-grown mat samples, respectively. These values are very small compared to those of metals and graphite at room temperature due to the random
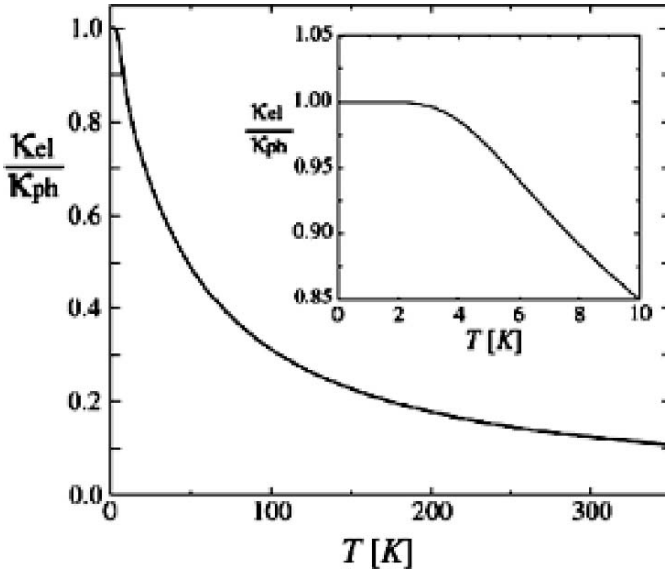
FIGURE 7.6. Temperature-dependence of the ratio of electrical to thermal conductance assuming ballistic phonon transport [9].

orientation of nanotubes within the mat samples. They also measured the electrical conductivity σ of the samples and calculated Lorenz number $\kappa/\sigma T$ which indicated a negligible electron contribution to the thermal conductivity below 30 K compared to phonon contribution. Additionally, they predicted thermal conductivity of ideal SWNT would range from 1750 to 5850 W/m-K at room temperature by assuming that the relationship between intrinsic and bulk electrical σ and thermal conductivity κ were related in the same fashion.

The measured thermal conductivity shown in Figure 7.7a reveals a linear temperature dependence behavior below $T = 30$ K with a monotonic increase over the full temperature range. The irregular distribution and orientation of nanotubes within the mat, however, made it impossible to determine any information about the thermal conductivity $\kappa_\perp$ in a direction perpendicular to the nanotube axis. In order to reduce the irregularity and randomness of SWNT distribution within mat samples, the thermal conductivity was measured from 10 to 400 K on magnetically aligned thin films of single-wall nanotube ropes in [11]. Figure 7.7b shows that the thermal conductivity $\kappa_\parallel$ in a direction parallel to the tube axis exhibits a monotonic increase up to 400 K reaching a value of 200 W/m-K at room temperature which is about an order of magnitude larger than that of SWNT mat and is within an order of magnitude of that of diamond. They also measured the electrical conductivity of the same samples and confirmed the dominant phonon contributions to κ to 10 K, the lowest temperature in their measurements.
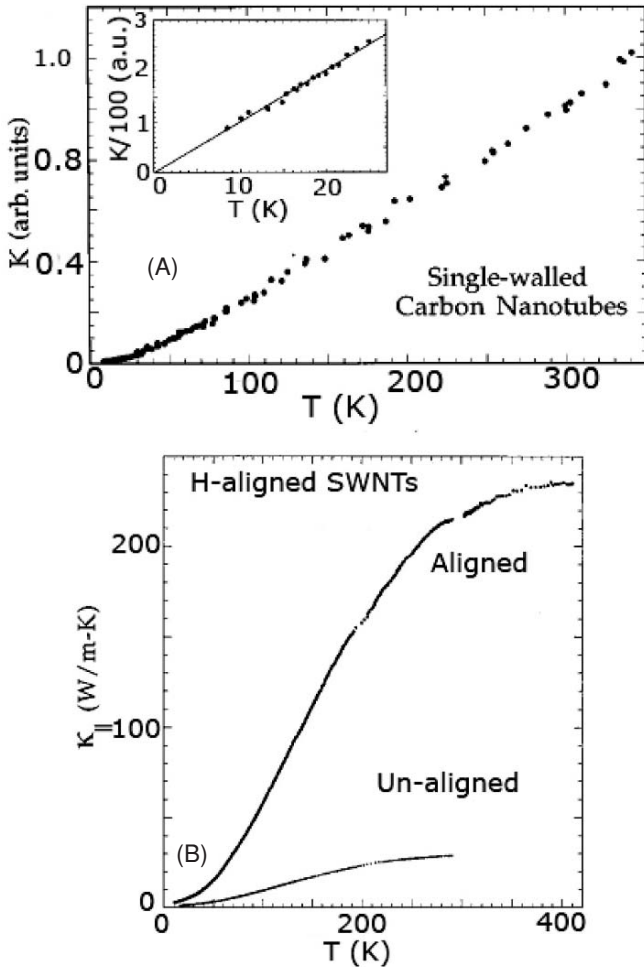
FIGURE 7.7. Temperature-dependence of the thermal conductivity of (a) SWNT mat, (b) aligned SWNT bundles [10, 11].

The thermal conductivity of oriented MWNT bundles was measured from 10 to 300 K using the self-heating 3 ω method [3]. The MWNT diameter distributions ranged from 20 to 40 nm with an average intertubule distance of 100 nm and 10 to 30 walls per tubule. The measured thermal conductivity, shown in Figure 7.8a, exhibits a smooth increase in thermal conductivity with temperature increase reaching a maximum of 25 W/m-K at room temperature. The measured κ of MWNT at 300 K is about two orders of magnitudes lower than graphite and diamond at room temperature. This was attributed to the imperfections introduced during growth
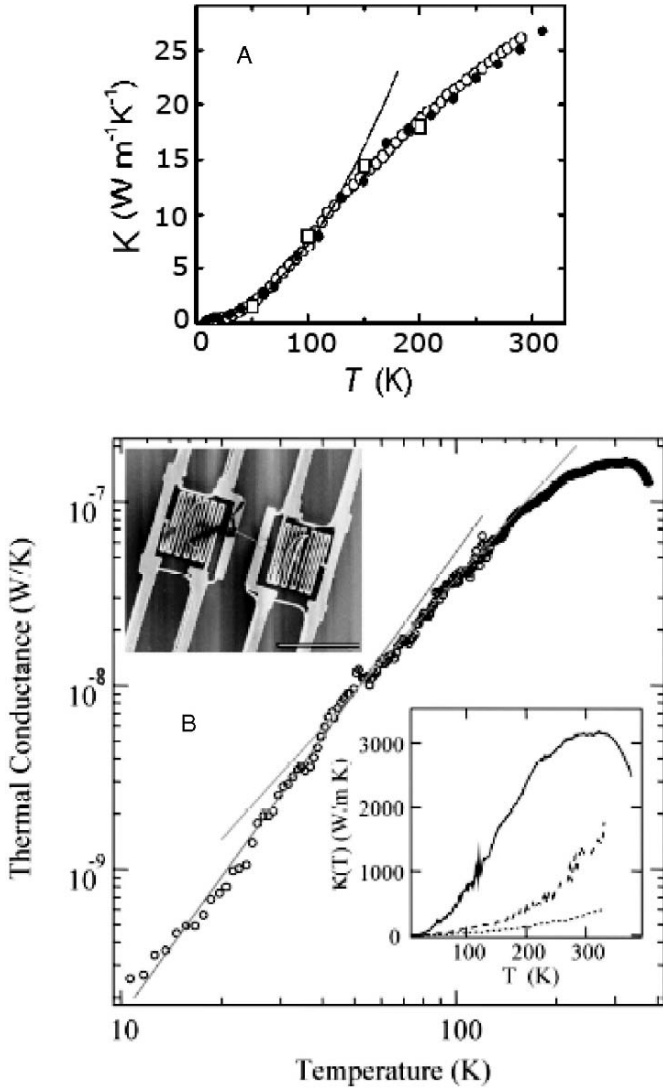
FIGURE 7.8. Temperature-dependence of the thermal conductivity of (a) aligned MWNT bundle, (b) individual MWNT [3,13].

which significantly reduce phonon mean free path length. The measurements also revealed a change in temperature dependence of κ from quadratic below 120 K to linear above that. The thermal conductivity of MWNT films at 300 K was also measured using pulsed photothermal reflectance (PPR) technique in [12]. The MWNT film was vertically grown using microwave plasma inside grove structures etched

in silicon with the length of MWNTs ranging from 10 to 50 μm and diameters from 40 to 100 nm. The measured value at room temperature after corrections for the air gaps between bundles was 200 W/mK. Furthermore, they measured the electrical conductivity which confirmed the dominant contribution of phonons to the thermal conductivity of MWNTs. The scattering from defects, intergraphene layer, and intertube coupling was thought to be responsible for the low measured thermal conductivity.

In order to isolate the contribution of intertube scattering and the effect of different nanotube length and diameters in the multiwall films, the thermal conductance of individual suspended MWNTs with diameters 14 nm, 80 nm, and 200 nm was measured over the temperature range from 8 K to 370 K in [13]. The MWNT had 14-nm diameter and a length of 2.5 μm corresponding to the gap between the two suspended islands is shown in the insert of Figure 7.8b. The measured thermal conductance in Figure 7.8b shows a smooth monotonic increase with temperature up to 320 K. As can be seen in the insert of Figure 7.8b, the room temperature thermal conductivity exceeds 3000 W/m-K which is an order of magnitude higher than that reported in [11]. However, the measured κ for 80-nm and 200-nm diameter MWNTs were smaller and closer to that of MWNT bundles reported in [3]. The measured $\kappa(T)$ had a T^α dependence with gαg 2.5 at low temperatures ($8 < T < 50$ K) and $\alpha \approx 2$ in the $50 < T < 150$ K range. The $T^{2.5}$ was assumed to be due to the weak three-dimensional nature of $\kappa(T)$ at temperatures below the Debye temperature for interlayer phonons $\Theta_\perp$ whereas the T^2 dependence above $\Theta_\perp$ indicated the two-dimensional nature of $\kappa(T)$ for MWNT. Table 7.1 provides a summary of measured thermal conductivities of carbon nanotubes and other materials.

TABLE 7.1 Thermal conductivity of nanotubes and other high conductivity materials.

Material	κ (J/mK)	References
SWNT mat	35	10
Aligned SWNT	220	11
Individual MWNT	3000	13
MWNT film	15–25	3, 12
MWNT (after correction)	200	12
0.07% ^{13}C diamond (enriched)	3320	20
Type II natural diamond	2190	20
CVD diamond	1300–2200	20, 21
Graphite	1800–2000	19
Cubic boron nitride	760	20
Silicon carbide	490	20
Copper	400	20
Aluminum nitride	320	20
Silicon	160	20

7.4. Thermal Conductivity Simulations

7.4.1. *Molecular Dynamic Approach*

The molecular dynamics (MD) method provides an attractive tool for understanding the processes involved in heat transfer at the molecular level. Furthermore, by nature this method allows controlling or modifying the parameters that may not be accessible by experiments which may lead to better understanding of a given phenomenon under investigation [36,37]. The nature of heat flow at moderate temperatures in carbon nanotubes is dominated by vibrational phonons and the electronic contribution can be neglected. Under these conditions, atomic-level MD simulations with many body anharmonic interaction potentials, such as the Tersoff–Brenner bond order potential [38,39], are most suited to examine lattice thermal properties in materials. Due to the anharmonic nature of the many-body bonding and nonbonding interactions, the vibrational modes are inherently coupled with each other and all the scattering processes are naturally included. The MD simulations at any given temperature provide complete information about the positions and momentum as a function of time; the energy dissipation and many correlated processes can be simulated in a natural way. The quantum effects can be incorporated through proper force potential and thermal distribution parameters, and a variety of dynamic information under equilibrium, nonequilibrium, and transient conditions can be computed from the atomic dynamics variables.

Thermal transport through carbon nanotubes is sensitive to the choice of good atomic interaction potential, including the anharmonic part because the atomic displacements far from equilibrium positions are also sampled. The room temperature (300 K) phonon spectra or density of states and vibrational amplitudes have been computed recently [40]. The spectra were simulated through Fourier transform of temperature-dependent velocity autocorrelation functions computed from MD trajectories using the Tersoff–Brenner potential for C–C interactions [38,39]. Good agreement with zero temperature phonon spectra, computed with higher accuracy ab initio DFT and tight-binding methods [41–45] was obtained. Additionally, the line-width of the computed spectra provides temperature-dependent life and correlation time of the phonon excitations involved. The spectra were also used to assign the low-frequency Raman modes of carbon nanotube bundles [40]. A simplified version of the Tersoff–Brenner bond order potential was also used in MD simulation of thermal properties of nanotubes [46].

The thermal conductivity coefficient still remains one of the difficult transport coefficients to calculate using MD simulations. The direct simulation approaches can be divided into two main categories: equilibrium MD methods that use the Green–Kubo formula, and nonequilibrium MD methods based on forcing temperature gradients explicitly or implicitly on the system. A detailed comparison of the different MD approaches to compute the thermal conductivity, their advantages, and shortcomings is given in [47].

This equilibrium MD approach uses current fluctuations to calculate the thermal conductivity κ via the fluctuation dissipation theorem. The MD approach is used to compute the autocorrelation function of the heat flux, which is related to the thermal conductivity by the Green–Kubo formula given by:

$$\kappa = \frac{V}{k_B T^2} \int_0^\infty \langle J_z(0) J_z(t) \rangle dt, \tag{12}$$

where T is the system temperature, $J_z(t)$ is the z-component of the heat flux, k_B is the Boltzmann constant, and V is the volume of the sample under investigation. For carbon nanotubes, the z-axis is assumed to be parallel to the nanotube axis. In general the heat flux J_q is given by:

$$\vec{J}_q(t) = \sum \vec{v}_i \varepsilon_i + \frac{1}{2} \sum_{i,j} \sum_{k,l} \vec{r}_{ik} \left(\vec{F}_{ij}^{kl} \cdot \vec{v}_i \right), \tag{13}$$

where ε_i is the total energy that includes the many-body potential energy term [15]. Quantum corrections to the thermal conductivity calculated from the classical autocorrelation function were found to be six orders of magnitude smaller in diamond [15]. The use of periodic boundary conditions in this approach may also lead to size-dependence of the thermal conductivity if the simulation region length is shorter than the mean free path of phonons and results in underestimation of the thermal conductivity. For example, the computed thermal conductivity of (10,10) single-wall carbon nanotubes using the Green–Kubo equilibrium MD approach converged to a constant value for samples longer than 20 nm at 300 K [15]. The advantage of this approach is that simulations are done under equilibrium conditions at any given temperature without imposing any driving forces such as temperature gradient or fictitious force as in the nonequilibrium MD approach. Unfortunately, as the upper limit of the integration indicates, very long simulation times (5×10^5 to 5×10^6 time steps) are required to ensure the convergence of the current-current autocorrelation function.

The nonequilibrium MD approach, on the other hand, involves either applying a temperature gradient across the system under investigation (also known as the direct method) or the use of a fictitious exchange term (force) and modification of the equations of motion which forces the system out of equilibrium and results in a heat flux to counter the effects of temperature gradient or the external force. MD simulations using the fictitious external force approach have been used to compute the thermal conductivity of single-wall nanotubes and their chirality dependence in [14,48]. The direct method involving temperature gradients can either use periodic or nonperiodic boundary conditions and the Fourier approximation is used to calculate the thermal conductivity κ. In the nonperiodic case, the two ends of a simulation cell are held at two different temperatures, which causes a heat flux through the system. The temperatures at both ends are kept at constant values by rescaling the velocities of the atoms at each time step to achieve the desired temperature. The periodic direct approach was used to calculate the thermal
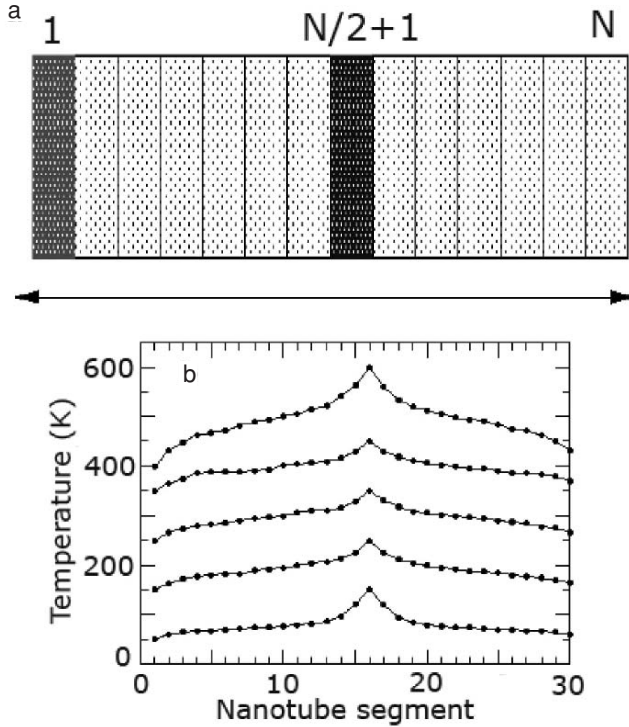
FIGURE 7.9. (a) Simulation system setup for periodic boundary conditions. (b) Temperature profile along (10,10) nanotube at 100 K to 500 K equilibrium temperatures [16].

conductivity of single-wall nanotubes [16] and the nonperiodic method in the case of Y-junction nanotubes and single-wall nanotubes [17,18].

The direct periodic approaches to calculating κ of interest here are (1) the velocity exchange approach to generate a temperature gradient and (2) the velocity scaling approach to maintain a specified temperature gradient. In the velocity exchange approach proposed in [49], the simulation domain is divided into several slabs of equal width as shown in Figure 7.9. A single slab (or group of slabs) near one boundary is designated as the cold slab and a slab (or group of slabs) at the center of the simulation domain is chosen as the hot slab (slabs). MD simulation is first run to achieve equilibrium at a given temperature T_o. To generate a heat flux, the velocity vectors of the hottest atom in the cold slab are exchanged with those of the coldest atom in the hot slab. This causes an energy transfer from the cold slab to the hot slab assuming that the energy of the hottest atom in the cold slab has higher kinetic energy than the coldest atom in the hot slab. This gradually leads to a difference in temperature between the cold and hot slabs and results in a temperature gradient in the region separating them. At steady state, the heat flux due to the temperature gradient balances the energy transfer by velocity exchange. Therefore, the heat flux can be computed from the net energy transfer by velocity

exchange. The choice of the locations of the hot and cold slabs in Figure 7.9a allows applying periodic boundary conditions along the straight nanotube axis in order to eliminate edge effects [49]. Furthermore, the resulting temperature profile at the end of the simulations (shown in Figure 7.9b) yields two thermal conductivities (depending on the temperature gradients) which can be averaged to arrive at the thermal conductivity at a given temperature or instant.

The thermal conductivity is calculated from the following relationship,

$$\kappa = -\frac{1}{2t A \left(\partial T / \partial z\right)} \sum_{transfers} \frac{m}{2} \left(v_h^2 - v_c^2\right). \tag{14}$$

Here A is the cross-sectional area, t is the simulation time, $v_h(v_c)$ is the velocity of the hot (cold) atom involved in velocity exchange, and m is the mass of the atoms (assumed to be identical). For materials with large thermal conductivity, the temperature gradient can be very small due to efficient heat transfer. Therefore, the temperature difference in the hot and cold slabs is very small. Also, the assumption that the velocity of the hottest atom in the cold slab remains larger than the velocity of the coldest atom in the hot slab may not be valid for all individual exchanges due to thermal fluctuations. The instantaneous thermal flux may oscillate between positive and negative directions, and the overall time-averaged flux may register lower values as compared to the simulations where hot and cold slab conditions are imposed directly by the velocity scaling methods. Additionally, this approach also assumes that each velocity exchange results totally in the exchange of kinetic energy between hot and cold slabs. In a covalently bonded, strongly interacting, solid-state system such as nanotubes and graphite this approximation may not be valid and not all the exchanged kinetic energy may go towards affecting the temperatures of the slabs. Any sudden change in the atomic velocity at each step (due to velocity exchange) may not conform to the requirement of the forces due to underlying potential energy surface, and part of the gain/loss in the atomic kinetic energy may be used to conform the dynamics to the underlying potential energy surface. For both of the above reasons, in general, we expect the thermal flux and hence the thermal conductivity computed using the velocity exchange approach to be less than the values computed by the velocity scaling approach under similar conditions.

The velocity scaling procedure proposed in [50] involves imposing a temperature gradient by setting the temperature at the hot slab to $T_o + \Delta T$ and that of the cold slab to $T_o - g\Delta T$, where T_o is the equilibrium temperature. The temperatures are maintained at these values throughout the simulations by scaling the velocities of each atom i in the cold and hot slabs from initial value of v_i to final v_i' at each time step. This amounts to adding (or subtracting) energy $\Delta E = \Delta E_{kin}$ to the slab of interest.

$$\Delta E = \frac{1}{2} \sum_{i=1}^{N_L} m_i (v_i'^2 - v_i^2), \tag{15}$$

where N_L is the number of atoms in the slab. The energy flux J is then given by:

$$J = \frac{\langle \Delta E \rangle}{A \Delta t} = -\kappa \frac{2\Delta T}{(L/2)}, \tag{16}$$

where $\langle \Delta E \rangle$ is the average energy per time step Δt, κ is the thermal conductivity, L is the length of the simulation region, and $2\Delta T$ is the temperature difference between the cold and hot slab. If energy is added/removed in the hot/cold slabs at each time step the net $\langle \Delta E \rangle$ is the sum of the values of the added/removed heat energy at the hot/cold slabs. A large jump in the temperature between the hot/cold slabs and the closest ones also generally occurs due to discontinuity in the temperature constraint conditions on the hot/cold slabs.

The temperature gradient defined by $2\Delta T/(L/2)$ does not give an accurate representation of the temperature gradient in the "full" region between the hot and cold slabs in nanotubes. To remedy this, the temperatures in the slabs between the hot and cold ones are not only time-averaged during the final 20 ps of the simulation, but also the temperature and length data from the nearest neighboring cells are omitted in computing the temperature gradient. The temperature gradients are determined on both sides of the hot slab from the linear square fit to the temperature distribution and length data from the remainder of the cells with no sharp discontinuities. This configuration yields two temperature gradients in a single trajectory which allows calculations of two values of κ in each trajectory. Furthermore, due to the short time step used in MD simulations (0.5 fs), it is not always true that $\Delta E_h > 0$ (i.e., energy added to the hot slab) and $\Delta E_c < 0$ (energy removed from the cold slab) due to the statistical fluctuations inherent in the MD approach. In reality, values of both ΔE_h and ΔE_c fluctuate between positive and negative values and the time average is zero. As explained above, the net energy flux through the nanotube is due to energy added/removed at both slabs, therefore the net energy exchange between the nanotube and external reservoirs is $|\Delta E_h + \Delta E_c|/2$ to account for thermal energy transport on both sides of the central hot slab. Because the instantaneous values of both ΔE_h and ΔE_c fluctuate between positive and negative, the absolute value of the sum therefore reflects the net energy added to or removed from the system at each step to maintain the flux at that step. With $|\Delta E_h + \Delta E_c|/2$ responsible for heat flux, the instantaneous thermal conductivity due to the energy exchange during time Δt is

$$\frac{|\Delta E_h + \Delta E_c|}{2A\Delta t} = -\kappa \frac{\partial T}{\partial z}. \tag{17}$$

The temperature gradients and heat flux are further time-averaged over the last N time steps ranging between 20–50 ps depending on simulation temperature. The time-averaged thermal conductivity is

$$\kappa = -\frac{1}{\left\langle \frac{\partial T}{\partial z} \right\rangle} \frac{\sum\limits_{i=1}^{N} |\Delta E_h + \Delta E_c|_i}{2NA\Delta t}. \tag{18}$$

Although the procedure appears to be simple, one has to take into account size effects and make sure the length of the simulation box is greater than the mean free path of the phonons and the system remains in the linear response region.

In many cases one can only simulate very small sample sizes and the imposed temperature gradients can lead to deviations from the linear response. To account for these issues, simulations are usually done for samples of different length and then extrapolated to determine κ for a sample infinite length or micron scale [18,47]. The values of κ calculated by the equilibrium MD approach was used to check the consistency of the MD simulations results and adjust the length of simulated sample in [16].

7.4.2. Single-Wall Nanotubes

A typical temperature distribution inside a nanotube at the end of the simulation is shown in Figure 7.9b at different equilibrium temperatures. This temperature distribution yields two gradients $\partial T/\partial z$ that are used to compute the thermal conductivities κ_L and κ_R corresponding to the temperature distributions to the left and right of the hot slab, respectively. These are averaged to yield the thermal conductivity at a given temperature. The thermal conductivity of SWNTs was computed using the direct MD simulation methods in [14–16]. The typical room temperature thermal conductivity of single-wall carbon nanotubes of 1–3 nm diameters is found to be around 2500 W/mK as shown in Figure 7.10a. The thermal conductivity shows a peaking behavior as a function of temperature because as the temperature is raised from very low values, more and more phonons are excited and contribute towards heat flow in the system. However, at higher temperatures, phonon–phonon scattering starts to dominate and streamlined heat flow in the CNTs decreases, causing a peak in thermal conductivity in the intermediate temperature range. For all the simulated CNTs (1–2 nm diameter) as a function of the tube diameter and chirality, it was found that the peak position is around room temperature and sensitive to the radius of the CNTs and not the chirality or the helicity [16]. This means that the thermal transport in SWNTs is mostly through excitations of the low-frequency radial phonon mode and the coupling of the radial mode with the axial or longitudinal phonons in the low-frequency region [15,51]. In addition, NEMD simulations using the periodic velocity exchange approach [16] and external force approach [49] predict higher thermal conductivities for zigzag SWNTs compared to armchair SWNT at low temperatures. Figure 7.10b shows the temperature dependence of the thermal conductivity of (5,5) and (10,0) SWNTs. The higher value was attributed to higher strain in the sigma bonds along the circumference in armchair SWNT compared to zigzag SWNT. The convergence of the thermal conductivity as a function of the length of the CNT, however, is still an issue in all the direct MD simulation results reported so far. A significant variation in the room temperature thermal conductivity of (10,10) CNT has been reported partly because some of the studies have used very small CNT lengths in the simulations [14]. Preliminary investigations of the convergence with respect to the temperature gradient $\partial T/\partial z$ across the CNT length have shown an inverse power-law dependence of the thermal conductivity on the thermal gradient. Rigorous, long time- and length-scale simulations are required to investigate the
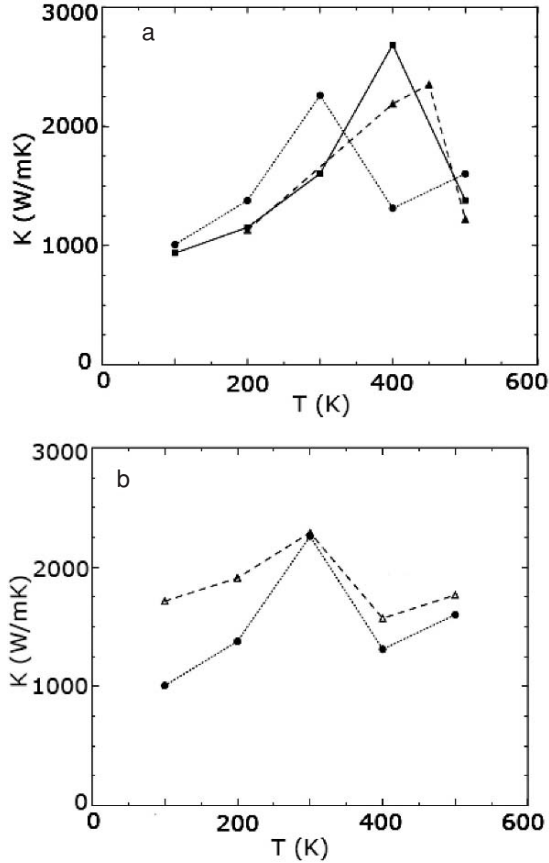
FIGURE 7.10. Thermal conductivity of SWNTs with (a) different diameters; (b) different chirality [16].

convergence behavior as a function of CNT length. It is noted, however, only the absolute value of thermal conductivity changes and not the qualitative behavior of the relative peak heights and position as a function of temperature.

7.4.3. Y-Junction Nanotubes

The steady-state thermal properties of a Y-junction nanotube consisting of a (14,0) trunk splitting into two (7,0) branches was investigated using molecular dynamics simulations in [19]. The thermal conductivity, shown in Figure 7.11, exhibits an increase with temperature similar to what has been reported experimentally for straight carbon nanotubes [10]. Figure 7.11 also indicates that the thermal conductivity of the isolated straight (14,0) nanotube was consistently larger than that of the Y-junction structure due to the discontinuity in the crystal structure

FIGURE 7.11. Temperature-dependence of the thermal conductivity of Y-junction nanotube. (14,0), squares; the triangles represent the forward heat flow configuration of the Y-junction tube, and the circles represent the reverse heat flow configuration of the Y-junction tube [17].
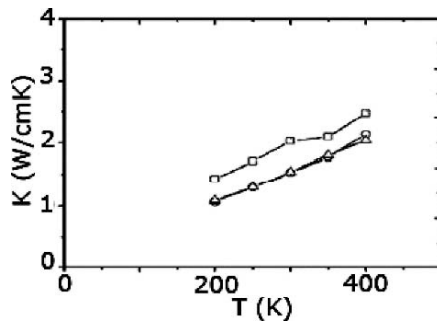
present at the hub of the Y-junction. The led to discontinuity in the temperature profile of the Y-junction nanotube discontinuity similar to that observed in crystal grain boundaries [52], junctions between nanotubes of different diameters [53], and in nanotubes with vacancy defects [19]. A study of the phonon modes in the Y-junction tubes demonstrated that the presence of defects reduces the density of axial and radial phonon modes. This relationship between temperature discontinuity and atomic vibrations also indicates that both the axial and the radial modes are at least partly responsible for the transfer of heat along a nanotube, and that the interruption of these modes results in an interruption of heat transfer.

Thermal transport in Y-junction nanotubes under steady state does not show any anisotropy with respect to the direction of the heat flow as can be seen in Figure 7.11, which is in contrast to the evidence of electrical rectification in the same structure. The calculation of the electrical properties of Y-junction nanotubes used the Green's function approach which accounts for the effects of quantum states on electrical conduction in Y-junction carbon nanotubes [27]. Recent measurements of the specific heat of carbon nanotubes revealed a quantized 1-D phonon spectrum at temperatures below 8 K. The temperature range for quantization of electrons and phonons is significantly different in CNTs. For phonons, the threshold energy at low temperatures is characterized by $\hbar\omega_{op}$, corresponding to the radial breathing mode frequency, and is typically a few meV. On the other hand, the characteristic energy for electrons is about 0.1 eV which corresponds to the energy at a Van Hove singularity relative to the Fermi level [9]. Consequently, the quantized nature of electrical and/or thermal conductance may survive up to room temperature. Therefore, quantum thermal effects are not seen at the temperatures used in these simulations. Furthermore, experimental measurements have also shown that the electron contribution to thermal conductivity is an order of magnitude smaller than the phonon contribution [10,11]. In addition, the use of Fourier's classical law of heat flow in the MD simulations precludes the inclusion of quantum thermal effects. Fourier's law provides an aggregate measure of the thermal conductivity by summing over all of the present phonon modes [35], but in doing so wipes out information about the contribution of individual phonon modes to heat flow. As the thermal conduction in carbon nanotubes at any temperature is dominated by phonons [2,11], it is possible that a more detailed model including

a consideration of individual phonon modes may reveal thermal rectification in Y-junction nanotubes at very low temperatures.

7.4.4. CNT–Polymer Composites

One of the main reasons for studying the thermal properties of individual SWNTs or MWNTs is to explore the possibility of using CNTs for lightweight, very strong, multifunctional composite materials with well-defined thermal characteristics for heat management in complex systems. The structural strength or thermal characteristics of such composite materials depend on the transfer characteristics of such properties from the fiber to the matrix and the coupling between the two. In some cases, the coupling is through chemical interfacial bonds, which can be covalent or noncovalent in nature, whereas in other cases the coupling could be purely physical in nature through nonbonded van der Waals (VDW) interactions. In addition, the aspect ratio of fiber, which is defined as L/D (L is the length of the fiber and D is the diameter), is also an important parameter for the efficiency of mechanical load or thermal energy transfer across the interfaces. Thermal characterization of CNT–polymer or other matrices involves (1) structural characterization as a density versus temperature phase diagrams, and (2) thermal conductance across CNT matrix interfaces, which can be used in percolation theory-based approaches to compute the increase in the net thermal conductivity of the composite materials by mixing very small volume fractions of carbon nanotubes in the matrix.

The MD simulations of the temperature-dependent structural properties of polymer composite with embedded carbon nanotubes have been performed recently [54]. The coupling at the interface was through nonbonded van der Waals interactions. The density of CNT–polyethylene composite for short (10 monomers) and long (100 monomers) polymer chains has been simulated as a function of temperature [54]. For example, the density versus temperature plot for the long chain CNT–polyethylene composite is shown in Figures 7.12 and 7.13. The position
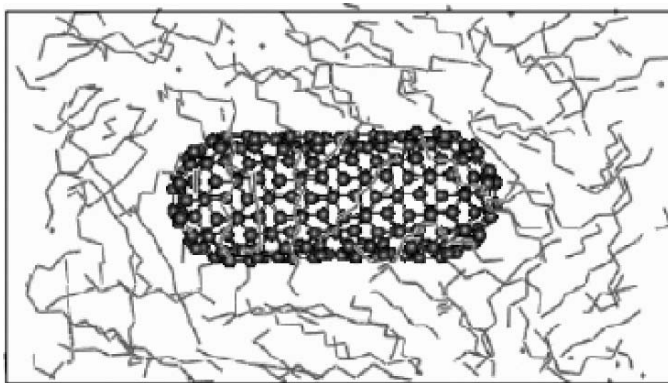
FIGURE 7.12. MD simulation unit cell for a composite system with $20\,\mathring{A}$ long capped (10,0) CNTs embedded in polyethylene matrix. Periodic boundary condition is used [54].

FIGURE 7.13. Density as a function of temperature for short-chained PE ($NP = 10$) and its composite with 20 Å long (10,0) CNTs embedded (averaged from six sample sets; the error bars are shown in the plot). Below T_g, the systems are glassy state, and above T_g, will be in a rubberlike or liquid state if temperature is higher than melting point T_m [54].
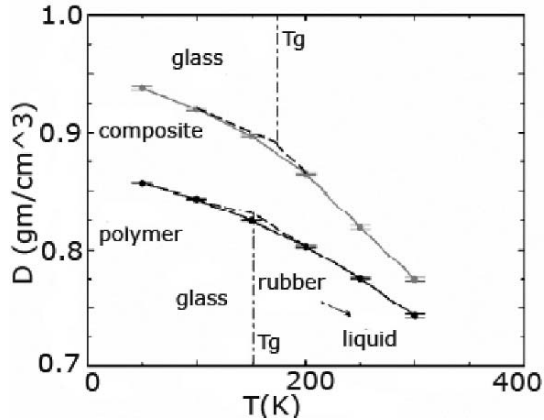
of the change in the slope of the linear behavior in the two cases corresponds to the glass transition temperature for pure polymer and the nanotube–polymer composite. The results show that, due to mixing of 8% by volume of SWNT in polyethylene the glass transition temperature increases by about 20% and more significantly, the thermal expansion coefficient above glass transition temperature increases by as much as 142%. The enhanced thermal expansion coefficient of the composite is attributed mostly due to an equivalent increase in the excluded volume of the embedded CNT as a function of temperature.

Because both excited vibrational phonon modes and Brownian motion contribute to the dynamic excluded volume of the embedded CNT, as the temperature is increased their contributions towards excluded volume increase significantly. The cross-linking of polymer with CNT was not allowed in these initial simulations. It is possible that the cross-linking of polymer matrix with embedded CNTs may further reduce the motions of polymer molecules or the CNT; the predicted changes in the glass transition temperature and the thermal expansion coefficients in that scenario could be different. The increase in glass transition temperature and thermal expansion coefficients of carbon nanotube polymer composites has been also observed in experiments [55].

The simulation and experimental observations of thermal conductivity or thermal conductance across polymer–CNT interfaces are few and have been attempted recently. The pico-second transient absorption spectra have been measured to deduce interface thermal conductance for carbon nanotubes suspended in surfactant micelles in water. The experimental findings have been analyzed using the MD simulations of heat transfer from a carbon nanotube to a model hydrocarbon liquid surrounding it. The heat transport in a nanotube composite material has been found to be limited mainly by exceptionally small interface thermal conductance $\sim$12 MW/m^{2}K. The net thermal conductivity of the composite thus has been found to be significantly smaller than the intrinsically high thermal conductivity

of carbon nanotubes and that would be allowed by the homogeneous mixing rule [56].

The observed low interface thermal conductance in the above case has been explained by a limited coupling between only a small number of low-frequency modes of carbon nanotubes and the surrounding matrix molecules. The energy contained in the high-frequency modes of the carbon nanotubes thus needs to be transferred to the low-frequency modes before it can be transported across the interface. The interface thermal resistance has been investigated also as a function of nanotube length. The longer nanotubes have been characterized by smaller thermal resistence or larger thermal conductance [57]. The thermal coupling between rather rigid carbon nanotubes and the soft polymer molecules has been attributed to the low-frequency weak dispersion forces, which limit the thermal transport across the CNT–polymer molecule interfaces. At higher temperatures and/or compressed composites, perhaps, the thermal interface conductance can be increased by increasing the coupling between the carbon nanotubes and the polymer matrix materials.

7.5. Heat Pulse Propagation in SWNT

MD simulations in [16] showed higher thermal conductivity for the (10,0) zigzag SWNT compared to the (5,5) armchair nanotube especially as can be seen in Figure 7.7b. Further MD simulations in [48] also showed that zigzag (20,0) SWNT had higher thermal conductivity compared to armchair (11,11) and chiral (10,13) nanotubes. Also calculations using lattice dynamics in [58] confirmed the same trend. The diameter of the (10,0) nanotube is only 16% larger than that of the (5,5) nanotube. This raises a question about the nature of energy transfer mechanisms in each nanotube and whether the mechanism is affected by chirality or the diameter of the nanotube. For example, excitation of different phonon modes may be responsible for the earlier reported difference in the thermal conductivities of zigzag and armchair nanotubes of same diameter [9,48,58]. The Fourier approximation used in steady-state thermal conductivity calculations, however, does not provide any information about the participating phonon modes and the energy carried by each phonon mode.

The application of strong heat pulses, on the other hand, generates several waves propagating at different speeds corresponding to different phonon modes, and can provide information about individual modes and their contribution towards the overall heat transport [59–61]. Heat pulse measurements in NaF at low temperatures revealed ballistic LA and TA phonon mode propagation as well as second sound waves at temperatures below 14 K [60]. Therefore heat pulse experiments provide quantitative information on transport by diffusion, ballistic phonons, and second sound waves. The second sound waves can be observed, as in the experiments reported in [60], when the momentum-conserving normal phonon scattering processes are dominant compared to the momentum-randomizing Umklapp

phonon scattering processes. Both experimental measurements on thermal conductivity and some theoretical models as well point to the long phonon mean free path length as being responsible for the higher thermal conductivity and its increase up to room temperature. As Umklapp processes mainly determine the mean free path length, one can also raise the question about whether this implies that normal phonon–phonon scattering processes (N-processes) dominate up to room temperature or at least over a wider range of temperatures compared to that in NaF. If this is true, then one can expect second sound waves to be observed in nanotubes. The speed of the leading edges of pulses arriving at the detector is determined from the arrival time and the sample length and used to determine the ballistic phonon mode (LA or TA) [59,60]. This approach assumes accurate knowledge of the speed of each phonon mode in the material under investigation. Consequently, heat pulse simulations can provide insight into how heat flow occurs in nanotubes, the important contributing phonon modes, and their dependence on the nanotube chirality and diameter.

Earlier molecular dynamics studies on pulsed heat propagation in alpha iron demonstrated energy flow by LA and TA modes and second sound waves [59]. Low temperatures and pure crystalline materials are required to observe second sound waves that are not attenuated by dissipative scattering processes. The molecular dynamics simulations thus provide an ideal platform for investigating these properties by controlling the temperature of the CNT, shape, and duration of heat pulses assuming the perfect crystalline structure. Thermal energy transport in single-wall carbon nanotubes subjected to intense heat in $(7,0)$, $(10,0)$, and $(5,5)$ single-wall carbon nanotubes with particular emphasis on the role of nanotube chirality and diameter was examined in [62]. The heat pulse was found to generate wave packets that move at the speed of sound corresponding to different phonon modes, second sound waves, and diffusive components. The waves corresponding to ballistic LA, TW phonon modes, and second sound in zigzag nanotubes carried more heat energy than in armchair nanotubes of similar diameter [62]. The thermal conductivity of zigzag nanotubes due to the ballistic phonon contribution therefore is expected to be larger as compared to the armchair nanotubes as reported recently [16,48].

For MD simulations, each nanotube was divided into 250 slabs. The number of atoms per slab was 40 atoms in a $(10,0)$ nanotube resulting in 10,000 atoms for the whole nanotube. The number of atoms per slab increases as the diameter of the nanotube increases. The axis of the tube was aligned along the z-axis with the free end of the nanotube at $z = 0$, and the far end of the nanotube was held rigid. In order to apply heat pulse and ensure smooth temperature transition from the boundary to the region of interest on the nanotube, the boundary region was chosen to extend over five slabs and the temperature was adjusted equally during the rise and fall times of the pulse. Additionally, the temperature at each slab was spatially averaged over 5 slabs centered at the slab of interest. The resulting temperature was also time-averaged over 200 time steps. The boundary at the far end of the nanotube consisted of several slabs with the outermost slab rigidly held in place. The remaining slabs

were held in equilibrium at the simulation temperature by applying a Gaussian random force, satisfying the fluctuation–dissipation theorem, which ensured that no reflection from the boundary to the oncoming propagating waves occurred. The one-dimensional nature of the nanotube simplifies the boundary conditions, as one does not have to worry about the scattering in the transverse directions. The atom's motion and configurations in the transverse or radial directions are governed by the intrinsic forces that maintain the shape of the nanotube.

Initially, MD simulations of single-wall carbon nanotubes were run to achieve thermal equilibrium at low temperatures close to 0.1 K. This was followed by the application of a strong heat pulse of finite duration, and rise and fall times. The simulation was stopped before the leading waves reached the right boundary, even though the boundary slabs and conditions would have ensured no reflection back into the system. The instantaneous temperature distribution along the nanotube was recorded every 200 time steps in addition to the time and spatially averaged temperatures. The minimum time scale τ_m for time-averaging is taken to be the time required for a ballistic LA mode to traverse a single slab which corresponds to about 25 fs for a (5,5) nanotube which is significantly larger than the time step of 0.5 fs used in the simulations. In order to determine the propagation speeds of the leading stress waves, the slab numbers corresponding to the peak locations at given time intervals are recorded. The speed is then determined from the spatial distance traversed by the particular wave during a given time interval. The average speed for each peak is determined from linear fit of the peak locations versus time.

An example of the temporal and spatial variation of the kinetic temperature in a (10,0) nanotube obtained from the MD simulations is shown in Figure 7.14. The
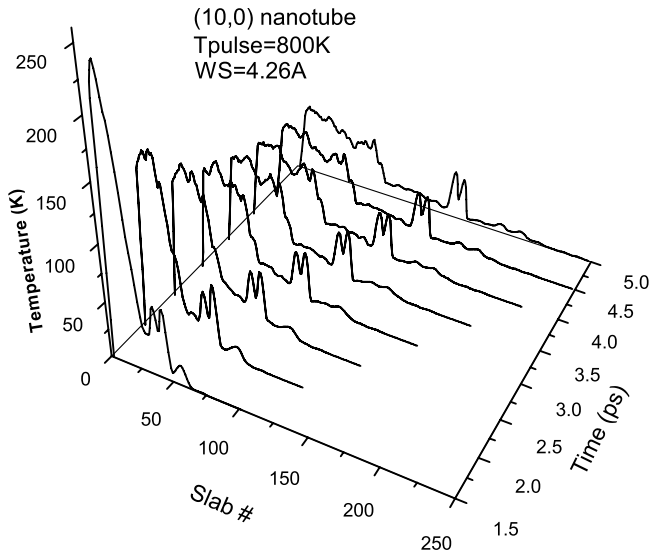
FIGURE 7.14. Spatial and temporal distribution of kinetic temperature along a (10,0) SWNT [62].
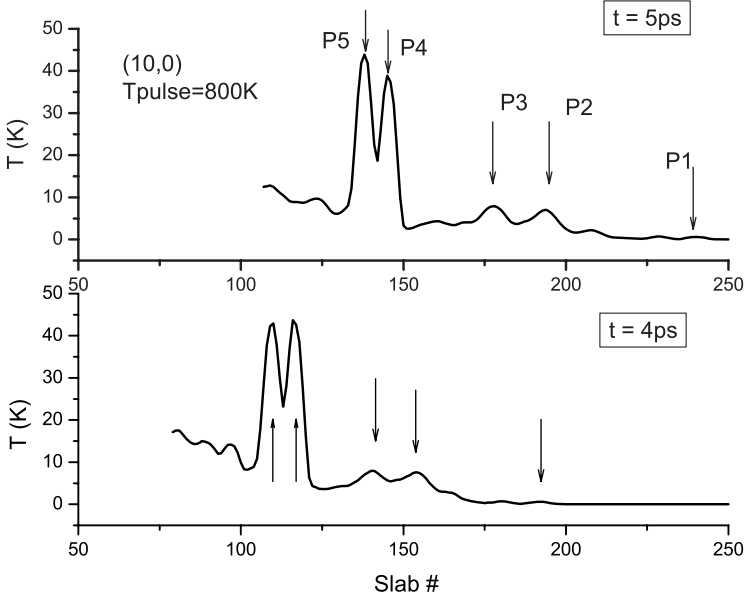
FIGURE 7.15. Spatial distribution of kinetic temperature along (10,0) nanotube at time 3 and 4 ps after the application of the heat pulse [62].

heat pulse induces clearly defined wave packets that propagate on the nanotube. The leading wave packets move at higher speeds as compared to the diffusive background. The shapes of wave packets P2 and P3, as shown in Figure 7.15, change and the peak intensity of P2 decreases by 15% between 3 ps and 5 ps whereas that of P3 stays constant during the same period. On the other hand, the peak intensity of the weak leading wave packet P1 stays constant and the shape does not change with time. The leading wave packets are followed by a dual-peak wave packet that undergoes very minor changes in its shape and the peak intensities slowly decay to a final kinetic temperature around 40 K at 5 ps. The time axis for this analysis was started at 1.5 ps to avoid the initial transient large kinetic temperature values that make it difficult to observe and analyze the low-intensity leading propagating waves from left to right. By shifting the time axis to 1.5 ps, the plotted maximum temperature has been reduced from 400 K to less than 100 K, which allows for better resolution of wave packets with smaller peaks. The distance along the nanotube axis has been normalized by the slab width and is plotted as slab numbers.

The three-dimensional view in Figure 7.14 provides a clear picture of how waves develop and propagate as separate wave packets on the nanotube. The details of the low-amplitude higher-speed wave packets are not clearly seen in the figure because of the slow-moving large diffusive components. Figure 7.15 shows the details of the frontal leading waves after leaving out the diffusive part of temperature distributions at times 4 and 5 ps. The average speed of peaks P1
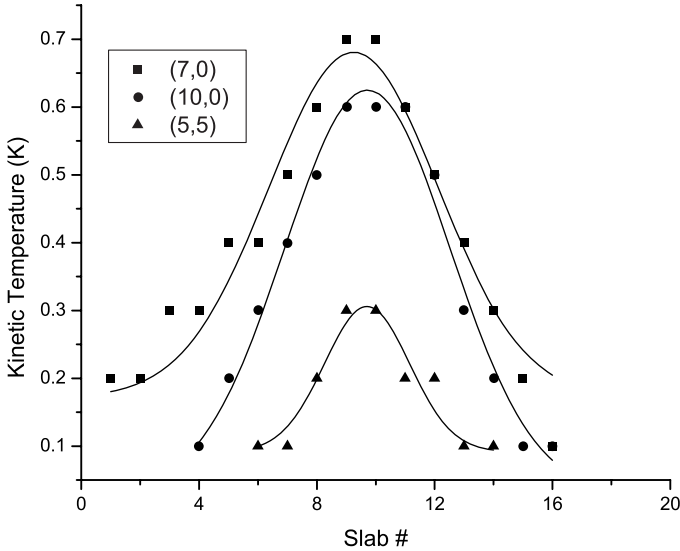
FIGURE 7.16. Shape of LA leading mode peak in (10,0), (7,0), and (5,5) SWNT at time = 4 ps. The line through the data points represents the best Guassian fit [62].

and P2 were found to be 20.6 km/s and 16.6 km/s, respectively. These speeds are very close to the speed of sound associated with longitudinal acoustic and twisted phonon modes, respectively [22]. The values obtained from the MD simulations are similar to theoretically calculated sound velocities of LA and TW phonons, in (10,10) armchair nanotubes, which were reported to be 20.35 km/s and 15 km/s, respectively [22]. The shape of the leading wave packet (identified as arising from the LA mode) did not change and had a peak kinetic temperature of 0.6 K and a full width at half maximum of 2.4 nm as shown in Figure 7.16. However, the wave packet P2, corresponding to the TW mode, has higher peak energy and has a fast decay from an initial value of 17 K to 7.0 K at 5 ps with a decay time constant of 1.06 ps as shown in Figure 7.17a. For comparison, the peak temperature for P1 is shown in Figure 7.17b. At 5 ps after the onset of the pulse, wave packet P2 had a much higher peak kinetic temperature of 7 K and a width at half maximum of 4.3 nm. Therefore the atomic motions within the TW wave packet P2 carry about 20 times higher overall kinetic energy as compared to the atomic motions within the P1 wave packet

The strongest wave packets in Figure 7.15 are P4 and P5 and they propagate together at a speed of 12.2 Km/s. The peak energies for P4 and P5 in a (10,0) nanotube decay with time constants of 2.1 and 1.0 ps, respectively, as shown in Figure 7.17a. At 5 ps after the onset of the pulse, wave packets P4 and P5 had peak temperatures 39.0 K and 44.0 K and full width at half maximum of 1.9 nm and 2.3 nm, respectively. Note that these two wave packets also remain spatially confined as compared to the leading wave packets P1, P2, and P3. Furthermore,
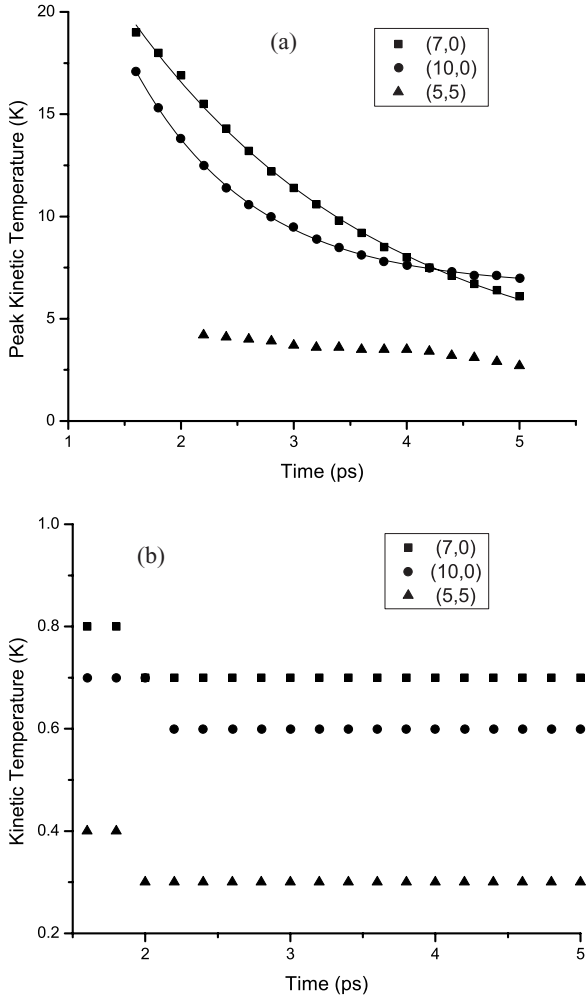
FIGURE 7.17. Temporal change of peak temperature of (a) TW mode wave packets; (b) second sound wave packet. The line through the data points represents the best exponential decay fit [62].

the total energy in the wave packets P4 and P5, as computed from the area of the curve under the Gaussian fit, is three times larger than the combined P2 and P3 wave packets. Consequently, one can conclude that the leading wave packets in zigzag (10,0) nanotubes propagate at the sound velocities of LA and TW modes. However, the largest amount of energy is carried by wave packets propagating at 12.2 Km/s. Additional simulations of (7,0) and (5,5) SWNT also revealed a similar trend. The results for the sound speed of wave packets P1 through P5 in (10,0), (5,5), and (7,0) nanotubes are summarized in Table 7.1.

TABLE 7.2 Speeds in km/sec of the leading propagating
wave packets in (10,0), (7,0), and (5,5) single-wall carbon
nanotubes (from heat pulse simulation).

Peak	(10,0)	(7,0)	(5,5)
P1	20.6 (LA)	21.3 (LA)	20.3 (LA)
P2	16.4 (TW)	18.1 (TW)	16.2 (TW)
P3	15.8 (TW)	16.2 (TW)	17.0 (TW)
P4	12.2	12.7	12.9
P5	12.2	12.6	12.3

The wave packets P4 and P5 propagate at speed approximately equal to 12 Km/sec in all the nanotubes as can be seen from Table 7.2. These wave packets can also be analyzed in comparison with the propagation speed data of known phonon modes. The propagation speed data, as seen in Table 7.3, shows that for TW modes propagation speeds vary from 12.0 km/s to 15.0 km/s whereas for the transverse breathing (TB) phonon modes vary from 12.3 km/s to 42.0 km/s [22,63–67]. The TB modes are also considered optical modes because their frequency is nonzero at $q = 0$. This large variation, however, arises from the differences in values of force constants and Young's modulus values used in different methods. To examine the possibility of the occurrence of the second sound wave, the ratio R of the speed of wave packet P1 (V_{LA} mode) to the average speed of the wave packets P4 and P5 (V_{S2}), was computed for all three nanotubes. The ratio R was found to be 1.69 in (10,0), 1.68 in (7,0), and 1.62 in (5,5) nanotubes. These ratios deviate from $\sqrt{3}$, by 2%, 3%, and 6% in (10,0), (7,0), and (5,5) nanotubes, respectively. This ratio was used to predict the presence of second sound waves at low temperatures in α-iron and NaF [59–61], and it is expected to be $\sqrt{3}$ for second sound waves in good crystalline materials. The second sound waves arise when momentum-conserving phonon-scattering events (N-processes) are far more frequent as compared to momentum-destroying collisions (U-processes) as temperature increases in the material. Under such conditions, the energy propagates as a collective temperature pulse characterized by velocity (second sound wave velocity) that is determined by the interaction of different phonon modes in the system [61].

TABLE 7.3 Speeds of sound waves associated with longitudinal (V_L), transverse (V_T), twisted (V_{TW}), and breathing (V_B) phonon modes in carbon nanotubes.

V_L (km/s)	V_T (km/s)	V_{TW} (km/s)	V_B (km/s)	References
20.35	9.43	15.0	—	1
21.7	—	14.0	42.8 Km/s	2
20.35	24.0, 9.0	15.0	—	3
20.7	14.1	14.1	—	4
19.9	—	12.3	—	5,6
19.9	—	12.3	12.3	6
—	—	15.0 (13.0)	—	7

In carbon nanotubes, the momentum-destroying Umklapp scattering processes are far less frequent at low temperatures as compared to the N-process and only begin to play a major role above room temperature which is responsible for the monotonic increase in the thermal conductivity of carbon nanotubes up to room temperature [10–13]. The local kinetic temperature within P4 and P5 wave packets is well below room temperature and the nanotube temperature is below 0.1 K which makes N-processes dominant. Furthermore, as can be seen from the three dimensional plot in Figure 7.14, other modes (TW) are generated as the peaks of modes P4 and P5 decay; this supports the selection that the peaks P4 and P5 represent second sound waves. Further dynamic investigations with the Tersoff–Brenner potential to analyze the dynamics of individual phonon modes are required to confirm the peak assignments. We note, however, that the above assignment of P4 and P5 as the second sound wave does not affect in any way the main results and conclusions of this work; that is, in general the nondiffusive energy carried by the modes P1–P5 for zigzag type nanotubes (7,0) and (10,0) are larger than the energy carried by similar modes in the armchair type (5,5) nanotube.

Assuming that similar propagating modes carry the bulk of thermal energy transport under equilibrium conditions as well, the above comments support the observation that for the same temperature gradient, one can expect higher heat flux in (10,0) zigzag nanotubes as compared to the (5,5) armchair nanotubes [16,58]. Furthermore, even the energy carried by second sound waves is smaller in (5,5) compared to (10,0) and (7,0) nanotubes. This translates to higher thermal conductivity for the zigzag nanotubes compared to armchair nanotubes. As the nanotube diameter increases, more modes are excited which can also contribute to heat flow. A more detailed analysis of the propagation speeds of the individual phonon modes and simulation of larger-diameter nanotubes are required to obtain more quantitative dynamic results.

References

[1]   S. Iijima, *Nature*, **354**, 56, 1991.
[2]   L.X. Benedict, et al., *Solid State Comm.* **100**, 177, 1996.
[3]   W. Yi, et al., *Phys. Rev. B* **59**, R9015, 1999.
[4]   A. Mizel, et al., *Phys. Rev. B* **60**, 3264, 1999.
[5]   J. Hone, et al., *Science* **289**, 1730, 2000.
[6]   J.C. Lasjaunisas, et al., *Phys. Rev. B* **65**, 113409, 2000.
[7]   V.N. Popov, *Phys. Rev. B* **66**, 153408, 2002.
[8]   S. Zhang, et al., *Phys. Rev. B* **68**, 075415, 2003.
[9]   T. Yamamoto, S. Watanabi, and K. Watanabe, *Phys. Rev. Lett.***92**, 075502, 2004.
[10] J. Hone, et al., *Phys. Rev. B* **59**, R2514, 1999.
[11] J. Hone, et al., *Appl. Phys. Lett.* **77**, 666, 2000.
[12] D. J. Yang, *Phys. Rev. B* **66**, 165440, 2002.
[13] P. Kim, , *Phys. Rev. Lett.* **87**, 215502, 2001.
[14] S. Berber, Y. K. Kwon, and D. Tomanek, *Phys. Rev. Lett.* **84**, 4613, 2000.
[15] J. Che, T. Cagin, and W. A. Goddard, *Nanotechnology* **11**, 65, 2001.
[16] M.A. Osman and D. Srivastava, *Nanotechnology* **12**, 21, 2001.

[17]   A. Cummings, M.A. Osman, and D. Srivastava, *Phys. Rev. B.* **70**, 115405, 2004.

[18]   S. Maruyama, *Physica B* **323**, 193, 2002.

[19]   B.T. Kelly, *Physics of Graphite,* Applied Science, London, 1981.

[20]   T.R. Anthony, *Phys. Rev. B* **42**, 1104, 1990.

[21]   J.E. Graebner, et al., *Appl. Phys. Lett.*

[22]   R. Saito, G. Dresselhaus. and M.S. Dresselhaus, *Physical Properties of Carbon Nanotubes*, London: Imperial College Press, 1998.

[23]   D. Zhou and S. Seraphin, *Chem. Phys. Lett.* **238**, 286, 1995; P. Nagy, et al., *Appl. Phys. A: Material Sci. Process.* **70**, 481, 2000.

[24]   J. Li, C. Papadopoulos, and J. Xu, *Nature(London)* **402**, 253, 2000.

[25]   B.C. Satishkumar, et al., *Appl. Phys. Lett.* **77**, 2530, 2000.

[26]   V. Crespi, *Phys. Rev. B* **58,** 12671, 1998.

[27]   A. Anderiotis, et al., *Phys. Rev. B* **65,** 165418, 2002.

[28]   R. Saito, et al., *Phys. Rev. B* **46**, 1804, 1992.

[29]   R. Saito, et al., *Appl. Phys. Lett.* **60**, 2204, 1992.

[30]   L. Chico, et al., *Phys. Rev. Lett.* **76**, 971, 1996.

[31]   Z. Yao, et al., *Nature* **402**, 273, 1999.

[32]   M. Menom and D. Srivastava, *Phys. Rev. Lett.,* **79**, 4453, 1997.

[33]   M. Menom and D. Srivastava, *J. Mat. Res.* **13**, 2357, 1998.

[34]   C. Papadopoulos, et al., *Phys. Rev. Lett.* **85**, 3476, 2000.

[35]   R. Berman, *Thermal Conduction in Solids,* Oxford: Oxford University Press, 1976.

[36]   M. P. Allen and D. J. Tildsley, *Computer Simulations of Liquids*, Oxford: Oxford Science, 1987.

[37]   D. Srivastava, M. Menon, and K. Cho, *Comput. Sci. Eng.* **3**, 42, 2001.

[38]   J. Tersoff, *Phys. Rev. B* **39**, 5566, 1989.

[39]   D.W. Brenner, O.A. Sherendova, and A. Areshkin, *Rev. in Comp. Chem.,* New York: VCH, 213, 1998.

[40]   V.P. Sokhan, D. Nicholson, and N. Quirke, *J. Chem. Phys.* **113,** 2007, 2000.

[41]   S. Portal, *Phys. Rev. B* **59**, 12678, 1999.

[42]   A. M. Rao, et al., *Science* **275,** 187, 1997.

[43]   J. Yu, R. K. Kalia, and P. Vashishta, *J. Chem. Phys.* **103**, 6697, 1995.

[44]   R. Ernst, and K.R. Subbaswami, *Phys. Rev. Lett.* **78**, 2738, 1997.

[45]   R. Saito, et al., *Phys. Rev. B* **59**, 2388, 1999.

[46]   S. Maruyama, *Adv. Numer. Heat Transfer* **3**, 186, 2000.

[47]   P.K. Schelling, S.R. Phillpot, and P. Keblinski, *Phys. Rev. B* **65**, 144306, 2002.

[48]   W. Zhang et al., *Nanotechnology* **15**, 936, 2004.

[49]   F. Muller-Plathe, *J. Chem. Phys.* **106,** 6082, 1997.

[50]   C. Oligschleger and J.C. Schön, *Phys. Rev. B* **59**, 4125 1999.

[51]   E. G. Noya, et al., *Phys. Rev. B* **70**, 115416, 2004.

[52]   A. Maiti, G. Mahan, and S. Pantelides, *Solid State Comm.* **102**, 517, 1997.

[53]   S. Maruyama, Y. Taniguchi, and Y. Shibuta, *Eurotherm* **75**, 2003.

[54]   C. Wei, D. Srivastava, and K. Cho, *Nano Lett.* **2**, 647, 2002.

[55]   J. Brandrup, E. H. Immergut, and E.A. Grulke, Eds., *Polymer Handbook* Vol. 17, 4th edition, New York: John Wiley, 1999.

[56]   S.T. Huxtable, D.G. Cahill, S. Shenogin, L. Xue, R. Ozisik, P. Barone, M. Usrey, M.S. Strano, G. Siddons, M. Shim, and P. Kablinski, *Nature Mater.* **2**, 731, 2003.

[57]   S. Shenogin, L. Xue, R. Ozicik, P. Kablinski, and D.G. Cahill, *J. Appl. Phys.* **95**, 8136, 2004.

[58]   J.X. Cao, et al., *Phys. Rev. B* **67**, 045413, 2003.

[59]   R.A. McDonald and D.H. Tsai, *Phys. Rep.* **46,** No. 1, 1, 1978.
[60]   H.E. Jackson and C.T. Walker, *Phys. Rev. B* **3**, 1428, 1971.
[61]   T.F. McNelly, et al., *Phys. Rev. Lett.* **24**, 100, 1970.
[62]   M.A. Osman and D. Srivastava, *Phys. Rev. B* **72**, 125413, 2005.
[63]   G.D. Mahan, *Phys. Rev. B* **65**, 235402, 2002.
[64]   M.S. Dresselhaus and P.C. Eklund, *Adv. Phys.* **49**, 705, 2000.
[65]   S.S. Savinskii and V.P. Peterovskii, *Phys. Solid State* **44**, 1802, 2002.
[66]   H. Suzuura and T. Ando, *Phys. Rev. B* **65**, 235412, 2002.
[67]   A. De Martino and R. Egger, *Phys. Rev B* **67**, 235418, 2003.

8
Chemical Vapor Deposition of Organized Architectures of Carbon Nanotubes for Applications

ROBERT VAJTAI, BINQING WEI, THOMAS F. GEORGE, AND PULICKEL M. AJAYAN

8.1. Introduction

Carbon nanotubes have been studied extensively since their discovery [1] in 1991, because of the extraordinary physical properties they exhibit in electronic, mechanical, and thermal processes. A single-walled nanotube may be considered as a specific, one-dimensional giant molecule composed purely of carbon, whereas properties of multiwalled nanotubes are closest to those of graphite's in-plane properties, having sp^2 hybridization of carbon bonds. To prepare closed-shell structures, one needs to insert topological defects into the hexagonal structure of graphene sheets. The extraordinary physical and chemical properties [2] and possible applications derived from these properties are attributed to the one-dimensionality and helicity of the nanotube structure.

For different applications, different properties and structures are important. Perfect carbon nanotubes have a high Young's modulus, or others are full of defects, thus providing the possibility for covalent or noncovalent functionalization; individual ones make use of quantum effects; and organized structures have millions of nanotubes to harness their synergy. Above all, the helicity in nanotubes is the most revealing feature to have emerged out of the first experimental [3] and theoretical papers [4–6]. This structural feature has great importance, because electrical properties of nanotubes pronouncedly change as a function of helicity and tube diameter.

Carbon nanotube growth methods can be classified based on the number of walls in a given tube. First, both multiwalled nanotubes [7] and single-walled nanotubes [8, 9] have been grown via arc-discharge carried out in an inert gas atmosphere between carbon or catalyst-containing carbon electrodes. Nowadays, carbon nanotubes and related materials are produced via a wide variety of processes [10], such as several types of the high-temperature arc-discharge method and laser vaporization of graphite targets, as well as numerous different techniques using chemical vapor deposition. The electric arc and laser methods are inherently impossible to scale up; however, these techniques are used routinely to make gram quantities of nanotubes. Nanotube samples produced by these methods are now commercially available in smaller quantities in "as-grown" or purified form.

Chemical vapor deposition (CVD) is a versatile and powerful tool in modern chemistry, chemical engineering, materials science, and nanotechnology. It is presently the most common method for carbon nanotube production, and it is also a well-known method [11] of carbon fiber production. In contrast to other methods, CVD can be scaled up, and there already exist industrial-scale production methods using this technique for nanofibers [12] which are dimensionally similar to the nanotubes discussed above. Furthermore, CVD can be tailored; that is, it can also be used to create oriented nanotube arrays on flat and 3-D substrates. Recent results point to the flexibility and power of the CVD technique, and ultimately, by tailoring the catalyst particles on substrates and controlling the CVD conditions, one hopes to achieve precise control of the nanotube architectures. By providing further control, the ultimate goal of the nanotechnology community is to provide carbon nanotube growth with a predefined number of tubes, with given diameter, helicity, and length along predefined locations.

In the first part of this chapter, we summarize the short history and achievements of the last several years of carbon nanotube growth. We also demonstrate our state-of-the-art methods of tailored nanotube growth and efforts to prepare nanotube structures capable of fulfilling the high expectations for these new and highly advanced materials. We then address applications of carbon nanotubes. Devices based on electron-field emission, low-voltage gas breakdown, filtering on the micro-, nano-, and even molecular scale, and equipment based on the enhanced properties of different composite materials consisting of nanotubes, are explored.

8.2. CVD: The Process and the Structures Grown via CVD

8.2.1. History and State of the Art of CVD of Carbon Nanotubes

In the CVD process, in general, catalytic metal particles are exposed to a medium containing hydrocarbon gases, and the formation of nanotubes is catalyzed. During growth, good uniformity in the size of the tubes is achieved (controlled by the size of the seeded catalyst particles). In some cases, when the catalysts are prefabricated into patterned arrays, well-aligned nanotube assemblies can be readily produced. Similarly, template-based approaches are also in use, where the aligned pores of a nanoporous membrane (such as electrodeposited porous alumina, zeolite, or porous silicon) are filled with carbon species through vapor deposition and later graphitized to produce nanotubes.

In the early years of study of chemical vapor deposition, different parameter ranges for distinguishing multi- and single-walled growth, as well as differentiating the product from carbon nanofibers, were outlined [13–15]. These results basically were the establishment of chemical vapor deposition as a route for carbon nanotube production. After receiving the first batches of carbon nanotubes by this new technique, a wide parameter range opened up for investigation; namely, it turned out that the reaction temperature, catalyst type, geometry, and substrate can

change the properties of the product dramatically. Logically, one needs to optimize the process for purity of the product and also for the yield, where both of these optimizations are still a challenge for scientists. Parallel with this problem, new challenges have arisen: further tailoring the properties of the product distinguishing not only between MWNTs and SWNTs but predefining the diameter, length, and number of walls, and eventually chirality of the tubes needs to be controlled. Success has been achieved in almost all of the directions of tailoring these parameters, although open questions still exist; for example, growth of nanotubes with predefined chirality has not been solved.

Among the processes developed for mass production of carbon nanotubes (SWNTs), we need to emphasize the HiPCO process, optimized for relatively high yield and production rate by scientists at Rice University [16]. The quantity of the product is still behind the amount predicted [17] and its price has not dropped as was expected. Nowadays, this is the most widely available and used SWNT product on the market produced by the CVD technique.

Parallel with the experimental and theoretical work done to explain the role of different parameters in the growth process, it turned out that the mechanism of the growth may be different for every group [10, 18], which means that solving the problem of predefined carbon nanotube growth is equivalent to solving the same problem for a series of independent processes. By now, good progress has been shown in the tailoring of the carbon nanotube length and diameter [19, 20], and the number of nanotube walls also has became a well-controlled parameter. Along with SWNTs and MWNTs, double-walled carbon nanotubes (DWNTs) were also prepared via the CVD method, and their purification was reported [21]. Catalyst material and particle size have been widely investigated [22–28] given their critical role in growth.

Beyond the properties of individual nanotubes, their collective behavior (synergy) is also important for a wide range of applications. First, the most obvious question was investigated: what are the methods to grow carbon nanotubes parallel to each other, and thus produce them in an aligned layer? The first papers reported the growth of blanket nanotube films [29] using a porous template and catalyst layer, or tailoring the location of the growth by focusing the laser beam in order to etch the substrate/catalyst [30, 31].

To think further along these lines, there is a need to control the location of growth while keeping some level of alignment. Most of the methods are based on catalyst deposition onto planar substrates, so patterning the catalyst on the sample surface was evidently a way to control the growth location: a nanotube layer was developed only on that part of the sample covered by catalyst. To prepare the pattern into the catalyst layer, several methods were applied. Dai et al. [32] prepared organized nanotube towers by CVD growth involving catalyst patterning and rational design of the substrate to enhance catalyst–substrate interactions and to control the catalyst particle size. The substrate was planar porous silicon, and the catalyst was a thin iron film evaporated through a shadow mask. The resulting structure consisted of multiwalled carbon nanotubes bound to each other by van der Waals interactions. Similar structures were achieved when the shadow mask

was applied in the CVD process itself [33] to prevent carbon nanotube growth on unwanted locations, and also to keep the shape of the grown nanotube towers. Furthermore, microcontact printing is a simple but powerful method to prepare a large area of lower-resolution catalyst patterns. A stamp may be applied to print catalyst-containing ink onto the substrate, and later carry out selective nanotube growth only on the printed areas [34].

A higher-level control was established in the CVD process when Duesberg et al. produced small vertical bundles of carbon nanotubes in lithographically defined, submicrometer-sized holes of the template [35, 36]. Similarly high-level control was achieved in the structures when Dai et al. [32] presented a method for controlled synthesis for free-standing single-walled and multiwalled nanotubes with directed orientations. Their process starts with silicon/silica tower fabrication, followed by catalyst deposition from the liquid phase using a block copolymer providing the necessary catalyst parameters. Extensive calcination and subsequent CVD growth with the substrate yielded SWNTs emanating from the towers. Directed freestanding SWNT networks are formed by nanotubes growing to adjacent towers and suspended above the surface.

In summary, we list the main parameters of the chemical vapor deposition of carbon nanotubes: the temperature of the growth, the carbon source, the materials and size of the catalyst, and the materials and surface properties of the substrate.

8.2.2. Floating Catalyst Method for Selective Growth of Carbon Nanotube Layers Using Ferrocene as a Catalyst

According to our experimental results [37], selectivity may be achieved by gas-phase catalyst delivery [38–40] on lithographically machined planar and nonplanar templates consisting of oxidized silicon surfaces. Our bottom-up fabrication approach is easy to carry out, scalable to large areas, and compatible with standard silicon microfabrication technology. In this specific CVD process, nanotube structures are designed and built first on planar patterns composed of SiO_2 and Si; most of the substrates used in this study were Si(100) wafers capped with a 100-nm-thick silica layer, however, below we discuss the case of thick silica layers (up to 8.5 μm).

In this process, patterns of Si/SiO_2 of various shapes were generated by photolithography. No catalyst material—generally required for CVD growth of nanotubes—was deposited or patterned on the substrates, thereby simplifying the template preparation to a great degree and diminishing the possibility of catalyst size changes in the heating-up period of the CVD process. Instead, growth of nanotubes is stimulated by exposing the substrate to a xylene/ferrocene vapor mixture at 750–850°C. A schematic of the experimental setup is demonstrated in Figure 8.1

In our experiments, nanotubes are grown on thermally oxidized silicon wafers by the CVD of xylene (C_8H_{10}), and ferrocene ($Fe(C_5H_5)_2$). Ferrocene is dissolved in xylene at concentrations of 0.01 g/ml, preheated at about 150–180°C, co-evaporated and fed into the CVD chamber, which was pumped down to a

Gas Flow
Control

Sample in Alumina Boat

Tube Furnace

Liquid Nitrogen Trap

Flow
Control

Temperature Control
of the Tube Furnace

Tank for Carbon Source/
Catalyzer Mixture

Thermocouples

Pressure Gauges

Evaporator &
Control
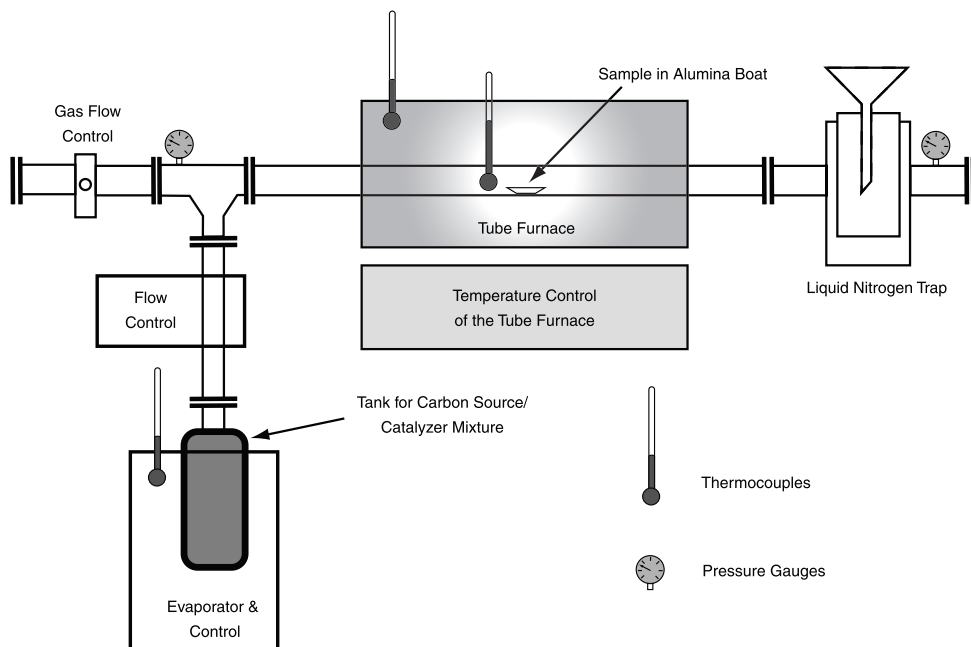
FIGURE 8.1. Experimental setup (schematic) for CVD of carbon nanotubes onto substrates using the floating catalyst method. The inert gas flow provides oxygen-free atmosphere, and the carbon source/catalyst solution is evaporated from a separate bubbler.

vacuum level on the order of 10^{-3} torr, backfilled with flowing argon to a pressure of about 100 mtorr, and heated up gradually to the desired reaction temperature.

8.3. Carbon Nanotube Structures Grown by Chemical Vapor Deposition

Another interesting and even more useful property of our floating catalyst method is the substrate selectivity [41,42], namely nanotubes grown perfectly aligned with respect to each other and normal to the substrate, and on the oxide only (neither on Si nor on the native oxide layer of Si). This allows one to obtain predefined carbon nanotube structures very easily and with all complexity by simply patterning SiO_2 on Si wafers (a common technique in the semiconductor industry); examples of this growth are displayed in (Figure 8.2).

Results for the structures grown by this method were published [37,43] where nanotube platelets were selectively placed on specified sites. Highly aligned nanotubes grow on the SiO_2 patterns in a direction normal to the substrate surface, and the selectivity is retained down to micron-sized SiO_2 templates. No nanotube
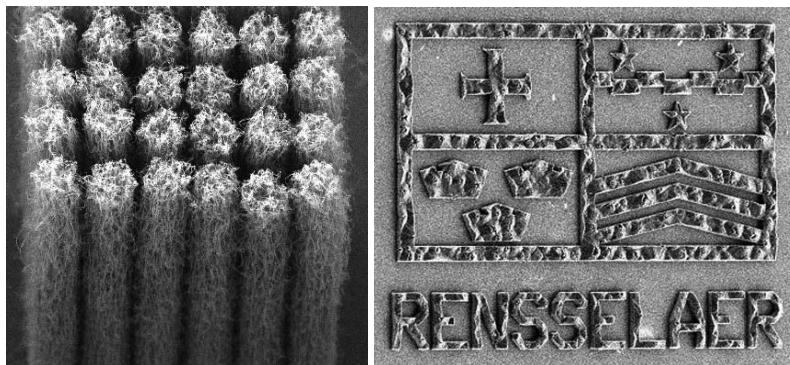
FIGURE 8.2. Substrate-dependent growth of multiwalled carbon nanotubes on planar SiO_2 and Si substrates by exposing them to a precursor of ferrocene and xylene at 800°C. (a) Platelets of aligned carbon nanotube arrays (SEM images) grown vertically on the micron-sized patterns. Alignment of nanotubes can be easily identified on the sidewalls. (b) Micromachined flag and name of RPI created from vertical arrays of carbon nanotubes.

growth is observed on pristine Si surfaces or on the native oxide layer, but micron-sized platelike blocks of vertically oriented nanotubes are grown from the underlying SiO_2 pattern. The height of these blocks can be precisely controlled to obtain microscale domains in the range of 10 to 100 μm (for the best results) by tuning the deposition time. The key characteristics of our process, its substrate-selectivity and normal growth to the surface provide the foundation for assembling tailored nanotube architectures of various shapes by machining the appropriate SiO_2/Si pattern by conventional lithography. In addition to the simple platelet blocks, one can build other shapes (e.g., circular, square, triangular, rectangular, trapezoidal) and blanket nanotube films with predefined hole size, density, and shape, or follow any arbitrary shape (Figure 8.2b).

In all cases of the growth, we observe reasonably good adhesion between individual nanotubes within each geometrical block and between the nanotubes and the substrate, presumably through van der Waals attraction. Each nanotube block, however, can be detached from the substrate and can be manipulated individually. Similar substrate-selective growth can be achieved on different faces of MgO crystals [44], Ni wires [45], by gold masking [46], and promoted growth on Pd seeds [47].

The task of finding the reason for substrate selectivity naturally arises. In the process, an abundance of particles is formed and depleted on the silicon surface, but these particles apparently do not aid the carbon nanotube growth. A very similar film of particles is observed on the silicon oxide surface where nanotubes grow. The particle size was characterized to be around 20–40 nm on the silicon oxide region, but slightly larger in the Si region. Measurements made by an electron probe microanalyzer (EPMA) and by Auger electron spectroscopy

(AES) indicate that iron and carbon are dispersed over both the silicon and the silicon oxide region. Cross-sectional TEM observation [42] of the substrates show that particles on top of silicon oxide surfaces are made of pure gamma iron (fcc Fe), and the silicon surface diffraction patterns show the presence of iron silicide and iron silicate, where such materials are not effective for carbon nanotube catalysis.

8.4. Directed Growth of Carbon Nanotubes by Floating Catalyst Method on 3-D Substrates

As mentioned above, the site-selectivity of the floating catalyst CVD method is a powerful tool to design structures used in three-dimensional structures such as MEMs and NEMs. To demonstrate this feat, we have shown simultaneous multidirectional growth and multilayered growth of ordered nanotubes. To provide depth for horizontal growth, thick silica layers (up to ~8.5 μm) were deposited by plasma-enhanced chemical vapor deposition (PECVD) to create high aspect ratio silica features. Similarly to the thin silica layers we used for planar substrates, patterns of Si/SiO_2 of various shapes were generated by photolithography followed by a combination of wet and/or dry etching. CVD growth of nanotubes is stimulated by exposing the substrate to xylene/ferrocene vapor mixture at 800°C, as described above.

Simultaneous multidirectional growth of highly oriented nanotubes can be harnessed to simultaneously grown nanotubes in several predetermined directions. For instance, we can realize nanotube growth in mutually orthogonal directions by using templates consisting of deep etched trenches separating at least several-μm-tall and -wide SiO_2 towers or lines. Figure 8.3). displays vertically and horizontally aligned nanotube arrays as well as more complex multidirectional growth of the MWNT layers. In the case of trenched substrate, MWNT layers are adjacent to each other, providing an excellent example that demonstrates the concept.

We are also able to create structures where the nanotubes have oblique inclinations (i.e., neither orthogonal nor planar with respect to the substrate plane) by using deep-trench templates with inclined silica surfaces into the displayed "daisy" shape or other illustrative examples, where nanotubes grow normal to the walls of such circular trenches, resulting in membranelike iris-shaped structures. These examples also show the flexibility of our approach to obtain radially oriented nanotubes with the entire spectrum of in-plane orientations on the substrate plane. Multilayer growth of ordered nanotubes may be carried out by selective nanotube growth on SiO_2 in a direction normal to the surface on partially free-standing silica architectures. Figure 8.3c shows an example of this type of growth, where nanotubes grow in two opposite directions (up and down) from a suspended SiO_2 layer. This suspended transparent layer of silicon oxide (thickness is about 8 μm) on a silicon base pillar is generated by photolithography and deep etching (40–50 μm) of Si wafer.
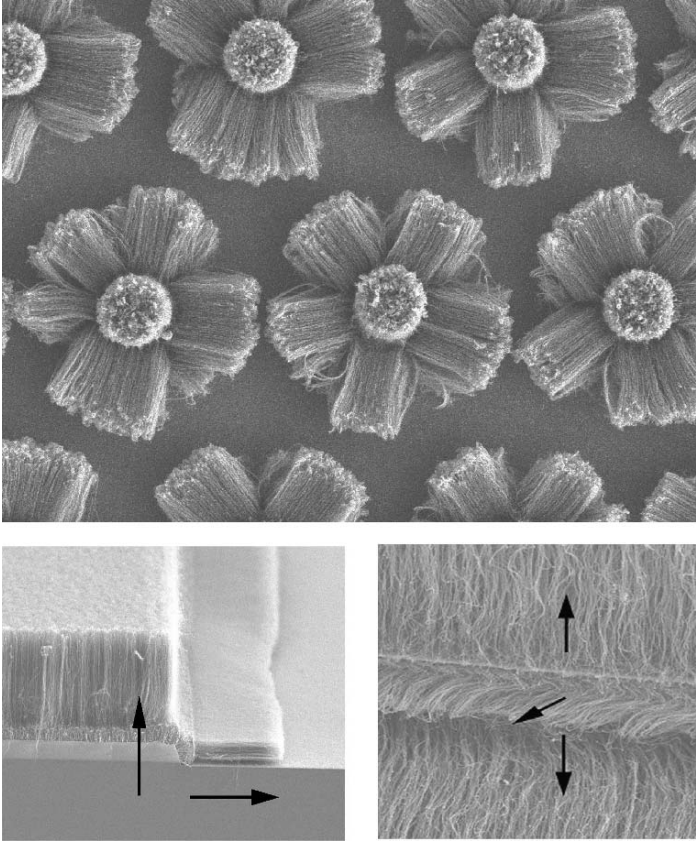
FIGURE 8.3. Extended three-dimensional patterns made of ordered multiwalled carbon nanotube films provide insight into multidirectional growth on a complex surface. (a) "Daisies" grown from truncated cones of SiO_2 on a silicon wafer. (b) Simultaneous vertical and horizontal aligned nanotube arrays of nanotubes grown on a template with deep etched trenches, where the length of nanotubes in both vertical and horizontal growth is about 60 micrometers, and the thickness of the SiO_2 layer is 8.5 micrometers. (c) Multilayer growth of carbon nanotubes into three dimensions on the edge of a free-standing plate of an 8.5-micron thick silica disk (up, down, and out) identified by arrows.

8.5. Freestanding Macroscopic Tubes Made of Carbon Nanotubes

By fabricating these robust membranelike structures made of multiwalled carbon nanotubes, we have demonstrated [48] for the first time that such a large number of nanotubes can be organized into one structure, and at the same time that the resulting macroscopic structure can be used for various separation processes with its nanoscale structures. Utilizing the continuous CVD method, we have
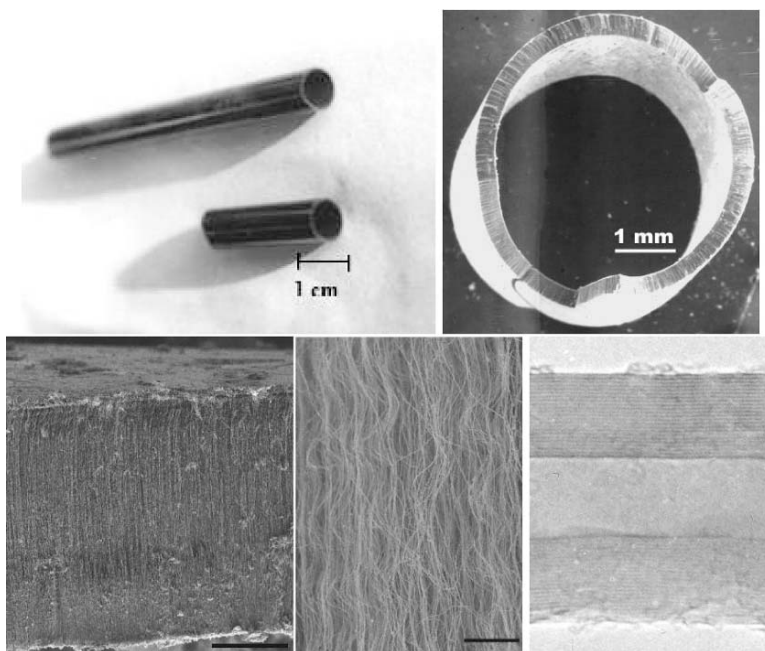
FIGURE 8.4. Macroarchitecture and structure of aligned nanotubes grown for use in filtration applications. (a) Photograph of the bulk tube made of exclusively carbon nanotubes. (b)–(d) Different magnification SEM images of the aligned tubes with radial symmetry resulting in hollow cylindrical structure. (e) HR-TEM image to depict the structure of the carbon layers of a multiwalled nanotube.

synthesized macroscale hollow carbon cylinders up to the centimeter scale in diameter and several centimeters in length, with wall thickness of 300 to 500 μm. The aligned nanotubes grow in radial directions on the walls of removable silica tube templates, leading to the formation of freestanding and continuous hollow cylindrical carbon tubes (Figure 8.4). Detailed structural characterization of the CNT (carbon nanotube) macrotube is shown in Figure 8.4c–e.

The length of the MWNTs corresponds to the wall thickness of the bulk structure, and the dense packing of these aligned structures is also visible. Figure 8.4e displays a high-resolution TEM image of a typical nanotube in the macrotube assembly, showing the well-graphitized walls of the MWNT. The ranges of inner and outer diameters of these nanotubes are found to be 10–12 nm and 20–40 nm, respectively, from TEM analysis. The macrotube is found to be mechanically very stable. The macroscopic tube remains stable even after ultrasonic treatment, showing the high mechanical stability of the assembled carbon architectures. We also have performed direct tensile tests on various small pieces (1–2 mm wide) of the assembled structure by applying a load parallel to the bulk tube axis. Three-point bend tests on these bulk structures have been performed to quantify the

breaking strength; the fracture load (at the weakest point) of the tube is found to be 2 N.

8.5.1. Microbrushes Made from Carbon Nanotubes

Applying our experience in three-dimensional, selective carbon nanotube growth techniques, we have constructed multifunctional conductive brushes with carbon nanotube bristles grafted on fiber handles, and demonstrated their several unique tasks such as cleaning of nanoparticles from narrow spaces, coating of the inside of holes, selective chemical adsorption, and as movable electromechanical brush contacts and switches [49]. The nanotube brush consists of a silicon carbide fiber as the handle and aligned multiwalled carbon nanotubes grafted on the fiber ends as bristles.

In the CVD process to produce multifunctional nanotube brushes, the continuous version of the above-mentioned CVD process was applied: a solution made by dissolving 0.3 g ferrocene into 30 ml xylene was injected into the furnace at a constant speed (0.5 ml min^{-1}). Argon was flowed to carry the solution into a preheated steel bottle (180°C) before entering the furnace. SiC fibers were placed into the middle of the furnace in an alumina boat. The typical reaction temperature was 800°C, and the growth time took 10 minutes to 1 hour.

Vertical placement of SiC fibers usually yields three nanotube prongs surrounding the fiber. (Figure 8.5). The formation of a three-pronged morphology is due to the self-organized growth of dense nanotube arrays as they grow outwards from the cylindrical surface, having circular cross-section, as the circumference surrounding the nanotube front surface is enlarged as the front moves away from the fiber nanotube interface. Two- and one-pronged structures were obtained by laying the
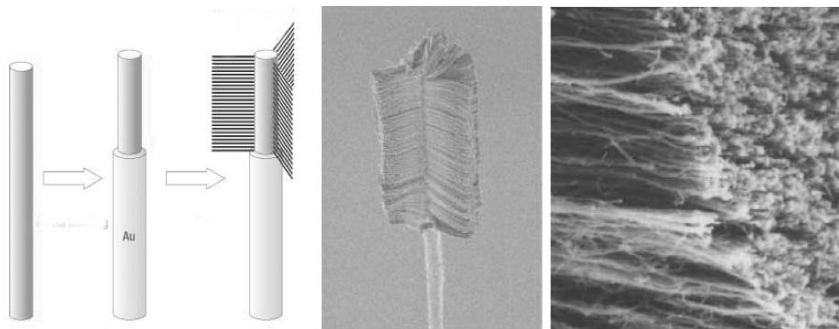
FIGURE 8.5. Nanotube brush preparation via masking the unwanted areas of the SiC fiber with gold and the resulting structure. (a) Ilustration of partial masking of SiC fibers in order to grow nanotubes only on the top part of the fiber. (b) SEM image of an as-grown brush (resembling a dust sweeper) consisting of nanotube bristles and a fiber handle. The bristles have a length of 60 μm, and span of over 300 μm along the handle. (c) Higher-magnification SEM image to demonstrate the structure of the tip of the nanotube brush.

fibers down on a flat surface during CVD, to block the nanotube growth in several directions. Shadow-masking of gold on the fibers was applied in a 50-mtorr Ar plasma at constant current of 30 mA with fiber ends (or other portions) covered by an aluminum foil. A 15-nm-thick Au layer was used for effective masking (inhibiting nanotube growth).

8.5.2. Controlled Fabrication of Hierarchically Branched Carbon Nanotubes in Pores of Porous Alumina

Along with the floating catalyst method, we have developed a rational approach for creating hierarchically branched nanoporous anodic aluminum oxide (AAO) templates and have fabricated a whole generation of branched nanowires and nanotubes inside these templates [50]. First, AAO templates were prepared by using a modified two-step anodization process. The first-step anodization was the same for all templates: high-purity Al foils were anodized in 0.3 M oxalic acid solution at 8–$10°$ C under a constant voltage. Then, the formed anodic aluminum layer was removed. In the second-step anodization, templates with different pore architectures underwent different processes of anodization, namely, the voltage of the anodization was changed in order to receive different number of channels. Reduction of the voltage by $2^{-1/2}$ results in Y-branched pores, and using this reduction multiple times, two-, three-, and four-generation Y-branched pores could be obtained. To form multiple channels we needed to diminish the anodization voltage by factor of $n^{-1/2}$, where n is the number of the created channels. Typically, after the anodization for the stem pores, we cleaned the remaining oxalic acid solution in the pores in deionized water and thinned the barrier layer at the pore bottom by immersing the samples in phosphoric acid. Of course, by subsequent reduction of the anodizing voltage by the above factors, we can generate second-generation multibranched pores growing from each of the first-generation multibranched pores.

To grow carbon nanotubes in an AAO template, we applied pyrolysis of acetylene [51–53] at $650°$C for 1–2 h with a flow of gas mixture of Ar (85%) and C_2H_2 (15%) at a rate of 35 mL/min. After the CVD process, carbon nanotubes were released from AAO templates by dissolving the templates in HF solution and then washed with deionized water several times. The nanotubes are deposited inside the pores by the pyrolysis of acetylene without using any catalyst material. The nanotubes grown here were multiwalled ($\sim$4–10 walls), have a diameter range of 20–120 nm, and are graphitic in nature. The wall thickness (and hence the number of walls) falls within a very narrow range of 1–4 nm. We normally observed a small reduction in the number of walls (approximately two or three walls) as a larger tube changed into smaller ones, and this reduction seemed to happen quite abruptly. To demonstrate these structures, Figure 8.6 shows an example of a complex structure, where two levels of multiple branching are grown. The primary stem splits first into three branches, each of which further splits into three subbranches. The high-magnification SEM images of the interface reveal the junctions, showing the branching and the reduction in diameters as the branching occurs.
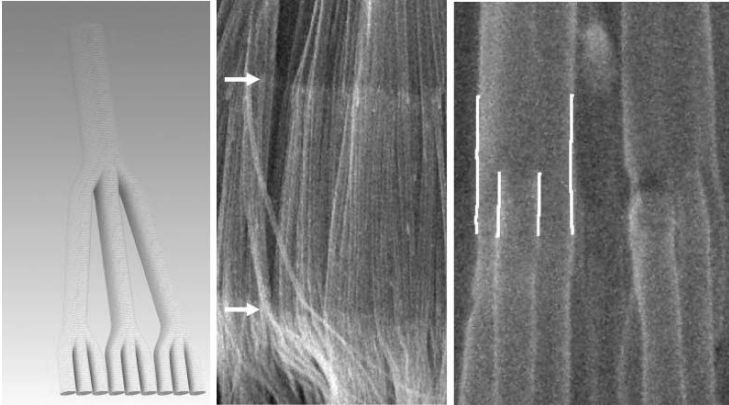
FIGURE 8.6. Hierarchically branched, open-ended nanotubes grown by the template-based chemical vapor deposition technique. (a) Schematic displaying a carbon nanotube stem splitting into three branches, and afterward again into three branches (1-‹ 3-‹3 structure, where the symbol -‹ denotes the branching). (b) SEM image of the branched nanotubes, where the location of the junctions are highlighted with white arrows. (c) Higher-magnification SEM image showing several stems and the branches emerging from them.

8.6. Applications of the Structures

Carbon nanotubes have many advantages over conventional materials and devices because of their unique electrical, mechanical, and physical properties [54]. They show promise in a large number of areas, and are being researched and studied exhaustively as flat panel displays [55], ionization sensors [56], fuel cell technology [57], energy storage [58], molecular electronic interconnects for an IC chip [59], advanced composites [60], and as tips of scanning probe microscopes [61]. A key obstacle to commercialization continues to be the need for cost-effective, large-scale production methods.

Other applications of carbon nanotubes include their potential use as atomic force microscopy/scanning tunneling microscopy (AFM/STM) tips, for analyzing DNA, and to create longer-lasting batteries/supercapacitors. Nanotube ropes and fibers show promise and can be revolutionary structures for the future, more than 100 times stronger than steel wool and may be used in armor and, eventually, even cars [62–66]. High-quality flat-screen televisions might be made in the future using field emitter arrays, whose performance is very much better than the liquid crystal display and plasma screen televisions of today. These wide ranges of applications have suggested the exciting and versatile nature of carbon nanotubes. Below, we cover only a fraction of all the prospective applications of ordered nanotube architectures for electron field emission sources, ionization sensors, membrane filters, and nanocomposites.

8.6.1. Electron Field Emission Sources

Carbon nanotubes exhibit very good field emission compared to metallic emitters. Such application as an emitter was first reported in 1995 [67,68] and has since been studied intensively on various CNT materials, including individual nanotubes [69], multiwalled nanotubes (MWNT) embedded in epoxy matrices [70, 71], MWNT films [68, 72], single-walled nanotubes (SWNT) [73–76], and aligned MWNT films [77]. A potential difference is applied between a nanotube or film of nanotubes as a cathode and Al-coated silicon surface as an anode, while maintaining a pressure of around 10^{-6} torr in the inert atmosphere in the chamber. Single nanotubes are used as electron guns for emitting a highly coherent electron beam. A film of nanotubes can be used for flat panel displays. The gap between the electrodes is very small, tens of micrometers. Applying a voltage/electric field to the carbon nanotubes causes electrons to be emitted from the sharp tip of the nanotubes, producing a current. The required turn on the field is low, around 5 V/μm, making the carbon nanotube a promising alternative to metallic emitters. Typical currents of a few A/cm^2 have been obtained on samples of sizes around 4 cm^2 for these low fields. The low voltage required is due to the concentration of the electric field at the tips of the tubes, called the "field amplification effect." This effect is pronounced for long vertical nanotubes with a small diameter, that is, high aspect ratio.

From ultraviolet photoelectron spectroscopy measurements, the aligned MWNTs are found to have a larger density of states at the Fermi level and a slightly lower work function than the random MWNTs, which is attributed to the difference between the electronic states of the tip and the sidewall of the CNT [78]. Because the electrons are emitted from the tips of the CNTs, intuitively one would expect that the vertically aligned CNTs are better emitters than the random films. However, this issue is complicated by the effect of electrical screening. Most of the vertically aligned MWNTs fabricated by the CVD process comprise densely packed CNTs. As a result, they do not show enhanced emission properties as expected. By lithographically patterning the location of the catalysts on the substrates as described in the previous sections, we could have patterned aligned CNTs with controlled spacing to minimize the screening effects.

Today, the most mature technology to produce gated microfield electron emitter arrays is the so-called Spindt-type metal microtip process. The drawbacks of the Spindt-type process are the expensive production, the critical lifetime in a technical vacuum, and the high operating voltages. Carbon nanotubes can be regarded as the potential second-generation technology to Spindt-type metal microtips. The use of carbon nanotubes as field-enhancing structures in field emission electron sources can bring several advantages such as longer lifetime and operation in poor vacuum due to the high chemical inertness as well as low operation voltages and perhaps most important, very low cost production techniques. In addition, carbon nanotubes do not suffer from thermal runaway at high temperatures.

Several prototype applications have been reported. For example, cathode ray lighting elements with carbon nanotubes as field emitters have been fabricated by Ise Electronics Co. in Japan, and they have twice the intensity as those of conventional thermionic cathode ray tube lighting elements operating under similar

conditions [79], flat panel displays developed at Sony and Samsung [55], and gas discharge tube (GDT) protectors demonstrated by the University of North Carolina at Chapel Hill and Raychem Co. for telecom network applications [80]. The enhanced performance shows that the nanotube-based GDTs are attractive over-voltage protection units in advanced telecom networks such as an asymmetric digital signal line, where the tolerance is narrower than what can be provided by current commercial GDTs.

8.6.2. *Ionization Sensors*

Taking advantage of the low electron emission voltages from nanotube sharp tips, an interesting application of the aligned nanotube arrays as ionization sensors, which was used to detect different gases in a mixture [56], has been recently reported based on our experimental results. The CNTs enjoy advantages over the currently used ionization sensors in terms of size, a simple operation, and not being affected by external conditions such as temperature and humidity. The setup used is similar to that for field emission with the nanotubes as anode and an Al sheet as cathode, separated by a vacuum at a pressure of 10^{-4} torr with a small spacing of about 150 μm. The gas that needs to be analyzed then is allowed to flow into the chamber. The voltage and current are monitored by an ammeter and voltmeter, which is important because as the voltage is increased, the gas is ionized within a small portion of the tips of the nanotubes. This cloud of ions then gains energy from the field and generates more electron-hole pairs. Furthermore, more electron-hole pairs are formed until an avalanche breakdown of the gas occurs by a discharge between the two electrodes. This voltage at which the breakdown occurs is unique for each gas and is referred to as the "breakdown voltage," which is a fingerprint of each gas. The surge current plays an important role, indicating the concentration of that gas. Proper measurement of the breakdown voltage can identify the gas present in the chamber. Some examples of the gases detected are helium, ammonia, argon, and oxygen, at a constant gas concentration of 4×10^{-2} mol/l as shown in Figure 8.7. The breakdown voltage values for individual gases remain the same even at different concentrations of the gas, showing unique values for the gases.

8.6.3. *Membrane Filters*

As discussed before, aligned carbon nanotubes can be synthesized controllably not only on flat or patterned substrates, but also on curved substrates, and could be easily removed from the substrates. We have reported the fabrication of freestanding monolithic uniform macroscopic hollow cylinders having radially aligned carbon nanotube walls, with diameters and lengths up to several centimeters [48]. These cylindrical membranes are used as filters to demonstrate their utility in two important settings: the elimination of multiple components of heavy hydrocarbons from petroleum—a crucial step in postdistillation of crude oil—with a single-step filtering process, and the filtration of bacterial contaminants such as *Escherichia coli* or nanometer-sized poliovirus (∼25 nm) from water (Figure 8.8). These macrofilters
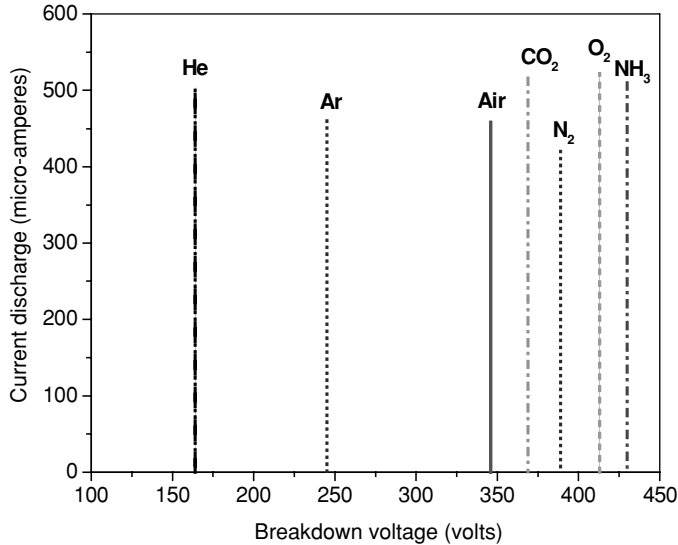
FIGURE 8.7. I–V curves for NH_3, CO_2, N_2, O_2, He, Ar and air, showing distinct break-down voltages. Ammonia displays the highest breakdown voltage, and helium the lowest [56].
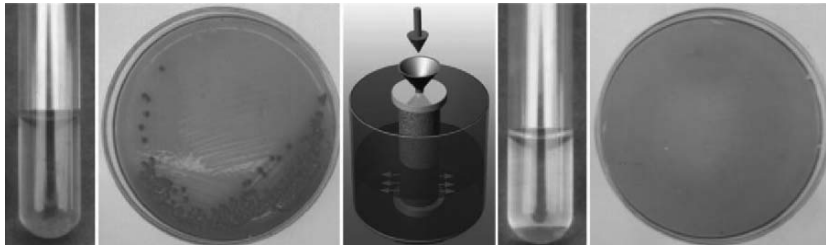
FIGURE 8.8. Removal of bacteria using a nanotube filter. (a) Unfiltered water containing E. coli bacteria; the turbid and light color is suggestive of the presence of bacteria colonies scraped from the surface of MacConey agar, which contains Phenol red as an indicator. (b) Colonies of *E.coli* bacteria grown by the culture of the polluted water. (c) Assembly for the filtration experiment. The nanotube filter with the bottom end-capped is placed inside a container, and the liquid flows through the macrotube (shown by the vertical arrow). The horizontal arrows show the flow direction of the filtered liquid. (d) Water filtered through the nanotube macrofilter. The product obtained is relatively clear compared with the original bacterial suspension in (a), indicating the absence of the bacteria (as well as coloring particles) in the filtrate. (e) Filtrate after culture, showing the absence of the bacterial colonies [48].

can be cleaned for repeated filtration through ultrasonication and autoclaving. The exceptional thermal and mechanical stability of nanotubes, and the high surface area, ease, and cost-effective fabrication of the nanotube membranes, may allow them to compete with ceramic- and polymer-based separation membranes used commercially.

A major advantage of using nanotube filters over conventional membrane filters lies in the fact that they can be cleaned repeatedly after each filtration process to regain their full filtering efficiency. A simple process of ultrasonication and autoclaving ($\sim$121°C for 30 min) has been found to be sufficient for cleaning these filters; cleaning can also be achieved by purging for the reuse of these filters. In conventional cellulose nitrate/acetate membrane filters used in water filtration, however, strong bacterial adsorption on the membrane surface affects their physical properties preventing their reusability as efficient filters [81]; most of the typical filters used for virus filtration are not reusable [82]. Because of the high thermal stability of nanotubes, nanotube filters can also be operated at temperatures of $\sim$400°C, which are several times higher than the highest operating temperatures of the conventional polymer membrane filters ($\sim$52°C). The nanotube filters, owing to their high mechanical and thermal stability, may compete with commercially available ceramic filters; furthermore, these filters may be tailored to specific needs by controlling the nanotube density in the walls and the surface character by chemical functionalization.

8.6.4. Nanocomposites

Nanocomposites based on carbon nanotubes have always been at the research front owing to their tremendous applications [83]. Recently, there has been significant scientific and technological interest in developing nanotube–polymer composites for applications requiring unique combinations of properties [84]. Nanotube polymer composites have shown promise in applications such as ultrafast all-optical switches [85], electromagnetic interference (EMI) shielding [86], photovoltaic devices [87, 88] gas sensors [89], and biocatalytic films [90]. The potential of these nanocomposites, however, has yet to be fully exploited. Some of the main limitations are lack of control over the orientation and dispersion of nanotubes in a polymer matrix, as well as the tailoring of the nanotube–polymer interface [83, 91, 92].

One approach to simultaneously control the nanotube alignment (especially in the third dimension) and the nanotube dispersion in a polymer is to infiltrate monomers into the prealigned arrays of nanotubes, followed by in situ polymerization [84]. The nanotubes grown by CVD are homogeneously distributed, and not bundled, which is an advantage over the bulk nonaligned nanotubes prepared by other techniques. The resulting composite films have good distribution, dispersion, and alignment of nanotubes in a polymer matrix, and they also provide reinforcement in the out-of-plane direction (Figure 8.9). In addition, MWNTs retard the oxidative thermal degradation of polymethyl-methacrylate (PMMA) by stabilization of macroradicals formed during the degradation process. The thermal stability of PMMA from thickness-aligned MWNT-PMMA films is improved due
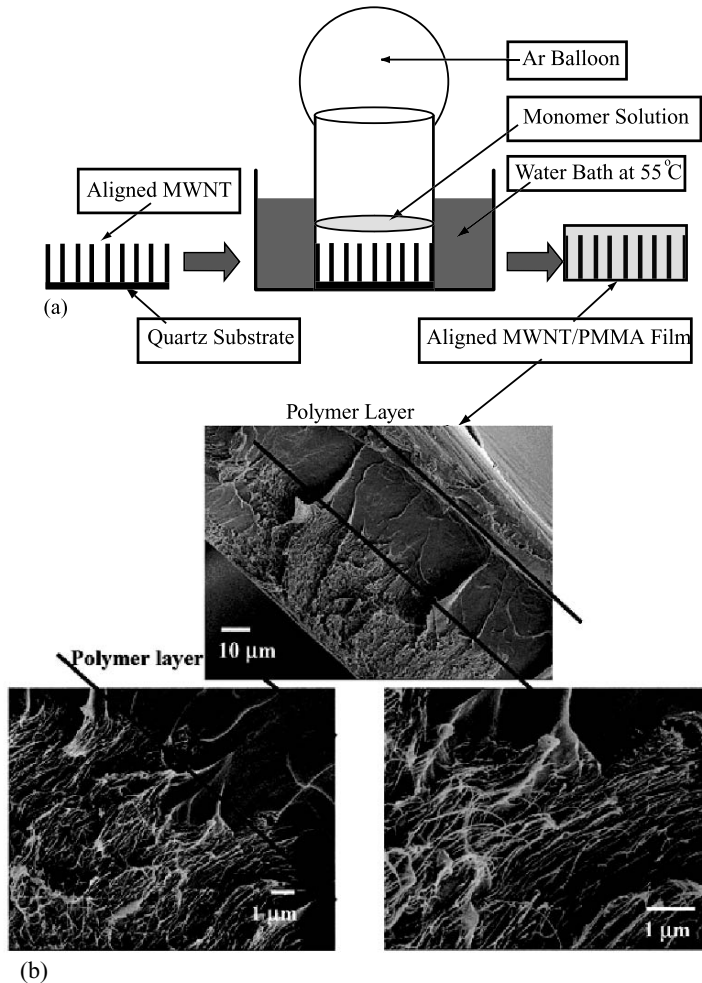
FIGURE 8.9. Schematics of process for making thickness-aligned MWNT/PMMA films: (a) Composite synthesis; (b) Cross-section of MWNT/PMMA films shows thickness-aligned MWNT (∼30 μm long) in PMMA matrix. An extra polymer (∼20 μm) is observed over the nanotube arrays [84].

to the large surface area offered by well-dispersed MWNT for interactions with PMMA macroradicals. This novel, two-step synthesis strategy has tremendous implications toward building some of the novel architectures with nanotubes and polymers, having unique properties (Figure 8.11).

Another important application for nanotube composites is based on their unique mechanical properties, that is, damping behavior [60, 93]. We have found that by using nanotube-epoxy films as interlayers within laminate composite systems (schematics in (Figure 10), the nanotube layer reinforces the interfaces between
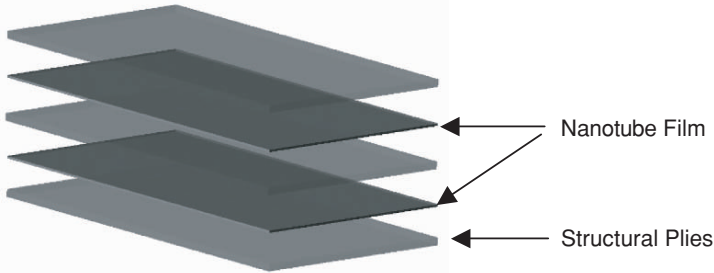
FIGURE 8.10. Composite laminates with integrated carbon nanotube films [94].

composite plies, enhancing laminate stiffness as well as structural damping. The experiments conducted using a piezosilica composite beam with an embedded nanotube-film sublayer indicate up to 200% increase in the inherent damping level and 30% increase in the baseline bending stiffness with minimal increase in structural weight. Scanning electron microscopy (SEM) characterization of the nanotube-film reveals a fascinating network of densely packed, highly interlinked multiwalled nanotubes [94]. This intertube connectivity results in strong interactions between adjacent nanotube clusters as they shear relative to each other, causing energy dissipation within the nanotube-film. The cross-links between nanotubes also serve to improve load transfer within the network, resulting in improved stiffness properties (Figure 11).

The advantages of using a nanotube-epoxy film as a damper are obvious. Firstly, traditional viscoelastic polymers degrade in performance at elevated temperatures. The operating range for commercial damping films varies in the range of 0–100°C. Carbon nanotubes can withstand high temperature without any significant degradation in nanotube structure-properties. Typically, oxidation of carbon nanotubes in air begins at 600°C. Within composite laminates (embedded films), the nanotubes could potentially sustain even higher temperatures without significant loss in performance. Consequently, for high-temperature applications nanotube films would offer superior performance and reliability.

Secondly, the stiffness of traditional viscoelastic damping polymers is much lower than the host composite structure. Carbon nanotube films on the other hand offer multifunctionality in terms of enhanced strength, stiffness, and fracture toughness, in addition to damping augmentation. The specific stiffness (stiffness/density ratio) of the nanotube-epoxy film developed is about three orders of magnitude greater than the Dyad-606 polymer film [94, 95].

Thirdly, the integration of viscoelastic damping films within composite systems poses significant technical challenges [94, 96]. When damping materials are co-cured with the host composite, the viscoelastic material experiences the temperature cycle of the cure. Commercially available damping materials have maximum recommended temperatures below that of the composite cure cycles. Moreover, there is a strong interaction between the resin (epoxy) and the damping material at elevated temperatures. Resin penetration into the damping material can result in up to 93% reduction in the material loss factor [94]. Carbon nanotubes are stable
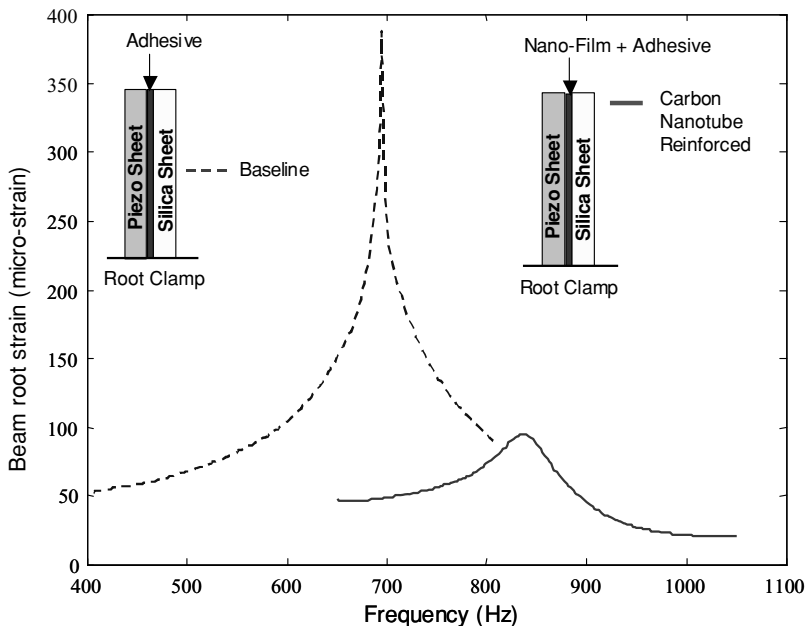
FIGURE 8.11. Comparison of the dynamic response of the baseline beam and nanotube reinforced sandwich beam for a frequency-sweep test at 50 Vrms. (cantilevered length of 22.86 mm) [60].

at temperatures well beyond composite cure cycles and do not exhibit degradation in structure/properties due to resin penetration; for these reasons carbon nanotube films could potentially be seamlessly integrated within composite/heterogeneous systems.

8.7. Future Perspectives, Challenges, and Possible Solutions

The CVD technique has become quite a versatile technique in the fabrication of carbon nanotubes, particularly in designing vertically aligned multiwalled carbon nanotubes on various substrates, as we have discussed in the previous chapters. It will be interesting to see the perspective on what awaits this technique in the controlled growth of nanotubes in the future. Certainly the technique has evolved over the years to accommodate a large number of precursor hydrocarbons and catalysts to produce structures that otherwise would have been thought difficult to grow. One good example is the growth of vertically aligned growth of single-walled nanotube (SWNT) arrays [97]. Recent developments incorporating water, or the use of oxygen-containing precursors (e.g., methanol) in the CVD process have produced beautiful aligned arrays and patterns of SWNT, similar to those we have shown here for MWNT. Applications of these dense SWNT arrays in microelectronics could be more compelling than MWNT. Similarly the CVD technique could be precisely

controlled (by adding elements such as sulphur, e.g.) to produce precise numbers of walls for individual nanotubes; large assemblies of nanotubes, all of which contain just two walls [21, 98] is a case in point. As we learn more about the conditions, process windows, catalyst promoters and poisons, and the growth mechanisms that produce nanotubes of different kinds, we are slowly being able to optimize CVD to design and fabricate nanotubes and nanotube patterns to our liking.

The growth mechanism of nanotubes grown by CVD is still somewhat of a puzzle, although new revelations are being reported. A recent paper [18] that looks at the growth in situ inside an electron microscope suggests that the structure and stability of the catalyst particles have a lot to do with the nanotubes that are formed during the process. The particles seem to remain in a constantly fluctuating structural state, driven by the energetics involved in the absorption and removal of carbon arising from the high-temperature vapor phase interaction of the metal particle with hydrocarbon gas, and the shape changes (spherical to elongated and vice versa) dictate the way nanotube morphologies precipitate around the particle (Figure 12).

These are still only small pieces of the puzzle pertaining to specific interactions between catalysts and carbon precursors and a general mechanism, which would explain how the nanotubes form at the atomic scale, is still a problem at large. We only know that a metal particle is responsible for the catalytic growth of a nanotube but not the sequence of steps that lead to its formation. It is only when this puzzle is resolved, either through some intuitive and large-scale simulations or through a sophisticated set of time-resolved experiments, that we will be able to churn out designer nanotubes of any kind in structure (e.g., chirality, which still remains a holy grail in nanotube growth), morphology, and dimensions. Until then the growth of nanotubes by CVD will remain a trial-and-error method, with optimized schemes
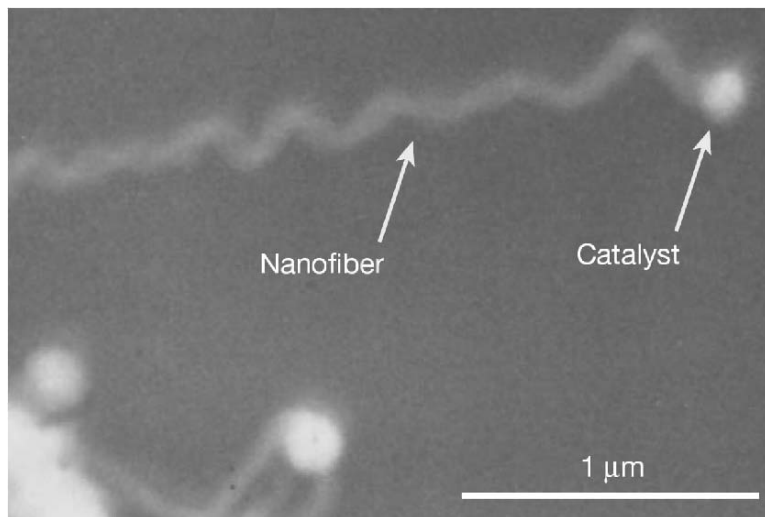
FIGURE 8.12. Nanofiber growth: At high temperatures, and in the presence of a catalyst, vapor phase hydrocarbon molecules dissociate. This process is the base of the growth mechanism on the atomic scale [99].

that produce nanotubes of various kinds growing within predefined process windows. Still it remains to our credit that we have come a long way in this game and the structures we can controllably fabricate today are quite compelling for many applications that we have envisioned for nanotube-based technologies.

References

[1]   Iijima, S. (1991). *Nature* **354**: 56.

[2]   Ajayan, P.M. (1999). *Chem. Rev*. **99**: 1787.

[3]   Ajiki, H. and Ando, T. (1993). *J. Phys. Soc. Jpn*. **62**, 1255.

[4]   Hamada, N., Sawada, S., and Oshiyama, A. (1992). *Phys. Rev. Lett*. **68**: 1579.

[5]   Mintmire, J.W., Dunlap, B.I., and White, C.T. (1992). *Phys. Rev. Lett*. **68**: 631.

[6]   Saito, R., Fujita, M., Dresselhaus, G., and Dresselhaus, M.S. (1992). *Phys. Rev. B* **46**: 1804.

[7]   Ebbesen, T.W. and Ajayan, P.M. (1992). *Nature* **358**: 220.

[8]   Iijima, S. and Ichihashi, T. (1993). *Nature* **363**: 603.

[9]   Bethune, D.S., Klang, C.H., de Vries, M.S., Gorman, G., Savoy, R., Vazquez, J., and Beyers, R. (1993). *Nature* **363**: 605.

[10]   Terrones, M. (2004). *Int. Mater. Rev*. **49**: 325.

[11]   Baker, R.T.K. (1989). *Carbon* **27**: 315.

[12]   See, e.g., http://www.apsci.com/ppi-about.html.

[13]   Endo, M., Takeuchi, K., Igarashi, S., Kobori, K., Shiraishi, M., and Kroto, H.W. (1993). *J. Phys. Chem. Solids*. **54**: 1841.

[14]   Jose-Yacaman, M., Miki-Yoshida, M.M., Rendon, L., and Santiesteban, J.G. (1993). *Appl. Phys. Lett*. **62**: 657.

[15]   Ivanov, V., Nagy, J.B., Lambin, P., Lucas, A., Zhang, X.B., Zhang, X.F., Bernaerts, D., Van Tendeloo, G., Amelinckx, S., and Van Landuyt, J. (1994). *Chem. Phys. Lett*. **223**: 329.

[16]   Hafner, J.H., Bronikowski, M.J., Azamian, B.R., Nikolaev, P., Rinzler, A.G., Colbert, D.T., Smith, K.A., Smalley, R.E. (1998). *Chem. Phys. Lett*. **296**: 195.

[17]   Ball, P. (2001). *Nature* **414**: 142.

[18]   Helveg, S., Lopez-Cartes, C., Sehested, J., Hansen, P.L., Clausen, B.S., Rostrup-Nielsen, J.R., Abild-Pedersen, F., Norskov, J.K. (2004). *Nature* **427**: 426.

[19]   Sinnott, S.B., Andrews, R., Qian, D., Rao, A.M., Mao, Z., Dickey, E.C., and Derbyshire, F. (1999). *Chem. Phys. Lett*. **315**: 25.

[20] Cheung, C.L., Kurtz, A., Park, H., and Lieber, C.M., (2002). *J. Phys. Chem. B*. **106**: 2429.

[21] Endo, M., Muramatsu, H., Hayashi, T.Y.A., Kim, M., Terrones, M., Dresselhaus, S. (2005). *Nature* **433**: 476.

[22] Rodriguez, N.M., Chambers, A., and Baker, R.T.K. (1995). *Langmuir* **11**: 3862.

[23] Shibuta, Y. and Maruyama, S. (2003). *Chem. Phys. Lett.* **382**: 381.

[24] Moisala, A., Nasibulin, A.G., and Kauppinen, E.I. (2003). *J. Phys. Condens. Matter* **15**: S3011.

[25] Juang Z.Y., Lai, J.F., Weng, C.H., Lee, J.H., Lai, H.J., Lai, T.S., and Tsai, C.H. (2004). *Diamond Related Mater.* **13**: 2140.

[26] Kobayashi, Y., Nakashima, H., Takagi, D., and Homma, Y. (2004). *Thin Solid Films* **464–465**: 286.

[27] Lastella, S., Jung, Y.J., Yang, H.C., Vajtai, R., Ajayan, P.M., Ryu, C., Rider, D.A., and Manners, I. (2004). *J. Mater. Chem.* **14(12)**: 1791.

[28] Ng, H.T., Chen, B., Koehne, J.E., Cassell, A.M., Li, J., Han, J., Meyyappan, M. (2003). *J. Phys. Chem. B*, **107**: 8484.

[29] Li, W.Z., Xie, S.S., Qian, L.X., Chang, B.H., Zou, B.S., Zhou, W.Y., Zhao, R.A., and Wang, G. (1996). *Science* **274**: 1701.

[30] Terrones, M. et al. (1997). *Nature* **388**: 52.

[31] Grobert, N. et al. (2000). *Appl. Phys*. A **70**, 175.

[32] Fan, S.S., Chapline, M.G., Franklin, N.R., Tombler, T.W., Cassell, A.M., and Dai, H.J. (1999). *Science* **283**: 512.

[33] Pan, Z.W., Zhu, H.G., Zhang, Z.T., Im, H., Dai, S., Beach, D.B., and Lowndes, D.H. (2003). *J. Phys. Chem. B*, **107**: 1338.

[34] Kind H., Bonard, J.M., Emmenegger, C., Nilsson, L.O., Hernadi, K., Maillard-Schaller, E., Schlapbach, L., Forro, L., and Kern, K. (1999). *Adv. Mater*. **11**: 1285.

[35] Duesberg, G.S., Graham, A.P., Liebau, M., Seidel, R., Unger, E., Kreupl, F., and Hoenlein, W. (2003). *NanoLetters* **3**: 257.

[36] Duesberg, G.S, Graham, A.P., Kreupl, F., Liebau, M., Seidel, R., Unger, E., and Hoenlein, W. (2004). *Diamond Related Mater*. **13**: 354.

[37] Wei, B.Q., Vajtai, R., Jung, Y., Ward, J., Zhang, R., Ramanath, G., and Ajayan, P.M. (2003). *Chem. Mater.* **15**(8): 1598.

[38] Andrews, R., Jacques, D., Rao, A.M., Derbyshire, F., Qian, D., Fan, X., and Dickey, E.C., and Chen, J. (1999). *Chem. Phys. Lett.* **303**, 467.

[39] Rao, C.N.R., Sen, R., Satishkumar, B.C., and Govindaraj, A. (1998). *Chem. Commun.* **15**: 1525.

[40] Cao, A.Y., Ci, L.J., Wu, G.W., Wei, B.Q., Xu, C.L., Liang, J., and Wu, D.H. (2001). *Carbon* **39**: 152.

[41] Zhang, Z.J., Wei, B.Q., Ramanath, G., and Ajayan, P.M. (2000). *Appl. Phys. Lett.* **77**: 3764.

[42] Jung, Y.J., Wei, B.Q., Vajtai, R., Ajayan, P.M., Homma Y., Prabhakaran, K., and Ogino, T. (2003). *Nanoletters* **3:** 561.

[43] Wei, B.Q., Vajtai, R., Jung, Y., Ward, J., Zhang, R., Ramanath, G., and Ajayan, P.M. (2002). *Nature* **416(6880)**: 495.

[44] Wei, B.Q., Vajtai, R., Zhang, Z., Ramanath G., and Ajayan, P.M. (2001). *J. Nanosci. Nanotechnol.* **1**: 35.

[45] Wei, B.Q., Zhang, Z., Ramanath, G., and Ajayan, P.M. (2000). *Appl. Phys. Lett.* **77**: 2985.

[46] Cao, A., Baskaran, R., Frederick, M.J., Turner, K., Ajayan, P.M., and Ramanath, G. (2003). *Adv. Mater.* **15**: 1105.

[47] Vajtai, R., Kordás, K., Wei, B.Q., Békési, J., Leppävuori, S., George, T.F., and Ajayan, P.M. (2002). *Mater. Sci. Eng. C* **19**: 271.

[48] Srivastava, A., Srivastava, O.N., Talapatra, S., Vajtai, R., and Ajayan, P.M. (2004). *Nature Mater.* **3:** 610.

[49] Cao, A., Veedu, V.P., Li, X., Yao, Z., Ghasemi-Nejhad, M.N., and Ajayan, P.M. (2005). *Nature Mater.* **4**: 540.

[50] Meng, G.W., Jung, Y.J., Cao, A., Vajtai, R., and Ajayan, P.M. (2005). *PNAS* **102**(20): 7074.

[51] Li, J., Papadopoulos, C., and Xu, J. (1999). *Nature* **402**: 253.

[52] Davydov, D.N., Sattari, P.A., AlMawlawi, D., Osika, A., Haslett, T.L., Moskovits, M. (1999). *J. Appl. Phys.* **86**: 3983.

[53] Sui, Y.C., Cui, B.Z., Martınez, L., Perez, R., and Sellmyer, D.J. (2002). *Thin Solid Films*, **406**: 64.

[54] Dresselhaus, M.S., Dresselhaus, G., and Avouris, P. (2001). *Carbon Nanotubes: Synthesis, Structure, Properties, and Applications*. Berlin/New York: Springer.

[55] Choi, W.B., Jin, Y.W., Kim, H.Y., Lee, S.J., Yun, M.J., Kang, J.H., Choi, Y.S., Park, N.S., Lee, N.S., and Kim, J.M. (2001). *Appl. Phys. Lett.* **78**: 1547.

[56] Modi, A., Koratkar, N., Lass, E., Wei, B.Q., and Ajayan, P.M. (2003). *Nature* **424**: 171.

[57] Matsumoto, T., Komatsu, T., Nakano, H., Arai, K., Nagashima, Y., Yoo, E., Yamazaki, T., Kijima, M., Shimizu, H., Takasawa, Y., and Nakamura, J. (2004). *Catalysis Today* **90**: 277

[58] Ma, R.Z., Liang, J., Wei, B.Q., Zhang, B., Xu, C.L., and Wu, D.H. (1999). *J. Power Sources* **84**: 126

[59] Kreupl, F., Graham, A.P., Duesberg, G.S., Steinhogl, W., Liebau, M., Unger, E., and Honlein, W. (2002). *Microelectron. Eng.* **64:** 399.

[60] Koratkar, N., Wei, B.Q., and Ajayan, P.M. (2002). *Adv. Mater.* **14**: 997.

[61] Tang, J., Yang, G., Zhang, Q., Parhat, A., Maynor, B., Liu, J., Qin, L.-C., and Zhou, O. (2005). *Nano Lett.* **5**: 11.

[62] Dalton, A.B., Collins, S., Munoz, E., Razal, J.M., Ebron, V.H., Ferraris, J.P., Coleman, J.N., Kim, B.G., and Baughman, R.H. (2003). *Nature* **423**: 703.

[63] Davis, V.A., Ericson, L.M., Parra-Vasquez, A.N.G., Fan, H., Wang, Y.H., Prieto, V., Longoria, J.A., Ramesh, S., Saini, R.K., Kittrell, C., Billups, W.E., Adams, W.W., Hauge, R.H., Smalley, R.E., and Pasquali, M. (2004). *Macromolecules* **37**: 154.

[64] Ericson, L.M., Fan, H., Peng, H.Q., Davis, V.A., Zhou, W., Sulpizio, J., Wang, Y.H., Booker, R., Vavro, J., Guthy, C., Parra-Vasquez, A.N.G., Kim, M.J., Ramesh, S., Saini, R.K., Kittrell, C., Lavin, G., Schmidt, H., Adams, W.W., Billups, W. E., Pasquali, M., Hwang, W.F., Hauge, R.H., Fischer, J.E., and Smalley, R.E. (2004). *Science* **305**: 1447.

[65] Zhu, H.W., Xu, C.L., Wu, D.H., Wei, B.Q., Vajtai, R., and Ajayan, P.M. (2002). *Science* **296**: 884.

[66] Zhang, M., Atkinson, K.R., and Baughman, R.H. (2004). *Science* **306**: 1358.

[67] Rinzler, A.G., Hafner, J.H., Nikolaev, P., Lou, L., Kim, S.G., Tomanek, D., Colbert, D., and Smalley, R.E. (1995). *Science* **269**: 1550.

[68] de Heer, W., Chatelain, A., and Ugarte, D. (1995). *Science* **270**: 1179.

[69] Saito, Y., Hamaguchi, K., Nishino, T., Hata, K., Tohji, K., Kasuya, A., and Nishina, Y. (1997). *Jpn. J. Appl. Phys.* **36**: L13440.

[70]   Collins, P. and Zettl, A. (1996). *Appl. Phys. Lett.* **69**: 1969.

[71]   Wang, Q.H., Corrigan, T.D., Dai, J.Y., Chang, R.H., and Krauss, A.R. (1997). *Appl. Phys. Lett.* **70**: 3308.

[72]   Kuttel, O.M., Groning, P., Emmenegger, C., and Schlapbach, L. (1998). *Appl. Phys. Lett.* **73**: 2113.

[73]   Bonnard, J.M., Salvetat, J.P., Stockli, T., de Heer, W.A., Forro, L., and Chatelain, A. (1998). *Appl. Phys. Lett.* **73**: 918.

[74]   Zhu, W., Bower, C., Zhou, O., Kochanski, G.P., and Jin, S. (1999). *Appl. Phys. Lett.* **75**: 873.

[75]   Dean, K.A. and Chalamala, B.R. (1999). *Appl. Phys. Lett.* **75**: 3017.

[76]   Dean, K.A. and Chalamala, B.R. (2000). *Appl. Phys. Lett.* **76**: 375.

[77]   Bower, C., Zhou, O., Zhu, W., Ramirez, A.G., Kochanski, G.P., and Jin, S. (2000). *Mat. Res. Soc. Symp. Proc.*

[78]   Suzuki, S., Watanabe, T., Kiyokura, T., Nath, K.N., Ogino, T., Heun, S., Zhu, W., Bower, C., and Zhou, O. (2001). *Phys. Rev. B* **63**: 2454181.

[79]   Saito, Y., Uemura,, S., and Hamakuchi, K. (1998). *Jpn. J. Appl. Phys.* **37**: L346.

[80]   Rosen, R., Simendinger, W., Debbault, C., Shimoda, H., Fleming, L., Stoner, B., and Zhou, O. (2000). *Appl. Phys. Lett.* **76**: 1668.

[81]   Chwickshank, R., Duguid, N.P., Marmion, B.P., and Swain, R.H.A. (1975). *Medical Microbiology*. London: Churchill.

[82]   http://www.millipore.com/publications.nsf/docs/DS1180EN00.

[83]   Ajayan, P.M., Schadler, L.S., Giannaris, C., and Rubio, A. (2000). *Adv. Mater.* **12**: 750.

[84]   Raravikar, N.R., Schadler, L.S., Vijayaraghavan, A., Zhao, Y., Wei, B.Q., and Ajayan, P.M. (2005). *Chem. Mater.* **17**: 974.

[85]   Chen, Y.-C., Raravikar, N.R., Schadler L.S., Ajayan, P.M. Zao, Y.-P., Lu, T.-M,. Wang, G.-C., and Zhang, X.-C. (2002). *Appl. Phys. Lett.* **81**: 975.

[86]   Kim, H.M., Kim, K., Lee, C.Y., Joo, J., Cho, S., Yoon, H.S., Pejakovic, D.A., Yoo, J.W., and Epstein, A.J. (2004). *Appl. Phys. Lett.* **84**, 589.

[87]   Ago, H., Petritsch, K., Shaffer, M.S.P. Windle, A.H., and Friend, R.H. (1999). *Adv. Mater.* **11**: 1281.

[88]   Kymakis, E. and Amartunga, G.A. (2002). *Appl. Phys. Lett.* **80**: 112.

[89]   Philip, B., Abraham J.K., Chandrasekhar, A., and Varadan, V.K., (2003). *Smart Mater. Struct.* **12**: 935.

[90]   Rege, K. Raravikar, N.R. Kim, D.-Y. Schadler, L.S. Ajayan, P.M. and Dordick, J.S. (2003). *Nano Lett.* **3**: 829.

[91]   Wagner, H.D. (2002). *Chem. Phys. Lett.* **361**: 57.

[92]   Lau, K.-T. (2003). *Chem. Phys. Lett.* **370**: 399.

[93]   Suhr, J., Koratkar, N., Keblinski, P., and Ajayan, P. M. (2005). *Nature Mater*. **4**: 134.

[94]   Koratkar N., Wei, B.Q., and Ajayan, P.M. (2003). *Composites Sci. Technol.* **63**: 1525.

[95]   Maly J.R. and Johnson, C.D. (1996). *SPIE Proceedings on Smart Structures and Materials*, p. 365.

[96]   Biggerstaff, J.M. and Kosmatka, J.B. (1998). *J. Comp. Mater.* **32**: 21.

[97]   Hata, K., Futaba, D.N., Mizuno, K., Namai, T., Yumura, M., and Iijima, S. (2004). *Science*, **306**: 1362.

[98]   Ci, L.J., Rao, Z.L., Zhou, Z.P., Tang, D.S., Yan, X.Q., Liang Y.X., Liu, D. F., Yuan, H.J., Zhou, W.Y., Wang, G., Liu, W., and Xie, S.S. (2002). *Chem. Phys. Lett.* **359**: 63.

[99]   Ajayan, P.M. (2004). *Nature*, **427**: 402.

9
Online Size Characterization of Nanofibers and Nanotubes

C. J. Unrau, R. L. Axelbaum, P. Biswas, and P. Fraundorf

9.1. Introduction

Nanofibers are commonly found in industry and nanotubes are quickly growing in importance and applications. As the production and use of these materials expands, the need to quickly and accurately size their lengths and diameters in the aerosol phase is becoming increasingly important. This need can arise from a desire to obtain feedback for process control and monitoring, or to understand and monitor the effect of these materials on human health. For example, nanofibers such as asbestos can present severe health risks when airborne and the toxicity of such fibers may be directly related to nanofiber dimensions [1]. This concern has been the motivation for developing online methods of sizing nanofibers in aerosols [2].

Although asbestos and other nanofibers can present severe health risks, such fibers can also have excellent commercial properties. Asbestos possesses properties such as chemical resistance and thermal insulation characteristics, which make it useful for applications such as high-temperature insulating materials [2]. Carbon nanofibers are used for material reinforcement due to their high tensile strength [3]. In addition to nanofibers, carbon nanotubes possess many unique properties making them desirable for a wide variety of applications including nanotransistors and field emission sources [4]. The properties of nanofibers and, in particular, carbon nanotubes are strongly size-dependent. Thus, optimizing the production of a particular size of nanofibers or nanotubes is desirable.

In this chapter, size *classification* refers to the separation of particles by size so that the resulting aerosol contains particles of a given size, whereas size *characterization* is the determination of the size distribution of the aerosol. Size characterization of nanofibers and nanotubes is commonly performed by transmission electron microscopy (TEM). TEM analysis has proven invaluable for examining the structure and composition of individual particles and is also valuable for size characterization if immediate feedback is not needed. Inasmuch as the particles must first be collected and then analyzed, the process is slow and laborious.

Clearly, an online method of analysis is needed to provide immediate feedback from changing process variables that includes measurement of number concentration, size, and purity. Such a method would result in faster optimization of a particular production process. TEM analysis could then be used to confirm the online measurements and to analyze quantities such as structure and composition. In addition, this method could also be valuable for online air quality measurements related to nanofibers and nanotubes.

In this chapter, online size classification techniques for both diameter and length of gas phase nanofibers are reviewed. In addition, unipolar diffusion charging theories for fibers are discussed. Based on the findings of this review, an approach to online size characterization of carbon nanotubes (and nanofibers) is developed and experimental results are presented. Because of the importance of TEM analysis for size measurement confirmation and for structure and compositional analysis, a brief discussion of microscopy sample preparation and analysis is also presented.

9.2. Size Classification of Nanofibers

Spherical particles are classified by their diameter, whereas nanofibers are classified by diameter, length, or a combination of the two. Classification devices for nanofibers have generally been separated into either or diameter and length classification devices. The common diameter classification devices exploit the aerodynamic properties of nanofibers, and length classification devices employ the motion of nanofibers in an electric field. Light-scattering techniques have also been used to characterize nanofibers using a combination of length and diameter [2] but these will not be discussed. For the purposes of this discussion, the term "fiber" is used for fibers with diameters on the order of 1 μm or greater and "nanofiber" refers to fibers with diameters on the order of 100 nm or less.

9.2.1. Diameter Classification

Nanofibers can be classified by an aerodynamic diameter via inertial impaction or centrifugation [5–9]. Inertial impactors, as illustrated in Figure 9.1, classify particles based on the Stokes number, a nondimensional grouping of parameters defined as [10]

$$Stk = \frac{\rho_0 U_0 d_{ar}^2}{9\mu W},$$ (1)

where ρ_0 is a standard reference physical density equal to 1 g/cm^3, U_0 is the calculated average velocity of the air stream at the jet exit, μ is the gas viscosity, and W is the jet diameter (for cylindrical jets). The aerodynamic resistance diameter, d_{ar}, in Eq. (1) is defined for a spherical particle [11] as

$$d_{ar} = d_{ae}\sqrt{C(d_{ae})} = \sqrt{\frac{\rho C(d_s)}{\rho_0}}d_s,$$ (2)
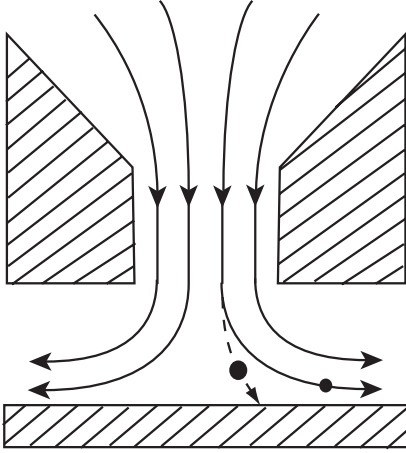
FIGURE 9.1. An illustration of the separation of spherical particles in an impactor.

where ρ is the particle density, d_s is the particle diameter, d_{ae} is the aerodynamic equivalent diameter, and $C(d_s)$ is the slip correction factor defined as

$$C(d_s) = 1 + \frac{2\lambda}{d_s} \left[1.142 + 0.558 \exp\left(\frac{-0.999 d_s}{2\lambda} \right) \right], \tag{3}$$

where λ is the mean free path of the gas [12, 13].

The impaction of spherical particles depicted in Figure 9.1 depends on the fluid properties and the particle diameter and density as described by the Stokes number. Those particles with an aerodynamic diameter larger than a well-defined cutoff size will collide with an impaction plate due to their larger inertia. Smaller particles will follow the flow field and pass by the plate. The impaction of nanofibers, however, depends on their length in addition to diameter and density. Cheng et al. [14] have outlined a theoretical approach to this and confirmed their theory via experimental studies. For nanofibers, the aerodynamic equivalent diameter is defined as

$$d_{ae}\sqrt{C(d_{ae})} = \sqrt{\frac{\rho C(d_a)}{\rho_0 \chi_0}} d_v, \tag{4}$$

where d_a is an adjusted sphere diameter, d_v is the equivalent volumetric diameter equal to $(1.5 D^2 L)^{1/3}$ where D and L are the diameter and length of the fiber, respectively, and χ_0 is the dynamic shape factor in the continuum regime [11]. The dynamic shape factor depends not only on shape but also on orientation relative to the flow field. Simplified equations to fit experimental data for cylinders in the perpendicular and parallel orientations are given by Cheng et al. [15–17] as follows.

$$\chi_\perp = 0.862 \beta^{1/3}, \tag{5}$$

$$\chi_{||} = 0.619 \beta^{1/3}, \tag{6}$$

where β is the aspect ratio [14]. The adjusted sphere diameter in Eq. (4) is given by [14,18,19]:

$$d_a = \frac{d_v G}{\chi},\tag{7}$$

where

$$G_\perp = 0.216\beta^{-2/3}(0.763 + 4.436\beta),\tag{8}$$
$$G_\| = 0.216\beta^{-2/3}(3.693 + 1.526\beta).\tag{9}$$

If the slip correction factors in Eq. (4) are close to 1 ($Kn = 2\lambda/d < 1$), it can be shown by substitution that the equivalent aerodynamic diameter is a function of $D^{5/6}$ and $L^{1/6}$. Cheng et al. confirmed this experimentally with silicon carbide whiskers ranging from 50 nm to 1 μm in diameter and from less than 2 μm to more than 15 μm in length. Experiments were carried out for both a centrifuge and an inertial impactor [14], and a relatively narrow diameter distribution for classified nanofibers was achieved in each case.

9.2.2. Length Classification

Classification of nanofiber length has proven to be more difficult than diameter and therefore has been the main focus of online size classification research. The principle method of classifying nanofibers by length is electrostatic classification. Other methods include wire screen penetration [20] and gravitational settling [21] but these will not be discussed. The electrostatic classification method can be further divided into two categories: dielectrophoretic and electrophoretic classification.

9.2.2.1. Dielectrophoretic Classification

Dielectrophoresis describes the motion of an *uncharged* particle in a nonuniform electric field due to an induced polarization on the particle. A device developed by Baron et al. for fiber length classification based on this motion is illustrated in Figure 9.2 [22].

In this device, uncharged particles enter the annulus between two concentric cylinders. The outer cylinder is grounded and a high voltage is applied to the inner cylinder. The electric field induces a polarization on the particles, causing them to move towards the inner electrode. The magnitude of this motion depends on particle size.

Lipowicz and Yeh [23] characterized this fiber motion and went on to examine the applicability of dielectrophoresis for fiber classification. The dielectrophoretic velocity, as derived by Lipowicz and Yeh is given by

$$v = \frac{K_m \varepsilon_0}{36\mu} DL \left(g(\beta) \left[\frac{\alpha}{\alpha - 1} - f(\beta) \right] \right)^{-1} \nabla E^2,\tag{10}$$

where E is the electric field, ε_0 is the permittivity of vacuum, K_f and K_m are, respectively, the dielectric constants of the fiber, and the electrically insulating medium
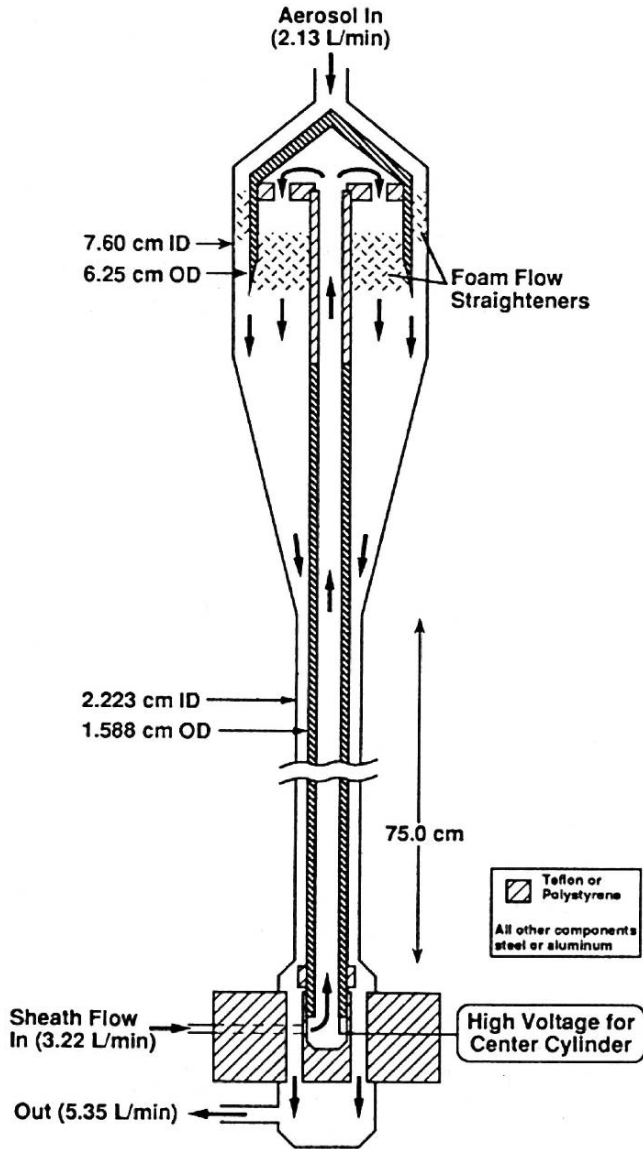
FIGURE 9.2. An illustration of a dielectrophoretic separation device [22].

where $K_f > K_m$, $\alpha = K_f/K_m$, and

$$f(\beta) = \xi[(1 - \xi^2)\coth^{-1}\xi + \xi] \tag{11a}$$

$$\xi = \beta(\beta^2 - 1)^{-1/2} \tag{11b}$$

$$g(\beta) = \frac{8}{3}\left[\frac{-2\beta}{\beta^2 - 1} + \frac{2\beta^2 - 1}{(\beta^2 - 1)^{3/2}}\ln\frac{\beta + (\beta^2 - 1)^{1/2}}{\beta - (\beta^2 - 1)^{1/2}}\right]^{-1}. \tag{12}$$

Lipowicz and Yeh showed that as β goes to infinity for nonconducting fibers, the velocity is proportional to D^2 whereas for conducting fibers, it is proportional to L^2. Based on this result, a classifier was designed to separate conductive fibers by length. To test the theory, macroscopic aluminum wires were placed in a medium of mineral oil between two cylindrical electrodes. Good agreement was achieved between theory and experiment and length separation was achieved. The dielectrophoretic force is inherently weak because it relies on induced polarization and becomes weaker with decreasing length, and thus Lipowicz and Yeh predicted a lower limit of 10 μm for length classification using this techique.

Based on this work, Baron et al. [22] developed and tested a classifier (Figure 9.2) for airborne nanofibers. Although most nanofibers are dielectric by nature, the conductivity of the nanofibers was not an issue because most airborne microscopic particles, whether conducting or nonconducting, can be considered conductive due to surface adsorption of water [24,25]. Lilienfeld demonstrated this by aligning dielectric fibers in an electric field [25]. Baron et al. tested their classifier using chrysotile fibers in humid air with a median diameter of about 80 nm and a median length of about 4 μm. They were able to demonstrate length classification of nanofibers down to 8 μm with standard deviations ranging from 1.55 to 7.31, where the shortest fibers exhibited the least deviation. The variability was higher than expected, but several explanations were proposed including machining imperfections.

The previous classifier of Ref. [22] could be operated either as a low-pass filter, leaving only shorter fibers airborne, or as a fiber collection device, collecting based on length. Baron et al. [26] went on to develop a differential mobility classifier using dielectrophoresis to allow for production of monodisperse length nanofibers in the gas phase, which was combined with an aerodynamic sizing instrument for near real-time measurement of length and diameter. The performance of the length classifier was tested by Deye et al. [27]. The flow field in the classifier was modeled and the resolution of length classification was evaluated experimentally using three methods: TEM, a split flow technique, and an electrical mobility technique. The results of these tests revealed that the classifier did not reach theoretical resolution. Nonetheless, the classifier was shown to be reliable for measurement of nanofiber aerosols and for production of monodisperse length aerosols.

9.2.2.2. Electrophoretic Classification

Electrophoresis describes the motion of a charged particle in an electric field. To classify nanofibers by length using this motion, the nanofibers must first be charged either with bipolar or unipolar ions and then classified according to their electrical mobility. A review of this type of classification using bipolar and unipolar charging is given below.

(a) Electrophoretic Classification with Bipolar Charging

Although unipolar charging is often preferred for electrophoretic classification of nanofibers, bipolar charging has also been used. Wen et al. conducted an extensive

study of bipolar charging, the first part of which discussed bipolar charging theories for both spherical and nonspherical particles [28], and the second was a detailed look at the charging and electrical mobility of linear chain aggregates [29].

Wen et al. reviewed the two common approaches to bipolar charging of spherical particles: the Boltzmann charge distribution and the steady-state ion diffusion flux toward a sphere [30–33]. Using these approaches, an equivalent charge diameter was introduced to extend the use of these approaches to include prolate particles. The equivalent charge diameter is defined as

$$D_{QE} = \frac{d_1 \beta}{\ln(2\beta)}, \tag{13}$$

where d_1 is the minor axis diameter [28]. The charging probability, f_n, for a conducting spheroid according to the Boltzmann distribution with $e^2 D_{QE} kT \gg 1$ is

$$f_n = \frac{e}{\left(\pi D_{QE} kT\right)^{1/2}} \exp\left[-\frac{(n-\bar{n})^2 e^2}{D_{QE} kT}\right], \tag{14}$$

where e is the elementary charge, k is the Boltzmann constant, T is the temperature, n is the integer number of charges, and $\bar{n}$ is the median charge [28]. The median number of charges is given as

$$\bar{n} = \frac{D_{QE} kT}{2e^2} \ln\left[\frac{N_+ Z_+}{N_- Z_-}\right], \tag{15}$$

where N_+ and N_- are the concentrations of positive and negative ions and Z_+ and Z_- are the ion electrical mobilities of positive and negative ions, respectively [29]. Both approaches were compared and it was demonstrated that most calculations for submicron aggregates can be based on the Boltzmann charge distribution. This conclusion was reached because even though Eq. (14) is written for the continuum regime, noncontinuum and image charge effects were appreciable only for very long particles with $d_1 < 0.04$ μm [28].

In the second part of their study, Wen et al. conducted charge and electrical mobility measurements on γ-Fe_2O_3 linear chain aggregates ranging from 40 to 80 nm in diameter with lengths on the order of 10 μm [29]. The measurements were performed with a DMA in combination with a Faraday cup electrometer and a condensation nuclei counter (CNC). A ^{85}Kr bipolar ion source provided the charging mechanism [29]. An aerosol centrifuge was used to obtain the aerodynamic diameter distribution. These measurements, in combination with an analysis of the DMA transfer function, were used to calculate the charge and electrical mobility distributions. The experimental distributions were compared with the Boltzmann distribution given in Eq. (14). The Boltzmann distribution was found to approximate the charge distribution and can be used to calculate the electrical mobility distribution to within 10% [29].

In summary, this study demonstrated a method of calculating charge distributions for linear chain aggregates, which should be comparable to nanofibers. It can

also be inferred from [29] that bipolar charging does not provide a feasible method for length classification of nanofibers because a nanofiber can have a distribution of charges. Consequently, a narrow length distribution cannot be achieved for a given electrical mobility, that is, instrument setting.

(b) Electrophoretic Classification with Unipolar Charging

Most electrophoretic techniques employ unipolar charging when classifying based on length. Before discussing any of the specific techniques, however, a review of current unipolar diffusion charging theories for nanofibers and nanotubes is presented to provide a basis of understanding for this particular classification method. Field charging theories are not discussed due to the fact that field charging does not play a significant role in charging nanofibers and nanotubes [34]. For theoretical analysis of field charging and combined field and diffusion charging of fibers, the reader is referred to Han and Gentry [34].

Unipolar diffusion charging theories for nonspherical particles fall into either the continuum or the free molecular regime. The continuum regime theory was developed by Zebel et al. [35] and Laframboise and Chang [36]. Zebel et al. solved the diffusion equation to obtain the ion flux, neglecting the image force term [35]. Laframboise and Chang developed a similar approach for particles of arbitrary shape [36]. Their approach also assumes the continuum regime and neglects image forces. By solving the continuum flux equations, they were able to obtain an expression for the particle current I for very elongated particles:

$$I = eN_0 D_{\text{ion}} \frac{2\pi L}{\ln(2\beta)} \cdot \frac{\phi_p \exp(-\phi_p)}{1 - \exp(-\phi_p) + 0.5\pi \phi_p K / \ln(2\beta)}, \tag{16}$$

where N_0 is the ion concentration at infinity, D_{ion} is the ion diffusion coefficient, $\phi_p = eV_p/kT$ is the dimensionless electric potential of the particle, V_p is the electric potential of a particle relative to the potential at large distance from it, and

$$K = \frac{2 - \gamma}{\gamma} \frac{\bar{c}}{3\bar{c}_{\|}} Kn, \tag{17}$$

where $\bar{c}$ is the mean ion thermal velocity, $\bar{c}_{\|}$ is the mean velocity parallel to the ion number flux, γ is the ion sticking probability per collision, and $Kn = 2\lambda/D$ [36]. Equation (16) is similar to that obtained for spherical particles with the exception of the K-term. This term indicates more sensitivity to departure from the free molecular regime for an elongated particle than for a spherical particle. (For the continuum regime, $K = 0$.)

Wang et al. [37] were the first to develop a diffusion charging theory for the free molecular regime, and they also extended the theory into the transition regime. Han and Gentry also developed a theory for the free molecular regime [38]. They

defined the ion flux to the fiber, $\dot{n}_f$, as

$$\dot{n}_f = \frac{1}{4} N_0 \bar{c} \exp\left[-\phi_c\left(r\right)\right], \tag{18}$$

where $\phi_c(r)$ is the potential function [38]. Equation (18) can be nondimensionalized and integrated to obtain the number of charges n as

$$n = \frac{1}{4}\pi \bar{c} N_0 t \, DL\bar{r}_m \exp[-\phi_c(\bar{r}_m)], \tag{19}$$

where t is the charging time, $\bar{r}_m$ is the distance at which the total flux is a minimum, and the dimensionless potential function, $\phi_c(\bar{r}_m)$, is defined as

$$\phi_c(\bar{r}_m) = \frac{2sn\psi_0}{\beta} \ln\left[\frac{\beta + \sqrt{(\beta^2 + \bar{r}_m^2)}}{\bar{r}_m}\right] - \frac{\psi_0}{2\bar{r}_m^2\left(\bar{r}_m^2 - 1\right)}, \tag{20}$$

where $s = 1$ or -1 for a repulsive or attractive force, respectively, between the incoming ions and the particle, and ψ_0 is the charging parameter, $2e^2/DkT$ [38]. Equation (20) was based on a model for a point charge and a cylinder using the image potential of a circular cross-section of the cylinder. The distance at which the total flux is a minimum, $\bar{r}_m$, appears in Eqs. (19) and (20) due to the use of the extension of the minimum flux criteria developed by Gentry [39] to this charging theory in the free molecular regime.

Han and Gentry conducted simulations based on their free molecular theory and the theory developed by Zebel et al. [35] to compare the charge acquired by a fiber with that of a sphere of equal surface area and to compare the charging rates predicted by the free molecular and continuum theories. Fibers with diameters of 0.120 to 0.180 μm and aspect ratios of 190 to 310 were used in the simulations. Based on the free molecular theory, the amount of charge on the fibers was found to be greater than the charge carried by equal surface area spheres for a given ion concentration and charging time. The amount of charge on the fibers calculated using the free molecular theory was also found to be greater than the amount of charge determined by the continuum theory for all particles considered. Finally, the simulations demonstrated that the number of charges increased at about the same rate for both increasing length and diameter using the free molecular theory, whereas the continuum theory predicted the number of charges would increase much faster with increasing length than with increasing diameter [38].

With these results and a basic knowledge of unipolar diffusion charging theories in mind, specific techniques based on electrophoretic classification with unipolar charging are now discussed. The devices used for this type of classification vary and two such devices are reviewed here. The first is an electrical mobility separator of the Hochrainer type [40]. Griffiths et al. [41] improved this device and their version is shown in Figure 9.3. In this device, a fiber aerosol enters the separating chamber after passing through a unipolar charger. The separating chamber consists of an outer grounded cylinder and a filter at the bottom with a centered high voltage electrode positioned just beneath it. Thus, particles arrange themselves on the filter
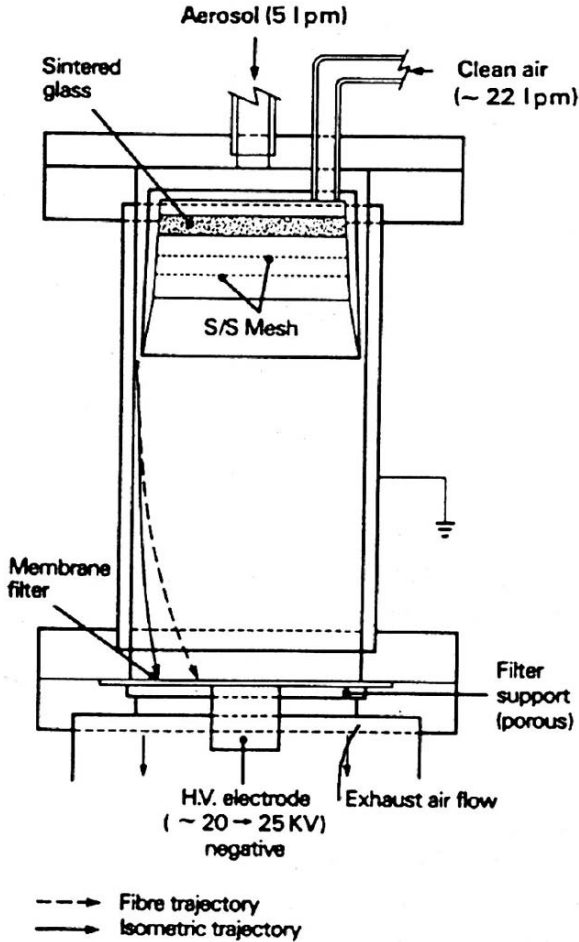
FIGURE 9.3. A schematic of the Hochrainer type mobility separator [41].

according to their electrical mobility with the particles having highest mobility being at the center.

Hochrainer et al. [40] and Griffiths et al. [41] tested micron-sized fibers and found that longer fibers were collected near the center of the filter whereas shorter fibers were collected farther out. Zebel et al. had observed similar results earlier using a slightly different mobility separator [35]. These results indicate that larger aspect ratio fibers acquired charge much faster than the smaller fibers. The difference in drag force is overcome by the greater charges leading to a higher electrical mobility. In addition, all three studies showed that isometric particles could be separated from fibers with the isometric particles being collected toward the edge of the filter [35,40,41]. The explanation suggested for this was that fibers become charged more rapidly than equal volume spheres due to their larger surface area.
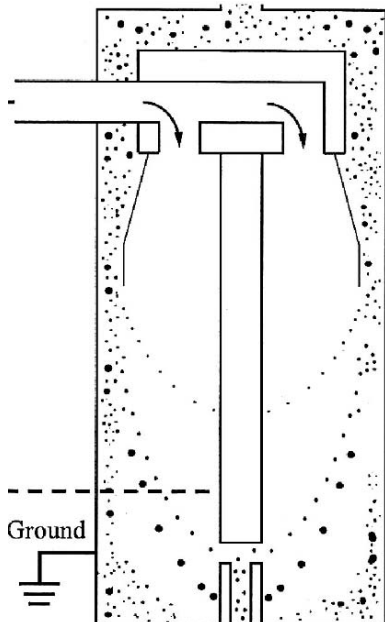
FIGURE 9.4. A schematic of a DMA [43].

Ground

Yu et al. demonstrated this theoretically [42] based on the charging theory for nonspherical particles developed by Laframboise and Chang [36].

A second type of device used in electrophoretic length classification is the differential mobility analyzer (DMA), which was mentioned in the preceding section. This device has two concentric cylinders, as shown in Figure 9.4; the outer one is grounded and the inner is at high potential. After passing through a unipolar or bipolar charger, the particles pass between the cylinders and collide with the inner electrode. Particles with higher electrical mobility collide farther up on the electrode than less mobile particles. In the schematic of the DMA shown in Figure 9.4, only particles within a narrow range of electrical mobilities exit the DMA. Thus, particles can be classified by their electrical mobility with high resolution.

Yu et al. used a similar device called a variable voltage differential analyzer [42]. Using actinolite nanofibers with a mean diameter of 300 nm and a mean length of 3 μm, they found that a reasonably narrow classified length distribution could be achieved. Based on the theory of Laframboise and Chang [36], they calculated the mean number of charges on nanofibers of different aspect ratios as a function of residence time in the charger. For a given residence time, it was demonstrated that the number of charges increases with aspect ratio, indicating that high aspect ratio nanofibers gain more charge than short aspect ratio nanofibers in the same amount of time and thus have the highest electrical mobilities. This is consistent with the results obtained using the electrical mobility separator discussed previously.

Chen et al. used a DMA with Mylar segments on the inner electrode to collect carbon fibers [44]. The carbon fibers were monodisperse in diameter (3.74 μm) and

polydisperse in length. After classification, the fibers were found to have narrow length distributions with geometric standard deviations between 1.08 and 1.25. The longest fibers had the highest electrical mobilities in these experiments, which is consistent with the findings discussed above. Chen et al. also calculated the charge distribution on the classified fibers and found that the mean number of charges increased with aspect ratio [44], which is consistent with the findings of Yu et al. [42].

In a later, more extensive study, Chen et al. used micrometer-long glass fibers of polydisperse diameter and length [45]. A virtual impactor was used to classify the fibers by diameter with geometric standard deviations ranging from 1.21–1.25. The fibers were subsequently classified by length using a differential mobility analyzer with a slit in the central electrode, allowing the classified fibers to exit the DMA. This configuration is particularly useful for the production of uniform dimension test aerosols. As in the previous study, classified fibers had a narrow length distribution [45]. This was also the case for other glass and carbon fibers of monodisperse diameter and polydisperse length. The relationship between charge and aspect ratio for all fibers was similar to previous studies [45].

Based on this review of fiber length classification studies, the best method for classifying nanofibers and nanotubes by length appears to be electrophoretic classification with a unipolar charger/DMA combination. Dielectrophoretic classification provides accurate classification but is restricted by a minimum length. Nanofibers cannot be separated by length using electrophoretic classification with bipolar charging due to the fact that a charge distribution exists for a particular nanofiber. Electrophoretic classification with unipolar charging, on the other hand, allows for accurate length classification with no minimum length restriction.

9.3. Online Size Characterization of Carbon Nanotubes

The above review provides a comparison of current online size classification techniques for nanofibers. Based on the findings of this review, electrophoretic classification with unipolar charging was employed to develop an online size characterization technique for carbon nanotubes (or nanofibers). As mentioned in the introduction, such a technique is necessary for efficient optimization of any nanotube production process. In this section, after a brief background on carbon nanotubes is given, an approach to online size characterization is presented along with experimental results obtained using this methodology and the aforementioned online size classification technique.

9.3.1. Background on Carbon Nanotubes

Since their discovery in 1991, carbon nanotubes (CNTs) have been the subject of intense research due to their unique electrical and mechanical properties. Because of these properties, CNTs are desirable for many applications including material

reinforcement [46], catalyst-support media [47–49], hydrogen storage [50], gas detectors [51], field emission displays [52], and many others. For several of these applications, only modest quantities of nanotubes will be needed. In this respect, current production methods such as chemical vapor deposition (CVD) may be satisfactory because nanotubes can be produced with good control and low impurities at a reasonable cost [53]. On the other hand, applications such as composite materials require industrial-scale quantities of carbon nanotubes.

In general, carbon nanotubes are produced in one of two ways: either on a supported catalyst or on a free-floating catalyst. In the supported catalyst method, particles such as iron are attached to a substrate and a carbon source such as a hydrocarbon or CO is passed over the substrate in a high-temperature environment. The nanotubes then grow from the catalyst particles. With the free-floating (aerosolized) catalyst method, particles are produced in the gas phase by flowing a catalyst precursor into the high-temperature environment with a source of carbon. The precursor typically decomposes to form the catalyst particles as an aerosol.

Aerosol methods have perhaps the highest probability of succeeding in the area of mass production of CNTs because they are continuous. Unfortunately, gas phase methods including laser ablation of composite metal targets [54,55], spray pyrolysis [56–59], the HiPCO process [60], and flame synthesis [61–66] do not approach kg/hr production rates due to current limitations of each method. Surpassing these limitations is hindered by a slow optimization process, requiring feedback from time consuming TEM studies. Recognizing the importance of production of carbon nanotubes in aerosols, we have, in this section, developed an approach to online size characterization.

To rapidly evaluate the effects of process variables, online characterization of size, number concentration, and purity of carbon nanotubes is needed, and in this section we describe such an approach, wherein a DMA is employed. As noted in Section 9.2.2, the DMA is capable of online classification of fibers [42,44,45]. In addition, Maynard et al. have classified nanotubes using the DMA, although a method for determining CNT size was not explicitly developed [67].

As mentioned above, the DMA classifies particles by their electrical mobility. Following the mobility theory described in Section 9.3.2, the electrical mobility of a classified nanotube can be determined as a function of CNT dimensions within the uncertainty of the number of charges carried by a nanotube. We show in Section 9.3.3 that a system-specific charge parameter can be established as a function of the diameter, length, and number of charges carried by a nanotube. Using this expression and electrical mobility theory, if one dimension of the CNT is known, the other can be measured. In addition, the number concentration can be obtained for each size using a scanning mobility particle sizer (SMPS), which is a combination of the DMA and a condensation particle counter (CPC). Finally, we show in Section 9.3.5 that carbon nanotubes can be distinguished from excess catalyst particles that do not produce nanotubes. This is possible using a DMA in combination with weak particle charging because under conditions of only a few charges, the mobility of the nanotubes is small relative to spherical particles as has

been experimentally demonstrated by Nasibulin et al. [68]. Distinguishing excess catalyst particles from CNTs is important in order to minimize impurities due to excess catalyst particles.

To test this approach to online size characterization of CNTs, multiwall carbon nanotubes (MWNTs) ranging from 10 to 100 nanometers in diameter and 0.5 to 40 μm in length with a purity of 95% were aerosolized and the DMA was used to size-select CNTs by their electrical mobility. These CNTs were subsequently collected directly onto TEM grids using an electrostatic sampler. Transmission electron microscopy was used to determine the dimensions of the carbon nanotubes. These dimensions were then used to test the methodology, and the results are presented in Section 9.3.5.

9.3.2. Theory of Electrical Mobility

For nonspherical aerosol particles, the electrical mobility is defined as [69,70]

$$Z = \frac{neC(d_a)}{3\pi\mu\chi_0 d_v}. \tag{21}$$

The dynamic shape factor, χ_0, for a nanotube is assumed to be the shape of a cylinder with an orientation perpendicular to the flow (Figure 9.5). The perpendicular orientation is assumed in this work because in a differential mobility analyzer the electric field is normal to the direction of the flow and it has been demonstrated that when CNTs are in the presence of an electric field, they align themselves with the direction of the field [71]. In addition, Lilienfeld [25] states that fibers tend to be aligned with electric fields due to an induced polarization and a torque exerted on the particle because of this polarization. This torque is increased further by the fact that the nanotubes are carrying charge and this charge is in the presence of the field gradient in the DMA. Finally, Kousaka et al. [72] experimentally demonstrated the alignment of doublets of spheres in a DMA. Consequently, we expect nanotubes to be aligned perpendicular to the flow when in the DMA as illustrated in Figure 9.5. The corresponding dynamic shape factor based on the slender body
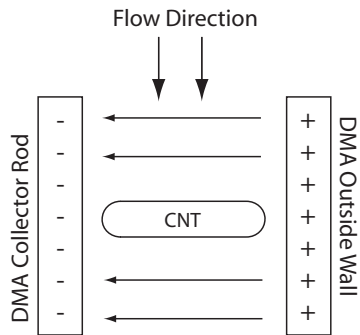
FIGURE 9.5. A schematic of a nanotube in the field of a DMA showing the CNT aligned with the electric field and normal to the flow direction.

approximation is given as

$$\chi_\perp = 2\left(\frac{2}{3}\right)^{\frac{4}{3}} \beta^{\frac{2}{3}} \left[\frac{\varepsilon + 0.307\varepsilon^2}{1 + \varepsilon/2} + 0.119\varepsilon^2\right], \tag{22}$$

where $\varepsilon = (\ln 2q)^{-1}$ [73].

The slip correction factor in Eq. (21) is defined by Eq. (3). The adjusted sphere diameter, d_a, although defined by Eq. (7), can alternatively be defined as [74]

$$d_a = \frac{2\lambda(1.142 + 0.558)F_{free}}{F_{cont}}, \tag{23}$$

where F_{free} and F_{cont} are the drag forces in the free molecular and continuum regimes, respectively, and are given by

$$F_{cont} = -3\pi \chi_0 \mu d_v U, \tag{24}$$

where U is the settling velocity, and

$$F_{free} = -\frac{\pi \mu D^2 U}{8\phi\lambda} \left[\begin{array}{l}(2\beta + 1) f + \left(2 - \dfrac{6 - \pi}{4} f\right) \times \\ (2\beta \sin^2 \theta + 2\cos^2 \theta)\end{array}\right], \tag{25}$$

where ϕ is a constant relating the gas mean free path and the gas viscosity and is equal to 0.491 for air and θ is the angle between the polar axis and flow direction and is equal to 90 degrees in this case [69,74]. The accommodation coefficient, f, in Eq. (25) is given by [69],

$$f = \frac{1}{\pi} \left[\left(\frac{36\phi}{1.142 + 0.558}\right) - 8\right]. \tag{26}$$

Substituting Eq. (3) and Eqs. (22) through (26) into Eq. (21), the electrical mobility of a nanotube can be found as a function of diameter, length, and the number of charges carried by a nanotube.

The electrical mobility of a spherical particle, Z_s, is defined as

$$Z_s = \frac{n_s e C(d_s)}{3\pi \mu d_s}, \tag{27}$$

where d_s is the diameter of the spherical particle and n_s is the number of charges carried by the particle. By equating Eqs. (21) and (27) and letting $d_s = D_{EM}$ and $n_s = 1$, an expression for the equivalent sphere mobility diameter can be defined as

$$\frac{D_{EM}}{C(D_{EM})} = \frac{\chi_0 d_v}{n C(d_a)}, \tag{28}$$

where D_{EM} is the equivalent sphere mobility diameter and $C(D_{EM})$ is the slip correction factor. In other words, for a given nanotube, D_{EM} in Eq. (28) is the diameter that a spherical particle carrying one charge would need to possess to have the same electrical mobility as the nanotube. Note that the right-hand side
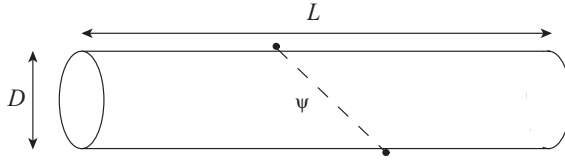
FIGURE 9.6. An illustration of the charge parameter, ψ, representing a characteristic distance between charges on the nanotube.

of Eq. (28) is constructed of only terms that include the actual nanotube diameter and length and the number of charges carried by the nanotube.

The electrical mobility of classified particles can also be defined in terms of the DMA voltage and sheath flow rate:

$$Z = \frac{Q_{sh} \ln(r_2/r_1)}{2\pi V \ell},$$

(29)

where r_1 and r_2 are the inner and outer radii of the DMA, respectively, ℓ is the length of the DMA, V is the applied voltage, and Q_{sh} is the sheath flow rate. By equating Eqs. (27) and (29) and letting $d_s = D_{EM}^*$ and $n_s = 1$, the electrical mobility diameter of a spherical particle carrying one charge is defined by

$$\frac{D_{EM}^*}{C(D_{EM}^*)} = \frac{2eV\ell}{3\mu Q_{sh} \ln \frac{r_2}{r_1}}.$$

(30)

The right-hand side of Eq. (30) is known and thus, the mobility diameter calculated in Eq. (28) can be compared to Eq. (30) to test the electrical mobility theory for nanotubes.

9.3.3. Semi-Empirical Estimate of Nanotube Charging

Equation (21) shows that the electrical mobility of a carbon nanotube is a function of diameter, length, and number of charges. This implies that different size nanotubes can have the same mobility, which leads to ambiguity as to the dimensions of the nanotubes. Therefore, it is necessary to obtain an additional expression relating the number of charges carried by a nanotube to the nanotube dimensions. If such an expression can be derived, the electrical mobility can be calculated knowing the diameter and length of the nanotube.

To derive such an equation, we rely on a semi-empirical concept based on simple geometric considerations. Considering the schematic of a nanotube shown in Figure 9.6, the charge parameter, ψ, can be defined as

$$\psi = \left[\left(\frac{L}{n} \right)^2 + D^2 \right]^{0.5},$$

(31)

where ψ represents a characteristic distance between charges.
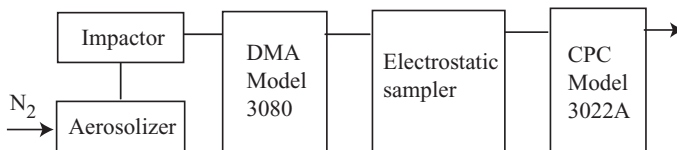
FIGURE 9.7. A flow diagram for the experimental setup.

The parameter, ψ in Eq. (31) can be determined experimentally if the diameter, length, and number of charges are known. The number of charges, however, is dependent upon the charging mechanism used so it should be noted that ψ is not a unique function but rather a system-dependent parameter. Finally, if ψ is determined for a specific system, Eq. (31) can be solved for n and rounded to the nearest integer for the number of charges. Substituting this into Eq. (21) defines the electrical mobility as a function of the nanotube dimensions alone.

9.3.4. Experimental

Multiwall carbon nanotubes (Helix Material Solutions, Inc.) with a size range of 10 to 100 nm in diameter and 0.5 to 40 μm in length were aerosolized in nitrogen gas with a flow rate of 0.1 lpm by flowing the gas through an impinger filled with nanotubes. The aerosolization process also provided the charging mechanism for the nanotubes. The resulting size distribution was measured using a TSI Model 3081 classifier and a TSI Model 3022A CPC. For the TSI Model 3081, the values for r_1, r_2, and ℓ in Eqs. (29) and (30) are 0.937 cm, 1.96 cm, and 44.4 cm, respectively. The sheath flow rate, Q_{sh}, used was 15 lpm. From this size distribution, four voltages were used to size-select CNTs, which were subsequently collected on separate TEM grids using an electrostatic sampler. Figure 9.7 illustrates a schematic of the experimental setup.

The electrostatic sampler used a strong electric field to collect the carbon nanotubes on holey carbon TEM grids. The use of an electrostatic sampler ensured that no sampling bias occurred. The importance of sampling without bias is discussed further in Section 9.4.1. Finally, the CNTs collected were observed using a transmission electron microscope (see Section 9.4). Diameters and lengths were obtained for the nanotubes and the results were used to test the electrical mobility theory and charge expression.

9.3.5. Results

As mentioned in Section 9.3.1, the differential mobility analyzer can provide online size distribution information (with a CPC) as well as discriminate between excess catalyst particles and nanotubes. In this section, a theoretical analysis of particle discrimination is presented. In addition, an analysis of size classification of carbon

nanotubes using a DMA in combination with a unipolar charger is described. Finally, experimental results for online size characterization of CNTs are presented, demonstrating the usefulness of the methodology outlined above.

9.3.5.1. Theoretical Analysis of DMA Size Classification and Particle Discrimination

Catalyst particles range in size from about 2 to 10 nm in diameter whereas most nanotubes of interest range from 2 to 10 nm in diameter and up to tens of microns in length. The ability of the DMA to distinguish between nanotubes and catalysts can be demonstrated theoretically by using Eqs. (21) and (27) for the mobilities of a carbon nanotube and a catalyst particle, respectively. The number of charges for the catalyst particles is assumed to be one for the worst-case scenario, that is, the most difficult to distinguish. The number of charges for the nanotubes can be calculated using Eqs. (19) and (20) which are based on the diffusion charging theory for fibers in the free molecular regime developed by Han and Gentry [38] as described in Section 9.2.2. Practical values for the $N_0 t$ product in Eq. (19) were chosen ranging from 10^6 to 10^8 ion-s/cm^3. The simulations conducted based on these equations and charging parameters demonstrate three key aspects of the DMA as an online characterization tool: length characterization, diameter characterization, and the ability to distinguish between excess catalyst particles and nanotubes.

Figure 9.8 is an illustration of the DMA potential required to classify nanotubes with a diameter of 2 nm and lengths ranging from 10–1000 nm (assuming ideal
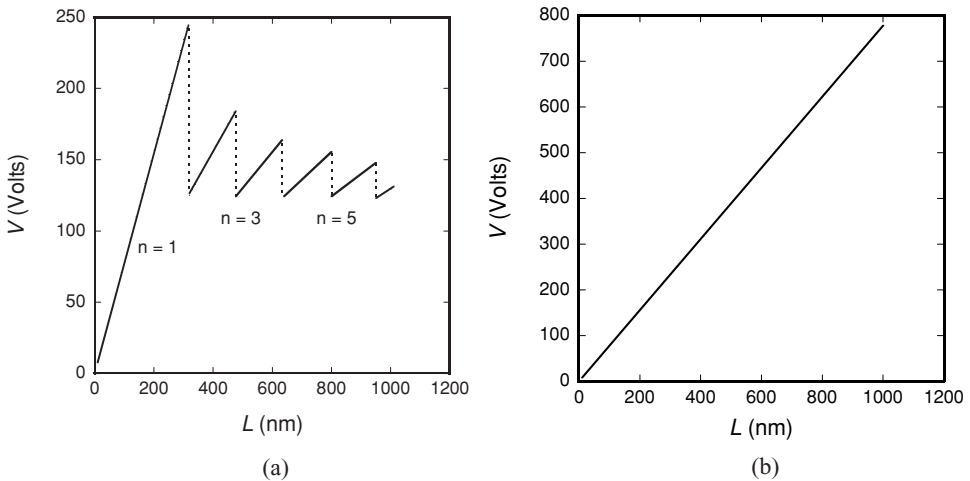
FIGURE 9.8. DMA potential versus length for 2-nm CNTs with $N_0 t$ equal to (a) 10^7 ion-s/cm^3; (b) 10^6 ion-s/cm^3.
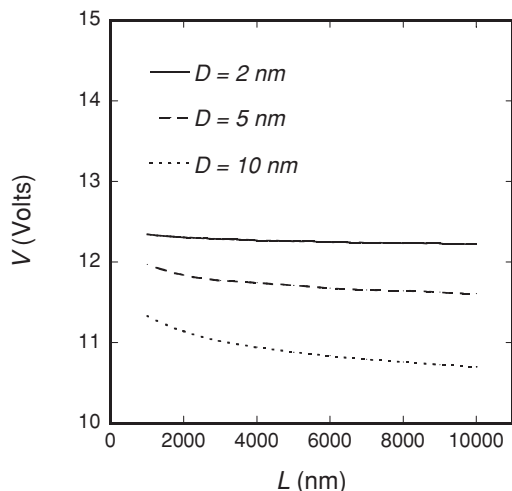
FIGURE 9.9. DMA potential versus length for 2-, 5-, and 10-nm CNTs with $N_0 t$ equal to 10^8 ion-s/cm^3.

resolution). The $N_0 t$ product is 10^7 ion-s/cm^3 in Figure 9.8a and 10^6 ion-s/cm^3 in Figure 9.8b. The saw-toothed shape in Figure 9.8a is due to an incremental increase in charge. When the nanotube is beyond a certain size, an additional charge is added, lowering the classification potential, which results in a step increase in mobility. The shape of this graph also indicates that length classification is not possible because in the 120–150 V range many different lengths would be classified at a single DMA voltage. On the other hand, Figure 9.8b illustrates the result when a value of 10^6 ion-s/cm^3 is used for the $N_0 t$ product. Due to the lower $N_0 t$ product, no multiple charging takes place, which makes length classification possible.

Figure 9.9 is an illustration of the DMA potential required to classify nanotubes with diameters of 2, 5, and 10 nm and lengths ranging from 1–10 μm. The $N_0 t$ product is 10^8 ion-s/cm^3. As the nanotubes approach large aspect ratios, an asymptote is reached. This asymptotic behavior can be attributed to the increase of the electrical mobility by the addition of one charge being balanced by a decrease in mobility due to an increase in drag force (due to increased length). Clearly, length classification is not possible based on this value of the $N_0 t$ product. On the other hand, because the simultaneous increase of charge and length has a canceling effect, the classification potential is a function of diameter only, which makes diameter classification possible. Consequently, length and diameter classification may be possible using the DMA by varying the $N_0 t$ product. It should also be noted from Figure 9.9 that the decrease in mobility due to an increase in drag force by increasing diameter or length is overcome by the increase in mobility due to an increase in charge. Therefore, larger nanotubes are classified at smaller potentials, which is consistent with results presented in Section 9.2.2.

Figure 9.10 is an illustration of the DMA potential required to classify spherical catalyst particles ranging from 2 to 10 nm in diameter and carrying one charge. By comparing this figure to Figure 9.8a (or 9.8b), it can be seen that only single-walled nanotubes less than 40 nm in length will be classified at a comparable DMA potential to that of 8 nm or less catalyst particles. This makes it possible to not

FIGURE 9.10. DMA potential versus catalyst particle diameter.
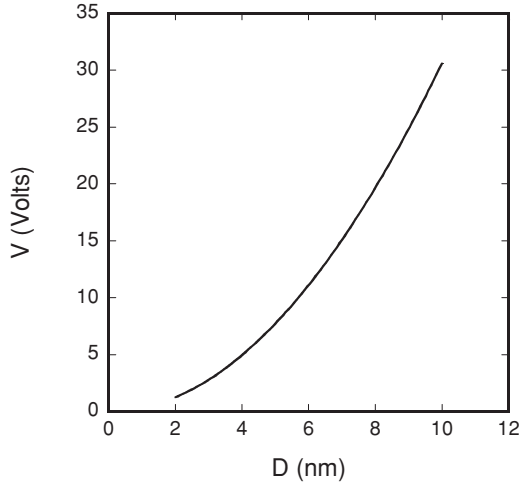
only distinguish between catalyst particles and nanotubes but also to measure the growth rates of the nanotubes. In contrast, a comparison of Figures 9.10 and 9.9 demonstrates that the DMA cannot distinguish between nanotubes and catalyst particles for an N_0t product of 10^8 ion-s/cm^3. The larger N_0t product causes overlap between the catalyst particle and nanotube classification potential, not allowing for discrimination between the two.

9.3.5.2. Experimental Results for Online Size Characterization of CNTs

As demonstrated above, the DMA is capable of online size classification of nanotubes and nanofibers. Therefore, in addition to providing information about number concentration and catalyst impurities, the DMA can provide information about the physical size of the nanotubes. Once classification is achieved, online size characterization is possible using electrical mobility theory and the charge parameter, ψ, described above. To test the methodology, CNTs were classified by their electrical mobility with a DMA and the actual dimensions of the classified particles were measured by TEM. Table 9.1 lists the voltages used to collect the nanotube samples. Also listed are the corresponding spherical mobility diameters calculated using Eq. (30).

TABLE 9.1 Experimental parameters.

V [Volts]	D_{EM}^* [nm]
−1619	79
−2710	106
−3862	130
−5500	161

V DMA voltage, D_{EM}^* spherical mobility diameter

Not all nanotubes observed in the TEM were recorded due to limitations of the electrical mobility theory. The theory applies only to nanotubes that are separate and straight and cannot predict electrical mobility diameters of tubes that are curved or bundled together. An example of an acceptable nanotube is shown in the middle of Figure 9.11, and an unacceptable tube is shown in the upper left.

Using the measured dimensions of the nanotubes, the corresponding equivalent electrical mobility diameters D_{EM} were calculated using Eq. (28). The number of charges on each nanotube was estimated by choosing the value of n in Eq. (28) that led to the best match between D_{EM} and D_{EM}^* listed in Table 9.1. A similar technique was used by Chen et al. to calculate the mean number of charges on length-classified uniform diameter carbon fibers [44]. A graph of D_{EM}^* versus D_{EM} is shown in Figure 9.12.

As illustrated in Figure 9.12, there is a good correlation between the spherical and equivalent electrical mobility diameters. This is expected because the number of charges used was a best fit. The spread in the data points represents the uncertainty of one charge. Although this gives some indication that the theory is correct, it is still desirable to determine the number of charges as a function of the nanotube dimensions. In order to do this, the charge parameter ψ must be determined. This parameter was calculated from Eq. (31) for each nanotube using the corresponding diameter, length, and best-fit number of charges. A graph of ψ versus V is shown in Figure 9.13 where V is the voltage of the collected samples given in Table 9.1.

The error bars in Figure 9.13 represent the standard deviation. Due to the relatively small error bars it can be concluded that the nanotubes measured from each sample clustered around an average value. It is also interesting to note that ψ increases linearly with voltage. Consequently, by fitting the data, ψ for this system can be represented by

$$\psi = 0.039 \cdot V + 60. \tag{32}$$
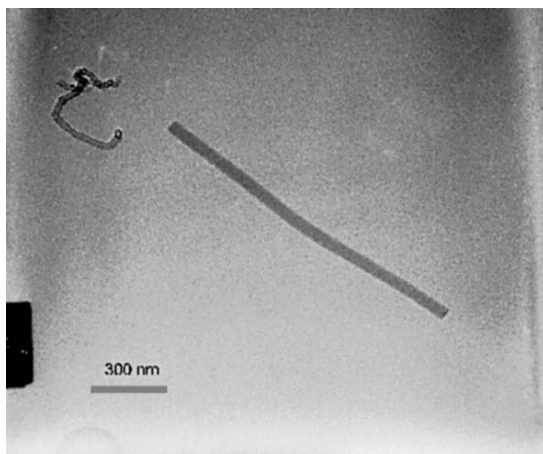
FIGURE 9.11. TEM image of a single, straight carbon nanotube and a curved nanotube.

300 nm
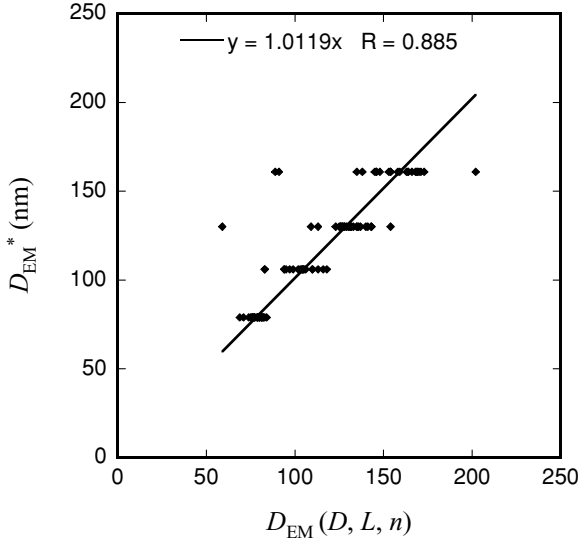
FIGURE 9.12. A comparison of D^*_{EM} and D_{EM}.

Solving Eq. (31) for the number of charges and substituting Eq. (32) for ψ, the number of charges, n, is

$$n = \frac{L}{\sqrt{(0.039 \cdot V + 60)^2 - D^2}}. \tag{33}$$
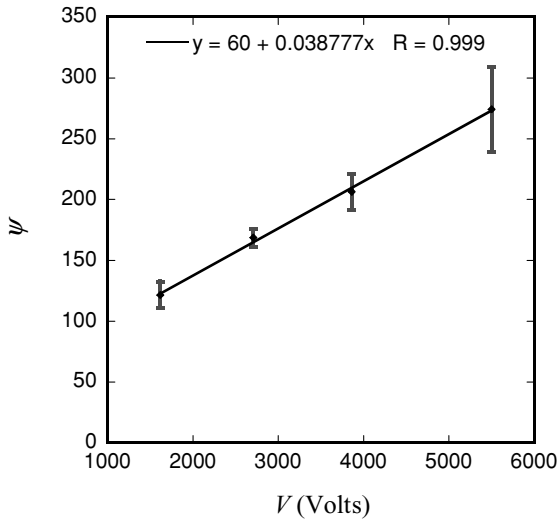
FIGURE 9.13. A graph of the charge parameter versus the DMA voltage.
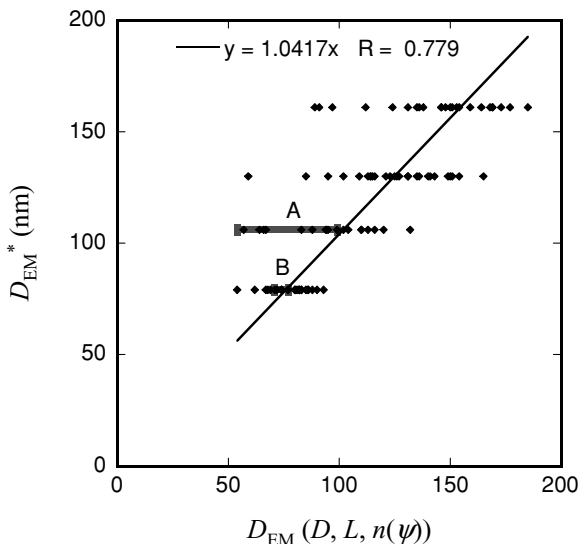
FIGURE 9.14. Sample diameter as a function of the equivalent mobility diameter: Error bars A and B correspond to two nanotubes: one with few charges (A) and the other with many (B).

The number of charges found from Eq. (33) was then used to recalculate the equivalent mobility diameter in Eq. (28) for each nanotube. Figure 9.14 illustrates the result.

From this figure it can be seen that there is again a correlation between the spherical and equivalent spherical mobility diameters as indicated by a slope of nearly one for the linear fit. There is a significant spread in the data but it is expected that the spread will reduce with increasing aspect ratio. Smaller aspect ratio tubes carry less charge, which results in large uncertainties if the charge expression (Eq. (33)) is off by just one charge. This is illustrated by error bar A in Figure 9.14, which corresponds to a nanotube of 26 nm in diameter and 275 nanometers in length carrying two charges as predicted by Eq. (33). On the other hand, for long tubes that carry many charges, the error is much less, as indicated by error bar B, which corresponds to a nanotube of 100 nm in diameter and 1 μm in length carrying 12 charges as predicted by Eq. (33).

Equation (21) can now be used to describe the electrical mobility of a carbon nanotube as a function of the dimensions of the nanotube and the DMA settings. Equating Eqs. (21) and (29) leads to an expression that includes only nanotube diameter and length as variables:

$$\frac{k_0 d_v}{n C(d_a)} = \frac{2 e V \ell}{3 \mu Q_{sh} \ln \dfrac{r_2}{r_1}}, \tag{34}$$

where n is found from Eq. (33) and the right-hand side is a constant based on the DMA settings. It should be noted that Eq. (34) is not a unique expression because the expression for n is system-dependent. Therefore, this expression must be calibrated for each system. Since calibration of Ψ is critical to use of the above methodologys in the next section we discuss the use of microscopy methods to obtain accurate measurements of the size of nanofibers and nanotubes.

9.4. Size Characterization of Nanofibers and Nanotubes by Microscopy

Offline methods of analysis such as TEM, SEM, and scanning probe microscopy (SPM). In addition to obtaining distributions of lengths and diameters, microscopy can directly investigate the detailed structure and composition of individual fibers. Although each of these types of microscopy is useful for providing size-distribution analysis in selected applications [75–79], only TEM permits diffraction analysis, compositional analysis of zeptoliter-sized (10^{-21}) volumes, plus atomic lattice and internal defect-structure imaging. With fibers for which confirmation of atomic structure and/or composition is relevant (e.g., in analysis of asbestos [80] and carbon nanotubes), TEM may therefore provide the most definitive results even when it does not offer the best counting statistics. Thus, this review focuses on TEM analysis of nanotubes and nanofibers.

Modern electron and scanning probe microscopes are becoming more like nanolaboratories, capable of fielding a wide range of experiments on specimens whose field of view has been magnified by factors of 10^{10} to 10^{16}. The main issues facing the microscopist, therefore, are (1) getting the specimen into the microscope without size bias, and (2) defining a limited set of experiments that will provide adequate statistics in a reasonable amount of time. These are therefore the topics of the next two sections.

9.4.1. Microscopy Specimen Prep and Sampling

Deposition of fibers by impaction from the gas phase onto a substrate is one mechanism for discriminating according to fiber diameter as discussed in Section 9.2.1. If the fibers are being deposited for microscopy directly onto a special surface (e.g., a 3-mm TEM grid with a lacey carbon film suspended between grid bars), the properties of that surface (e.g., propensity to charge electrostatically) might result in segregation relative to fibers elsewhere on the collector. If the fibers are instead transferred from the standard substrate to a microscope grid after deposition, the possibility of segregation during the transfer process must be considered. The high surface-to-volume ratios of nanoscale fibers make segregation effects during transfer particularly likely. In either case, a known size distribution of similar fibers may provide the best measure of segregation during either deposition onto a TEM grid or transfer to the TEM grid from the substrate.

(a)   (b)
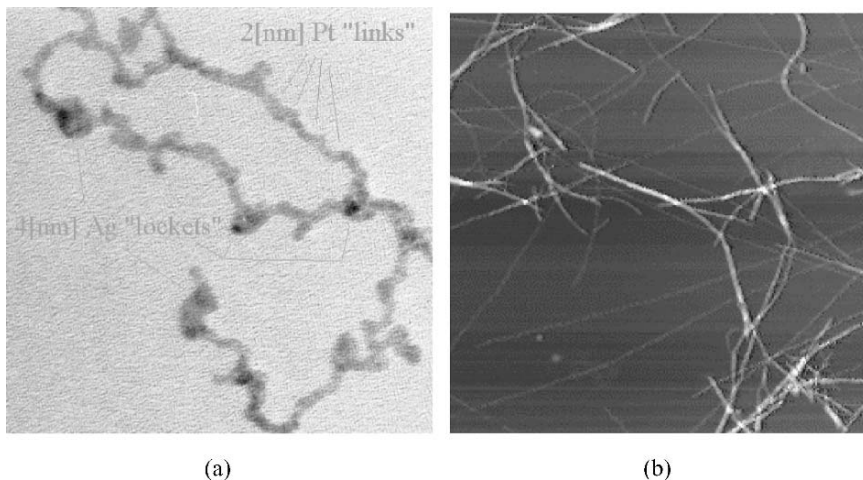
FIGURE 9.15. Two wet-mounted nanoassemblages: (a) "necklace" of 2-nm Pt crystals with Ag "lockets" in a 90-nm field, mounted on holey carbon film for TEM [82]; (b) 10-μm field of 10-nm wide amyloid protein fibrils mounted for SPM work on mica. Molecule affinities played a role in both (see text).

When transfer of nanofibers is unavoidable, molecule affinities play a large role. For example, the Pt necklaces in Figure 9.15a spread out beautifully on the carbon support film, but were attracted to the carbon too much to allow themselves to be draped over holes in the support film and thus allow high-resolution TEM (HRTEM) imaging without the intervening support. If deposited near a hole, the necklace particles instead pile up on the carbon film.

If liquids are involved in the transfer, for example, the particles are suspended in a liquid and then this liquid is deposited onto the grid and allowed to dry, surface tension effects can also massively disturb the homogeneity of deposit. One way to avoid this is to remove the liquid without allowing it to dry. For example, the protein nanofibers in the SPM image of Figure 9.15b deposited themselves voluntarily when a drop of solution containing them was placed in contact with the mica. The drop was then removed with a pipette and the surface was further washed with deposited water droplets and then removed intact. In this way molecule/surface affinities have been used [81] to make transfers from liquid to surface both predictable and homogeneous.

The SPM image of Figure 9.15a illustrates two other challenges to the mounting process: high aspect ratio and fiber overlap. With aspect ratios over 1000, seeing the fiber's width in a field of view large enough to also see both ends is not easy. Having many such fibers in each field of view then becomes virtually impossible without a great deal of overlap. These issues have been addressed in attempts to standardize methods applied to asbestos fiber analysis [80], but the problems are exacerbated for particles with even higher aspect ratios, that is, the protein

protofibrils shown above or single-walled carbon nanotubes. For example, when aspect ratios exceed the number of pixels along one side of an image, the image cannot record both length and width of fibers running in that direction. For a 3-millimeter-long nanotube only 3 nm in diameter, this suggests the need for images a million pixels on a side. Even if the data could be acquired in a reasonable amount of time, such an image might require 10^{12} bytes of storage.

Microscopy of single-walled carbon nanotubes has additional challenges, for example, the contrast mechanisms available in microscopy. Large-diameter nanotubes have edges, which show up clearly in TEM because of the large number of atoms viewed edge-on. On the other hand, the scattering from small-diameter single-walled carbon nanotubes is extremely small. Even a 15-wall carbon nanotube can be almost invisible without contrast enhancement in the presence of larger tubes. The microscopist in this context must be very careful about detection biases. This is also true in the SPM and one reason that, for example, quantitative work is preferably performed on flat reconstructed (100) silicon surfaces that provide "dimer-row graph paper lines" only 1.3 angstroms in height as local evidence of the microscope's height sensitivity in a given field of view.

9.4.2. Obtaining and Interpreting Information from the Sample

The TEM image in Figure 9.16a illustrates some of the challenges associated with measuring size by microscopy. In general, if the fibers are arrayed side-on without overlap in the field of view and show contrast that is uniformly darker or brighter than their surroundings (including any contaminants), then available image-processing software can easily determine their lengths and diameters. These conditions are rarely met. For example, the fibers in the image are not uniformly darker than the carbon lace that supports them, and they are neither free from overlap nor lying side-on in the viewing field.

Most image-processing programs will have trouble determining fiber sizes from the source image in Figure 9.16 [83,84]. Nonetheless, there is ample information with which to work. Individual nanofibers have their own distinctive internal structure [85], so a close look at the source image allows one to easily distinguish fibers from the support and to follow fibers from beginning to end. Moreover, the majority of the fibers have internal partitions, which can be counted for a length estimate even as tube segments move in the third dimension (into and out of the plane of the image). This is labor intensive, however, and the job of putting statistical limits on the accuracy of microscopy assertions about the distribution of fiber sizes will continue to be a challenge, just as it was for asbestos testing in past decades [80]. Quantifying the extra microscopic details themselves (e.g., fiber curvature, cross-sectional circularity, fibrillation, inside-diameter, and chirality) is a developing challenge as well [75–79, 86].

(a)   (b)
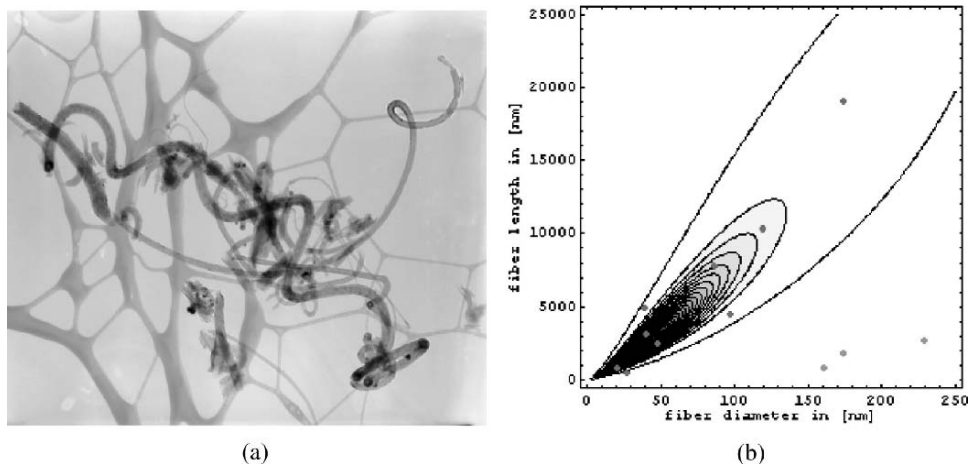
FIGURE 9.16. Carbon nanofiber dimensions from a TEM image: (a) brightfield image 8.3-μm wide; (b) fiber length versus diameter superposed on a bivariate log-normal distribution inferred from a subset of the fibers.

The incentive for doing statistically significant work of this type of analysis is high for two reasons. First, it allows one to quantify correlations between diameter and length as illustrated in Figure 9.16b above. This is important in terms of online analysis as discussed in previous sections. If a quantitative relationship between the length and diameter of a collection of fibers can be determined, even if both vary over wide ranges, a classification process that depends on knowledge of one to infer the other can put the relationship to use and constrain both unambiguously. For example, in its simplest form, the relationship between length L and diameter D in nanometers for the fitted subset of fibers in Figure 9.16 might look like $L \cong 8.1\ D^{1.5}$.

Secondly, the connection between these variables and other physical features of each fiber is often important. The microscopy techniques described here give broad access to other properties of fiber structure. For example, the source image for Figure 9.16 suggests that only some of the smaller carbon fibers in the field of view are hollow. Additional properties include crystallinity along with internal defect structure and surface reconstructions along with surface facet/edge/kink geometry. Other properties accessible to microscopy include the relationship of fibers to, and the structure of, additional nonfiber components (e.g., nanocatalyst particles), as well as the relationship between fibers and their matrix and/or support (e.g., the silicon substrate upon which fibers in a nanoelectronic display are fastened).

Finally, as the thrust of this chapter is online methods for accurately characterizing particles by size, microscopy of individual particles is a natural tool for calibration and monitoring their effectiveness. Structures of known geometry (such as nanotubes and nanospheres) can allow one to infer mass or volume indirectly

and thus relate local measurements to bulk constraints on quantities such as number concentration. In addition to elemental ratios by X-ray spectroscopy [87], the number of atoms per unit area in a field of view can sometimes be determined directly by electron energy loss spectroscopy [88,89]. Inasmuch as microscopes also quantify the area in a field of view, the number of a given image feature per gram may thus be measured as well.

9.5. Conclusions

Online size classification techniques were reviewed for nanofibers. Diameter classification via impaction and length classification using dielectrophoretic and electrophoretic techniques were presented along with a review of unipolar diffusion charging theories for fibers. Based on the results of this review, a DMA operated with unipolar charging of the incoming aerosol was used with a CPC for online size characterization of carbon nanotubes. Simulations were conducted to test the ability of the DMA to not only classify carbon nanotubes but also distinguish between CNTs and catalyst particles. Both appeared possible by adjusting the $N_0 t$ product. A method of online size characterization was developed for nanotubes using a system-specific charge parameter along with electrical mobility theory for elongated particles. This methodology allows one dimension of the nanotube/nanofiber to be measured if the other is known or can be estimated. The method was tested and confirmed using commercial carbon nanotubes classified by a DMA. This method of online size characterization allows for faster optimization of gas phase carbon nanotube production. In addition, it could also be valuable for online air quality measurements related to nanofibers and nanotubes. Finally, TEM sample preparation and analysis methods were discussed due to the important role of microscopy in calibrating or validating online measurements. In particular, by identifying functional relationships between length and width, microscopy can make it possible for the online techniques described here to infer the size distribution of both.

Nomenclature

$\bar{c}$	mean ion thermal velocity
$\bar{c}_{\parallel}$	mean ion velocity parallel to ion flux
C	slip correction factor
d_a	adjusted sphere diameter
d_{ae}	equivalent aerodynamic diameter
d_v	equivalent volumetric diameter
d_1	minor axis diameter
d_s	spherical particle diameter
D	fiber/nanotube diameter
D_{QE}	charge equivalent diameter

D_{EM}	equivalent mobility diameter
D_{EM}^*	mobility diameter of a sphere carrying one charge
D_{ion}	ion diffusion coefficient
e	elementary charge
E	electric field
f	accommodation coefficient
f_n	charging probability for a conducting spheroid
F	drag force
I	particle current
k	Boltzmann constant
K_f	fiber dielectric constant
K_m	dielectric constant of electrically insulated medium ($K_m < K_f$)
Kn	Knudsen number ($2\lambda/d$)
ℓ	DMA length
L	fiber/nanotube length
n	integer number of charges
$\bar{n}$	median number of charges
N_0	ion concentration at infinity
N_+, N_-	concentrations of positive and negative ions
Q_{sh}	DMA sheath flow rate
r_1	inner radius of DMA column
r_2	outer radius of DMA column
$\bar{r}_m$	distance of minimum total flux
s	+1 or −1 indicates repulsive or attractive force
t	charging time
T	temperature
U	relative velocity between particle and bulk flow
U_0	average velocity of the air stream at impactor jet exit
v	dielectrophoretic velocity
V	applied electrical potential of the DMA
V_p	electric potential of a particle
W	impactor jet diameter (circular jet)
Z	electrical mobility
Z_+, Z_-	electrical mobilities of positive and negative ions

Greek Letters

α	constant equal to K_f/K_m
β	aspect ratio (L/D)
γ	ion sticking probability
ε_0	permittivity of vacuum
ϕ	constant relating the gas viscosity to the mean free path
ϕ_c	dimensionless potential function
λ	gas mean free path
ρ_0	unit density (1 g/cc)

ρ particle density
θ orientation angle between polar axis and direction of flow
μ gas viscosity
$\chi_\perp$ dynamic shape factor with long axis perpendicular to the flow
$\chi_\parallel$ dynamic shape factor with long axis parallel to the flow
ψ system-specific charge parameter
ψ_0 charging parameter

References

[1]   Lippmann, M. (1988). Asbestos exposure indexes. *Environ Res* **46**:86–106.

[2]   Baron, P.A., Sorensen, C.M., and Brockman, J.E. (2001). Nonspherical particle measurement: Shape factors, fractals and fibers. In: Willike, K., Baron, P.A. (Eds.) *Nonspherical Particle Measurement: Shape Factors, Fractals and Fibers*. Wiley, New York, pp. 705–749.

[3]   Mordkovich, V.Z. (2003). Carbon nanofibers: A new ultrahigh-strength material for chemical technology. *Theor Found Chem Eng* **37**:429–438.

[4]   Terrones, M. (2004). Carbon nanotubes: Synthesis and properties, electronic devices and other emerging applications. *Int Mater Rev* **49**:325–377.

[5]   Stober, W., Flaschsbart, H., and Hochrainer, D. (1970). The aerodynamic diameter of latex aggregates and asbestos fibers. *Staub–Reinhalt Luft* **30**:1–12.

[6]   Burke, W. and Esmen, N.A. (1978). The inertial behavior of fibers. *Amer Ind Hyg Assoc J* **39**:400–405.

[7]   Martonen, T.B. (1990). Measurement of aerodynamic size and related risk of airborne fibers. *World Congress-Particle Technology*, Kyoto Japan, Society of Powder Technology, Japan.

[8]   Griffiths, W.D. and Vaughn, N.P. (1986). The aerodynamic behaviour of cylindrical and spheroidal particles when settling under gravity. *J Aerosol Sci* **17**:53–65.

[9]   Asgharian, B. and Godo, M.N. (1999). Size separation of spherical particles and fibers in an aerosol centrifuge. *Aerosol Sci Tech* **30**:383–400.

[10]   Raabe, O.G., Braaten, D.A., Axelbaum, R.L., Teague, S.V., and Cahill, T.A. (1988). Calibration studies of the drum impactor. *J Aerosol Sci* **19**:183–195.

[11]   Raabe, O.G. (1976). Aerosol aerodynamic size conventions for inertial sampler calibration. *J Air Pollut Control Assoc* **26**:856–860.

[12]   Allen, M.D. and Raabe, O.G. (1985). Slip correction measurements of spherical solid aerosol particles in an improved Millikan apparatus. *Aerosol Sci Tech* **4**:269–286.

[13]   Cheng, Y.S., Allen, M.D., Gallegos, D.P., Yeh, H.C., and Peterson, K. (1988). Drag force and slip correction of aggregate aerosols. *Aerosol Sci Tech* **8**:199–214.

[14]   Cheng, Y.S., Powell, Q.H., Smith, S.M., and Johnson, N.F. (1995). Silicon-carbide whiskers—Characterization and aerodynamic behaviors. *Am Ind Hyg Assoc J* **56**:970–978.

[15]   Heiss, J.F. and Coull, J. (1952). The effect of orientation and shape on the settling velocity of non-isometric particles in a viscous medium. *Chem Eng Progress* **48**:133–140.

[16]   Youngren, G.K. and Acrivos, A. (1975). Stokes flow past a particle of arbitrary shape: A numerical solution. *J Fluid Mech* **69**:377–403.

[17]   Kasper, G., Niida, T., and Yang, M. (1985). Measurements of viscous drag on cylinders and chains of spheres with aspect ratio between 2 and 50. *J Aerosol Sci* **16**:535–556.

[18] Chen, B.T., Irwin, R., Cheng, Y.S., Hoover, M.D., and Yeh, H.C. (1993). Aerodynamic behavior of fiber-like and disk-like particles in a millikan cell apparatus. *J Aerosol Sci* **24**:181–195.

[19] Dahneke, B.E. (1973). Slip correction factors for nonspherical bodies: The form of the general law. *J Aerosol Sci* **4**:163–170.

[20] Myojo, T. (1998.) A length-selective technique for fibrous aerosols. In: Spurny, K.R. (Ed.) *Advances in Aerosol Filtration*, Boca Raton, FL: Lewis, pp. 481–498.

[21] Spurny, K.R., Stober, W., Opiela, H., and Weiss, G. (1979). Size-selective preparation of inorganic fibers for biological experiments. *Am Ind Hyg Assoc J* **40**:20–38.

[22] Baron, P.A., Deye, G.J., and Fernback, J. (1994). Length separation of fibers. *Aerosol Sci Tech* **21**:179–192.

[23] Lipowicz, P.J. and Yeh, H.C. (1989). Fiber dielectrophoresis. *Aerosol Sci Tech* **11**:206–212.

[24] Fuchs, N.A. (1964). *The Mechanics of Aerosols*. New York: Permagon.

[25] Lilienfeld, P. (1985). Rotational electrodynamics of airborne fibers. *J Aerosol Sci* **16**:315–322.

[26] Baron, P.A., Deye, G.J., Fernback, J.E., and Jones, W.G. (1998). Direct-reading measurement of fiber length/diameter distributions. *Advances in Environmental Measurement Methods for Asbestos*, Boulder, CO: American Society for Testing Materials.

[27] Deye, G.J., Gao, P., Baron, P.A., and Fernback, J. (1999). Performance evaluation of a fiber length classifier. *Aerosol Sci Tech* **30**:420–437.

[28] Wen, H.Y., Reischl, G.P., and Kasper, G. (1984a). Bipolar diffusion charging of fibrous aerosol particles: Charging theory. *J Aerosol Sci* **15**:89–101.

[29] Wen, H.Y., Reischl, G.P., and Kasper, G. (1984b). Bipolar diffusion charging of fibrous aerosol particles: Charge and electrical mobility measurements on linear chain aggregates. *J Aerosol Sci* **15**:103–122.

[30] Keefe, D., Nolan, P.J., and Rich, T.A. (1959). Charge equilibrium in aerosols according to the Boltzmann law. *Proc R Ir Acad* **60A**:27–45.

[31] Gunn, R. (1955). The statistical electrification of aerosols by ionic diffusion. *J Colloid Interface Sci* **10**:107–119.

[32] Natanson, G.L. (1960). Theory of charging submicroscopic aerosol particles as a result of capturing gas ions. *J Tech Phys* (Russian) **30**:573–588.

[33] Fuchs, N.A. (1963). On the stationary charge distribution on aerosol particles in a bipolar ionic atmosphere. *Geofis Pura Appl* **56**:185–193.

[34] Han, R.J. and Gentry, J.W. (1993). Field and combined diffusional and field charging of fibrous aerosols. *Aerosol Sci Tech* **18**:165–179.

[35] Zebel, G., Hochrainer, D., and Boose, C. (1977). A sampling method with separated deposition of airborne fibers and other particles. *J Aerosol Sci* **8**:205–213.

[36] Laframboise, J.G. and Chang, J.S. (1977). Theory of charge deposition on charged aerosol particles of arbitrary shape. *J Aerosol Sci* **8**:331–338.

[37] Wang, C.C., Pao, J.R., and Gentry, J.W. (1988). Calculations and measurements of the charge distribution for non-spherical particles. *J Aerosol Sci* **19**:805–808.

[38] Han, R.J. and Gentry, J.W. (1993). Unipolar diffusional charging of fibrous aerosols—theory and experiment. *J Aerosol Sci* **24**:211–226.

[39] Gentry, J.W. (1972). Charging of aerosol by unipolar diffusion of ions. *J Aerosol Sci* **3**:65–76.

[40] Hochrainer, D., Zebel, G., and Prodi, V. (1978). Ein gerat zur trennung von fasern und isometrischen partikeln bei der probenahme. *Staub–Reinhalt Luft* **38**:425–429.

[41] Griffiths, W.D. (1987). The shape selective sampling of fibrous aerosols. *J Aerosol Sci* **19**:703–713.

[42] Yu, P.Y., Wang, C.C., and Gentry, J.W. (1987). Experimental measurement of the rate of unipolar charging of actinolite fibers. *J Aerosol Sci* **18**:73–85.

[43] TSI Incorporated. (2000). *Model 3080 Electrostatic Classifier: Instruction Manual.* pp. b–5.

[44] Chen, B.T., Yeh, H.C., and Hobbs, C.H. (1993). Size classification of carbon–fiber aerosols. *Aerosol Sci Tech* **19**:109–120.

[45] Chen, B.T., Yeh, H.C., and Johnson, N.F. (1996). Design and use of a virtual impactor and an electrical classifier for generation of test fiber aerosols with narrow size distributions. *J Aerosol Sci* **27**:83–94.

[46] Calvert, P. (1997). Potential applications of nanotubes. In: Ebbesen, T.W. (Ed.) *Carbon Nanotubes: Preparation and Properties*, Boca Raton, FL:CRC, pp. 277–292.

[47] Saito, R., Dresselhaus, G., and Dresselhaus, U.S. (1998). *Physical Properties of Carbon Nanotubes*. London: Imperial College Press.

[48] Planeix, J.M., Coustel, N., Coq, B., Brotons, V., Kumbhar, P.S., Dutartre, R., Geneste, P., Bernier, P., and Ajayan, P.M. (1994). Application of carbon nanotubes as supports in heterogeneous catalysis. *J Am Chem Soc* **116**:7935–7936.

[49] Schlitter, R.R., Seo, J.W., Gimzewski, J.K., Durkan, C., Saifullah, M.S.M., and Welland, M.E (2001) Single crystals of single-walled carbon nanotubes formed by self-assembly. *Science* **292**:1136–1139.

[50] Liu, C., Fan, Y.Y., Liu, M., Cong, H.T., Cheng, H.M., and Dresselhaus, M.S. (1999). Hydrogen storage in single-walled carbon nanotubes at room temperature. *Science* **286**:1127–1129.

[51] Kong, J., Franklin, N.R., Zhou, C.W., Chapline, M.G., Peng, S., Cho, K.J., Dai, H.J. (2000). Nanotube molecular wires as chemical sensors. *Science* **287**:622–625.

[52] de Jonge, N., Lamy, Y., Schoots, K., and Oosterkamp, T.H. (2002). High brightness electron beam from a multi-walled carbon nanotube. *Nature* **420**:393–395.

[53] Liu, J., Fan, S., and Dai, H. (2004). Recent advances in methods of forming carbon nanotubes. *Mrs Bull* **29**:244–250.

[54] Dillon, A.C., Parialla, P.A., Alleman, J.L., Perkins, J.D., and Heben, M.J. (2000). Controlling single-wall nanotube diameters with variation in laser pulse power. *Chem Phys Lett* **316**:13–18.

[55] Puretzky, A.A., Geohegan, D.B., Fan, X., and Pennycook, S.J. (2000). Dynamics of single-wall carbon nanotube synthesis by laser vaporization. *Appl Phys A* **70**:153–160.

[56] Kamalakaran, R., Terrones, M., Seeger, T., Kohler-Redlich, P., Ruhle, M., Kim, Y.A., Hayashi, T., and Endo, M. (2000). Synthesis of thick and crystalline nanotube arrays by spray pyrolysis. *Appl Phys Lett* **77**:3385–3387.

[57] Andrews, R., Jacques, D., Rao, A.M., Derbyshire. F., Qian, D., Fan, X., Dickey, E.C., and Chen, J. (1999). Continuous production of aligned carbon nanotubes: A step closer to commercial realization. *Chem Phys Lett* **303**:467–474.

[58] Nikolaev, P., Bronikowski, M.J., Bradley, R.K., Rohmund, F., Colbert, D.T., Smith, K.A., and Smalley, R.E. (1999). Gas-phase catalytic growth of single-walled carbon nanotubes from carbon monoxide. *Chem Phys Lett* **313**:91–97.

[59] Cheng, H.M., Li, F., Sun, X., Brown, S.D.M., Pimenta, M.A., Marucci, A., Dresselhaus, G., and Dresselhaus, M.S. (1998). Bulk morphology and diameter distribution of single-walled carbon nanotubes synthesized by catalytic decomposition of hydrocarbons. *Chem Phys Lett* **289**:602–610.

[60] Nikolaev, P. (2004). Gas-phase production of single-walled carbon nanotubes from carbon monoxide: A review of the hipco process. *J Nanosci Nanotech* **4**: 307–316.

[61] Van der Wal, R.L., Ticich, T.M., and Curtis, V.E. (2000). Diffusion flame synthesis of single-walled carbon nanotubes. *Chem Phys Lett* **323**:217–223.

[62] Height, M.J., Howard, J.B., Tester, J.W., and Sande, J.B.V. (2004). Flame synthesis of single-walled carbon nanotubes. *Carbon* **42**:2295–2307.

[63] Lee, G.W., Jurng, J., and Hwang, J. (2004). Formation of nickel-catalyzed multi-walled carbon nanotubes and nanofibers on a substrate using an ethylene inverse diffusion flame. Combust Flame **139**:167–175.

[64] Diener, M.D., Nichelson, N., and Alford, J.M. (2000). Synthesis of single-walled carbon nanotubes in flames. *J Phys Chem B* **104**:9615–9620.

[65] Saveliev, A.V., Merchan-Merchan, W., and Kennedy, L.A. (2003). Metal catalyzed synthesis of carbon nanostructures in an opposed flow methane oxygen flame. *Combust Flame* **135**:27–33.

[66] Pan, C.X., Liu, Y.L., Cao, F., Wang, J.B., and Ren, Y.Y. (2004). Synthesis and growth mechanism of carbon nanotubes and nanofibers from ethanol flames. *Micron* **35**:461–468.

[67] Maynard, A.D., Baron, P.A., Foley, M., Shvedova, A.A., Kisin, E.R., and Castranova, V. (2004). Exposure to carbon nanotube material: Aerosol release during the handling of unrefined single-walled carbon nanotube material. *J Toxicol Env Heal A* **67**:87–107.

[68] Nasibulin, A.G., Moisala, A., Brown, D.P., Jiang, H., and Kauppinen, E.I. (2005). A novel aerosol method for single walled carbon nanotube synthesis. *Chem Phys Lett* **402**:227–232.

[69] Cheng, Y.S. (1991). Drag forces on nonspherical aerosol particles. *Chem Eng Commun* **108**:201–223.

[70] Hinds, W.C. (1999). *Aerosol Technology: Properties, Behavior, and Measurement of Airborne Particles.* New York: John Wiley.

[71] Koratkar, N., Modi, A., Kim, J., Wei, B.Q., Vajtai, R., Talapatra, S., and Ajayan, P.M. (2004). Mobility of carbon nanotubes in high electric fields. *J Nanosci Nanotechn* **4**:69–71.

[72] Kousaka, Y., Endo, Y., Ichitsubo, H., and Alonso, M. (1996). Orientation-specific dynamic shape factors for doublets and triplets of spheres in the transition regime. *Aerosol Sci Tech* **24**:36–44.

[73] Batchelor, G.K. (1970). Slender-body theory for particles of arbitrary cross-section in stokes flow. *J Fluid Mech* **44**:419–440.

[74] Dahneke, B.E. (1973). Slip correction factors of nonspherical bodies. I. Free molecule flow. *J Aerosol Sci* **4**:147–161.

[75] Rothbard, D.R. (2003) Electron microscopy for the pulp and paper industry. In: Li, Z.R. (Ed.) *Industrial Applications of Electron Microscopy*, New York: Marcel Dekker

[76] Chan, I.Y. (2003). Characterization of petroleum catalysts by electron microscopy. In: Li, Z.R. (Ed.) *Industrial Applications of Electron Microscopy*, New York: Marcel Dekker.

[77] Kubic, T.A. (2003). Forensic applications of scanning electron microscopy with x-ray analysis. In: Li, Z.R. (Ed.) *Industrial Applications of Electron Microscopy*, New York: Marcel Dekker.

[78] Choi, W.B. and Lee, Y.H. (2003). Carbon nanotube and its application to nanoelectronics. In: Li, Z.R. (Ed.) *Industrial Applications of Electron Microscopy*, New York: Marcel Dekker.

[79] Liang, L. and Li, Z.R. (2003). Digital imaging in electron microscopy. In: Li, Z.R. (Ed.) *Industrial Applications of Electron Microscopy*, New York: Marcel Dekker.

[80] NIOSH. *NIOSH manual of analytical methods* (4th). ONLINE. (1994). U.S. Division of Health and Human Services: National Institute of Occupational Safety and Health. Available: http://www.cdc.gov/niosh/nmam/.

[81] Nichols, M.R., Moss, M.A., Reed, D.K., Lin, W., Mukhopadhyay, R., Hoh, J.H., and Rosenberry, T.L. (2002). Growth of â-amyloid(1–40) protofibrils by monomer elongation and lateral association. Characterization of distinct products by light scattering and atomic force microscopy. *Biochemistry* **41**:6115–6127.

[82] Mandell, E., Fraundorf, P., and Bertino, M.F. (2004). Powder patterns from nanocrystal lattice images. *Microsc Microanal* **10**:1254–1255.

[83] Russ, J.C. (1999). *The Image Processing Handbook*. Boca Raton, FL: CRC and IEEE.

[84] Rasband, W. *Imagej*. http://rsbinfonihgov/ij/.

[85] Gupta, S., Wang, Y.Y., Garguilo, J.M., and Nemanich, R.J. (2005). Imaging temperature dependent field emission from carbon nanotube films: Single- versus multi-walled. *Appl Phys Lett* **86**:063109/1–063109/3.

[86] Henn, A. and Fraundorf, P. (1990). A quantitative measure of the degree of fibrillation of short reinforcing fibers. *J Mater Sci* **25**:3659–3663.

[87] Cliff, G. and Lorimer, G.W. (1975). The quantitative analysis of thin specimens. *J Microscopy* **103**:203–207.

[88] Gibbons, P., Bradley, C.R., and Fraundorf, P.B. (1987). How to remove multiple scattering from core-excitation spectra iii: Varying the mean free path. *Ultramicroscopy* **21**:305–312.

[89] Egerton, R.F. (1996). *Electron Energy Loss Spectroscopy in the Electron Microscope.* New York: Plenum.

10
Theoretical Investigations in Retinal and Cubane

G. P. Zhang and Thomas F. George

10.1. Introduction

Successful isolation and characterization of higher diamondoids has revitalized the interest in this compound [1]. Diamondoids represent a group of hydrocarbon molecules with a structure similar to part of a typical diamond structure. In fact, one can successively construct different diamondoids by excising from the diamond crystal lattice and saturating dangling carbon bonds with hydrogen atoms. Recent molecular simulation studies [2] reveal more details about this compound and suggest some possible applications in nanotechnology. Adamantane has important pharmaceutical applications. Adamantane and cyclopentane are also known as "plastic crystals" [3]. The theoretical challenge to simulate those diamondoids mainly comes from the system size. For instance, the smallest one, called adamantane (from $\alpha\delta\alpha\mu\alpha\chi$, the Greek word for diamond) is a tricyclodecane $C_{10}H_{16}$ (see Figure 10.1). Within the Hartree–Fock approximation and multiple-configuration interaction with a limited basis set, adamantane can be easily handled by much state-of-art software such as Molpro, Gaussian, and GAMES. In this respect, theoretical computations are much easier than those in transition metal oxide compounds and clusters where the electron correlation plays an important role. However, when the system size becomes larger, which is most like those in real experiments, a theoretical investigation becomes rather difficult, especially if one is interested in studying the properties at the first-principles level.

There are numerous references to diamondoids in the literature. In this chapter, we focus our attention on the optical and mechanical properties. Our aim is to lay the groundwork to compare theoretical results with experimental atomic force microscopy (AFM) measurements. AFM is a powerful tool for probing intermolecular interactions because it can resolve forces down to a piconewton, and has extremely high spatial resolution. But it does not have the chemical group sensitivity, which motivates the development of the so-called chemical force microscopy [4]. Consequently, when we present the theoretical study below, we always keep this in mind. The theoretical study can be roughly categorized into two groups: semiclassical and pure quantum mechanical simulations. In the following, we address these two problems sequentially.

FIGURE 10.1. Adamantane.
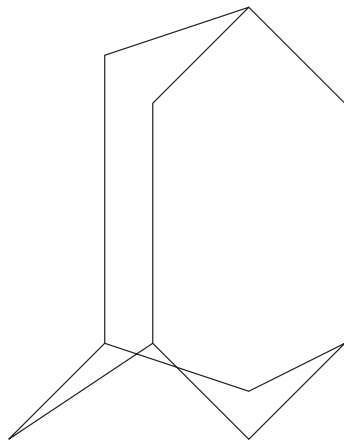
10.2. Semiclassical and Empirical Method

The semiclassical approach heavily relies on the empirical interactions. As in many molecular systems, diamondoids have both intramolecular and intermolecular interactions. Intramolecular interactions reflect the bonding nature of the system. For instance, C–H bonds have very different potential surfaces from those of C–C bonds, to which they are also related whether the bonds are single, double, or triple. The Lennard–Jones potential is probably the simplest one to use. In general, a two-body potential can be expanded as

$$V(\vec{r}_i, \vec{r}_j) = V_{el} + V_{dipole} + V_{quad} + \cdots, \tag{1}$$

where V_{el}, V_{dipole}, and V_{quad} are the electronic contribution, dipole, and quadruple terms, respectively. Some common potentials are listed in Table 10.1. For many-body interactions, direct calculations become very difficult, and consequently an approximation has to be made at some step. Intermolecular interactions are those that occur between molecules. Due to the finite size of the molecules, the orientation of the molecules has to be taken into account properly when constructing a potential. Consequently, the intermolecular interaction is known to be

TABLE 10.1 Some common potentials. Δr refers to the distance between two atoms or molecules. K is the spring constant. D, a, b, and σ are fitting parameters.

Name	Form	Applicability
Harmonic	$\frac{K}{2}\Delta r^2$	Short-range, weak
Morse	$\epsilon[(1 - e^{-\alpha\Delta r})^2 - 1]$	Chemically bonded
Lennard–Jones	$4\epsilon[(\sigma/\Delta r)^{12} - (\sigma/\Delta r)^6]$	Nonbonding
Buckingham	$Ae^{-\Delta r/\sigma} - C(\sigma/\Delta r)^6$	Short-range

orientation-dependent. The beauty of classical simulations is that it enables us to treat very large systems.

From these potentials, the effective force can be computed by taking the derivatives of the potential with respect to the position, which can be compared with the force from atomic force microscopy. However, a realistic experimental measurement complicates such a comparison. Experimentally, a measurement of the atomic force is done by scanning a very sharp tip across a sample. This force depends on the surface morphology and local type of binding: covalent, ionic, metallic, or van der Waals. The change of force versus distance reflects the joint effect from the interactions among the electrons, atoms, and molecules on the surface and those on the tip. This is not an easy task, because entirely different bonds would result in the same magnitude and displacement relation. A systematic and element or bond-specific AFM is needed in order to compare with the theoretical simulations.

10.3. First-Principles Calculations

Classical simulations often lack the crucial insight into the problem, because one cannot simply use the force to characterize all the possible interactions. Fortunately, with decades of development, theoretical calculations have become quite sophisticated for crystals and molecules, although not yet for realistic nanometer-sized materials. For solids, the pseudopotential as well as the full-potential linearized augmented plane-wave (FLAPW) method within the density functional theory are well developed. Modern quantum chemical techniques (Gaussian98 [5] and MOLPRO [6]) are quite efficient to compute the potential surfaces for a given molecule. In order to illustrate those possibilities, we show some of our own results in simulating the reaction path for a segment of the retinal molecule in rhodopsin [7].

10.3.1. Segment of Retinal Molecule

Retinal molecules are the basic element in human eyes that initiates our vision. Malfunctioning of these molecules could lead to eye illness or even blindness. In order to avoid such malfunctioning, one must first understand the so-called photo-induced isomerization in retinal, or conformation change of the molecule upon excitation of light.

Figure 10.2 shows the rhodopsin structure. Isomerization occurs around the bond 11–12 with angle $\theta_{11,12}$. Here 11 and 12 refer to the numbers of the carbon
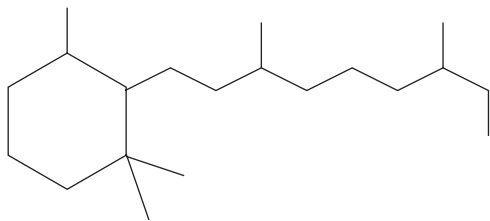
FIGURE 10.2. Rhodopsin. In the actual calculation, we only use a small segment, which contains nine carbon atoms and two methyl groups along the backbone.

FIGURE 10.3. Ground-state potential versus angle $\theta_{11,12}$ in a segment of rhodopsin.
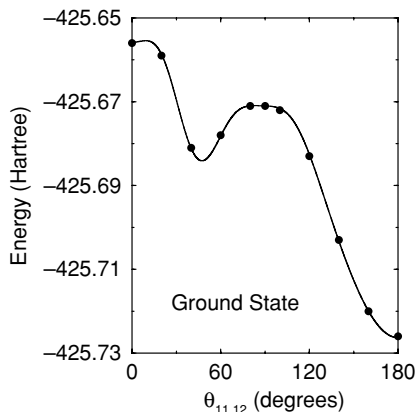
atoms counting from the left. In the present calculations, we have employed the multiconfiguration self-consistent field (MCSCF) [8] technique to compute the ground state and two excited states by the Molpro package [9]. The basis set used for hydrogen is (4S 1P)/[2S 1P], and for carbon, (9S 4P 1D)/[3S 2P 1D] is used, where both basis functions are correlation-consistent basis sets. After Hartree–Fock iterations, these basis sets are optimized for the later MCSCF calculations. We fully optimize the molecule structure and then calculate the ground-state and excited-state potentials as a function of the dihedral angle $\theta_{11,12}$.

In Figure 10.3, we plot the ground-state potential as a function of the dihedral angle $\theta_{11,12}$. Note that the configuration at $\theta_{11,12} = 0°$ corresponds to a *cis*-structure. A potential surface shaped like the Greek letter η is noted. The figure shows that due to the steric hindrance, the ground state has an all-*trans* configuration.

Within MCSCF, the excited-state potential surfaces are obtained simultaneously. The excited-state potentials are plotted in Figure 10.4. Note that in order to
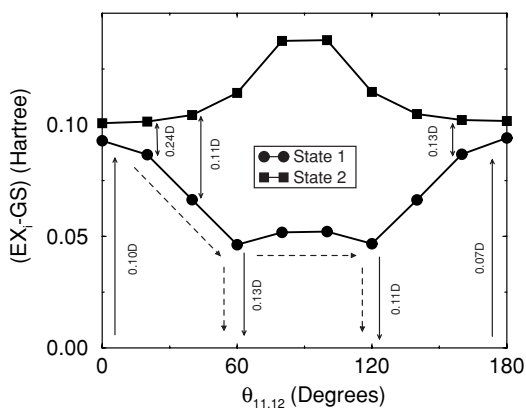
FIGURE 10.4. Potential for the excited state versus the angle around the bond 11–12. It is importantly to note, the transition matrix elements are also accurately obtained.

have a clear view of the change of the excited-state potentials with respect to the ground-state potential, the ground-state energies have been subtracted from the excited-state energies at each dihedral angle $\theta_{11,12}$. One prominent feature is that those surfaces are roughly symmetric with respect to $\theta_{11,12} = 90°$. For the first-excited state, a minimum appears around $\theta_{11,12} = 60°–120°$. This minimum is very important because it provides a barrierless decay channel for the isomerization. The traditional explanation of the efficient *trans* ↔ *cis* isomerization is that there is no barrier for undergoing this isomerization on excited-state potentials. Indeed, our ab initio results confirm this picture. Furthermore, we wish to present an optical reason for isomerization by calculating the dipole-matrix elements between the ground and excited states.

Those strongly dipole-allowed transitions are marked with arrows (with solid lines) in Figure 10.4, where their respective transition matrix elements are also provided [11] in Debye units. One important message from the figure is that the dipole-allowed transitions are rather selective in our model system. We focus on the first-excited state for a moment. The allowed transitions from and to the ground state appear around $\theta_{11,12} = 0°$, 60°, 120°, and 180°, with the corresponding transition moments of 0.10D, 0.123D, 0.11D, and 0.07D, respectively. Quite large transition moments at $\theta_{11,12} = 0°$ and 180° ensure that the system can be easily excited, which activates the initial event of isomerization. For the *trans* ↔ *cis* isomerization, the most important angles are 60° and 120°, as it is around these two angles that the *trans* ↔ *cis* isomerization can effectively occur. We use dashed-line arrows to show two possible decay channels: one is around 60°, and the other is around 120° (also see Figure 10.2). It is easy to see that once one reaches 60°, the molecular configuration will tend to *cis* and the other reaches *trans*.

The success of decay to the ground state at these two desired configurations is ensured by the large transition matrix elements between the ground and excited states. Note that we only consider the radiative decay. More interesting, from $\theta_{11,12} = 60°–120°$, the potential surface of the excited state is rather flat. This greatly facilitates not only *cis* → *trans* but also *trans* → *cis* isomerization [10]. The highly selective transitions are further supported by the fact that for those undesired configurations, such as at $\theta_{11,12} = 40°$, which are not favorable to isomerization, the transition elements are basically zero [11]. This means that once an electron is excited to the excited state, it is hard to decay to the ground state at these unfavorable configurations. The high selectivity greatly improves the efficiency of isomerizations, a phenomenon which is very common in biological processes [12]. Here we show the optical aspect of the high selectivity in a short polyene, which is essential to many photoinduced processes.

There are some other reasons why the isomerization is so efficient. In Figure 10.4, we also plot the second-excited-state potential as a function of $\theta_{11,12}$. This potential has a maximum instead of minimum around $\theta_{11,12} = 60–120°$. From the above, we know around $\theta_{11,12} = 60–120°$ is the particular range where the isomerization from the *trans* to *cis* configuration happens. Consequently, for

the second-excited state the isomerization is not favorable. This second-excited state, however, is also virtually dipole-forbidden from the ground state, as we find the transition matrix elements are very small. This guarantees that the second-excited state cannot be excited effectively. Interestingly, the transition matrix elements between the first- and second-excited states are fairly large, so that even if there are some electrons in the second-excited state, they can quickly transit to the first-excited state and finish the isomerization. This eventually ensures a very efficient isomerization.

10.3.2. Cubane

Cubane belongs to a typical class of molecular solids such as carbon clusters (C_{60}, C_{70}). Due to its peculiar structure (i.e., the C–C–C bond angle is 90° rather than the customary 109.5°), cubane stores a great deal of energy, which implies its explosiveness. Cubane was firstly synthesized in 1964 [13] but its remarkable properties, such as potential pharmaceutical applications, have been realized only recently. One of its derivatives, tetranitrocubane, is a very powerful explosive, yet it is extremely stable, a great advantage from a safety standpoint. Another derivative, the dipivaloylcubane compound, exhibits moderate activity against human immunodeficiency virus without impairing healthy cells. This greatly motivates extensive studies both experimentally and theoretically. For example, ab initio calculations provide valuable information on its bond structure and electronic properties. The numerical computations reproduce the experimental bond lengths quite satisfactorily [14]. Spectroscopic properties of cubane have also been explored recently. Miaskiewicz et al. [15] calculated the vibrational spectra of cubane by the density-functional theory. The infrared and Raman spectra have been independently studied by Vlahacos et al. [16] and Jursic [17]. Zakrzewski and Ortiz [18] reported the vertical ionization energies of cubane. On the other hand, the chemical stability of cubane structure is certainly interesting from an application point of view.

The remarkable structural properties of cubane greatly motivate us to investigate its underlying driving force. We employ an ab initio method to calculate its bond structure for a pure cubane. All the calculations are performed at the Hartree–Fock level by the Molpro package [9]. The basis set used for hydrogen is (4S 1P)/[2S 1P], whereas for carbon (9S 4P 1D)/[3S 2P 1D] is used. The basis functions are all valence triple zeta correlated basis sets.

Until Eaton and Cole [13] carried out the first synthesis of cubane, scientists did not believe it could be made. It was thought that even though one made cubane, it would explode spontaneously because a tremendous amount of energy is stored inside the molecule. But when Eaton and Cole made the compound, it turned out to be very stable. Previous calculations showed that the stable structure is cubic (see Figure 10.5) [19].

There are two kinds of bond lengths, namely the length $R_{C–C}$ between two neighboring carbon atoms and the length $R_{C–H}$ between neighboring hydrogen and carbon atoms. In the present study, the structure of cubane is fully optimized
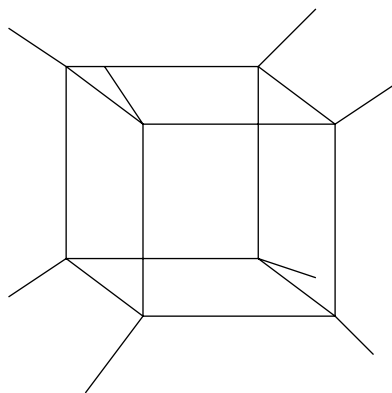
FIGURE 10.5. A typical cubane structure. The origin of the coordinate system is at the center.

without any constraints, which yields a cubic structure with only two kinds of bond lengths, $R_{C-C} = 1.56175$ Å, $R_{C-H} = 1.08774$ Å, in good agreement with both experimental [14] and theoretical results [19]. Experimentally, Hedberg et al. [14] found $R_{C-C} = 1.5618$ Å. Theoretical calculations using different basis sets show that $R_{C-C} = 1.557-1.580$ Å. Note that hereafter all the calculations are based on this fully–optimized structure. In order to see how the total energy changes as a function of one specific bond length, we fix one bond length while variating the other. In Figure 10.6, we plot the total energy as a function of R_{C-C}, where $R_{C-H} = 1.08774$ Å. One sees that with an increase in R_{C-C}, the energy decreases first and then increases. A minimum appears at 1.56175 Å. The estimated dissociation energy is 2.2 Hartree, which indicates that cubane is very stable. A polynomial fit shows that the potential energy changes as

$$V(R_{C-C}) = A_0 + \frac{A_1}{R_{C-C}^{A_2}} + A_3 e^{-A_4 R_{C-C}}, \tag{2}$$
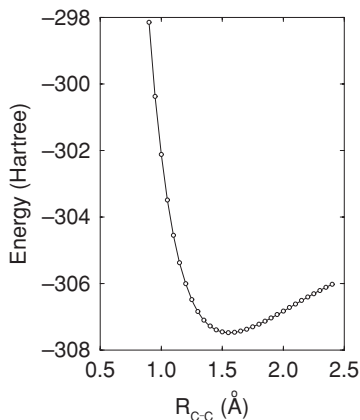
FIGURE 10.6. The potential energy first increases as the helium atom moves towards cubane and then decreases. A peak appears at about $z = -1.86$ Å. The vertical dashed line refers to the z−component of the neighboring hydrogen atom's position. Note that the cubane framework is fixed.

FIGURE 10.7. Analogously the total energy of cubane changes as a function of R_{C-H} whereas R_{C-C} is fixed at 1.56175 Å.
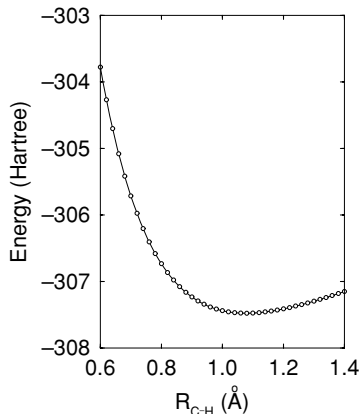
where $A_0 = -305.216$, $A_1 = 25.8292$, $A_2 = 2.20239$, $A_3 = -71.5941$, and $A_4 = 1.14699$. The units of the As are chosen such that the overall unit is Hartree. (The same is true for those Bs below). We notice that the potential form is very different from those listed in Table I. We in fact tried to use those potentials but none of them is able to reproduce our potential. In some sense, our potential does not follow Morse and Lennard–Jones potentials, but behaves more as the Buckingham potential.

Next we fix $R_{C-C} = 1.56175$ Å and change R_{C-H} from 0.6 Å to 1.4 Å. The total energy is plotted as a function of R_{C-H} in Figure 10.7. The minimum is around 1.08774 Å, which reasonably agrees with the previous results. The experimental length is 1.098 Å and the theoretical results range from 1.075 to 1.106 Å. The potential can be fitted as

$$V(R_{C-H}) = B_0 + \frac{B_1}{R_{C-H}^{B_2}} + B_3 e^{R_{C-H}}, \tag{3}$$

where $B_0 = -310.33$, $B_1 = 0.948781$, $B_2 = 3.36077$, and $B_3 = 0.717603$. Comparing $V(R_{C-C})$ with $V(R_{C-H})$, one finds that $V(R_{C-H})$ changes more smoothly. Similarly, the phenomenological potential [20] has a different form from our ab initio potentials, which reflects that cubane does not perfectly fall into the usual hydrocarbon category. This is a direct consequence of its unique structure as aforementioned. The dissociation energy for the hydrogen atoms is found to be 0.9 Hartree, corresponding to 10^5 K. Thus at room temperature, the framework of cubane is very stable.

These two potential forms suggest the complication of the potential in a real simulation. Those simple model potentials in Table 10.1 may have limited applications particularly for nanosystems. This is important for future investigations in other systems.

reflect the position or the policy of the federal government, and no official endorsement should be inferred.

References

[1]   J. E. Dahl, S. G. Liu, and R. M. K. Carlson, *Science* **299**, 96 (2003); A. P. Marchand, *Science* **299**, 52 (2003).

[2]   D. W. Brenner, O. A. Shenderova, D. A. Areshkin, J. D. Schall and S.-J. V. Franklan, *Comput. Model. Eng. Sci.* **3**, 643 (2002); K. E. Drexler, *Nanosystems: Molecular Machinery, Manufacturing, and Computation* (Wiley, new York, 1992).

[3]   J. E. Fisher and P. A. Heiney, *J. Phys. Chem. Solids* **54**, 1725 (1993)

[4]   A. Noy, D. V. Vezenov, and C. M. Lieber, *Ann. Rev. Mater. Sci.* **27**, 381 (1997).

[5]   M. J. Frisch, G. W. Trucks, H. B. Schlegel, G. E. Scuseria, M. A. Robb, J. R. Cheeseman, J. A. Montgomery, Jr., T. Vreven, K. N. Kudin, J. C. Burant, J. M. Millam, S. S. Iyengar, J. Tomasi, V. Barone, B. Mennucci, M. Cossi, G. Scalmani, N. Rega, G. A. Petersson, H. Nakatsuji, M. Hada, M. Ehara, K. Toyota, R. Fukuda, J. Hasegawa, M. Ishida, T. Nakajima, Y. Honda, O. Kitao, H. Nakai, M. Klene, X. Li, J. E. Knox, H. P. Hratchian, J. B. Cross, C. Adamo, J. Jaramillo, R. Gomperts, R. E. Stratmann, O. Yazyev, A. J. Austin, R. Cammi, C. Pomelli, J. W. Ochterski, P. Y. Ayala, K. Morokuma, G. A. Voth, P. Salvador, J. J. Dannenberg, V. G. Zakrzewski, S. Dapprich, A. D. Daniels, M. C. Strain, O. Farkas, D. K. Malick, A. D. Rabuck, K. Raghavachari, J. B. Foresman, J. V. Ortiz, Q. Cui, A. G. Baboul, S. Clifford, J. Cioslowski, B. B. Stefanov, G. Liu, A. Liashenko, P. Piskorz, I. Komaromi, R. L. Martin, D. J. Fox, T. Keith, M. A. Al-Laham, C. Y. Peng, A. Nanayakkara, M. Challacombe, P. M. W. Gill, B. Johnson, W. Chen, M. W. Wong, C. Gonzalez, and J. A. Pople (Gaussian Inc., Pittsburgh PA, 2003.)

[6]   MOLPRO is a package of ab initio programs written by H. J. Werner and P. J. Knowles, with contributions from J. Almlf, R. D. Amos, M. J. O. Deegan, S. T. Elbert, C. Hampel, W. Meyer, K. Peterson, R. Pitzer, A. J. Stone, P. R. Taylor, R. Lindh, M. E. Mura, and T. Thorsteinsson.

[7]   G. P. Zhang, X. F. Zong, and Thomas F. George, *J. Chem. Phys.* **110**, 9765 (1999).

[8]   Actually, we initially also attempted to employ density functional theory to calculate potentials, as it is faster and in some senses includes the exchange interaction, which seems to be superior to the Hartree–Fock approximation. Our calculation showed that even with the best density functional, the total energy is lower than that of the HF calculation, but the wavefunction was found to be poor after we checked the Mulliken population for each atom against other higher-level calculations. This certainly influences the dipole transition elements.

[9]   H.-J. Werner and P. J. Knowles, *J. Chem. Phys.* **82**, 5053 (1985); P. J. Knowles and H.-J. Werner, *Chem. Phys. Lett.* **115**, 259 (1985).

[10]   In retinal, whether it goes to the *cis* or *trans* configuration also depends on surrounding proteins, which regulate different barriers.

[11]   Transition elements smaller than 0.01 *D* are not shown.

[12]   F. Gai, K. C. Hasson, J. C. McDonald, and P. A. Anfinrud, *Science* **279**, 1886 (1998).

[13]   P. E. Eaton and T. W. Cole, Jr., *J. Am. Chem. Soc.* **86**, 3157 (1964).

[14]   L. Hedberg, K. Hedberg, P. E. Eaton, N. Nodari, and A. G. Robiettte, *J. Am. Chem. Soc.* **113**, 1514 (1991).

[15] K. Miaskiewicz and D. A. Smith, *Chem. Phys. Lett.* **270**,

[16] C. P. Vlahacos, H. F. Hameka, and J. O. Jensen, *Chem. Phys. Lett.* **259**, 283 (1996).

[17] B. S. Jursic, *J. Mol. Struct.: THEOCHEM* **394**, 15 (1997).

[18] V. G. Zakrzewski and J. V. Ortiz, *Chem. Phys. Lett.* **230**, 313 (1994).

[19] J. M. Schulman and R. L. Disch, *J. Am. Chem. Soc.* **106**, 1202 (1984).

[20] A. J. Pertsin and A. I. Kitaigorodsky, Eds., *The Atom-Atom Potential Method* (Springer-Verlag, Berlin, 1986).

11
Polyhedral Heteroborane Clusters for Nanotechnology

Fabio Pichierri

11.1. Introduction

Nanotechnology is concerned with the research and development of nanometer-scale (1∼100 nm) devices and materials [1,2]. In principle, two opposing routes towards the nanoscale can be pursued: top-down and bottom-up. The top-down route approaches the nanoscale starting from macroscopic objects and with the aid of lithographic techniques. These are the methods of choice in the manufacturing of microstructures and micromachines with sizes in the range of 1–100 μm [3]. The main factor limiting the sizes of features patterned with optical lithography is represented by the wavelength of the radiation employed. Both electron- and ion-beam lithographic techniques are currently capable of manufacturing patterns of sizes close to or below 200 nm thereby extending the resolution limits of conventional optical lithography [4].

The bottom-up route, on the other hand, arrives at nanostructures by assembling either atoms or molecules. Whereas physicists prefer using atoms as building blocks, chemists are well acquainted with the synthesis, modification, and study of molecules. Given that molecules are stable assemblies of atoms covalently linked to one another, we can expect the chemists' molecule-by-molecule bottom-up approach to nanostructures to be more effective and promising than that of manipulating "sticky" atoms one at a time.

Many research activities in nanotechnology are inspired by nature, which has successfully built marvelous and complex molecular-scale machines such as, for example, the bacterial flagellar motor [5]. This giant protein assembly couples mechanical motion to proton (or sodium ion) transfer to propel flagellated bacteria within fluids. Another important observation about the nanotech revolution concerns the convergence of traditional scientific disciplines (chemistry, physics, biology, medicine) and engineering. Scientists working on the most fundamental aspects of nanoscience and nanotechnology cannot forget about the technological implications of their research.

This chapter provides an overview of the structural and electronic properties of polyhedral heteroborane clusters and their potential use as building blocks in nanotechnology. These clusters comprise polyhedral boranes (boron hydrides),

256

carboranes (hydrides of boron and carbon), and metallacarboranes (carboranes incorporating transition metal ions) [6–11]. Their crystal structures have been searched within the Cambridge Structure Database (CSD), version 5.26 [12]. Each structure is labeled with a six-letter code (sometimes followed by a number) that can be used for data retrieval from the database. Structures are explicitly referenced only when they are relevant to the discussion.

The chemistry of boron hydrides [6–11] is as wide and fascinating as its sister field of hydrocarbon (organic) chemistry. So far, two scientists have been awarded the Nobel Prize in Chemistry for research carried out in this field [13]. William Lipscomb was awarded the prize in 1976 "for his studies on the structure of boranes illuminating problems of chemical bonding." Two years after, in 1979, Herbert C. Brown shared the prize with Georg Wittig "for their development of the use of boron- and phosphorus-containing compounds, respectively, into important reagents in organic synthesis." These scientists have followed the footsteps of Alfred Stock whose pioneer work on boranes started in 1912 [7]. Outstanding developments and advances in this research field have been contributed by the groups of Hawthorne, Grimes, Valliant, Wade, and many others. The next section provides the necessary background for understanding the molecular and electronic structure of polyhedral heteroborane clusters, which comprise boranes, carboranes, and metallacarboranes. Section 11.3 deals with the potential applications of these molecules to nanotechnology and Section 11.4 presents a general discussion about the computational design of functional materials.

11.2. Structural and Electronic Properties

11.2.1. Borane Clusters

Borane clusters have been classified according to the topology of their molecular frameworks. Accordingly, *closo* boranes (from the Greek *clovos*, meaning cage) are closed polyhedra, *nido* (from the Latin *nidus*, meaning nest) boranes are semi-closed polyhedra, and *arachno* (from the Greek *arachne*, meaning spider's web) boranes possess open structures [6]. Both *nido* and *arachno* boranes are neutral specie whereas *closo* boranes are stable as dianions of chemical formula $[B_nH_n]^{2-}$, with $n = 5–12$. Figure 11.1 displays the crystal structures of *nido*-B_5H_9 (GAC-WOW), *nido*-$B_{10}H_{14}$ (FUYYIH02), *arachno*-B_5H_{11} (FUYYUT) *closo*-$[B_6H_6]^{2-}$ (GIGRIX, O_h), and *closo*-$[B_{12}H_{12}]^{2-}$ (GAZLEY, I_h). The polyhedral clusters are often called deltahedra for their faces are made of triangular B_3 units. The experimentally determined B–B bond distances in both *nido* and *arachno* boranes are in the range from 1.77 to 1.98 Å. That of *closo*-$[B_6H_6]^{2-}$ is at ~1.77 Å and the B–B distance in *closo*-$[B_{12}H_{12}]^{2-}$ is at ~1.8 Å.

In comparison to carbon, boron is said to be electron-deficient inasmuch as its valence shell is made of four atomic orbitals (one s and three p) occupied by three electrons [6]. It follows that chemical bonding in boranes cannot be described only with the use of two-center–two-electron (2c–2e) interactions but

GACWOW   FUYYIH02   FUYYUT

GIGRIX   GAZLEY
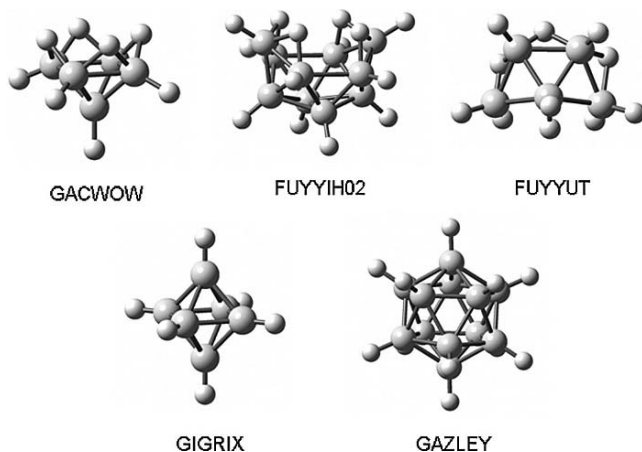
FIGURE 11.1. Crystal structures of some borane clusters.

one must resort on three-center–two-electron (3c–2e) interactions as well. The latter were introduced by Christopher Longuet-Higgins in 1949 and Lipscomb further developed a qualitative theory of localized bonding interactions in boranes [6]. This theory employs the 2c–2e interactions to describe both B–H and B–B bonds whereas the 3c–2e interactions are necessary for describing the chemical bonding within both B–H–B and B–B–B bridges as well that in the B_3 units of the deltahedron. Theoretical arguments based on molecular orbital (MO) theory are more powerful in describing the electronic structures of *closo* boranes of high symmetry such as *closo*-$[B_{12}H_{12}]^{2-}$. With the advent of fast computers and efficient algorithms, structurally complex boranes and their derivatives are amenable to quantitative theoretical treatment with the aid of computational quantum chemistry methods [14].

Functionalization of borane clusters has been successfully achieved following a variety of synthetic routes [6]. Particularly interesting are the derivatives of *closo*-$[B_{12}H_{12}]^{2-}$ some of which are shown in Figure 11.2. Both mono- and disubstituted derivatives have been prepared. An interesting compound is PAVWUE which contains a 1,2-oxalate dianion coordinated via two of its oxygen atoms to one edge of the polyhedron. The existence of many crystal structures, several of which are polymeric, where transition metals are coordinated to either side of the 1,2-oxalate dianion suggests the possibility of using this building block in the preparation of novel nanostructured materials.

The poly-functionalization of *closo*-$[B_{12}H_{12}]^{2-}$ has been achieved in *closo*-$[B_{12}F_{12}]^{2-}$ (GUZFOW) and *closo*-$[B_{12}Me_{12}]^{2-}$ (XETBON), whose crystal structures are shown in Figure 11.3. Hawthorne's group has recently discovered that the oxidation of *closo*-$[B_{12}H_{12}]^{2-}$ with hydrogen peroxide yields *closo*-$[B_{12}(OH)_{12}]^{2-}$ (JOQVAM) in which the OH groups have fully replaced the H atoms of the starting compound [15].

RIKRUY (X–NH$_3$)
RILQEI (X=Phenyl)   HIZYUK (Y=CO)   PAVWUE
SEPBIY (X=CH$_3$)   HIZZAR (Y=CO$_2$H$_2$)
TAKRAZ (X=SCN)
FADMUT (X=OH)
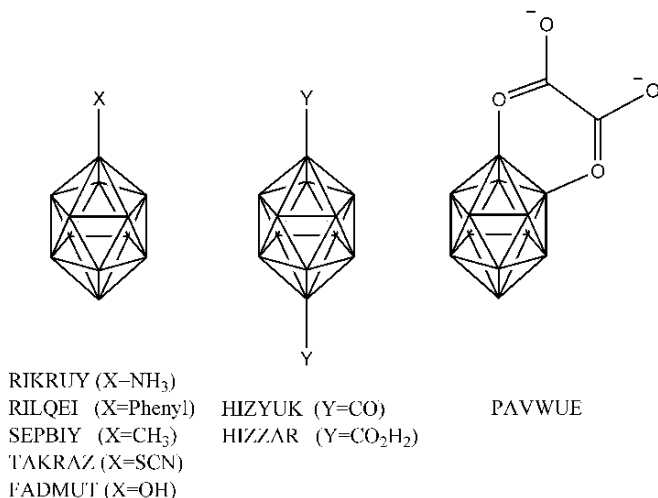
FIGURE 11.2. Some derivatives of *closo*-[B$_{12}$H$_{12}$]$^{2-}$. Each vertex of the polyhedron represents a BH moiety.

This novel reaction paves the way towards the synthesis of polyfunctionalized borane clusters (*closomers*) bearing large organic groups attached to the B$_{12}$ core. With diameters greater than 1 nm, these novel compounds can be considered true molecular nanoparticles. We discuss them in detail later on in this chapter. Further information on the preparation and reactivity of borane compounds can be found in the more specialized chemistry literature [6].

11.2.2. Carborane Clusters

Carborane clusters are formally obtained from the replacement of one or more BH$^-$ units with isoelectronic CH units [6]. More than 95% of the carboranes synthesized so far possess two carbon atoms embedded in their skeletons. This is the group of dicarba-*closo*-boranes with chemical formula C$_2$B$_n$H$_{n+2}$, with $n = 3$–10. Their

GUZFOW   XETBON   JOQVAM

FIGURE 11.3. Polyfunctionalized derivatives of *closo*-[B$_{12}$H$_{12}$]$^{2-}$.
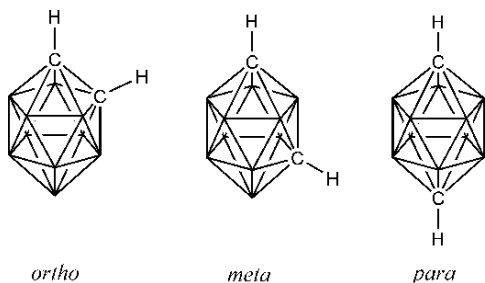
FIGURE 11.4. The three isomers of *closo*-$C_2B_{10}H_{12}$.

ortho   *meta*   *para*

structures are similar to those of the polyhedral boranes discussed above. Figure 11.4 shows the molecular structures of three isomers (*ortho, meta, para*) of *closo*-$C_2B_{10}H_{12}$. They differ from one another by the relative position of the two carbon atoms in the cage. The carbon atoms in these isomers are separated at 1.62 Å (*ortho*), 2.61 Å (*metha*), and 3.05 Å (*para*). Note that only the first interatomic distance corresponds to a covalent (2c–2e) bond.

Substituents have been attached to either one or both carbon atoms of *closo*-$C_2B_{10}H_{12}$ isomers. Relevant examples of derivatives whose structures have been characterized by single-crystal X-ray crystallography are displayed in Figure 11.5. Particularly interesting molecules are QUAFWOK and XATDOL containing one amide group and two acetyl groups, respectively. The former derivative suggests the possibility of introducing carborane clusters into proteins and the latter derivative represents a link between borane and acetylene chemistries.

11.2.3. Metallacarborane Clusters

Metallacarborane clusters are carboranes containing one or (generally not more than) two transition metal atoms. They can be prepared by following different synthetic routes [6]. One of them, originally discovered by Hawthorne in the 1960s, employs the *nido*-carborane anions shown in Figure 11.6. These anions, also termed *dicarbollides*, are obtained by treating the isomers of *closo*-$C_2B_{10}H_{12}$ with strong bases.

Then, the reaction between *nido*-carborane anion and $FeCl_2$ in the presence of NaCp ($Cp = C_5H_5^-$) affords the sandwich-type complex $Fe(\eta^5\text{-}Cp)(\eta^5\text{-}C_2B_{10}H_{11})$ whose structure (CYPCFE) is shown in Figure 11.7. Note that the dicarbollide anion acts as a formal 6-electron donor when bonding metals in the η^5 fashion.

Figure 11.7 displays the structures of two other metallacarboranes, one containing the $Re(CO)_3$ fragment (CSCREC) and one with $TaCl_3$ (VUPBAJ). Metallacarboranes in which either one or two metal ions are sandwiched between a pair of *nido*-carborane anions have also been synthesized. The structures of three such complexes are shown in Figure 11.8. The first structure (NIDBOR) contains a Ni(IV) ion sandwiched between two *nido*-7,8-$C_2B_9H_{11}$ (or 7,8-dicarbollide)
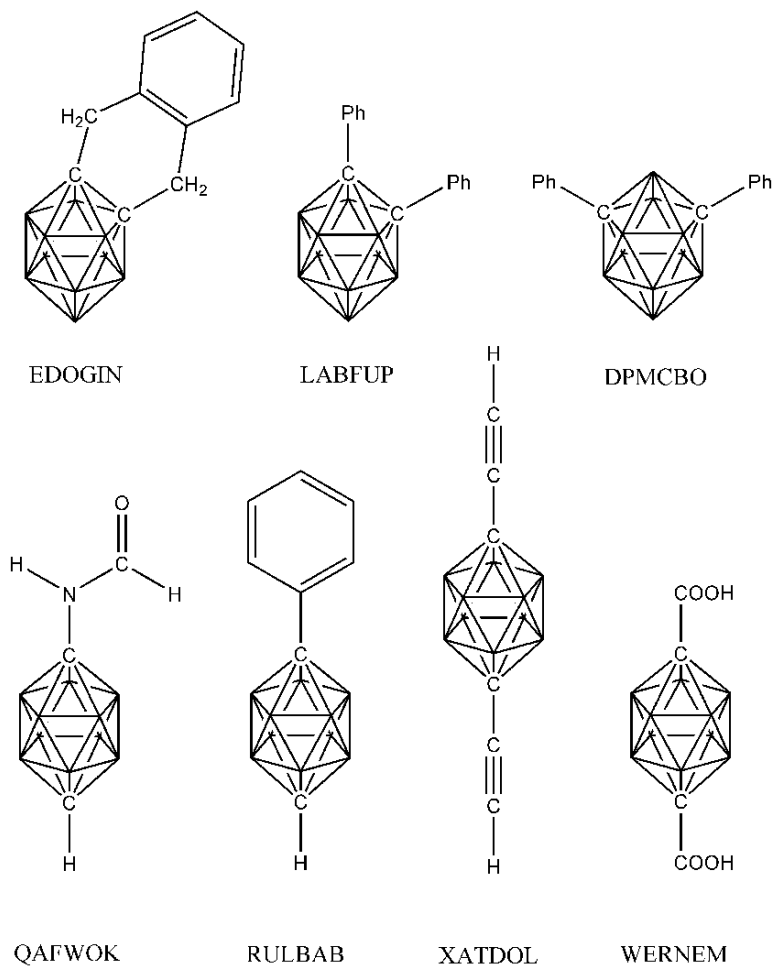
FIGURE 11.5. Some derivatives of *o*-, *m*-, and *p-closo*-$C_2B_{10}H_{12}$.

$[nido\text{-}7,8\text{-}C_2B_9H_{11}]^{2-}$ $[nido\text{-}7,9\text{-}C_2B_9H_{11}]^{2-}$
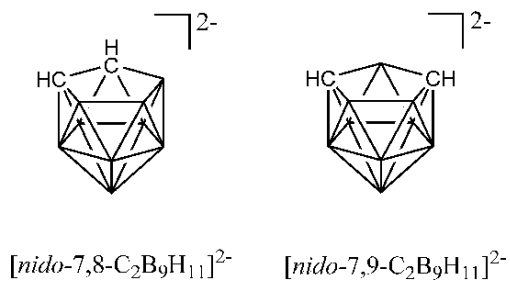
FIGURE 11.6. Two *nido*-carborane anion isomers.
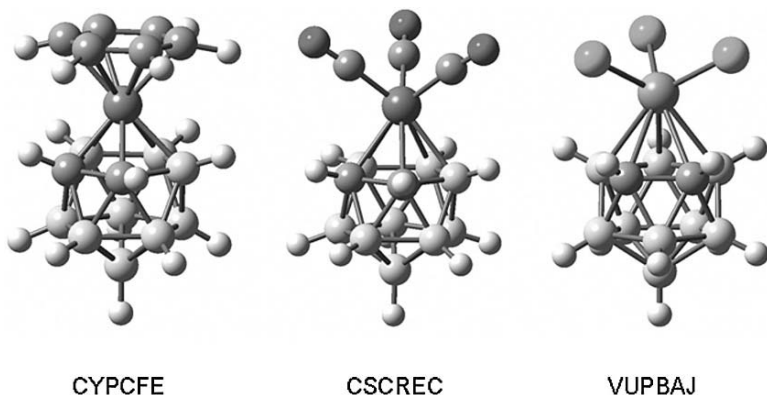
FIGURE 11.7. The structures of three metallacarboranes.

anions. The second structure (CAKXOC) contains a cobalt ion sandwiched between a pair of dicarbollide anions that are linked to each other through a disulfide bridge. The third and last structure shows Mo_2 (OFIQOJ) and W_2 (OFIREA) dimetal units capped on either side by a dicarbollide dianion and with four phenyl-thiolato groups (the phenyl rings have been omitted for clarity) bridging the metal–metal moiety.

In the next section, dedicated to the applications of polyhedral heteroboranes to nanotechnology, we discuss an interesting molecular machine made of a derivative of NIDBOR (Figure 11.8) that has been recently investigated by Hawthorne's group.
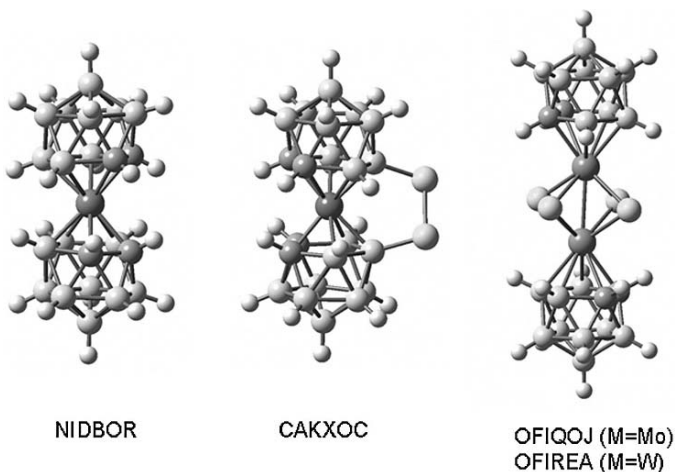
FIGURE 11.8. Metallacarboranes containing two dicarbollide ligands.

11.3. Applications

11.3.1. Nanoparticles

Nanoparticles are particles with diameters smaller than 100 nm [16]. Examples include colloidal suspensions, particles of metals (Au), and semiconductors (CdS, TiO_2). Their properties differ from those of the corresponding bulk making them attractive for novel technological applications. Giant molecules and proteins can also be included in this category.

We mentioned above the polyfunctionalized closomers synthesized and structurally characterized by Hawthorne and coworkers [15]. One of these molecules, derived by replacing the hydroxyl groups of *closo*-$[B_{12}(OH)_{12}]^{2-}$ with benzyloxy groups (QOZNAU), is shown in Figure 11.9. This spherical molecule has a diameter of about 1.5 nm. Polyfunctionalized closomers containing –OCOR substituents (with R = Me or Ph) attached to each vertex of the B_{12} polyhedron have also been synthesized and their structures (not shown here) characterized by X-ray crystallography (QOZMOH, QOZMUN).

Another interesting example of a boron-containing molecular nanoparticle is shown on the right side of Figure 11.9 (IKUYIW). This molecule, which has been recently synthesized by Valliant and coworkers [17], contains six isocyano-*para*-carborane groups coordinated with a central Re(I) ion. The carborane ligands assume an octahedral arrangement around the central metal and are coordinated with it via the carbon atom of their –N $\equiv$ C groups. The diameter of this spherical molecule is close to 1.5 nm like that of QOZNAU and the carborane units are separated from each other by about 0.5 nm. Valliant and co-workers have proposed using this Re(I) complex in the boron neutron capture therapy (BNCT), a binary treatment for cancer which we describe in more detail in the next section.

QOZNAU   IKUYIW
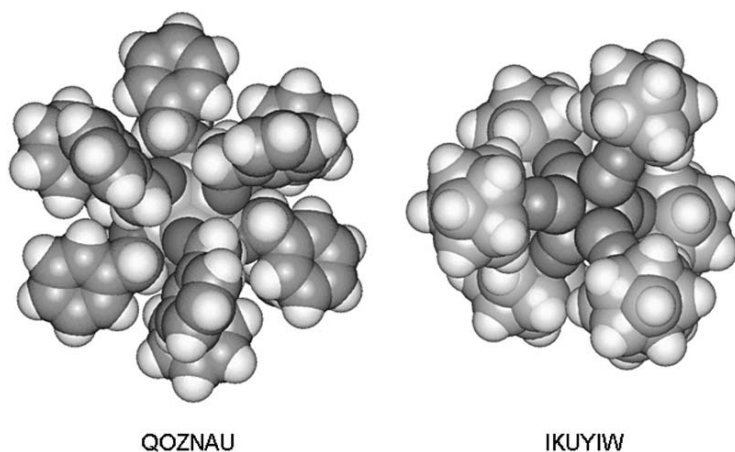
FIGURE 11.9. Boron-containing molecular nanoparticles.

11.3.2. Nanomedicine

Nanomedicine is concerned with the application of nanotechnology to medicine [18]. In addition to futuristic (and often scary) scenarios such as those represented by nanorobots operating inside the human body, more realistic applications of nanomedicine have been proposed. Among them, we mention the development of nanocapsules for drug delivery, fullerene-based drugs and sensors, artificial enzymes and antibodies, and tools for medical diagnostics and monitoring.

As far as polyhedral heteroboranes are concerned, several of their applications in medicinal chemistry have been recently reviewed by Valliant et al. [19]. Here we limit our discussion to boron neutron capture therapy (BNCT) [20]. An efficacious BNCT requires delivering large quantities of boron to the tumor cells. This can be achieved through the synthesis and use of large boron-containing molecular nanoparticles, such as the octahedral Re(I) complex (IKUYIW) described in the preceding section. Bombardment of the ^{10}B isotope with slow (thermal) neutrons initiates the following nuclear reaction,

$$^{10}B + {}^1n \rightarrow [{}^{11}B] \rightarrow {}^4He^{2+} + {}^7Li^{3+} + \gamma,$$
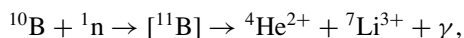
which produces one $^7Li^{3+}$ ion and one alpha particle ($^4He^{2+}$) along with gamma rays. Both particles have mean paths approximately equal to the cell's diameter. This assures that only the targeted tumor cells are destroyed and the surrounding cells are left intact. Among several requirements, BNCT compounds need to be nontoxic to the human body. Hence, heteroborane clusters are to be covalently linked to nontoxic molecules so that they can be delivered to the tumor. Among the large number of molecules synthesized so far, carborane-containing porphyrins and metalloporphyrins of Zn(II), Cu(II), and Ni(II) are very promising compounds for applications in BNCT.

Figure 11.10 shows the crystal structures of two Zn(II)-porphyrins bearing four carborane units, both of which have been synthesized by Vicente et al. [21,22]. The

QUERVEO   EJOGAL
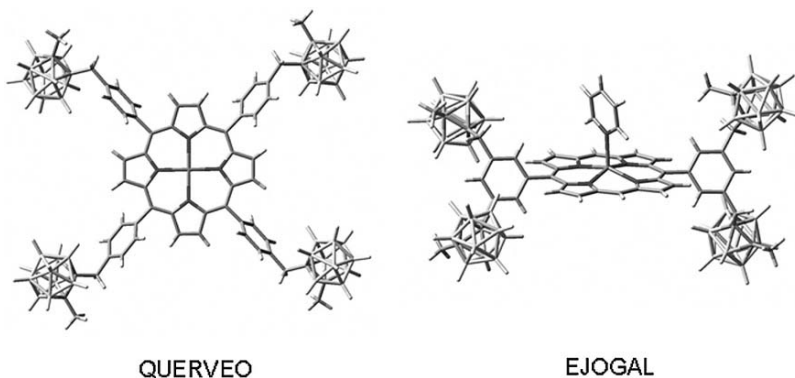
FIGURE 11.10. Two Zn(II)-porphyrin molecules bearing four carborane units for applications in BNCT.

first molecule (QUERVEO) has a carboranylmethyl group attached to each of the four peripheral phenyl groups [21] whereas the second molecule (EJOGAL) has a pair of carboranylmethyl groups attached to each of the two phenyl substituents. Note that the Zn(II) center of the second porphyrin is five-coordinated having a pyridine molecule axially coordinated with the metal. In their study the authors found that the Zn(II) porphyrin delivered greater amounts of boron to the tumor cells induced in mice than did its metal-free analogue [22]. On the other hand, the metal-free porphyrin compound provided greater tumor-to-blood boron concentration ratios than did its Zn(II)-containing form. Furthermore, the authors noted that the replacement of Zn(II) with other metal ions, such as Cu(II), represents a useful mean for modulating the properties of these medicines. The design, synthesis, and pharmacological testing of many more boron-containing porphyrins and metalloporphyrins are expected in the near future.

11.3.3. Molecular Machines

The field of molecular-scale machines and devices is a very hot one in modern chemistry research [23]. Simply put, taking inspiration from nature, chemists started to synthesize different kinds of molecules that are able to perform large-amplitude motions as a result of an energy input. The energy supplied to the molecule can be chemical (from the breaking of chemical bonds), photochemical, or electrochemical (from the reactions of oxidation and reduction). Depending on the type of motion (rotation, translation, bending, etc.) performed by each molecule, molecular rotors, turnstiles, cogwheels, brakes, and so on have been investigated.

Figure 11.11 shows the metallacarborane-based rotor recently investigated by Hawthorne and co-workers [24]. The system is an alkyl-substituted derivative of the Ni(IV)-bisdicarbollide complex (NIDBOR) discussed above (see Figure 11.8).
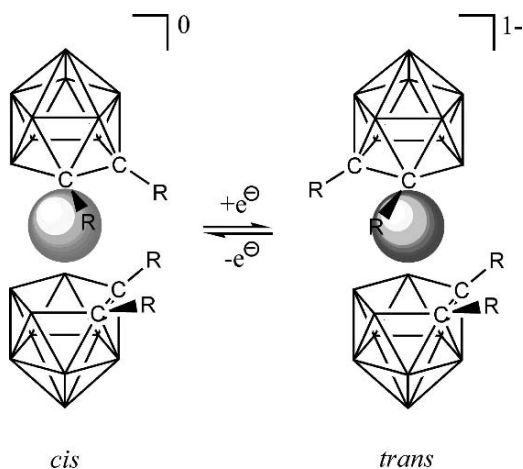
FIGURE 11.11. Oxidized (*cis*) and reduced (*trans*) conformers of $Ni(\eta^5\text{-}C_2R_2B_9H_9)_2$ with $R = H$ or alkyl group.

Upon either electrochemical reduction of Ni(IV) to Ni(III) or photoexcitation, the controlled rotation of one dicarbollide unit with respect to the other has been experimentally observed by the authors. Experiments have been complemented by theoretical (DFT) calculations showing that the minimum for the Ni(III) complex corresponds to the *transoid* configuration whereas that for the Ni(IV) complex occurs at the *cisoid* configuration. The authors further suggested that a complete molecular machine could be obtained by covalently attaching the metallacarborane complex to a surface so as to prevent the rotation of one dicarbollide unit with respect to the other. This suggestion is not too far-fetched if we consider the extraordinary advances made in the last 20 years in both chemical synthesis [25] and surface chemistry [26].

11.3.4. Nanoelectronics

Nanoelectronics is the area of nanotechnology concerned with the study and development of molecular-scale electronic devices [27]. One of the ultimate goals of nanoelectronics would be that of constructing a nanoscale computer made of molecular components. Hence, since the pioneering study by Aviram and Ratner published in 1974 [28], researchers have so far investigated, both experimentally and theoretically, a large number of molecules that are potential candidates for molecular wires, logic gates, rectifiers, transistors, and the like [29].

As far as polyhedral heteroboranes are concerned, some interesting and encouraging results have thus far been obtained. In 2002 a group of Russian scientists presented the results of an experimental study on several inorganic clusters that also included a thallium-substituted carborane cluster [30]. Although substantial differences among the properties of the clusters under study were not observed, the authors demonstrated that all clusters could operate as single-electron tunneling (SET) transistors at room temperature.

Another interesting study has been carried out by a British–Italian team who has performed electrochemical measurements (cyclic voltammetry) on a bimetallic complex of cobalt provided with a *closo*-1,12-carborane cage bridging the two metals [31]. The results of their experiments clearly showed that the carborane framework can participate in π-type delocalized bonding thereby permitting electronic communication between the metals. These experimental results are supported by recent ab initio calculations which, in addition, suggest that electron transport through the carborane cage strongly depends on the conformation of the chemical groups attached to the carbon atoms at the 1,12 positions [32].

The above studies suggest the possibility of constructing molecular wires out of *closo*-1,12-carborane units such as the one (LADFAX) shown in Figure 11.12. The distance between silicon atoms at the ends corresponds to ~2 nm. The synthesis of molecules bearing a discrete number of C-linked carborane units can provide molecular wires of different length. Also, providing the terminal alkyl chains with thiol groups (-SH) offers the possibility of attaching this molecular wire to metal surfaces such as that of gold.
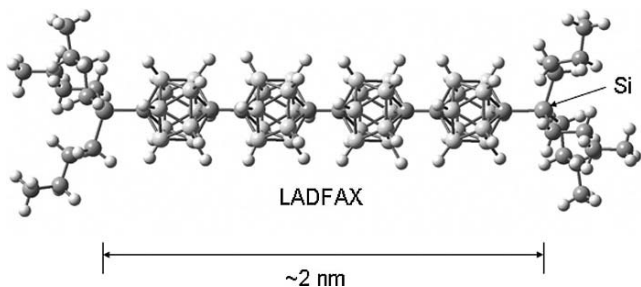
FIGURE 11.12. A carborane-based molecular wire.

Organic moieties with π-electrons can be inserted between a pair of *closo*-1,12-carborane units as shown in the structures of Figure 11.13. These C-linked carboranes are characterized by possessing different numbers of π-electrons delocalized over the carbonaceous bridges. In this regard, separating the carboranes with a biphenyl moiety (QINMOP) provides 12 π-electrons over a distance of 10.2 Å whereas inserting an additional alkynyl group between the phenyl rings (NEVCAS) provides 16 π-electrons over a distance of 12.7 Å. The third molecule (TINKIK) in this figure has a pair of carborane units separated by two alkynyl units (four C atoms) that provide 8 π-electrons over a length of 6.7 Å. Interestingly, we notice that the carbon chain is attached to the boron atoms of the carborane cage rather than to the carbon atoms as in the two molecules discussed before.

The last example of a potential carborane-based building block for nanoelectronics is shown in Figure 11.14. This molecule (FOSSIP) represents the molecular analogue of a three-way (or Y-type) junction with the carborane units that

QINMOP

NEVCAS
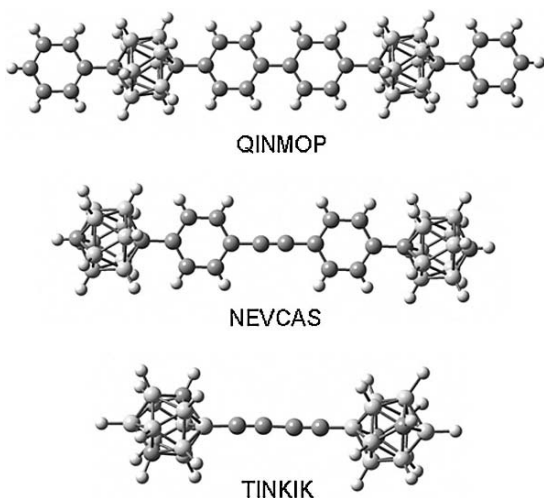
FIGURE 11.13. Carbon-linked carborane units.

TINKIK
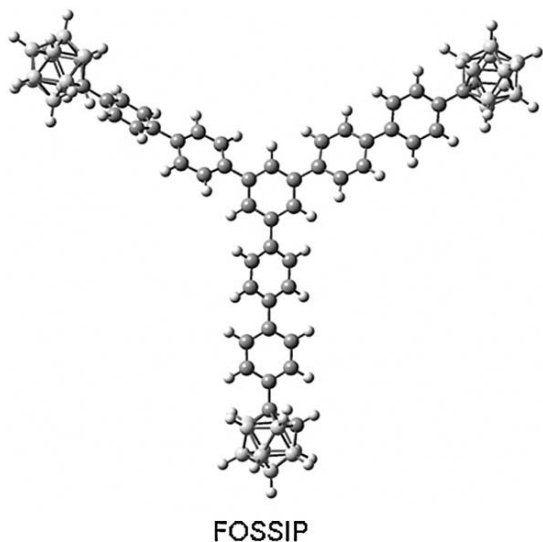
FIGURE 11.14. A three-way molecular junction.

FOSSIP

are connected in pairs through 5 six-membered arene rings. The total number of π-electrons in the carbonaceous part of the molecule corresponds to 42. We notice that this molecule could also be employed as a molecular logic gate upon functionalization of the three carborane units.

11.3.5. Nanostructured Materials

One of the main research activities in nanotechnology is the development of novel functional materials [33,34]. Control over the function of materials requires them to possess a high degree of structural ordering at the nanoscale. For this reason the materials are termed *nanostructured*. So far, several kinds of molecular clusters have been proposed as possible building blocks for the synthesis of nanostructured materials. Stang and co-workers [35] have suggested using high-symmetry coordination cages thus exploiting the directional properties of the metal–ligand dative bonds. Sanchez and co-workers [36] have investigated the use of silicon and tin oxide clusters provided with organic groups that facilitate the polymerization of the building units to yield organic–inorganic hybrid materials. Veith [37], on the other hand, suggested using alkoxides of Zr, Ba, and Ti as single-source precursors in the formation of nanostructured materials with the aid of chemical vapor deposition (CVD). All these proposals have in common the topological concept of a building unit (or building block) that can be assembled to generate novel architectures [38].

Polyhedral heteroborane clusters are ideal candidate building blocks for the design and synthesis of novel materials. For example, a few years ago Grimes [39] suggested using either carborane rings or cages in the assembly of 3-D organometallic networks. These interesting proposals, however, still remain

FIGURE 11.15. Hg-linked carbo-
rane building blocks.

AHIKEH

RULBEF
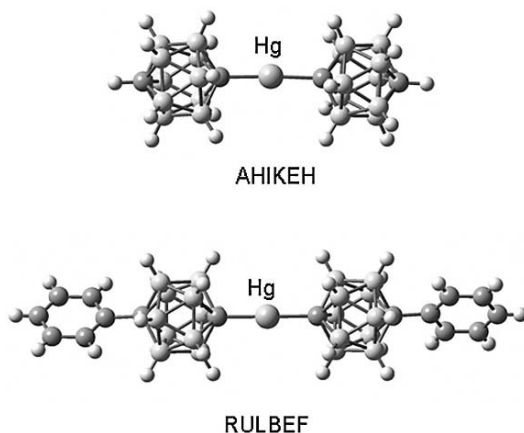
virtually unexplored. One possible reason for this state of affairs is related to the availability of many building units, such as those of polyhedral silsesquioxanes (POSS) [40], whose synthesis is cheaper than that of polyhedral heteroboranes.

Here we limit our discussion to the Hg-linked carborane building blocks shown in Figure 11.15. The choice of these metallic tectons (or metallatectons) stems from the possibility of exploiting the extracoordination ability of the Hg(II) ion towards N-containing ligands [41]. The Hg(II)-linked *p*-carborane AHIKEH has been functionalized with phenyl rings attached to its terminal carbon atoms to yield RULBEF. Subsequently, Michl and co-workers [42] mixed it with 2,2′-bipyrimidyl to obtain the supramolecular structure (RULBIJ) shown in Figure 11.16. Here the

RULBIJ   RULBUV
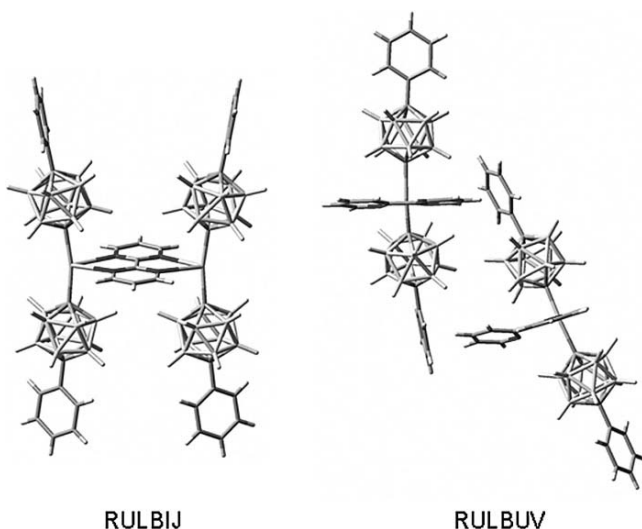
FIGURE 11.16. Control of the materials structure by ligand-based design.
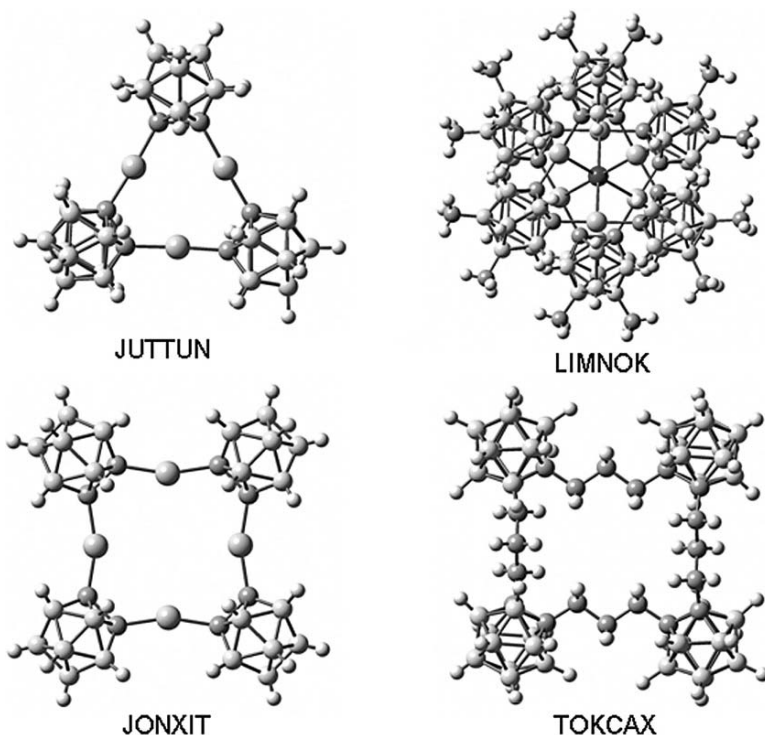
FIGURE 11.17. Molecular triangles and squares as potential building blocks for nanostructured materials.

nitrogen atoms of 2,2′-bipyrimidyl coordinate in pairs one Hg(II) ion to achieve the dimerization of the original building block.

Interestingly, when 2,2′-bipyridyl was employed, the presence of only a single pair of N-donor atoms yielded a material (RULBUV) with the building units that are separated from each other. This interesting study shows how the careful combination of building units and linker-type ligands can be exploited to control the architecture of solid-state materials.

Finally, it is worth mentioning that *o*-carborane clusters can also be linked through Hg(II) ions to yield useful building blocks as shown in Figure 11.17. Here three *o*-carborane units can be linked together by using three Hg(II) ions to yield a triangular building block (JUTTUN). When crystallized in the presence of iodide anions, the triangular building block (now functionalized with methyl groups) forms a superstructure with the spherical anion sandwiched between the molecular triangles (LIMNOK).

Molecular squares containing four Hg(II)-*o*-carborane units have also been synthesized and structurally characterized (JONXIT). These building blocks have sides of ∼1 nm and have been shown to act as receptors towards halide anions. Interestingly, the metal-free version of the molecular square has also been synthesized

(TOKCAX). Here four alkyl chains each made of three methylene (CH_2) groups replace a corresponding number of Hg(II) ions.

11.4. Computational Design of Materials

Traditional scientific disciplines such as chemistry and solid-state physics have so far made much use of computational methods to investigate the structural and electronic properties of existing materials [14,43]. These methods are mainly of two kinds: quantum mechanical methods that attempt to reach an approximate solution of the Schrödinger equation describing the physics of the atoms in the material, and methods based on atom–atom potentials and force-fields that are capable of modeling the chemical constituents of materials by employing the laws of classical mechanics. Each method has its advantages and disadvantages and the choice of one with respect to the other is often dictated by the specific problems and systems under investigation.

In addition to allowing the study of properties of existing materials, however, computational methods are an increasingly important tool in the hands of researchers for both property prediction and materials design [44–46]. Jansen and Schön [46] have recently proposed a general approach for the prediction of not-yet-synthesized materials that is based on the global exploration of the energy landscape of a chemical system. First, candidate structures are identified and their kinetic and thermodynamic stabilities are computationally assessed. Then, local free energies and physical properties are computed for a limited set of stable structures. In the final step, the candidates with the desired properties are selected. An important observation made by these authors concerns the applicability of their approach to materials that are capable of existence. In other words, materials design is not free but constrained by the building blocks that Nature offers.

In the spirit of Jansen and Schön's approach, we propose the general scheme for the design of nanostructured materials shown in Figure 11.18. The starting point
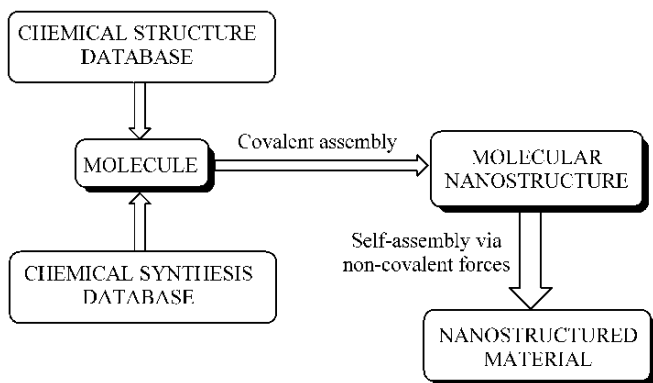
FIGURE 11.18. Proposed approach for the design of nanostructured materials.

of the flow chart is represented by the molecule whose structure can be obtained from a database of crystal structures such as CSD [12]. Molecules can be synthesized and modified according to the needs of a given design project. This can be achieved with the aid of a database of chemical reactions. Subsequently, molecular nanostructures with sizes larger than 1 nm are constructed either by assembling a discrete number of molecules or by attaching large chemical groups to a parent molecule (chemical functionalization). We call this step *covalent assembly*. It is here where computational quantum chemistry methods [14] can be highly effective in predicting the stability of the designer polyatomic system (molecular nanostructure). In this regard, we recently predicted a novel series of compact hydrocarbons obtained from the covalent assembly of cubane units [47]. These novel molecular nanostructures, which we dubbed *cubanoids*, were proposed to be the precursors of superhard materials. A similar approach could also be applied to the polyhedral heteroborane clusters discussed above.

The next and last step of Figure 11.18 represents the one leading to the bulk nanostructured material by self-assembly via noncovalent interactions. These comprise hydrogen bonds, Coulombic (ion–ion, ion–dipole, and dipole–dipole interactions) and van der Waals interactions. The possibility of automating the self-assembly step would be useful in extending the search for novel architectures. In this regard, Mellot-Draznieks et al. [48] have recently proposed an interesting approach based on the automated assembly of building units leading to hybrid organic–inorganic frameworks. The successful prediction of novel topologies can be partly ascribed to the use of fragments containing transition metal ions that are capable of forming directional metal–ligand bonds.

11.5. Summary

Polyhedral heterocarborane clusters are promising materials for nanotechnology. This is evident from the interesting applications discussed in this chapter, which include molecular nanoparticles, nanomedicines, and molecular-scale machines and devices. The use of carboranes as building blocks in the computational design of nanostructured materials remains open to novel discoveries that will be possible only by pursuing further research in this fascinating area of molecular chemistry.

References

[1]   Timp, G.L. (Ed.) (1998). *Nanotechnology.* New York: American Institute of Physics.
[2]   Wilson, M., Kannangara, K., Smith, G., Simmons, M., and Raguse, B. (2002). *Nanotechnology: Basic Science and Emerging Technologies.* Boca Raton, FL: Chapman & Hall.

[3]   Fujimasa, I. (1996). *Micromachines.* New York: Oxford University Press.

[4]   Sheats, J.R. and Smith, B.W. (Eds.) (1998). *Microlithography: Science and Technology*. New York: Marcel Dekker.

[5]   DeRosier, D.J. (1998). *Cell* **93**: 17–20.

[6]   Greenwood, N.N. and Earnshaw, A. (1998). *Chemistry of the Elements*, 2nd ed., Oxford: Butterworth Heinemann.

[7]   Stock: A. (1933). *Hydrides of Boron and Silicon*. Ithaca, NY: Cornell University Press.

[8]   Lipscomb, W.N. (1963). *Boron Hydrides*. New York: Benjamin.

[9]   Muetterties, E.L. and Knoth, W.H. (1968). *Polyhedral Boranes*. New York: Marcel Dekker.

[10] Brown, H.C. (1972). *Boranes in Organic Chemistry*. Ithaca, NY: Cornell University Press.

[11] Muetterties, E.L. (1975). *Boron Hydride Chemistry*. New York: Academic.

[12] Allen: F.H. (2002). *Acta Crystallogr. B***58**: 380–388.

[13] Hargittai, I. (2002). *The Road to Stockholm: Nobel Prizes, Science, and Scientists*. Oxford: Oxford University Press.

[14] Jensen, F. (1998). *Introduction to Computational Chemistry*. New York: John Wiley and Sons.

[15] Hawthorne, M.F. (2003). *Pure Appl. Chem*. **75**: 1157–1164.

[16] Kruis, F.E., Fissan, H., and Peled, A. (1998). *J. Aerosol Sci*. **29**: 511–535.

[17] Schaffer, P., Britten, J.F., Davison, A., Jones, A.G., and Valliant, J.F.J. (2003). *Organomet. Chem*. **680**: 323–328.

[18] Freitas, R. (2005). *Nanomedicine* **1**: 2–9.

[19] Valliant, J.F., Guenther, K.J., King, A.S., Morel, P., Schaffer, P., Sogbein, O.O., and Stephenson, K.A. (2002). *Coord. Chem. Rev*. **232**: 173–230.

[20] Fairchild, R.G., Bond, V.P., and Woodhead, A.D. (Eds.) (1989). *Clinical Aspects of Neutron Capture Therapy*. New York: Plenum.

[21] Vicente, M.G.H., Nurco, D.J., Shetty, S.J., Medforth, C.J., and Smith, K.M. (2001). *Chem. Commun*. 483–484.

[22] Vicente, M.G.H., Wickramasinghe, A., Nurco, D.J., Wang, H.J.H., Nawrocky, M.M., Makarc, M.S., and Miura, M. (2003). *Bioorg. Med. Chem*. **11**: 3101–3108.

[23] Balzani, V., Venturi, M., and Credi, A. (2003). *Molecular Devices and Machines*. Weinheim: Wiley-VCH.

[24] Hawthorne, M.F., Zink, J.I., Skelton, J.M., Bayer, M.J., Liu, C., Livshits, E., Baer, R., and Neuhauser, D. (2004). *Science* **303**: 1849–1851.

[25] Corey, E.J. and Cheng, X.-M. (1995). *The Logic of Chemical Synthesis*. New York: John Wiley & Sons.

[26] Somorjai, G.A. (2002). *J. Phys. Chem. B* **106**, 9201–9213.

[27] Waser, R. (Ed.) (2003). *Nanoelectronics and Information Technology*. Weinheim: Wiley-VCH.

[28] Aviram, A. and Ratner, M.A. (1974). *Chem. Phys. Lett*. **29**: 277–283.

[29] Joachim, C., Gimzewski, J.K., and Aviram A. (2000). *Nature* **408**: 541–548.

[30] Gubin, S.P., Gulayev, Y.V., Khomutov, G.B., Kislov, V.V., Kolesov, V.V., Soldatov, E.S., Sulaimankulov, K.S., and Trifonov, A.S. (2002). *Nanotechnology* **13**: 185–194.

[31] Fox, M.A., Paterson, M.A.J., Nervi, C., Galeotti, F., Puschmann, H., Howard, J.A.K., and Low, P.J. (2001). *Chem. Commun*. 1610–1611.

[32] Pati, R., Pineda, A.C., Pandey, R., and Karna, S.P. (2005). *Chem. Phys. Lett*. **406**: 483–488.

[33] Edelstein, A.S. and Cammarata, R.C. (Eds.) (1996). *Nanomaterials: Synthesis, Properties and Applications*. Bristol: Institute of Physics Publishing.

[34] Yang, P. (Ed.) (2003). *The Chemistry of Nanostructured Materials*. Singapore: World Scientific.

[35] Seidel, R.S. and Stang, P.J. (2002). *Acc. Chem. Res*. **35**: 972–983.

[36] Sanchez, C., Soler-Illia, G.J. de A.A., Ribot, F., Lalot, T., Mayer, C.R., and Cabuil, V. (2001). *Chem. Mater*. **13**: 3061–3083.

[37] Veith, M. (2002). *J. Chem. Soc*., *Dalton Trans*. 2405–2412.

[38] Ferey, G. (2000). *J. Solid State Chem*. **152**: 37–48.

[39] Grimes, R. (2000). *Coord. Chem. Rev*. **200–202**: 773–811.

[40] Phillips, S.H., Haddad, T.S., and Tomczak, S.J. (2004). *Curr. Opin. Solid State Mater. Sci*. **8**, 21–29.

[41] Henry, M. and Hosseini, M.W. (2004). *New J. Chem*. **28**: 897–906.

[42] Schoberl, U., Magnera, T.F., Harrison, R.M., Fleischer, F., Pflug, J.L., Schwab, P.F.H., Meng, X., Lipiak, D., Noll, B.C., Allured, V. S., Rudalevige, T., Lee, S., and Michl, J. (1997). *J. Am. Chem. Soc*. **119**: 3907–3917.

[43] Kaxiras, E. (2003). *Atomic and Electronic Structure of Solids*. Cambridge: Cambridge University Press.

[44] Raabe, D. (2002). *Adv. Mater*. **14**: 639–650.

[45] Eberhart, M.E. and Clougherty, D.P. (2004). *Nature Mater*. **3:** 659–661.

[46] Jansen, M. and Schön, J.C. (2004). *Nature Mater*. **3:** 838.

[47] Pichierri, F. (2004). *Internet Electron. J. Mol. Des*. **3**: 134–142.

[48] Mellot-Draznieks, C., Dutour, J., and Féréy, G. (2004). *Angew. Chem. Int. Ed*. **43**: 6290–6296.

12
Squeezing Germanium Nanostructures

K. L. Teo and Z. X. Shen

12.1. Introduction

The motivation of the present high-pressure studies is to investigate the strain effects in Germanium (Ge) nanostructures [1–6]. Germanium islands nucleate in the Stranski–Krastanov growth mode as a result of strain accumulated due to the 4% lattice mismatch between Si and Ge [7]. Although the structure of the formed QDs and NCs has been studied using atomic force microscopy, transmission electron microscopy, X-ray photoemission spectroscopy, and other methods, Raman spectroscopy is a tool very well suited for investigating their structural information under high pressure. The Raman peak position and width allow us to discuss strain and quantum confinement in nanostructures [8]. Raman scattering has been extensively used to study the phonon modes of Ge QDs and NCs and to predict the phonon confinement and strain effects [9–12]. However, all these experiments were carried out at ambient pressure. On the other hand, Raman scattering at high pressure offers an attractive means for investigating phonon properties of solids [13]. In addition to the reduction of interatomic distances, the effect of pressure also reduces the strain in Ge layers due to the difference between the bulk moduli of Si and Ge. Consequently, the biaxial strain can be tuned by varying the applied pressure. In this work, we utilize Raman spectroscopy with the application of hydrostatic pressure using a diamond anvil cell to access information on strain in embedded Ge nanostructures. The samples of interests are self-assembled Ge quantum dots (QDs) and Ge/Si dot superlattices as well as Ge nanocrystals (NCs) embedded in different matrices such as Ge/SiO$_2$ on Si substrate and Ge/SiO$_2$ on quartz substrate.

There have been many reports of quantum confinements of electron-hole pairs or excitons in Ge NCs [14–16]. However, these efforts have been mainly restricted to the study of the fundamental band-gap only. Figure 12.1 shows the band structure of bulk Ge. The indirect and direct band-gap energies of Ge are 0.65 eV $\left(\Gamma_8^+ \to L_6^-\right)$ and 0.88 eV $\left(\Gamma_8^+ \to \Gamma_7^-\right)$, respectively. In bulk Ge, the higher-energy excitons such as the E$_1$ transitions around 2.2 eV, also possess quite large oscillator strength [17]. For probing transitions well above the fundamental gap, resonant Raman scattering (RRS) is superior to both absorption and emission, which are the
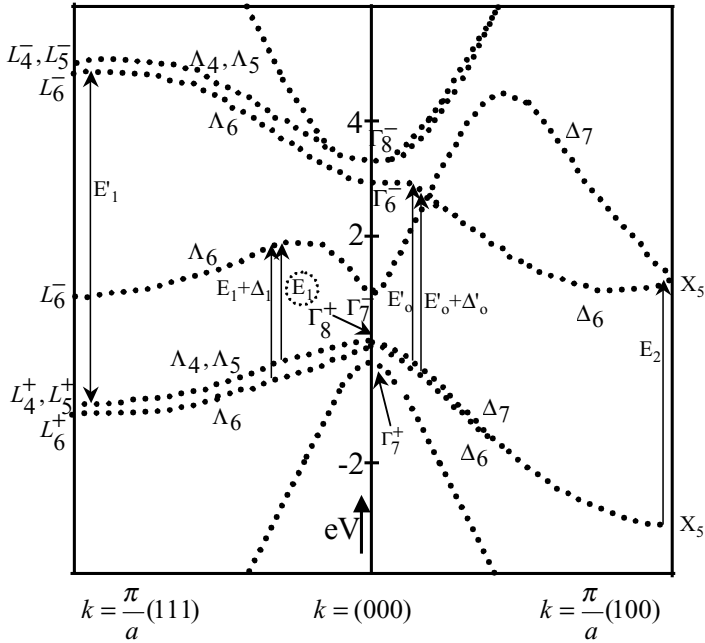
FIGURE 12.1. Band structure of bulk Ge. The E_1 transition is indicated by dotted circle [17].

standard techniques for studying confinement of excitons. In addition to electronic transitions, RRS can also provide information on phonons and their interactions with electrons [18]. The latter capability is significant because it has been established that confinement effects can change the vibrational modes and hence the electron–phonon interaction of semiconductor nanostructures [12,19,20]. In this work, we also describe the use of high pressure to tune the electronic transition (E_1 excitons) through the laser excitation energies resulting in resonance Raman scattering (RRS) in the Ge phonon mode.

12.2. Experimental Techniques

The Raman experiments were performed in a backscattering geometry at room temperature using 514.5 nm (2.41 eV), 496.8 nm (2.496 eV), and 488 nm (2.541 eV) lines from an argon–ion laser and the 632.8 nm (1.96 eV) line from a He–Ne laser. The Raman spectra were analyzed using a JY T64000 micro-Raman system with a liquid nitrogen cooled CCD detector. The pressure-dependent measurements were carried out using a diamond anvil cell (DAC) with a 4:1 mixture of methanol and ethanol as the pressure-transmitting medium. Figure 12.2 shows a schematic diagram of the high-pressure experimental setup. A small sample with dimensions of $\sim 100 \times 100 \times 30 \ \mu m^3$ was prepared by mechanical polishing and cutting before
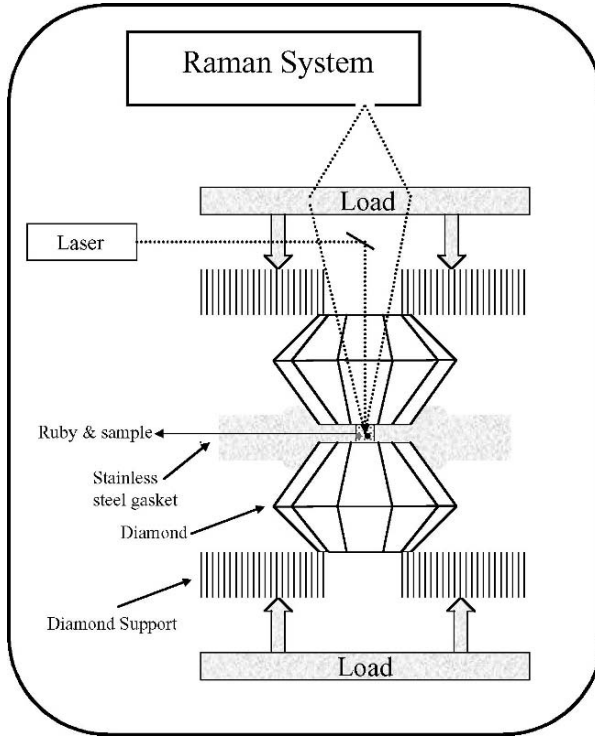
FIGURE 12.2. A schematic diagram of the high-pressure Raman experimental setup.

loading into the gasket of the DAC. The applied pressure was measured by the shift of the ruby R1 line [21]. Because the frequency of the first-order Si Raman peak shows a blue shift with a pressure coefficient of 0.52 cm^{-1}/kbar [22], we can use it as an internal pressure calibration. The signal collected from DAC is at least an order of magnitude weaker than that obtained outside the DAC.

12.3. Germanium Quantum Dots

The samples used for Raman investigations were grown by solid-source molecular beam epitaxy on n–Si (001) substrates and underwent the following growth procedure: deoxidation at 900°C, growth of a ~400 nm Si buffer layer while ramping the growth temperature down to 500°C, followed by 7 monolayers (ML) Ge and a 160-nm-thick Si cap layer. A growth interruption of 5 s was introduced between the Ge and Si layers. Typical growth rates of 1.2 and 0.07 Å/s were used for Si and Ge, respectively [23]. The sample for atomic force microscopy (AFM) follows an almost identical growth procedure but without the Si cap and the Ge deposition is 5.8 ML instead of 7 ML.
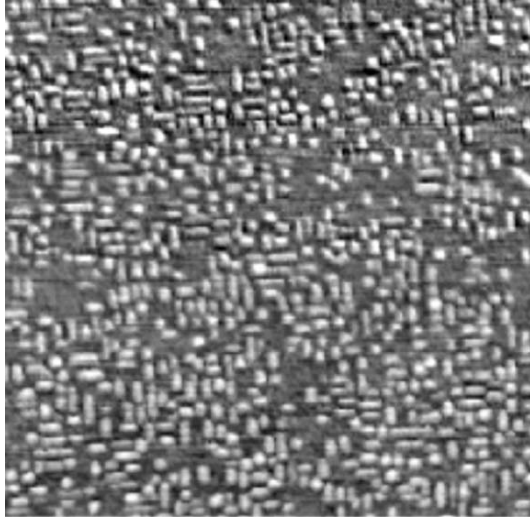
FIGURE 12.3. A 0.8×0.8 μm^2 AFM scan of a 5.8 ML Ge QDs layer grown on Si substrate at 500°C [1].

It has been shown that pyramids and domes can coexist at certain conditions and that pyramids are metastable structures that can directly transform into domes with increasing Ge deposition or postannealing treatment [24]. Pyramids and domes usually form at high temperatures, whereas the much smaller hut clusters nucleate at lower temperatures. Figure 12.3 shows a 0.8×0.8 μm^2 atomic force microscopy (AFM) scan of nominally 5.8 ML Ge QDs grown at 500°C. The image reveals small hut clusters of diameters ∼20 nm with areal density of 1×10^{11} cm^{-2}.

12.3.1. Raman Peak Assignments

In many Raman scattering studies of Ge nanostructures grown on Si substrates, the Si acoustical-overtone {2TA(X) and 2TA(Σ) phonons [22] (abbreviated as Si–2TA)} from the Si substrate can be erroneously attributed to the Ge–Ge vibrations of the sample due to the fact that both the Ge–Ge mode and Si–2TA are located at the same frequency (∼300 cm^{-1}) [8]. Except in the case of high compressive built-in strain in the Ge layers [2], these two phonon modes are hardly resolved at ambient pressure. This fact is totally ignored in many studies and thus it makes the information obtained based on these spectra on the Ge nanostructures of little value.

The Raman peaks from the Ge QDs sample and the Si substrate obey different selection rules and are observable at different polarization configurations, which can be used to distinguish these two peaks [25]. Figure 12.4 shows the polarized Raman spectra of a Ge QDs sample on Si substrate and that of a reference Si substrate sample. All spectra were taken with the same data accumulation time. Figure 12.4a plots the spectrum recorded from the reference Si substrate in the

FIGURE 12.4. Raman spectra of the Ge QDs sample and Si substrate under different polarization configurations: (a) substrate: $001(110, 110)00\bar{1}$; (b) substrate: $001(100, 010)00\bar{1}$; (c) sample: $001(100, 010)00\bar{1}$; and (d) sample: $001(110, 110)00\bar{1}$ [1].
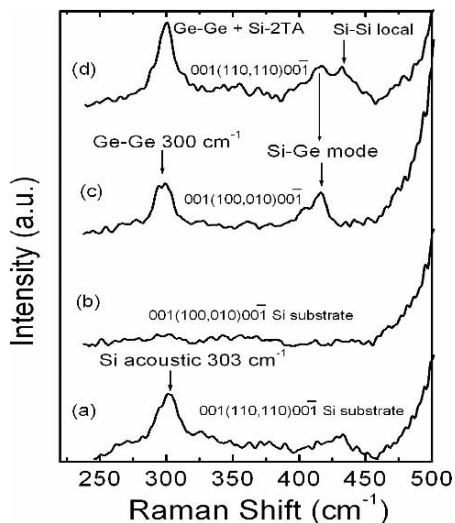
$001(110, 110)00\bar{1}$ backscattering geometry which shows a strong Si–2TA peak at $\sim$300 cm^{-1}. In the $001(100, 010)00\bar{1}$ backscattering geometry, however, as illustrated in Figure 12.4b, the Si–2TA peak is suppressed. Figure 12.4c shows the spectrum in the $001(100, 010)00\bar{1}$ backscattering geometry from the Ge QDs sample so as to minimize the Si–2TA peak. Although the lineshape and the intensity of the peak at $\sim$300 cm^{-1} from the sample are quite similar to the Si–2TA peak shown in Figure 12.4a, the Raman peak in Figure 12.4c should be that of the Ge–Ge mode in the QDs due to the scattering configuration used.

In order to ascertain the above assignment, we recorded the spectrum from the sample (see Fig. 12.4d) in the same geometry as that of Fig. 12.4(a). This spectrum should include a strong contribution from the Si–2TA peak. Indeed, the integrated intensity of the peak at $\sim$300 cm^{-1}is about a factor of two stronger than the peak observed at 300 cm^{-1} in Figure 12.4c. We can conclude that the Raman peak in Figure 12.4c contains only contributions from the Ge–Ge mode. In addition, we argue that the Ge–Ge peak in Figure 12.4c is mainly from the Ge QDs rather than the Ge wetting layer. This is because in the $001(100, 100)00\bar{1}$ configuration, the signals from the Ge wetting layers are forbidden according to the selection rules [26]. This point is confirmed by the fact that in this configuration, the intensity of the Ge–Ge modes in our sample does not change much compared with that in Figure 12.4c.

12.3.2. High-Pressure Raman Studies

Figure 12.5 shows the high-pressure Raman spectra of Ge QDs up to 67 kbar using the laser excitation at 2.41 eV without polarization. At ambient pressure, four peaks are identified: Ge–Ge or Si–2TA (304 cm^{-1}), Si–Ge (419 cm^{-1}),
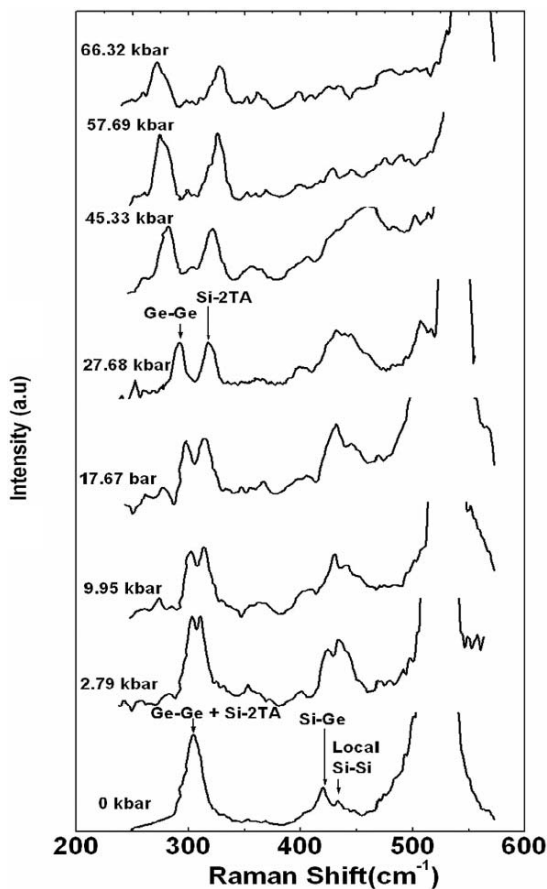
FIGURE 12.5. Room temperature Raman spectra at various pressures for the Ge QDs taken in the $001(100, -)00\bar{1}$ configuration [1].

Si–Si local mode (435 cm^{-1}), and optical phonon mode from the Si substrate at 521 cm^{-1}. The peak at 419 cm^{-1} is due to the Si–Ge interface phonon mode localized at the surfaces of the Ge quantum structures [10] or due to Si–Ge inter-mixing in the islands [27–29]. In our case, the islands are grown at a relatively low temperature, ~500°C. The strain-driven alloying of Ge clusters should not be very pronounced [28]. It is likely that there is more than 70% Ge in the dots. In addition, the Si–Si vibrational mode seen at 435 cm^{-1} suggests the existence of strain in Si underneath the Ge dots induced by the dots [30]. We note that the Ge–Ge mode in the bulk sample is located at 300 cm^{-1}. However, for Ge deposited on Si substrate, a compressive strain in the Ge layer due to lattice mismatch between Ge and Si is expected to increase the Ge–Ge mode to 315.8 cm^{-1}. The fact that we observed this mode at about 304 cm^{-1} suggests that the confinement effect in our Ge QDs decreases the Ge–Ge mode by ~12 cm^{-1}. This is consistent with the fact that in Ge QDs a compressive built-in strain leads to a Raman blue shift of the Ge–Ge mode, and the confinement effect causes a red shift [19]. For pseudomorphically

grown Ge on Si substrate, the lattice mismatch between Si and Ge gives rise to
~4 % of compressive strain in the Ge layer. In QDs, this lattice-mismatch induced
strain is partially reduced and nonuniform across the structure as a result of island
formation [29].

With increasing pressure, the first-order Si Raman peak at 521 cm^{-1} shifts to
higher frequencies with a pressure coefficient of 0.52 cm^{-1}kbar^{-1}, which can be
used as an internal measure of the pressure [22]. It is noteworthy that the linewidth
of the Si–Ge mode, observed at 419 cm^{-1} at ambient pressure, broadens and the
peak blueshifts with pressure. As pressure increases, the spectrum at ~304 cm^{-1}
splits into two peaks. As discussed earlier in Section 12.3.1, the Ge–Ge and Si–2TA
modes overlap at ambient pressure, making it hard to distinguish them. Under
pressure, the Ge–Ge mode shows a blueshift and the Si–2TA mode shows a redshift.
As a result, these two peaks are clearly resolved. We have also used different laser
excitation energies E_L for the measurement of Raman spectra at various pressures
in the Ge QDs as shown in Figure 12.6. The spectra are normalized to the substrate
Si phonon intensity.

Figure 12.7 shows the Raman shifts, $\Delta v = v(P) - v(0)$, of the Si substrate at
521 cm^{-1}, and Ge–Ge and Si–2TA peaks as a function of pressure P. The
solid curves correspond to the least squares fit to the experimental data. The
rates of Raman shift of these modes with pressure are: Si-substrate (0.51 ±
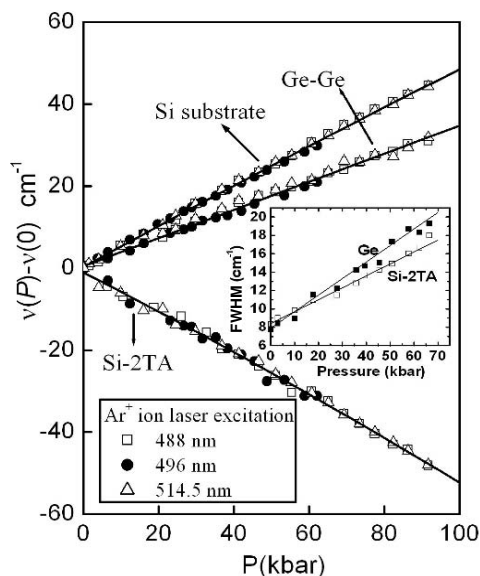
FIGURE 12.7. Raman shifts $v(P) - v(0)$ as a function of pressure. The excitation energies are 2.541 eV (squares), 2.496 eV (circles), 2.41 eV (triangles). The inset shows the FWHM of Ge–Ge (solid squares) and Si–2TA modes (open squares) as a function of pressure and the solid lines correspond to the linear fits to the experimental data.

0.01) $\mathrm{cm}^{-1}\mathrm{kbar}^{-1}$, Ge–Ge$(0.34 \pm 0.03)\,\mathrm{cm}^{-1}\mathrm{kbar}^{-1}$, Si–2TA$(-0.47 \pm 0.03)\,\mathrm{cm}^{-1}$ kbar^{-1}. The inset in Figure 12.7 shows the full width half maximum (FWHM) Γ of the Ge–Ge and Si–2TA phonon modes as a function of pressure. The fitted linear relations for Γ in cm^{-1} are given by

$$\Gamma_{Ge}(P) = (7.9 \pm 0.4) + (0.177 \pm 0.008)P \tag{1}$$

$$\Gamma_{Si-2TA}(P) = (8.4 \pm 0.2) + (0.135 \pm 0.006)P. \tag{2}$$

The Murnaghan equation [31] of state was used to relate the lattice constant a and pressure P,

$$\frac{a}{a_o} = \left[\frac{B_o'}{B_o} + 1\right]^{\frac{-1}{3B_o'}}, \tag{3}$$

where a_o is the lattice constant at ambient pressure, B_o is the bulk modulus of material concerned, and B_o' is its pressure derivative.

Using the parameters listed in Table 12.1, we plot the Raman shift of the Ge–Ge mode against relative compression $(-\Delta a/a_o)$ as shown in Figure 12.8. The least

TABLE 12.1 Parameters for bulk Si and Ge at room temperature [32].

	Si	Ge
B_o (kbar)	978.8	750.2
B_o'	4.2	4.76
$a_o(\text{Å})$	5.431	5.646

FIGURE 12.8. Raman shift of the
Ge–Ge mode as a function of lat-
tice compression. The symbols for
excitation energies are the same as
in Figure 12.7. The solid curve cor-
responds to the least squares fit to the
experimental data.
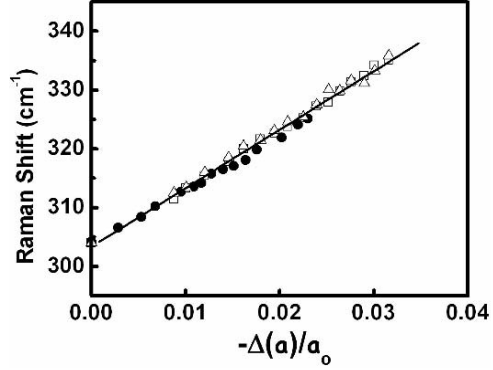
squares fit gives:

$$\omega_{Ge}(p) = (304.1 \pm 0.3) + (996 \pm 12)\left[-\frac{\Delta a}{a_o}\right]. \tag{4}$$

We use the following relation to calculate the mode Grüneisen parameter γ_i.

$$\gamma_i = \frac{B_o}{\omega_i}\frac{d\omega_i}{dP}. \tag{5}$$

With the linear pressure coefficient $d\omega/dP = 0.34\,\mathrm{cm^{-1}kbar^{-1}}$ and $B_o = 750.2$ kbar in bulk Ge, we obtain a value of $\gamma = 0.84 \pm 0.01$ in our Ge QDs. This value is ~25% smaller than the corresponding value found in the bulk Ge (1.12) [33]. If we assume the Ge QDs are constrained by the surrounding Si lattice so that the bulk modulus of Ge becomes the same as that of Si, we obtain $\gamma = 1.09$, which is only about 3% smaller than the expected value. In other words, the smaller compressibility of Si "isolates" the Ge QDs from external pressure, reducing $d\omega/dP$ for Ge QDs as compared to the bulk Ge value of $0.39\,\mathrm{cm^{-1}}$/kbar [34]. The shift $\Delta\omega_{strain}$ of the optical-phonon frequency induced by a biaxial strain together with the applied hydrostatic pressure P can be shown to be [34]

$$\Delta\omega_{strain} = \frac{1}{\omega_o}\left(q - p\frac{C_{12}^{Ge}}{C_{11}^{Ge}}\right)\left(\frac{a_o^{Si}}{a_o^{Ge}} - 1\right) - \frac{p + 2q}{2\omega_o\left(C_{11}^{Ge} + 2C_{12}^{Ge}\right)}P$$
$$+ \frac{1}{\omega_o}\frac{a_o^{Si}}{a_o^{Ge}}\left(q - p\frac{C_{12}^{Ge}}{C_{11}^{Ge}}\right)\left[\frac{1}{C_{11}^{Ge} + 2C_{12}^{Ge}} - \frac{1}{C_{11}^{Si} + 2C_{12}^{Si}}\right]P, \tag{6}$$

where ω_o is the optical phonon frequency of the Ge–Ge mode, p and q are deformation potentials of the optical phonon in Ge, C_{11}^i and C_{12}^i are components of the fourth rank elastic (stiffness) tensor, and a_o is the lattice constant at ambient pressure. The first term is the lattice mismatch due to compressive strain in the Ge layer at ambient pressure. The second term is due to hydrostatic pressure applied to the Ge layer; which gives the pressure coefficient of the bulk Ge. The third term arises because Ge and Si have different compressibility.

Using the parameters listed in Table 12.2, we compute the second term in Eq. (6) to be $d\omega/dP = +0.36\,\mathrm{cm^{-1}}$/kbar. It is important to note that in Eq. (6), the second

TABLE 12.2 Parameters for bulk Si and Ge at room temperature.

	Si	Ge
C_{11} (kbar)	1656[a]	1288[a]
C_{12} (kbar)	638.6[a]	482.5[a]
a_o(Å)	5.431[a]	5.646[a]
$p(s^{-2})$	-1.345×10^{28}[b]	-4.7×10^{27}[b]
$q(s^{-2})$	-1.946×10^{28}[b]	-6.167×10^{27}[b]

(a): Ref. [35]; (b): Ref [36].

term is essentially the pressure coefficient of the bulk Ge sample and the third term represents the effect on the Ge phonon frequency as a result of the change in the biaxial strain induced by the pressure. Because the second and third terms have opposite signs, the third term reduces the pressure coefficient of the Ge phonon in the QDs. The reduction in the pressure coefficient of the Ge phonon frequency in QDs (i.e., the third term obtained from Eq. (6)) is ~ -0.04 cm^{-1}/kbar. This value agrees well with what was observed experimentally.

12.3.3. Resonance Raman Scattering via High Pressure

It has been known that the optical phonon Raman-scattering efficiency of bulk Ge exhibits a resonance peak at 2.23 eV [37]. The inset of Figure 12.9 shows the normalized intensity profile of Ge–Ge mode versus pressure for three different excitation energies (2.541 eV, 2.496 eV, and 2.41 eV) as obtained from Figure 12.6. It is evident that the Ge–Ge mode exhibits enhancement at different pressures for the given excitation energies. We interpret the enhancement for the Ge–Ge mode in our Ge QDs to be resonant scattering within the Ge layers as pressure tunes the electronic transition through the excitation energies.
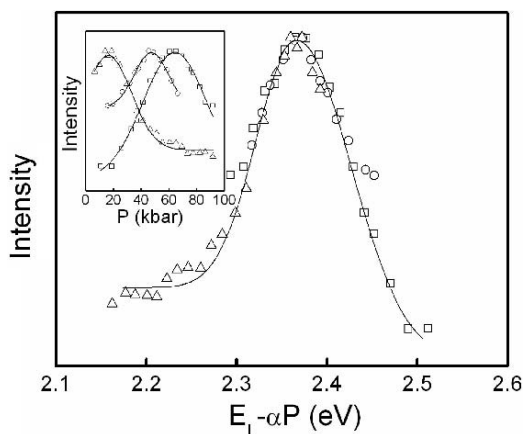
FIGURE 12.9. Normalized intensities of the Ge–Ge mode versus energies $(E_L - \alpha P)$. The inset shows the normalized intensities of Ge–Ge mode resonant at different pressures for different excitation energies at 2.541 eV (squares), 2.496 eV (circles), and 2.41 eV (triangles). The solid curves are guides for the eye [3].

We plot in Figure 12.9 the normalized intensities of the Ge–Ge mode versus $(E_L - \alpha P)$ where α $(= dE_1/dP)$ is the pressure coefficient of the electronic transition at resonance. With $\alpha = 2.7 \pm 0.5$ meV/kbar, we obtain the best agreement for the intensity profiles of the three excitation lines. The maximum enhancement resulting from this analysis is near 2.37 eV with a FWHM of 120 meV as compared with the resonant FWHM of 150 meV found in bulk Ge. This observed sharpness of the E_1 peak suggests that a rather homogeneous strain with resonance occurs in the Ge QDs. We note that the α value in the Ge QDs is 64% smaller than the value found for the E_1 transition in bulk Ge (7.5 meV/kbar) [38]. This deviation could be due to the difference in the deformation potential of Ge QDs as compared to the bulk value. Thus, we relate dE_1/dP to the deformation potential [38] $dE_1/d(lnV)$ through the volume compressibility $K = 1/B_o$:

$$\frac{dE_1}{d(lnV)} = -\frac{1}{K}\frac{dE_1}{dP}. \tag{7}$$

We take $1/K = B_o = 978.8$ kbar for Si, to be consistent with our previous argument that the Ge QDs are constrained by the Si host. We obtain the deformation potential of -2.6 ± 0.5 eV as compared to the bulk Ge value (-4.5 ± 0.4 eV) in Ref. [39]. Other contributions to the smaller α value may originate from the nonlinear dependence of the peak energy on pressure inasmuch as any sublinear dependence will tend to decrease the pressure coefficient. It is noteworthy that a pressure coefficient of 4 ± 1 meV/kbar has been obtained in Ge_nSi_m multiple quantum wells [40].

12.4. Germanium Nanocrystals

One of the promising ways to fabricate Ge nanostructures is to make embedded Ge nanocrystals (NCs) in SiO_2 using techniques such as co-sputtering and ion-implantation, followed by subsequent annealing [41–43]. Considering the large interface-to-volume ratio in nanocrystal–matrix systems, the interface strain plays an important role in deciding the physical and thermodynamic properties of NCs. On Si(001), the NCs of epitaxial Ge were found to effectively repel one another strongly via the strain fields that are produced in the Si substrate [44]. It has also been found that the interface strain has a great effect on the growth and evolution of nanocrystalline Ge in matrices [27,28,44]. Thus, investigations on the elastic field in the nanocrystal–matrix systems would enhance our understanding of the strain mechanism of the NCs as well as the exploitation of their novel functions. The SiO_2/Si interface is also the most important interface system technologically. Knowledge on the interface strain and its dependence on SiO_2 thickness are critical in Si device applications. In the next two sections, we report the Raman scattering under hydrostatic pressure in two kinds of Ge nanosystems: Ge NCs embedded in (a) SiO_2 matrix on quartz substrate (abbreviated as Ge/SiO_2/quartz nanosystem) and (b) SiO_2 matrix on Si substrate (abbreviated as Ge/SiO_2/Si nanosystem).
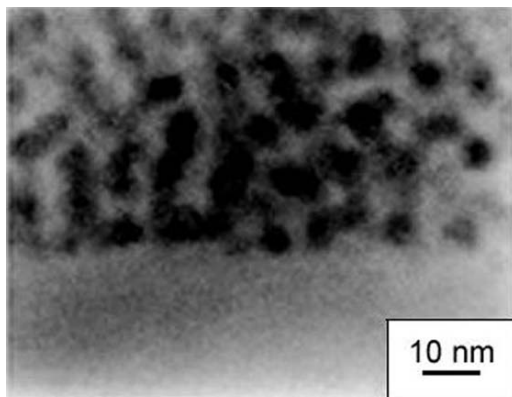
FIGURE 12.10. TEM image of the annealed Ge NCs [5].

12.4.1. Ge/SiO₂/Quartz Nanosystem

In this section, we describe the effect of hydrostatic pressure on the nanocrystallite Ge embedded in a rather soft matrix such as SiO_2. The evolution of the interface strain between Ge NCs and the matrix with pressure is discussed in terms of a simple elastic model. Such information provides an insight in understanding the formation mechanism of nanocrystallite Ge embedded in SiO_2.

The samples used for investigation were prepared by co-deposition of Ge and SiO_2 by radio-frequency (rf) magnetron sputtering onto quartz substrate with about 3–5-nm-thick native oxide. The sample thickness is ~1 μm and Ge concentration is ~60 mol%. After deposition, the sample was annealed for 1 h at 800°C in an argon atmosphere which produced the NCs. More details on the sample preparation are given in Ref. [14]. Figure 12.10 shows the transmission electron microscopic (TEM) image of the annealed Ge NCs [45]. One can see clearly that the size of the Ge NCs is ~5 nm and they form a kind of continuous network.

Figure 12.11 shows the Raman spectra for as-deposited and annealed Ge samples. The appearance of a strong and sharp peak upon annealing indicates the
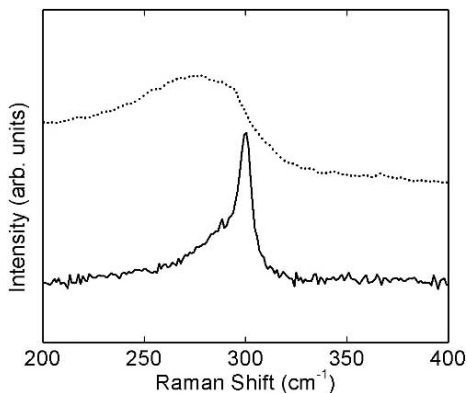
FIGURE 12.11. Raman spectra for as-deposited sample (dashed lines) and annealed (solid lines) Ge NCs [5].

FIGURE 12.12. Raman spectra of Ge NCs at various pressures with 488-nm laser excitation [5].
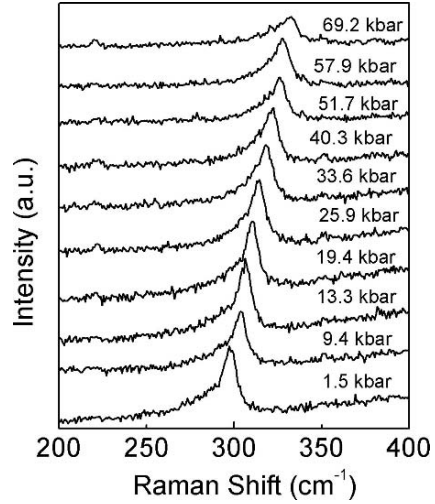
formation of the crystalline phase. In comparison with bulk Ge, the peak position of the Ge NCs is at 298 cm^{-1}, with an asymmetric profile at the lower frequency. The asymmetric shape of the peak obtained is characteristic of the small crystals [42]. It is noteworthy that the Ge–Ge mode shifts to lower frequency as the laser intensity increases. To prevent any laser-induced heating, the laser power is kept to a minimum.

Figure 12.12 shows the Raman spectra of Ge NCs at various pressures under the laser excitation of 488 nm. With increasing pressure the Ge–Ge mode shifts to a higher frequency. The rate of frequency shift of this mode with pressure is shown in Figure 12.13. The frequency shift of the bulk Ge mode (ω_{bulk}^{Ge}) is also shown for comparison. In order to take into account the behavior of shoulder peak at 284 cm^{-1} of the Ge–Ge mode in the Ge NCs, the spectrum is fitted with two Lorentzian peaks. At ambient pressure, the main peak (ω_1^{Ge}) occurs at 298 cm^{-1} with a FWHM of $\sim$7 cm^{-1} and the shoulder peak (ω_2^{Ge}) at 284 cm^{-1} with FWHM of $\sim$20 cm^{-1}.

The solid curves correspond to the least squares fit to the experimental data as given by

$$\omega_{bulk}^{Ge}(P) = (299.7 \pm 0.1) + (0.39 \pm 0.01)P, \tag{8}$$

$$\omega_1^{Ge}(P) = (297.8 \pm 0.2) + (0.77 \pm 0.01)P - (0.004 \pm 0.001)P^2, \tag{9}$$

$$\omega_2^{Ge}(P) = (283.9 \pm 0.8) + (0.93 \pm 0.05)P - (0.006 \pm 0.001)P^2. \tag{10}$$

Comparing with bulk Ge, we obtain $\alpha_{NC} = d\omega/dP = 0.77$ cm^{-1}kbar^{-1} for the Ge–Ge mode in Ge NCs. This value is very large compared with that for Ge QDs (size $\sim$20 nm) in Section 12.3 and that of self-assembled Ge/Si dot superlattice (size $\sim$8 nm) [2], both with $\alpha_{QD} = d\omega/dP \cong 0.34$ cm^{-1}kbar^{-1}, despite their size difference. Consequently, the $d\omega/dP$ should be independent of the size but related to the matrix. Both the Ge hut cluster and Ge/Si dot superlattice samples can be
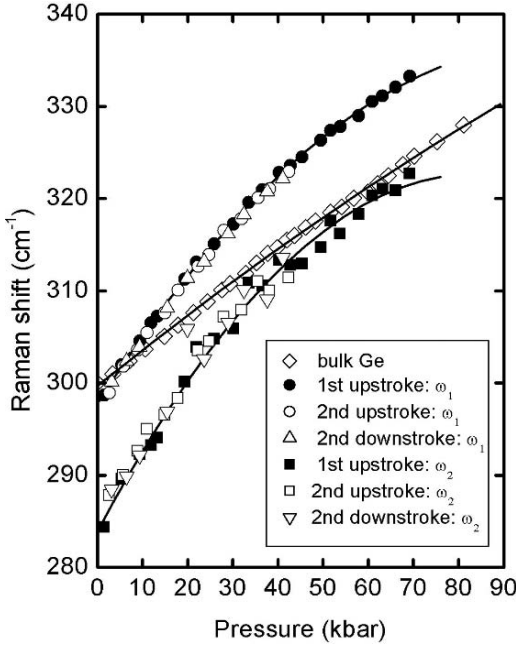
FIGURE 12.13. Raman shift as function of pressure P of Ge–Ge mode in bulk Ge, Ge NCs, and the asymmetric part of the Ge–Ge mode in the Ge NCs [5].

considered as Ge dots in Si host. The large $d\omega/dP$ observed in our NCs (in SiO$_2$ host) can be explained if we assume that the effective pressure acting on the NCs is different from the applied pressure. This effect has been observed by Haselhoff et al. [46] for CuCl NCs in alkali–halide matrices. However, in their model the strain at the interface between the NCs and the matrix was not taken into account.

As shown in Figure 12.13, we have performed the pressure dependence study of the Ge–Ge modes of the NCs for one pressure cycle and there is no hysteresis observed. This confirms that the pressure-induced strain in the NCs is reversible. With this elastic behavior of our Ge/SiO$_2$ NCs-matrix system, we assume both the NCs and the matrix as isotropic elastic continua [46]. We modeled the NC as a sphere of radius r_1 in a spherical SiO$_2$ matrix of radius r_2, where $r_2 \gg r_1$. The system is subjected to a hydrostatic pressure P. Using spherical co-ordinates with the origin at the center of the NC sphere, our system has a spherical symmetry where the displacement vector $\vec{u}$ is everywhere radial and can be written as $u = ar + b/r^2$. The components of the strain tensor are $u_{rr} = a - 2b/r^3$ and $u_{\theta\theta} = u_{\phi\phi} = a + b/r^3$. The constants a and b are determined from the boundary conditions. At the interface between the NC and the matrix, the interface strain is given as $\delta = u_{\theta\theta}^1 - u_{\theta\theta}^2$, where $u_{\theta\theta}^1$ and $u_{\theta\theta}^2$ are the strain tensor of the NC and the matrix, respectively. From the boundary conditions at $r_1 = r_2$, the effective pressure P_{NC} at the NC is given by [47]

$$P_{NC} = P\frac{9K_1(1 - \sigma_2)}{2E_2 + 3(1 + \sigma_2)K_1} + \delta\frac{6E_2K_1}{2E_2 + 3(1 + \sigma_2)K_1}, \tag{11}$$

where E_1, σ_1, K_1 and E_2, σ_2, K_2 are the Young's modulus, Poisson ratio, and bulk modulus of the NC and the matrix, respectively. From (11), we have

$$\frac{dP_{NC}}{dP} = \frac{9K_1(1-\sigma_2)}{2E_2 + 3(1+\sigma_2)K_1} + \frac{6E_2K_1}{2E_2 + 3(1+\sigma_2)K_1}\frac{d\delta}{dP} = k_1 + k_2\frac{d\delta}{dP}. \quad (12)$$

In our case for the Ge NCs, Eq. (12) gives $dP_{NC}/dP = \alpha_{NC}/\alpha_{bulk} = 0.77/0.39 = 1.97$. Using the elastic constants of Ge ($E_1 = 131.66$ GPa, $\sigma_1 = 0.20748$, $K_1 = 75.02$ GPa) [32], and that of the SiO$_2$ ($E_1 = 73$ GPa, $\sigma_2 = 0.162$, $K_2 = 36.1$ GPa) [48], we find from (12) that $k_1 = 1.39$ and $k_2 d\delta/dP = 0.58$. A positive $d\delta/dP$ value suggests that the accumulated strain at the interface induces a compressive stress on the NCs as pressure increases. This is possible because SiO$_2$ ($K_2 = 36.1$ GPa) is much easier to compress than Ge ($K_1 = 75.02$ GPa). As such, the large pressure coefficient for Ge NCs comes from the contribution of the stress at the interface evolving with pressure. On the other hand, for the case of Ge QDs, (12) gives $dP_{NC}/dP = \alpha_{QD}/\alpha_{bulk} = 0.34/0.39 = 0.87$. With the Si matrix of elastic constant values ($E_2 = 162.91$ GPa, $\sigma_2 = 0.22262$, $K_2 = 97.8$ GPa) [32], we obtain $k_1 = 0.87$ and thus $k_2 d\delta/dP \approx 0$. This is consistent with the fact that the smaller compressibility of Si "isolates" the Ge QDs from the external pressure, reducing α_{QD} for Ge QDs (0.34 cm^{-1}kbar^{-1}) as compared to the bulk Ge value of 0.39 cm^{-1}kbar^{-1}.

12.4.2. Ge/SiO$_2$/Si Nanosystem

In the previous section, we have shown that for Ge NCs embedded in a quartz matrix, the pressure coefficient ($\alpha = 0.77$ cm^{-1} kbar^{-1}) obtained for the Ge mode is almost twice as large as its corresponding bulk value [5]. This can be explained using a simple elastic model that describes the effective pressure transmitted from the matrix to the nanocrystals. However, the interface strain/stress effects under applied hydrostatic pressure have not been fully understood in a more complicated nanosystem, such as Ge NCs embedded in SiO$_2$ on Si substrate. In order to elucidate the strain/stress effect on the NCs in the nanostructures, it is necessary to carry out high-pressure research on the multicomponent nanosystem, Moreover because desired functional characteristics of semiconductor heterostructure depend critically on their structure and geometry which are generally influenced by the local elastic field distribution during its fabrication or application, further investigations on multicomponent nanostructures, such as the Ge/SiO$_2$/Si nanosystem, may cast insight on exploring the formation or application of semiconductor nanostructures.

The preparation of samples is the same as in previous section except that Si substrate instead of quartz is used for co-deposition of Ge and SiO$_2$. Figure 12.14(a) shows the transmission electron microscopic (TEM) image of the annealed Ge NCs [45]. Interestingly, the NCs are preferentially formed in the area away from the sample surface, and near the interface with the silicon substrate the density of the NCs is somewhat higher. High-resolution (HR) TEM images (Figures 12.14b,c) reveal other features of the formed NCs [45]. The NCs formed in the bulk of the
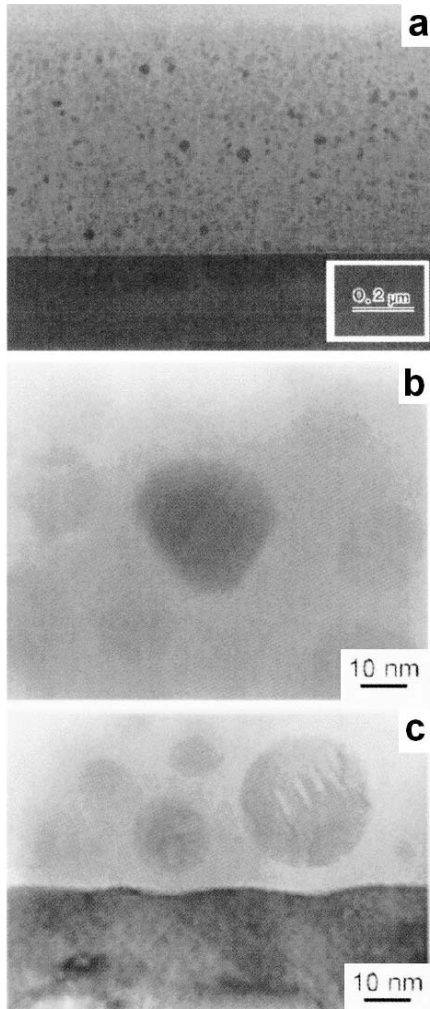
FIGURE 12.14. (a) TEM image of Ge/SiO$_2$/Si NCs sample; (b) HR-TEM image of a Ge/SiO$_2$/Si NCs sample with Ge NCs formed in the bulk of the sample; and (c) in the vicinity of the Si(001) interface [6].

sample have clearly pronounced facets and are single crystals, in very few cases with twinning defects. The NCs formed in the direct vicinity of the Si substrate, on the other hand, are spherical and the interface under these NCs is no longer flat. In both cases, the size of the NCs is ~20 nm.

For high-pressure Raman scattering study, the Ge NCs and the Si substrate have different first-order optical phonon modes (Ge mode at ~300 cm^{-1} and Si mode at ~521 cm^{-1}), making it much easier to study the strain effects on the NCs and the substrate than in the Si NCs/SiO$_2$/Si nanosystem, where the Raman modes of Si NCs and substrate Si overlap. We have shown in Section 12.3 and Figure 12.4 that the Si–2TA at ~300 cm^{-1} can be eliminated by specific polarization configuration. Moreover, our experiments [1–5] suggested that the Raman

FIGURE 12.15. (a) Raman spectra for Ge/SiO$_2$/Si NCs samples at ambient pressure; pressure dependence of Raman shift of the Ge mode (b); and (c) the Si mode. The inset shows the enlarged portion of the Si mode near transition P $\sim$ 23 kbar [6].
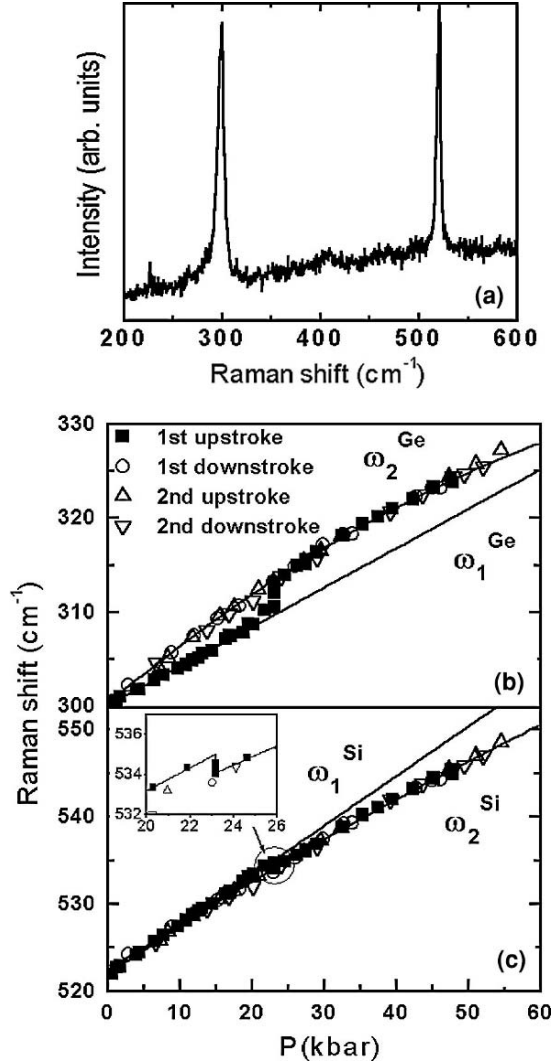
shifts with pressure ($\alpha = d\omega/dp$) are independent of the size of the NCs, which is consistent with results derived from high-pressure Raman experiments on CdS and CdSe, showing that the potential energy as a function of unit cell volume is identical in both the harmonic and the first anharmonic term in tetrahedrally bonded bulk and nanocrystal systems [49]. This simplifies the study of the elastic field evolution with the surrounding hydrostatic pressure because we can neglect the size effect of the NCs.

Figure 12.15a shows the Raman spectra of the Ge/SiO$_2$/Si system at ambient pressure. The Ge mode occurs at $\sim$300 cm^{-1} with a FWHM of about 5 cm^{-1}

whereas the Si mode from the substrate is at $\sim$521 cm^{-1} with a FWHM of about 4 cm^{-1}. The appearance of a strong and sharp peak of Ge mode indicates the formation of the crystalline phase. We have used the $001(100, 010)00\bar{1}$ scattering configuration to minimize the Si–2TA peak at $\sim$300 cm^{-1}. We note that the Ge mode shifts to lower frequency as the laser intensity increases. To prevent any laser induced heating, the laser power on the sample is kept to a minimum with a power density of $\sim$5 $\times$ 10^4 W/cm^2.

The Raman shifts of the Ge mode and the Si mode with pressure P for two pressure cycles were shown in Figure 12.15b,c, where both the Ge and Si peaks were fitted with a Lorentzian profile. During the first pressure upstroke, the Ge mode shifts linearly with P and then shows a step jump from 310.4 to 313.8 cm^{-1} at $P \sim$ 23 kbar, and subsequently shifts with P at a larger pressure coefficient (α). On the other hand, at $P \sim$ 23 kbar, the Si mode shows a downshift by $\sim$0.9 cm^{-1}, and thereafter the Si mode shifts at a smaller pressure coefficient (α). The step jump at $P \sim$ 23 kbar occurs only in the first pressure upstroke, indicating an irreversible transition of the Ge/SiO$_2$/Si nanosystem. In the subsequent pressure change, up- or downstroke, both the Ge and Si modes are reversible. It is noteworthy that although the present high-pressure experiment is performed on Ge NCs of size $\sim$20 nm, we have also observed similar behavior in Ge NCs of size 4 to 12 nm with the same SiO$_2$ layer thickness indicating the observed phenomenon is independent of NCs size.

As shown in Figure 12.15c, the solid curves correspond to the least squares fit to the experimental data, where the Raman modes for the first upstroke up to $P \sim$ 23 kbar (ω_1) and subsequent pressure change (ω_2) were fitted separately:

$$\omega_1^{Ge}(P) = (300.0 \pm 0.1) + (0.42 \pm 0.01)P, \tag{13}$$

$$\omega_2^{Ge}(P) = (300.2 \pm 0.2) + (0.64 \pm 0.02)P - (0.003 \pm 0.001)P^2, \tag{14}$$

$$\omega_1^{Si}(P) = (521.7 \pm 0.1) + (0.57 \pm 0.01)P, \tag{15}$$

$$\omega_2^{Si}(P) = (522.3 \pm 0.2) + (0.53 \pm 0.01)P - (0.001 \pm 0.0002)P^2. \tag{16}$$

From the fitting results above, at the irreversible transition pressure 23 kbar, the pressure coefficient α(Ge) of the Ge mode changes from 0.42 to 0.64 cm^{-1}kbar^{-1} and α(Si) of the Si mode changes from 0.57 to 0.53 cm^{-1}kbar^{-1}. We note that the elastic field distribution would not be uniformly homogeneous in the Ge/SiO$_2$/Si nanosystem, especially near the interface between the SiO$_2$ matrix and the Si substrate. Thus, it is necessary to investigate the elastic field distribution in the Ge/SiO$_2$/Si nanosystem to enhance our understanding of the pressure dependence of the Raman shifts of the Ge and Si modes.

In our simulation, we used a finite element package (ABAQUS/Standard) and an axisymmetric model structure as shown in Figure 12.16, where the Ge NCs sphere is located along the rotational z-axis, and the Si substrate and SiO$_2$ matrix cylindrical layers are separated by a sharp interface. In the calculation of the elastic field distribution in the nanosystem, an external hydrostatic pressure of 10 kbar was assumed. For simplicity, the Ge NCs, SiO$_2$ matrix, and Si substrate were considered as isotropic elastic continua, with elastic constants of Ge ($E_1 = 1316.6$ kbar, $\sigma_1 = 0.20748$, $K_1 = 750.2$ kbar) [32], SiO$_2$ ($E_2 = 730$ kbar, $\sigma_2 = 0.162$,

FIGURE 12.16. Schematic diagram of the Ge/SiO$_2$/Si axis symmetrical nanosystem [6].
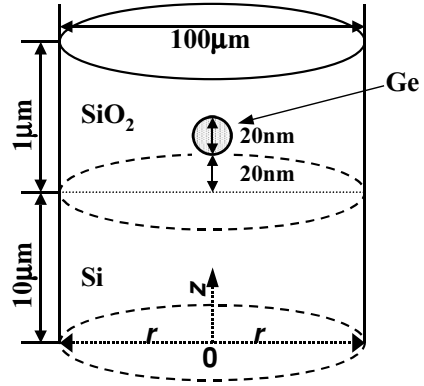
$K_2 = 361$ kbar) [48], and Si ($E_3 = 1629.1$ kbar, $\sigma_3 = 0.22262$, $K_3 = 978.8$ kbar) [32]. Here $(E_i, \sigma_i, K_i)_{i=1,2,3}$ are the Young's modulus, Poisson ratio, and bulk modulus, respectively.

Figure 12.17 shows the r–z plane stress distributions of σ_{rr}, σ_{rz}, σ_{zz}, $\sigma_{\theta\theta}$, and σ_{Mises} for the disk-shaped Ge/SiO$_2$/Si nanosystem, where the negative values indicate compressive stress. All five stress tensors are distributed rather nonhomogeneously around the surface of the nanosystem, and near the SiO$_2$/Si interface. But in the central part of the nanosystem away from the edges ($r = 50$ µm), the five tensors are distributed uniformly in the layers parallel to the SiO$_2$/Si interface. At the SiO$_2$/Si interface, there is a significant discontinuity for σ_{rr} and $\sigma_{\theta\theta}$. The values of σ_{rr} and $\sigma_{\theta\theta}$ are almost identical and there a big jump across the interface from –5.70 kbar in the SiO$_2$ matrix to about –11.77 kbar in the Si substrate. This can be ascribed to the fact that SiO$_2$ ($K_2 = 361$ kbar) is much easier to compress than Si ($K_3 = 978.8$ kbar), but both of them have to shrink together at the interface under pressure. As a result, the SiO$_2$ matrix experiences more tensile stress near the SiO$_2$/Si interface than anywhere else.

On the other hand, the Si substrate has to undergo a more compressive stress. Accordingly, the absolute values of σ_{rr} and $\sigma_{\theta\theta}$ for SiO$_2$ matrix become smaller from the top surface to the SiO$_2$/Si interface, and σ_{rr} and $\sigma_{\theta\theta}$ of the Si substrate become bigger from the bottom surface to the SiO$_2$/Si interface. Consequently, below 23 kbar, the α of Ge ($\sim$0.42 cm-^{1}kbar^{-1}) and Si modes ($\sim$0.57 cm^{-1}kbar^{-1}) can be due to the discontinuous distribution of σ_{rr} and $\sigma_{\theta\theta}$ in the nanosystem introduced by the SiO$_2$/Si interface. As a result of the concentration of the discontinuous stresses, the interface strain would accumulate, which may induce the debonding of the SiO$_2$/Si interface, that is, the delamination between the SiO$_2$ matrix and the Si substrate layers. The delamination dynamics of the SiO$_2$/Si interface can be further understood by Figure 12.18a, which shows the local distribution of (Von) Mises stress [50] σ_{Mises} at the SiO$_2$/Si interface edge, as indicated by the circle in Figure 12.17. Figures 12.18b–f show the local stress distribution of σ_{Mises}, σ_{rr}, σ_{rz}, σ_{zz}, and $\sigma_{\theta\theta}$ around Ge NCs as shown in Figure 12.16. The distribution of σ_{Mises} concentrates strongly at the outer SiO$_2$/Si interface edge ($r = r_{MAX} = 50$ µm),
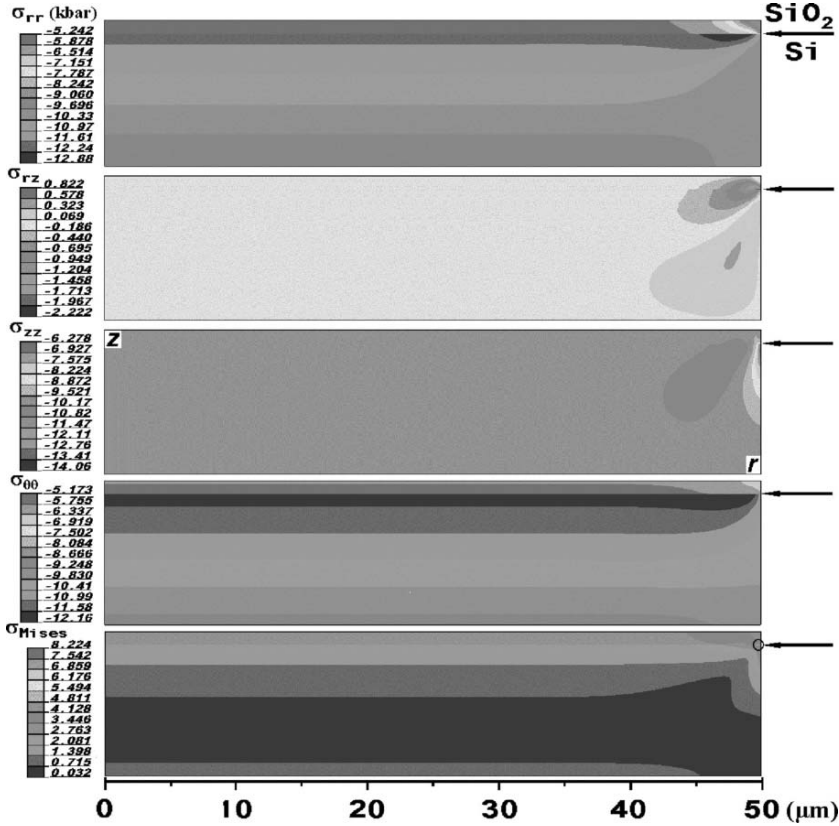
FIGURE 12.17. Global r–z plane stress distributions of σ_{rr}, σ_{rz}, σ_{zz}, $\sigma_{\theta\theta}$, and σ_{Mises} for the disk-shaped Ge/SiO$_2$/Si nanosystem. The horizontal axis represents r with $r = 0$ being the center and $r = 50$ μm being the edge of the disk. The vertical is the z-axis and the arrows indicating the SiO$_2$/Si interface [6].

indicating further that the delamination starts from the edge where the largest strain energy is accumulated and gradually moves inward. Due to this delamination behavior, we are able to explain our experimental observation for the discontinuity at $P \sim 23$ kbar in the first pressure upstroke.

As the optical penetration depth of a 514.5-nm laser in Si(001) is about 1.0 μm [51], only about a 1-μm-thick layer of the Si substrate layer below the SiO$_2$/Si interface contributes to the observed Si Raman signal. Due to the bonding at the SiO$_2$/Si interface, the strains near the interface are different from those in the Si substrate. Close to the SiO$_2$/Si interface, the calculated Si substrate strains are: $\varepsilon_{rr} \cong \varepsilon_{\theta\theta} \cong -4.24 \times 10^{-3}$, and $\varepsilon_{zz} \cong -2.92 \times 10^{-3}$. The Si strain values at a layer 1.0 μm below the SiO$_2$/Si interface are: $\varepsilon_{rr} \cong \varepsilon_{\theta\theta} \cong -4.15 \times 10^{-3}$, $\varepsilon_{zz} \cong -2.98 \times 10^{-3}$, and $\varepsilon_{rz} \cong 0$. As it is known that when a strain exists along the major crystal axes of a cubic crystal, the triply degenerate optical mode (the
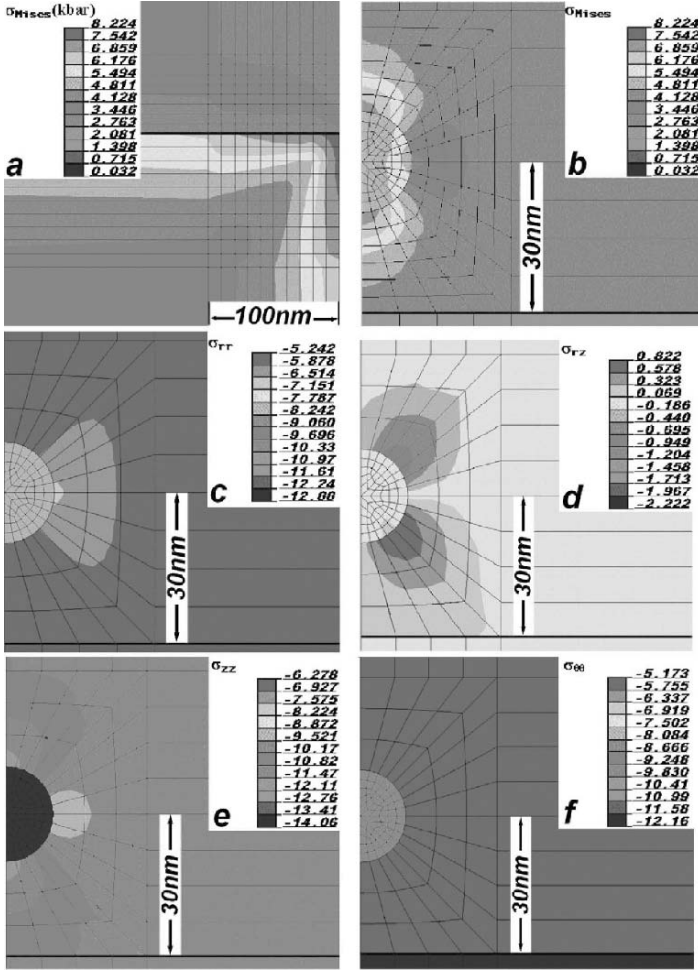
FIGURE 12.18. (a) Local $r-z$ plane (Von) Mises stress σ_{Mises} distribution near the SiO$_2$/Si interface edge (the circle in Figure 12.4); The local $r-z$ plane stress distribution of (b) σ_{Mises}, (c) σ_{rr}, (d) σ_{rz}, (e) σ_{zz}, and (f) $\sigma_{\theta\theta}$ around a Ge NC. The thin solid lines indicate the mesh used in the calculation and the thicker line indicates the SiO$_2$/Si interface [6].

$\Gamma_{25'}$ optical phonon for Si) near a zero wave vector splits into a singlet and a doublet [34,36]. In Raman experiments with backscattering geometry along the [001] direction, only the singlet is observable. In the absence of interfacial disorder, the Raman frequency of this Si mode is given by

$$\omega = \omega_0 + (1/2\omega_0)[p\varepsilon_{zz} + q(\varepsilon_{rr} + \varepsilon_{\theta\theta})], \qquad (17)$$

where $\omega_0 (= 0.9849 \times 10^{14} s^{-1})$ is the frequency of the c-Si zone-center LO phonon, and $p(= -1.345 \times 10^{28} s^{-2})$ and $q(= -1.946 \times 10^{28} s^{-2})$ are the Si deformation potentials [36].

Before delamination, the pressure coefficient $\alpha(\text{Si}) = 0.55 \text{ cm}^{-1}\text{kbar}^{-1}$ near the SiO_2/Si interface and $\alpha(\text{Si}) = 0.54 \text{ cm}^{-1}\text{kbar}^{-1}$ at a location 1.0 μm below the interface. After delamination, the interface no longer exists and the Si substrate becomes a stand alone crystal. Hence its properties should be the same as that of the bulk Si, with $\alpha(\text{Si}) = 0.48 \text{ cm}^{-1}\text{kbar}^{-1}$ and $\varepsilon_{rr} = \varepsilon_{\theta\theta} = \varepsilon_{zz} = 3.405 \times 10^{-3}$ under a hydrostatic pressure of 10 kbar. From the $\alpha(\text{Si})$ values before and after delamination, we calculated a downshift of the Si mode at 23 kbar to be 1.4 cm^{-1}. This result agrees well with our experimentally observed downshifts of $\sim 0.9 \text{ cm}^{-1}$ within the experimental error.

We now discuss the local stress distributions around the Ge NCs (Figure 12.18), which will help us further understand the characteristics of the Ge/SiO_2/Si nanosystem. Due to the smaller compressibility of Ge ($K_1 = 750.2 \text{ kbar}$) NCs than the SiO_2 ($K_2 = 361 \text{ kbar}$) matrix, Ge NCs undergo rather larger stresses of σ_{rr}, σ_{zz}, and $\sigma_{\theta\theta}$ than the surrounding SiO_2 matrix. Moreover, the discontinuous and nonuniform stress distribution of $\sigma_{rr}, \sigma_{rz}, \sigma_{zz}$, and $\sigma_{\theta\theta}$ can be observed around the Ge/SiO_2 interface. In the SiO_2 matrix, the existence of Ge NCs effectively modified the surrounding elastic field with a scale comparable with the size of the NCs. Similarly, nonuniform local stress can also arise during cooling or heating in the high-temperature growth of the Ge/SiO_2/Si nanosystem due to different thermal expansion coefficients of the GeNCs and the SiO_2 host. The interface roughness directly under the NCs shown in Figure 12.14c can be due to the nonhomogeneous local stress distribution induced by the embedded Ge NCs (see Figure 12.18b–f).

We also calculated the dependence of σ_{rr} and $\sigma_{\theta\theta}$ on the thickness of the SiO_2 matrix layer, where the axisymmetric model structure as shown in Figure 12.16 was still used but with the thickness of the SiO_2 layer varied from 0.2 μm to 3.0 μm. Figure 12.19 shows the σ_{rr} and $\sigma_{\theta\theta}$ in SiO_2 at a location close to the SiO_2/Si interface near the central rotation axis (i.e., $r \to 0$) as a function of the
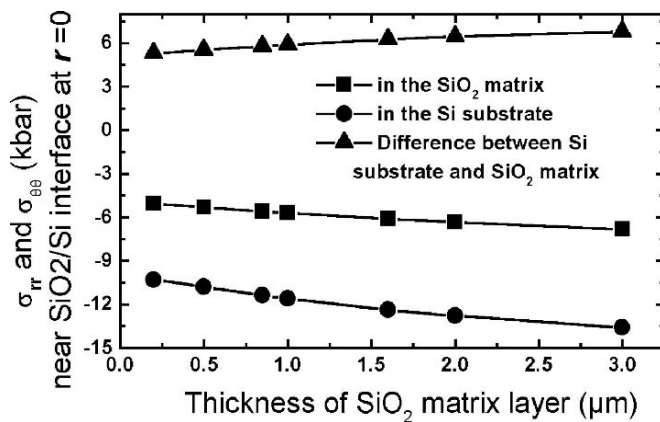
FIGURE 12.19. SiO_2 film thickness dependence of σ_{rr} and $\sigma_{\theta\theta}$ in SiO_2 near the interface at $r = 0$ [6].

SiO$_2$ matrix layer thickness. We found that as the thickness of the SiO$_2$ matrix layer increases, the stress concentration of σ_{rr} and $\sigma_{\theta\theta}$ in the Si substrate becomes stronger and the difference on the two sides of the interface also becomes bigger, resulting in more strain energy accumulating around the SiO$_2$/Si interface. Thus, under the same pressure, the delamination occurs more easily for the thicker SiO$_2$ matrix layer.

12.5. Conclusion

In summary, Ge QDs grown by solid-source molecular-beam epitaxy were investigated by Raman scattering under hydrostatic pressure at room temperature. The pressure coefficient of Ge–Ge mode in QDs is smaller than the corresponding quantity in bulk Ge. We also utilize the effect of pressure to tune the electronic transition through laser excitation energies in the Ge QDs. A clear resonant enhancement at $E_1 = 2.37$ eV is obtained for the normalized intensity of the Ge–Ge mode as a function of pressure. The pressure coefficient of this resonating electronic transition thus obtained is $\sim 2.7 \pm 0.5$ meV/kbar, which is significantly smaller than the pressure shift of the E_1 transition in bulk Ge. This is attributed to the fact that the Ge QDs are strongly constrained by the surrounding Si lattice, leading to a smaller deformation as compared to the bulk Ge, when subjected to the same pressure.

We have also investigated the Ge NCs embedded into a SiO$_2$ matrix on a quartz-glass substrate (Ge/SiO$_2$/quartz nanosystem) by Raman scattering under hydrostatic pressure. We found a larger pressure coefficient for the Ge–Ge mode in Ge NCs as compared to its corresponding bulk value. The observed effect can be explained in terms of a simple elastic model, which describes the significant contribution of the interface stress. Thus the pressure acting on the NCs is not necessarily the same as the pressure applied from outside. For Ge NCs embedded in a SiO$_2$ matrix on a Si substrate, we found that delamination between SiO$_2$ film and Si substrate occurs at ~ 23 kbar due to the large difference between the compressibility of the SiO$_2$ matrix and Si substrate. The observed effect can be understood by the nonhomogeneous distribution of the elastic field in the Ge/SiO$_2$/Si nanosystem. Although our investigation focuses on the Ge/SiO$_2$/Si nanosystem, our results could provide a general understanding on the elastic properties of different multicomponent nanosystems.

References

[1]   Teo, K.L., Qin, L., Noordin, L.M., Karunasiri, G., Shen, Z.X., Schmidt, O.G., Eberl, K., and Queisser, H.J. (2001). *Phys. Rev. B* **63**: 121306.

[2]   Qin L, Teo, K.L., Shen, Z.X., Peng, C.S., and Zhou, J.M. (2001). *Phys. Rev. B* **64**: 075312.

[3]   Teo, K.L., Qin, L., Shen, Z.X., and Schmidt, O.G. (2002). *Appl. Phys. Lett*. **80**: 2919.

[4]   Qin, L., Shen, Z.X., Teo, K.L., Peng, C.S., Zhou, J.M., Tung, C.H., and Tang, S.H. (2003). *Thin Solid Films* **424**: 23.

[5]   Liu, L., Shen, Z.X., Teo, K.L., Kolobov, A.V., and Maeda, Y. (2003). *J. Appl. Phys*. **93**: 9392.

[6]   Liu, L., Teo, K.L., Shen, Z.X., Sun, J.S., Ong, E.H., Kolobov, A.V., and Maeda, Y. (2004). *Phys. Rev. B* **69**: 125333.

[7]   Floro, J.A., Sinclair, M.B., Chason, E., Freund, L.B., Twesten, R.D., Hwang, R.Q., Lucadamo, G.A. (2000). *Phys. Rev. Lett*. **84**: 701; Jesson, D.E., Kastner, M., and Voigtlander, B. (2000). *ibid* **84**: 330; Kastner, M. and Voigtlander, B. (1999). *ibid* **82**: 2745; Wedler, G., Walz, J., Hesjedal, T., Chilla, E., and Koch, R. (1998) *ibid* **80**: 2382; Ross, F.M., Tersoff, J., and Tromp, R.M. (1998). *ibid* **80**: 984; Goldfarb, I., Hayden, P.T., Owen, J.H.G., and Briggs, G.A.D. (1997). *ibid* **78** 3959; Steinfort, A.J., Scholte, P.M.L.O., Ettema, A., Tuinstra, F., Nielsen, M., Landemark, E., Smilgies, D.M., Feidenhansl, R., Falkenberg, G., Seehofer, L., and Johnson, R.L. (1996). *ibid* **77**: 2009.

[8]   Kolobov, A.V. and Tanaka, K. (1999). *Appl. Phys. Lett.* **75**: 3572; Kolobov, A.V. (2000). *J. Appl. Phys*. **87**: 2926.

[9]   Liu, J.L., Wan, J., Jiang, Z.M., Khitun, A., Wang, K.L., Yu, D.P. (2002). *J. Appl. Phys.* **92**: 6804.

[10]   Kwok, S.H., Yu, P.Y., Tung, C.H., Zhang, Y.H., Li, M.F., Peng, C.S., and Zhou, J.M. (1999). *Phys. Rev. B* **59**: 4980.

[11]   Boscherini, F., Capellini, G., Gaspare, L.D., Rosei. F., Motta, N., Mobilio, S. (2000). *ibid* **76**: 682; Liu, J.L., Jin, G., Tang, Y.S., Luo, Y.H., Wang, K.L., and Yu, D.P. (2000). *Appl. Phys. Lett*. **76**: 586; Groenen, J., Carles, R., Christiansen, S., Albrecht, M., Dorsch, W., Strunk, H.P., Wawra, H., and Wagner, G. (1997). *ibid* **71**: 3856; Persans, P.D., Deelman, P.W., Stokes, K.L., Schowalter, L.J., Byrne, A., and Thundat, T. (1997). *Ibid* **70**: 472.

[12]   Bottani, C.E., Mantini, C., Milani, P., Manfredini, M., Stella, A., Tognini, P., Cheyssac, P., and Kofman, R. (1996). *Ibid* **69**: 2409.

[13]   Anastassakis, E. and Cardona, M. (1998). *Semiconductor Physics and Semimetals*, Eds. Suski, T. and Paul, W., Academic, 55:118.

[14]   Maeda, Y. (1995). *Phys. Rev. B* **51**: 1658.

[15]   Lockwood, D.J., Lu, Z.H., and Baribeau, J.M. (1996). *Phys. Rev. Lett*. **76**: 539.

[16]   van Buuren, T., Dinh, L.N., Chase, L.L., Siekhaus, W.J., Terminello, L.J. (1998). *Phys. Rev. Lett*. **80**(17): 3803.

[17]   Yu, P.Y. and Cardona, M. (2003). *Fundamentals of Semiconductors: Physics and Material Properties*, Third edn., New York: Springer, Chap. 6.

[18]   Yu, P.Y. and Cardona, M. (2003). *Fundamentals of Semiconductors: Physics and Material Properties*, Third edn., New York: Springer, Chap. 7.

[19]   Fauchet, P.M. and Campbell, I.H. (1988). *Cri. Rev. Solid State Mater. Sci.* **14**: S79.

[20]   Kobayashi, T., Endoh, T., Fukuda, H., Nomura, S., Sakai, A., and Ueda, Y. (1997). *Appl. Phys. Lett*. **71**: 1195.

[21] Piermarini, G. J., Block, S., Barnett, J.D., and Forman, R.A. (1975). *J. Appl. Phys.* **46**: 2774.

[22] Weinstein, B.A. and Piermarini, G.J. (1975). *Phys. Rev. B* **12**: 1172.

[23] Schmidt, O.G., Lange, C., and Eberl, K. (1999). *Appl. Phys. Lett.* **75**: 1905.

[24] Kamins, T.I., Carr, E.C., Williams, R.S., and Rosner, S.J. (1997). *J. Appl. Phys.* **81**: 211; Floro, J.A., Locadomo, G.A., Chason, E., Freund, L.B., Sinclair, M., Twesten, R.D., and Hwang, R.Q. (1998). *Phys. Rev. Lett.* **80**: 4717; Kamins, T.I., Medeiros-Ribeiro, G., Ohlberg, D.A.A., and Williams, R.S. (1999). *J. Appl. Phys.* **85**: 1159.

[25] Liu, J.L., Jin, G., Tang, Y.S., and Wang, K.L. (1999). *Appl. Phys. Lett.* **75**: 3574.

[26] Schorer, R., Abstreiter, G., de Gironcoli, S., Molinari, E. , Kibbel, H., and Presting, H. (1994). *Phys. Rev. B* **49**: 5406.

[27] Liu, C.P., Gibson, J.M., Cahill, D.G., Kamins, T.I., Basile, D.P., and Williams, R.S. (2000). *Phys. Rev. Lett.* **84**: 1958.

[28] Chaparro, S.A., Drucker, J., Zhang, Y., Chandrasekhar, D., McCartney, M.R., and Smith, D.J. (1999). *Phys. Rev. Lett.* **83**: 1199.

[29] Magidson, V., Regelman, D.V., Beserman, R., and Dettmer, K. (1998). *Appl. Phys. Lett.* **73**: 1044.

[30] Liu, J.L., Tang, Y.S., Wang, K.L., Radetic, T., and Gronsky, R. (1999). *Appl. Phys. Lett.* **74**: 1863.

[31] Olego, D. and Cardona, M. (1982). *Phys. Rev.* B **25**: 1151.

[32] Ledbetter, H. and Kim, S. (2001). *Handbook of Elastic Properties of Solids, Liquids, and Gases*, II: 99∼100 M. Levy, H.E. Bass, R.R. Stern, M. Levy, L. Furr, and V. Keppens (Eds.) San Diego: Academic.

[33] Buchenauer, C.J., Cerdeira, F., and Cardona, M. (1970). *Proceedings of the Second International Confertence on Light Scattering in Solids*, M. Balkanski (Ed.), Paris: Flammarian, p. 280.

[34] Sui, Z.F., Herman, I.P., and Bevk, J. (1991). *Appl. Phys. Lett.* **58**: 2351; Sui, Z.F., Burke, H.H., and Herman, P. (1993). *Phys. Rev. B* **48**: 2162.

[35] Mitra, S.S. and Massa, N.E. (1981). In: *Handbook on Semiconductor*. T. S. Moss (Ed.), Amsterdam, New York: North Holland.

[36] Cerdeira, F., Buchenauer, C.J., Pollak, F.H., and Cardona, M. (1972). *Phys Rev B* **5**: 580.

[37] Renucci, M.A., Renucci, J.B., Zeyher, R., and Cardona, M. (1974). *Phys. Rev. B* **10**: 54309.

[38] Zallen, R. and Paul, W. (1967). *Phys. Rev.* **155**: 703.

[39] Pollak, F.H. and Cardona. M. (1968). *Phys. Rev.* **172**: 816.

[40] Seon, M., Holtz, M., Park, T.R., Brafman. O., Bean, J.C. (1998). *Phys. Rev. B* **58**: 4779.

[41] Craciun, V., Boyd, I.W., Reader, A.H., and Vandenhoudt, E.W. (1994). *Appl. Phys. Lett.* **65**: 3233.

[42] Teo, K.L., Kwok, S.H., Yu, P.Y., and Guha, S. (2000). *Phys. Rev. B* **62**: 1584.

[43] Shen, J.K., Wu, X.L., Tan, C., Yuan, R.K., and Bao, X.M. (2002). *Phys. Lett. A* **300**: 307.

[44] Williams, R.S., Medeiros-Ribeiro, G., Kamins, T.I., and Ohlbergy, D.A.A. (2000). *Annu. Rev. Phys. Chem.* **51**: 527.

[45] Kolobov, A.V., Wei, S.Q., Yan, W.S., Oyanagi, H., Maeda, Y., and Tanaka, K. (2003). *Phys. Rev. B* **67**: 195314.

[46] Haselhoff, M., Reimann, K., and Weber, H.J. (1999). *Eur. Phys. J. B* **12**: 147.

[47]   Landau, L.D. and Lifschitz, E.M. (1970). *Theory of Elasticity*, second edn., London: Pergamon.

[48]   Duffrène, L. and Kieffer. J. (1998). In: D. Hewak (Ed.) *Properties, Processing and Applications of Glass and Rare Earth-Doped Glasses for Optical Fibres*, London: IEE, INSPEC, p. 29.

[49]   Tolbert, S.H. and Alivisatos, A.P. (1995). *Annu. Rev. Phys. Chem.* **46**: 595.

[50]   Saxena, A. (1998). *Nonlinear Fracture Mechanics for Engineers*, Boca Raton, FL: CRC Press, Chap. 2, p.27.

[51]   Jellison, G.E., Jr. (1992). *Opt. Mater.* **1**: 41.

13
Nanoengineered Biomimetic Bone-Building Blocks

R. Murugan and S. Ramakrishna

13.1. Introduction

Bone is a paradigm for a dynamic tissue because it has a unique capability of self-regenerating or self-remodeling throughout its life without leaving a scar. However, many circumstances call for bone grafting owing to bone defects arising either from traumatic or nontraumatic destruction. Bone grafting is a field of intensive investigation in human health care as it directly affects the quality and length of human life. Basically, bone grafting is a surgical method that repairs or regenerates the defective bone with the help of bone graft materials.

Of course, the need for such bone grafts truly depends on the complication of bone defects. For example, if the defect is minor, bone has its own capability to self-regenerate its functions within a few weeks time concerning applied stress of cellular and other metabolic components. Therefore, bone grafting is not required in such a situation. But, in the case of severe defect and when the loss of volume is too high, bone will not heal by itself. Under these circumstances, bone grafting is actually required to repair or regenerate the defective bone into normal healthy bone without damaging living tissues. There are several methods available for the treatment of bone defects, including customary methods of autografting and allografting. Although they are clinically considered good therapies and have saved several lives, still they encounter some practical complications. For example, the supply of autograft is limited and there is a possibility of pathogen transfer from allograft. Accordingly, there is a great need for engineering synthetic bone grafts equivalent to natural bone tissue in all aspects.

Currently, numerous synthetic bone grafts are available for clinical use that are capable of alleviating some of the practical complications associated with autograft or allograft. Although there has been good progress in bone grafting using synthetic bone grafts, the way in which they execute their functions in vivo is quite different from each other and they still have uncertain competence. The characteristics of the currently available synthetic bone grafts are drastically different from those of natural bone tissue in many aspects, in particular molecular interaction between minerals and organic components. This is mainly due to the result of the absence

of peculiar self-organizing interaction between the apatitic crystals and the proteic components as occur in natural bone tissue.

Furthermore, most synthetic bone grafts available today are considerably different from natural bone either compositionally or structurally or a combination of each. It is well known that natural bone tissue is a nanocomposite matrix, constituted of nanosize bladelike crystals of hydroxyapatite (HA) grown in intimate contact with a proteic matrix rich with collagen nanofibers [1,2]; thereby choosing the HA/collagen as a precursor for making synthetic bone grafts is an added advantage and, of course, could easily be adapted to the body environment. Therefore, engineering of bone grafts analogous to natural bone tissue, in terms of composition and structure, at the nano or molecular level is a goal to be pursued. There are several methods currently employed for the processing of bone grafts. The biomimetic approach is one among them that has recently gained much interest and is perceived to be more beneficial than conventional methods owing to their possibility of processing synthetic bone grafts by mimicking the biological mechanism of natural bone tissue.

Keeping these points in view, it is therefore necessary to emphasize the current trend of the biomimetic HA/collagen system in bone grafting, which may also stimulate research on biomimetic bone grafts in a new direction. This chapter also discusses some of the critical issues and scientific challenges that might be faced in further research and development of this emerging field, bone biomimetics. For the benefit of readers, the basics of bone science and its nanostructural self-assembling strategy, the current scenario of bone grafting, how the concept of biomimetics originated from conventional processing methods, and the recently developed biomimetic bone grafts are briefly described. We hope it will be useful for readers to learn facts on the state of the art of nanoengineered biomimetic bone grafts.

13.2. Nanostructural Strategy of Bone

13.2.1. Nanoscale Bone-Building Blocks

Bone is an amazing and, in fact, a natural nanocomposite self-organized with approximately 70% minerals and 30% proteins. The design strategy of biomimetic bone grafts is not straightforward without understanding at least the rudiments of bone composition, structure, and the way in which it is organized. Bone, in general, is a well-organized connective tissue made of several building blocks at multiple levels that consist of, in decreasing proportions, minerals, collagen, water, noncollagenous proteins, lipids, vascular elements, and cellular components. An overall composition of the bone is given in Table 13.1 [3–5]. Bone minerals are chiefly enriched with HA nanocrystals and bone proteins mainly consist of collagen nanofibers. Collagen acts as a structural framework in which nanocrystals of HA are embedded to strengthen the bone tissue [6–8]. Bone collagen has a typical fibrous structure, whose diameter varies from 100 to 2000 nm. Similarly, HA in bone minerals is in the form of platelike nanocrystals with dimensions of about 4 nm by 50 nm by 50 nm.

TABLE 13.1 The composition of bone tissue.[a]

Inorganic phase (wt.%)	Organic phase (wt.%)
Hydroxyapatite ~60	Collagen ~20
Carbonate ~4	Water ~9
Citrate ~0.9	Noncollagenous proteins ~3
Sodium ~0.7	(osteocalcin, osteonectin, osteopontin,
Magnesium ~0.5	thrombospondin, morphogenetic proteins,
Other traces:	sialoprotein, serum proteins),
Cl^-, F^-, K^+ Sr^{2+}, Pb^{2+},	Other traces:
Zn^{2+}, Cu^{2+}, Fe^{2+}	Polysaccharides, lipids, cytokines.
	Primary bone cells:
	osteoblasts, osteocytes, osteoclasts.

[a]Compiled from Refs. [3–5]; Composition slightly varied from species to species and from bone to bone.

The structural and compositional strategies, in which they are precisely built, make the bone a true nanocomposite. The bone minerals are also enriched with a few trace elements, including carbonate, citrate, sodium, magnesium, fluoride, chloride, potassium, and iron which are used for various metabolic functions [7,8]. The prime role of minerals is to provide toughness and rigidity to the bone, whereas collagen provides tensile strength and flexibility. It is really amazing to know how nature built extremely hard and tough bone using such soft (collagen) and brittle (HA) ingredients. Bone not only provides mechanical support for the organism but also elegantly serves as a reservoir for minerals, particularly calcium and phosphate.

The complete biological mechanism involved in the bone-building strategy is still unclear and thus research still progresses in this direction around the world. It is believed that the key to bone strength is the complex structural hierarchy into which it is organized in a self-assembling mode. It is important to note that the minerals are not directly bound to collagen, but bound through noncollagenous proteins. The process involved in this strategy is often called biological mineralization or biomineralization. The noncollagenous proteins make up approximately 3 to 5% of the bone, and provide active sites for biomineralization. Water, which is one of the most essential substances of the body because no cells survive without water, is also found in sufficient quantity in all bones. Lipids are also necessary for cellular functions, and account for about 2% of the bone. They play an important role in the process of initial biomineralization. It is worthwhile to note that, in general, biomineralization typically begins only 10 days after the organic matrix is laid down. The concept of biological mineralization is briefly discussed in Section 13.2.4.

13.2.2. Cellular Functions of Bone Tissue

Bone formation is accomplished by synchronized multicellular actions and hence studying the functions of cellular components is significant in the context of bone
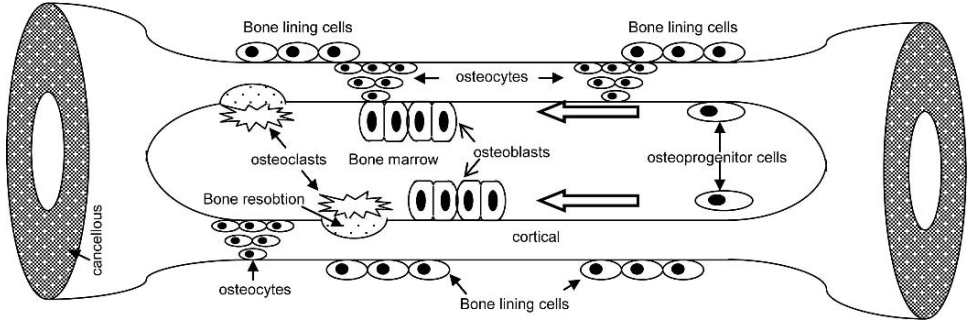
FIGURE 13.1. Diagrammatic representation of cellular factors influencing bone remodeling.

metabolism, which further helps to understand their roles in biological mineraliza-
tion. There are five distinct types of cells associated with the bone tissue with regard
to their functions, which are called osteoprogenitor cells, osteoblasts, osteocytes,
osteoclasts, and bone-lining cells (see Figure 13.1) [9–11].

Bone, like other connective tissues in the embryo, is derived from mesenchymal
cells. These cells have the ability to proliferate and differentiate into bone cells,
which are known as osteoprogenitor cells. They are also called bone-precursor
cells. Osteoblasts are the cells that are responsible for the formation of new bone
tissue. They start with secreting collagen macromolecules followed by coating
noncollagenous proteins, which are similar to glue that has the ability to bind the
minerals, mostly calcium and phosphate, from the bloodstream. Osteocytes are
mature cells derived from the osteoblasts that are responsible for the maintenance of
the bone tissue. They function as transporting agents of minerals between bone and
blood. Osteoclasts are the large cells that are found at the surface of the bone mineral
next to the resorbing bone. They are responsible for the resorbtion of the bone
tissue. They use acids or enzymes to dissolve the minerals as well as collagen
from the mature bone. The dissolved minerals then re-enter the bloodstream and
are carried to different parts of the body. Bone-lining cells are found along the
surface of the mature bone, which are responsible for regulating the transportation
of minerals in and out of the bone tissue. They also respond to hormones by
making some exclusive proteins that activate the osteoclasts. These five types of
cells are together responsible for building the bone matrix with hierarchical self-
assembly, maintenance, and remodeling as required. All these processes must be
in equilibrium to ensure a healthy bone tissue.

13.2.3. Hierarchical Tactics of Bone

Bone is considered an assemblage of hierarchical structural units or building blocks
elegantly designed at many length scales, macro to nano and so, to meet multi-
ple functions, including strength to the body. When bone is initially laid down,
it is structurally weak and unorganized. But within a few days, the primary bone
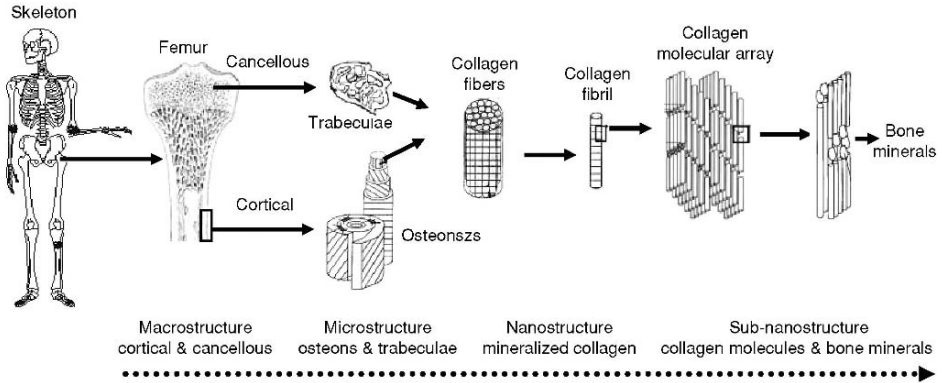
FIGURE 13.2. The hierarchical structure of bone, from macro- to nanoassembly.

* Adapted and re-drawn from Ref. [12]

remodels to become lamellar bone and gradually mature, and has a perfect alignment of collagen fibers and minerals. At the macrostructural level, the mature lamellar bone can be distinguished into two types, namely, spongy bone and compact bone. As their names imply, they radically vary in density. They are organized with multilevel pores, macro to nano, for the establishment of multiple functions, including transportation of nutrients, oxygen, and body fluids.

The dimension-dependent hierarchical structure of the bone tissue is shown in Figure 13.2 [12]. The spongy bone occupies about 20% of the total bone. It is also often called trabecular or cancellous bone. It is lighter and lesser dense than compact bone (see Figure 13.2). It has high porosity and a higher concentration of blood vessels compared to compact bone. The porous architecture is easily visible under the lower-power microscopes and/or even to the naked eyes if the pores are very large. The diameter of the pores may be from a few micrometers to millimeters. On the other hand, compact bone is much denser than spongy bone. It is also called cortical or dense bone. It occupies about 80% of the total bone. It has less porosity and thus it has less concentration of blood vessels. Its porous architecture is not visible to naked eyes owing to less porosity. They may be perhaps 10–20 μm in diameter and are mostly separated by intervals of 200–300 μm. Compact bone functions mechanically in tension, compression, and torsion, whereas spongy bone functions mainly in compression.

At the microstructural level, the repeated structural unit of compact bone is mostly of osteon or the Haversian system, which acts as weight-bearing pillars. In contrast, spongy bone contains no such osteon units, but they are made of an interconnecting framework of trabeculae. The trabeculae have three types of cellular structures: plate/platelike, plate/barlike, and bar/barlike. At the nanostructural level, the bone tissue chiefly consists of collagen nanofibers and nanocrystals of bone minerals, particularly HA. Although several structural levels of bone have been identified, a complete understanding of how the mineral–matrix interactions

are related to their mechanical reliability at the thus-far identified seven hierarchical levels of the bone tissue is still required. Furthermore, rationales of cell–matrix and cell–cell interactions are also important aspects to be considered at the atomic or molecular level.

13.2.4. Mechanism of Biological Mineralization

Biological mineralization or biomineralization is defined as a process by which living organisms generate biominerals that crystallize and mature in a precisely well-organized way for the growth of bone tissue, which gives structural strength to bone. The field of biomineralization is a multidisciplinary theme that combines the basic sciences of physics, chemistry, and biology in association with the modern sciences of structural biology and nanobioengineering, towards the development of new generation of biomaterials for bone grafting. With reference to available data reported in the various literature during the past decade, biomineralization is a promising as well as primary process for the fabrication of such a new class of bone grafts.

The process of biomineralization usually involves the nucleation and growth of biominerals within a matrix of either cellular or extracellular organisms in a well-organized fashion, which occurs only under mild and ambient conditions at low temperature [13,14]. It should also be noted that biomineralization does not occur without a matrix, which acts as a mineral nucleating agent. The matrix is thought to be important in binding various ions at anionic or cationic sites. Calcium and phosphates are the primary biominerals involved in the various stages of biomineralization of human bone tissue.

In general, the biomineralization process occurs in two steps. In the first step, phosphate accumulates within the matrix through the enzymatic hydrolysis of phyrophosphates, a kind of calcium phosphate-based inorganic phase. The accumulated phosphates then react with calcium ions and subsequently produce apatite crystals, particularly HA, in the case of bone tissue growth. It is believed that anions (phosphate, for example) assist nucleation by providing a negatively charged surface that interacts electrostatically with cations (calcium, for example) [15]. Certain ions have a strong attraction for electrons in oxygen-containing anions (phosphate, for example) which further reduces the attraction of water molecules, leading to HA formation as follows: $10Ca^{2+} + 6HPO_4^{2-} + 2H_2O \rightarrow Ca_{10}(PO_4)_6(OH)_2 + 8H^+$.

In the second step, the crystal within the matrix grows and is exposed to the cartilage matrix fluid; note that cartilage is a precursor of bone or an earlier stage of bone formation. The exposed apatite into the matrix fluid then gradually matures owing to the supersaturated fluid containing apatite crystals. The highly matured apatite crystal deposits radically surrounding the collagen nanofibers, followed by biomineralization. In addition, the distribution of the anions in the matrix may provide a steriochemical template for adsorbing a layer of cations, thereby controlling both the phases and orientation of the nuclei as well as their location (see Figure 13.3) [16].

The collagen matrix spatially or temporally defines the space with bound side chain groups and free calcium and/or phosphate ions (Pi) as shown in Figure 13.3. It
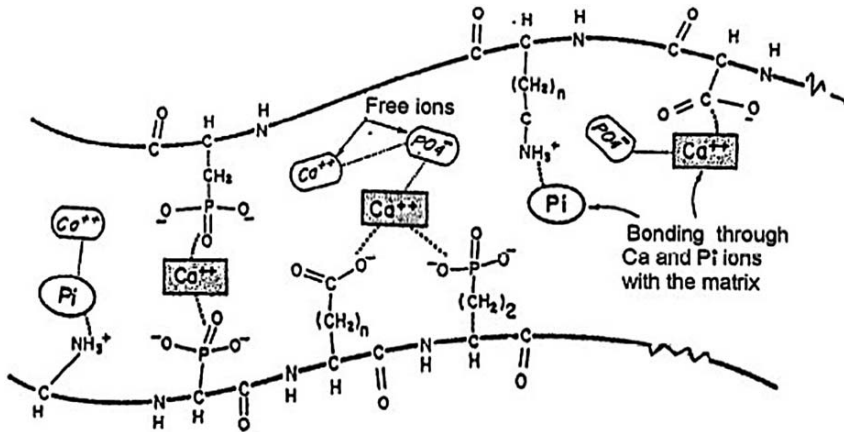
FIGURE 13.3. Mineral–protein (matrix) interaction of biological mineralization. Adapted from Ref. [16].

is also believed that the anions in matrix fluid can influence crystal shape by selective adsorption onto certain faces [17]. The inhibition of biological mineralization occurs only in regions where the matrix fluid tends to conditions of supersaturation for those involved minerals, that is, in sites where the solubility produces a particular type of bone crystals (HA, for example). The size of such bone crystals is extremely ultrafine (nano or subnano level), which means they have very high surface area-to-volume ratio and thus high affinity to biological or biochemical compounds essential for biomineralization.

It is well known that collagen (type I) was the first predominant matrix to support biomineral deposition [18]. It should also be noted that collagen alone is not always the initiation site of biomineralization, but also noncollagenous proteins such as proteoglycans or bone sialoproteins are offering sites for the initial biomineralization. A major issue in the biomineralization process is whether collagen or noncollagenous proteins nucleate the biominerals. Despite numerous investigations, however, the exact role of those biological substances in biomineralization is still unclear. In addition, phosphoproteins, polysaccharides, and lipids are also actively involved in the process of biomineralization [19,20]. They are all responsible for the initiation, growth, and regulation of biomineral deposition into the cellular or extracellular matrix (ECM).

Furthermore, the process of biomineralization truly depends on various systemic and local factors in the body fluids. For example, blood plasma contains various proteins that are significantly involved in the biomineralization process and its growth also responds to local stresses but complete knowledge on how the stress is being sensed or transduced is not yet available. On the other hand, the degree of biomineralization is the most essential factor in determining the biomechanical competence of bone tissue. Nevertheless, the actual mechanism involved in biomineralization remains poorly understood even with the advances of biosciences. All these basic and, of course, critical data are highly necessary for the design of an ideal biomimetic bone graft.

13.3. Current Scenario of Bone Grafting

Bone grafting is a surgical method that repairs or replaces the defective bones with healthy bones with the aid of materials or substances either from the patient's own body or from synthetic sources. The materials used for bone grafting are known as bone graft materials or bone grafts. They are widely used in orthopedic surgery, plastic surgery, oral and maxillofacial surgery, and dental surgery. It should be noted that bone is the second most transplanted tissue in humans. Bone grafts not only fill defective gaps, but also eventually provide mechanical and structural support; thereby enhancing bone tissue growth. By this method, bone defect-healing time gets reduced and new bone formation strengthens the defective area by bridging implanted bone grafts with host bone. There is a variety of bone grafting methodologies available, including autografting, allografting, xenografting, and alloplastic or synthetic bone grafting, each varying with their own advantages and disadvantages [21–26]. A diagrammatic representation of typical bone grafting in humans is shown in Figure 13.4. The selection of the grafting method is purely dependent on the nature and complication of the bone defects as well as the choice of available bone grafts and, of course, the key decision depends on the surgeon's own experience.

Autografting is a class of method in which bone tissue is transplanted from one site to another site of the same individual. The concept is basically the patient's own bone collected from a donor site and transplanted to another site of the same body that requires bone regeneration. It is commonly harvested from the patient's iliac crest in the form of cancellous bone. Mowlem clinically proved it in 1944 [27], and he had successfully treated about 75 critical cases using cancellous bone from the
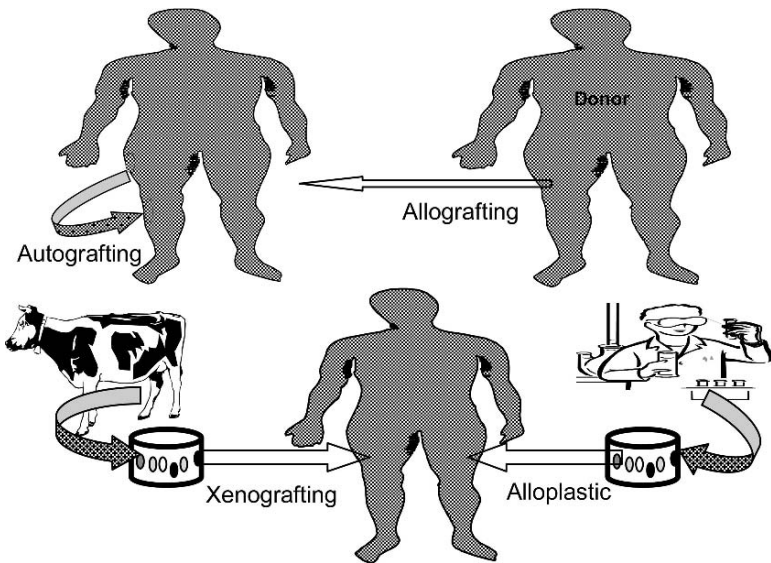
FIGURE 13.4. A scheme for bone grafting strategies.

iliac crest. Another recently explored source of autogenic graft is the osteoblastic stem cells found in bone marrow, also familiarly known as bone marrow aspirate (BMA). These cells can be harvested from the patient's own body with the help of a syringe needle and transplanted to the defective site without complicated surgery as in the above cases. BMA extensively provides osteogenic and osteoinductive factors necessary for fast bone regeneration. They can also be transplanted by blending or mixing with other bone graft materials in a composite form [28,29]. The latter method is a good choice because there is a chance of migration of cells from the implanted site if we deliver them without a suitable carrier system.

So far, in general, the best clinical success rate has been achieved by this autografting method because it provides osteogenic cells as well as essential osteoinductive factors for the activation of bone growth; thereby it is clinically considered as a gold standard [30,31]. This method is also recognized as the safest transplant owing to histocompatiblility of the grafts and thus there is no chance for rejection. The microstructural features of the graft perfectly match with host tissue. However, it has a few disadvantages in several clinical situations, including (1) insufficient amount of grafts, particularly in children and when dealing with large bone defects; (2) significant postoperative risk of morbidity at the donor site; and (3) complexity in making the required shape.

Allografting is another kind of bone grafting method, which can be defined as tissue transplantation between individuals of the same species but of nonidentical genetic composition. Lexer carried out the first clinical use of allograft in 1908 [32]. The materials used as allografts are mostly cancellous, cortical, or a combination of each. The bone banks stock this type of grafts, which are usually harvested from cadavers. Typically, they are frozen or freeze-dried bones. However, after sterilization, most of them seem to lose much of their strength and, of course, they will not be resorbed absolutely after implantation; therefore they often remain as dead tissue or act as a foreign body. The dead portion then gradually becomes brittle and gives further medical complications with surrounding tissues. The advantages of allografting are the elimination of harvesting a surgical site, the related postoperative pain, and the added expense of a second operative procedure. The disadvantages are the slight chance of disease transmission such as hepatitis B, C, and acquired immune deficiency syndrome (AIDS), and reduced effectiveness because the bone growth cells and proteins are removed during the cleansing and disinfecting process [33,34]. This method is, therefore, of particular importance only if the bone defect is considerably large or the defect is not amenable to repair by autografting owing to insufficient quantity of the graft materials.

Xenografting is a method of transplanting tissue from one species to another; bone from animal to human, for example. It comes from the Greek word *xenos*, meaning strange. The feasibility of using animals as a source of bone tissue for transplantation has been the focus of research for many decades. Most of the bone transplantations using xenografts were performed in the early 1960s. The bone banks usually stock an abundant quantity of xenografts because of their easy harvesting compared to bone from humans. Currently, multiple xenografts are being processed, including frozen calf bone, freeze-dried calf bone, decalcified ox bone, deproteinized bovine bone, and anorganic bone [35]. Kiel bone is one
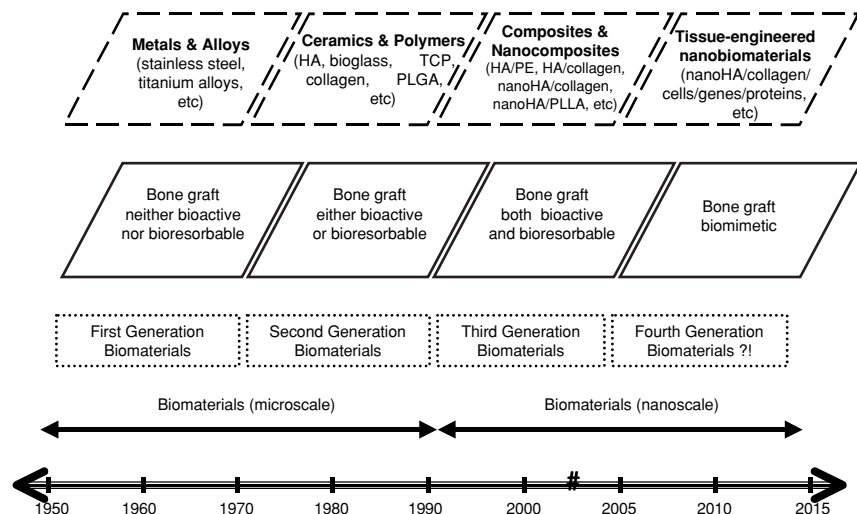
FIGURE 13.5. Evolution of bone grafts.

of the few commercially available xenografts, consisting of deproteinized bone of freshly sacrificed calves [36]. Xenografting is not very successful compared to autografting or allografting, probably due to the peril of antigenicity. However, the shortage of organs has prompted continued research in this field and thus extensive research is still ongoing throughout the world.

As an alternative to the above three types of bone grafts, synthetic substances are gaining much interest in use as bone graft materials. A surgical method that uses synthetic substances to repair or regenerate defective bone tissue is known as alloplastic or synthetic bone grafting. The synthetic substances used in bone grafting are called synthetic bone grafts. Over the past four decades a variety of synthetic bone grafts had been developed with the aim of eliminating or minimizing the above said complications associated with autografts, allografts, and xenografts [37–40]. Evolution of bone grafts with their past, present, and future trends are schematically illustrated in Figure 13.5 for the easy understanding of readers and for the comparison of their tremendous growth during the last few decades.

The compiled data imply that a variety of synthetic materials has been exploited for bone grafting. It is should be noted that each material has different characteristic functions either in vitro or in vivo or both; thereby it is quite difficult to judge which is the best system for bone grafting. Each of them has many advantages as well as disadvantages with respect to a specific need. In general, synthetic grafts eliminate some of the shortcomings of autografts or allografts associated with the donor shortage and the chance for rejection or transmission of infectious disease, respectively; therefore they are considered a good choice for bone grafting. In addition, synthetic grafts are abundantly available, reproducible, shapeable, sterilizable, and cost-effective. Although synthetic grafts have many desirable characteristics, currently none resembles natural bone tissue in many

aspects, which is mainly due to the lack of appropriate designing technique. In this regard, the so-called biomimetic approach is considered one of the promising methods in designing such a bone-resembling graft. Now, research is progressing in this direction and the next decade may witness many breakthroughs in the fascinating field of biomimetics.

13.4. Key Factors of an Ideal Bone Graft

Although most of the synthetic grafts available possess favorable characteristics for bone regeneration currently none resembles autogenic bone, which further stimulates research in bone grafting. It is worthwhile to recall that reconstruction of bone tissue by synthetic bone grafts having structure, composition, and biological features that mimic natural bone tissue is the ultimate goal to be pursued for any bone grafting. Therefore, engineering a bone graft with these features is a real challenge for the biomaterialist. The prime role of bone grafts is to provide a perfect framework for the host bone to regenerate new bone tissue, soft tissue, and vascular and other metabolic components. In this regard, selection of bone grafts is of great importance inasmuch as the clinical success rate depends in part on the characteristics of those grafts. Essentially they must satisfy a few characteristics, particularly osteoconductive, osteoinductive, and osteogenic, which are given in Table 13.2 with their critical comments. Any material that holds all these key factors can probably be considered as an ideal bone graft. Although several synthetic grafts satisfy some of these factors, none have the ability of satisfying all these factors together, except autogenic bone; therefore investigations are still in action to recognize an ideal synthetic bone graft. In the subsequent sections we provide detailed information on bone grafts with regard to their osteogenic characteristic functions (see Table 13.3) [41–46], the most critical factors of an ideal bone graft.

13.4.1. Osteoconductive Bone Grafts

Osteoconduction is a physical effect wherein the matrix of the graft acts as a scaffold on which cells are able to form new bone tissue. In other words, the bone-healing response is conducted through the graft. Accordingly, osteoconductive bone grafts are to serve as a structural framework through which host bone infiltrates and regenerates new bone tissue. The best examples of osteoconductive grafts are autogenic- and allogenic-cancellous bones, HA, and purified collagen (see Table 13.3). Among them, HA and collagen are widely used not only in bone grafting but also in other medical applications owing to their abundant availability, easy processing, amazing functional properties, and, in fact, ingredients of natural bone tissue; therefore we describe them in this section in a detailed fashion.

13.4.1.1. Hydroxyapatite and Its Use in Bone Grafting

Hydroxyapatite is a class of calcium phosphate-based bioceramic material, frequently used as a bone graft substitute owing to its chemical and structural

TABLE 13.2 Basic characteristics of an ideal bone graft.

Characteristics	Comments
Biocompatible	Biologically compatible to host tissue (i.e., should not provoke any rejection, inflammation, and immune responses).
Bioactive	To facilitate a direct biochemical bonding to host tissue.
Biodegradable in a controlled fashion	The rate of biodegradation has to be adjusted to match the rate of bone tissue formation.
Degradation time	Preferably less than six months, but depends on case by case.
Mode of degradation	Bulk or surface erosion.
Osteoconductive	Capable of supporting in-growth of sprouting capillaries, perivascular mesenchymal tissues, and osteoprogenitor cells from the recipient host into the 3-D structure of a graft that acts as a scaffold.
Osteoinductive	A process in which biomolecules enriched within the graft convert the patient's cells into cells capable of forming a new bone.
Vascular supportive	Should provide channels for blood supply for fast and healthy bone regeneration.
Nontoxic	Should not evoke toxicity to host tissue.
Nonimmunogenic	Should not evoke immunogenic response to host tissue.
High porosity with interconnected pores	To maximize the space for cellular adhesion, growth, ECM secretion, revascularization, adequate nutrition, and oxygen supply. However, it should not compromise mechanical strength of the graft.
Pore size	To allow cell penetration.
<50 μm	Sufficient to in-growth of fibrous tissue.
>100 μm	Needed for new bone generation.
>200 μm	Required for mature osteons to form.
3-D structure	For the assistance of cellular in-growth and transport of nutrition and oxygen.
High surface area-to-volume ratio	Needed for high density of cellular attachment.
Surface modifiable	To functionalize additional chemical or biomolecular groups in order to enhance cellular adhesion and bone tissue growth.
Adequate mechanical strength	To withstand in vivo stimuli.
Ultrapure	Needed for better performance of graft.
Sterilizable	To avoid toxic contamination.
Cost-effective	Affordable to all; thereby making the patient happier.

similarity with natural bone mineral [47,48]. The HA derived either from natural sources or from synthetic sources is regarded as a bioactive substance because it forms a strong chemical bond with host bone tissue, and hence it is recognized as a good bone graft material. HA is not only bioactive but also osteoconductive, nontoxic, nonimmunogenic, and its structure is crystallographically similar to that of bone mineral. All the critical properties of the HA such as physiochemical, biomechanical, and biological are compiled and listed in Table 13.4 [22,49–53], which makes the HA a possible and perhaps the most appropriate bone graft material. The stoichiometric HA has a chemical composition of $Ca_{10}(PO_4)_6(OH)_2$ with a Ca/P ratio of 1.67. Crystallographic studies are one of the important parameters for the selection of stoichiometric HA.

TABLE 13.3 Classification of bone grafts upon tissue response.

Types of bone grafts	Description	Examples	References
Osteoconductive graft	Bone grafts that serve as a structural framework through which bone-forming cells can attach, migrate, and grow, leading to new bone tissue	AutoB, AlloB, HA, Collagen	[41,42]
Osteoinductive graft	Bone grafts that induce a biochemical process capable of promoting or accelerating new bone tissue	AutoB, BMP, DBM	[43,44]
Osteogenic graft	Bone grafts that convert the transplanted living tissue into new bone tissue	AutoB, BMA	[45,46]

AutoB: Autogeous bone; AlloB: Allogenous bone

A complete understanding of the crystal structure of HA can be acquired from the in-depth knowledge of the spatial orientation or organization of a small number of constituent ions. The unit cell, a basic structural pattern of the constituent ions, of HA is a right rhombic prism that forms a simple hexagonic crystal lattice. The

TABLE 13.4 Critical properties of HA.[a]

Properties	Experimental data
Chemical composition	$Ca_{10}(PO_4)_6(OH)_2$
Ca/P molar	1.67
Color	Mostly white
Crystal system	Hexagonal
Space group	$P6_3/m$
Cell dimensions (Å)	$a = b = 9.42, c = 6.88$
Young's modulus (GPa)	80–110
Elastic modulus (GPa)	114
Compressive strength (MPa)	400–900
Bending strength (MPa)	115–200
Density (g/cm^3)	3.16
Relative density (%)	95–99.5
Fracture toughness (MPa.m$^{1/2}$)	0.7–1.2
Hardness (HV)	600
Decomposition temp.(°C)	>1000
Melting point (°C)	1614
Dielectric constant	7.40–10.47
Thermal conductivity (W/cm.K)	0.013
Biocompatibility	High
Bioactivity	High
Biodegradation	Low
Cellular compatibility	High
Osteoinduction	Nil
Osteoconduction	High

[a]Compiled from Refs. [22, 49–53].
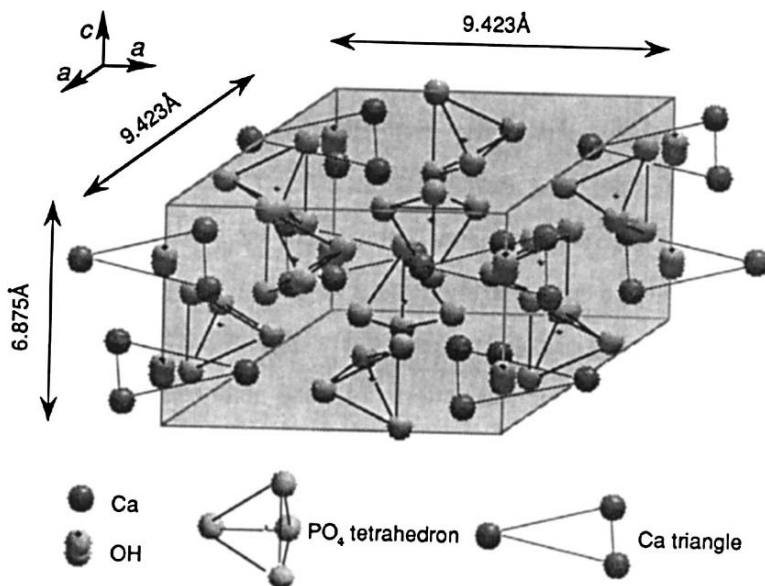
FIGURE 13.6. A diagrammatic view of crystal structure of HA. Courtesy: Prof. H. Aoki, Tokyo Denki University, Japan.

length along an edge of the basal plane of the unit cell is $a = b = 9.42$ Å and the height of the unit cell is $c = 6.88$ Å [54]. The spatial symmetry (i.e., space group) symbolized as $P6_3/m$, cannot be completely specified with fewer than this number of atoms. The arrangement of these constituent atoms is projected along the c-axis onto the basal plane. A schema of the crystal structure of HA viewed diagonally is shown in Figure 13.6 [54].

For simplicity, the chemical composition of HA can be written as $Ca_4(I)Ca_6(II)(PO_4)_6(OH)_2$, where the Ca atoms occupy two series of nonequivalent sites. The Ca(I) atoms are on the fourfold symmetry 4(f) positions and the Ca(II) atoms are in the sixfold symmetry 6(f) position. The P atom is surrounded by four atoms and forms a tetrahedron. The PO_4 tetrahedron is almost regular with only slight distortion. The hydroxyl ions lie, in projection, at the corners of the rhombic base of the unit cell. Furthermore, hydroxyl ions are always perpendicular to the nearest plane of calcium with the hydrogen ion facing away from this plane in such a way that the O–H band never overlaps the plane. Of course, the crystal structure and crystallization behavior of HA are strongly dependent on the substitution nature of the ionic species and the pattern ordering. Even the crystal structure can be changed by the manipulation of the calcium to phosphorous (Ca/P) ratio, which leads to possible changes in their solubility.

As per a literature survey, HA has a long history of being used as a good bone graft. Its possible clinical uses range from augmenting atrophic alveolar ridges to repairing long bone defects, ununited bone fractures, middle ear prostheses, spinal fusions, cranioplasty, craniofacial repair, and vertebral fusions. On the other hand, it

has also been used in various dental surgeries and biomolecular delivery. Basically, HA is a family of apatite phase. The name apatite was derived from the Greek word, meaning "to deceive," which was coined by Werner in 1786 [55]. Apatite belongs to a family of components having similar structure but not necessarily having identical phase composition. The first synthesis of apatite was carried out by Daubree in 1851 [56], in which apatite was produced by just passing phosphorous trichloride vapor over red hot lime. In 1951, a synthetic HA was prepared by Ray and Ward [57], suitable for bone defects. They implanted their processed HA at surgically created bone defects in the long bones and iliac wings of dogs and the skulls of cats and monkeys and obtained affirmative results. In 1970s and 1980s, Aoki and Kato [58], De Groot [59], and Jarcho [60] pioneered multishapeable HA suitable for clinical orthopedics.

Since then, a variety of preparation methodologies of HA has been reported. It is worthwhile to note that HA can also be processed from animal bone [61,62] and coral exoskeleton [63,64]. In all these, however, different processing methods are involved in the production of microsize HA in various forms such as powder or dense or porous blocks, corresponding to clinical applications. In the past few years, significant research efforts have been devoted to the production of nanosize HA in order to obtain high surface reactivity with adequate physical, chemical, and biological properties similar to natural bone mineral.

The nano HA has unique advantages over conventional micro HA in terms of high surface area-to-volume ratio and ultrafine structure, which are the most imperative properties essential for cell–substrate interactions in vivo. For example, compared to conventionally crystallized HA, nanocrystallized HA promotes osteoblast cell adhesion, differentiation, proliferation, osteointegration, and deposition of calcium-containing minerals on their surface, thereby enhancing new bone growth within a short period [65]. Keeping these points in view, nano HA can be considered as a unique class of bone grafting material. The nano HA can be synthesized by many different methods, which include solid state [66], wet chemical [67,68], hydrothermal [69,70], mechanochemical [71], pH shock wave [72], and more recently microwave processing [73]. Critical comments on these processing methods are specified in Table 13.5 and detailed descriptions about them are given in the following sections, respectively.

(a) Solid-State Reaction

Solid-state reaction has generally been used for the processing of bioceramic powders at high temperature. The HA powders prepared by this method usually have irregular shapes with larger grain size and they quite often exhibit heterogeneity in the phase composition due to chemical reactions resulting from small diffusion coefficients of ions within the solid. An example for the formation of HA using the solid-state method is given below:

$$4CaCO_3 + CaHPO_4.2H_2O \rightarrow Ca_{10}(PO_4)_6(OH)_2 + 4CO_2$$
$$+14H_2O \text{ at} 1000 - 1300°C.$$
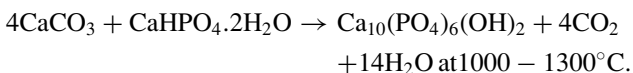
TABLE 13.5 Methods involved in the synthesis of nano HA.

Methods	Grain size (nm)	General remarks	References
Solid state	500	Inhomogeneous, large grain size (micro to nano), irregular shapes, reaction condition 900 to 1300°C	[66]
Wet chemical	20–200	Nanograin size, low crystallinity, homogeneous, reaction condition: room temp. to 100°C	[67,68]
Precipitation/ hydrothermal	10–25	Homogeneous, ultrafine particles, low crystallinity, reaction condition: room temp. to 200°C (1 to 2 MPa)	[69]
Hydrothermal	10–80	Homogeneous, fine crystals, high temperature, and high-pressure atmosphere	[70]
Mechanochemical	<20	Easy production, semi-crystallinity, ultrafine crystals, room temp. process	[71]
pH shock wave	20–100	High-energy dispersing, nonporous, monocrystalline particles with Ca/P molar ratio 1.43 to 1.66	[72]
Microwave	100–300	Uniformity, nanosize particles, time and energy saving	[73]

The key ingredients of this reaction are basically in solid phase in which both act as Ca and P precursors in the formation of HA. Typically, solid-state reaction takes place at very high temperature, that is, above 1000°C.

A method for the preparation of HA fibers was established using a solid phase reaction [66]. With this method, the HA fibers were fabricated by heating a compact consisting of calcium metaphosphate fibers with calcium hydroxide particles at 1000°C in air atmosphere, and subsequently treated with dilute aqueous HCl solution to remove unwanted secondary phase substitution such as CaO. The obtained HA fibers were characterized and found that the nanostructural characteristic features of HA are quite similar to the natural bone mineral apatite phase. Therefore, the solid-state reaction can be considered as one of the capable methods for the production of nanostructure HA.

(b) Wet-Chemical Method

The wet-chemical route is one of the promising and most frequently used methods to synthesize HA as it is relatively easy to process even at low temperature, in contrast to solid-state reaction. The materials synthesized by using this method are almost in homogeneous phase composition, but are poorly crystallized owing to the low-temperature process. One common wet-chemical method of synthesizing HA is based on using calcium hydroxide with orthophosphoric acid according to following equation:

$$10Ca(OH)_2 + 6H_3PO_4 \rightarrow Ca_{10}(PO_4)_6(OH)_2 + 13H_2O.$$
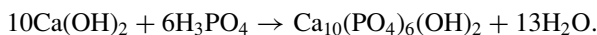
A free-flowing form of nanocrystalline HA was synthesized by using this method [74]. The obtained powder agglomerates were consolidated into bulk form to

test their mechanical reliability. The experimental data clearly showed that the compressive strength of the bulk nano HA could be increased up to fourfold in comparison to natural bone, whereas bending strength was found to be almost equivalent to that of bone.

Recently, Ahn et al. [75] processed a bioactive nanocrystalline HA through nanostructure processing to achieve superior chemical homogeneity and structural uniformity in order to manufacture high-quality apatites. They have attained nanostructural HA by using the precipitation route with $Ca(NO_3)_2.4H_2O$ and $(NH_4)_2HPO_4$ and studied the optimal condition by changing the reaction parameters such as precursor pH, aging time, and temperature to achieve nano HA particles with tailored composition and morphology. This investigation clearly indicated that the nanostructure processing offers an alternative solution to challenges encountered in conventional HA processing and concluded that nanostructured HA results in a 70% improvement over the best conventional HA.

Our group has also processed HA nanoparticles by using the wet-chemical method [67,68] and studied their physicochemical and physiological properties at body pH. The investigations clearly showed the resorbable characteristic of nano HA over conventional micro HA owing to their larger surface area-to-volume ratio that ultimately makes the nano HA highly surface reactive. A typical SEM micrograph of HA obtained by using the wet-chemical method is shown in Figure 13.7 [76], indicating a spherical form of HA nanoparticles approximately 100 nm in diameter. With reference to the overall experimental results, the wet-chemical method is one of the most promising methods for the production of nano HA and, perhaps, the easiest method too.
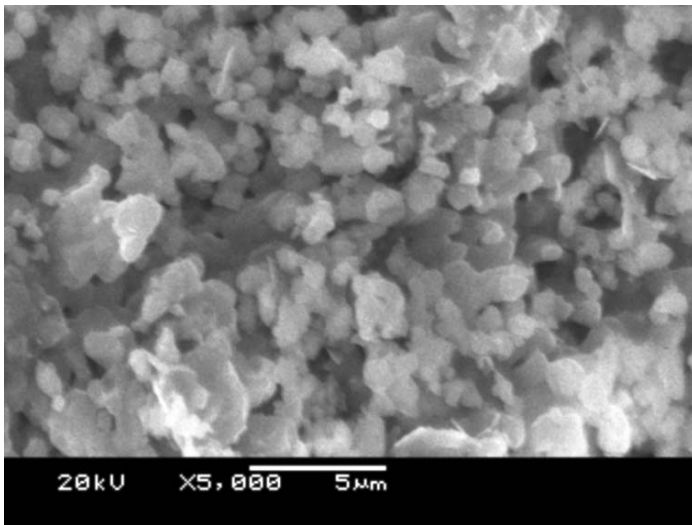
FIGURE 13.7. SEM micrograph of HA nanoparticles.

(c) Hydrothermal Reaction

The hydrothermal method enables the synthesis of a crystallized phase of HA with homogeneous phase composition at high temperature and at high-pressure atmosphere. The HA processed by using this method are easily sinterable owing to the effects of high temperature and high-pressure aqueous solutions. Zhang and Consalves [69] synthesized nanosize HA by precipitating the calcium and phosphate precursors under hydrothermal conditions, and they studied its thermal stability. By using this technique, they obtained HA with a rod shape and an average crystal size of 10 to 24 nm with respect to compositions of precursors. They produced a variety of calcium phosphate powders with respect to starting materials with a Ca/P ratio ranging from 1.66 to 1.73, meaning that they have different solubility features.

Another interesting method was recently reported by Zhang et al. [69], in which they synthesized HA in the form of nanorods in the presence of anionic starburst dendrimer polyamidoamine with surface carboxylate groups through a hydrothermal method. The reaction conditions are as follows. First, Ca^{2+} (0.01 mol/l) and PO_4^{3-} (0.01 mol/l) were prepared separately by dissolving the desired amount of $Ca(NO_3)_2$ and $(NH_4)_2HPO_4$ in distilled water. Then, 0.1 g polyamidoamine was added to the Ca^{2+} containing solution. The two solutions were kept 3 h to ensure the cooperative interaction and self-assembly process were completed. Then, the $(NH_4)_2HPO_4$ solution was added dropwise (about 1 s/drop) to the Ca^{2+} containing solution under stirring condition. After blending, the suspension was kept for about 3 h before separating the precipitate. The resulting white precipitate was filtered, washed thoroughly with distilled water, and oven-dried at about 60°C. The same process was carried out to form a suspension; then it was transferred to an autoclave, sealed tightly, and hydrothermally treated at 150°C for 10 h. The obtained products were analyzed by several techniques, and the results indicated that HA nanorods can be prepared by using this hydrothermal method with narrow particle distribution within nanosize range (80 nm by 10 nm, with aspect ratio about 8). The investigation suggested that the dendrimer-mediated hydrothermal method is a relatively new processing method for the manufacture of HA.

(d) Mechanochemical Route

Production of nano HA by using the mechanochemical route is a versatile process owing to its simplicity, which differs slightly from the conventional wet-chemical route. Although HA have been synthesized by the conventional wet-chemical method, the purity of the HA products depends on their reaction pH, whereas reaction through the mechanochemical route need not be under precise pH control. Nakamura et al. [71] recently reported the synthesis of nano HA by using the mechanochemical method. The HA was obtained directly by milling a mixture comprising $Ca(OH)_2$, an aqueous solution of H_3PO_4, and a dispersant, an ammonium salt of polyacrylic acid. The reaction was carried out at room temperature. The obtained HA had relatively crystallized particles in the nanometer regime. The average crystallite size of HA was found to be below 20 nm, but the obtained product was calcium-deficient HA (1.51, Ca/P molar ratio) as compared to that

of stoichiometric HA (1.67, Ca/P molar ratio). Furthermore, they suggested some of the merits of this mechanochemical route, which include (1) assisting deprotonation from brushite to form HA, and (2) keeping high dispersability and low viscosity of reaction sol. Overall, the production of nanocrystalline HA through the mechanochemical route is straightforward.

(e) pH Shock Wave Method

Another interesting method for the production of HA is the pH shock wave method. Recently, Koumoulidis et al. [72] reported the processing of HA using this pH shock wave method. They synthesized HA in the form of lathlike monocrystalline particles by using high-energy dispersing equipment with the precursors of $Ca(H_2PO_4)_2.H_2O$ and $CaCl_2$ with a Ca/P molar ratio of 1.66, which is almost similar to the stoichiometric Ca/P ratio of HA. The obtained products were characterized well using various analytical methods to determine their phase composition, structure, and texture. The products have a very different Ca/P molar ratio ranging from 1.43 to 1.66 with respect to the preparation methodology. This method produces nonporous monocrystalline HA particles with average grain size of ~140 to 1300 nm in length, 20 to 100 nm in width, and 10 to 40 nm in thickness. The Ca/P atomic ratio of nano HA was found to be 1.66, which is very close to the reported theoretical value of stoichiometric HA (1.67). As per their investigation, this seems to be a unique method, because it creates appropriate hydrodynamic conditions for lathlike particle growth in the [001] direction that could not be obtained by using conventional mechanical stirring equipment.

(f) Microwave Treatment

Microwave processing is relatively a new class of method, which has recently gained much interest and has been perceived to be beneficial in the synthesis of HA. Many investigations reported the processing of HA using microwaves. This method offers high-purity materials with minimized reaction time and energy saving over conventional methods [77–79]. The preparation and characterization of nanosize HA under microwave irradiation was investigated recently [78]. The nano HA was synthesized by the precipitation method using $NH_4H_2(PO_4)$ and $Ca(NO_3)_2.4H_2O$. The precipitate was subjected to microwave sintering after being washed with distilled water using a high-speed centrifuge. The microwave generated the power input of 980 W and power output of 490 W with a frequency of 2.45 GHz for a period of 5 to 15 minutes.

This method offers several advantages over normal furnace heating corresponding to time and energy savings. The experimental results suggested that there was a slight increase in the microhardness value of the sintered HA with increasing microwave exposure time. The major problem associated with microwave densification is in getting large samples without microcracks. The formation of cracks is believed to result from the nonuniform packing of crystallite in the green compact as well as due to the nonuniform heating profile occurring inside the microwave cavity. Another interesting investigation is that in which Yang et al. [79] reported the sintering effect of HA by using the microwave-processing technique. They

synthesized HA by using the chemical precipitation method at 95°C with a pH from 9 to 11.5. The prepared HA was characterized systematically by various analytical methods. They found that the prepared HA had a Ca/P ratio of 1.67, which is similar to that of stoichiometric HA. The HA green samples were sintered by microwave heating at 1050 to 1100°C for 5 to 10 min, and the results were compared with other HA green samples sintered by using the conventional heating method. The results clearly indicated that the HA prepared by microwave processing were denser and had a finer grain size as compared to those prepared by the conventional heating method. Accordingly, the HA prepared under microwave irradiation seem to be a unique class of material owing to their characteristic functional properties.

Although nano HA is an excellent bone graft material, its inherent low fracture toughness has limited its use in certain orthopedic applications, in particular heavy load-bearing implantation. The fracture toughness of HA is about 1.0 MPa.m$^{1/2}$, which is very low as compared to natural bone (2–12 MPa.m$^{1/2}$) and the Weibull modulus is also sufficiently low, such that it depromotes the reliability of HA for heavy-loaded implants. The Weibull modulus of the HA is in the range between 5 and 18, which means that HA behaves as a typically brittle biomaterial; therefore it is used only in low-weight-bearing orthopedic applications such as bone defect filler, coating agent on metallic bioimplant, and biomolecular delivery. In order to improve reliability, it is necessary to introduce some biocompatible reinforcement agents or matrix materials. However, introduction of foreign materials may lead to a decrease in reliability of HA; therefore choosing the reinforcement agents or matrix materials is of great importance. Recently, a composite of nano HA with natural polymer, in particular collagen, has been preferred to improve the reliability of nano HA. Collagen is a natural choice of ECM, abundantly found in human bone tissue; thus choosing collagen as a matrix material could enhance the reliability of bone grafts. Moreover, in fact, they are the basic structural building blocks of natural bone tissue.

13.4.1.2. Collagen and Its Use in Bone Grafting

Collagen is a major protein of the native ECM that primarily serves as a structural protein in biological mineralization. Collagen comprises as much as one third of the total proteins in human body. In general, it has many desirable functional properties favorable for bone metabolism. The purified collagen has excellent biocompatibility, biodegradability, nontoxicity, and nonantigenecity that make the collagen a prime and safe source in a variety of biomedical applications, including bone grafting [80–82]. The way in which it interacts with the host tissue further makes it a more unique class of biomaterial than the other natural or synthetic polymers. Some of the merits and demerits of collagen that make it an excellent substrate for bone tissue engineering are listed in Table 13.6.

There are many types of collagen available based on their molecular sequences. So far, 27 distinct types with at least 42 distinct polypeptide chains of collagen have been identified. The different types of existing collagen are formed according to the twists and turns between the hydrogen bonds holding the structure together. Although many types of collagen exist in a living organism, the most abundant form of

TABLE 13.6 Merits and demerits of collagen as a bone graft.

Collagen	
Merits	Demerits
Biocompatible	High cost
Bioresorbable	More hydrophilic
Hemostatic	Antigenic if it has telopeptides
Osteoconductive	
Superior cellular adhesion	
Regulatable biodegradability	
Surface modifiable	
Nontoxic	
Weak-antigenic	
Tunable mechanical strength	
Shapeable	
Sterilizable	
Abundant availability	
Best ion exchanger and binder of electrolyte metabolites	

collagen in the connective tissue is type I. Type I collagen is composed of two α_1 (I) chains and one α_2 (I) chain in the form of a triple helix pattern with a fiber diameter of about 50 nm [81,82]. All collagens are composed of three polypeptide chains, designated as α-chains, that are each coiled into a left-handed helix. These three chains are then wrapped around each other into a right-handed triple helix; therefore the final structure is a triple helical ropelike fashion. The triple-helical structure of collagen is shown in Figure 13.8 [83]. The triple-helical domain has a characteristic

α-chain

FIGURE 13.8. Triple-helical structure of collagen. Adapted from Ref. [83].

primary structure, where glycine in every third amino acid generates repeating (Gly X–Y)$_n$ units; X is alanine or praline, and Y is hydroxyproline [81,82].

In general, collagen extracted from the natural tissues is capable of eliciting immunogenic response to a certain extent upon implantation; thus direct use of this type of collagen is limited. Nowadays, a purified form of collagen known as reconstituted collagen is processed by various biochemical methods and commercially sold. The reconstituted collagen is relatively less immunogenic than native collagen. Collagen can also be chemically modified by various methods (succinylation, e.g.) to increase its surface reactivity by inducing more negative charges, which in turn aids the collagen in dissolving even in the neutral pH; therefore its usage can be widened significantly in biomedical applications. However, it does not have significant strength or stiffness and so it cannot be used as such for a variety of bone grafting applications, which leads to the concept of composite bone grafts.

There is a possibility of enhancing its functionality by incorporating other bone graft substances (e.g., HA, bone morphogenetic protein (BMP) and osteoprogenitor precursors). Such a composite bone graft is also commercially available for clinical use. Collagraft, BioOss, and Healos are a few notable examples of such a kind of bone graft [84–86]. Collagraft (Zimmer Inc., U.S.A.), which is made of calcium phosphates and collagen, is used for low-weight-bearing orthopedic applications,. Bio-Oss (Geistlich Biomaterials Inc., U.S.A.) is a craniofacial graft, which is made of bovine collagen and deorganified bovine bone. Healos (CE Mark, CA) is a spongelike mineralized collagen fiber, mainly used as an osteoconductive matrix. Accordingly, collagen can be considered as an accomplished biomaterial for bone grafting.

13.4.2. Osteoinductive Bone Grafts

Osteoinduction is a chemical process in which biomolecules enriched within the graft converts the patient's cells into cells that are capable of forming new bone tissue. Examples of osteoinductive grafts are autogenic bone, BMP, and demineralized bone matrix (DBM) (see Table 13.3). The osteoinductive bone grafts are capable of inducing differentiation of undifferentiated stem cells into osteogenic cells or to induce the stem cells to proliferate. In 1965, Urist discovered that the DBM would be able to promote new bone formation in the bone defective sites [87].

It was noticed, after systematic investigations, that the intact proteins within the matrix are responsible for bone formation owing to their osteoinductive ability. These proteins were later named bone morphogenetic proteins (BMPs). They are considered one of the most promising biological substances and have a wide range of potential benefits for bone grafting, which have been extensively studied in native and recombinant forms. The experimental evidence describes native BMPs as immunogenic, and recombinant BMPs (rhBMPs) as nonimmunogenic [88,89]. Among them, a variety of rhBMPs, rhBMP-2 has been widely used for bone grafting and clinically proven to exhibit a very high osteoinductivity [90].

However, the mode of delivery of BMPs into the defective site is still under quest because they need a carrier matrix in order to stipulate their function effectively. Although a few systems have been tried for delivery, there is still no optimal one. With hope, probably, nanocomposite could be utilized for this purpose. Ono et al. [91] used HA as an osteoconductive carrier matrix for the delivery of rh-BMP-2. They hypothesized that the combinations of HA and rhBMP-2 could provide a potent alternative to autogenic bone grafts. They implanted HA in the form of rods treated with 1.7 g and 5.7 g of rhBMP-2 into the cranial bone of rabbits and found that bone formation was inclined to be greater at the higher dose of rhBMP-2 (5.7 g). The induction of new bone is dose-dependent on rhBMP-2. Even with a small dose, a considerable increase in the strength of HA was observed compared to pure HA. As a result, early bone ingrowth in the pores of HA was noticed, which is a good sign for the efficiency of the carrier system.

Recently, Jung et al. [92] clinically studied 11 partially edentulous patients to evaluate whether the addition of rhBMP-2 to a commercial bone graft product of BioOss (a bioengineered graft from bovine source) would improve guided bone regeneration therapy regarding bone volume, density, and maturation. They found that the combination of the BioOss with rhBMP-2 could enhance the maturation process of bone regeneration and could increase the osteointegration between graft and host bone. These studies clearly demostrated that the rhBMP-2 has the osteoinductive potential to improve and accelerate bone regeneration tremendously.

13.4.3. Osteogenic Bone Grafts

Osteogenesis is an ability of the graft to produce a new bone. Inasmuch as only living cells are able to construct or regenerate new bone tissue, the success rate of bone healing extremely depends on the living bone cells that are enriched within the graft. These cells are actively involved in the early stages of bone formation in order to fuse the implanted bone graft with the host bone. The ability of osteogenesis is extensively and, perhaps, only, found in fresh autogenic bone and in BMA (see Table 13.3). As osteogenic bone grafts, they are responsible for bone growth by converting the transplanted living tissue into new bone tissue.

Recently great interest has been shown in BMA in bone grafting owing to its osteogenic potential, quite similar to autogenic bone [93]. As it is well known that living bone cells can only regenerate new bone tissue, using BMA in the treatment of bone defects is highly remarkable. The osteogenic potential cells derived from bone marrow are effectively used in various clinical orthopedics to improve bone growth. However, the effectiveness of the BMA depends a great deal on the density and activity of stem cells intact within the aspirate. The advantage of BMA over autogenic bone is that it could be harvested from the patient's own body with the help of a simple needle, without any complicated surgery and ensuing pain, and could be delivered at the bone defects. This type of transplantation is termed minimally invasive bone grafting.

However, the efficiency of the BMA truly depends on its carrier system, therefore the selection of the carrier system is the most important factor for its clinical use. It

can be mixed with other bone graft materials as well, in particular osteoconductive grafts, and then can be transplanted at the defective sites. It is reported that there is a possibility of increasing the rate of differentiation and proliferation of bone marrow stem cells by delivery in conjunction with DBM [94], collagen [95], and HA [96] in the form of composite bone grafts.

13.5. Biomimetic Nanocomposites—A New Approach

It should be noted that the above studies clearly indicate that single-phase components do not always provide all the properties necessary for bone grafting, thus considerable attention has been paid to composites. The term composite can be defined as a heterogeneous combination of two or more materials, differing in morphology or composition on a microscale, in other words, a microcomposite [97]. Composite grafts are a good choice among the synthetic bone grafts owing to the possibility of incorporating most of the favorable features of various single-phase components and to eliminate or minimize the problems associated with the monolithics as discussed in previous sections. The composite, therefore, can be treated as the only material that uniquely exhibits a range of properties equivalent to bone, and thus it could be possible to eliminate some of the problems associated with current synthetic bone grafts. Some of the bone grafts used in the last few decades for clinical bone therapy are shown in Figure 13.9, including composites.

Recently, an extensive and informative review written by Ramakrishna et al. [98] described the recent trends and potential applications of those composites in various biomedical applications, including bone reconstruction. As bone is a dynamic living tissue, it should be noted that unless we make bioactive bonelike composites with intact favorable osteoinductive and/or osteogenic components, synthetic bone grafts would only have limited survivability. Accordingly, much attention has been paid to the manufacture of bioactive composites over the past two decades. An important advantage of the bioactive composite lies in its strong interfacial bonding ability with host tissue and its improved mechanical strength. It is, therefore, possible to match certain properties of the bioactive composites to natural bone.

Considerable attention has been paid in the past two decades to bioactive composite grafts that consist of bioactive ceramic filler in a polymeric matrix. In 1980s, Bonfield et al. developed a bioactive composite based on HA and PE [99,100]. It has been demonstrated that it has the capability of promoting extensive bone-bonding functions upon implantation. Later, it was also commercialized under the name of HAPAX[TM] after a thorough clinical test. Unfortunately, it is not a good biodegradable graft, which limits its wider usage in clinical medicine. It is primarily being used as a middle ear implant, which is one of the promising bioactive composite grafts used for such an application. The exciting news is that the clinician could readily shape it during surgery with respect to the size and shape of the bone defect.

Cranial Bone Defects
HA, HA-collagen, bioactive glass, alumina, autogenic bone, allogenic bone, DBM

Maxillofacial Reconstructions
HA, bioactive glass, alumina, zirconia, HA-PE, bioglass-PE, PTFE-carbon, autogenic bone, allogenic bone

Periodontal Defects
HA, TCP, bioactive glass, HA-PLA, HA-PLGA, HA-collagen, autogenic bone, allogenic bone, DBM

Alveolar Ridge Augmentations
HA, TCP, bioglass, alumina, HA-PLA, HA-collagen, HA-PLGA, autogenic bone, allogenic bone, HA-DBM composite

Bone Void Fillers
HA, TCP, biocoral, calcium sulfate, PMMA, HA-collagen, bioactive glass-ceramic composite, autogenic bone, demineralized allograft, demineralized xenograft, patient-derived osteoblasts in conjunction with HA matrix

Spinal Surgery
HA, bioactive glass, HA-collagen, PET-silicon, bioglass-PU, autogenic bone, DBM, tissue-engineered HA, HA-BMA composite

Orthopedic Prostheses
Alumina, zirconia, stainless steel, Ti, Ti-6Al-4V, Co-Cr-Mo-Ni, A-W glass ceramics, HA-PE, HA-collagen, bioactive glass-coated biometals, HA-coated biometals, carbon fibers-PE, osteogenic cells intact HA-and bioactive glass-coated porous surfaces

PE: Polyethylene; PET: Polyethylene terephthalate; PLA: Polylactic acid; PLGA: Poly(lactide-co-glycolide); PMMA: Polymethyl methacrylate; PTFE: Polytetrafluoroethylene; PU: Polyurethane.

FIGURE 13.9. Commonly used bone grafts in clinical bone therapy.

Simultaneously, bioresorbable composites are developed and investigated as bone grafts. For example, Laurencin et al. [101] developed a composite containing HA and PLGA and demonstrated its cellular-compatibility suitable for bone tissue regeneration. It was found that the composite highly supported osteoblast proliferation, differentiation, and deposition of calcium phosphate minerals. The cells were proliferated for up to 21 days and formed a mineralized layer on the composite. However, some studies report that the physical properties of the composite, made of the same ingredients, are not completely satisfied upon implantation because of the conventional mode of processing technology [102]. Perhaps there may be a reason for their inadequate properties in that their constituents are dissimilar to the ingredients of natural bone.

We have also explored the possibility of utilizing HA, both at the micro- and nanolevel, in conjunction with natural and synthetic polymers in the form of composites suitable for bone grafting and bone drug delivery [103–107]. It should also be noted that most of the above composites differ from host bone either

compositionally or structurally. These features are highly essential for the appreciation of better functioning of grafts with host tissue upon implantation. Of particular interest in this context is the combination of HA with collagen into a bioactive composite form, which appears a natural choice for bone grafting; that is, it mimics the ingredients of a real bone.

A composite based on HA and collagen has been developed and investigated [108]. It shows great promise because of its resemblance to natural bone in terms of biocompatibility and bioactivity. For example, the bone grafts made of HA and collagen demonstrated a more enhanced osteoconductivity [109] and other properties (e.g., biomechanical) than did their constituent phases upon implantation. Accordingly, choosing HA and collagen as precursors to design osteoconductive composite bone grafts is perfect and competent, and can also be utilized as a carrier system for the delivery of osteoinductive and osteogenic factors. Nevertheless, most HA/collagen composites are conventionally processed by anchoring HA particulates into the matrix of collagen. Using this method, it is quite difficult to obtain a uniform or a homogeneous composite graft. Furthermore, most of the HA used in this process are sintered and large-size crystallites, which is in contrast to the natural bone apatite; therefore it may take a longer time to remodel into bone tissue upon implantation. In addition, some of the composites processed by this method exhibit very poor mechanical properties [110,111], probably owing to the lack of a strong interfacial bonding between their constituents.

As mentioned earlier, this kind of composite truly mimics natural bone in terms of composition, but differs structurally owing to the grain size and form of the reinforcing agent, which might impede the interfacial bonding between their constituents; thereby it may lose osteointegration considerably. There is a chance of improving the osteointegration by reducing the grain size of the reinforcing agent or by activating the nucleation of ultrafine apatite growth onto the matrix, which may lead to enhanced mechanical strength with improved biological and biochemical affinity to the host tissue. Collectively, it should be noted that microcomposites have been processed with microsize inclusions; therefore it is quite difficult to achieve appropriate interfacial bonding between the constituents. They are also in contrast to biological mineralization of natural bone, which indicates that an alternative method is needed to precisely process a composite bone graft that mimics biological mineralization.

Recently, with advances of nanotechnology and biosciences, biomimetic nanocomposites have gained much interest and are perceived to be beneficial over microcomposites in many aspects as bone grafts, which, of course, opens a new arena in the field of bone grafting. Nanocomposites play a pivotal role in bone grafting as a new class of bone graft material owing to their amazing characteristics, including larger surface area-to-volume ratio and superior mechanical strength, which uses a combination of several nanoscale bone graft materials and/or in conjunction with osteoinductive growth factors and osteogenic cellular components. The latter are supplement stimuli for bone growth. The term nanocomposite can be defined as a heterogeneous combination of two or more materials in which at
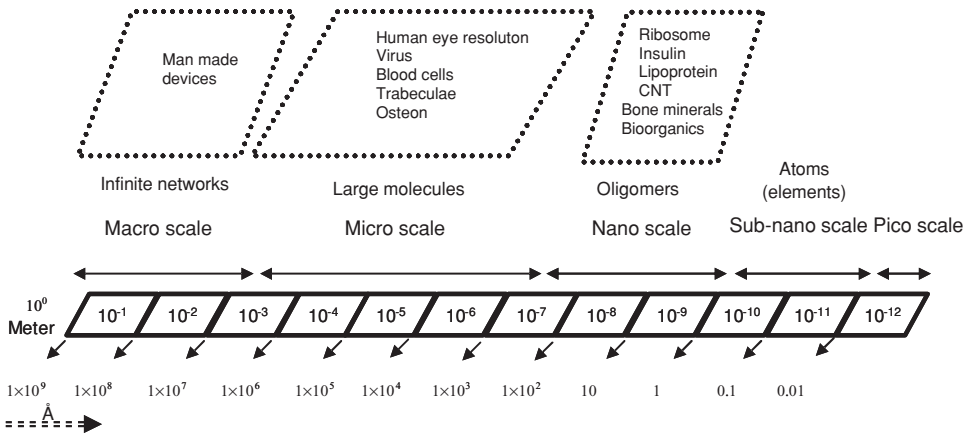
* Adapted and re-drawn from Ref. [22]

FIGURE 13.10. Dimensions of various substances with highlights of biological systems.

least one of those materials should be in a nanometer-scale range. A nanometer is equal to 10^{-9} m. The dimensions of some of the biological systems are highlighted in Figure 13.10.

It is surprising to realize that most biological systems begin with a nanoscale mechanism that might be the basis for the success of their unbelievable characteristic functions. For example, bone is the toughest natural nanocomposite, precisely evolved by nature's proficiency in using a nanoscale hierarchical assembly with the basic ingredients of HA and collagen; therefore researchers are trying to imitate such a process, through so-called biomimetics, for making nanocomposite materials into synthetic bone grafts and perceiving these to be the right choice over microcomposites. Therefore, it is considered that engineering nanocomposite bone grafts through the biomimetic approach is a somewhat new class of method.

As per a literature survey, there are numerous methods for the processing of nanocomposites suitable for bone grafting. A current research trend on the HA–polymer nanocomposites in bone grafting applications is given in Table 13.7 [112–127]. It should be noted that, from the compiled data, HA/collagen is the only system so far studied up to in vivo animal studies as compared to other HA–polymer nanocomposite systems, which further suggests their impact. In addition, they are anticipated to provide all the factors essential for bone regeneration for long-term survivability. There is also a possibility of improving interfacial bonding between the constituents of the composites and superior surface reactivity of the whole composite with the host tissues by nanostructural and biomimetic strategies. Inasmuch as this field is still in its infancy, there is as yet no standardized method for making such nanocomposite grafts. The following sections describe their impact and recently developed processing methodology with suitable illustrated examples.

TABLE 13.7 Current trend on HA–polymer nanocomposites for bone grafting.

Nanocomposite systems	Methods	Materials characterization	In vitro cell culture	In vivo animal study	References
HA/Natural Polymer Nanocomposite Systems					
HA/collagen	Precipitation	+	−	−	[112]
HA/collagen	Biomimetics	+	+	−	[113]
HA/collagen	Biomimetics	+	−	+	[114]
HA/collagen	Biomimetics	+	+	+	[115]
HA/collagen/PLA	Biomimetics	+	+	+	[116]
HA/collagen/alginate	Biomimetics	+	+	−	[117]
HA/chitosan	Precipitation	+	−	−	[118]
HA/gelatin	Biomimetics	+	−	−	[119]
HA/silk fibroin	Mechanochemical	+	−	−	[120]
HA/Synthetic Polymer Nanocomposite Systems					
HA/PCL	Solvent-casting	+	−	−	[121]
HA/PLA	Solvent-casting	+	−	−	[122]
HA/PEG/PBT	Precipitation	+	−	−	[123]
HA/PHMA	Biomimetics	+	−	−	[124]
HA/Polyanhydride	Photo polymerization	+	−	−	[125]
HA/PHEMA	Biomimetics	+	−	−	[126]
HA/PAA	Insitu polymerization	+	−	−	[127]

13.6. Biomimetic Bone Grafts—Designs from Nature's Lessons

13.6.1. Rationale and Benefits of Biomimetics

It is quite common to realize that the birth of a new method in any field is always an indication of the shortcomings of conventional methods for their assigned work or because of the enhanced performance of the new method over conventional ones. It is, of course, particularly true for bone grafting. It should be noted that characteristics of the synthetic bone grafts are drastically different from that of natural bone in many aspects, in particular mineral–protein (matrix) interaction. Although natural bone is chiefly made up of HA and collagen compounds, engineering synthetic bone grafts that consist of these components are substantially different from the natural ones. The reason behind this strategy mostly involves the absence of peculiar self-organizing interaction between those two phases. Nowadays, therefore, many investigations attempt to mimic the composition and structural features of natural bone tissue while engineering synthetic bone grafts at nano or molecular level.

One of the processing methods to emulate such features is the biomimetic or bioinspired approach. This nascent field has recently entered bone engineering in the design and assembly of bone graft materials, mimicking biological mechanisms. The term biomimetic can be defined as a microstructural processing

technique that either mimics or inspires the biological mechanism, in part or in whole, for the design of accurate and specific systems [128]. It was derived from the Greek words *bios* meaning life and *mimesis* meaning imitation. It is also called by several distinct names: bionics, biognosis, bioinspired, and biomimicry are a few of them. Biomimetics is a branch of science that deals with the design of a new class of bone grafts that seek to emulate the biological processes involved in the formation of new bone at the molecular level. It is the right choice to select biomimetics to engineer a new class of bone graft for orthopedic applications. Basically, it involves the design of synthetic bone graft systems using the information obtained from biological ones (e.g., biomineralization).

A basic understanding of the mechanism involved in biological mineralization would yield much exciting information about how nature accomplishes such an elegant process, as discussed in Section 13.2.4, which is also helpful in the design of exquisite nanocomposite bone grafts. The biological process generates highly ordered minerals with hybrid composition, complex texture, and ultrafine crystallites through hierarchical self-assembly. Even with the advances of bioscience, however, the complete biological strategy involved in the hierarchical self-assembling mechanism is not understood yet. Accordingly, designing synthetic bone grafts, mimicking real bone, using the mechanism found in biological strategy, is extremely complicated and, perhaps, the most challenging process.

Interestingly, the smallest building blocks of bone are precisely built at the nanoscale architecture using nanocrystals of HA embedded with fibrous collagen matrix. So, it is believed that making nanocomposite grafts with certain features of natural bone either compositionally or structurally using biomimetic self-assembly may replicate nature's process. This method involves a bottom-up approach, which begins by designing and synthesizing molecules that have the ability to self-assemble or self-organize spontaneously into the higher order of microscale or macroscale structures [129,130].

Self-assembly of nanocomposite is a relatively new paradigm in the processing of novel bone grafts, mimicking the biological process either in whole or in part. Self-assembly can be defined as the spontaneous organization of individual components into an ordered structure without human involvement [131]. The greatest challenge in self-assembly is to engineer molecular building blocks that can undergo spontaneous organization into a well-defined and stable macroscopic structure using noncovalent bonds. These types of interactions typically involve hydrogen bonds, ionic bonds, water-mediated hydrogen bonds, dipolar interactions, and hydrophobic and van der Waals interactions. Although each of these forces is rather weak, their collective interactions can produce very stable structures (e.g., bone). Among them, the water-mediated hydrogen bond is especially important for living organisms because all biological tissues must interact with water [132]. Biomimetic growth of bone apatite is a good example for this kind of self-assembly that applies the bottom-up approach. The following section describes such a process with suitable illustrated examples.

13.6.2. Design Strategy of Biomimetic Nanocomposite Bone Grafts

The need for the development of bone grafts is continuously stimulated by the unsatisfactory performance of available grafts and, of course, lack of an appropriate technique to fabricate bone-resembling grafts. A novel way of fabricating nanocomposite bone grafts using strategies found in nature have recently received much attention and have been found to be more beneficial than other conventional methods. This section describes more on nanostructured bonelike composite grafts processed by biomimetic self-assembly suitable for bone-grafting applications.

Of particular interest, in this section, attention is given to HA/collagen systems because they are currently widely accepted osteoconductive bone grafts and also they are the basic ingredients of natural bone tissue. Biomimetic HA/collagen composite offers enormous promise for the repair of defective bone tissue owing to its structure, composition, and other factors similar to natural bone. In fact, bone is a family of nanocomposites in which the basic building blocks are the mineralized collagen nanofibers; nature thereby provides critical ideas on how to engineer such biomimetic bone grafts with a well-organized structure and composition. However, it is clear that the current approaches have not yet led to the design of optimal bone grafts owing to the lack of understanding of the complete mechanism involved in the natural bone-building strategy. With the advances of nanotechnology and structural biology, it is now possible to develop a new class of bone-resembling nanocomposite grafts that could help in bone regeneration similar to some extent to naturally occurring bone matrices.

A key step in the biomimetic strategy is to achieve a controlled nucleation and crystal growth of apatite phase onto collagen matrix (see Figure 13.11). This process partly mimics the biological phenomenon and demonstrates a good system for bone regeneration with enhanced osteoconductivity from a pure HA and a pure collagen [133,134]. A biomimetic nanocomposite was developed by self-assembling of HA nanocrystals onto collagen fibers [134]. The direct nucleation of HA nanocrystals onto collagen fibers has been performed by starting from an aqueous suspension of $Ca(OH)_2$ and H_3PO_4 together with a collagen solution of pH 9 to 10 at 25°C. The obtained composite product was freeze-dried at –40°C and then gradually warmed up to 35°C for 36 h. The characteristic results indicate that the nanocrystals of HA are elegantly aligned with their c-axis preferentially oriented along the collagen fibers, suggesting a close interaction between HA and collagen phases.

As this process mimics biological mineralization to some extent, it was suggested that the HA/collagen nanocomposite can be used for bone repair in orthopedic and maxillofacial surgeries. A similar bonelike nanocomposite consisting of HA and collagen, by a self-organization mechanism using $Ca(OH)_2$, H_3PO_4, and porcine atelocollagen as precursors, was developed by Kikuchi et al. [133,135]. The composite has elegantly self-organized into a nanostructure quite similar to that of natural bone, which might have occurred through a chemical interaction between HA and collagen. The length of self-assembled fiber bundles was found
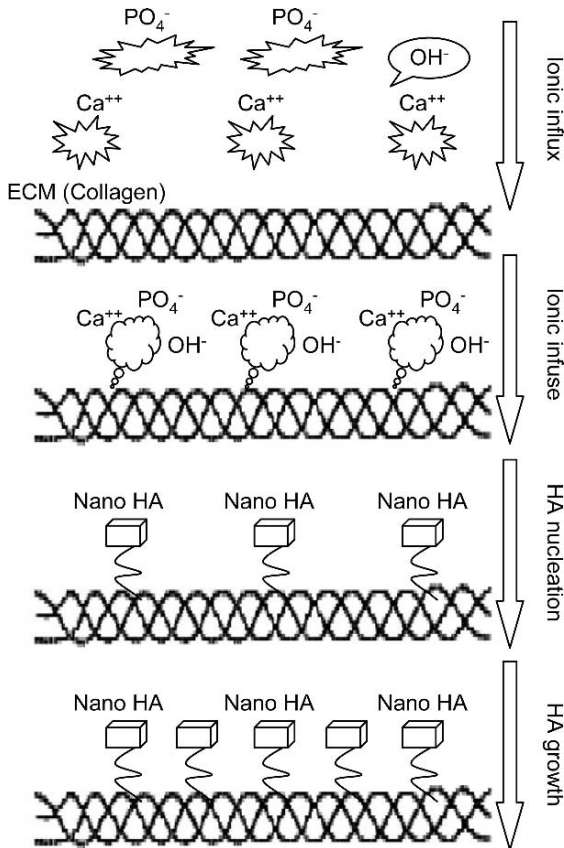
FIGURE 13.11. A scheme for a self-assembly of HA/collagen nanocomposite graft.

to be 20 μm in which each bundle consisted of many collagen fibrils of 300 nm
length embedded with bladelike HA nanocrystals of 50 nm in size. They found that
increasing the degree of self-assembling eventually increases the bending strength
of the composite, suggesting that high mechanical strength can be attained by op-
timizing the self-assembling mechanism between HA and collagen. The in vivo
performance of this nanocomposite was evaluated in beagle dogs by creating an
artificial bone defect. The results of the animal study proved excellent biocom-
patibility, osteocompatibility, and bioactivity of the composite with surrounding
tissues and stimulated the formation of new bone growth with an Haversian system
(see Figure 13.12).

Furthermore, it enhanced the conventional biomaterials' rate of bone-healing
within a short period, which might have resulted from its nanostructural self-
assembly and compositional similarity to natural bone tissue, therefore a biomimet-
ically processed HA/collagen system can be considered as a good bone graft. This
kind of composite can readily be incorporated into bone metabolism rather than
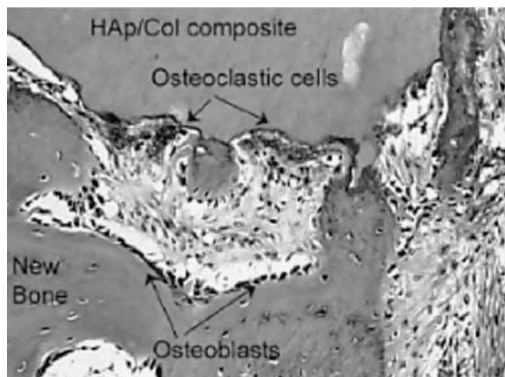
FIGURE 13.12. Histological section of a biomimetically processed HA/collagen system, indicating its osteocompatibility. Adapted from Ref. [133].

being a permanent implant. Accordingly, the biomimetic processing of composites is perceived to be highly preferable to conventional processing methods.

It is also good to know that, nowadays, there are many advanced techniques and sophisticated instrumentations available for the study of biomineralization that tremendously helps the development of this interesting multidisciplinary field. Some of them are listed in Table 13.8 with their few critical comments. Recently, Zhai et al. [136] demonstrated the features of biomineralized recombinant human-like collagen. They analyzed the mineral growth using various analytical tools. The morphology of the mineralized collagen was examined by scanning electron microscopy (SEM) and transmission electron microscopy (TEM). The respective micrographs are shown in Figure 13.13. It can be seen that a flowerlike morphological structure of the mineralized collagen fibrils on the powder surface and the leaves of the flower are entangled and perpendicular to that surface (Figure 13.13a). The length of the fibrils is found to be about 20 nm in width and 500 nm in length. Furthermore, a TEM micrograph (Figure 13.13b) confirmed that biomineralization has taken place on the surface of collagen, that is, deposition of nano HA. The nano HA is about 6 to 25 nm in size and its c-axis is parallel to the collagen fibrils' orientation.

Another interesting method was developed for the self-assembly of HA coating onto collagen membrane [137]. The membrane was soaked in a stimulated body fluid (SBF) solution, very close to human blood plasma, with and without citric acid, the role of which was exclusively investigated during the nucleation of HA. It should be noted that the researchers have chosen collagen membrane that had no HA-forming ability in the SBF solution. They found that there was no nucleation of apatite crystals on the surface of the membrane when it was soaked in SBF without citric acid. Interestingly, the membrane soaked in SBF with citric acid gradually stimulated the nucleation of HA crystals. Therefore, it can be suggested that citric acid has a nucleating ability and can accelerate the coating of apatite onto membrane.

Later, many research groups demonstrated the ability of nucleation of HA crystals onto collagen through a chemical interaction of carboxylate groups of collagen macromolecules [138–140]. All the reports suggested that the nucleation process

TABLE 13.8 Commonly used techniques in biomineralization study.

Techniques	Comments
X-Ray Diffraction Techniques	
Wide angle x-ray diffraction	Provides a specific proof for the mineral identification with their crystal structure and unit cell dimensions.
Small angle x-ray scattering	Determines mineral's crystal size, shape, and orientation. It is also widely used in structural analysis of proteins.
Synchrotron diffraction	A relatively new technique to study mineral composition with high resolution.
Neutron Diffraction Technique	
Neutron diffraction	Provides qualitative information on mineral texture and crystal orientation.
Electron Diffraction Techniques	
Scanning electron microscopy	Provides morphological structure of the minerals with their size, shape, and related structural information.
Transmission electron microscopy	Provides ultrastructure of minerals and their size and shape. Crystal orientation and texture can also be studied.
Microscopic Techniques	
Atomic force microscopy	Provides details on molecular interaction between minerals and protein components through which mineral binding and deposition can be determined. Surface topology of the crystals can also be identified.
Magnetic resonance force microscopy	Provides complete details on chemical specificity, composition, three-dimensional subsurface structure.
Infrared spectroscopy	Facilitates differentiation of symmetric and asymmetric vibration and stretching bonds of the mineral components and allows estimating mineral contents.
Raman spectroscopy	Provides all information on symmetric and asymmetric vibration and stretching bonds of the mineral components and allows estimating mineral contents, such as infrared.

is critically dependent on the carboxylate groups of the collagen. On the other hand, mechanical reliability of the nanocomposite does not match exactly with that of the host bone in many cases. It is an essential factor to be considered for all bone grafts as it directly measures their strength. In order to enhance the mechanical reliability of the mineralized collagen, a glutaraldehyde cross-linked porous HA/collagen nanocomposite was developed [141]. Here, $Ca(OH)_2$, H_3PO_4, and collagen were used as precursors to formulate the composite. An homogeneous suspension of 0.1994 mol of $Ca(OH)_2$ dispersed in 2000 ml of H_2O and 59.7 mM of H_3PO_4 was gradually added to the aqueous solution of 5 g collagen. The pH of the reaction mixture was adjusted to 8.4 and the reaction was maintained at 38°C and finally aged for 12 h by adjusting the pH to 7. In order to mimic the cross-linking process in the toughening of natural bone, 0.2% aqueous glutaraldehyde solution was slowly added into the slurry solution at the same reaction temperature. The composite was thoroughly analyzed and its 3-D porous nanostructure that could be able to support cellular growth was confirmed. They noticed that if the cross-linking agent was added, the size of the reaction precipitate was found
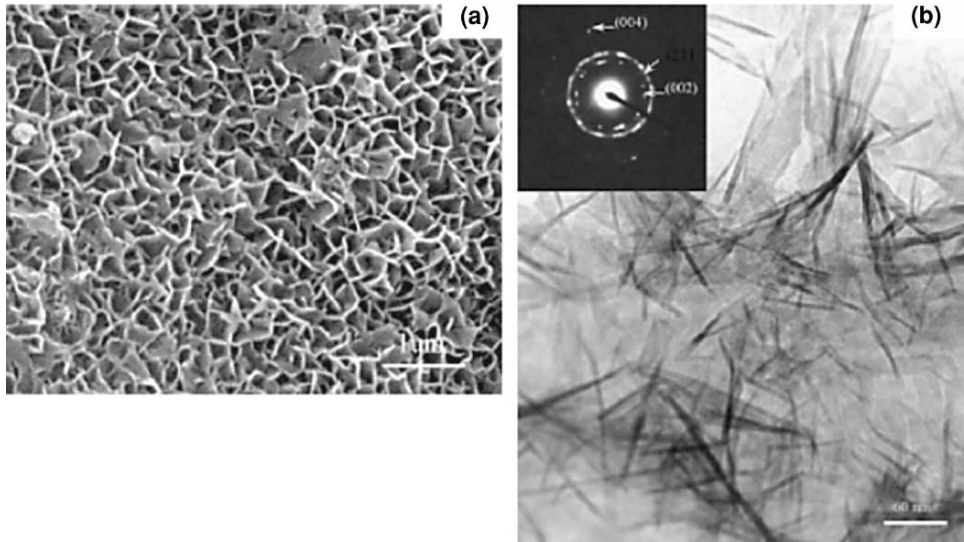
FIGURE 13.13. Micrographs of biomineralized recombinant human-like collagen: (a) SEM; (b) TEM. Adapted from Ref. [136].

to grow and seemed to be triggered by the assembly of HA nanocrystals (50 nm) around the collagen fibers (300 nm), leading to the formation of a thick composite bundle. The thickness of the mineralized collagen depends on the amount of glutaraldehyde added. Because this system has relatively good toughness, it was suggested for use as a bone graft.

Although many investigations have been carried out to mimic bone artificially, using HA and collagen, with compositional, structural, biological, or mechanical functions comparable to its natural counterpart, it should be noted, however, that bone is not a simple mixture of HA crystals and collagen fibers in many ways. In addition to collagen, bone contains many traces of bioorganics such as glycoproteins or glycosaminoglycans, which play a pivotal role in controlling the functions of bone cells. In this regard, attempts were made to mimic both the bioorganic compositions of bone and peculiar configurational arrays of HA nanocrystals on those bioorganics [142,143].

A design strategy for making such a nanocomposite using HA, collagen, and chondroitin sulfate (proteoglycans) was developed with an intention of using it as a biomimetic bone graft for cartilage repair (a premature bone) as well as for bone repair. The hypothesis was that the cartilage is a key tissue of all growing bones because bone formation is initiated from the calcification of cartilage and then it would be replaced by the bone through endochondral ossification. Therefore, cartilage is regarded as a precursor of bone. The chondroitin sulfate is best known for its ability to promote the binding of chondronectin, which is the chondrocyte attachment factor, to collagen and thus gradually stimulates chondrocyte adhesion. Accordingly, this nanocomposite system is likely to provide specific

binding sites for chondrocytes. The crystallographic results confirmed the orientation of the *c*-axis of the HA nanocrystals along the longitudinal direction of the collagen and chondroitin sulfate complex. The distribution of HA was found to be almost uniform within the matrix and has substantial mechanical strength with fracture toughness 35–50 MPa and hardness 119–219 MPa. In addition, it has a potential capacity of bone remodeling through the process of endochondral ossification. Based on these results, the proteoglycans-immobilized HA/collagen nanocomposite may be used as a promising bone substitute.

Nanocomposite grafts can also be used as a carrier vehicle for the delivery of growth factors. Recently, an HA/collagen nanocomposite system was biomimetically developed and used as a carrier for the delivery of rhBMP-2 [144,145]. The performance study of this kind of system is based on the hypothesis that the controlled release of rhBMP-2 biomolecules facilitates early callus and new bone growth upon implantation, as compared to other conventional biomaterials. As discussed earlier, the rhBMP-2 is a well-known osteoinductive protein. It should be noted that both naturally occurring BMPs and recombinant BMPs have long been used as osteogenic initiators in various bone-defective models in order to enhance the bone-healing process quite similar to autogenic bone. The studies found that the mechanical reliability of this system corroborated well with the strength of autogenic cancellous bone. The overall experimental results indicated that the in vivo performance of the nanocomposite with rhBMP-2 is better than the nanocomposite without rhBMP-2.

Early bone formation occurred with the use of rhBMP-2 treated composites, which implies their efficacy as a good bone graft. Based on these findings, this biomimetically processed system is considered as a perfect osteoconductive as well as osteoinductive bone graft. It can be used for anterior fusion of the cervical spine as well as inlay grafting bone defects in weight-bearing orthopedic sites. Although biomimetic design of bone grafts is still in the infant stage, there is a bright future for creating a new generation of bone grafts with improved toughness and structural analogy to natural bone, evidence of which can be found in recent and rapid publications.

13.7. Bone Tissue Engineering

Engineering synthetic bone tissues that are capable of serving in vivo-like natural bone tissue in all the functional aspects is our ultimate goal to discover in bone tissue engineering. Because only living bone cells can ultimately generate new bone tissue, a unique approach is to develop bone grafts that are cell-responsive upon implantation. A new wave of advances in nanotechnology and cell biology enables the production of novel cell/tissue-engineered bone grafts, quite resembling autogenic or living bone. Bone tissue engineering is a nascent multidisciplinary field that applies the principles of bioengineering and biosciences towards the development of novel biological substitutes capable of restoring, maintaining, or improving a tissue function that fails to regenerate or heal spontaneously [146].
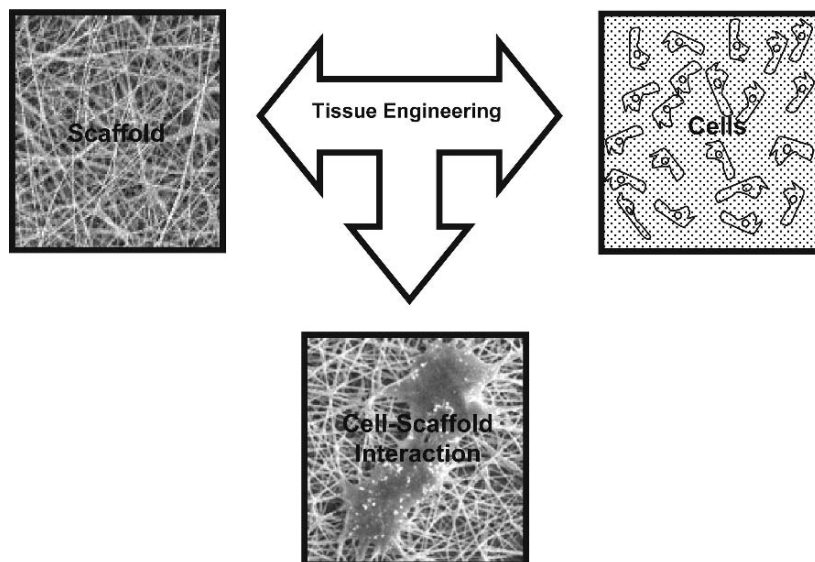
FIGURE 13.14. Factors contributing to the success of tissue engineering.

This method offers a new kind of therapy that differs from conventional implants in that the engineered bone tissue becomes integrated within the patient, affording a potentially permanent and specific cure of the disease state. The prime concept of tissue engineering is; (1) to isolate a small biopsy of specific cells from a patient, (2) to allow them to culture on a perfect scaffold (probably biomimetic nanocomposites), (3) to transplant the cell-engineered scaffold into the defective site of the patient's body that needs bone regeneration, and (4) to guide or direct new tissue formation into the scaffold that can be biodegraded over time. In this aspect, three key factors have to be considered for the success of bone tissue engineering. They are cells, scaffold, and cell–matrix (scaffold) interaction (see Figure 13.14).

The term scaffold is known as artificial ECM, which plays a pivotal role in accommodating the cells. These cells then undergo proliferation, migration, and differentiation, leading to the formation of a specific tissue while secreting the ECM that is required for tissue regeneration. On the other hand, direct delivery of cell suspension has been tried in some cases without using scaffolds [147,148], but this process encountered some difficulties in controlling the localization of transplanted cells. It is also known that most of the cells are anchorage-dependent, in other words scaffold-dependent, and thus they will not survive if delivered without a suitable scaffold. In addition, the scaffold provides adequate mechanical support against the body's stimuli upon implantation. Accordingly, designing a scaffold with maximum features of the native ECM is of great importance and a prerequisite for any tissue engineering, particularly bone tissue engineering.

Of course, the success rate of bone tissue engineering depends in part on the behavior of the scaffold. It is also perceived to be beneficial if biomimetically processed osteoconductive scaffolds interact with osteoinductive growth factors and osteogenic bone cells. Upon implantation, they must encourage the osteoprogenitor cells to attach, differentiate, and migrate into the matrix and, subsequently, should dynamically participate in new bone formation. For example, the scaffold loaded with appropriate osteoinductive growth factors (e.g., BMP) has been proven to enhance and regulate cellular ingrowth [115]. In this manner, it is possible to promote bone tissue ingrowth in the defective bone sites, leading to fast bone growth.

Keeping the above points in view, a bone tissue engineering approach to treat bone defects must involve the use of an osteoconductive scaffold with osteogenic cells and osteoinductive or growth factors, which may create an ideal bone graft. Figure 13.15 shows a schematic design strategy of a tissue-engineered biomimetic nanocomposite graft with all those factors. A tissue-engineered HA/collagen nanocomposite matrix seems to be the most promising system for bone reconstructive or regenerative surgery and such a matrix was developed mimicking the composition as well as microstructure of natural bone tissue suitable for bone tissue engineering [149]. The study demonstrated the ability of mineralized collagen matrix for its preferential orientation similar to a process that occurred during biological mineralization. Here, the collagen matrix serves as a template for HA nucleation and growth. The merit of this system lies not only in its structural reliability but also on the size-controlled nucleation of crystal growth with low crystallinity like natural bone minerals.
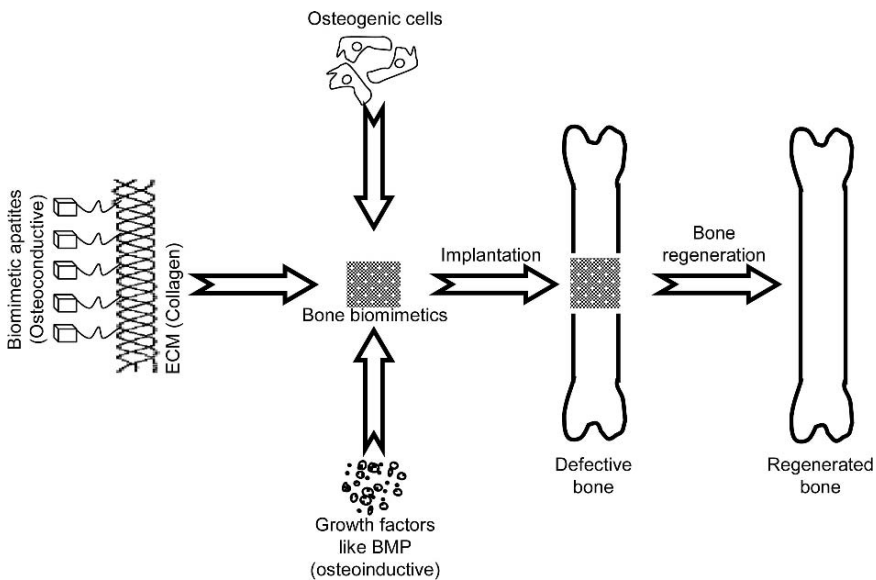
FIGURE 13.15. Design strategy of tissue-engineered biomimetic nanocomposite bone graft.

The efficacy of this matrix for bone tissue engineering was examined with osteogenic potential cells. The osteogenic cells/nanocomposite scaffolds were developed by organ culture technique as well as by conventional method and their in vitro cellular functions were systematically investigated. It was noticed that the scaffolds supported cellular growth and related functions well, leading to new bone formation. Based on the experimental results, this bone-resembling nanocomposite could be used as a promising system for engineering bone tissue.

An interesting article on biomimetic collagen by Yang et al. [115] examined the ability of the cell-binding domain of collagen (type I) to promote cellular adhesion, proliferation, and differentiation onto the scaffold. For this, they selected human bone marrow stromal cells, expanded, and cultured onto HA (a processed anorganic bone matrix) adsorbed with or without collagen (P-15 peptide) under osteogenic conditions. The experimental results clearly demonstrated the potential adsorption, cell-binding, and signaling molecule of collagen to the scaffold to facilitate appropriate biomimetic structures for human osteoprogenitor and osteoblast adhesion, proliferation, and differentiation. These findings indicate the ability of biomimetic structures in promoting osteogenic cellular growth and in supporting biomineralization, which ultimately leads to bone regeneration capability of biomineralized bone matrix.

13.8. Challenges and Future Directions

Despite recent advances in the development of biomimetic bone grafts, several challenges still remain that are to be taken into consideration while engineering bone grafts, which are briefly listed below.

- Standardizing a promising method for engineering biomimetic bone grafts is really a great challenge to be elucidated because of the ways in which the growth of biomineralization appears to be quite different with respect to processing methodology and key ingredients employed. Furthermore, of course, it may help to promote further research and development needed for this fascinating field.
- Although numerous studies intend to elucidate the biological mechanism that determines where, when and how mineral crystals form in living organisms, the complete mechanism involved in biomineralization remains uncertain.
- Another challenge is to mimic the hierarchical structure and composition of natural bone tissue while processing synthetic bone grafts or scaffolds. Despite many advances in structural biology, the nucleation mechanism involved in bone tissue formation is far from being understood. Although many proteins or macromolecules are involved in the initiation and growth of the biomineralization process, however, there are no data available to declare which is the most essential for that purpose.
- To understand how the exact functional mechanism of cell-responsive bone grafts behaves in body environments, particularly cell–matrix and cell–cell interaction

at the atomic or molecular level is perhaps a major challenge in bone tissue engineering. A complete molecular mechanism by which the cells and scaffold matrix interact with each other in vivo to promote bone regeneration is not implicit yet. Even with the advances of biosciences, we still lack elucidation of this strategy.

- Lastly, the ability to improve angiogenesis within the nanocomposite bone graft is probably the most significant challenge in bone tissue engineering because cells without a proper blood supply will not survive.

Future research is, therefore, precisely focused on what are the essential factors required for the initiation of biomineralization, synthetically, and how to regulate the deposition or growth of biominerals in a controlled fashion on extremely small length scales, which are essentially required for engineering ideal bone grafts using a biomimetic approach. The next decade may witness many breakthroughs in this emerging field that ultimately lead to the process of an ideal bone graft. It is believed that, in spite of the several challenges, biomimetic design and processing of nanocomposite bone grafts are likely to prove invaluable in the future development of bone grafting. A significant amount of work on this emerging topic is now being published, which is a good sign for the growth of this fascinating field. A real revolution may occur in bone grafting if it is possible to engineer a graft that could imitate all the functional aspects of natural bone tissue, which may also lead to a healthy and long life expectancy for many patients.

13.9. Conclusions

Being the first inventor, nature sets high standards for the biomaterial scientists and engineers who design bone grafts to assist in the repair or regeneration of the functions of defective bone tissues into normal healthy tissues. The most elusive and preferred goal, in this regard, is to produce bone grafts that mimic all the functional properties of natural bone in terms of the physical, mechanical, chemical, and biological. Recently, biomimetic design of nanocomposite bone grafts (HA/collagen), has gained much interest and has been perceived to be beneficial not only because they are the basic ingredients of natural bone tissue but also because they provide a larger surface area and surface reactivity owing to their nano characteristics; therefore they are compositionally and structurally similar to host bone and able to promote bone-related cellular functions extensively.

Many investigations also suggested that the composites made of bioactive HA and collagen precursors are probably the best suitable system for bone grafting. However, no synthetic graft is yet able to match the performance of natural bone tissue even with the advances of science and technology. It is believed that a combination of osteoconductive matrix with osteogenic cells and osteoinductive growth factors creates an ideal bone graft. The biomimetic approach is a good choice and, perhaps, one of the more promising methods for making such bone grafts with enhanced functions, mimicking a real bone that may even alleviate the

demerits of the currently available bone-grafting procedures including donor site morbidity of autogenic bone and possible disease transformation of allogenic bone. Biomimetic design of bone grafts is, however, still at the laboratory research level, and the development of such grafts in all length scales is in fact a critical task for the biomaterialist. With the advances of nanotechnology and tissue engineering, there is a bright chance in the near future to formulate biomimetic nanocomposite bone grafts in the place of autogenic bone grafts.

Acronyms

μm	Micrometer
3-D	Three-dimensional
AIDS	Acquired immune deficiency syndrome
BMA	Bone marrow aspirate
BMP	Bone morphogenetic protein
Ca/P	Calcium-to-phosphorous ratio
ChS	Chondroitin sulfate
DBM	Demineralized bone matrix
ECM	Extracellular matrix
HA	Hydroxyapatite
nm	Nanometer
PE	Polyethylene
PET	Polyethylene terephthalate
PLA	Polylactic acid
PLGA	Poly(lactide-co-glycolide)
PMMA	Polymethyl methacrylate
PTFE	Polytetrafluoroethylene
PU	Polyurethane
rhBMP	Recombinant human bone morphogenetic protein
SBF	Stimulated body fluid
SEM	Scanning electron microscopy
TCP	Tri-calcium phosphate
TEM	Transmission electron microscopy

Glossry

Allografting
Tissue transplantation between individuals of the same species, but of nonidentical genetic.

Alloplast
Substitution of synthetic biomaterials to repair or replace defective parts of the body.

Artificial organ
A medical device or implant intended to replace the body organs.

Autografting
Transplantation of the tissue within the same body.

Bioactivity
Ability of the implant to play a vital role in the metabolic processes of living body.

Bioactive material
A material that is capable of directing a chemical bond with living tissue.

Biocompatibility
Ability of the implant to perform with an appropriate host response in a specific application.

Biodegradability
Susceptibility of an implant to be decomposed by a living organism.

Biomaterial
Any synthetic material that is biocompatible with the host tissue and with the body upon implantation. It can be metal, ceramic, polymer, or a composite of each.

Biomimetics
The development of synthetic systems based on information gained from biological systems (e.g., biomineralization).

Biopsy
Removal of a small portion of tissue, usually for the purpose of making a diagnosis.

Bone
A rigid, yet dynamic connective tissue consisting of calcium phosphate-based minerals embedded with collagen fibers in conjunction with osteogenic cells.

Bone marrow
A soft tissue found inside the bones in the body that produces platelets and red and white blood cells.

Bone grafting
A surgical procedure that repairs or replaces a defective bone with the help of materials, either from natural or synthetic sources.

Calcium
The most important mineral that is rich in the bone.

Cancellous bone
A spongy tissue of the bone with high porosity.

Cell
Fundamental, structural, and functional unit of all living beings that is composed of an outer membrane enclosing protoplasm and nucleus.

Cellular bone grafts
Bone grafts that have living cells.

Collagen
A fibrous protein having a triple helical structure that functions to hold tissues together.

Composite
A heterogeneous combination of two or more materials.

Connective tissue
Any of the tissues of the body that support specialized elements or parenchyma.

Cortical bone
A hard (dense) tissue of bone with functional osteons.

Extracellular matrix
The material that surrounds cells, which consists of many biological substances including proteins and polysaccharides.

Fracture
Broken bones.

Graft
A transplant.

Growth factors
A heterogeneous group of substances whose general purpose is to enhance the rate of healing, for example, BMP.

Hard tissue
The general term for calcified structures of our body such as bone and tooth.

Hydroxyapatite
A calcium phosphate-based material with chemical composition $Ca_{10}(PO_4)_6(OH)_2$, rich in bone minerals.

Immunogenic
Capable of stimulating an immune response.

Implant
Any medical device made from single- or multiphase materials intended for human health care.

Implantation
A surgical procedure by which a medical device or prosthesis is placed either temporarily or permanently in the human body.

In vitro
A biological study performed in the laboratory. In other words, outside the living body.

In vivo
A biological study performed inside the living body.

Metabolism
A general term used to designate all biochemical changes that occur to substances within the body by either anabolism or catabolism.

Micro
A unit prefix meaning one millionth (1/1,000,000).

Monolithic
Made from a single material.

Nano
A unit prefix meaning one billionth (1/1,000,000,000).

Nanocomposite
A heterogeneous combination of two or more materials in which one should be on the order of the nanometer scale.

Nanomaterials
Materials composed of particles having nanometric tolerances; a nanometer is equal to 10^{-9} meters.

Nontraumatic fracture
Any fracture caused by disease. Also known as pathologic fracture (e.g., osteoporosis).

Organ
A differentiated part of an organism adapted for a definite function.

Orthopedics
The medical specialty concerned with the skeletal system.

Osteoblasts
Bone cells that are responsible for the formation of bone.

Osteoclasts
Bone cells that are responsible for resorbtion of bone.

Osteoconduction
An action associated with in-growth of capillaries and migration of bone-forming cells from the host into a 3-D matrix to form a new bone.

Osteocytes
Bone cells that are responsible for the maintenance of bone.

Osteogenesis
A process of development of bone tissue.

Osteoinduction
A biochemical process of promoting or accelerating new bone.

Pathogen
Any organism that is capable of producing disease.

Polymer
A large molecule formed by the combination of many similar smaller molecules, that is, monomers.

Prosthesis
A medical device that is capable of replacing the organs or tissues of the body.

Protein
A large biomolecule composed of one or more chains of amino acids in a specific sequence.

Resorbtion
Dissolution of a substance.

Scaffold
A temporary structural construct or matrix used to support the cells for accommodation during tissue fabrication.

Stem cells
Undifferentiated cells that develop specialized cells, which are located in the bone marrow.

Strain
The change in size or shape of a body as a result of applied force.

Stress
An internal force that resists a load, expressed in force per unit area.

Surface area
The total area of exposed surface of an object.

Tissue
A collection of similar cells and their surrounding intercellular substances.

Tissue engineering
Development and manipulation of laboratory grown molecules, cells, tissues, and organs for repair or replacement of the defective body parts.

Toughness
The amount of energy absorbed by a material before breakage.

Transplantation
Surgical transfer of tissue or organ from one place to another.

Trauma
Any injury or wound caused by an external force.

Tumor
An uncontrolled growth of cells that are not capable of serving their specific function, which may be benign or malignant.

Vascular
A term pertaining to a blood vessel.

Xenografting
Tissue transplantation between two different species (e.g., bone from animal to human).

References

[1] Lakes, R. (1993). Materials with structural hierarchy. *Nature* **361**: 511–5.

[2] Hartgerink, J.D., Beniash, E., and Stupp, S.I. (2001). Self-assembly and mineral-ization of peptide-amphiphile nanofibers. *Science* **294**: 1684–8.

[3] LeGeros, R.Z. (1994). In: Brown, P.W. and Constantz, B., Eds. *Biological and Synthetic Apatites*. Boca Raton, FL: CRC.

[4] Park, J.B. (1984). *Biomaterials Science & Engineering*. New York: Plenum.

[5] Murugan, R. and Ramakrishna, S. (2005). In: Nalwa, H.S., Ed. *Handbook of Nanos-tructured Biomaterials and Their Applications*. California: American Scientific.

[6] Currey, J.D. (2002). *Bones:Structure and Mechanics*. Princeton, NJ: Princeton University Press.

[7] Lowenstam, H.A. and Weiner, S. (1989). *On Biomineralization*. New York: Oxford University Press.

[8] McConnell, D. (1962). The crystal structure of bone. *Clin. Orthop. Relat. Res.* **23**: 253–68.

[9] Frost, H.M. (1964). In: Frost, H.M., Ed. *Bone Biodynamics*. Boston: Little Brown; p. 315–34.

[10] Aubin, J.E. and Liau, F. (1996). *Principles of Bone Biology*. 1st ed. San Diego: Academic.

[11] Ducy, P., Schinke, T., and Karsenty, G. (2000). The osteoblast: A sophisticated fibroblast under central surveillance. *Science* **289**: 1501–4.

[12] Cowin, S.C., van Buskirk, W.C., and Ashman, R.B. (1987). In: Skalak, R. and Chien, S. Eds. *Handbook of Bioengineering*. New York: McGraw-Hill.

[13] Majeska, R.J. and Wuthier, R.E. (1975). Studies on matrix vesicles isolated from chick epiphyseal cartilage: Association of pyrophosphatase and ATPase activities with alkaline phosphatase. *Biochim. Biophys. Acta* **391**: 51–60.

[14] Anderson, H.C. (1969). Vesicles associated with calcification in the matrix of epi-physeal cartilage. *J. Cell Biol.* **41**: 59–72.

[15] Inoue, S. and Okazaki, K. (1978). Biocrystals. *Sci. Am.* **236**: 82–92.

[16] Ahmad, Z. and Mark, J.E. (1998). Biomimetic materials: Recent developments in organic-inorganic hybrids. *Mater. Sci. Eng. C* **6**: 183–96.

[17] Berman, A., Addadi, L., and Weiner, S. (1988). Interactions with sea-urchin skeleton macromolecules and growing calcite crystals: A study of intracrystalline proteins. *Nature* **331**: 546–48.

[18] Mergenhagen, S.E., Martin, G.R., Rizzo, A.A., Wright, D.N., and Scott, D.B. (1960). Calcification in vivo of implanted collagen. *Biochim. Biophys. Acta* **43**: 563–5.

[19] Simkiss, K. (1975). *Bone and Biomineralization*. London: Edward Arnold.

[20] Simkiss, K. and Wilbur, K.M. (1989). *Biomineralization: Cell Biology and Mineral Deposition.* New York: Academic.

[21] Damien, C.J. and Parsons, J.R. (1991). Bone graft and bone graft substitutes: A review of current technology and applications. *J. Appl. Biomater.* **2**: 187–208.

[22] Murugan, R. and Ramakrishna, S. (2004). Nanostructured biomaterials. In: Nalwa, H.S., Ed. *Encyclopedia of Nanoscience and Nanotechnology*, California: American Scientific, 7: 595–613.

[23] Welch, R.D., Zhang, H., and Bronson, D.G. (2003). Experimental tibial plateau fractures augmented with calcium phosphate cement or autologous bone graft. *J. Bone Joint Surg. Am.* **85**: 222–31.

[24]   Myerson, M.S., Neufeld, S.K., and Uribe, J. (2005). Fresh-frozen structural allo-grafts in the foot and ankle. *J. Bone Joint Surg. Am.* **87**: 113–20.

[25]   Li, X.D. and Hu, Y.Y. (2001). The treatment of osteomyelitis with gentamicin-reconstituted bone xenograft-composite. *J. Bone Joint Surg. Br.* **83**: 1063–8.

[26]   Cypher, T.J. and Grossman, J.P. (1996). Biological principles of bone graft healing. *J. Foot Ankle Surg.* **35**: 413–7.

[27]   Mowlem, R. (1944). Cancellous chip bone-grafts: Report on 75 cases. *Lancet* **2**: 746–8.

[28]   Connolly, J.F. (1995). Injectable bone marrow preparations to stimulate osteogenic repair. *Clin. Orthop. Relat. Res.* **313**: 8–18.

[29]   Tiedeman, J.J., Garvin, K.L., Kile, T.A., and Connolly, J.F. (1995). The role of a composite, demineralized bone matrix and bone marrow in the treatment of osseous defects. *Orthopedics* **18**: 1153–8.

[30]   Gazdag, A.R., Lane, J.M., Glaser, D., and Forster, R.A. (1995). Alternatives to autogenous bone graft: Efficacy and indications. *J. Am. Acad. Orthop. Surg.* **3**: 1–8.

[31]   Asahina, I., Sato, I., Oda, M., Marukawa, E., Imranul, A.M., and Enomoto, S. (1999). In: *Bone Engineering.* 1st edition. Toronto: Em Squared; p. 526.

[32]   Lexer, E. (1908). Substitution of whole or half joints freshly amputated extermities by free plastic operation. *Surg. Gynec. Obstet.* **6**: 601–7.

[33]   Mankin, H.J. and Gebhardt, M.C. (1996). Long-term results of allograft replace-ment in the management of bone tumours. *Clin. Orthop. Relat. Res.* **324**: 86–97.

[34]   Simonds, R.J., Holmberg, S.D., Hurwitz, R.Z., et al. (1992). Transmission of human immunodeficiency virus type 1 from a seronegative organ and tissue donor. *N. Engl. J. Med.* **326**: 726–32.

[35]   Salama, R. (1983). Xenogeneic bone grafting in humans. *Clin. Orthop. Relat. Res.* **174**: 113–21.

[36]   Salama, R. (1973). Recombined grafts of bone and marrow. *J. Bone Jt. Surg. Br.* **55**: 402–17.

[37]   Mears, D.C. (1977). Metals in medicine and surgery. *Inter. Metals Rev.* **218**: 119–55.

[38]   De Boer, H.H. (1988). The history of bone grafts. *Clin. Orthop.* **226**: 292–8.

[39]   Perry, C.R. (1999). Bone repair techniques, bone graft, and bone graft substitutes. *Clin. Orthop. Relat. Res.* **360**: 71–86.

[40]   Bohner, M. (2000). Calcium orthophosphates in medicine: From ceramics to cal-cium phosphate cements. *Injury* **31**: SD37–47.

[41]   Betz, R.R. (2002). Limitations of autograft and allograft: New synthetic solutions. *Orthopedics* **25**: S561–70.

[42]   Cornell, C.N. and Lane, J.M. (1998). Current understanding of osteoconduction in bone regeneration. *Clin. Orthop. Relat. Res.* **355**: S267–73.

[43]   Tuli, S.M. and Singh, A.D. (1978). The osteoinductive property of decalcified bone matrix: An experimental study. *J. Bone Jt. Surg. Br.* **60**: 116–23.

[44]   Sakou, T. (1998). Bone morphogenetic proteins: From basic studies to clinical approaches. *Bone* **22**: 591–603.

[45]   Connolly, J.F. (1995). Injectable bone marrow preparations to stimulate osteogenic repair. *Clin. Orthop. Relat. Res.* **313**: 8–18.

[46]   Connolly, J.F., Guse, R., Lippiello, L., and Dehne, R. (1989). Development of an osteogenic bone-marrow preparation. *J. Bone Jt. Surg. Am.* **71**: 684–91.

[47]   Jarcho, M. (1981). Calcium phosphates ceramics as hard tissues prosthetics. *Clin. Orthop. Relat. Res.* **157**: 259–78.

[48] De Groot, K. and Ducheyne, P. (1981). In vivo surface activity of a hydroxyapatite alveolar bone substitute. *J. Biomed. Mater. Res*. **15**: 441–5.

[49] Black, J. and Hastings, G.W. (1998). *Handbook of Biomaterials Properties*. London: Chapman and Hall.

[50] De Groot, K. (1990). In: Yammamuro, T. and Hench, L.L., Eds. *Chemistry of Calcium Phosphates*. Boca Raton, FL: CRC.

[51] Hench, L.L. (1998). Bioceramics. *J. Am. Ceram. Soc*. **81**: 1705–28.

[52] LeGeros, R.Z. and LeGeros, J.P. (1993). In: Hench, L.L. and Wilson. J., Eds. *An Introduction to Bioceramics*. Singapore: World Scientific, pp.139–80.

[53] Kay, M.I., Young, R.A., and Posner, A.S. (1964). Crystal structure of hydroxyapatite. *Nature* **204**: 1050–2.

[54] Aoki, H. (1994). *Medical Applications of Hydroxyapatite*. Tokyo: Ishiyaku EuroAmerica.

[55] Werner, Gerhard's Grundr. (1786). 281.

[56] Daubree, A. (1851). *Comp. Rend. Acad. Sci. Paris* **32**: 625.

[57] Ray, R.D. and Ward, A.A. (1951). A preliminary report on studies of basic calcium phosphate in bone replacement. *Surg. Forum* **2**: 429–34.

[58] Aoki, H. and Kato, K. (1973). Synthesis of hydroxyapatite under hydrothermal conditions. Part 1: Effects of pH and temperature. *J. Dent. App. Mater*. **14**: 36–9.

[59] DeGroot, K. (1980). Bioceramic consisting calcium phosphate salts. *Biomaterials* **1**: 47–50.

[60] Jarcho, M. (1976). Hydroxyapatite synthesis and characterization in dense polycrystalline forms. *J. Mater. Sci* .**1**: 2027–35.

[61] Murugan, R., Rao, K.P., and Kumar, T.S.S. (2003). Heat-deproteinated xenogeneic bone from slaughterhouse waste: Physico-chemical properties. *Bull. Mater. Sci*. **26**: 523–8.

[62] Murugan, R., Kumar, T.S.S., and Rao, K.P. (2002). Fluorinated bovine hydroxyapatite: Preparation and characterization. *Mater. Lett*. **57**: 429–33.

[63] Murugan, R. and Ramakrishna, S. (2004). Coupling of therapeutic molecules onto surface modified coralline hydroxyapatite. *Biomaterials* **25**: 3073–80.

[64] Murugan, R., Rao, K.P., and Kumar, T.S.S. (2002). Microwave synthesis of bioresorbable carbonated hydroxyapatite using goniopora. *Bioceramics* **15**: 51–4.

[65] Webster, T.J., Siegel, R.W., and Bizios, R. (2000). Enhanced functions of osteoblasts on nanophase ceramics. *Biomaterials* **21**: 1803–10.

[66] Ota, Y. and Iwashita, T. (1998). Novel preparation method of hydroxyapatite fibers. *J. Am. Ceram. Soc*. **81**: 1665–8.

[67] Murugan, R. and Ramakrishna, S. (2005). Aqueous mediated synthesis of bioresorbable nanocrystalline hydroxyapatite. *J. Cryst. Growth* **274**: 209–13.

[68] Murugan, R. and Ramakrishna, S. (2004). Bioresorbable composite bone paste using polysaccharide based nano hydroxyapatite. *Biomaterials* **25**: 3829–35.

[69] Zhang, S. and Consalves, K.E. (1997). Preparation and characterization of thermally stable nanohydroxyapatite. *J. Mater. Sci. Mater. Med*. **8**: 25–8.

[70] Zhang, F., Zhou, Z.H., Yang, S.P., Mao, L.H., Chen, H.M., and Yu, X.B. (2005). Hydrothermal synthesis of hydroxyapatite nanorods in the presence of anionic starburst dendrimer. *Mater. Lett*. **59:** 1422–5.

[71] Nakamura, S., Tsobe, T., and Senna, M. (2001). Hydroxyapatite nano sol prepared via a mechanochemical route. *J. Nanopart. Res*. **3**: 57–61.

[72] Koumoulidis, G.C., Vaimakis, T.C., Sdoukos, A.T., Boukos, N.K., and Trapalis, C.C. (2001). Preparation of hydroxyapatite lath-like particles using high-speed dispersing equipment. *J. Am. Ceram. Soc.* **84**: 1203–8.

[73] Yang, Y. and Ong, J.L. (2002). Rapid sintering of hydroxyapatite by microwave processing. *J. Mater. Sci. Lett.* **21**: 67–9.

[74] Edward, S.A., Nathaniel, J.G., Atsushi, N., and Jackie, Y.Y. (1998). In: Xiao, D. and Ying, J., Eds. *MRS 1998 Fall Meetings*. Private communication; p. 611.

[75] Ahn, E.S., Gleason, N.J., Nakahira, A., and Ying, J.Y. (2001). Nanostructure processing of hydroxyapatite-based bioceramics. *Nano Lett.* **1**: 149–53.

[76] Murugan, R. and Ramakrishna, S. 2006.

[77] Bissell, M.J. and Barcellos-Hoff, M.H. (1987). The influence of extracellular matrix on gene expression: Is structure the message? *J. Cell. Sci. Suppl.* **8**: 327–43.

[78] Vijayan, S. and Varma, H. (2002). Microwave sintering of nanosized hydroxyapatite powder compacts. *Mater. Lett.* **56**: 827–31.

[79] Yang, Y., Ong, J.L., and Tian, J. (2002). Rapid sintering of hydroxyapatite by microwave processing. *J. Mater. Sci. Lett.* **21**: 67–9.

[80] Lee, C.H., Singla, A., and Lee, Y. (2001). Biomedical applications of collagen. *Int. J. Pharm.* **221**: 1–22.

[81] Nimni, M.E. and Harkness, F.D. (1988). In: Nimni, M.E., Ed. *Collagen Biochemistry*. Boca Raton, FL: CRC, 1:1–79.

[82] Ramachandran, G.N. (1967). *Chemistry of Collagen*. New York: Academic.

[83] Lehninger, A.L., Nelson, D.L., and Cox, M.M. (2000). In: Freeman, W.H., Ed. *Principles of Biochemistry*. Third edition. New York: Marcel Dekker.

[84] Cornell, C.N., Lane, J.M., Chapman, M., Merkow, R., Seligson, D., Henry, S., Gustilo, R., and Vincent, K. (1991). Multicenter trial of Collagraft as bone graft substitute. *J. Orthop. Trauma* **5**: 1–8.

[85] Terheyden, H., Knak, C., Jepsen, S., Palmie, S., and Rueger, D.R. (2001). Mandibular reconstruction with a prefabricated vascularized bone graft using recombinant human osteogenic protein-1: An experimental study in miniature pigs. Part I: Prefabrication. *Int. J. Oral Maxillofac. Surg.* **30**: 373–9.

[86] Tay, B.K., Le, A.X., Heilman, M., Lotz, J., and Bradford, D.S. (1998). Use of a collagen-hydroxyapatite matrix in spinal fusion: A rabbit model. *Spine* **23**: 2276–81.

[87] Urist, M.R. (1965). Bone: Formation by autoinduction. *Science* **150**: 893–9.

[88] Sandhu, H.S. (1998). Biologic enhancement of spinal fusion. *Orthop. Clin. North. Am.* **29**: 621–31.

[89] Wang, E.A., Rosen, V., D'Alessandro, J.S., Bauduy, M., Cordes, P., Harada, T., Israel, D.I., Hewick, R.M., Kerns, K.M., LaPan, P., Luxenberg, D.P., McQuaid, D., Moutsasos, I.K., Nove, J., and Wozney, J.M. (1990). Recombinant human bone morphogenetic protein induces bone formation. *Proc. Natl. Acad. Sci. USA* **87**: 2220–4.

[90] Boyne, P.J., Marx, R.E., Nevins, M., Triplett, G., Lazaro, E., Lilly, L.C., Alder, M., and Nummikoski, P. (1997). A feasibility study evaluating rhBMP-2/absorbable collagen sponge for maxillary sinus floor augmentation. *Int. J. Periodon. Restor. Dent.* **17**: 11–25.

[91] Ono, I., Tateshita, T., Inoue, M., and Kuboki, Y. (1998). In vivo strength enhancement of hydroxyapatite combined with rhBMP-2. *J. Bone Mineral Metab.* **16**: 81–7.

[92] Jung, R.E., Glauser, R., Schärer, P., Hämmerle, C.H.F., Sailer, H.F., and Weber, F.E. (2003). Effect of rhBMP-2 on guided bone regeneration in humans. *Clin. Oral Imp.l Res.*. **14**: 556–68.

[93] Bianco, P., Riminucci, M., Gronthos, S., and Robey, P.G. (2001). Bone marrow stromal stem cells: Nature, biology, and potential applications. *Stem Cells* **19**: 180–92.

[94] Tiedmann, J.J., Connolly, J.F., Strates, B.S., and Lippiello, L. (1991). Treatment of nonunion by percutaneous injection of bone marrow and demineralized bone matrix. An experimental study in dogs. *Clin. Orthop. Relat. Res.* **268**: 294–302.

[95] Cornell, C.N., Lane, J.M., Chapman, M., Merkow, R., Seligson, D., Henry, S., Gustilo, R., and Vincent, K. (1991). Multicenter trial of Collagraft as bone graft substitute. *J. Orthop. Trauma* **5**: 1–8.

[96] Bozic, K.J., Glazer, P.A., Zurakowski, D., Simon, B.J., Lipson, S.J., and Hayes, W.C. (1999). In vivo evaluation of coralline hydroxyapatite and direct current electrical stimulation in lumbar spinal fusion. *Spine* **24**: 2127–33.

[97] Holliday, L. (1966). *Composite Materials*. New York: Elsevier.

[98] Ramakrishna, S., Mayer, J., Wintermantel, E., and Leong, K.W. (2001). Biomedical applications of polymer-composite materials: A review. *Comp. Sci. Tech.* **61**: 1189–224.

[99] Bonfield, W., Grynpas, M.D., Tully, A.E., Bowman, J., and Abram, J. (1981). Hydroxyapatite reinforced polyethylene: A mechanically compatible implant material for bone replacement. *Biomaterials* **2**: 185–6.

[100] Bonfield, W., Doyle, C., and Tanner, K.E. (1986). In: Cristel, P., Meunier, A., and Lee, A.J.C., Eds. *Biological and Biomechanical Performance of Biomaterials*. Amsterdam: Elsevier; p.153.

[101] Laurencin, C.T., Attawia, M.A., Elgendy, H.E., and Herbert, K.M. (1996). Tissue engineered bone-regeneration using degradable polymers: The formation of mineralized matrices. *Bone* **91**: S93–9.

[102] Daniels, A.U., Chang, M.K.O., and Andriano, K.P. (1990). Mechanical properties of biodegradable polymers and composites proposed for internal fixation of bone. *J. Appl. Biomat*. **1**: 57–78.

[103] Murugan, R. and Ramakrishna, S. (2004). Coupling of therapeutic molecules onto surface modified coralline hydroxyapatite. *Biomaterials* **25**: 3073–80.

[104] Murugan, R. and Ramakrishna, S. (2004). Bioresorbable composite bone paste using polysaccharide based nano hydroxyapatite. *Biomaterials* **25**: 3829–35.

[105] Murugan, R. and Rao, K.P (1998). In: Srinivasan, K.S.V., Ed. *Proceedings of IUPAC Macromolecules*. New Delhi: Allied, pp. 638–41.

[106] Murugan, R. and Rao, K.P. (2002). Controlled release of antibiotic from surface modified coralline hydroxyapatite. *Trends Biomater. Artif. Organs* **16**: 43–5.

[107] Murugan, R. and Rao, K.P. (2002). Biodegradable coralline hydroxyapatite composite gel using natural alginate. *Bioceramics* **15**: 407–10.

[108] TenHuisen, K.S., Martin, R.I., Klimkiewicz, M., and Brown, P.W. (1995). Formation and properties of a synthetic bone composite: Hydroxyapatite-collagen. *J. Biomed. Mater. Res.* **29**: 803–10.

[109] Hoexter, D.L. (2002). Bone regeneration graft materials. *J. Oral Implantol*. **28**: 290–4.

[110]   Okazaki, M., Ohmae, H., Takahashi, J., Kimura, H., and Sakuda, M. (1990). Insolu-
        bilized properties of UV-irradiated CO3 apatite-collagen composites. *Biomaterials*
        11: 568–72.

[111]   Hirota, K., Nishihara, K., and Tanaka, H. (1993). Pressure sintering of apatite-
        collagen composite. *Biomed. Mater. Eng.* **3**: 147–51.

[112]   Tampieri, A., Celotti, G., Landi, E., Sandri, M., Falini, G., and Roveri, N. (2003).
        Biologically inspired synthesis of bone-like composite: self-assembled collagen
        fibers/hydroxyapatite nanocrystals. *J. Biomed. Mater. Res.* **67A**: 618–25.

[113]   Du, C., Cui, F.Z., Zhu, X.D., and De Groot. K. (1999). Three-dimensional nano-
        HAp/collagen matrix loading with osteogenic cells in organ culture. *J. Biomed.
        Mater. Res.* **44**: 407–15.

[114]   Itoh, S., Kikuchi, M., Koyama, Y., Takakuda, K., Shinomiya, K., and Tanaka, J.
        (2004). Development of a hydroxyapatite/collagen nanocomposite as a medical
        device. *Cell Transplant* **13**: 451–61.

[115]   Yang, X.B., Bhatnagar, R.S., Li, S., and Oreffo, R.O. (2004). Biomimetic collagen
        scaffolds for human bone cell growth and differentiation. *Tissue Eng.* **10**: 1148–59.

[116]   Liao, S.S., Cui, F.Z., Zhang, W., and Feng, Q.L. (2004). Hierarchically biomimetic
        bone scaffold materials: Nano-HA/collagen/PLA composite. *J. Biomed. Mater. Res.
        Appl. Biomat.* **69B**: 158–65.

[117]   Zhang, S.M., Cui, F.Z., Lioa, S.S., Zhu, Y., and Han, L. (2003). Synthesis and bio-
        compatibility of porous nano-hydroxyapatite/collagen/alginate composite. *J. Mater.
        Sci. Mater. Med.* **14**: 641–5.

[118]   Yamaguchi, I., Tokuchi, K., Fukuzaki, H., Koyama, Y., Takakada, K., Monma,
        H., and Tanaka, J. (2001). Preparation and microstructure analysis of chi-
        tosan/hydroxyapatite nanocomposites. *J. Biomed. Mater. Res.* **55**: 20–7.

[119]   Chang, M.C., Ko, C.C., and Douglas, W.H. (2003). Preparation of hydroxyapatite-
        gelatin nanocomposite. *Biomaterials* **24**: 2853–62.

[120]   Memoto, R., Nakamura, S., Isobe, T., and Senna, M. (2001). Direct synthesis of
        hydroxyapatite-silk fibroin nano-composite sol via a mechanochemical route. *J. Sol.
        Gel. Sci. Tech.* **21**: 7–12.

[121]   Hao, J., Liu, Y., Zhou, S., Li, Z., and Deng, X. (2003). Investigation of
        nanocomposites based on semi-interpenetrating network of [L-poly (epsilon-
        caprolactone)]/[net-poly (epsilon-caprolactone)] and hydroxyapatite nanocrystals.
        Biomaterials **24**: 1531–9.

[122]   Deng, X., Hao, J., and Wnag, C. (2001). Preparation and mechanical properties of
        nanocomposites of poly(D, L-lactide) with Ca-deficient hydroxyapatite nanocrys-
        tals. *Biomaterials* **22**: 2867–73.

[123]   Liu, Q., De Wijn, J.R., and Van Blitterswijk, A. (1997). Nano-apatite/polymer com-
        posites: mechanical and physicochemical characteristics. *Biomaterials* **18**: 1263–
        70.

[124]   Wang, X., Li, Y., Wei, J., and De Groot, K. (2002). Development of biomimetic
        nano-hydroxyapatite/poly(hexamethylene adipamide) composites. *Biomaterials*
        23: 4787–91.

[125]   Li, H., Chen, Y., and Xie, Y. (2003). Photo-crosslinking polymerization to pre-
        pare polyanhydride/needle-like hydroxyapatite biodegradable nanocomposite for
        orthopedic application. *Mater. Lett.* **57**: 2848–54.

[126]   Song, J., Saiz, E., and Bertozzi, C.R. (2003). A new approach to mineralization
        of biocompatible hydrogel scaffolds: an efficient process toward 3-dimensional
        bonelike composites. *J. Am. Chem. Soc.* **125**: 1236–43.

[127]   Liou, S.C., Chen, S.Y., and Liu, D.M. (2003). Synthesis and characterization of needlelike apatitic nanocomposite with controlled aspect ratios. *Biomaterials* **24**: 3981–8.

[128]   Green, D., Walsh, D., Mann, S., and Oreffo, R.O.C. (2002). The potentials of biomimesis in bone tissue engineering: lessons from the design and synthesis of invertebrate skeletons. *Bone* **30**: 810–5.

[129]   Stupp, S.I. and Brawn, P.V. (1997). Molecular manipulation of microstructures: Biomaterials, ceramics, and semiconductors. *Science* **277**: 1242–8.

[130]   Stupp, S.I., LeBonheur, V., Walker, K., Li, L.S., Huggins, K.E., Keser, M., and Amstutz, A. (1997). Supramolecular materials: Self organized nanostructures. *Science* **276**: 384–9.

[131]   Bates, F. (1991). Polymer-polymer phase behavior. *Science* **251**: 898–905.

[132]   Zhang, S. (2003). Fabrication of novel biomaterials through molecular self-assembly. *Nature Biotech.* **21**: 1171–77.

[133]   Kikuchi, M., Ikoma, T., Itoh, S., Matsumoto, H.N., Koyama, Y., Takakuda, K., Shinomiya, K., and Tanaka, J. (2004). Biomimetic synthesis of bone-like nanocomposites using the self-organization mechanism of hydroxyapatite and collagen. *Comp. Sci. Tech.* **64**: 819–25.

[134]   Roveri, N., Falini, G., Tampieri, A., Landi, E., Sandri, M., Sidoti, M.C., and Parma, B. (2003). Biologically inspired growth of hydroxyapatite nanocrystals inside self-assembled collagen fibers. *Mater. Sci. Eng. C* **23**: 441–6.

[135]   Kikuchi, M., Itoh, S., Ichinose, S., Shinomiya, K., and Tanaka, J. (2001). Self-organization mechanism in a bone-like hydroxyapatite/collagen nanocomposite synthesized in vitro and its biological reaction in vivo.*Biomaterials* **22**: 1705–11.

[136]   Zhai, Y., Cui, F.Z., and Wang, Y. (2005). Formation of nano-hydroxyapatite on recombinant human-like collagen fibrils. *Curr. Appl. Phys.* **5**: 429–32.

[137]   Rhee, S.H. and Tanaka, J. (1998). Hydroxyapatite coating on a collagen membrane by a biomimetic method. *J. Am. Ceram. Soc.* **81**: 3029–31.

[138]   Rhee, S.H., Lee, J.D., and Tanaka, J. (2000). Nucleation of hydroxyapatite crystal through chemical interaction with collagen. *J. Am. Ceram. Soc.* **83**: 2890–2.

[139]   Lin, X., Li, X., Fan, H., Wen, X., Lu, J., and Zhang, X. (2004). In situ synthesis of bone-like apatite/collagen nano-composite at low temperature. *Mater. Lett.* **58**: 3569–72.

[140]   Zhang, W., Liao, S.S., and Cui, F.Z. (2003). Hierarchical self-assembly of nano-fibrils in mineralized collagen. *Chem. Mater.* **15**: 3221–6.

[141]   Chang, M.C., Ikoma, T., Kikuchi, M., and Tanaka, J. (2001). Preparation of a porous hydroxyapatite/collagen nanocomposite using glutataldehyde as a crosslinkage agent. *J. Mater. Sci. Lett.* **20**: 1199–201.

[142]   Rhee, S.H., Suetsugu, Y., and Tanaka, J. (2001). Biomimetic configurational arrays of hydroxyapatite nanocrystals on bio-organics. *Biomaterials* **22**: 2843–7.

[143]   Rhee, S.H. and Tanaka, J. (2001). Synthesis of a hydroxyapatite/collagen/chondroitin sulphate nanocomposite by a novel precipitation method.*J. Am. Ceram. Soc.* **84**: 459–61.

[144]   Itoh, S., Kikuchi, M., Koyama, Y., Takakuda, K., Shinomiya, K., and Tanaka, J. (2002). Development of an artificial vertebral body using a novel biomaterial, hydroxyapatite/collagen composite. *Biomaterials* **23**: 3919–26.

[145]   Itoh, S., Kikuchi, M., Koyama, Y., Takakuda, K., Shinomiya, K., and Tanaka, J. (2004). Development of a hydroxyapatite/collagen nanocomposite as a medical device. *Cell Transplant* **13**: 451–61.

[146]   Langer, R. and Vacanti, J.P. (1993). Tissue engineering. *Science* 260: 920–6.

[147]   Brittberg, M., Lindahl, A., Nilsson, A., Ohlsson, C., Isaksson, O., and Peterson, L. (1994). Treatment of deep cartilage defects in the knee with autologous chondrocyte transplantation. *N. Engl. J. Med.* **331**: 889–95.

[148]   Ponder, K.P., Gupta, S., Leland, F., Darlington, G., Finegold, M., Demayo, J., Ledley, F.D., Chowdhury, J.R., and Woo, S.L. (1991). Mouse hepatocytes migrate to liver parenchyma and function indefinitely after intrasplenic transplantation. *Proc. Natl. Acad. Sci. USA* **88**: 1217–21.

[149]   Du, C., Cui, F.Z., Zhu, X.D., and De Groot, K. (1999). Three-dimensional nano-HAp/collagen matrix loading with osteogenic cells in organ culture. *J. Biomed. Mater. Res.* **44**: 407–15.

14
Use of Nanoparticles as Building Blocks for Bioapplications

YONG ZHANG AND FENG WANG

14.1. Introduction

Nanoparticles (NPs) are a new class of advanced materials with sizes ranging from 1 nm to 100 nm. They have special physicochemical properties that are very different from those of bulk materials. For example, metal nanoparticles smaller than 5 nm show remarkable quantum size effects, which endow them with peculiar physical and chemical properties. The superlattices of metal nanoparticles exhibit novel electronic and optical properties that are not present in the isolated particles. The sizes of the nanoparticles are close to those of biomolecules, which allows an integration of nanotechnology and biotechnology, leading to major advances in multiplexed bioassays [1–3], clinical therapies [4], ultrasensitive biodetection, and bioimaging [5,6]. Moreover, nanoparticles can be used as building blocks for the fabrication of micro/nanoscale constructs with highly ordered architectures.

Increasing interest has been attracted to building close-packed solids of nanoparticles, controlling their microstructure, and engineering their properties on a nanometer scale. There are a number of strategies available for the ordering of nanoparticles into structured assemblies, and construction of large and complex systems, for example, shape-directed assembly and programmed assembly of nanoparticles comprising surface-attached molecules, ligands, and recognition sites, the formation of complex hybrid nanostructures by in situ transformation of unstable nanoparticle-based precursors, and template-directed assembly using nanoparticle building blocks [7]. These materials can bring new and unique capabilities to a variety of biomedical applications ranging from diagnostics to therapies.

14.2. Synthesis and Surface Modification of Nanoparticles

Nanoparticles can be made with a wide variety of materials. In particular, metal, metal oxide, semiconductor, and polymer nanoparticles are potentially useful for research in cellular and molecular biology, biosensing, bioimaging, and so on. A variety of synthetic methodologies is currently available for the preparation
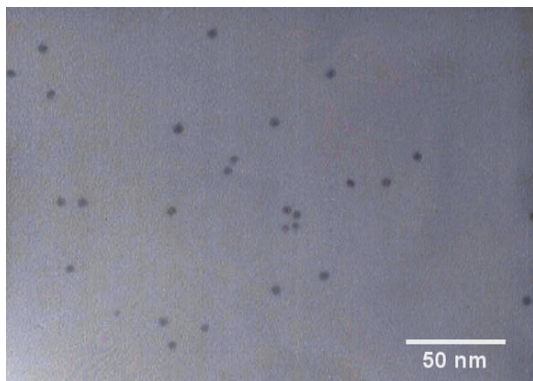
FIGURE 14.1. SEM image of Au nanoparticles.

50 nm

of nanoparticles with unique shape and narrow size distribution. Typically, the nanoparticles are synthesized via wet-chemical approaches, in which clusters of atoms or molecules are formed in the presence of surfactants. The surfactants bind to the surfaces of the clusters, control particle growth, and prevent the particles from aggregation.

14.2.1. Synthesis of Nanoparticles

Metal nanoparticles such as Au colloids have been used extensively as specific staining agents in biological light and electron microscopy [8,9]. The small sizes of these nanoparticles (diameters as small as 1.4 nm) allow them to be physically close to the structures they stain, thus providing high resolution (Figure 14.1). Au colloids can be synthesized with high quality via a variety of approaches [10,11]. Among these approaches, the most popular one is citrate reduction of $HAuCl_4$ in water, introduced by Turkevitch in 1951 [12]. The particles synthesized are nearly monodispersed with sizes controlled by changing the initial concentrations of reagents [13]. Nanoparticles of other noble metals may also be synthesized by citrate reduction, such as silver particles from $AgNO_3$, palladium from $H_2[PdCl_4]$, and platinum from $H_2[PtCl_6]$ [14,15]. Alloy nanoparticles, which may have properties different from individual metal nanoparticles, can also be synthesized [16,17]. For example, the reduction of the mixture of noble metal salts can lead to "alloy" or "mixed grain" particles. Furthermore, core-shell structured nanoparticles can be built up by the synthesis of a small colloidal nucleus followed by its enlargement with a different metal [18] or some other materials [14,19,20]. These nanoparticles have been studied extensively because their properties differ from those of the core or shell materials [20,21].

Magnetic metal oxide nanoparticles can be prepared in the form of either single-domain or superparamagnetic magnetite (Fe_3O_4), greigite (Fe_3S_4), maghemite (γ-Fe_2O_3), various types of ferrites (MeO·Fe_2O_3, where Me = Ni, Co, Mg, Zn, Mn, . . .), and so on. Magnetite nanoparticles are usually synthesized using wet-chemical methods through direct precipitation of magnetite by contacting ferrous

and ferric salts in alkaline media [22]. The synthesis and control of size, shape, and composition of magnetite nanoparticles have been widely studied using different iron salts [23], and through changing the Fe(II)/Fe(III) ratio, pH, ionic strength, and concentrations of the media [24–26]. Nonetheless, the nanoparticles produced via the above conventional methods are mobile in solution and thus easy to coalesce to form agglomerates. To make the mixture of the agglomerated and dispersive nanoparticles usable for biomedical applications, the agglomerated particles were usually sedimented and the supernatant colloid containing dispersed nanoparticles were collected [27].

Semiconductor nanoparticles, usually known as quantum dots (QDs), were first prepared in aqueous solution. This method yielded low-quality QDs with large size variations and poor fluorescence efficiencies. In 1993, Bawendi et al. developed a high-temperature route using a pyrolytic reaction [28], which forms the basis of various methods to produce high-quality, monodispersed QDs consisting of elements from group II to group IV in the periodic table. The method basically entails the combination of an appropriate metallic or organometallic precursor (such as Zn, Cd, or Pb) with a corresponding chalcogen precursor (such as S, Se, or Te) in a solvent at high temperature. The commonly used solvents are tri-N-octylphosphine oxide (TOPO), in conjunction with tri-N-octylphosphine (TOP), hexadecylamine (HDA), or steric acid [29–31]. To improve surface passivation, a shell of semiconductor materials with a higher band-gap such as ZnS or CdS is epitaxially grown around the initial core QDs [32,33].

Polymer latex nanoparticles can be prepared in many materials such as polystyrene and acrylate with controllable size, through radical-initiated polymerization in heterogeneous media (Figure 14.2). The sizes of latex nanoparticles are very dependent on the polymerization conditions. To yield nanosized particles, the polymerization is usually carried out in microemulsions [34]. For some applications, two or more monomers are used. For example, for polystyrene nanoparticles, divinylbenzene (DVB) is used as a cross-linker to improve the structural performance [35] and methacrylic acid (MAA) or methacrylate (MMA) is used as a co-monomer to provide the nanoparticles with desirable surface chemistry [36,37]. Furthermore, some fluorochromes or magnetic materials are incorporated into polymer nanoparticles, to render the particles multifunctional [38,39].

14.2.2. Surface Modification of Nanoparticles

Nanoparticles need to be surface modified if they are not water soluble, monodisperse, or biocompatible. Most of the biological reactions are carried out in an aqueous environment. However, some nanoparticles such as QDs are synthesized in organic solvents and are insoluble in water. Furthermore, nanoparticles have a large surface area-volume-ratio and tend to agglomerate to reduce their surface energy. When nanoparticles agglomerate, or adsorb plasma proteins, they are quickly eliminated from the blood stream by macrophages of the mononuclear phagocyte system (MPS) before they can reach target tissues [40], causing biocompatibility problems. One of the effective approaches to solving these problems is to modify
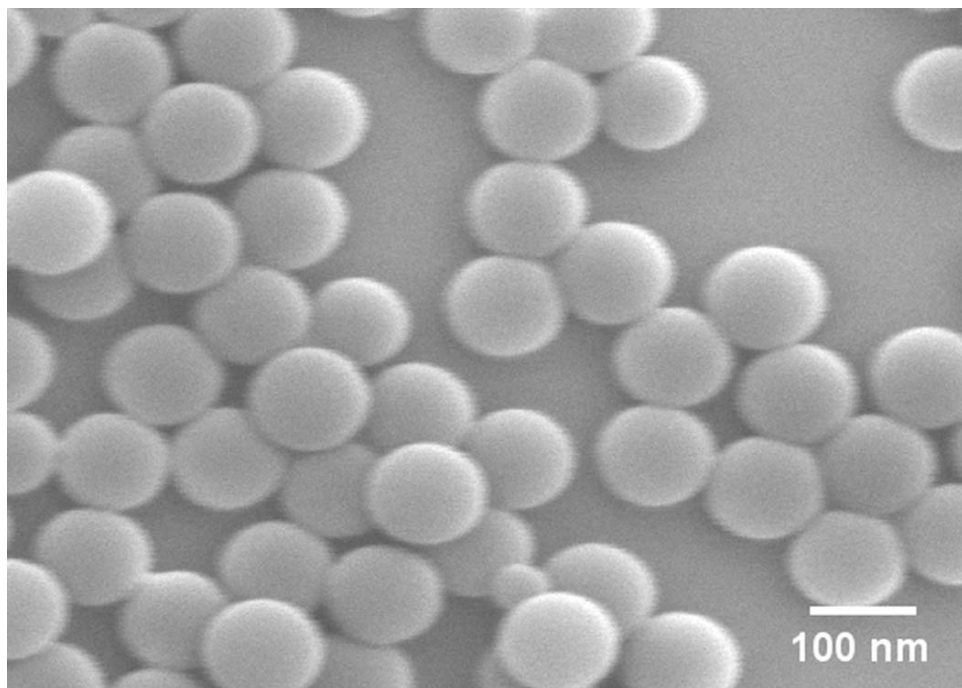
FIGURE 14.2. SEM image of polystyrene nanoparticles.

the surfaces of nanoparticles with some coatings of desirable functionality, and thus change the intrinsic physicochemical properties of nanoparticles. Coating nanoparticles with self-assembled monolayers of surfactant molecules has demonstrated prevention of the agglomeration and improvement of the biocompatibility [41]. Here we use QDs as an example to show how to do surface modification on QDs.

One method involves the surface exchange of hydrophobic surfactant molecules for polar species. It has also shown that the TOPO ligands on the QD surface may be replaced with heterobifunctional linker molecules, which provides both hydrophilic character and functional groups for further bioconjugation [6,42]. This method was initially shown to work well for linker molecules such as mercaptoacetic acid, mercaptosuccinic acid, glutathione, dithiothreitol, and histidine. Later, it was found that it could be applicable to a wide range of bifunctional compounds containing sulf-hydryl groups [43–45]. However, QDs capped with small bifunctional linker molecules are easily degraded by hydrolysis or oxidation of the capping ligand [46]. To overcome this problem, a more laborious but more stable method was developed [5,47]. The first step in the surface silanization is to replace the surfactant TOPO by thiol-containing silane monomers to form an initial silica shell (Figure 14.3). Subsequently, phosphonate-, polyethyleneglycol-, or ammonium-containing silane monomers, along with the thiol-containing monomer can be added to increase the thickness of the silica shell. This allows the QDs to
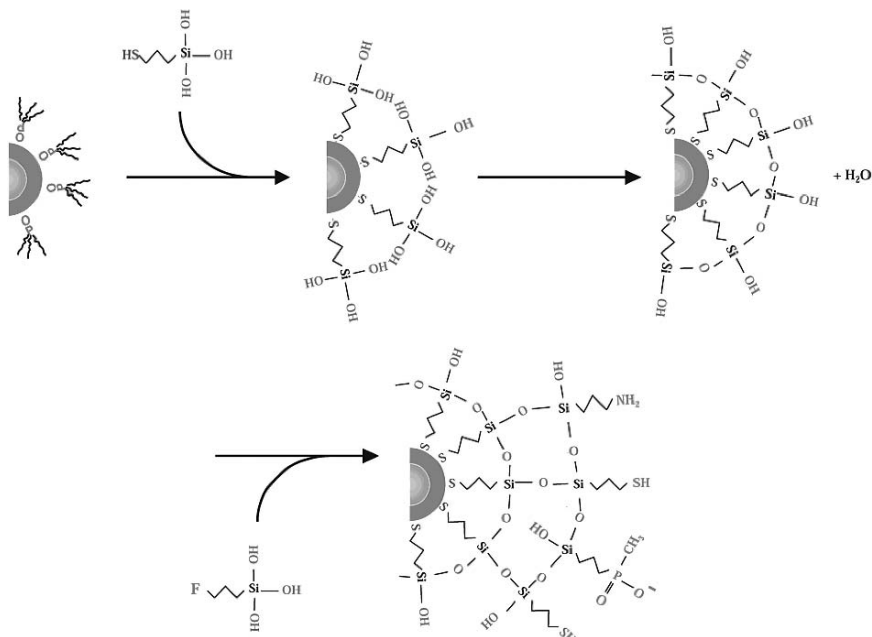
FIGURE 14.3. Surface modification of CdSeZnS quantum dots with silane. (Reprinted with permission from [47]. Copyright (2001) American Chemical Society.)

have a hydrophilic surface and functional groups on the surface for conjugation with biomolecules [47,48].

Another method involves phase transfer using amphiphilic molecules that behave as detergents for solubilizing the QDs coated with hydrophobic groups. This method is especially advantageous as it allows for the retention of the original surfactant molecules, which seem to increase the stability and fluorescence efficiency of the QDs over those where the original surface has been completely changed or exchanged with a heterobifunctional linker molecule [49]. The original TOPO ligands on the QD surface are used to interact with an amphiphilic polymer such as octylamine-modified polyacrylic acid and finally lead to the formation of a stable hydrophilic shell around the QD [50]. Another example is to encapsulate TOPO-coated QDs with phospholipid molecules. The hydrocarbon tails of the phospholipids are interlocked with the alkyl chains on the QD surfaces, and the polar phosphate head groups are self-assembled to form micelles in the solution [51].

14.3. Conjugation of Biomolecules to Nanoparticles

Biomolecules such as proteins, antibodies, and DNA have been extensively used for numerous bioapplications after being immobilized onto polymer or inorganic substrates, due to their unique recognition, transport, and catalytic properties. The

immobilization of biomolecules on the substrate materials are readily carried out through a variety of techniques including physical adsorption, electrostatic binding, specific recognition, and covalent coupling [52,53].

14.3.1. Attachment of Biomolecules to Nanoparticles

Typically, the water-soluble nanoparticles prepared via wet-chemical approaches are surface-capped with a ligand layer, which is formed either in situ or through postmodification of the as-prepared nanoparticles. According to the properties of the capping layer, the methods for conjugation of the biomolecules are varied.

When nanoparticles are stabilized by anionic ligands such as carboxylic acid derivatives (citrate, tartrate, lipoic acid), biomolecules are often coupled through noncovalent electrostatic interactions. For instance, gold and silver nanoparticles synthesized by citrate reduction are functionalized with immunoglobulin G (IgG) molecules at pH values that lie slightly above the isoelectric point of the citrate ligand [54]. This allows effective binding between the positively charged amino acid side chains of the protein and the negatively charged citrate groups of the nanoparticles. Other examples of protein coating through electrostatic interactions include the direct adsorption of heme-containing redoxenzymes at citrate-stabilized Ag nanoparticles [55–57] and the binding of basic leucine zipper proteins to lipoic acid stabilized semiconductor $CdSe_{core}/ZnS_{shell}$ particles [58]. Similarly, the adsorption of DNA molecules to positively charged Cd^{2+}-rich CdS nanoparticles has been studied [59–63]. Furthermore, the electrostatic deposition of biomolecules, particularly proteins or enzymes, is also used to form multilayer assemblies [64].

In the presence of a labile capping layer such as citrate on nanoparticles, biomolecules can be linked to the nanoparticles directly through chemisorption by exchanging with the original ligands. This method is usually used for the conjugation of proteins with Au nanoparticles, based on the binding of thiol groups of cysteine residues of the proteins (e.g., serum albumin) to the Au surface [65]. If no thiolated residues are available in the protein structure, thiol groups can be incorporated by chemical means [66,67] or through genetic engineering [68–71]. Similarly, nucleic acids can be synthesized with tethered alkanethiol groups by using appropriate phosphoramidate precursors in a solid-phase synthesis. The n-alkylthiolated nucleic acids have been extensively used for the preparation of DNA-functionalized gold [72–74] and semiconductor [62,75] nanoparticles. As an alternative, DNA functionalized with a steroid–disulfide derivative also binds to Au nanoparticles with high adsorption stability [76].

Some low-molecular bifunctional linkers, which have anchor groups for their attachment to nanoparticle surfaces and functional groups for covalent coupling to the target biomolecules, can be used for the generation of covalent-tethered conjugates of biomolecules with nanoparticles (Figure 14.4). Anchor groups such as thiols, disulfides, or phosphine ligands are often used for the binding of the bifunctional linkers to Au, Ag, CdS, and CdSe nanoparticles [52]. They may readily substitute weakly adsorbed molecules to stabilize the nanoparticles or may
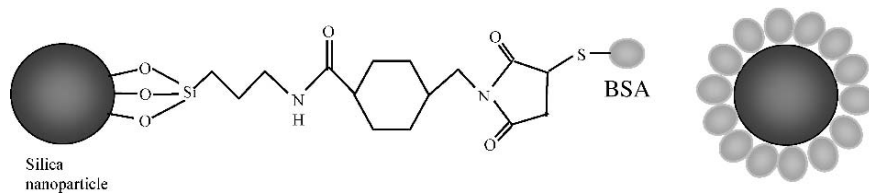
FIGURE 14.4. Conjugation of bovine serum albumin (BSA) to silica nanoparticles through 3-[(2-aminoethyl) amino] propyltrimethoxysilane (APTES) and 4-(N-maleimidomethyl) cycohexane-1-carboxylic acid 3-sulfo-N-hydroxysuccinimideester (sulfo-SMCC).

be used for the synthesis of the nanoparticles as surfactants. Different bifunctional linkers may have various terminal functional groups such as amine, active ester, and maleimide, which can be coupled to biomolecules covalently via carbodiimide-mediated esterification, amidation reactions, or reactions involving thiol groups [52,53].

14.3.2. *Biofunctionality of Biomolecules on Nanoparticles*

It is well known that bioconjugation of nanoparticles often leads to the degradation and inactivity of the biomolecules. In particular, the conjugation of protein with nanoparticles is a very complex process and many factors play a part in determining the extent of change in the structure of the protein. During the past decade, studies of different assay formats have been applied for measurement of bioaffinity employing nanoparticles. Some of the earlier studies indicated that the conjugation process altered the structure of the protein and led to the loss of protein functionality to various extents [77–79]. On the other hand, some other studies employing different detection methods showed that, using surface modification [80] and special covalent binding technique [81], the structure of the protein could be retained upon adsorption and hence the functionality remained favorable for the application of the nanoparticles in protein assays.

A study performed by McGuire et al. [77] suggested that protein adsorption on nanoparticles caused it to undergo significant conformational changes and ultimately led to the loss of protein functionality. The investigation was done on three variants of T4 lysozyme after they were attached to 9-nm colloidal silica particles using a circular dichroism (CD) technique to observe their secondary structure before and after adsorption. The results demonstrated that the lysozyme variants with less thermal stability bind more strongly to the nanoparticles than more stable ones. These unstable variants were also the ones that lost their secondary structure and catalytic activity.

Based on these results, Dordick et al. [78] did another study to investigate how the sizes of the silica nanoparticles influence the structure and enzymatic activity of adsorbed lysozyme. The same CD technique was used to observe the protein structure, and calorimetric activity assays were used to monitor the enzyme activity after adsorption. The results from the two analysis techniques were then used to

derive the overall effect of the nanoparticle size. It was concluded that lysozyme undergoes significant change in its structure upon adsorption onto silica particles. However, it is strongly dependent upon the size of the nanoparticles and the pH of the solution. Furthermore, an earlier study performed by Kondo and Mihara [79] on human hemoglobin and horse myoglobin on several inorganic nanoparticles (silica, zirconia, and titania) indicated that adsorption of proteins on these particles does not only affect the secondary structure of the proteins, but also their tertiary structure. The results also showed that the extent of conformational changes also depends on the type of nanoparticles used: silica nanoparticles cause fewer changes than zirconia and titania nanoparticles.

For all the abovementioned studies, the common method used to examine the changes in protein structure was circular dichroism (CD), which is the most direct method to show the exact structure of the protein. However, it is important to realize that a loss in the structure of the protein does not always provide a strong relation with the loss of activity or functionality of the protein. As reported by Dordick [78], about 60% of the enzyme activity was retained even when more than 70% of the α-helix structure of lysozyme was damaged. More experiments were performed to find out how the nanoparticles affect the functionality of proteins. Margel et al. [82] conducted a study involving the use of immobilized polyacrolein (PA) microspheres in a diagnostic assay to detect the amount of α_1-antitrypsin in human serum. The surface of the polyacrolein microspheres was modified with aldehyde end groups to bind with both the substrate and the trypsin molecules needed to detect the complementary α_1-antitrypsin. The surface analytical methods used in this study were the FTR/ATR spectra, electron spectroscopy for chemical analysis (ESCA), and scanning electron microscopy. Three types of assays were used and the result of each assay was compared to the others to check the activity of the trypsin after adsorption to the PA microspheres. One assay used radial immunodiffusion where human serum was introduced into wells prepared in an agar gel containing a specific antibody against α_1-antitrypsin. After incubation, a ring of immune precipitate was formed due to the antigen–antibody reaction and the diameter of the ring indicated the amount of trypsin detected in the serum. The other two assays made use of trypsin in solution and trypsin bound to the PA microspheres. The result of the study proved that trypsin bound to the PA microspheres was more stable and its enzymatic activity could be retained for a much longer period (up to one year) compared to trypsin in free solution. This was supported by the strong correlation of results with the immunodiffusion assay method when human serum was tested using both assays under similar conditions. From this result, we could infer with high probability that much of the structure of trypsin had to be retained even after adsorption to the microspheres as it was able to maintain a high level of activity even after storage over a long period of time.

Lee et al. conducted a study of protein and enzyme immobilization on non-porous microspheres of polystyrene (PS) materials and discovered that the activity of the enzyme bound to the PS microsphere was retained much longer than when it was in a free solution [81]. In his study, he used β-lactamase and concanavalin A (Con A) proteins that were attached to an amino-containing PS microspheres

through several methods of covalent binding. By comparing the activity of the enzyme in a fixed amount of time, Lee discovered that the best method of preparation was to activate glutaraldehyde cross-linking between the β-lactamase and the microspheres. This indicated that success in retaining the activity of the enzyme after adsorption to microspheres can be increased by using a special covalent binding technique that does not interfere too much with the structure of the enzyme.

Another study showed that protein functionality could be greatly conserved even after adsorption to microspheres [80]. The recombinant firefly luciferase (FFL) tagged with histidene was used, which is able to produce bioluminescence in its active form. A hydrophilic and protein-repelling Pluronic surfactant was used to provide an activity-preserving base on the microsphere. A metal-chelating nitrilotriacetic acid (NTA) group, which has a high affinity to the histidine tags bound to the FFL protein, was then coupled to the terminal hydroxyl groups of Pluronic. The results showed that the PS microspheres with chelating Pluronic surface retained about 93% of its bioluminiscence activity on the microspheres. This clearly demonstrated that FFL's functionality was successfully conserved after adsorption to modified PS microspheres and little damage was done to its protein structure.

14.4. Nanoparticles as Building Blocks for Bioapplications

14.4.1. Self-Assembly of Nanoparticles Using Biomolecules as Templates

Much attention has been directed to organizing nanoparticles into an ordered structure. A number of strategies such as solvent evaporation [83,84], Langmuir–Blodgett techniques [85], and shape-directed assembly [86] are available for ordering of nanoparticles into structured assemblies, and construction of large and complex systems. Alternatively, nanoparticles can be assembled through chemical coupling in solution via bivalent cross-linkers. An example is the alkyldithiol-directed aggregation of gold colloid [87]. In a similar way, nanoparticles can be self-assembled using biomolecules as cross-linkers. Driven by biospecific interactions, nanoparticles are connected to form a network or grow into 3-D materials with ordered structure. In particular, nanoparticles can be self-assembled using a biomolecular scaffold as a template [7]. Due to the high complexity of biomolecules and their particular ability to adapt themselves, very complex systems can be formed in a programmable way. The interactions that have been exploited to drive nanoparticles to organize along the biomolecular scaffold include molecular recognition and electrostatic absorption.

14.4.1.1. Self-Assembly of Nanoparticles via Molecular Recognition

One of the most fascinating capabilities of many biomolecules is that of molecular recognition [88]. Certain biomolecules can recognize and bind to another one

with extremely high selectivity and specificity. This is similar to a lock-and-key combination, but on a molecular level. Out of millions of keys, or ligand molecules, only one fits a particular lock, or receptor molecule. After the ligand molecules are attached to the surface of nanoparticles, they can specifically bind to receptors that "fit" the molecular recognition of the ligand molecules with high sensitivity and selectivity. In other words, nanoparticles with receptors can be directed to positions where ligand molecules are present. Generally, there are three classes of receptor–ligand pairs: antibody–antigen, oligonucleotide–complementary oligonucleotide, and avidin (streptavidin)–biotin, among which the complementary interactions of DNA have been widely used to facilitate the assembly of nanoparticles. DNA can mediate the assembly of nanoparticles in two different ways: DNA itself acts as a template or DNA directs nanoparticles to organize along other biomolecule templates.

DNA has been used as an attractive scaffolding material because of its very long linear structure and its mechanical rigidity over short distances. DNA-directed arrangement of nanoparticles on a surface can be demonstrated with a sorting experiment. Different parts of a surface are patterned with oligonucleotides of different sequences. Different nanoparticles are conjugated with oligonucleotides that are complementary to the oligonucleotides immobilized at particular positions on the substrate. The surface is incubated with the oligonucleotide–nanoparticle conjugates and rinsed after hybridization. The DNA-directed nanoparticle patterning is realized when nanoparticles only bind to the surface immobilized with oligonucleotides complementary to that conjugated to the nanoparticles. DNA-mediated sorting has been demonstrated using Au [89] and CdSe/ZnS nanoparticles [90].

Formation of nanoparticle assemblies in solution has also been conducted. Self-assembly of nanoparticles in solution minimizes or eliminates nonspecific binding of the nanoparticles to the substrate. DNA oligonucleotides were attached to metal colloids (sizes >10 nm) bearing thiolated DNA complements based on the specific molecular recognition of the DNA sequence [1,74,91], producing analytically useful optical information. Alivisatos et al. used a similar approach to produce two- or three-dimensional assemblies of nanoparticles [92,93].

Many biomolecules including microorganisms can be self-assembled to form ordered structures, which in turn can be used as templates for the organization of nanoparticles. One example is an aquatic organism known as a diatom which has a self-assembled rigid structure. The total number of extant diatom species is on the order of 10^5, with each forming a frustule of unique shape, in size from the microscale to the nanoscale [94]. However, silica-based diatom frustules lack the ability to recognize nanoparticles with certain ligands and thus cannot be used directly for the assembly of nanoparticles. Recently, Rosi et al. showed that diatom cell walls can be covalently bound with DNA and used as templates for the assembly of DNA-functionalized nanoparticles (Figure 14.5), and multilayers of nanoparticles can be assembled onto the template [95].
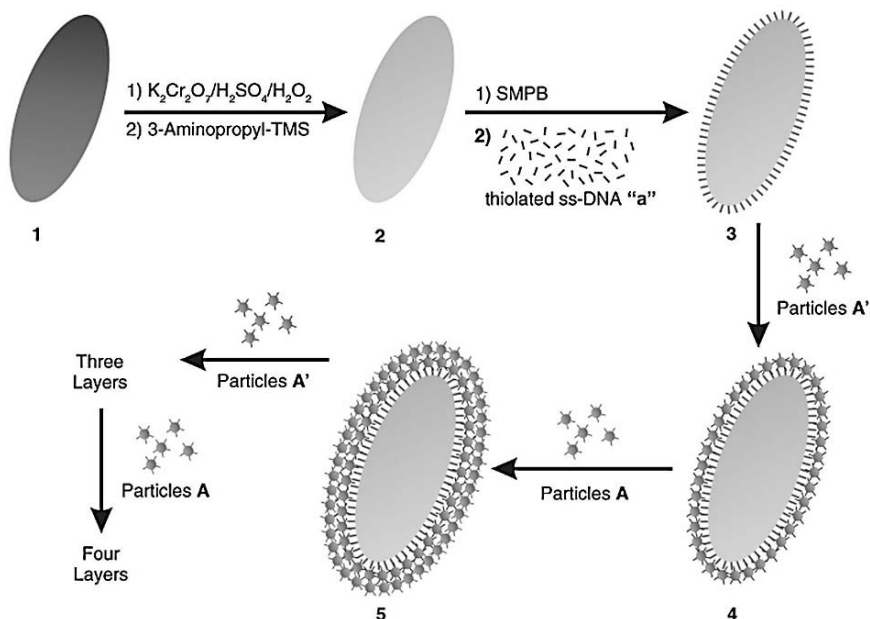
FIGURE 14.5. Scheme depicting the functionalization of diatom templates with DNA and DNA-functionalized nanoparticles. (From [95], reproduced with permission from John Wiley & Sons.)

14.4.1.2. Self-Assembly of Nanoparticles via Electrostatic Adsorption

Except for molecular recognition, many biomolecules can bind to each other through electrostatic absorption. Electrostatic binding is a robust interaction and has been proved to be a successful route to assemble nanoparticles using biomolecules as a template.

Because of the negatively charged phosphate backbone of DNA, nanoparticles with a cationic surface can be electrostatically bound to it in a controllable way. Synthetic thiocholine iodide [(2-mercaptoethyl) trimethylammonium iodide] is used as a cationic thiol compound to provide CdS nanoparticles with positive charges and guide the nanoparticles to electrostatically bind to a DNA template predeposited at the air–water interface [96]. By using amino acid lysine instead of the cationic capping agent, colloidal gold nanoparticles are self-assembled in solution [97] and in thin films [98]. This approach results in the formation of a linear superstructure of the gold nanoparticles, which can be used for generation of nanowires.

Electrostatic immobilization of nanoparticles to DNA in solution is of special interest. Warner and Hutchison [99] exploited the electrostatic interactions between the negatively charged phosphate backbone of DNA and functionalized gold nanoparticles with a cationic headgroup in the ligand shell, and described

a systematic approach to obtaining a DNA-templated assembly of nanoparticles in solution. The results showed that electrostatic assembly of thiocholine-stabilized nanoparticles onto double-stranded DNA in solution is a viable approach to preparing close-packed, templated 2-D and 3-D structures as well as linear nanoparticle assemblies. Wang and Murray [100] further demonstrated that assembly of nanoparticles can be controlled by varying the molar ratios of nanoparticles and DNA base pairs and the length of the DNA chains employed, opening up a possibility to assemble nanoparticles in a more programmable way.

Microorganisms can also be used as versatile templates for the organization of nanostructured materials into larger-scale functional architectures. Specially organized bacterial superstructures, with charged functional groups such as carboxylic or amino groups in well-defined positions of the protein meshwork, have been widely used as templates for the assembly of nanoparticles through electrostatic interactions. Davis reported the formation of superstructures of Fe_3O_4 and CdS nanoparticles on bacterial threads produced from a mutant strain of the bacterium Bacillus subtilis, in which mineralized bacterial composites can be prepared either from nanoparticles or by in situ deposition [101,102]. In addition, bacterial surface layers (S-layers) can be used as templates for organization of nanoparticles as well. The structural diversity of S-layers, their feasibility of forming self-assembly on a wide range of substrates, and the potential for surface chemical modification suggest that they could be exploited to produce a wide range of ordered nanoparticle arrays. Shenton et al. demonstrated the in situ formation of ordered two-dimensional arrays of CdS quantum dots using self-assembled bacterial S-layers [103].

Another template used to assemble nanoparticles is virus. Tobacco mosiac virus (TMV) is used for the synthesis and organization of inorganic nanoparticles [104]. The charged amino acid residues (such as glutamate, aspartate, arginine, and lysine) on the surface of the proteins may be used as nucleation sites for deposition of inorganic nanoparticles, as demonstrated by the growth of CdS and PbS quantum dots, iron oxides, and silica on the surface of TMV [104]. Recently, Mao and co-workers reported a virus-based template for the synthesis of single-crystal ZnS and CdS, and freestanding chemically ordered CoPt and FePt nanowires [105]. By using a biomolecular template, a programmable control over the composition, phase, and self-assembly of nanoparticles can be realized.

14.4.2. Self-Assembly of Nanoparticles on Solid Substrates

Nanoparticles have been assembled on a wide range of conductive, semi-conductive, and insulating materials. Techniques have been developed to produce nanoparticle microarrays or close-packed nanoparticle monolayers on a solid substrate [10]. Layer-by-layer assembly has also been conceived to direct the formation of thin films containing nanoparticles [106,107]. Nanoparticle multilayers are constructed using the same nanoparticle, or different nanoparticles even in the

same architecture [10,107]. These ordered nanoparticles on the substrate provide numerous new functionalities that are absent in bulk materials, leading the way toward the construction of novel biomedical devices.

The unique photonic and conductive properties of some nanoparticles can be employed to detect biological recognitions on a surface. With dimensions similar to those of biomolecules, nanoparticles are a natural choice for detecting biomolecules, which can be used in both electrochemically and optically based biosensors. Upon the assembly of nanoparticles on a solid surface, the biomolecules adsorbed on the surfaces of nanoparticles can be detected by means of surface plasmon resonance (SPR), surface enhanced Raman spectroscopy (SERS), and surface-enhanced fluorescence spectroscopic techniques. Furthermore, the unique size-controlled optical properties of semiconductor nanoparticles imply that the organization of combinatorial libraries of biomolecule–semiconductor nanoparticle hybrid systems or the assembly of these hybrids in array configurations may lead to the high-throughput parallel analysis of numerous analytes [53].

The nanoparticle assemblies can also be used to enhance the chemical reactivity of biomolecules. Au nanoparticles assembled on polyurethane microspheres are used as permeable high-surface supports for the immobilization of enzymes such as pepsin to provide easy access of the substrate molecules to the enzyme active centers in the multilayer enzyme assembly. Proteins immobilized in this way exhibit biocatalytic activity higher than that of the free enzyme in solution and significantly enhanced temperature and pH stability [108]. In another approach, the layer-by-layer deposition of enzymes and magnetic particles is applied to prepare a bioreactor, which allows the biocatalytic layer to be stripped out with an external magnet when it is deactivated, so that the surface could be reloaded with a new active biocatalyst layer [109].

The use of nanoparticles for micropatterning of proteins on solid substrate has also been demonstrated [110]. Micropatterning of proteins can be achieved by immobilizing proteins on silica nanoparticles followed by self-assembly of the nanoparticles in patterned microwells (Figure 14.6). Because the placement of
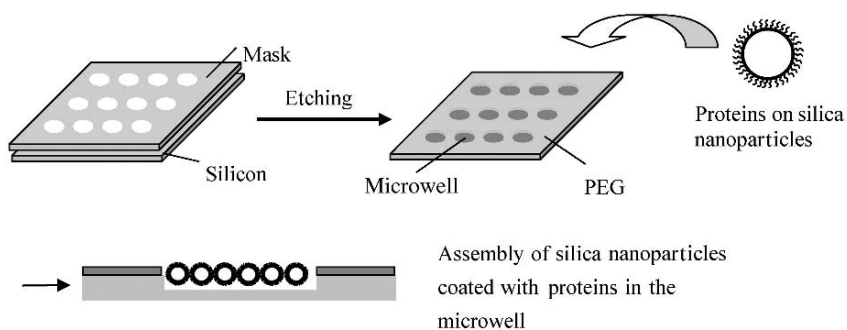
FIGURE 14.6. Schematic diagram of protein micropatterning via self-assembly of nanoparticles.
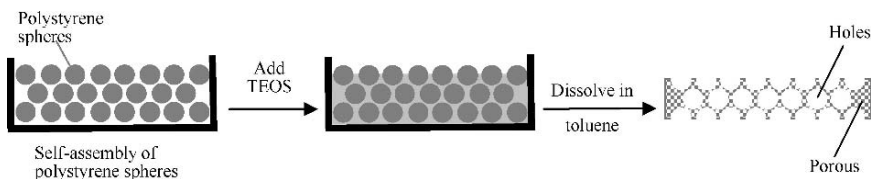
FIGURE 14.7. Schematic diagram of fabrication of porous materials using polymer nanoparticles as templates. TEOS: tetraethylorthosilicate.

protein–nanoparticle conjugates into the microwells is at the last step of the process, denaturing or contamination of proteins by the chemicals used in lithography can be avoided. This technique can be used to fabricate a planar protein microarray integrated with nonplanar spots, which also provides a universal route to the spatial positioning of other biomolecules.

14.4.3. Preparation of Hollow Spheres and Porous Materials Using Nanoparticles as Templates

Nanoparticles can also be used as a template for fabrication of porous materials, which can find a variety of applications such as hosting biomolecules, controlled release, and constructing biosensors. A large range of silica-based [111] and non-siliceous [112–114] porous materials are generally synthesized via precipitation from supersaturated solutions, by using ordered arrays of surfactants as templates. Precipitation routes are best suited to siliceous materials, which are thermally stable at high temperatures up to 800°C [115]. Nonsiliceous porous materials are often more difficult to synthesize by precipitation routes and often exhibit poor crystallinity and low thermal stability. Alternatively, porous materials can be synthesized by forming a self-assembly of nanoparticles in a solid and subsequently removing the templated nanoparticles (Figure 14.7). This approach can provide a general route to yield porous materials with various chemical compositions and controlled pore morphology [116,117].

Furthermore, various approaches to producing hollow spheres with controlled composition and pore structure are available. Caruso et al. [118] reported the fabrication of silica and silica–polymer hollow spheres by consecutively coating silica nanoparticles or some polymers onto colloidal polystyrene (PS) beads. The templated polystyrene beads can be removed either by calcination or decomposition upon exposure to some organic solvents (Figure 14.8). The wall thickness of the hollow spheres or the size of the holes can be readily controlled by varying the number of nanoparticle–polymer deposition cycles, and the size and shape are dependent on the morphology of the templating polystyrene beads. Alternatively, the hollow spheres can be synthesized without a sacrificial template. Silica/Au hollow spheres have been fabricated through the formation of Au/poly(L-lysine-b-l-crysteine) nanoparticles and their subsequent encasement within a shell composed of silica nanoparticles [119]. The flocculation-based self-assembly (or

FIGURE 14.8. Hollow silica spheres prepared by using polystyrene nanoparticles as templates. Polystyrene nanoparticles are dissolved in toluene.
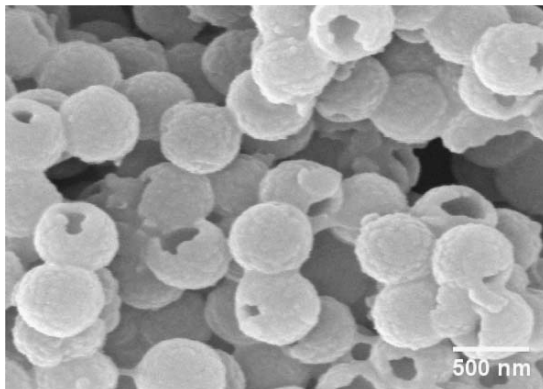
"flocculation assembly") of nanoparticles into hollow microspheres has also been demonstrated [120].

A general approach to prepare hollow spheres of ceramic materials with functionalized interior surface has also been reported [121]. The outer surfaces of the templating PS beads are first coated with submonolayers of silver nanoparticles, and they are assembled into a three-dimensional crystalline lattice. The beads are then coated with a titania layer. After the PS beads are dissolved in toluene, uniform hollow spheres are generated, with their interior surfaces being functionalized with the silver nanoparticles. Meanwhile, silver nanoparticles can be selectively removed using another wet etchant to produce an array of nanosized cavities on the interior surface of the hollow sphere. These nanoscale cavities may have functionality similar to that of the nanoscale template, as demonstrated in the area of molecular imprinting [122,123].

The use of nanoparticle building blocks for the fabrication of porous bulk solids has been extensively studied. Norris and co-workers used CdSe nanoparticles as building blocks to produce ordered three-dimensional porous solids of high- and low-refractive indexes as potential photonic band-gap materials [124]. The CdSe nanoparticles are induced to self-assemble inside a self-organized silica template. Subsequently, the template is removed and a three-dimensionally patterned material consisting solely of densely packed CdSe nanoparticles is obtained. The nanoparticles can be further sintered at high temperature to form a porous bulk semiconductor. Sakka and co-workers proposed a heterocoagulation method to prepare porous materials with controlled pore size and porosity [116]. Monodispersed polymer nanoparticles are used as a template and ceramic nanoparticles are used as building blocks (Figure 14.9). After surface modification, well-dispersed suspensions of polymer and ceramic nanoparticles with highly opposite surface charges are obtained at the same pH condition. Upon mixing the two suspensions, core-shell structures are formed via electrostatic attraction. The flocculated particles are subsequently closely packed by vacuum filtration. The polymers are finally removed by calcination, resulting in the porous structure. Bacterial threads
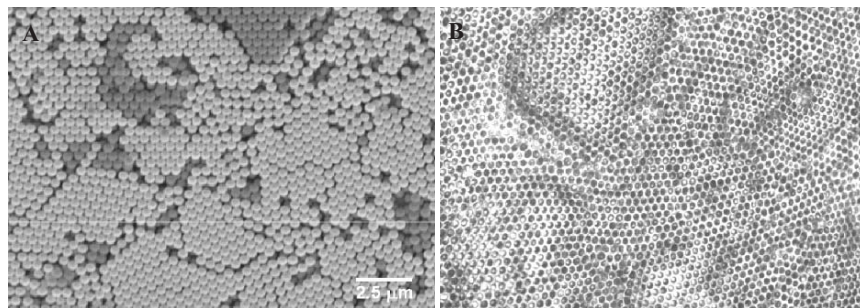
FIGURE 14.9. SEM image of polystyrene nanoparticles self-assembled on silicon substrate (A) and optical photograph of porous silica film fabricated using polystyrene nanoparticles as templates (B).

and polymer gels are also used as template to construct a porous material [102,125]. The materials have been found to retain the characteristic shape and length of the organic templates and do not generally have a large surface area and pore volume. Other templates include liquid-crystals, based on the interactions between the liquid-crystal and surface modified nanoparticles [117].

References

[1]   Elghanian, R., Storhoff, J.J., Mucic, R.C., Letsinger, R.L., and Mirkin, C.A. (1997). Selective colorimetric detection of polynucleotides based on the distance-dependent optical properties of gold nanoparticles. *Science* **277**:(5329), 1078–1081.

[2]   Dubertret, B., Calame, M., and Libchaber, A.J. (2001). Single-mismatch detection using gold-quenched fluorescent oligonucleotides. *Nature Biotechnol.* **19**:(4), 365–370.

[3]   Reynolds, R.A., Mirkin, C.A., and Letsinger, R.L. (2000). Homogeneous, nanoparticle-based quantitative colorimetric detection of oligonucleotides. *J. Amer. Chem. Soc.* **122**:(15), 3795–3796.

[4]   Gruttner, C., Teller, J., and Schutt, W. (1997). In: *Scientific and Clinical Applications of Magnetic Carriers*. U. Häfeli, W. Schütt, J. Teller, and M. Zborowski (Eds.) New York: Plenum, p. 53.

[5]   Bruchez, M., Moronne, M., Gin, P.,Weiss, S., and Alivisatos, A.P. (1998). Semiconductor nanocrystals as fluorescent biological labels. *Science* **281**:(5385), 2013–2016.

[6]   Chan, W.C.W. and Nie, S.M. (1998). Quantum dot bioconjugates for ultrasensitive nonisotopic detection. *Science* **281**:(5385), 2016–2018.

[7]   Davis, S.A., Breulmann, M., Rhodes, K.H., Zhang, B., and Mann, S. (2001). Template-directed assembly using nanoparticle building blocks: A nanotectonic approach to organized materials. *Chem. Mater.* **13**:(10), 3218–3226.

[8]   Nie, S.M. and Emery, S.R. (1997). Probing single molecules and single nanoparticles by surface-enhanced Raman scattering. *Science* **275**:(5303), 1102–1106.

[9]   Emery, S.R., Haskins, W.E., and Nie, S.M. (1998). Direct observation of size-dependent optical enhancement in single metal nanoparticles. *J. Amer. Chem. Soc.* **120**:(31), 8009–8010.

[10] Shipway, A.N., Katz, E., and Willner, I. (2000). Nanoparticle arrays on surfaces for electronic, optical, and sensor applications. *Chemphyschem* **1**:(1), 18–52.

[11] Daniel, M.C. and Astruc, D. (2004). Gold nanoparticles: Assembly, supramolecular chemistry, quantum-size-related properties, and applications toward biology, catalysis, and nanotechnology. *Chem. Rev.* **104**(1), 293–346.

[12] Turkevitch, J., Stevenson, P.C., and Hillier, J. (1951). Nucleation and growth Process in the synthesis of colloidal gold. *Discuss. Faraday Soc.* **11**: 55–75.

[13] Hostetler, M.J., Wingate, J.E., Zhong, C.J., Harris, J.E., Vachet, R.W., Clark, M.R., Londono, J.D., Green, S.J., Stokes, J.J., Wignall, G.D., Glish, G.L., Porter, M.D., Evans, N.D., and Murray, R.W. (1998). Alkanethiolate gold cluster molecules with core diameters from 1.5 to 5.2 nm: Core and monolayer properties as a function of core size. *Langmuir* **14**:(1), 17–30.

[14] Cassagneau, T. and Fendler, J.H. (1999). Preparation and layer-by-layer self-assembly of silver nanoparticles capped by graphite oxide nanosheets. *J. Phys. Chem. B* **103**:(11), 1789–1793.

[15] Bright, R.M., Musick, M.D., and Natan, M.J. (1998). Preparation and characterization of Ag colloid monolayers. *Langmuir* **14**:(20), 5695–5701.

[16] Schmid, G. (1992). Large clusters and colloids—Metals in the embryonic state. *Chem. Reviews* **92**:(8), 1709–1727.

[17] Toshima, N. and Yonezawa, T. (1998). Bimetallic nanoparticles–Novel materials for chemical and physical applications. *New J. Chem.* **22**:(11), 1179–1201.

[18] Keating, C.D., Kovaleski, K.M., and Natan, M.J. (1998). Protein: Colloid conjugates for surface enhanced Raman scattering: Stability and control of protein orientation. *J. Phys. Chem. B* **102**:(47), 9404–9413.

[19] Kamat, P.V. and Shanghavi, B. (1997). Interparticle electron transfer in metal/semiconductor composites. Picosecond dynamics of CdS-capped gold nanoclusters. *J. Phys. Chem. B* **101**:(39), 7675–7679.

[20] Roos, C., Schmidt, M., Ebenhoch, J., Baumann, F., Deubzer, B., and Weis, J. (1999). Design and synthesis of molecular reactors for the preparation of topologically trapped gold clusters. *Adv. Mater.* **11**:(9), 761–766.

[21] Freeman, R.G., Hommer, M.B., Grabar, K.C., Jackson, M.A., and Natan, M.J. (1996). Ag-clad Au nanoparticles: Novel aggregation, optical, and surface-enhanced Raman scattering properties. *J. Phys. Chem.* 100:(2), 718–724.

[22] Kim, D.K., Zhang, Y., Voit, W., Rao, K.V., and Muhammed, M. (2001). Synthesis and characterization of surfactant-coated superparamagnetic monodispersed iron oxide nanoparticles. *J. Magnet. Magnetic Mater.* **225**:(1–2), 30–36.

[23] Tronc, E., Belleville, P., Jolivet, J.P., and Livage, J. (1992). Transformation of ferric hydroxide into spinel by Fe(Ii) adsorption. *Langmuir* **8**:(1), 313–319.

[24] Nakatsuka, K. and Jeyadevan, B. (1994). Initial susceptibilities of magnetic fluids dispersing Mn–Zn ferrite and cobalt ferrite particles. *IEEE Trans. Magnet.* **30**:(6), 4671–4673.

[25] Davies, K.J., Wells, S., and Charles, S.W. (1993). The effect of temperature and oleate adsorption on the growth of maghemite particles. *J. Magnet. Magnetic Mater.* **122**:(1–3), 24–28.

[26] Davies, K.J., Wells, S., Upadhyay, R.V., Charles, S.W., Ogrady, K., Elhilo, M., Meaz, T., and Morup, S. (1995). The observation of multiaxial anisotropy in ultrafine

cobalt ferrite particles used in magnetic fluids. *J. Magnet. Magnetic Mater.* **149**:(1–2), 14–18.

[27]   Kim, D.K., Zhang, Y., Voit, W., Kao, K.V., Kehr, J., Bjelke, B., and Muhammed, M. (2001). Superparamagnetic iron oxide nanoparticles for bio-medical applications. *Scripta Mater.* **44**:(8–9), 1713–1717.

[28]   Murray, C.B., Norris, D.J., and Bawendi, M.G. (1993). Synthesis and characterization of nearly monodisperse Cde (E = S, Se, Te) semiconductor nanocrystallites. *J. Amer. Chem. Soc.* **115**:(19), 8706–8715.

[29]   Talapin, D.V., Haubold, S., Rogach, A.L., Kornowski, A., Haase, M., and Weller, H. (2001). A novel organometallic synthesis of highly luminescent CdTe nanocrystals. *J. Phys. Chem. B* 105:(12), 2260–2263.

[30]   Talapin, D.V., Rogach, A.L., Kornowski, A., Haase, M., and Weller, H. (2001). Highly luminescent monodisperse CdSe and CdSe/ZnS nanocrystals synthesized in a hexadecylamine-trioctylphosphine oxide-trioctylphospine mixture. *Nano Lett.* **1**:(4), 207–211.

[31]   Qu, L.H., Peng, Z.A., and Peng, X.G. (2001). Alternative routes toward high quality CdSe nanocrystals. *Nano Lett.* 1:(6), 333–337.

[32]   Hines, M.A. and Guyot-Sionnest, P. (1996). Synthesis and characterization of strongly luminescing ZnS-Capped CdSe nanocrystals. *J. Phys. Chem.* **100**:(2), 468–471.

[33]   Peng, X.G., Schlamp, M.C., Kadavanich, A.V., and Alivisatos, A.P. (1997). Epitaxial growth of highly luminescent CdSe/CdS core/shell nanocrystals with photostability and electronic accessibility. *J. Amer. Chem. Soc.* **119**:(30), 7019–7029.

[34]   Lopez-Quintela, M.A., Tojo, C., Blanco, M.C., Rio, L.G., and Leis, J.R. (2004). Microemulsion dynamics and reactions in microemulsions. *Curr. Opin. Colloid Interface Sci.* **9**:(3–4), 264–278.

[35]   Okubo, M., Minami, H., and Morikawa, K. (2003). Influence of shell strength on shape transformation of micron-sized, monodisperse, hollow polymer particles. *Colloid Polym. Sci.* **281**:(3), 214–219.

[36]   Larpent, C., Bernard, E., Richard, J., and Vaslin, S. (1997). Synthesis of functionalized nanoparticles via copolymerization in microemulsions and surface reactions. *React. Function. Polym.* **33**:(1), 49–59.

[37]   Tang, L.S., Yang, J.W., Zhang, S.F., Yang, J.Z., and Wu, Y.M. (2004). Emulsifier-minor emulsion copolymerization of BA-MMA-St-MAA (or AA)-N-MA. *J. Appl. Polym. Sci.* **92**:(5), 2923–2929.

[38]   Gao, H.F., Zhao, Y.Q., Fu, S.K., Li, B., and Li, M.Q. (2002). Preparation of a novel polymeric fluorescent nanoparticle. *Colloid Polym. Sci.* **280**:(7), 653–660.

[39]   Song, G.P., Bo, J., and Guo, R. (2004). The characterization and property of polystyrene compounding of alpha-Fe2O3 in the nano-scale. *Colloid Polym. Sci.* **282**:(6), 656–660.

[40]   Allemann, E., Gurny, R., and Doelker, E. (1993). Drug-loaded nanoparticles—preparation methods and drug targeting issues. *Euro. J. Pharmaceut. Biopharmaceut.* **39**:(5), 173–191.

[41]   Andrade, J.D., Hlady, V., and Jeon, S.I. (1996). Poly(ethylene oxide) and protein resistance—Principles, problems, and possibilities. In: *Hydrophilic Polymers*, Vol. 248, pp. 51–59.

[42]   Rogach, A.L., Kornowski, A., Gao, M.Y., Eychmuller, A., and Weller, H. (1999). Synthesis and characterization of a size series of extremely small thiol-stabilized CdSe nanocrystals. *J. Phys. Chem. B* **103**:(16), 3065–3069.

[43] Pathak, S., Choi, S.K., Arnheim, N., and Thompson, M.E. (2001). Hydroxylated quantum dots as luminescent probes for in situ hybridization. *J. Amer. Chem. Soc.* **123**:(17), 4103–4104.

[44] Aldana, J., Wang, Y.A., and Peng, X.G. (2001). Photochemical instability of CdSe nanocrystals coated by hydrophilic thiols. *J. Amer. Chem. Soc.* **123**:(36), 8844–8850.

[45] Willard, D.M., Carillo, L.L., Jung, J., and Van Orden, A. (2001). CdSe-ZnS quantum dots as resonance energy transfer donors in a model protein-protein binding assay. *Nano Lett.* **1**:(9), 469–474.

[46] Chen, Y.F. and Rosenzweig, Z. (2002). Luminescent CdSe quantum dot doped stabilized micelles. *Nano Lett.* **2**:(11), 1299–1302.

[47] Gerion, D., Pinaud, F., Williams, S.C., Parak, W.J., Zanchet, D., Weiss, S., and Alivisatos, A.P. (2001). Synthesis and properties of biocompatible water-soluble silica-coated CdSe/ZnS semiconductor quantum dots. *J. Phys. Chem. B* **105**:(37), 8861–8871.

[48] Parak, W.J., Gerion, D., Zanchet, D., Woerz, A.S.. Pellegrino, T.. Micheel, C., Williams, S.C., Seitz, M., Bruehl, R.E., Bryant, Z., Bustamante, C., Bertozzi, C.R., and Alivisatos, A.P. (2002). Conjugation of DNA to silanized colloidal semiconductor nanocrystalline quantum dots. *Chem. Mater.* **14**:(5), 2113–2119.

[49] Bailey, R.E., Smith, A.M., and Nie, S.M. (2004). Quantum dots in biology and medicine. *Physica E-Low-Dimen.Syst. Nanostruct.* **25**:(1), 1–12.

[50] Wu, X.Y., Liu, H.J., Liu, J.Q., Haley, K.N., Treadway, J.A., Larson, J.P., Ge, N.F., Peale, F., and Bruchez, M.P. (2003). Immunofluorescent labeling of cancer marker Her2 and other cellular targets with semiconductor quantum dots. *Nature Biotechnol.* **21**:(1), 41–46.

[51] Dubertret, B., Skourides, P., Norris, D.J., Noireaux, V., Brivanlou, A.H., and Libchaber, A. (2002). In vivo imaging of quantum dots encapsulated in phospholipid micelles. *Science* **298**:(5599), 1759–1762.

[52] Niemeyer, C.M. (2001). Nanoparticles, proteins, and nucleic acids: Biotechnology meets materials science. *Angew. Chem. Int. Edit.* **40**:(22), 4128–4158.

[53] Katz, E. and Willner, I. (2004). Integrated nanoparticle-biomolecule hybrid systems: Synthesis, properties, and applications. *Angew. Chem. Int. Edit.* **43**:(45), 6042–6108.

[54] Shenton, W., Davis, S.A., and Mann, S. (1999). Directed self-assembly of nanoparticles into macroscopic materials using antibody-antigen recognition. *Adv. Mater.* **11**:(6), 449–452.

[55] Broderick, J.B., Natan, M.J., Ohalloran, T.V., and Vanduyne, R.P. (1993). Evidence for retention of biological-activity of a nonheme iron enzyme adsorbed on a silver colloid—a surface-enhanced resonance raman-scattering study. *Biochemistry* **32**:(50), 13771–13776.

[56] Macdonald, I.D.G. and Smith, W.E. (1996). Orientation of cytochrome c adsorbed on a citrate-reduced silver colloid surface. *Langmuir* **12**:(3), 706–713.

[57] Rospendowski, B.N., Kelly, K., Wolf, C.R., and Smith, W.E. (1991). Surface-enhanced resonance raman-scattering from cytochromes-p-450 adsorbed on citrate-reduced silver sols. *J. Amer. Chem. Soc.* **113**:(4), 1217–1225.

[58] Mattoussi, H., Mauro, J.M., Goldman, E.R., Anderson, G.P., Sundar, V.C., Mikulec, F.V., and Bawendi, M.G. (2000). Self-assembly of CdSe-ZnS quantum dot bioconjugates using an engineered recombinant protein. *J. Amer. Chem. Soc.* **122**:(49), 12142–12150.

[59] Mahtab, R., Rogers, J.P., and Murphy, C.J. (1995). Protein-sized quantum-dot luminescence can distinguish between straight, bent, and kinked oligonucleotides. *J. Amer. Chem. Soc*. **117**:(35), 9099–9100.

[60] Mahtab, R., Rogers, J.P., Singleton, C.P., and Murphy, C.J. (1996). Preferential adsorption of a "kinked" DNA to a neutral curved surface: Comparisons to and implications for nonspecific DNA-protein interactions. *J. Amer. Chem. Soc.* **118**:(30), 7028–7032.

[61] Mahtab, R., Harden, H.H., and Murphy, C.J. (2000). Temperature- and salt-dependent binding of long DNA to protein-sized quantum dots: Thermodynamics of "inorganic protein"-DNA interactions. *J. Amer. Chem. Soc.* **122**:(1), 14–17.

[62] Lakowicz, J.R., Gryczynski, I., Gryczynski, Z., Nowaczyk, K., and Murphy, C.J. (2000). Time-resolved spectral observations of cadmium-enriched cadmium sulfide nanoparticles and the effects of DNA oligomer binding. *Analyt. Biochem.* **280**:(1), 128–136.

[63] Bigham, S.R. and Coffer, J.L. (2000). Thermochemical passivation of DNA-stabilized Q-cadmium sulfide nanoparticles. *J. Cluster Sci.* **11**:(2), 359–372.

[64] Caruso, F. (2001). Nanoengineering of particle surfaces. *Adv. Mater.* **13**:(1), 11–22.

[65] Hayat, M.A. (1989). *Colloidal Gold: Principles, Methods, and Applications*, New York: Academic.

[66] Ghosh, S.S., Kao, P.M., McCue, A.W., and Chappelle, H.L. (1990). Use of maleimide-thiol coupling chemistry for efficient syntheses of oligonucleotide-enzyme conjugate hybridization probes. *Bioconjug. Chem.* **1**:(1), 71–76.

[67] Droz, E., Taborelli, M., Descouts, P., Wells, T.N.C., and Werlen, R.C. (1996). Covalent immobilization of immunoglobulins G and Fab′ fragments on gold substrates for scanning force microscopy imaging in liquids. *J. Vacuum Sci. Technol. B* **14**:(2), 1422–1426.

[68] Hong, H.G., Bohn, P.W., and Sligar, S.G. (1993). Optical Determination Of Surface-Density In Oriented Metalloprotein Nanostructures. *Analyt. Chem.* **65**:(11), 1635–1638.

[69] Hong, H.G., Jiang, M., Sligar, S.G., and Bohn, P.W. (1994). Cysteine-specific surface tethering of genetically-engineered cytochromes for fabrication of metalloprotein nanostructures. *Langmuir* **10**:(1), 153–158.

[70] Firestone, M.A., Shank, M.L., Sligar, S.G., and Bohn, P.W. (1996). Film architecture in biomolecular assemblies. Effect of linker on the orientation of genetically engineered surface-bound proteins. *J. Amer. Chem. Soc.* **118**:(38), 9033–9041.

[71] Kanno, S., Yanagida, Y., Haruyama, T., Kobatake, E., and Aizawa, M. (2000). Assembling of engineered IgG-binding protein on gold surface for highly oriented antibody immobilization. *J. Biotechnol.* **76**:(2–3), 207–214.

[72] Park, S.J., Lazarides, A.A., Mirkin, C.A., Brazis, P.W., Kannewurf, C.R., and Letsinger, R.L. (2000). The electrical properties of gold nanoparticle assemblies linked by DNA. *Angew. Chem. Int. Edit.* **39**:(21), 3845–3848.

[73] Demers, L.M., Mirkin, C.A., Mucic, R.C., Reynolds, R.A., Letsinger, R.L., Elghanian, R., and Viswanadham, G. (2000). A fluorescence-based method for determining the surface coverage and hybridization efficiency of thiol-capped oligonucleotides bound to gold thin films and nanoparticles. *Analyt. Chem.* **72**:(22), 5535–5541.

[74] Mirkin, C.A., Letsinger, R.L., Mucic, R.C., and Storhoff, J.J. (1996). A DNA-based method for rationally assembling nanoparticles into macroscopic materials. *Nature* **382**:(6592), 607–609.

[75]   Mitchell, G.P., Mirkin, C.A., and Letsinger, R.L. (1999). Programmed assembly of DNA functionalized quantum dots. *J. Amer. Chem. Soc.* **121**:(35), 8122–8123.

[76]   Letsinger, R.L., Elghanian, R., Viswanadham, G., and Mirkin, C.A. (2000). Use of a steroid cyclic disulfide anchor in constructing gold nanoparticle-oligonucleotide conjugates. *Bioconjug. Chem.* **11**:(2), 289–291.

[77]   Bower, C.K., Xu, Q., and McGuire, J. (1998). Activity losses among T4 lysozyme variants after adsorption to colloidal silica. *Biotechnol. Bioeng.* **58**:(6), 658–662.

[78]   Vertegel, A.A., Siegel, R.W., and Dordick, J.S. (2004). Silica nanoparticle size influences the structure and enzymatic activity of adsorbed lysozyme. *Langmuir* **20**:(16), 6800–6807.

[79]   Kondo, A. and Mihara, J. (1996). Comparison of adsorption and conformation of hemoglobin and myoglobin on various inorganic ultrafine particles. *J. Colloid Interface Sci.* **177**:(1), 214–221.

[80]   Ho, C.H., Limberis, L., Caldwell, K.D., and Stewart, R.J. (1998). A metal-chelating pluronic for immobilization of histidine-tagged proteins at interfaces: Immobilization of firefly luciferase on polystyrene beads. *Langmuir* **14**:(14), 3889–3894.

[81]   Wu, C.W., Lee, J.G., and Lee, W.C. (1998). Protein and enzyme immobilization on non-porous microspheres of polystyrene. *Biotechnol. Appl. Biochem.* **27**: 225–230.

[82]   Dolitzky, Y., Sturchak, S., Nizan, B., Sela, B.A., and Margel, S. (1994). Synthesis, characterization, and use of immobilized polyacrolein microspheres in diagnostics—a model determination of alpha(1)-antitrypsin in human serum. *Analyt. Biochem.* **220**:(2), 257–267.

[83]   Murray, C.B., Kagan, C.R., and Bawendi, M.G. (1995). Self-organization of cdse nanocrystallites into 3-dimensional quantum-dot superlattices. *Science* **270**:(5240), 1335–1338.

[84]   Wang, Z.L. (1998). Structural analysis of self-assembling nanocrystal superlattices. *Adv. Mater.* **10**:(1), 13–30.

[85]   Collier, C.P., Saykally, R.J., Shiang, J.J., Henrichs, S.E., and Heath, J.R. (1997). Reversible tuning of silver quantum dot monolayers through the metal-insulator transition. *Science* **277**:(5334), 1978–1981.

[86]   Li, M., Schnablegger, H., and Mann, S. (1999). Coupled synthesis and self-assembly of nanoparticles to give structures with controlled organization. *Nature* **402**:(6760), 393–395.

[87]   Brust, M., Bethell, D., Schiffrin, D.J., Kiely, and C.J. (1995). Novel gold-dithiol nano-networks with nonmetallic electronic-properties. *Adv. Mater.* **7**:(9), 795–797.

[88]   Fritz, J., Baller, M.K., Lang, H.P., Rothuizen, H., Vettiger, P., Meyer, E., Guntherodt, H.J., Gerber, C., and Gimzewski, J.K. (2000). Translating biomolecular recognition into nanomechanics. *Science* **288**:(5464), 316–318.

[89]   Niemeyer, C.M., Ceyhan, B., Gao, S., Chi, L., Peschel, S., and Simon, U. (2001). Site-selective immobilization of gold nanoparticles functionalized with DNA oligomers. *Colloid Polym. Sci.* **279**:(1), 68–72.

[90]   Gerion, D., Parak, W.J., Williams, S.C., Zanchet, D., Micheel, C.M., and Alivisatos, A.P. (2002). Sorting fluorescent nanocrystals with DNA. *J. Amer. Chem. Soc.* **124**:(24), 7070–7074.

[91]   Park, S.J., Lazarides, A.A., Mirkin, C.A., and Letsinger, R.L. (2001). Directed assembly of periodic materials from protein and oligonucleotide-modified nanoparticle building blocks. *Angew. Chem. Int. Edit.* **40**:(15), 2909–2912.

[92]   Alivisatos, A.P., Johnsson, K.P., Peng, X.G., Wilson, T.E., Loweth, C.J., Bruchez, M.P., and Schultz, P.G. (1996). Organization of 'nanocrystal molecules' using DNA. *Nature* **382**:(6592), 609–611.

[93]   Loweth, C.J., Caldwell, W.B., Peng, X.G., Alivisatos, A.P., and Schultz, P.G. (1999). DNA-based assembly of gold nanocrystals. *Angew. Chem. Int. Edit.* **38**:(12), 1808–1812.

[94]   Sandhage, K.H., Dickerson, M.B., Huseman, P.M., Caranna, M.A., Clifton, J.D., Bull, T.A., Heibel, T.J., Overton, W.R., and Schoenwaelder, M.E.A. (2002). Novel, bioclastic route to self-assembled, 3D, chemically tailored meso/nanostructures: Shape-preserving reactive conversion of biosilica (diatom) microshells. *Adv. Mater.* **14**:(6), 429–433.

[95]   Rosi, N.L., Thaxton, C.S., and Mirkin, C.A. (2004). Control of nanoparticle assembly by using DNA-modified diatom templates. *Angew. Chem. Int. Edit.* **43**:(41), 5500–5503.

[96]   Torimoto, T., Yamashita, M., Kuwabata, S., Sakata, T., Mori, H., and Yoneyama, H. (1999). Fabrication of CdS nanoparticle chains along DNA double strands. *J. Phys. Chem. B* **103**:(42), 8799–8803.

[97]   Kumar, A., Pattarkine, M., Bhadbhade, M., Mandale, A.B., Ganesh, K.N., Datar, S.S., Dharmadhikari, C.V., and Sastry, M. (2001). Linear superclusters of colloidal gold particles by electrostatic assembly on DNA templates. *Adv. Mate.* **13**:(5), 341–344.

[98]   Sastry, M., Kumar, A., Datar, S., Dharmadhikari, C.V., and Ganesh, K.N. (2001). DNA-mediated electrostatic assembly of gold nanoparticles into linear arrays by a simple drop-coating procedure. *Appl. Phys. Lett.s* **78**:(19), 2943–2945.

[99]   Warner, M.G. and Hutchison, J.E. (2003). Linear assemblies of nanoparticles electrostatically organized on DNA scaffolds. *Nature Mater.* **2**:(4), 272–277.

[100] Wang, G.L., and Murray, R.W. (2004). Controlled assembly of monolayer-protected gold clusters by dissolved DNA. *Nano Lett.* **4**:(1), 95–101.

[101] Davis, S.A., Patel, H.M., Mayes, E.L., Mendelson, N.H., Franco, G., and Mann, S. (1998). Brittle bacteria: A biomimetic approach to the formation of fibrous composite materials. *Chem. Mater.* **10**:(9), 2516–2524.

[102] Davis, S.A., Burkett, S.L., Mendelson, N.H., and Mann, S. (1997). Bacterial templating of ordered macrostructures in silica and silica-surfactant mesophases. *Nature* **385**:(6615), 420–423.

[103] Shenton, W., Pum, D., Sleytr, U.B., and Mann, S. (1997). Synthesis of cadmium sulphide superlattices using self-assembled bacterial S-layers. *Nature* **389**(6651), 585–587.

[104] Shenton, W., Douglas, T., Young, M., Stubbs, G., and Mann, S. (1999). Inorganic-organic nanotube composites from template mineralization of tobacco mosaic virus. *Adv. Mater.* **11**:(3), 253–256.

[105] Mao, C.B., Solis, D.J., Reiss, B.D., Kottmann, S.T., Sweeney, R.Y., Hayhurst, A., Georgiou, G., Iverson, B., and Belcher, A.M. (2004). Virus-based toolkit for the directed synthesis of magnetic and semiconducting nanowires. *Science* **303**:(5655), 213–217.

[106] Mamedov, A.A. and Kotov, N.A. (2000). Free-standing layer-by-layer assembled films of magnetite nanoparticles. *Langmuir* **16**:(13), 5530–5533.

[107] Ai, H., Jones, S.A., and Lvov, Y.M. (2003). Biomedical applications of electrostatic layer-by-layer nano-assembly of polymers, enzymes, and nanoparticles. *Cell Biochem. Biophys.* **39**:(1), 23–43.

[108]   Phadtare, S., Kumar, A., Vinod, V.P., Dash, C., Palaskar, D.V., Rao, M., Shukla, P.G., Sivaram, S., and Sastry, M. (2003). Direct assembly of gold nanoparticle "shells" on polyurethane microsphere "cores" and their application as enzyme immobilization templates. *Chem. Mater.* **15**:(10), 1944–1949.

[109]   Fang, M., Grant, P.S., McShane, M.J., Sukhorukov, G.B., Golub, V.O., and Lvov, Y.M. (2002). Magnetic bio/nanoreactor with multilayer shells of glucose oxidase and inorganic nanoparticles. *Langmuir* **18**:(16), 6338–6344.

[110]   Wang, C. and Zhang, Y. (2005). Protein micropatterning via self-assembly of nanoparticles. *Adv. Mater.* **17**:(2), 150–153.

[111]   Zhao, D.Y., Huo, Q.S., Feng, J.L., Chmelka, B.F., and Stucky, G.D. (1998). Non-ionic triblock and star diblock copolymer and oligomeric surfactant syntheses of highly ordered, hydrothermally stable, mesoporous silica structures. *J. Amer. Chem. Soc.* **120**:(24), 6024–6036.

[112]   Yang, P.D., Zhao, D.Y., Margolese, D.I., Chmelka, B.F., and Stucky, G.D. (1999). Block copolymer templating syntheses of mesoporous metal oxides with large ordering lengths and semicrystalline framework. *Chem. Mater.* **11**:(10), 2813–2826.

[113]   Antonelli, D.M. and Ying, J.Y. (1995). Synthesis of hexagonally packed meso-porous Tio2 by a modified sol-gel method. *Angew. Chem. Int. Edit. English* **34**:(18), 2014–2017.

[114]   Antonelli, D.M. and Ying, J.Y. (1996). Synthesis of a stable hexagonally packed mesoporous niobium oxide molecular sieve through a novel ligand-assisted templating mechanism. *Angew. Chem. Int. Edit. English* **35**:(4), 426–430.

[115]   Chen, L.Y., Jaenicke, S., and Chuah, G.K. (1997). Thermal and hydrothermal sta-bility of framework-substituted MCM-41 mesoporous materials. *Micropor. Mater.* **12**:(4–6), 323–330.

[116]   Tang, F.Q., Fudouzi, H., Uchikoshi, T., and Sakka, Y. (2004). Preparation of porous materials with controlled pore size and porosity. *J. Euro. Ceram. Soc.* **24**:(2), 341–344.

[117]   Chane-Ching, J.Y., Cobo, F., Aubert, D., Harvey, H.G., Airiau, M., and Corma, A. (2005). A general method for the synthesis of nanostructured large-surface-area materials through the self-assembly of functionalized nanoparticles. *Chem. A Euro. J.* **11**:(3), 979–987.

[118]   Caruso, F., Caruso, R.A., and Mohwald, H. (1998). Nanoengineering of inor-ganic and hybrid hollow spheres by colloidal templating. *Science* **282**:(5391), 1111–1114.

[119]   Wong, M.S., Cha, J.N., Choi, K.S., Deming, T.J., and Stucky, G.D. (2002). Assem-bly of nanoparticles into hollow spheres using block copolypeptides. *Nano Lett.* **2**:(6), 583–587.

[120]   Murthy, V.S., Cha, J.N., Stucky, G.D., and Wong, M.S. (2004). Charge-driven flocculation of poly(L-lysine)-gold nanoparticle assemblies leading to hollow mi-crospheres. *J. Amer. Chem. Soc.* **126**:(16), 5292–5299.

[121]   Yin, Y., Lu, Y., Gates, B., and Xia, Y. (2001). Synthesis and characterization of mesoscopic hollow spheres of ceramic materials with functionalized interior sur-faces. *Chem. Mater.* **13**:(4), 1146–1148.

[122]   Wulff, G. (1995). Molecular imprinting in cross-linked materials with the aid of molecular templates—A way towards artificial antibodies. *Angew. Chem. Int. Ed. English* **34**:(17), 1812–1832.

[123]   Mayes, A.G. and Mosbach, K. (1997). Molecularly imprinted polymers: use-
        ful materials for analytical chemistry? *Trac-Trends Analyt. Chem.* **16**:(6),
        321–332.
[124]   Vlasov, Y.A., Yao, N., and Norris, D.J. (1999). Synthesis of photonic crystals for
        optical wavelengths from semiconductor quantum dots. *Adv. Mater.* **11**:(2), 165–
        169.
[125]   Breulmann, M., Davis, S.A., Mann, S., Hentze, H.P., and Antonietti, M. (2000).
        Polymer-gel templating of porous inorganic macro-structures using nanoparticle
        building blocks. *Adv. Mater.* **12**:(7), 502–507.

15
Polymer Nanofibers for Biosensor Applications

S. Ramakrishna, Neeta L. Lala, Hota Garudadhwaj,
Ramakrishnan Ramaseshan, and V. K. Ganesh

15.1. Biosensors: Definition

A biosensor is a device that uses a biological element (e.g., enzyme, antibody, whole cell, etc.) to monitor the presence of various chemicals on a substrate by enabling highly specific interactions between biological molecules to be detected and utilized. Typically antibodies or enzymes are coupled to microelectronics to enable their interactions with the substances of interest to be monitored. The ability of biomolecules to react with very low concentrations of substances allows biosensors to be used in various applications such as the monitoring of pollutants in water, air, and soil, and in the detection of medically important molecules such as hormones, sugars, and peptides in body fluids.

The sensing part of a biosensor consists of a biological element, which is the bio-receptor, having remarkable properties concerning the specific molecular recognition of a target analyte as shown in Figure 15.1. The biological element is closely associated with a transducer that converts the physicochemical signal occurring during the molecular recognition phenomenon into an electrical signal.

In a biosensor, the biological element acts as an extremely selective filter compared to a chemical system. This makes the biosensor a powerful tool when a high selectivity is needed.

15.2. Classification and Types

Biosensors are classified into four categories as shown in Figure 15.2.

15.2.1. Electrochemical Sensors

The main types of electrochemical sensing techniques include:

1. *Potentiometry.* These sensors work by measuring the electrical potential developed by an electrode in an electrolyte solution at zero current flow. The Nernst
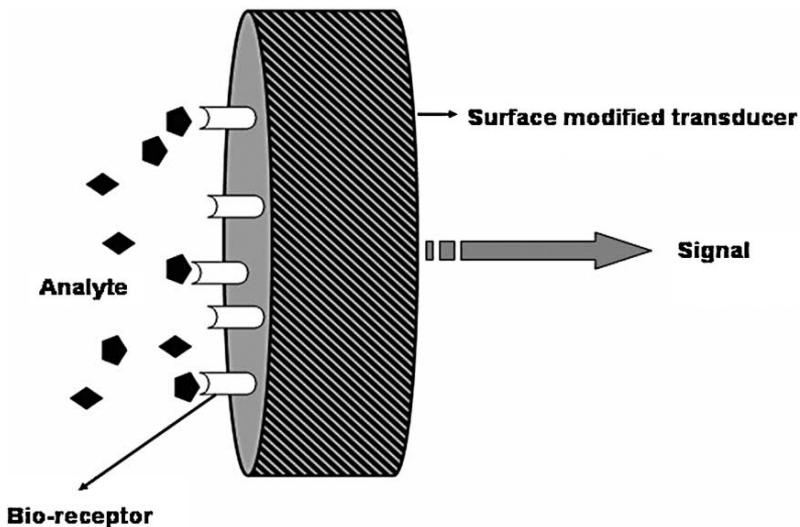
FIGURE 15.1. The biosensor principle.

equation, Eq. (1), is employed to relate the potential and concentration of the analyte to be measured.

$$E = E_o - RT/nF \ln[\text{oxidized}]/[\text{reduced}]. \tag{1}$$

2. *Voltammetry.* In a voltammetric sensor the concentration of an ion that is to be measured causes a change in the potential and thereby gets recorded as a function of output voltage. Various standard electrodes are used to generate the initial or zero potential, such as calomel electrodes, standard silver chloride electrodes, and others. If a dropping mercury electrode is used, the method is termed polarography.
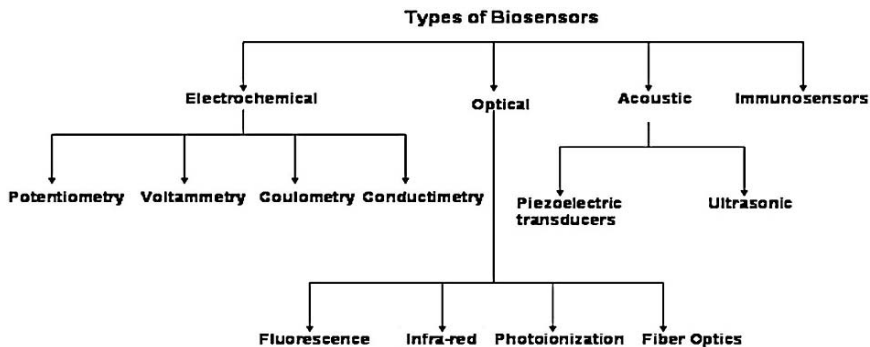
FIGURE 15.2. Classification of biosensors.

3. *Coulometry*. This is the terminology given when a current or electric charge is passed through a solution and by the use of Faraday's law it is related to the concentration of the measured substance. (Faraday's law essentially states that it takes 9.65×10^4 Coulombs of electrical charge to cause electrolysis of 1 mole of a univalent electrolyte species.)

4. *Conductimetry*. In this method the conductance of a solution is measured, using inert electrodes, alternating current, and an alternating null current. However, it is noteworthy that there is no electric current or potential gradient and the concentration of the analyte is measured as a function of the conductance of ions.

15.2.2. Optical Sensors

The principle of this sensor is that any change in the concentration of its surroundings produces a change in its optical properties. Therefore, there is a noticeable change in the amount of radiation reflected or emitted. Infrared, UV, and fluorescence are the spectra commonly used. Fluorescence is the most applied method for optical biosensors.

15.2.2.1. Fluorescence

Fluorescence is a luminescence emitted by certain substances due to the absorption of radiation at one wavelength and the almost instantaneous re-emission of radiation at another, usually longer wavelength. The emission stops almost as soon as the incident radiation is halted, thus distinguishing this phenomenon from phosphorescence, in which reradiation of light may continue for some time after the incident radiation is halted. The color of the radiated light typically differs from the apparent color of the material, as when green crystals of fluor spar afford blue reflections. It is due not to the difference in the color of a distinct surface layer, but to the power that the substance has of modifying the light incident upon it, by first absorbing the light to achieve an excited state and then radiating light to resume the ground energy level. The light emitted by fluorescent substances is in general of longer wavelength than the incident light. The radiation can also be induced by ionizing radiation that is not electromagnetic, such as alpha or beta rays and cathode rays. This property is possessed by fluorspar, uranium glass, sulphide of calcium, and many other substances. It finds use in analytical instruments to detect or measure radiation and in some commercial applications.

15.2.3. Acoustic Sensors

This works on the principle that any change in the environment concentration is reflected as a change in mass of the sensing interface which is then measured as a variation in vibration frequency. Sensors working by this principle are alternately termed "surface acoustic wave (SAW) resonators."

15.2.3.1. Piezoelectric Effect

The piezoelectric effect is due to the fact that certain crystals contain positively and negatively charged ions, which separate when the crystals are subjected to stress. Vibration of a crystal involves its passing from a deformed configuration through its equilibrium configuration to an opposite deformed configuration and then back through the equilibrium configuration to the original deformed configuration.

When the vibrating crystal is piezoelectric, this cycle of oscillating deformity produces an oscillating electrical field; the frequency of the electrical oscillation is identical to the vibrational frequency of the crystal. At the same time, placing a piezoelectric crystal in an oscillating electrical field causes it to vibrate at its frequency. This transfer of energy from the electric field to the crystal is highly inefficient except when the frequency of the oscillating electrical field is the same as the resonant frequency of the crystal.

The crystals most commonly used are 5, 9, and 10 MHz quartz of 10–16-mm disks, squares, or rectangles that are approximately 0.15-mm thick. The metal electrodes are 3000–10,000-Å thick and 3–8 mm in diameter and can be made of gold, silver, aluminum, or nickel.

The quartz wafer is sandwiched between two electrodes bonded to the wafer surface. These electrodes are used to induce an oscillating electrical field perpendicular to the surface of the water. The electrical field then produces a mechanical oscillation, a standing wave, in the bulk of the quartz wafer as described in Eq. (2). Mechanical oscillation of the crystal is maximum where the electrode pads overlap and diminishes rapidly in areas where the oscillating electrodes do not overlap.

$$\Delta f_0 = -\left[\frac{f_0(0)}{A X_q \rho_q}\right]\Delta m = -S\Delta m, \tag{2}$$

where

Δf_o = Change in the resonant frequency
f_o = Initial (applied) frequency at zero mass
A = Surface area of the resonator
X_q = Shear modulus of the quartz crystal
ρ_q = Density of the resonator
S = Proportionality constant.

15.2.4. Immunosensors

Immunosensors are biosensors that embody antibodies as their selective binding components. They take advantage of the high selectivity provided by the molecular recognition of antibodies. Because of significant differences in affinity constants antibodies may confer an extremely high sensitivity to immunosensors in comparison to enzyme sensors.

Immunosensors can be divided in principle into two categories: nonlabeled and labeled immunosensors. Nonlabeled immunosensors are designed so that the immunocomplex that is the antigen–antibody complex is directly determined

by measuring the physical changes induced by the formation of the complex. In contrast, in a labeled immunosensor a sensitively detectable label is incorporated.

15.3. Limitations of Biosensors

The typical disadvantages encountered using isolated biological components in biosensors, are primarily problems of stability, lifetime of the biological component, and limited dynamic ranges. In addition to this they may also need a longer time to return to the baseline signal after use and so reversibility may be a problem. There is also the possibility of variation in the responses of biosensors produced from different batches of cells or organisms. Therefore, the growth condition must be monitored closely to ensure that each batch is as similar as possible. Culture age, temperature, population, and aeration during the induction of the response can all affect the response of the biosensor.

15.4. Significance of Nanofibers for Biosensor Applications

Thin films are often employed in sensors in order to improve their performance. It is well known that the sensitivity of a film is proportional to the surface area of the film per unit mass. Thin films made of nanofibers (NF) have surface area approximately one to two orders of magnitude larger than continuous films and therefore their sensitivities are potentially as large. The large available surface is the advantage that polymer nanofibers have over the existing sensor substrates. Nanofibrous supports with designed hierarchical pore structure architecture can provide a unique environment for biosensing due to controlled fluid delivery, retention, and ability to facilitate direct electron transfer.

Two main nanofiber fabrication techniques were compared: particle coagulation spinning (PCS) and electrospinning [1]. Three types of nanofibrous supports were studied to test their applicability for biosensor packaging: nonporous fibers made of single-wall carbon nanotubes by PCS process, electrospun nanowebs made of conductive polymer nanofibers, and polymer nanofiber/carbon nanotube composite webs. It was concluded that electrospun fibers had better strength, uniformity during fabrication, and gave reproducible results.

Nanofiber films are used as a sensing interface for thickness shear mode (TSM) piezoelectric sensors. TSM sensors coated with nanofiber films made of poly-lactic acid-co-glycolic acid (PLAGA) polymers were studied under various ambient conditions and were reported to possess better sensitivities than their thin film counterparts [2]. For TSM resonators, the resolution varies linearly with the surface area of the sensing interface. Hence, polymer nanofiber would be an ideal material for this purpose.

Recently, efforts were undertaken in the production of nanofibers for electrochemical sensors as well. Metal ions such as Pd, Pt, and Au are coated or

electrodeposited onto the surface of the fibers to improve the conductivity and resolution. The literature shows that polymers such as polyaniline, polypyrrole, and polyamic acid have been electrospun and successfully used as sensing interfaces [3]. For electrochemical sensors, the resolution varied in proportion to the conductivity of the interface; in this case, it is the number of electrons transferred that govern the sensitivity. Therefore, nanofibers that have a very high surface area would be idealistic for electrochemical biosensors as well.

Optical sensors are relatively new and not much work has been carried out in this field. From first principles, the sensitivity of an optical sensor would depend on the amount of fluorescence emitted which in turn is proportional to the available area of the interface. Thus by change in morphology, if pores or pockets could be introduced the sensitivity would also increase proportionately. In the case of nanofibers this is inadvertent as the available area by itself is quite large and when porous fibers are used, the further increase is manifold. Thus, nanofibers would be the best-suited materials for fabrication of optical sensors.

Recent progress in biomedical technology has resulted in the development of novel sensor products with new applications. Modern biomedical sensors with advanced microfabrication and signal-processing techniques are becoming more and more accurate and inexpensive [4]. With the burden of accuracy and reliability removed, the focus is now on miniaturization of the bulky instrumentation and development of portable sensors. Also, a lot of work has been previously accomplished in developing various specific target molecules for different analytes that has exhausted all possibilities. So, the focus is again on miniaturization by detection of multianalytes on a single chip.

This idea is the base of the "lab-on-a-chip" projects that are presently being carried out in various laboratories across the world. Although microelectronics has sufficiently minimized the instrumentation and made it portable, the sensing interface is still critical as it forms the heart of the sensor. Therefore, no compromise can be had with regard to the available area of the sensor (which is proportional to the number of active sites). Hence the solution would be to adapt such a morphology that is small yet possesses a large surface area for interaction. The obvious key would be nanofibers. Nanofibers have been recently tested for biomedical applications as well as for fabrication of nanofiber-based immunosensors [5]. Specific target molecules such as antibodies can be tailored on the surface of the nanofibers at high concentrations. It is also possible to attach more than one antibody on the nanofiber mesh which would create a basis for multianalyte detection capability. All said, the nanofibers rule the sensor domain.

15.5. Biosensors from Polymer Nanofibers—Review

The section below presents a brief review of the existent nanofiber biosensor configurations. Starting from the glucose sensor which was the earliest sensor developed in the history of biosensing, each realm is being replaced with nanofibers for improving sensor properties. An outline of the modifications made by incorporation

of nanofibers, the sensor parameters studied, and the results are presented under each category.

15.5.1. Fabrication of Biosensors Using Polymer Nanofibers

Electrospinning [6] makes it possible to create self-supporting nonwoven meshes from polymer melts as well as lacy porous coatings on a variety of substrates. Membranes are one of the essential components of a biosensor. They are used for (1) preventing fouling, (2) eliminating interference, and (3) controlling the operating regime of the biosensor; for example, when a small molecule is the analyte, macromolecules such as proteins can be prevented from entering the active site.

The approach of fabrication [7] onto the nanofibers is highly sensitive to optical sensors [8]. Combining the two techniques of electrospinning and electrostatic layer-by-layer adsorption was made possible where a fluorescent probe was electrostatically assembled onto the surface of electrospun nanofibrous membranes whose fluorescence could be quenched on using extremely low concentrations of aqueous methyl viologen (MV_{2+}) and cytochrome C solutions. The high sensitivity is attributed to the high surface area-to-volume ratio of the electrospun membrane and efficient interaction between the fluorescent conjugate polymer and the analytes [9].

Virus-based micro- and nanofibers were fabricated using wet-spinning and electrospinning processes. When M13 viruses were blended with PVP fibers, an intact structure of the viruses was formed. These fibers demonstrated that novel biomaterials can be fabricated from a programmed organism to extend the dimension of engineered viruses into fibers providing useful biological functions and highly sensitive catalytic functions in the future for biomedical biosensor applications [10].

Madhugiri et al. [11] have employed a novel dual syringe electrospinning method to prepare a composite fiber network of a semiconducting, electroluminescent. polymer MEH-PPV and mesoporous SBA-15 silica. The idea behind using two different solutions was to make an interwoven network of fibers containing a polymer and a molecular sieve material and study the optical properties of the resulting composites. The composite fibers obtained by electrospinning MEH-PPV and SBA-15 silica together exhibit a blueshift in the emission, which can also be altered by introducing organic moieties into the inorganic material. The shift in emission is mainly attributed to non-aggregation of the polymer chains, which occurs due to the polymer chain conformation. The silica mesoporous fibers acted as a nanospacer thereby reducing interchain interactions, resulting in the blueshift in the emission. Hence, dual syringe electrospinning is a way to alter the optical properties of the fluorescent polymers in fibrous form, which will have interesting applications in molecular electronics.

There are several technologies proposed for urea detection through use of immobilized urease. Most of them offer a narrow detection limit in either low or high concentrations of urea. Srivastava et al. [12], described a urea biosensor utilizing

urease immobilized on gelatin beads. This system was successful at achieving long storage stability, with a half-life of 240 days. The sensors' drawbacks were a detection limit from 0.8 to 23 mM and a response time of 6 mins. Another sensing system proposed was on porous glass beads [13], presenting a linear relation between current and urea concentration within a narrow range of 0–600 μM urea solutions. The chemical field effect transistor with a pH-sensitive gate has been proposed due to the photosensitive layers of PVA. Sant et al. [14] detected urea between concentrations of 5 and 25 mM. Castillo-Ortega and Rodriguez [15] prepared electroconductive PAn–PBMA homogenous composite films by casting, offering the detection limits of small range 3–20 mM. Seki's group [16] used urea immobilized on SiO_2 film as a pH-sensitive layer in light addressable potentiometric sensors (LAPS) and once again had a narrow range of detection from 5 to 15 mM. No detailed discussion of longevity for the mentioned product was provided.

With increasing demand for nanotechnology, electrospinning became a novel technique; biocomposite nanofibers were electrospun using Urease with PVP solution [17]. The immobilized enzyme remained active inside the polymer solution. Most importantly, the reactivity was maintained inside the electrospun nonwoven mats. The electrospun membrane acted as catalyst in the hydrolysis with different concentrations of urea solutions. The proposed material connects the rising world of nanotechnology with the biosensing field offering cost-efficient urea-sensing material applicable in medical diagnosis and environmental and bio-industrial analysis. The biggest improvements are the fast response time, sensitivity to low concentrations of urea, and a more versatile design. This successful immobilization of urease implies reproducibility with other enzymes used for biosensing, such as glucose oxidase and horseradish peroxidase among others.

So, we begin with some preliminary work that has presently had success in fabricating a nanofiber-based system for glucose biosensor applications.

15.5.2. Glucose Sensor

15.5.2.1. Brief Classification

Ever since Clarke and Lyons, glucose sensing has come a very long way. The techniques for glucose measurement have also developed beyond capabilities. There are innumerable possibilities that one could follow to measure glucose concentration from a particular medium as classified in Figure 15.3.

15.5.2.2. Principle

Most of the reported sensors with which continuous measurements have been made are electrochemically based taking advantage of the reaction of glucose with oxygen.

The amperometric response of the sensor originates from the oxidation current of H_2O_2, which could be effectively measured to decipher glucose concentration

•Optical

•Acoustic

•Colorimetric

Glucose Sensors

•Thermoelectric

•Piezoelectric and   Immunosensors

•Electrochemical (Biosensors)

                                                    •Potentiometric

                               Enzyme Sensors   •Conductometric

                                                    •Amperometric   •H_2O_2 electrode

                                                                        •Oxygen electrode
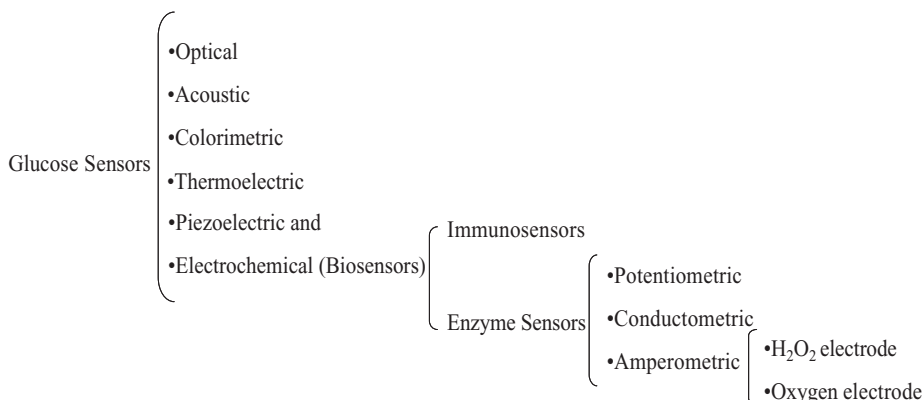
FIGURE 15.3. Classification for the measurement of a glucose sensor.

levels. Glucose oxidase (GOx) is an enzyme that catalyzes the oxidation of glucose as explained below:

$$C_6H_{12}O_6 + O_2 + H_2O \xrightarrow{(GO_X)} C_6H_{12}O_7 + H_2O_2 \qquad (3)$$

(glucose)

$$H_2O_2 \rightarrow 2e^- + 2H^+ + O_2 \qquad (4)$$
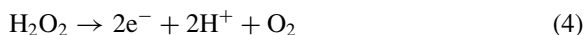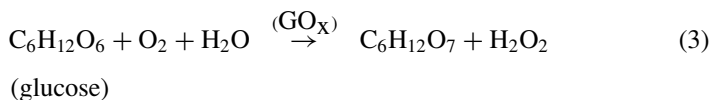
Glucose present in solution or any body fluid reacts with the oxidized form of the enzyme to form glucolactone/gluconic acid ($C_6H_{12}O_7$), with the evolution of two protons and electrons, thus reducing GOx on the electrode. Glucose oxidase has been selected as a model as it has been very well studied, and is stable, inexpensive, and practically applicable. The oxygen dissolved in the surrounding fluid reacts with GOx, accepting the aforementioned protons and electrons to form hydrogen peroxide and regenerating oxidized GOx, which is ready to react once more with glucose. To measure the amount of glucose, either one can measure the change in oxygen concentration in the solution or, as an alternative, the increase in H_2O_2 concentration. This choice turns out to be more reliable because the sensor is less sensitive to varying background oxygen concentrations in the sample. Either way, the glucose concentration can be directly correlated to the output of the potentiostat. The response time and sensitivity could be calculated by observing the output voltage/current with time.

15.5.2.3. Background Literature

The ability to detect, quickly and reliably, the presence or absence of specific chemicals can be a matter of life or death. Leaks of toxic gases, monitoring of glucose in the bloodstream, testing for harmful compounds in foods, and early alert of chemical and biological warfare agents all require reliable and sensitive sensing devices. The demand for such devices is ever more urgent and the

capability of many relevant technologies to build these devices is unprecedented. Due to the importance of glucose detection in diabetics, enzyme biosensors are important in clinical, environmental, and food analysis. They are becoming more and more important as analytical tools, for enzymes have the unique ability of quickly and accurately recognizing target molecules even in a complicated system. Determining the concentrations of glucose in blood has been recognized as an important clinical diagnostic test for diabetes during hyper- and hypoglycemic conditions. The diagnosis of diabetes requires a tight monitoring of blood glucose levels and electrochemical biosensors for glucose are playing a leading role in this direction [18]. Glucose monitoring systems can provide alarms greatly facilitating intensive glucose control regimes. The normal clinical range for glucose in blood is between 3.5 and 6.1 mM, and abnormal glucose levels can reach as high as 20 mM. Clark and Lyons developed the first enzyme electrode in 1962 [19], suggesting the coupling of enzymatic reaction to an electrochemical monitor, which was subsequently called an "enzyme electrode." From then on, it was established that it is possible to detect glucose in both serum and whole blood, however, in vivo measurements proved much more difficult.

A significant breakthrough occurred in the early 1980s, when self-monitoring of blood glucose became possible through the development of dry chemical strips for use with a single drop of blood. The resulting reaction could be followed by monitoring the formation of product spectrophotometrically or electrochemically. Recently, monitoring glucose by noninvasive means such as near-infrared technique [20], optical rotation [21], colorimetric [22], and fluorescence detection [23] to name but just a very few, has also been proposed which would eliminate the painful and annoying step of pricking the finger to obtain blood.

Biosensors such as Glucowatch are worn on the wrist, which when subjected to environmental conditions (temperature fluctuations, mechanical shocks, etc.) could adversely affect the sensor signal [24]. Other technologies, that are presently emerging include glucose-monitoring skin patches, which are deemed less painful than finger-pricking with a lancet. For practical application, the monitoring unit must be miniaturized to be compatible with its use as a wearable system. If patients are going to use these monitoring systems themselves, the system must be simple and inexpensive. A fundamental question is whether the sensor, which must necessarily be quite small, is properly sampling the site of implantation and whether this site is indicative of the region of our interest. Combining nanomaterials and biomolecules is of interest because nanoparticles can play an important role in immobilizing biomolecules due to the excellent biocompatibility and good conductivity.

Recently, many kinds of nanomaterials such as gold [25,26] and SiO2 nanoparticles [27–29] have been widely used in constructing electrochemical biosensors. Bharathi and co-workers [30] have demonstrated that gold nanoparticles can self-assemble both inside the network and on the surface of the silica gel. The gold nanoparticles immobilized by a silica gel three-dimensional network can act as

tiny conducting centers and facilitate the electron transfer [29]. Zhang et al. [31] have reported the gold nanoparticles can not only promote the electron transfer between the analyte and the electrode surface but could also act as a conducting base for the assembly of biomolecules. They can provide a favorable microenvironment for the active immobilization of GOx due to their excellent biocompatibility.

In addition, the combination of addressing with the high-affinity interaction of avidin–biotin (association constant $K_a = 10^{15}$ M^{-1}) leads to an affinity-driven immobilization protocol for enzymes involving solely a single attachment point that fully retains its biological activity [32–35].

15.5.2.4. Professor Ramakrishna Group's Results

Polymer nanofiber-based biosensors have been developed, based on the above-mentioned principle of the glucose sensor. Nylon-6 nanofibers have been electrospun, impregnated with Au nanoclusters (for increasing conductivity) and immobilized with glucose oxidase. The schematic diagram of the sensor is shown in Figure 15.4.

The results in Figures 15.5 to 15.7 show the fabrication of the biosensor at each stage. Avidin–biotin interaction was used to immobilize the enzyme onto the Nylon-6 nanofibers. Sensitivity was measured using electrochemical impedance spectroscopy. The results are also presented in the figures with comparative advantages over the existent sensor.
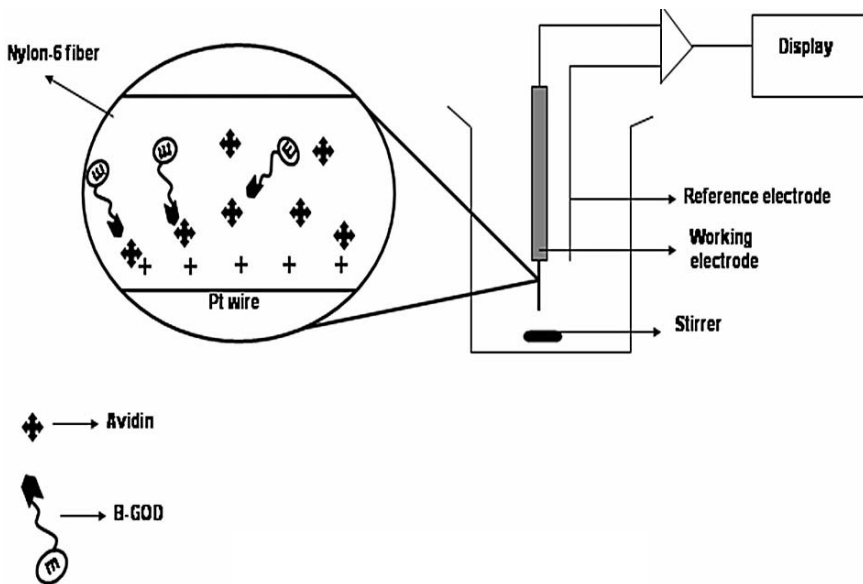
FIGURE 15.4. Schematic diagram for glucose biosensor.
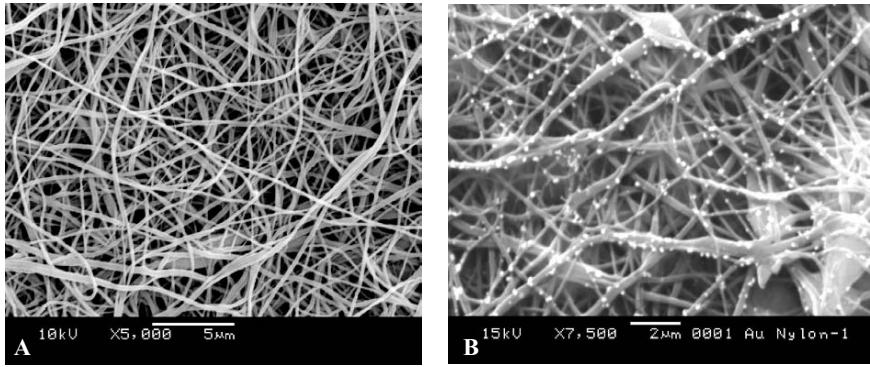
FIGURE 15.5. SEM micrographs of (A) electrospun Nylon-6, (B) (Au-Nylon-6).
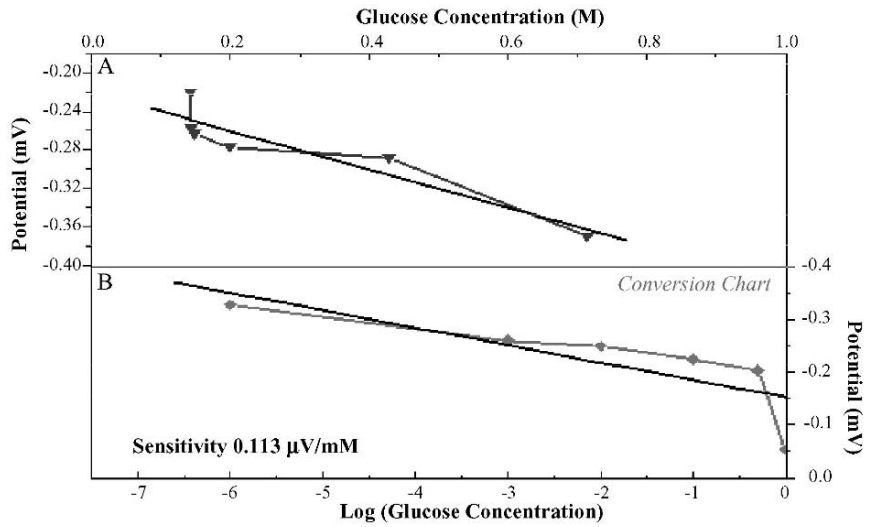
FIGURE 15.6. Shows the plot of (A) glucose concentration versus potential and (B) conversion chart of glucose concentration versus voltage for the nanofiber-based sensor.
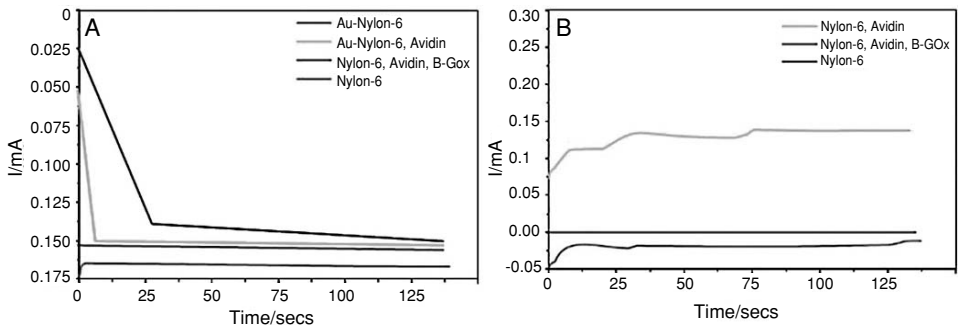
FIGURE 15.7. Transmembrane current measured (A) with and (B) without Au nanoparticles (higher currents in the presence of Au shows improved conductivity).

In brief the characteristics of our sensor are summarized as follows.

1. *Quick Response*: within 130 s.
2. *Accurate*: Glucose levels are found very accurately (fine resolution 0.113 µV/ mM compared to the existing nA levels); the measured values were found to be reproducible.
3. *Selective*: Minimum interference for lower concentrations implies high signal-to-noise ratio.
4. *Wide Range*: Works well from 1 M to 1 µM.
5. *Stable:* Membrane with immobilized enzyme is stable with time; experiments observed after two months gave results with less than 5% absolute error. The Pt wire was stored in the refrigerator at 4°C in phosphate buffer when not in use.
6. *Compatible:* For both in vivo as well as in vitro measurements, suits for continuous monitoring as well. Could be used as an implant beneath the skin for continuous monitoring.

15.6. Application

The application domains of biosensors can be broadly classified into two categories: biomedical and environmental. The typical applications are as follows.

15.6.1. Biomedical Application

15.6.1.1. Measurement of Metabolites

The initial impetus for advancing sensor technology came from the health care area, where it is now generally recognized that measurements of blood gases, ions, and metabolites are often essential and allow a better estimation of the metabolic state of a patient. In intensive care units, for example, patients frequently show rapid variations in biochemical levels that require an urgent remedial action. Also, in less severe patient handling, more successful treatment can be achieved by obtaining instant assays. At present, the list of the most commonly required instant analyses is not extensive. In practice, these assays are performed by analytical laboratories, where discrete samples are analyzed, frequently using the more traditional analytical techniques.

15.6.2. Environmental Monitoring

15.6.2.1. Air and Water Monitoring

Another assay situation that may involve a considerable degree of the unknown is that of environmental monitoring. The primary measurement medium here will be water or air, but the variety of target analytes is vast. At sites of potential pollution, such as in factory effluent, it would be desirable to install online real-time monitoring and alarms, aimed at specific analytes, but in many cases random or

discrete monitoring of both target species and general hazardous compounds would be sufficient. The possible analytes include biological oxygen demand (BOD) which provides a good indication of pollution, atmospheric acidity, and river water pH, detergent, herbicides, and fertilizers (organophosphates, nitrates, etc.). The survey of market potential has identified the increasing significance of this area and this is now substantiated by a strong interest from industry.

15.6.3. Multicomponent Analyzers

The potential for biosensor technology is enormous and is likely to revolutionize analysis and control of biological systems. It is possible therefore to identify very different analytical requirements and biosensor developments must be viewed under this constraint. It is often tempting to expect a single sensor aimed at a particular analyte to be equally applicable to online closed-loop operation in a fermenter and pinprick blood samples. In practice, however, the parallel development of several types of sensor, frequently employing very different measurement parameters, is more realistic.

15.7. Conclusion

This chapter gives a brief description of biosensors and their existing limitations. Much emphasis has been focused on the replacement of the sensing interface with polymer nanofibers and improvements in the sensor's performance have been highlighted. The various applications into which nanofiber-based biosensors could possibly fit have also been described. It is concluded that the polymer nanofibers have a great potential in sensor applications and the research needs exploration in greater detail.

References

[1]   Hong, K.H., Oh, K.W., and Kang, T.J. (2005). Preparation of conducting Nylon-6 electrospun fiber webs by the in situ polymerization of polyaniline. *J. Appl. Polymer. Sci*. **96:**(4), 983–991.

[2]   Kwoun, S.J., Lec, R.M., Han, B., and Ko, F.K. (2000). A novel polymer nanofiber interface for chemical sensor applications. In: *Proceedings of the 2000 IEEE/EIA International*, pp. 52–57.

[3]   Jianrong, C., Yuqing, M., Nongyue, H., Xiaohua, W., and Sijiao, L. (2004). Nanotechnology and biosensors. *Biotechnol. Adv.* **22**(7):505–518.

[4] Figeys, D. and Pinto, D. (2000). Lab-on-a-chip: A revolution in biological and med-ical sciences—A look at some of the basic concepts and novel components used to construct prototype devices. *Anal. Chem.* May 1, 330A–335A.

[5] Huang, J., Virji, S., Weiller, B.H., and Kaner, R.B. (2003). Polyaniline nanofibers: Facile synthesis and chemical sensors. *J. Am. Chem. Soc.* **125**(2): 314–315.

[6] Jayaraman, K., Kotaki, M., Zhang, Y., Mo, X., and Ramakrishna, S. (2004). Recent advances in polymer nanofibers, *J. Nanosci. Nanotech.* **4**:(1–2), 52– 65.

[7] Barker, S.A. (1987). Immobilization of biological component of biosensors. In: A.P.F. Turner, I. Karube, and G.S. Wilson (Eds.) *Biosensors: Fundamentals and Applications* Oxford:.Oxford Science, pp. 85–99.

[8] Wang, X., Drew, C., Lee, S.H., Senecal, K.J., Kumar, J., and Samuelson, L.A. (2002). Electrospun nanofibrous membranes for highly sensitive optical sensors. *Nano Lett.* **2**(11):1273–1275.

[9] Wang, X., Young-Gi, K., Christopher, D., Bon-Cheol, K., Jayant, K., and Lynne, A.S. (2004). Electrostatic assembly of conjugated polymer thin layers on electrospun nanofibrous membranes for biosensors. *Nano Lett.* **4**(2): 331–334.

[10] Seung-Wuk, L. and Angela, M.B. (2004). Virus-based fabrication of micro- and nanofibers using electospinning. *Nano Lett.* **4**(3): 387–390.

[11] Madhugiri, S., Dalton, A., Gutierrez, J., Ferraris, J.P., and Balkus, K.J., Jr. (2003). Electrospun MEH-PPV/SBA-15 composite nanofibers using a dual syringe method. *J. Am. Chem. Soc.* **125**(47):14531–14538.

[12] Srivastava, P.K., Kayastha, A.M., and Srinivasan (2001). Characterization of gelatin-immobilized pigeonpea urease and preparation of a new urea biosensor. *Biotechnol. Appl. Biochem.* **34**:55–62.

[13] Yoneyama, K., Fujino, Y., Osaka, T., and Satoh, I. (2001). Amperometric sensing system for the detection of urea by a combination of the pH-stat method and flow injection analysis. *Sens. Actuat. B.* **76**:152–157.

[14] Sant,W., Pourciel, M.L., Launay, J., Do Conto, T., Martinez, A., and Temple-Boyer, P. (2003). Development of chemical field effect transistors for the detection of urea. *Sens. Actuat. B* **95**(1-3):309–314.

[15] Castillo-Ortega, M.M., Rodriguez, D.E., Encinas J.C., Plascencia M., Mendez-Velarde A., and Olayo R. (2002). Conductometric uric acid and urea biosensor prepared from electroconductive polyaniline–poly (n-butyl methacry methacrylate) composites. *Sens. Actuat. B. Chem.* **85**(1-2):19–25.

[16] Seki, A., Ikeda, S., Kubo, I., and Karube, I. (1998). Biosensors based on light-addressable potentiometric sensors for urea, penicillin and glucose. *Anal. Chim. Acta.* **373:**(1), 9–13.

[17] Sawicka, K., Gouma P., and Simon, S. (2005). Electrospun biocomposite nanofibers for urea biosensing. *Sens. Actuat. B. Chem* **108**(1-2), 585 – 588.

[18] Wang, J. (2001). Glucose biosensor: 40 years of advances and challenges. *Electro-analysis.* **13**(12):983–988.

[19] Clark, L.C. and Lyones, C. (1962). Electrode systems for continuous monitoring in vascular surgery. *Acad. Sci.* **102**:29–45.

[20] Robinson M.R., Eaton, R. P., Haaland, D.M., Koepp, G.W., Thomas, E.V., Stallard, B.R., and Robinson, P.L. (1992). Noninvasive glucose monitoring in diabetic pa-tients: A preliminary evaluation. *Clin. Chem.* **38**:1618–1622.

[21] March, W.F., Rabinovitch, B., Adam, R., Wise, J.R., and Melton, M. (1982). Ocular glucose sensor. *Trans. Am. Soc. Artif. Intern. Organs* **28:**232–235.

[22] Clarke, W.L., Becker, D.J., Cox, D., Santiago, J.V., White, N.H., Betschart, J., Ecken-rode, K., Levandoski, L.A., Prusinki, E.A., Simineiro L. M., Snyder, A. L., Tideman, A.M., and Yaegar, T. (1988). Evaluation of a new system for self blood glucose monitoring. Diabetes. *Res. Clin. Pract.* **4**:209–214.

[23] Tolosa, L., Gryczynski, I., Eichhorn, L.R., Dattelbaum, J.D., Castellano, F.N., Rao, G., and Lakowicz, J.R. (1999). Glucose sensor for low-cost lifetime-based sensing using a genetically engineered protein. *Anal. Biochem.* **267**:114–120.

[24] Tierney, M.J., Tamada, J.A., Potts, R.O., Jovanovic, L., and Grag, S., and Cygnus Research Team. (2001). Clinical evaluation of the GlucoWatch ®_ biographer: A continual, noninvasive glucose monitor for patients with diabetes. *Biosens. Bioelectron.* **16**:621–629.

[25] Yu, A., Liang, Z., Cho, J., and Caruso, F. (2003). Nanostructured electrochemical sensor based on dense gold nanoparticle films. *Nano Lett.* **3**:1203–1207.

[26] Xiao, Y., Ju, H.X., and Chen, H.Y. (1999). Hydrogen peroxide sensor based on horseradish peroxidase-labeled Au colloids immobilized on gold electrode surface by cysteamine monolayer. *Anal. Chem. Acta.* **391**:73–82.

[27] Hilliard, L.R., Zhao, X., and Tan, W. (2002). Immobilization of oligonucleotides onto silica nanoparticles for DNA hybridization studies. *Anal. Chim. Acta.* **470**:51–56.

[28] Qhobosheane, M., Santra, S., Zhang, P., and Tan, W. (2001). Biochemically functionalized silica nanoparticles. *Analyst* **126**:1274–1278.

[29] Chen, Z.J., Ou, X.M., Tang, F.Q., and Jiang, L. (1996). Effect of nanometer particles on the adsorbability and enzymatic activity of glucose oxidase. *Colloids. Surf. B: Biointerf.* **7:**(3–4), 173–179.

[30] Bharathi, S., Nogami, M., and Ikeda, S. (2001). Novel electrochemical interfaces with a tunable kinetic barrier by self assembling organically modified silica gel and gold nanoparticles. *Langmuir* **17**:1–4.

[31] Zhang, S., Wang, N., Niu, Y., and Sun, C. (2005). Immobilization of glucose oxidase on gold nanoparticles modified Au electrode for the construction of biosensor. *Sens. Actuat. B* **109**: 367–374.

[32] Cosnier, S., Galland, B., Gondran, C., and Le Pellec, A. (1998). Electrogeneration of biotinylated functionalized polypyrroles for simple immobilization of enzymes. *Electroanalysis* **10**:808–813.

[33] Torres-Rodriguez, L.M., Roget, A., Billon, M., Bidan., G., and. Livache, T. (1998). Synthesis of biotin functionalized pyrrole and its electro polymerization: Toward a versatile avidin biosensor. *Chem. Commun.* **18**:1993–1994.

[34] Cosnier, S. and Lepellic, A. (1999). Poly (pyrrole–biotin): A new polymer for biomolecule grafting on electrode surfaces. *Electrochim. Acta* **44**:1833–1836.

[35] Cosnier, S., Stoytcheva, M., Senillou, A., Perrot, H., Furriel, R.P.M., and Leone, F.A. (1999). A biotinlyated conducting Polypyrrole for the spatially controlled construction of an amperometric biosensor. *Anal. Chem.* **71**:3692–3697.

16
High-Pressure Synthesis of Carbon Nanostructured Superhard Materials

V.D. Blank, S.G. Buga, G.A. Dubitsky, K.V. Gogolinsky, V.M. Prokhorov, N.R. Serebryanaya, and V.A. Popov

16.1. Introduction

The discovery of fullerenes with short C–C distances has revived hope for new superhard materials from carbon. Fullerenes are new allotropic forms of carbon with molecular structure. The fullerene molecules look like closed hollow spheres; their surface is lined with hexagons and pentagons from carbon atoms. The hexagon with atoms of carbon in its vertices is a structural element of both fullerenes and graphite.

Synthesis of fullerenes in condensed state (fullerites) opened up an opportunity not only to study the physical properties of a new material, but also enabled the development of new polymerized states by cycloaddition due to the rupture of the double bonds on the hexagons of adjacent molecules. Such polymerized phases should possess unique properties (high resistance to solvents, high strength and hardness) due to the formation of short covalent bonds between molecules instead of weak van der Waals bonds in molecular structures. The action of high pressures on a substance is the most efficient way of developing more dense modifications with short interatomic distances. It is well known that diamond is a polymorphic modification of carbon formed from graphite at high pressures. As interatomic distances in a graphite layer are shorter than in diamond (1.42 Å and 1.54 Å, respectively), graphene sheets are more rigid than diamond. The surface of fullerene molecules can be represented as a folded graphite layer, and the bulk elastic modulus of C_{60} molecule was theoretically estimated in 1991 to be higher than that of diamond. The same prediction was made for strongly compressed C_{60} solid, that is, for the case when the intermolecular distance approaches the length of an sp^3 bond. Novel fullerene superhard and ultrahard carbon materials were produced soon afterwards, first in microscopic amounts in high-pressure diamond chambers at room temperature, and then as macroscopic samples of up to 200 mg in heated high-pressure tungsten carbide apparatuses. Both crystalline and disordered structures with different physicomechanical and electrical properties were obtained and investigated. In this chapter, we studied these advanced materials.

16.2. Synthesis of Superhard Materials

Superhard phases of C_{60} were obtained using a toroid-type apparatus [1] improved to produce higher pressures up to 15 GPa [2]. High pressures were developed in a chamber consisting of two coaxial profiled anvils with a container with the sealing rings between them (Figure 16.1a). The chamber was placed into a hydraulic press with pressure multiplication. The force-transferring pistons in the press were of consecutively decreasing area to have the smallest-area piston exert the highest pressure on the chamber with the sample.
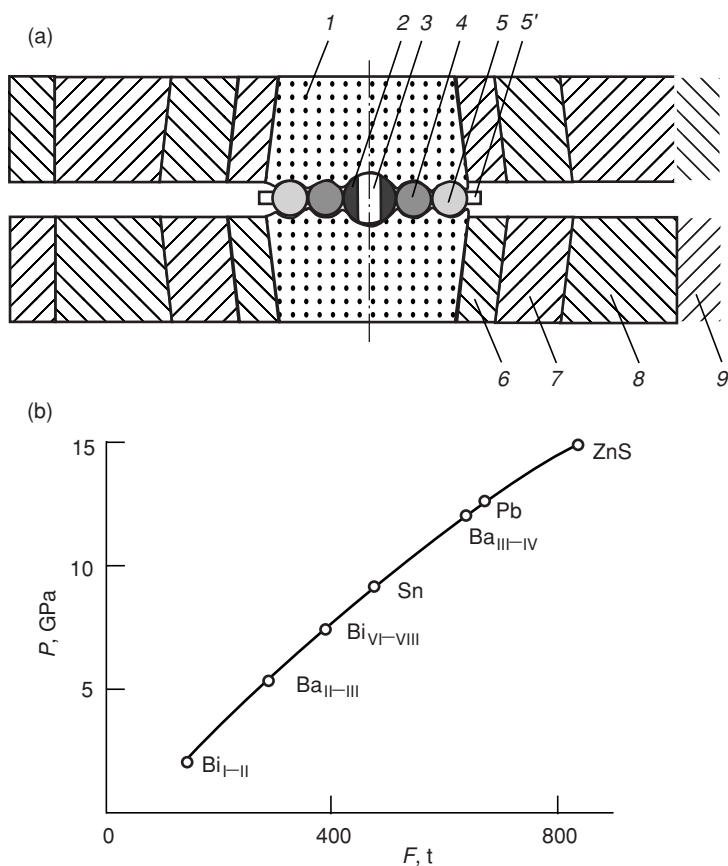
FIGURE 16.1. A method of high-pressure and high-temperature (HPHT) treatment of fullerenes. (a) The schematic of a toroid-type HPHT apparatus with the working-chamber diameter of 15 mm [1]. 1: hard-alloy punches; 6, 7, 8, 9: supporting steel rings; 3: zone where the heater and sample are placed; 2: container; 4: first sealing ring; 5 and 5′: second and third sealing rings; (b) A calibration curve plotted by the changes of electrical resistance of the reference metals.

The pressure in the chamber was determined by the chamber-pressure/press-force calibration curves. The calibration curves for each pair of anvils were plotted by the changes of electrical resistance at polymorphic transformations in reference metals: Bi (7.7 GPa), Sn (9.5 GPa), Ba (12.5 GPa), Pb (13 GPa), and ZnS (15 GPa) at room temperature (Figure 16.1b).

High temperatures were developed by resistive heating in a graphite heater. The temperature was measured by thermocouples: chromel–alumel, up to $1470° C$; platinum–platinum rhodium, up to $1870° C$; and tungsten–rhenium, for higher temperatures.

In order to avoid contamination by volatile components, samples were placed in refractory metal foil. The highest temperature was recorded near the side walls of the heater; the temperature gradient was ∼50 degrees. Taking into account the pressure and temperature gradients, the samples for studies were taken from the central part of the reaction zone.

A set pressure was developed at 0.15 GPa/min, the heating was at a rate of $50° C/min$, and the isothermal exposure was 1 min or, in special cases, 20 s. The samples were quenched as follows: the heating was switched off, the chamber was cooled at a rate of $400° C/s$, and the chamber was discharged at a rate of 0.1–0.15 GPa/min. The experiments were carried out at pressures of 8, 9.5, 12.5–13, and 15 GPa within the temperature range of 300–2100 K.

After the temperature and pressure were decreased, the samples obtained at high pressure were recovered from the chamber and analyzed under normal conditions.

16.3. Structure of Superhard Materials

The crystalline structure of the high-pressure phases of fullerites was studied using the powder diffraction method. The diffractograms of the metastable phases of C_{60} fullerite were obtained by a KARD-6 diffractometer with the two-dimensional area detector developed at the Institute of Crystallography, Russian Academy of Sciences [3]. The detector is a flat multichannel proportional chamber with fast delay lines. A graphite monochromator (transmission geometry, CuK_{α} radiation $(40 kV \times 30 mA)$ was used. Yttrium aluminum garnet served as external reference. The centers of gravity of the Bragg peaks were determined to an accuracy of $0.01°$.

Figure 16.2 shows the diffractograms of the C_{60} phases obtained by the action of 13 GPa within a broad temperature range [4]. The diffraction peaks become broader as the temperature is increased, and amorphous halos appear at $2\theta > 40°$. At $T > 1270 K$, the structure is completely amorphized. A temperature of 670 K proved to be a threshold for producing samples with the hardness higher than that of cubic boron nitride (cBN). The hardest were amorphous samples; their hardness was higher than that of diamond and they were named ultrahard. The amorphous structure of fullerites after high-pressure and high-temperature (HPHT) treatment was studied using a transmission electron microscope. The samples were obtained by polishing followed by ion etching. A characteristic structure is shown in Figure 16.3.
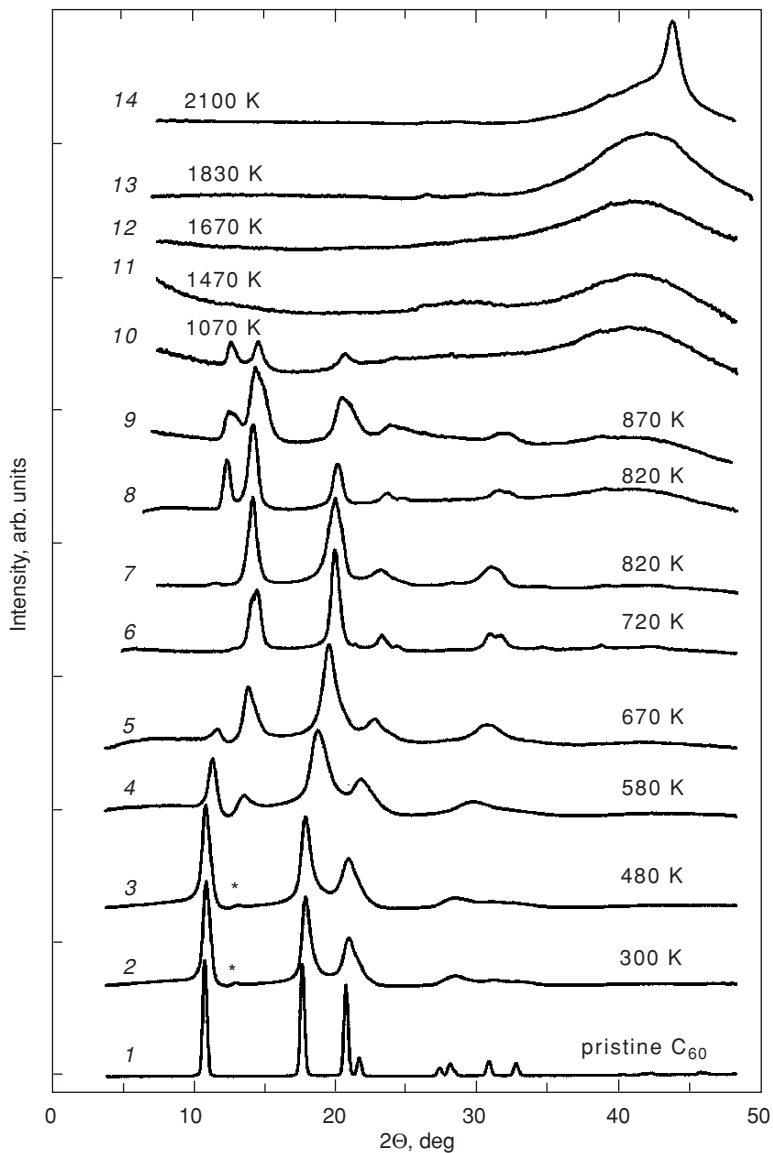
FIGURE 16.2. Diffractograms of the C_{60} phases. * is a (110) reflection occurring at the orthorhombic distortion of the initial fcc structure.

In ascending order of hardness and polymerization, we singled out three types of structures of crystalline superhard phases:
- Phase C (Figure 16.2, diffractogram 5) obtained at 9.5–13 GPa, $T \geq 670$ K; its hardness is higher than that of cBN;
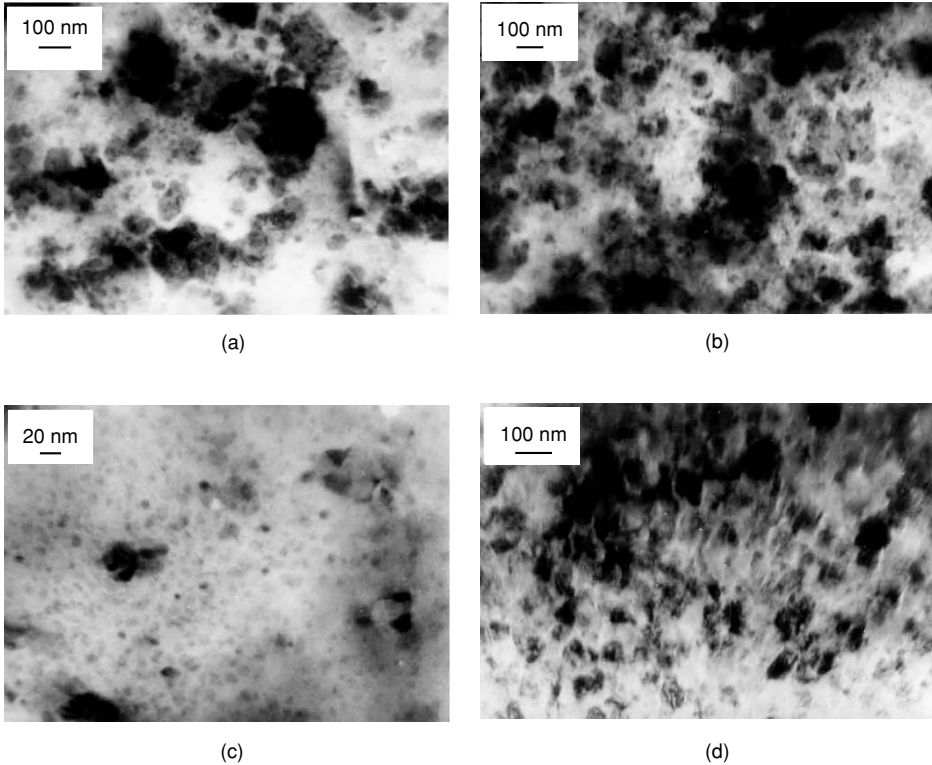
FIGURE 16.3. A characteristic structure of fullerites treated at a pressure of 15 GPa and high temperature.

- Phase B (Figure 16.2, diffractogram 7) with hardness of about that of the (100) face of diamond; obtained at pressures higher than 9.5 GPa and $T \approx 770$ K;
- The hardest phase A (Figure 16.2, diffractogram 8) with hardness higher than that of the (111) face of diamond was obtained at pressures greater than 13 GPa and $T > 670$ K.

Modeling the structures we assumed that polymerization begins with the formation of dimers along the diagonals of the faces (the shortest distance) of the fcc structure and its rhombic distortion.

A high pressure compresses the structure and thereby brings the dimers together and makes them bind into chains and layers of molecules in the (x, y) plane, and a high temperature increases the amplitude of anisotropic oscillations of atoms, thus promoting the appearance of bonds between (x, y) layers in the vertical direction. Nonhydrostatic compression reduces the symmetry to body-centered, in which the distances along the [111] space diagonals are the shortest; their further compression is the major principle of three-dimensional (3-D) polymerization. The primary goal in modeling the structure of 3-D phases is to find the atoms that would bridge the "frozen" molecules or cages of molecules along the [111] direction.
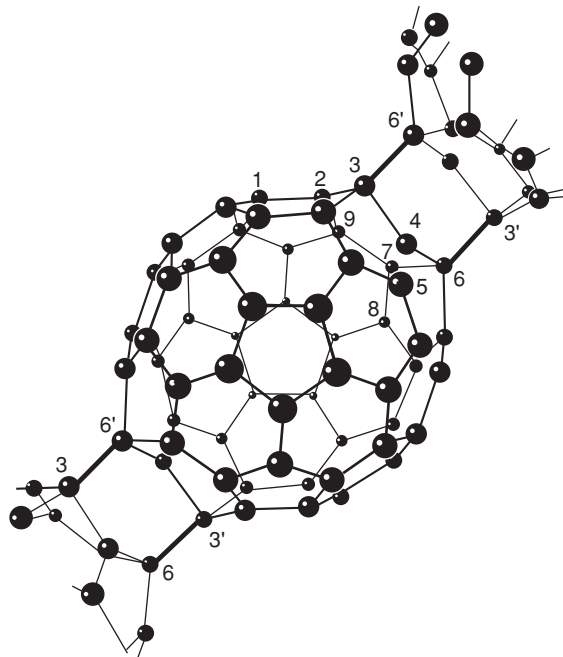
FIGURE 16.4. The cages of molecules in a rhombic 3-D structure are bridged along a [111] space diagonal. Thick lines indicate (3 + 3)-type bonds between C6–C3′ and C3–C6′ atoms on the adjacent cages of molecules.

Figure 16.4 shows the central molecule and its intermolecular bonds along the [111] direction. The structure was calculated by the molecular mechanics (MM+) methods in the assumption of the shortest distances between the C6–C3′ atoms. For the given size of a unit cell, the structure was the most stable, with a gain of 0.092 eV/atom in the formation energy as compared with the molecular structure. In bridging the C3′–C6 molecules by short distances, a new (3 + 3) type of cycloaddition is formed, which is shown by thick lines in Figure 16.4 [5].

Taking into account the different intensity-distribution patterns on the diffractograms of the superhard phases of C_{60} (samples 5, 7, 8 in Figure 16.2), it was assumed that the type of cycloaddition along the coordinate axes of the structures changes as the polymerization parameters (HPHT) increase, but the (3 + 3) cycles along the [111] direction are preserved.

Besides the (2 + 2) type of cycloaddition, in models of the structures of phases B and A we used dimer C_{120} theoretically calculated in [6] and representing a common four-sided ring. This dimer can be represented as a (2 + 2) cycloadduct turned 90° (Figures 16.4, 16.5), then the plane of the binding quadrangle becomes perpendicular to the axis of polymerization. In other words, molecules are spliced in polymerization, and the distances between them become smaller.

Figure 16.6 shows the results of the profile analysis of the superhard-phase diffractograms and the change of shape of the cages of "stiffened" fullerene
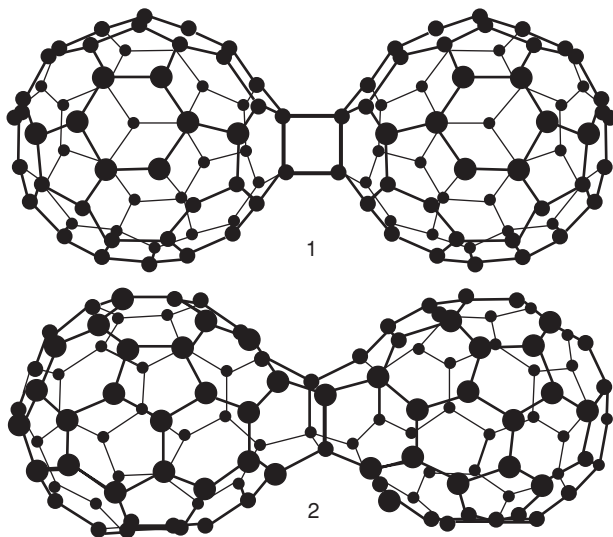
FIGURE 16.5. Dimers of C_{120}. 1: dimer formed by $(2 + 2)$ cycles; 2: dimer formed by a common four-sided ring.

molecules due to the formation of covalent bonds in polymerization. The initial coordinates of carbon atoms were calculated by the molecular mechanics (MM+) method and then verified by the method of profile analysis (Rietveld method, FULLProf [7]).

In the model of phase C structure, the axis a is polymerized by the type of $(2 + 2)$ cycloaddition with distances in the chain ($C8 - C8 = 1.64$ Å and 1.53 Å) corresponding to the length of the covalent bond in $(2 + 2)$ cycles, the distances in $(3 + 3)$ cycles are ~ 1.96 Å. Phase C is not a 1-D chain structure, as it has short non-van der Waals bonds fastening its cage along the space diagonal. The cage of the C_{60} molecule is almost spherical.

Due to significantly different distributions of intensity peaks in the diffractograms of phases C and B (Figure 16.6), we chose the common four-sided ring type of cycloaddition along axis b for modeling the structure of phase B. This type of cycloaddition is a caged structure, the distances C3–C6 in $(3 + 3)$ cycles are 1.71 Å. Due to the formation of shorter bonds in common four-sided ring cycles (C1–C1 $= 1.54$–1.6 Å) in phase B the C_{60} molecule is deformed stronger than in phase C; it is extended along axis b and acquires a barrellike form. Hexagons on the lateral surface of the molecule form fragments of the graphite plane. Each molecule is bound to ten adjacent molecules and contains 20 sp^3 atoms out of 60: eight pairs of atoms C3–C6 and two pairs of atoms C1–C1, $16 + 4 = 20$. In the structures of phases C and B, large zeolitelike channels are formed due to the presence of nonpolymerized directions [5, 8].

When choosing the model of phase A, we took into account the high value of hardness of this phase; that is, the structure should contain as many as possible
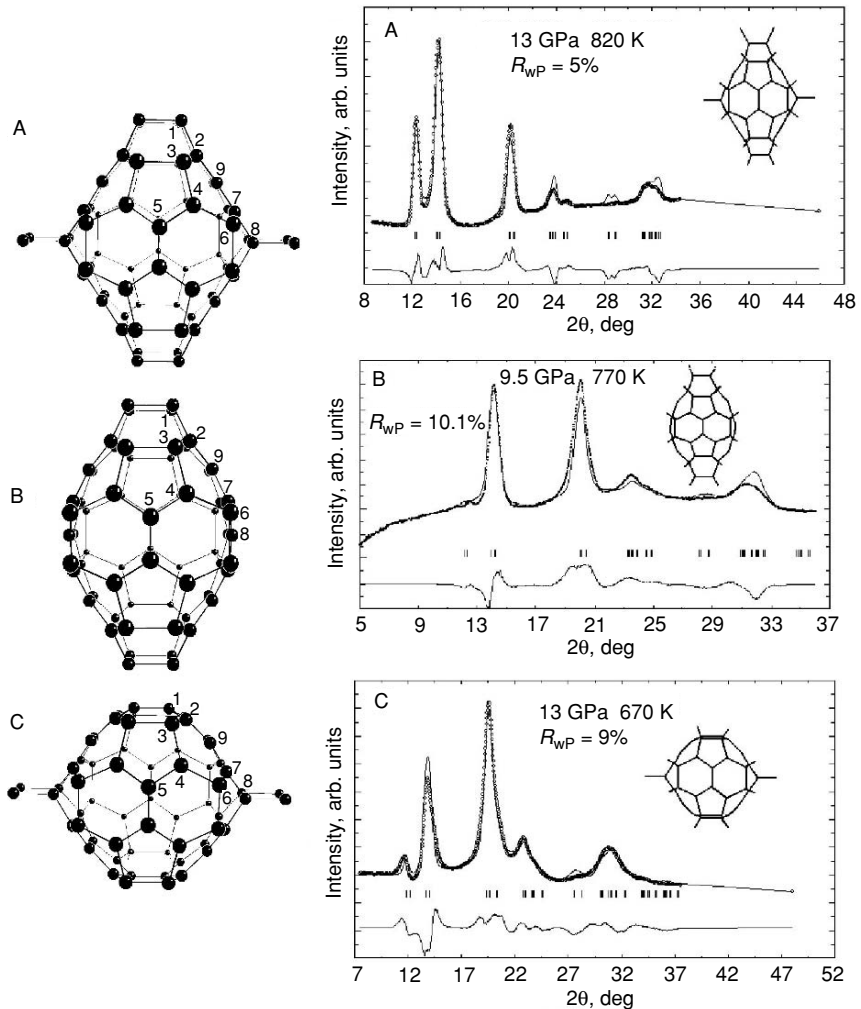
FIGURE 16.6. Models of polymerized C_{60} molecules in the superhard phases A, B, C (left) and the results of the profile analysis of the C_{60} superhard-phase diffractograms (right). The numerals are the numbers of independent carbon atoms whose coordinates are given in Table 16.1. The molecules are represented in projection (001): the axis c of the rhombic structure is perpendicular to the plane of the figure; the horizontal axis is axis a; the vertical axis is axis b. The amorphous halos were not taken into account at the adjustment of the diffractogram profiles.

sp^3-hybridized carbon atoms, and the distances between the molecules should be comparable with the length of a single diamond bond (1.54 Å). In its structure, the molecules are polymerized along both coordinate axes, a and b; by the type of $(2 + 2)$ cycloaddition, along axis a; and by the type of common four-sided ring cycles, along axis b.
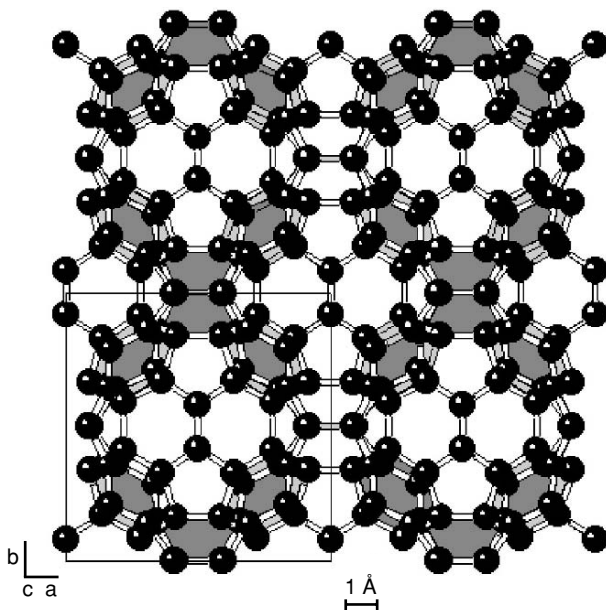
FIGURE 16.7. Projection (001) of the structure of phase A. Light grey elements are hexagons containing sp^3-hybridized carbon atoms. The unit cell is shown by thin lines. Intermolecular distances C8–C8: along axis $a = 1.61$ Å, along axis $b = 1.54$ Å; C1–C1 distances along axis b are equal to 1.55 Å, along $a = 1.58$ Å; distances C3–C6 are equal to 1.54 Å each (that is, are exactly equal to the length of a single diamond bond). The other distances between carbon atoms, forming the cage of a stiffened C_{60} molecule, also differ strongly from their values in pristine; their length varies from 1.40 up to 1.55 Å.

The nearest distances between carbon atoms for sp^3-hybridized atoms are within the limits of 1.52–1.54 Å. Each molecule is surrounded by 12 molecules: 4 molecules from above, 4 molecules from below, and 4 molecules in the (x, y) layer; each molecule contains 24 sp^3 carbon atoms out of 60. The molecule of superhard phase A is deformed even more strongly than in phases C and B. $(3 + 3)$ bonds transform the molecular structure of pristine C_{60} into a 3-D cage from carbon atoms. The basis projection of the structure of phase A (Figure 16.7) shows (in light grey) hexagons in which sp^3 bonds are formed between the atoms of adjacent molecules. Table 16.1 gives the verified parameters of unit cells and the coordinates for the atoms of three superhard phases A, B, and C.

Unusual ellipsislike diffraction reflections of the structure of phase A were revealed in studies using a 2-D "image plate" detector on ESRF synchrotron radiation [9].

Elongated ellipsislike Bragg reflections (Figure 16.8) were earlier observed only directly under pressure in nonhydrostatic conditions due to deviatory stresses caused by the uniaxial component of pressure. The elliptic shape of diffraction

TABLE 16.1 Crystallographic data for the structures of phases A, B, and C. Space group *Immm*, $Z = 120$ carbon atoms.

	Phase A			Phase B			Phase C		
	a, Å	b, Å	c, Å	a, Å	b, Å	c, Å	a, Å	b, Å	c, Å
Atom	8.674	8.810	12.601	8.693	8.878	12.698	8.73	9.16	12.94
	x	y	z	x	y	z	x	y	z
1	0.091	0.5000	0.0615	0.0915	0.5000	0.0620	0.0840	0.3690	0.0000
2	0.1559	0.3540	0.1100	0.1540	0.3420	0.0920	0.1617	0.3370	0.0950
3	0.0890	0.3370	0.2170	0.0865	0.3110	0.2010	0.0920	0.3020	0.2030
4	0.1370	0.1730	0.2380	0.1324	0.1614	0.2506	0.1270	0.1600	0.2490
5	0.0000	0.0799	0.2600	0.0000	0.0815	0.2866	0.0000	0.0760	0.2750
6	0.2800	0.0900	0.2180	0.2810	0.0868	0.2295	0.2620	0.0840	0.2140
7	0.3110	0.1380	0.0980	0.3220	0.1305	0.1168	0.3460	0.1300	0.1190
8	0.407	0.0000	0.0610	0.3712	0.0000	0.0560	0.4070	0.0000	0.0590
9	0.1710	0.1990	0.0580	0.2820	0.2610	0.0540	0.2920	0.2410	0.0570
	$R_{wP} = 4.8\%,$			$R_{wP} = 10\%,$			$R_{wP} = 9\%,$		
	$R_{Bragg} = 17\%,$			$R_{Bragg} = 26\%,$			$R_{Bragg} = 14\%,$		
	$\chi^2 = 1.3$			$\chi^2 = 2.3$			$\chi^2 = 1.5$		
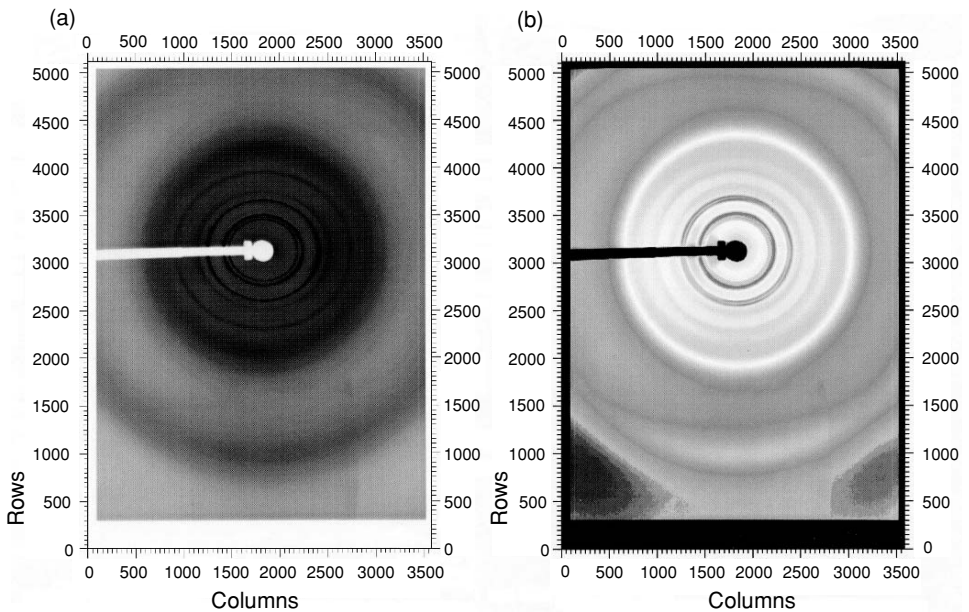
FIGURE 16.8. Two-dimensional diffraction patterns of superhard C_{60} phase A obtained using an image plate detector at the ESRF synchrotron facility. (a) Diffractional "ellipses" of the strong strained samples (see text); (b) normal diffractional circles of the equilibrium part of samples.
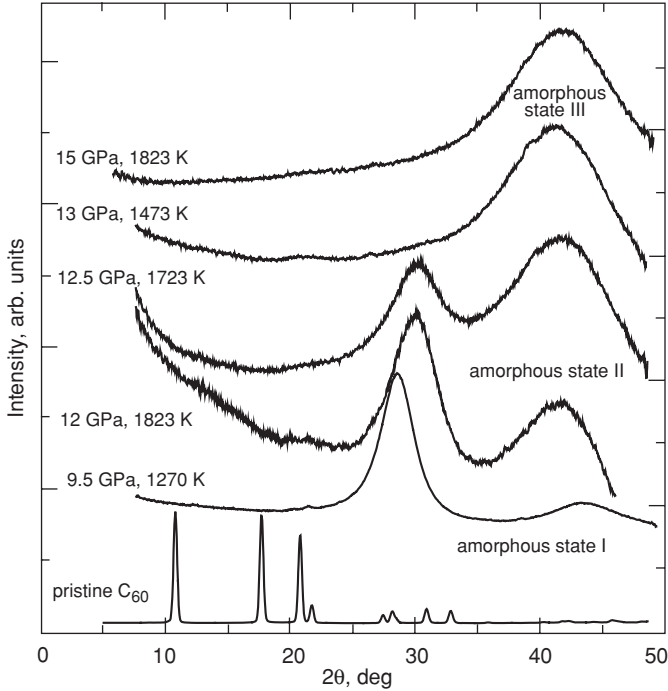
FIGURE 16.9. Diffractograms of three types of amorphous states of superhard phases.

reflections is the result of a nonuniform compression of coordinate axes of the unit cell: along the direction of the applied pressure it is compressed more than in the perpendicular direction. In 3-D polymerization of fullerene molecules the initial cubic structure is strongly and nonuniformly compressed due to the formation of covalent bonds between molecules. Elastic stresses are developed that cause deformation of the molecule. At nonuniform compression, the molecules approach along the directions of the greatest stress and thereby conditions for local reductions of interplane distances are created. New intermolecular covalent bonds prove so strong that they retain the 3-D polymerization-induced deformation of the structure after the pressure is removed. The deformation of the structure calculated from the eccentricity of diffraction "ellipses" is huge, $\sim 9\%$ $(\Delta a/a)$.

As the polymerization temperature increases, the diffraction reflections from the crystal phases broaden and blur, and they totally vanish at $T > 1000$–1100 K. Structures and, respectively, diffraction patterns of amorphous superhard phases of C_{60} differ depending on the type of the preceding crystal structures obtained within the given pressure range at a lower temperature. Figure 16.9 presents diffractograms of all three types of amorphous phases.

As there is only one polymerized direction in the structure of phase C in the (x, y) layer, we observe the formation of zeolite channels along the diagonal directions (Figure 16.10). The distance between the layers in $(3 + 3)$ cycles in the structure

FIGURE 16.10. Projections of the structures of superhard phases A, B, and C on the lateral faces. Thin lines are unit cells; hatched areas are zeolitelike channels on the projections of the structures of phases B and C.

A

B

a
b   c

C

b
a   c   1 Å
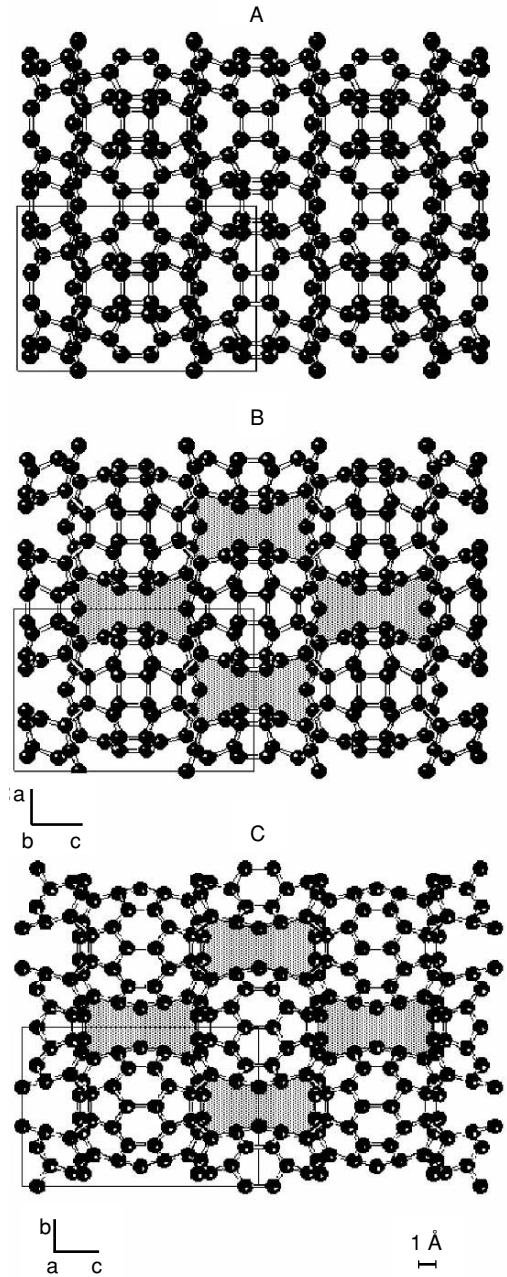
of phase C is still very large, 1.96 Å, so it is no wonder that the structure of the disordered state acquires a layered character (amorphous state I).

The second type of disordered state (Figure 16.9, II) is characteristic of ultrahard fullerites obtained by the action of high pressures (12–12.5 GPa) and temperatures

higher than 1200 K. The diffraction pattern has two halos with almost identical amplitudes but different angular widths. As compared with the previous state, the first halo is shifted to even more distant angles of reflection, and the second halo, in contrast, is moved up to smaller angles. This diffraction pattern could not be characterized as hexagonal, as we have here an almost cubic ratio between the centers of gravity of the halos. A decrease of the intensity of the first halo is also in favor of a more isotropic structure of the near order. The second type of amorphous state is obtained in disordering of superhard phase B at the increase of the synthesis temperature.

The third type of disordered state of ultrahard C_{60} is characterized by one halo on the diffraction pattern (Figure 16.9, state III) and is formed in the disordering of superhard phase A (Figure 16.9, 13–15 GPa). The structure of phase A has no channels (Figure 16.10).

Thus, amorphous states II and III we found have an original structure of short-range ordering, the basic structural unit of which is the cage of the C_{60} molecule, but not individual carbon atoms as in amorphous diamond films. Also, the hardness of amorphous state III is very high (170–200 GPa), higher than the hardness of the (111) face of diamond (167 GPa). The elastic properties of the ultrahard phases of C_{60} also proved unusual: the measurements of the speeds of longitudinal and transverse elastic waves by methods of acoustic microscopy showed the record values of $c_L = 17 \div 26$ km/s and $c_T = 7.2 \div 9.6$ km/s. The bulk modulus of elasticity ($K = 700$–800 GPa [10]) of these samples exceeds that of diamond (441 GPa, [11]). The high values of the bulk modulus, rather large shear moduli, and a significant value of the Poisson ratio, and also the unusual diffraction pattern (diffractograms of states II and III in Figure 16.9) indicate the drastic difference between the structure of ultrahard phases of fullerite C_{60} and the diamond structure. Diamond is synthesized only at the highest temperature of the effect on fullerite C_{60} at a pressure of 13 GPa (Figure 16.2, diffractogram 14); that is, the diamond structure is obtained as if in the annealing of the ultrahard state of fullerite C_{60}.

Figure 16.11 shows an unequilibrium (P, T) diagram of the conditions for the synthesis of the polymorphic modifications of C_{60}, plotted from the results of our studies. The structure and properties of the phases synthesized at pressures lower that 9.5 GPa are published in [12].

The phases are designated as follows.

■—The fcc structure of pristine with broadened diffraction peaks indicating a small amount of dimers

▫—Phases I and II

□—Orthorhombic + rhombohedral two-phase samples (dimers + 2-D polymers, from 7 to 40% of 2-D polymers)

◇—2-D polymer with rhombohedral structure + orthorhombic dimers (up to 25% dimers)

×—Orthorhombic superhard 3-D polymerized phases A, B, and C

M,▲ —Distorted crystalline 3-D polymerized phases with large amorphous halos in the range of $2\theta > 40°$
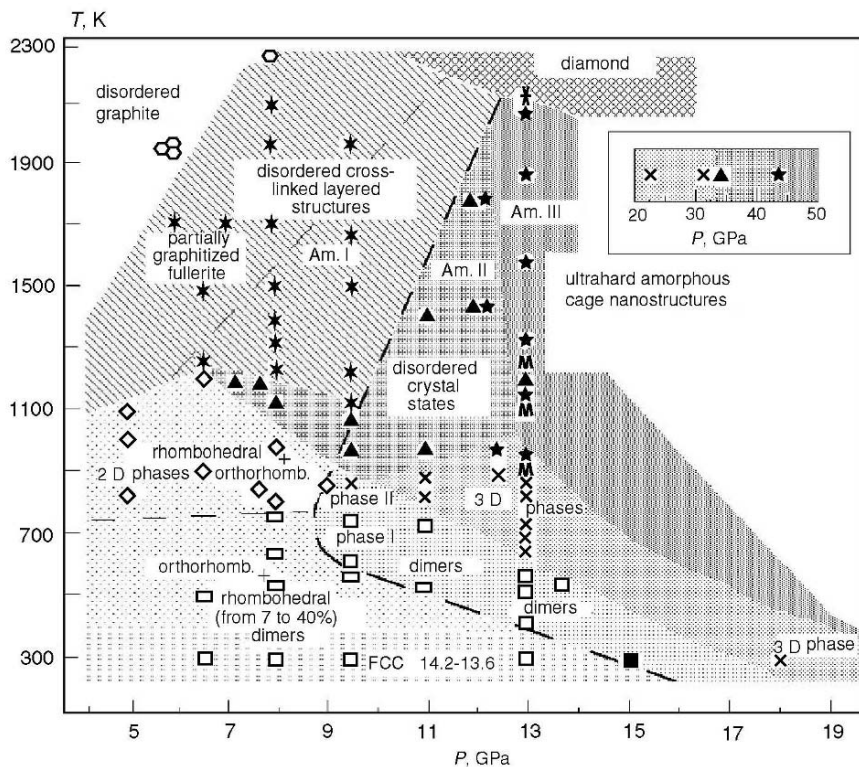
FIGURE 16.11. Unequilibrium (P, T) diagram of the conditions for the synthesis of poly-morphic crystalline phases and amorphous conditions of C_{60}. The insert shows the high-pressure part of the diagram plotted by the results of studies carried out at diamond anvil cells with shear deformations up to 50 GPa at room temperature [13]. The thin slanted dashed line in the left-hand side subdivides the first amorphous state into two parts depending on the hardness of the phases: the softer phases are formed above this line; their hardness decreases with the temperature increase and approaches the hardness of graphite. The dis-ordered structure of a 2-D polymerized phase also containing fragments of the hexagonal structure, with hardness of about 2 GPa, and formed at $\simeq$1000 K and 8 GPa, is at the right-hand side of this line. As the temperature is increased up to 1800 K at 8 GPa the hardness increases at a respective reduction of the average interlayer distance; at the further rise of temperature the hardness begins to decrease. 1800 K is the temperature of the rupture of C_{60} molecules and of the beginning of the formation of a graphitelike state, shown on the plot as a partially graphitized state. The semimetal character of conductivity of these layered disordered structures passes into a semiconductor character in phases obtained under (P, T) conditions to the right of the boundary shown by a thick dashed line.

✦—Amorphous state I (Am. I), layered disordered structure
★—Am. II and Am. III, amorphous states, on the diffractograms of which two
   halos (Am. II) or one halo (Am. III) are present
✕—diamond

The high mechanical properties of crystalline superhard phases and three amorphous states allowed them to be considered as a new class of superhard materials whose structure can be presented in a generalized form as a product of 3-D polymerization of C_{60} molecules.

The diagram of the conditions for the synthesis of C_{60} phases evidently shows the wonderful prospects of using high pressures to develop novel carbon modifications with unique properties. Formation of strong intermolecular bonds at high pressures results in a diversity of structures based on linear, planar, and bulk polymeric grids.

The thermal stability of polymerized phases was investigated by the method of differential scanning calorimetry (DSC) [14]; the maximal temperature of heating was 640 K. Several cycles of heating were carried out and the diffractograms were recorded before and after each cycle. The results of calorimetric annealing showed that all crystal phases, except for phase A, at heating to a temperature of 640 K undergo a polymorphic transformation into the structure of a monomere or are transformed into less dense phases at a gradual annealing to lower temperatures. The structure of phase A remained stable even at the maximal temperature of heating. Superhard amorphous states of C_{60} proved to be stable too; their diffractograms did not change after repeated annealing to maximal temperatures.

Depolymerization of superhard phase B is accompanied by the exothermal evolution of heat. During the heating of a sample of phase B up to the maximal temperature the reverse transformation into the molecular phase occured already in the first DSC cycle, and was accompanied by an exothermal peak with the maximum at 477 K (Figure 16.12) on the curve of the dependence of the specific heat capacity on temperature. The occurrence of an exothermal peak at ∼480 K characterizes the rupture of $(3 + 3)$ bonds, the thermal effect of this process is ∼60 J/g.

The structural transformations observed during the annealing and depolymerization (Figure 16.13) in high-pressure metastable phases of C_{60} are in full conformity with structural transformations during the polymerization (Figure 16.3), but in reverse sequence, passing the same stages with gradual weakening of polymerization.

16.4. Hardness

Hardness is the most important characteristic of superhard materials. It indicates the potential of the cutting tool: this is the field of application where superhard materials are used the most. Cutting (or scratching) is the basis of the first primitive Mohs hardness scale. Hardness is defined as the load on an indenter divided by the projected area. Several hardness measurement methods are used in practice, the major ones being indentation and sclerometry (scratch at a constant indenter load). A detailed comparison of the indentation and sclerometry methods is given in [15]. These methods conform well with each other. Sclerometry implies a greater plastic deformation as compared with indentation [15].
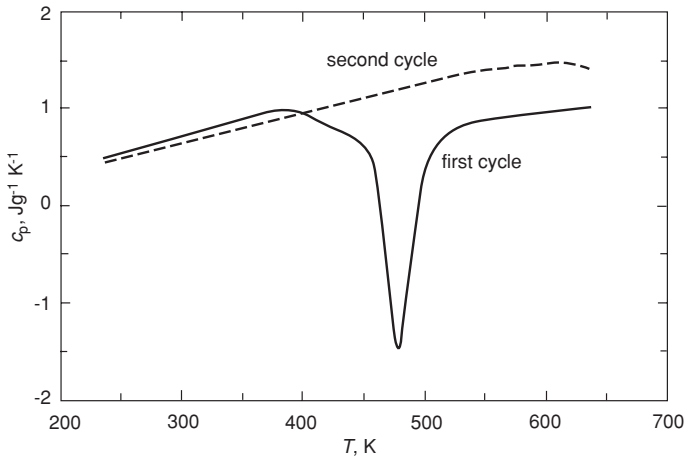
FIGURE 16.12. Change of the heat capacity of phase B during the heating for two cycles.
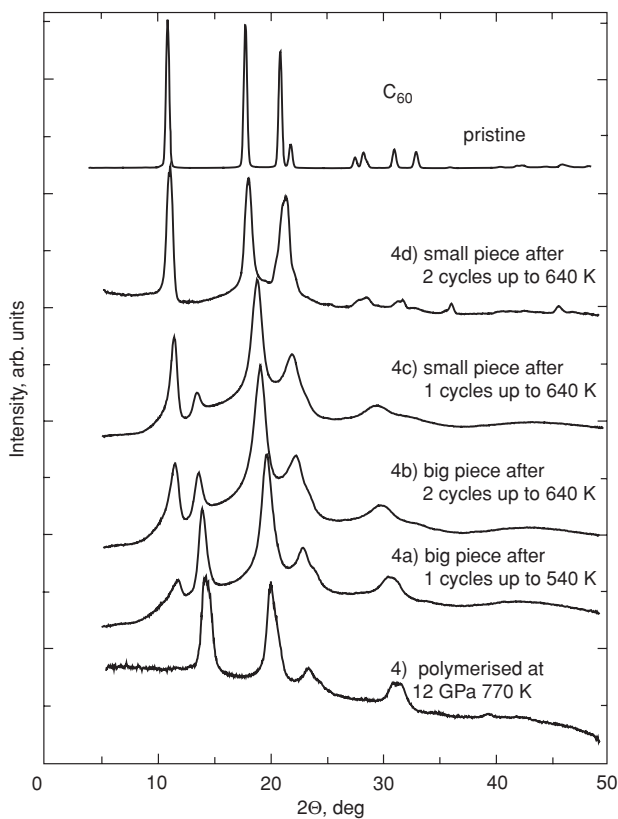
FIGURE 16.13. Reflection of the degree of polymerization on the diffractograms of C_{60} polymerized phases.

Obviously, the hardness of the indenter should exceed that of the material tested. For decades, this was the major obstacle for hardness measurements of diamond. Numerous papers discuss diamond hardness measurements [16–23]. The range of reported hardness values is 56–257 GPa. For comparison, the hardness of cBN is from 60 to 72 GPa depending on the so-called hardness anisotropy [15,18,22] (for a single crystal, hardness depends on the tested face orientation and the orientation of the indenter). The value of uncertainty of the diamond hardness covered the entire superhard hardness range. The problem was eventually solved when ultrahard fullerite C_{60} (U–C_{60}) was used as the indenter material [16–18]. It became possible to study the hardness of major types of diamond. Thus, in [18] it was found that synthetic diamond with nitrogen concentration of 0.3 ppm exceeds other diamond types by hardness and wear resistance and reveals a hardness anisotropy different from other diamond types. For this diamond type, the hardness varies from 139 to 175 GPa depending on the hardness anisotropy, whereas for diamond with a nitrogen concentration of 200 ppm it ranges from 115 to 151 GPa depending on hardness anisotropy.

The nanosclerometry hardness measurement procedure described in [16–18] is, possibly, a unique reliable procedure for hardness measurements within the diamond and hyperdiamond hardness range, so we discuss it in more detail. Hardness measurements are performed in this procedure using the NanoScan (NS) measurement system based upon the principles of scanning probe microscopy. The sclerometry method (scratch at a constant indenter load) was used for hardness measurements using the NS. As mentioned above, the sclerometry and indentation methods conform well to each other. According to the sclerometry method the hardness value H is calculated as

$$H = kP/b^2,\qquad(16.1)$$

where k is a coefficient of the tip shape, P is the indenter load, and b is the scratch width.

The shape of the indenter is a very important parameter for submicron hardness tests, but in practice it is difficult to make indenters with reproducible geometry. A special procedure was used in this study to calibrate the indenter. In accordance with the standard method of sclerometry, at a designated P the scratch width b is measured. In the proposed procedure b is a constant (in [16–18] it was about 0.6 μm), P_m is measured, and the hardness H_m is proportional to P_m according to (16.1). Thus, it is necessary to calibrate the tip with respect to a primary standard with the known hardness H_s in order to determine the load P_s at which the scratch with $b = 0.6$ μm is made.

According to (16.1), if b^2 and k are constant, we have:

$$H_m/H_s = P_m/P_s \quad \text{and} \quad H_m = H_s(P_m/P_s).\qquad(16.2)$$

The primary standard for this procedure must have mechanical properties close to those of the material tested. Sapphire was used as the standard.
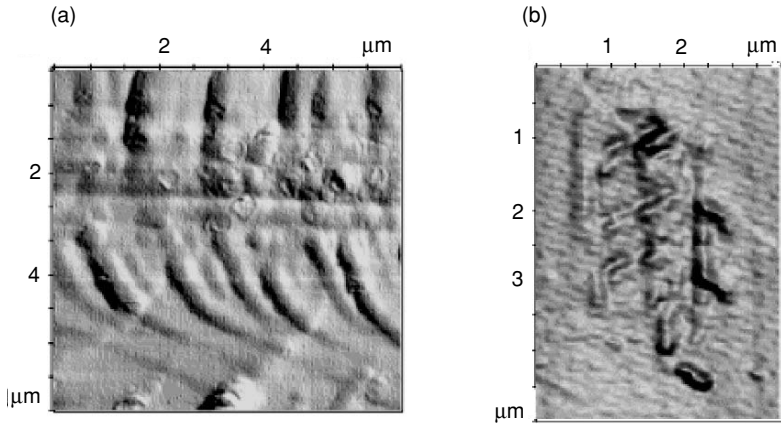
FIGURE 16.14. Scratching of the (111) diamond face with the diamond indenter is accompanied by the appearance of numerous cracks. The vertical scale (the difference between the highest and lowest parts of the relief in the z-direction) of (a) is 15 nm; at least two types of cracks are present in (a): macroscopic linear and microscopic hexagonal ring cracks. The vertical scale of (b) is 2 nm; only linear cracks are visible [16,17].

This new procedure illustrates the nature of uncertainty of the diamond hardness measurement using the diamond indenter [16–18]. The scratching of the diamond face with a diamond indenter is accompanied by the appearance of numerous cracks (Figure 16.14) (as shown in [16], cracks lead to a wrong hardness value), whereas the scratching with the U–C$_{60}$ tip causes the plastic deformation of diamond without fracture (Figure 16.15). This depends upon the fact that the hardness of U–C$_{60}$ is enough to create a sufficient pressure at the contact point for the plastic
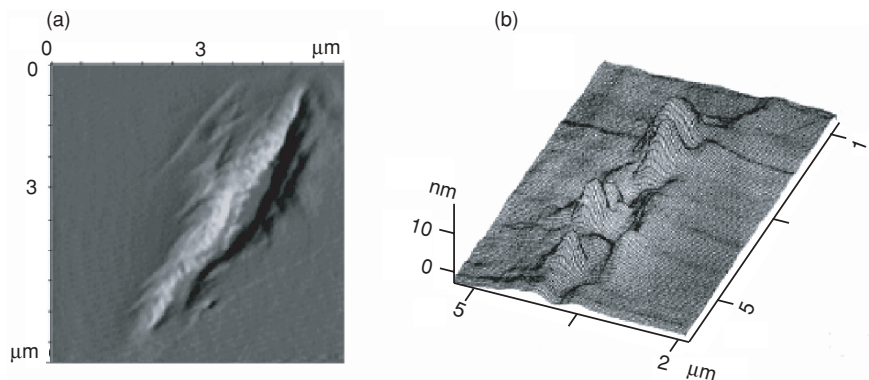
FIGURE 16.15. Scratches on the (111) diamond face made by U–C$_{60}$ indenter at room temperature. The scratching of diamond with the U–C$_{60}$ tip causes plastic deformation of diamond without fracture. The vertical scale of (a) is 90 nm (the difference between the highest and lowest parts of the relief in the z-direction) [16,17].

(a)   (b)

5 micron
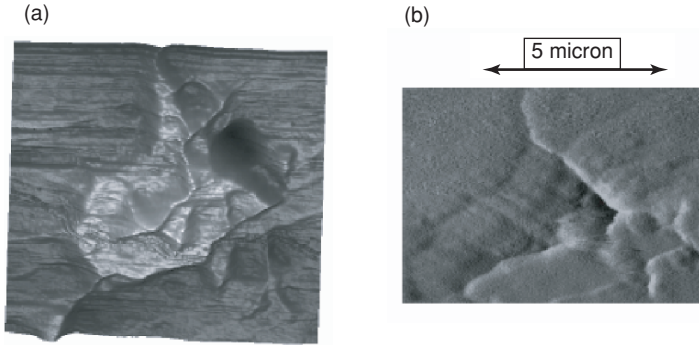
FIGURE 16.16. NS images of the indentations on the (111) diamond face. The indenter loads were 200 g (a) and 300 g (b); the vertical scale (the difference between the highest and lowest parts of the relief in the z-direction) was 50 nm.

flow of diamond at room temperature and the hardness of U–C_{60} exceeds that of diamond.

Interesting microscopic hexagonal ring cracks are visible in Figure 16.14a along with macroscopic linear cracks.

Using a U–C_{60} Vickers-type indenter, it is possible to perform the hardness measurements of diamond at the indenter load up to 1.3 kg. The hardness of the (111) diamond face obtained under these "macroscopic" conditions, 167 ± 7 GPa, corresponds to that measured at the indenter load of about 10 g.

The study using NS revealed unusual indentations on the (111) diamond face (while under load the indenter edges and the indentation were visible). The indentation after 300 g load is a wavy plate and a square cavity (in accordance with the indenter orientation) 50 nm deep (Figure 16.16). Small cracks are observed in the corners of the indentations. This feature of the diamond face indentation conforms with the phenomenon described in [18]. In some experiments using the indenter load below 10 g, the indented part of a diamond surface heaved after the scratching instead of forming the scratched cavity. In the present case, the wavy plate is formed at higher loads instead of the pyramidlike indentation visible under load. The sclerometry method used for hardness measurements implies a larger plastic deformation in comparison with the indentation method. As the result, the scratch profile is more significant than the indentation profile.

The hardness of U–C_{60} and other superhard fullerites was measured using the nanosclerometry hardness measurement procedure in comparison with diamond, cBN, and other hard materials [16, 17, 24]. It increases the validity of the data. The results of the hardness tests for fullerite C_{60} samples reported in [17] are presented in Figure 16.17. The hardness values versus synthesis temperature are plotted. The specimens were synthesized at nonhydrostatic pressures of 9.5 and 13 GPa as discussed in Section 16.2. The hardness levels of sapphire, cBN, and diamond are plotted for comparison.
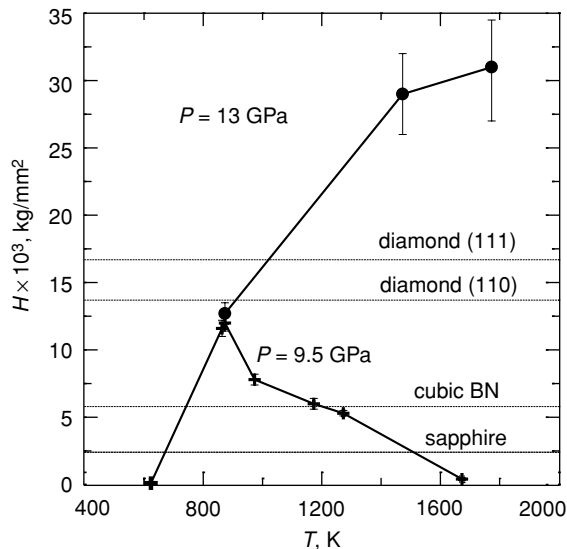
FIGURE 16.17. Hardness of fullerites versus synthesis temperature. The samples were synthesized at nonhydrostatic pressures of 9.5 and 13 GPa. The hardness levels of sapphire, cBN, and diamond are plotted for comparison [17].

16.5. Elastic Properties of C_{60}-Based Polymerized Fullerites

The unique method for studies of the elastic properties of small specimens is known as acoustic microscopy [25]. It allows not only to "screen" the sample and thereby to control the presence of defects but also to follow the mapping of local elastic properties. Because the elastic properties are specified by the intermolecular bonding and nanostructural organization of a substance their determination can provide the designation of specimen's microstructure.

The density of the specimens was measured by the flotation method using mixtures of diiodmethane and acetone liquids of different concentrations. The bulk densities ρ of the specimens were determined to an accuracy of ± 0.05 g/cm^3. They varied within the range of 1.75–3.28 g/cm^3 (Tables 16.2–16.5).

A wide-field pulse scanning acoustic microscope (WFPAM) was used in the reflection mode at the driving frequencies of $f = 25 - 50 - 100$ MHz to measure the local values of ultrasonic velocities and elastic moduli (the microacoustic technique) and to visualize the bulk microstructure of a specimen (scanning acoustic microscopy). The method makes it possible to measure the elastic characteristics of small specimens and inclusions [26, 27].

Local and averaging elastic moduli were calculated to an accuracy of $\pm 5 \div 25\%$ on the basis of the measured velocities and densities of the polymerized fullerite samples.

TABLE 16.2 C_{60} synthesized at $P = 8$ GPa.[a]

T, K	ρ g/mm	V_L km/s	V_t km/s	K GPa	E GPa	G GPa	σ
500	1.75	6.0±0.3	3.7±0.1	30±5	57±14	24±2	0.19±0.05
		7.4±0.4	4.8±0.2	40±6	90±20	40±4	0.14±0.04
900	1.90	6.8±0.3	4.1±0.2	45±5	80±20	30±3	0.20±0.03
		7.4±0.4	4.5±0.2	50±7	90±20	40±5	0.20±0.04
1650	2.22	8.6±0.6	4.3±0.2	110±20	110±30	40±5	0.33±0.08
		15.2±1.0	5.6±0.2	420±60	200±50	70±5	0.42±0.08

[a] The averaging values of density ρ, longitudinal V_L and shear V_t ultrasonic wave velocities, bulk modulus K, shear modulus G, Young's modulus E, and Poisson's ratio σ as a function of synthesis temperature T.

TABLE 16.3 C_{60} synthesized at $P = 9.5$ GPa.[a]

T, K	ρ, g/mm	V_L, km/s	V_t, km/s	K, GPa	E, GPa	G, GPa	σ
700	2.30	12.0	7.8	160	320	140	0.13
770	2.35	12.5	6.8	220	280	110	0.29
970	2.62	18.5	11.4	450	800	340	0.20
1070	2.30	18.5	11.4	420	690	280	0.22
1150	2.26	16.0	8.25	370	400	150	0.32
1400	2.32	18.0	12.0	310	700	330	0.10
1500	2.27	18.0	11.0	370	660	275	0.20

[a] Notations are identical to those for Table 16.2.

TABLE 16.4 C_{60} synthesized at $P = 11$, 12.5, and 13.5 GPa.[a]

P/T GPa/K	ρ g/mm	V_L, km/s	V_t, km/s	K, GPa	E, GPa	G, GPa	σ
11/1450	2.25	11.7	6.7	170	250	100	0.26
12.5/1000	3.10	17.0	9.4	540	660	280	0.28
13/1670	3.10	17.0	7.2	690	450	160	0.39
13/1770	3.30	18.4	8.7	790	680	250	0.36
13/1870[b]	3.15	26	9.7	1700	850	300	0.42

[a] Notations are identical to those for Table 16.2
[b] See [10] for details.

TABLE 16.5 C_{60} synthesized at $P = 15$ GPa.[a]

T, K	ρ, g/mm	V_L, km/s	V_t, km/s	K, GPa	E, GPa	G, GPa	σ
670	2.55	14.6	8.1	320	430	170	0.28
820	2.72						
1120	3.02	20.5	10.6	820	900	340	0.32
1470	3.27	19.5	10.9	730	990	390	0.27
1820	3.28	17.0	10.8	440	890	380	0.16

[a] Notations are identical to those for Table 16.2.

Together with the recording of oscillograms of echo signals, the acoustic microscope WFPAM was also used in B- and C-scanning modes. The acoustic microscopy images reflecting the microstructure of fullerite specimens were obtained. The regular acoustic images (C-scans) were used for visualization of the specimen surface and selecting spots for measurements on it.

Then from these data the elastic moduli, such as the bulk modulus K, shear modulus G, and Young's modulus E were calculated.

Some C_{60} samples have the value of local bulk and Young's moduli much higher than those of diamond.

The values in these tables represent the mean values of the samples' elastic parameters. However, we observed a large sound velocity variance along the line of scan direction. As this takes place, the sound velocity has the highest value near the specimen periphery and the lowest one at the central part (Table 16.2). It should be noted that the radial variation of sound velocity was not symmetric in each B scans, and varied at the angular variation of the scanning line.

16.6. Electrical Conductivity of 3-D-Polymerized Fullerites C_{60} Obtained by HPHT Treatment

The initial fullerite C_{60} has band-gap of 1.7 eV and possesses a high degree of localization of charge carriers on molecules due to the van der Waals character of intermolecular interaction in crystals.

In polymerization of pure fullerenes σ-orbitals are partially overlapped and strong cage nanostructures are synthesized based on molecules and clusters formed between molecules. Linear and planar polymers of fullerites obtained at a pressure of up to 8 GPa possess a strong anisotropy of electrical properties due to the presence of covalent interatomic bonds in the chains and planes of the polymer and van der Waals bonds between chains (planes) [28].

At pressures of 9.5–13 GPa and temperatures of synthesis T_s within the range of 300–800 K, 3-D-polymerized crystalline structures with densities within the range of 2.2–2.6 g/cm^3 were obtained as described in Section 16.3. At higher temperatures there occurs a disordering of the polymer to form new cluster structures with the maximal density within the range of 2.7–3.3 g/cm^3, depending on the actual values of pressure and temperature. All these structures have mixed interatomic bonds of sp^2 and sp^3 type.

Studies of the temperature dependence of the electrical resistance of 3-D-polymerized fullerites with various structures within the range of 2.5–300 K allow one to determine the activation energy of charge carriers and to draw conclusions on the degree of ordering of the structure. Measurements of the dependence of the electrical resistance on temperature were carried out by a four-contact method in a helium cryostat Oxford Instruments MagLab 2000 Cryostat System [29]. The results of measurements are shown in Figures 16.18 and 16.19 in Arrhenius coordinates and as power-law dependences. The characteristic values of conductivity at room temperature and activation energy of charge carriers are presented in Table 16.6.
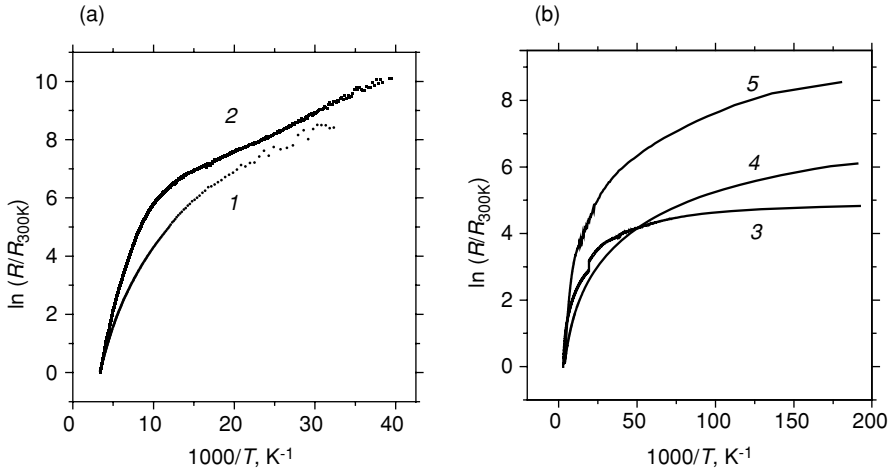
FIGURE 16.18. A temperature-dependence of the electrical resistance of samples in Arrhenius coordinates. The numbers of the curves correspond to those of the samples in Table 16.1.

Electrical conductivity of 3-D-polymerized fullerenes C_{60} strongly decreases at low temperatures which indicates its semiconductor character.

The characteristic Boltzmann exponential dependence of conductivity on temperature was observed only on samples with crystal 3-D-polymerized structure as, for example, in sample No. 2 (Figure 16.18a). As seen in Figure 16.18a, the curve
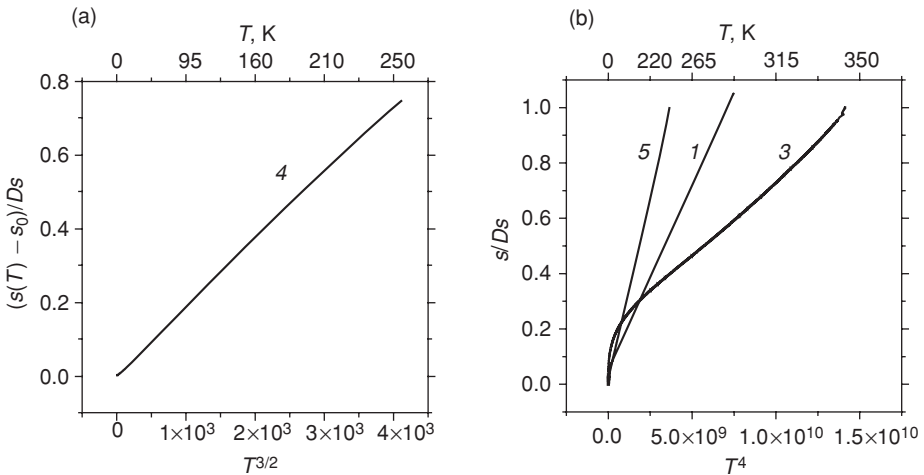
FIGURE 16.19. Power-law temperature dependences of the conductance of C_{60} samples with crystal and disordered 3-D-polymerized structures obtained at $P = 11.5$-15 GPa and various temperatures of synthesis.

TABLE 16.6 The values of specific electrical resistance ρ_{300K} and charge-carrier activation energy E_a at room temperature of 3-D-polymerized specimens of C_{60}, obtained at pressures of 11.5–12.5 GPa and temperatures of 820–1500 K.

No.	P, GPa	$T_{synthesis}$, K	n, g cm^{-3}	ρ_{300K}, Ωcm	E_a, eV
1	12.5	820	2.55	10^2	0.2
2	11.5	850	2.45	10^3	0.18
3	12	1000	2.7	10^3	0.2
4	11.5	1300	2.5	0.1	0.06
5	12.5	1500	3.05	10^4	0.18

of $\ln R(T^{-1})$ has two well-defined linear regions, giving two different values E_a of the activation energy of charge carriers. At $T > 130$ K $E_a \approx 0.18$ eV, and at $T < 130$ K $E_a = 2.3$ meV. The value of 0.18 eV can correspond to the band-gap width, as interatomic bonds in the model of this structure are mainly of sp^2 type as in graphite. This suggests that the band-gap in this intrinsic carbon semiconductor should not be large.

The dependences of $\ln R(T^{-1})$ for samples with disordered structure have almost no linear regions. The deviations from the Boltzmann law of activation of charge carriers in semiconductors are observed in the presence of a complex energy spectrum of carriers with various energy levels, in the presence of various types of doping impurities, and also due to various dimensional effects, such as quasi-1-D or 2-D conductivity channels. At low temperatures the conductivity is provided due to shallow impurity levels and defect states. With the rise in temperature the charge carriers occupying deeper energy levels become more active. In most samples at temperatures lower than 100 K the dependence of the resistance on temperature is proportional to $\exp(T_0/T)^{1/4}$, which testifies to the localization of charge carriers in the approximation of the 3-D system of charge carriers.

At the same time it was found that the dependences of conductivity on temperature had a clearcut power character. For the chosen samples 4 and 1,3,5 the conductivity was proportional to $T^{3/2}$ and T^4, respectively (Figure 16.19).

The experimentally observed dependence ($\sigma \sim T^{3/2}$) in a wide temperature range (4–300 K) may indicate that the temperature dependence of mobility is of exponential character and compensates the Boltzmann exponential component. It is known, for example, that in diamonds the mobility of holes depends as T^{-s} on temperature, where the parameter s smoothly changes from 1.5 below 400 K up to 3 above 400 K. In the assumption of two types of charge carriers the total conductivity is their superposition:

$$\frac{1}{\sigma} = \frac{1}{\sigma_1} + \frac{1}{\sigma_2} \,, \qquad \sigma_{1,2} = e\mu_{1,2}(T)N_{o1,2}T^{3/2}\exp(-E_{a1,2}/2kT)\,,$$

where e is the charge of electron, $\mu_{1,2}(T)$ is the Hall mobility of respective charge carriers as a function of temperature, and $N_{o1,2}$ is the density of states in a valent zone.

Figure 16.19b is a plot of the dependence of electrical conductivity of samples 1, 3, 5 with activation energy of 0.17–0.2 eV, showing the linear dependence on T^4 in a broad range of temperatures. This regularity represents a certain system and is characteristic of the samples obtained both from C_{60} and from C_{70}. Further studies are required to explain such power-law dependence of electrical conductivity on temperature at higher temperatures.

In fact, 3-D-polymerized fullerites are new unique intrinsic carbon semiconductors. Their uniqueness is that unlike initial fullerite C_{60} which is also a semiconductor, 3-D polymers are a covalent crystal, not a van der Waals crystal, as the initial C_{60}. This is the basic difference for applications of these new materials in solid-state electronics.

In general, crystalline 3-D polymerized fullerites are a new type of intrinsic carbon semiconductor and can be used for development of novel semiconductor devices.

16.7. Conclusion

The method of high-pressure treatment is an effective tool for development of new materials. In combination with high temperatures and large deformations it is possible to obtain really unique new structures of solids, unknown earlier in nature and possessing novel physical and chemical properties. The discovery of novel carbon forms—fullerenes—allowed the use of these nanostructures as initial materials for synthesis of novel superhard nanostructured allotropic forms of carbon: 3-D polymers of C_{60}. The basic types of their crystaline and disordered structures were established and the (P, T) diagram of synthesis was constructed. A distinctive feature of these polymers is extremely high values of hardness and the bulk module of elasticity, close to corresponding values for diamond and exceeding them. At the same time, the value of the shear modulus and Young's modulus are lower than the values for diamond. It is the basic difference from the structure of diamond. Three-dimensional polymers of C_{60} are more isotropic as compared with diamond. The presence of mixed sp^2 and sp^3 types of bonds results in a significant difference of band structure of charge carriers both from diamond (broadband semiconductor) and from graphite (semimetal). The width of the band gap in crystalline 3-D polymers is 0.2–0.5 eV.

Ultrahard fullerites with disordered structure and hardness of more than 200 GPa are already used as material for heavy-duty probes of scanning atomic force microscopes-nanoindenters. In combination with electrically conducting properties it enables one to investigate not only the mechanical properties of solid bodies by the AFM method, but also the electrical properties. Application of an ultrahard fullerite as an indentor material has allowed one to measure correctly for the first time the hardness of diamond at room temperature.

As a whole, 3-D-polymerized fullerites represent a new class of superhard materials that can find wide areas of applications as various functional materials and also as components of various composite, construction, and tool materials.

References

[1]   Blank V.D., Buga S.G., Serebryanaya N.R. et al.: *Phys. Lett. A*, 205, 208–216 (1995).
[2]   Blank V.D., Dubitsky G.A., Serebryanaya N.R. et al.: *Physica B*, 339, 39–44 (2003).
[3]   Sulyanov S.N., Popov A.N., Kheiker D.M.: *J. Appl. Cryst.*, 27, 934–942 (1994).
[4]   Blank V.D., Buga S.G., Serebryanaya N.R. et al.: *Phys. Lett. A*, 220, 149–157 (1996).
[5]   Chernozatonskii L.A., Serebryanaya N.R., Mavrin B.N.: *Chem. Phys. Lett.*, 316, 199–204 (2000).
[6]   Osawa S., Osawa E., Hirose Y.: *Fullerene Sci. Technol.*, 3(5), 565–585 (1995).
[7]   Rodriguez-Carvajal J.: Program FullProf, Internet version 3.5d Oct98-LLB-JRC (Laboratoire Leon Brillouin CEA-CNRS).
[8]   Serebryanaya N.R., Chernozatonskii L.A.: *Solid State Commun.*, 114, 537–541 (2000).
[9]   Marques L., Mezouar M., Hodeau J.-L. et al.: *Science*, 283, 1720–1723 (1999).
[10] Blank V.D., Levin V.M., Prokhorov V.M. et al.: *ZhETF*, 114, 1365–1374 (1998) (in Russian).
[11] McSkimin H.J., Andreatch P. Jr, Glynn P.: *J. Appl. Phys.*, 43, 985–987 (1972).
[12] Blank V.D., Buga S.G., Dubitsky G.A. et al.: *Carbon*, 36(4), 319ñ343 (1998).
[13] Serebryanaya N.R., Blank V.D., Ivdenko V.A., Chernozatonskii L.A.: *Solid State Commun.*, 118(4), 183–187 (2001).
[14] Buga S., Blank V., Fransson A., Serebryanaya N., Sundqvist B.: *J. Phys. Chem. Solids*, 63, 331–343 (2002).
[15] Grigorovich V.K.: *Hardness and Microhardness of Metals*. Nauka, Moscow (1976) (in Russian).
[16] Blank V., Popov M., Lvova N., Gogolinsky K., Reshetov V.: *J. Mat. Res.*, 12, 3109 (1997).
[17] Blank V., Popov M., Pivovarov G., Lvova N., Gogolinsky K., Reshetov V.: *Diamond Relat. Mater.*, 7, 427 (1998).
[18] Blank V., Popov M., Pivovarov G., Lvova N., Terentev S.: *Diamond Relat. Mater.*, 8, 1531 (1999).
[19] Field J.E. (Ed.): *The Properties of Natural and Synthetic Diamond*. Academic, San Diego, CA, p. 515 (1992).
[20] Westbrook J.H., Conrad H. (Eds.): *The Science of Hardness Testing and Its Research Applications*. American Society for Metals, Metals Park, OH, p. 209 (1973).
[21] Wilks J., Wilks E.: *Properties and Applications of Diamond*. Butterworth-Heinemann, Oxford (1991).
[22] Sumiya H., Toba N., Satoch S.: *Diamond Relat. Mater.*, 6, 1841 (1997).
[23] Novikov N.V., Dub S.N.: *Diamond Relat. Mater.*, 5, 1026 (1996).
[24] Blank V.D. et al.: *Phys. Lett. A*, 248, 415 (1998).
[25] Briggs A.: in: R. Brook et al. (Eds.), *Acoust. Microscopy*. Oxford Press (1992).
[26] Prokhorov V.M., Blank V.D., Buga S.G., Levin V.M.: *Synth. Metals*, 103, 2439 (1999).
[27] Levin V.M., Blank B.D., Prokhorov V.M. et al.: *J. Phys. Chem. Solids*, 61, 1017 (2000).
[28] Makarova T.L., Wagberg T., Sundqvist B. et al.: *Mol. Cryst. Liq. Crys. C*, 13, 151 (2000).
[29] Buga S., Blank V., Dubitsky G., Edman L., Zhu X.-M., Nyanchi E., Sundqvist B.: *J. Phys. Chem. Sol.*, 61, 1009 (2000).

Index